SYNTHESIS AND CHARACTERIZATIONS OF MULTIFUNCTIONAL LUMINESCENT LANTHANIDE DOPED MATERIALS

Albenc Nexha

UNIVERSITAT ROVIRA i VIRGILI

SYNTHESIS AND CHARACTERIZATIONS OF MULTIFUNCTIONAL LUMINESCENT LANTHANIDE DOPED MATERIALS

ALBENC NEXHA

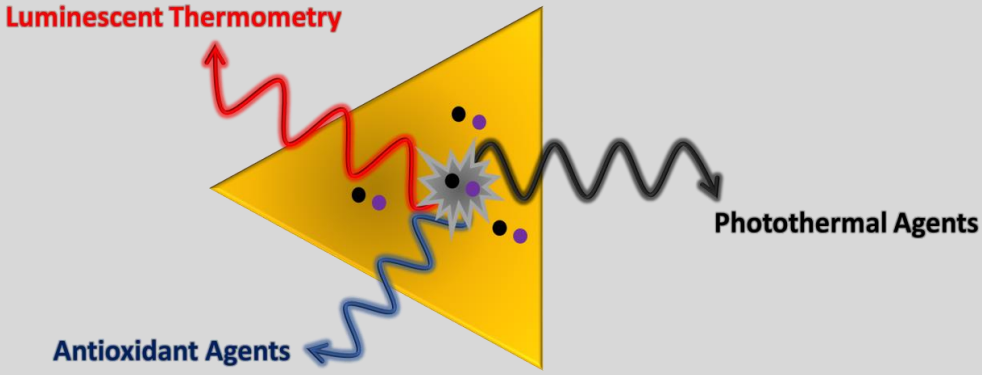

DOCTORAL THESIS
2020

UNIVERSITAT ROVIRA I VIRGILI
SYNTHESIS AND CHARACTERIZATIONS OF MULTIFUNCTIONAL LUMINESCENT LANTHANIDE DOPED MATERIALS
Albenc Nexha

SYNTHESIS AND CHARACTERIZATIONS OF MULTIFUNCTIONAL LUMINESCENT LANTHANIDE DOPED MATERIALS

ALBENC NEXHA

Doctoral Thesis

Supervised by: **Dr. Joan Josep Carvajal**

Dr. Maria Cinta Pujol

Prof. Dr. Magdalena Aguiló

Doctoral Programe in Nanoscience, Materials and Chemical Engineering

Departament de Química Física i Inorgànica

Física i Cristal·lografia de Materials i Nanomaterials (FiCMA - FiCNA)

UNIVERSITAT ROVIRA i VIRGILI

Tarragona

2020

UNIVERSITAT ROVIRA I VIRGILI
SYNTHESIS AND CHARACTERIZATIONS OF MULTIFUNCTIONAL LUMINESCENT LANTHANIDE DOPED MATERIALS
Albenc Nexha

SYNTHESIS AND CHARACTERIZATIONS OF MULTIFUNCTIONAL LUMINESCENT LANTHANIDE DOPED MATERIALS

ALBENC NEXHA

Departament de Química Física i Inorgànica

Física i Cristal·lografia de Materials i Nanomaterials (FiCMA - FiCNA)

Universitat Rovira i Virgili

C/ Marcel·lí Domingo, 1, E-43007, Tarragona, Spain

UNIVERSITAT ROVIRA I VIRGILI
SYNTHESIS AND CHARACTERIZATIONS OF MULTIFUNCTIONAL LUMINESCENT LANTHANIDE DOPED MATERIALS
Albenc Nexha

UNIVERSITAT ROVIRA i VIRGILI

WE STATE that the present study, entitled **"Synthesis and characterizations of multifunctional luminescent lanthanide doped materials"**, presented by Albenc Nexha for the award of the degree of Doctor, has been carried out under our supervision at the Department of Physical and Inorganic Chemistry of this university.

Tarragona, 30.09.2020

Doctoral Thesis Supervisors

UNIVERSITAT ROVIRA I VIRGILI
SYNTHESIS AND CHARACTERIZATIONS OF MULTIFUNCTIONAL LUMINESCENT LANTHANIDE DOPED MATERIALS
Albenc Nexha

Acknowledgments

In the end, you always go back to the people that were there in the beginning.

My deepest graditude to my supervisors, Dr. Joan Josep Carvajal, Dr. Maria Cinta Pujol and Prof. Dr. Magdalena Aguiló. Thanks for shining light inside the tunnel. Thanks for challenging me when challenge was needed. And thanks for supporting me when support was needed. Your input and patience has been priceless in helping me to learn how to do research and to navigate some of the more emotionally challenging aspects of this project. Your creativity and wisdom are inspirational.

To Joan, for always finding the needle in the haystack and putting order in disorder. To Cinta, for pursuing the unknown and thinking out of the box. And to Magdalena, for always enlightening the journey and keeping the balance.

I would like to express my gratitude to all the members of the group. Thanks to Prof. Dr. Francesc Díaz, Dr. Xavier Mateos, Dr. Jaume Massons, Dr. Rosa Sole and Dr. Josep Maria Serres, for all the help, support and valuable advices. Special thanks to the technicians Nicole, Gemma and Josue for being always there and embracing every problem with a smile. To my fellows, Esrom, Raja, Irina, Nisrine, Marc, Sami and Pauli, thanks for sharing your time with me. Special thanks to Raja for those cheering up indian songs during late friday afternoons.

I want to express my appreciation also to the technicians of the SRCiT (Rita, Francesc, Eric and Mercè), who helped me a lot in my research. Thanks to Rita for forgetting that I had to analyze other samples and wasted all the time with what she calls “the ninja”, the branched nanotriangles synthesized within this thesis. I am grateful to Francesc for always being punctual on delievering the data, sometimes even exceeding expectations.

“What can you do to promote world peace? Go home and love your family.” That’s what our beloved Mother Teresa used to say. I am blessed to share every second of this journey with my family and to feel their unconditional love. Words cannot describe the feelings. To my mom Dallandyshe and to my dad Kadri, thanks for supporting every step of my journey, thanks for being my backbone, thanks for providing me the wings to fly. To my brothers, Xhulio and Geni, thanks for being always there in the good and bad times. To my beloved fiancée Xhensila, you are my catalyst. Grateful for every glance of energy that you have provide during all these years. All that you are, is all that I'll ever need. I wouldn’t be here without you.

UNIVERSITAT ROVIRA I VIRGILI
SYNTHESIS AND CHARACTERIZATIONS OF MULTIFUNCTIONAL LUMINESCENT LANTHANIDE DOPED MATERIALS
Albenc Nexha

To 15.12 (2x)…

List of Publications

The following publications are based on the work described in this thesis:

Paper I. **A. Nexha**, J. J. Carvajal, M. C. Pujol, F. Díaz and M. Aguiló, "Lanthanide doped luminescence nanothermometers in the biological windows", To be submitted

Paper II. **A. Nexha**, J. J. Carvajal, M. C. Pujol, F. Díaz and M. Aguiló, "Short-wavelength infrared self-assessed photothermal agents based on Ho, Tm:$KLu(WO_4)_2$ nanocrystals operating in the third biological window (1.45-1.96 μm wavelength range)", *Journal of Materials Chemistry* C, **2020**, 8, 180-191.

Paper III. **A. Nexha**, M. C. Pujol, J. J. Carvajal, F. Díaz and M. Aguiló, "Effect of size and shape of Ho, Tm:$KLu(WO_4)_2$ nanocrystals in the performance as simultaneous luminescent nanothermometers operating in the third biological window and as photothermal agents", Submitted to *Journal of Alloys and Compounds*

Paper IV. **A. Nexha**, J. J. Carvajal, M. C. Pujol, F. Díaz and M. Aguiló, "Synthesis of monoclinic Ho, Tm:$KLu(WO_4)_2$ microrods with high photothermal conversion efficiency via thermal decomposition-assisted method", Submitted to *Journal of Materials Chemistry C*

Paper V. **A. Nexha**, M. C. Pujol, J. J. Carvajal, F. Díaz and M. Aguiló, "Controlling the growth of colloidal rare earth oxides via wet chemical methodologies", To be submitted

Paper VI. **A. Nexha**, J. J. Carvajal, M. C. Pujol, F. Díaz and M. Aguiló, "Evaluating the performance of Ho^{3+}, Tm^{3+} doped Y_2O_3 nanotriangles, nanohearts and self-assembled nanodiscs as luminescent nanothermometers and photothermal agents as a function of the morphology", To be submitted

Paper VII. **A. Nexha**, J. J. Carvajal, M. C. Pujol, F. Díaz and M. Aguiló, "Effect of the core@shell and layer-by-layer nanoarchitectures on the thermal sensing and photothermal conversion efficiency in triangular Ho, Tm:Y_2O_3 colloidal nanocrystals operating in the third biological window", To be submitted

Paper VIII. **A. Nexha**, M. C. Pujol, J. J. Carvajal, F. Díaz and M. Aguiló, "Luminescent nanothermometry via white light emission generated from Ho^{3+}, Tm^{3+}:Y_2O_3 colloidal nanocrystals", To be submitted

Paper IX. **A. Nexha**, J. J. Carvajal, M. C. Pujol, F. Díaz and M. Aguiló, "Engineering yttrium oxide antioxidant nanoagents", To be submitted

The following publications are not included in this thesis:

Paper X. **A. Nexha**, M. C. Pujol, J. J. Carvajal, F. Díaz and M. Aguiló, "Luminescence nanothermometry of self-assembled Er^{3+}, Yb^{3+} doped Y_2O_3 upconverting nanodiscs", To be submitted

Paper XI. J. J. Carvajal, O. Savchuk, **A. Nexha**, M. C. Pujol, M. Aguiló and F. Díaz, "Expanding luminescence thermometry detection range to the SWIR for biomedical applications", Proceedings Volume 10680, Optical Sensing and Detection V; 106800X (**2018**)

Participation in Conferences

- **Three Wise Men Winter School**, Madrid (Spain), 08-11.01.2020.
  Oral Presentation: "Luminescence nanothermometry of doped self-assembled Y_2O_3 colloidal nanodiscs based on their up/down conversion emissions"
- **NanoSpain**, Barcelona (Spain), 28-31.05.2019.
  Oral Presentation: "Synthesis, thermal sensing and photothermal conversion efficiency of Ho, Tm:Y_2O_3 colloidal nanocrystals with different morphologies"
- **International Conference in Phosphor Thermometry**, Magdeburg (Germany), 27-29.07.2020.
  Oral Presentation: “Thermal decomposition-assisted synthesis of Ho, Tm:$KLu(WO_4)_2$ rods with high light-to-heat conversion efficiency”
- **Advanced Laser Technologies**, Tarragona (Spain), 9-14.09.2018
  Oral Presentation: "Self-assessed photothermal agents based on Ho, Tm:$KLu(WO_4)_2$ nanocrystals operating in the SWIR region"
- **International School of Chemistry**, Camerino (Italy), 1-6.09.2020.
  Oral Presentation: “Sensing the temperature generated by self-assessed photothermal agents in ex-vivo experiments via lanthanide doped luminescence nanothermometers”

SYNTHESIS AND CHARACTERIZATIONS OF MULTIFUNCTIONAL LUMINESCENT LANTHANIDE DOPED MATERIALS

ALBENC NEXHA

2020

UNIVERSITAT ROVIRA I VIRGILI
SYNTHESIS AND CHARACTERIZATIONS OF MULTIFUNCTIONAL LUMINESCENT LANTHANIDE DOPED MATERIALS
Albenc Nexha

Abstract

The development of non-contact accurate and efficient luminescent lanthanide doped nanothermometers as fast diagnostic tools, have led to the replacement of the conventional contact thermal probes due to their versatility, stability and narrow emission band profiles. The application of lanthanide doped materials as temperature nanosensors, excited with ultraviolet, visible or near infrared lights, and the generation of light emissions lying in the biological windows spectral regions: I-BW (650 nm-950 nm), II-BW (1000 nm-1350 nm), III-BW (1400 nm-2000 nm) and IV-BW (centered at 2200 nm), are notably growing in interest because of the advantages of reduced phototoxicity and photobleaching, better image contrast and deeper penetration depth in biological tissues.

Among these biological windows, the III-BW allows for deeper thermal readings within specific biological tissues, attributed to their higher penetration depth (up to three times) due to the reduction of absorbance and scattering. Nevertheless, this spectral region has been scarcely explored up to now.

Here, we synthesize luminescent Ho^{3+} and Tm^{3+} doped nano- and submicroparticles with emissions located within the III-BW. The peculiar electronic configuration of these lanthanide ions gives rise to radiative and non-radiative processes, which can be used for temperature sensing purposes through luminescence nanothermometry, and heat generation, respectively that can make of these materials potential photothermal agents. Since these two functionalities can be achieved simultaneously, the materials doped with these ions can act as self-assessed photothermal agents.

We explored the possibilities of embedding Ho^{3+} and Tm^{3+} in different host materials, such as sesquioxides and double tungstates, as potential self-assessed photothermal agents operating in the III-BW. In addition, we analyzed how the size and shape of the material affect to these properties. Different hosts with different morphological characteristics were synthesized by applying already established sol-gel techniques, and developing novel solvothermal (microwave-assisted and conventional autoclave) and wet-chemical methodologies (thermal decomposition and digestive ripening).

We also explored if these nanoparticles might present additional functionalities, taking advantage of their peculiar electronic configuration and morphological characteristics, such as white light emitters and nanothermometers, and as *ex-vivo* antioxidant agents.

Keywords: nanoparticles, synthesis, luminescence nanothermometry, third biological window, photothermal agents, white light emitters, antioxidant agents

UNIVERSITAT ROVIRA I VIRGILI
SYNTHESIS AND CHARACTERIZATIONS OF MULTIFUNCTIONAL LUMINESCENT LANTHANIDE DOPED MATERIALS
Albenc Nexha

Table of Contents

UNIVERSITAT ROVIRA I VIRGILI
SYNTHESIS AND CHARACTERIZATIONS OF MULTIFUNCTIONAL LUMINESCENT LANTHANIDE DOPED MATERIALS
Albenc Nexha

Chapter I

Introduction

Lanthanide doped luminescent materials have triggered the development of highly sensitive thermometers, particularly if the operating regime of their emissions are located within the biological windows spectral regimes (I-BW: 650-950 nm, II-BW: 1000-1350 nm, III-BW: 1400-2000 nm and IV-BW: centered at 2200 nm). In this chapter, the current status of the performance of these lanthanide nanothermometers within a specific biological window spectral regime will be emphezised. Basic understading of different classes of luminescent nanothermometry and the figures of merits used to evaluate the performance of nanothermometers will be described. Within the different biological windows regimes, the performance of luminescent lanthanide doped materials will be evaluated and factors affecting this performance will be highlighted. Possible biological or nonbiological applications of these materials operating within the biological windows will be demonstrated. The chapter will conclude with the aims and structure of the thesis.

Paper I

Lanthanide doped luminescence nanothermometers in the biological windows

Albenc Nexha, Joan J. Carvajal,* Maria Cinta Pujol, Francesc Díaz, Magdalena Aguiló
Universitat Rovira i Virgili, Departament Química Física i Inorgànica,
Física i Cristal·lografia de Materials i Nanomaterials (FiCMA-FiCNA)-EMaS, Campus Sescelades, E-43007, Tarragona, Spain
**joanjosep.carvajal@urv.cat*

Abstract
The development of lanthanide doped non-contact luminescent nanothermometers with accuracy, efficiency and as fast diagnostic tools attributed to their versatility, stability and narrow emission band profiles, have spurred the replacement of conventional contact thermal probes. The application of lanthanide doped materials as temperature nanosensors, excited with ultraviolet, visible or near infrared light, and the generation of emissions lying in the biological windows regimes: I-BW (650 nm-950 nm), II-BW (1000 nm-1350 nm), III-BW (1400 nm-2000 nm) and IV-BW (centered at 2200 nm), are notably growing due to the advantages they present, including reduced phototoxicity and photobleaching, better image contrast and deeper penetration depths in the biological tissues. Here, the different mechanisms used in lanthanide ion doped nanomaterials to sense temperature in these biological windows for biomedical and other applications, are summarized, focusing towards factors that affect their thermal sensitivity, and consequently their temperature resolution. Comparing the thermometric performance of these nanomaterials in each biological window, we identified the strategies that allow boosting their sensing properties.

1.1. Introduction to contactless thermometers

Substantial chemical, physical and biological processes are temperature-dependent, thus precise and accurate measurement of the temperature is of paramount importance in countless industrial and research applications.[1-7]

Nowadays, temperature sensors account for 80% of the world-wide sensor market and expect to reach a value of $8.8 billion by 2027, according to Grand View Research, Inc.[8] However, most of these temperature sensors are based on contact thermometers, where the thermal reading is achieved by direct physical contact of an invasive probe material with the body in which temperature should be determined. Contact thermometers require conductive heat transfer and need to reach equilibrium between the sensor and the object under study. This connection disturbs the measurement of the temperature at the object, leading to an inappropriate determination of the exact temperature. These inaccurate measurements are especially enlarged when dealing with nanoscale dimensions, in which the size of the object under study, is smaller than the sensor head of the thermometer.[9-13] In addition, these thermometers are limited to surface-temperature measurements. Modern requirements for thermal readings in areas such as microelectronics, photonics, nanomedicine and diagnosis, and microfluidics, among others, have led to the replacement of contact thermometers and the development of non-contact nanoscale thermometers.[14-16]

Non-contact nanoscale thermometers can provide feedback of the local temperature of a given system with micro and nanoscale spatial resolution.[17] The precise determination of the temperature at the nanoscale has attracted great interest, especially in the nanomedicine and diagnosis fields, as many functions of the human body, including cell division, gene expression or enzyme reactions, are temperature-dependent.[18] Diseases, such as cellular pathogenesis of cancer, lead to heat generation.[19] In addition, temperature changes can also be induced

intentionally to kill locally infected cells.[20] Therefore, achieving precise thermal reading information is crucial to heal infected cells and simultaneously avoid destruction of surrounding healthy tissues.

High-resolution thermal non-contact measurement techniques operating in the micro/nanoscale are divided into several types using distinct criteria based on their operating principle. These methods provide different advantages and drawbacks,[21] hence the proper selection according to the required spatial, temporal and thermal resolutions, are essential. Non-contact techniques for the determination of the temperature include infrared thermometry, thermoreflectance, Raman scattering, interferometry, non-optical and luminescence nanothermometry.[17]
The principle of the infrared thermometry is to determine the temperature by the amount of the thermal radiation emitted from the target which is being monitored.[22] Knowing the amount of infrared energy emitted by the object and its emissivity, the target temperature can be determined. This non-contact method is a well-implemented commercial technique and grants a temperature image profile of the surface of the target, achieving spatial, temporal and thermal resolutions of ~10 μm, ~10 μs and ~0.1 K,[22] respectively. However, this technique requires an additional knowledge of the spatial resolution and the emissivity of the target in the micrometer scale.[2] These are serious drawbacks for the application of this technique in the nanoscale because with the determination of the temperature on the surface and not inside the target, the precise discrimination of the temperature of a living cell, for instance, strongly impacts on the analysis of its pathology and physiology and, in turn, on the optimization of therapeutic processes (*e.g.* in hyperthermal tumor treatments and photodynamic therapy).[23, 24]

Thermoreflectance thermometry extracts thermal readings from the dependence of refractive index of the material from the temperature.[25] This technique offers high thermal (~0.01 K) and temporal resolution (~0.1 μs), and combination of qualitative and quantitative measurements.[22] Despite this, it requires the calibration of the refractive index of the material of analysis, and its spatial resolution is limited by the light diffraction limit.[26]

Raman scattering thermometry is based on the dependence of the position of the Raman modes of the material of interest from the tempeature.[27] Raman thermometry can be applied to liquids and solids, including powders, achieving spatial, temporal and thermal resolutions of the order of ~1 μm, ~10^6 μs and ~0.1 K,[22] respectively. Regardless, it is a time-consuming technique and the number of the materials to which this technique can be applied is very small because the materials need to have a large Raman efficiency if applied as successful temperature probes.[28]
Optical interferometry provides dual information: local temperature and local deformation due to the thermal expansion of the material of analysis.[29] Interferometers depict the differences in optical paths between light beams that bypasses the test section and passes directly through it. Although this technique can be integrated in remote detection systems with spatial, temporal and thermal resolution of ~1 μm, ~0.001 μs and ~10^{-5} K,[22] respectively, drawbacks related to cross talk with other stimulus, such as strain/stress and bending and low spatial resolution in the transverse direction, limit their application.[22]
Non-optical thermometry methods include several techniques developed for nanoscale thermometric applications such as scanning thermal microscopy,[30] deposition of metallic thermal sensors by nanolithography,[31] carbon nanotubes thermometry,[32] and biomaterials thermometry.[33] Scanning thermal microscopy uses a small thermocouple with a junction diameter of the order of 20 to 100 nm, formed at the probe tip of an atomic force microscope, which is scanned over the surface of interest.[34] It can also consist on a combination of a thermocouple and a resistance temperature,[35] providing sub-micrometric spatial resolution.[22] This technique is limited to solid samples and offers slow acquisition times, requiring at the same time fundamental knowledge of the tip-sample heat transfer mechanisms.[22] Nanolithography can be applied to deposit a platinum strip to form a thermal sensor on the surface of the material of interest. However, ensuring the robustness of the sensor and its chemical consistency, are important challenges for this technique.[17] Carbon nanotubes as thermal probes were originally proposed using gallium as the thermometric liquid filling them, and with the support of a scanning electron microscope to observe their meniscus.[32] These nanotubes have been applied also to provide good thermal contact between a microscope and the sample with nanoscale resolution,[36] but it presents also some limitations, such as the thermal contact resistance formed between the tip and the surface, which can modify the probe response, especially for highly thermally conducting samples.[36]
Biomaterials, such as living cells, sense temperature by using their components (proteins, nucleic

acids and mRNAs).[33] The change of the temperature in these components is manifested either by modifying their conformational structure, directly or undergoing complex reactions that can be exploited to extract the temperature on the nanoscale level.[37-39] However, the molecular complexity associated to this temperature sensing is not yet fully understood, and the thermal response occurs within the physiological range of temperatures. Furthermore, this technique often induces conformational changes that are subtle and reversible.[33]
Luminescence thermometry (also called thermographic phosphor nanothermometry) refers to the relationship between temperature and the luminescence properties of the light emitted by the luminophore to achieve thermal sensing.[10] The major boost of the luminescence thermometry at the nanoscale is attributed to the high temperature sensitivity of different luminescent materials and the easy detection setups required for these signals. With the change of temperature, different luminescence characteristics such as intensity of the emission, spectral position, decay and rise time, band positions and widths, may all be modified, which gives rise to different luminescence thermometry classes.[10] Luminescence thermometry provides high spatial resolution (< 10 μm) in short acquisition times (< 10 μs) and high thermal resolution (0.1 K).[22] Additionally, luminescent thermometers can operate even in harsh conditions such as in biological fluids, strong electromagnetic fields, cryogenic temperatures and in fast moving objects, without restricting their resolutions.[10, 12, 40, 41]

1.2. Luminescence nanothermometry

1.2.1. Fundamental principles of luminescence nanothermometry

Luminescence refers to the emission of light from an excited electronic state of a given substance.[42] This substance (or phosphor), consist of a luminescence entity, molecule or activator ion, embedded in a host (or matrix) material, and sometimes accompanied by a second entity that favors the absorption of light and transfers this energy to the activator, called sensitizer. Sometimes, this substance may consist of only an activator embedded in a host, without the presence of a sensitizer. The characteristic luminescence properties of a given substance can be obtained by doping to the host with relatively small amounts of foreign ions (activator and a sensitizer). An activator incorporated into a host lattice gives rise to a center which can be excited to generate luminescence. A sensitizer incorporated into a host lattice is capable of absorbing more efficiency the energy from the excitation source and transfer it in a very efficient way to a neighboring activator, that at the end will generate luminescence.[43]

When exposed to temperature, the characteristics of the luminescence of the phosphor (intensity, spectral position, decay and/or rise time, the band position and width), may change. Exploring the way in which these characteristics change with the ultimate goal of determining the temperature of the phosphor, give rise to the luminescent thermometry. Figure 1.1 depicts a general schematic illustration of the basic mechanisms of the luminescence thermometry. For the sake of simplicity, a single center emission phosphor is illustrated, displaying a change in the intensity of the emissions as the temperature increases. This figure illustrates the class of band-shape luminescent thermometry, probably the widest explored class.

In the figure we show how the phosphor is excited with an energy source ($h\nu$) from the ground state level (indicated as 0) to an excited state level (indicated as 3), from where, according to the principle of conservation of energy, will decay back to an intermediate or to the ground state in the form of light or through the release of energy via non-radiative processes.[42, 43] The decay could occur directly from the excited state (3) back to the ground state (0) via a radiative relaxation process, generating an emission line (labelled as “Emission 1” with intensity I_1) or via a non-radiative relaxing process (showed with a golden curved arrow) through at lower intermediate excited level (either 2 or 1). From here, the second emission line (labelled as “Emission 2” with intensity I_2) can be generated when a second radiative relaxation process occurs to another lower intermediate excitation level, or to the ground state.[42] Please note that from the 2 and 1 intermediate excited states, additional emission lines can be generated but for simplicity reasons, they are not illustrated in Figure 1.1.

In order to be applied as luminescent nanothermometer, the generated emissions from the phosphor, must fulfill several requirements. These requirements are related to the quality of the emission generated: exhibit high quantum yield and should be temperature-dependent.[10] The

generated emissions of a phosphor are related to, among other different variables, the composition of the material, purity level and the local temperature of the system.[1] Thus, the principle of luminescence nanothermometry is to exploit the relationship between the properties of the luminescence emission process and temperature to achieve thermal sensing by temporal or spectral analysis of the emission.[10] For example, in our simplified single-center emission phosphor, upon increasing the temperature from T_1 to T_2 (presented in Figure 1.1 with the red curved arrows labelled as "Heat"), it induced changes on the intensity of the emissions. Investigating the variation of the ratio of the intensities of the emissions (I_1 and I_2), thermal reading of the system can be deduced from which the temperature can be determined prior a calibration of the luminescent thermometer.[10] When temperature changes are applied, the intensity of the emissions (and other luminescence properties as well) can vary due to the processes of population or depopulation of the energy levels.[1]

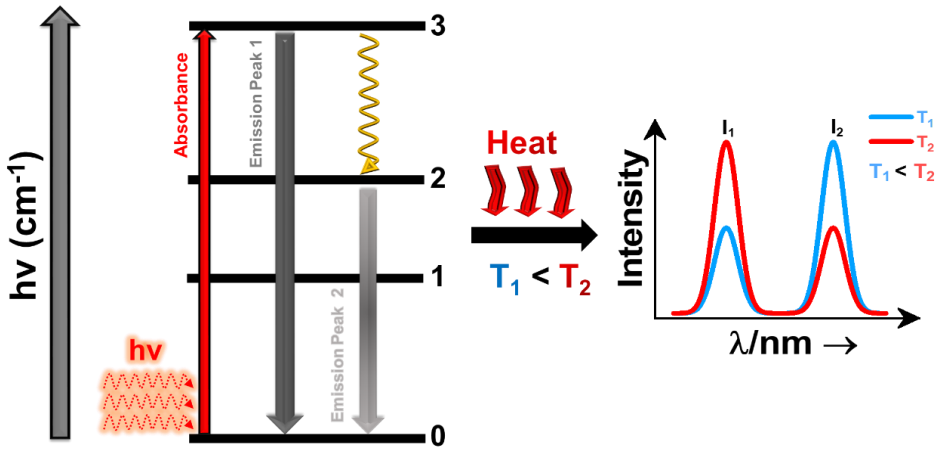

Figure 1.1. Basic working principle of luminescence nanothermometry, illustrated via the change of the intensity of the emissions with the increase of temperature, as an example.

1.2.2. Classes of luminescence nanothermometry

Temperature can affect the characteristics of the luminescence of the phosphor in different ways. Based on the particular parameter of luminescence whose temperature-dependence is analyzed, different classes of luminescence nanothermometry are developed. Figure 1.2 illustrates six parameters that define the luminescence of a given phosphor: band-shape, intensity, bandwidth, spectral shift, lifetime and polarization, and their variation with the increase of temperature.[10]

Band-shape nanothermometry refers to the relative intensity between the different spectral lines of the luminescence spectrum (see Figure 1.2 (a)).[10] The changes induced by the temperature on the luminescence intensity are related to the thermal activation of processes of quenching and increase on the probability of non-radiative mechanisms. This class of luminescence nanothermometry relates materials which possess radiative states with an energy gap (ΔE) of the order of 200 cm^{-1} to 2000 cm^{-1}, *i.e*, the so-called "thermally coupled levels" (hereafter TCLs) and the extraction of thermal knowledge is achieved by the fluorescence intensity ratio (FIR), based totally on Boltzmann type-distribution.[44] The main benefit of this class is its independency of signal losses and the possible fluctuations in the excitation intensity.[10] TCLs with too small ΔE (ΔE < 200 cm^{-1}) will lead to strong overlap of signals, while too large ΔE value (ΔE > 2000 cm^{-1}) will result in the weak coupling of the levels.[45] Furthermore, the performance of nanothermometers operating by the principles of this class, is strictly related to the energy gap.[46] In addition, this class of nanothermometry includes single or dual emitting center with a change on the intensity of at least two different emission bands in a material.[47]

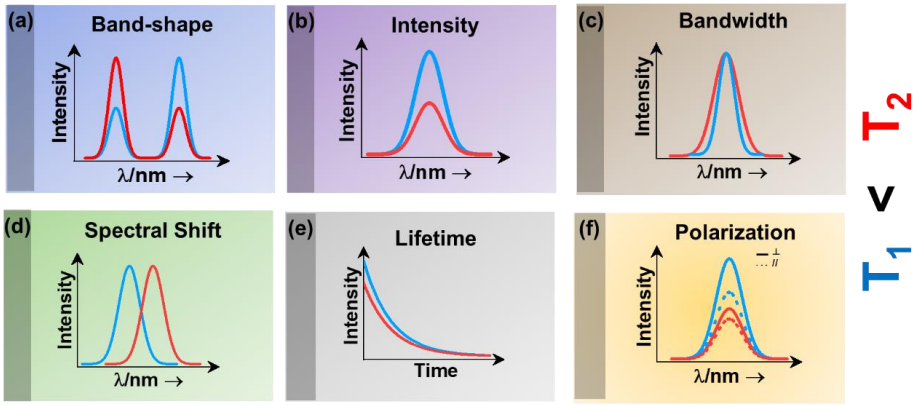

Figure 1.2. Classes of luminescence nanothermometry: (a) band-shape, (b) intensity, (c) bandwidth, (d) spectral shift, (e) lifetime and (f) polarization.

Intensity luminescence nanothermometry determines temperature through the analysis of the intensity of the generated luminescence (see Figure 1.2 (b)).[10] With the change of temperature, as for the case of band-shape luminescence nanothermometry class, processes like quenching and the increase of the probability of non-radiative mechanisms to happen, will display a decrease of the intensity of the luminescence that can be correlated with the temperature. With the change of temperature, the intensity of the emission spectrum becomes less (or more) intense due to an overall change in the number of emitted photons.[44, 48]

Bandwidth luminescence nanothermometry extracts temperature information from the effect that the change of temperature has on the width of the emission lines of the luminescence spectrum (see Figure 1.2 (c)).[10] Generally, with an increase of the temperature, the emission lines become broader because of the thermal vibration of the luminescent center and its neighboring atoms/molecules.[10] The degree of change of the emission line broadening is usually small, and as a result it can be only observed in systems showing inherent narrow emission lines and strongly-temperature dependent transitions.[10]

Spectral shift luminescence nanothermometry is based on the analysis of the spectral positions of the emission lines, which is changed due to their dependence from the temperature. When the temperature is increased, the energy value of the emitting level is changed, manifested by a shift in the emission wavelength (see Figure 1.2 (d)).[10] This energy gap depends on a large variety of temperature-dependent parameters of the emitting material, including the refractive index and the inter-atomic distances, among others.[10] The shift in the spectral position is usually related to thermally induced strains in the environment of the thermal probes, occurring as a result of the electron-phonon interaction.[15]

Lifetime nanothermometry analyzes the temperature dependence of the luminescence lifetime (see Figure.1.2 (e)). Luminescence lifetime studies the time that the emitted intensity decays down to 1/e of its value after a pulsed excitation.[10] The experimental lifetime is related to the contribution of the radiative, non-radiative or multiphonon and quenching mechanisms.[49] With the increase of the temperature, the lifetime is generally shorten due to the increase of the quenching mechanisms. Lifetime is also strictly related to the dimensions of the materials. The lifetime of nanocrystals are shorter compared to the macroparticles. This difference is related to the presence of larger lattice distortion, larger surface defects, higher surface-to-volume ratio in nanomaterials, which overall lead to increase of the radiative rates and larger quenching rates.[49]

Polarization luminescence nanothermometry is based on the influence of temperature in the “polarization anisotropy” parameter, which is the ratio between the luminescence intensities emitted at two orthogonal polarization states (see Figure 1.2 (f)).[10]

In the following sections, we will analyze how these different luminescence nanothermometry classes have been used to determine temperature using lanthanide-doped luminescent

nanothermometers operating in the biological windows, with special emphasis on the different strategies developed to improve their performance. For a detailed comprehensive understanding on the six luminescence thermometry classes and determination of their thermal sensing capacity, the reader is asked to refer to the review of Jaque *et al*.[10] and Brites *et al*.[47].

1.2.3. Materials used to develop luminescent nanothermometers

Different luminescent nanomaterials have been tested for providing a contactless thermal reading through luminescence nanothermometry. In order to boost their potential nanothermometric applications in different fields, but specially in biomedicine, several factors including strong luminescence, good photostability, no photobleaching effect, barely no toxicity, good dispersibility in biological media and outstanding optical properties that allow for deep tissue light penetration,[50] should be taken into account.

Luminescent materials tested as potential nanothermometers include fluorescent proteins,[51-55] nanogels,[3,56-58] polymers,[62-66] organic-inorganic hybrids,[59-63] nanodiamonds,[64-66] metal organic frameworks (MOFs),[41,67-69] organic dyes,[70-76] semiconductor quantum-dots (QDs),[77-84] and lanthanide (Ln^{3+})-doped nanomaterials.[47, 85-87]

Fluorescent proteins, either in their simple form or genetically encoded, can be used to extract temperature at the intracellular level.[51-55] These nanothermometers can be applied to obtain thermal images of heated single cells and to study thermogenesis, a fundamental process in cell biology. Regardless of the relatively high intracellular thermal sensitivity achieved with these nanothermometers, drawbacks, including time-consuming gene encoding, the need for specialized microscopy equipment and advanced molecular biology techniques for gene modification,[88, 89] have deprived their future applications.

Nanogels portray nanoscale sized three-dimensional hydrogel materials formed by crosslinked swellable polymer networks with a high capacity to hold water, without actually dissolving into the aqueous medium.[90] Below 303 K, the structure of the nanogel swells by absorbing water into its interior, which causes a quenching in the fluorescence that is gradually recovered when the temperature increases above 303 K and the nanogel shrinks because of the release of water molecules.[3, 56-58] As luminescent nanothermometers, nanogel compounds present an important advantage: the most relevant changes in their fluorescence intensity occur within the physiological range of temperatures. A particular disadvantage is that the emission intensity of the nanogels becomes highly temperature sensitive only in a reduced temperature range (298-338 K).[10]

Polymers stands for large macromolecules composed of repeated structural units, called monomers. The presence of luminescent monomers within the polymers, allows their use as luminescent thermometers.[62-66] The luminescence of these compounds is usually found in the visible (VIS) range (500-600 nm) after being excited with ultraviolet (UV) light,[62-66] which can induce phototoxicity if applied to extract thermal information in biological tissues.[91] Despite the good results demonstrated in thermal imaging, these thermometers usually exhibit drawbacks related to their low quantum yield,[92] relatively large sizes, and the dependence of the luminescence not only on temperature, but also from the local concentration of emitting centers.[10]

An organic-inorganic hybrid can be defined as a single particle that combines two different materials belonging to these categories.[93] In the field of luminescent nanothermometry, these materials can be used by exploiting the complementary functionalities of their constituent materials to develop multifunctional platforms, such as temperature sensing and heat generation for further applications.[61-63, 94] Regardless of their good temperature sensing properties, limitations are also faced. These limitations are related to nanothermometers being operative only in the VIS regime, which represent a low penetration depth in the biological tissues and the distortion of the spectra read due to the non-negligible absorption by the different components encountered in them.[95]

The application of nanodiamonds as luminescent nanothermometers is attributed to the presence of particular local point defects (nitrogen vacancy centers) in their structure.[96] These nanodiamonds are fluorescent and display a very sensitive temperature transition between two ground quantum spin states.[64-66] The advantages of these nanothermometers rely on their high

thermal sensitivity and on the fact that nitrogen vacancy centers are inner defects, hence, in theory rending these thermometers environment-independent.[96] However, when applied in biological tissues, the light generated from these materials might be affected by the biological tissue components. Furthermore, their emissions are often located at the VIS regime and the low fluorescence efficiency displayed by them, is a limiting factor, especially when acquiring cellular thermal images.[97]

Metal organic frameworks (MOFs) have emerged as an important class of luminescent materials due to their multiple luminescent centers and tunable optical properties.[41, 67-69, 98] The tunability of the optical properties of MOFs is related to the fact that the metal nodes, organic linkers, and guest molecules within porous MOFs, all can potentially generate luminescence. Furthermore, the inherent porosity and large surface areas of MOFs offer great opportunities for intermolecular interaction between frameworks and guest molecules, influencing the coordination environment and the energy transfer processes that can occur among them, thus modulating the luminescent properties of MOFs.[98] However, it should admitted that to use these luminescent thermometers in biological environments, besides high sensitivity and spatial resolution, non-toxicity and stability in the physiological environment are required, which often lack in MOFs based thermometers.[98]

Organic dyes are organic compounds with strong luminescence intensity, in general.[10] Despite their high temperature sensing properties and the ability to be easily incorporated into living cells, the spectral properties of the luminescence band depend on many factors, including temperature, solvent, concentration, pH and environment.[10, 97] Being specially dependent on the environment, it makes necessary to recalibrate the thermometers in each particular environment, and thus, the temperature sensing ability will strongly depend on the medium where the compound is embedded.[97]

Quantum dots (QDs) are highly attractive nanomaterials for application as luminescent nanothermometers, due to their size-tunable spectroscopic properties,[83, 84] narrow emissions, high photostability and high quantum yields.[99] For years, concerns regarding their phototoxicity and cytotoxicity towards biological matter due to UV light excitation,[91] and emission wavelengths limited to the range shorter than 1000 nm, have been resolved by the preparation of core@shell structures.[100, 101] Despite this, limitations concerning the variation of the luminescence parameters (intensity, lifetime and spectral shift) with the environment, including surfactants and ligands, which leads to a source of error in thermal readings,[102] and their genetic-induced changes,[105] still remain.

Lanthanide (Ln^{3+}) doped nanomaterials, due to their peculiar electronic configuration, exhibit stable and narrow emissions covering a wide range of the electromagnetic spectrum, upon proper selection of the dopants and the transparency of the host, with high emission quantum yields (> 50% in the visible).[103-106] In addition, these barely non-toxic materials,[107] can generate their emission lines upon excitation via near infrared (NIR) light, which stands for a low-cost excitation source with no photobleaching, no autofluorescence and no photoxicity upon biological matter.[21, 47] Furthermore, the use of NIR light instead of VIS or UV light, allows for deep-tissue penetration,[91] specifically when the wavelengths of the emissions fall within the so-called biological windows,[108, 109] (see Section 1.4). Thus, inspired by these properties of Ln^{3+} doped luminescent nanomaterials, the rest of this chapter, will be focused on the performance of these materials to extract information of the local temperature of a given system when the generated emissions fall on the biological windows regions. Furthermore, the strategies explored to boost their ability to achieve better thermal readings in the biological windows will be analyzed.

1.3. Performance of a lanthanide doped luminescent nanothermometer

Regardless of the luminescent nanothermometry class used to extract temperature information, the performance of a lanthanide doped nanothermometer can be evaluated and compared to other nanothermometers, based on their thermal sensitivity, temperature resolution, spatio-temporal resolution, repeatability and reproducibility. Detailed information about all these parameters were summarized by Brites *et al*.[47]. Thus, here we will emphasize, in general terms, how these parameters can be calculated.

The thermal sensitivity expresses the degree of change of the thermometric parameter (generally, denoted by Δ) per degree of temperature. The thermal sensitivity can be expressed as the absolute thermal sensitivity and the relative thermal sensitivity.

The absolute thermal sensitivity (S_{abs}) is defined as the rate of change of the thermometric parameter (Δ) with the temperature and is expressed as:[110]

$$S_{abs} = \frac{\partial \Delta}{\partial T} \qquad (1.1)$$

S_{abs} is expressed in units of inverse of kelvin (K^{-1}). This parameter is strictly related to the experimental setup used and the sample characteristics, thus, its use is restricted on comparing only nanothermometers of the same nature.

To compare the thermometric performance of different nanothermometers, independently of their nature or material employed, the relative thermal sensitivity (S_{rel}) can be used. S_{rel} expresses the maximum change in the thermometric parameter (Δ) for each temperature degree and it is defined:[44, 111, 112]

$$S_{rel} = \frac{1}{\Delta} \left| \frac{\partial \Delta}{\partial T} \right| x\ 100\ \% \quad (1.2)$$

S_{rel} is expressed in units of % change per degree of temperature change (% K^{-1}).

The temperature resolution (also defined as temperature sensitivity), δT, represents the smallest temperature change that can be detected in a given measurement. δT depends on the type of the material and the experimental setup used. Depending on the experimental detection setup used, the acquisition conditions applied and the signal-to-noise ratio in the experiment, δT might change.[112] δT is measured in kelvin (K) and it is expressed as:[113]

$$\delta T = \frac{1}{S_{rel}} \frac{\delta \Delta}{\Delta} \qquad (1.3)$$

where $\delta\Delta$ is the uncertainty in the determination of Δ.

Another interesting approach towards the determination of δT is by recording multiple consecutive emission spectra at a fixed temperature.[67,114] By using the calibration curve of the nanothermometer, the range of the variability of the calculated temperature can be determined. Results display a gaussian distribution with a mean value and a standard deviation value, corresponding to the average temperature and resolution (δT) of the measurement.[67, 114]

The spatial resolution represents the minimum distance between points presenting a temperature difference higher than δT, when the temperature is measured in different spatial positions.[30] The spatial resolution (δx) is expressed as:[30]

$$\delta x = \frac{\delta T}{|\vec{\nabla}\, T|_{max}} \qquad (1.4)$$

where $|\vec{\nabla}\, T|_{max}$ is the maximum temperature gradient of the temperature mapping performed.

The temporal resolution of the measurement (δt) is defined as the minimum time interval between measurements presenting a temperature difference higher than δT and is expressed as:

$$\delta t = \frac{\delta T}{|\frac{dT}{dt}|_{max}} \qquad (1.5)$$

where $|\frac{dT}{dt}|_{max}$ is the maximum temperature change per unit of time.

The repeatability indicates the ability of a nanothermometer to provide the same thermal performance under the same identical conditions,[115] and is defined as:

$$R = 1 - \frac{\max|\Delta_c - \Delta_i|}{\Delta_c} \qquad (1.6)$$

where Δ_c is the mean thermometric parameter and Δ_i is the value of each measurement of the thermometric parameter.

The reproducibility refers to the variation of the same measurements in different modified circumstances, including different measurement methods, different equipment in use, different observers, or measurements made over a period of time within the true level of the already measured data.[116]

1.4. Biological Windows

A good use of the luminescent thermometers in biological tissues requires knowledge about several parameters that influence the excitation of the nanothermometers by optical means, and also the detection of the emitted light by the materials. These parameters, including the emission characteristics, the optical path length through biological tissues and the volumetric energy distribution, are linked to the absorption and scattering properties of the biological sample.[117] The selection of these parameters should meet the overall goal of achieving a high penetration depth in real biological samples, allowing deeper thermal reading, and favoring an efficient and reliable phosphor for early detection and diagnosis of diseases.

Applying NIR light instead of UV or VIS as an excitation source, results in more efficient penetration in biological tissues due to the reduced scattering and absorption of light with longer wavelengths.[109] Spectral regions were both tissue absorption and scattering are minimized are known as biological windows (BWs).[109]

The main absorbers of light in biological tissues include water, hemoglobin, melanin and lipids, whereas their size, composition and morphology are the responsible for the scattering of light.[118] Water absorbs at the NIR region at around 980 nm and it is nearly transparent in the visible region.[119] Hemoglobin (oxy-hemoglobin and deoxy-hemoglobin), from its side, is the component responsible for the absorption of visible light by blood. The highest absorbance of hemoglobin is at the visible region and decreases above 600 nm.[120] The absorbance of melanin is inversely proportional to the increase of the wavelength from the visible to the NIR.[121] Regarding the absorbance of lipids *in vivo*, the data available in the literature are quite scarce, however as reported from Smith *et al*., the absorption contribution of fat in biological tissues is less important than that of water and blood.[109] Scatters of the light in the biological tissues include cell nuclei, mitochondria, cell membranes and the whole cells.[122] Light scattering decreases exponentially as the wavelength increases from visible to the NIR.[123]

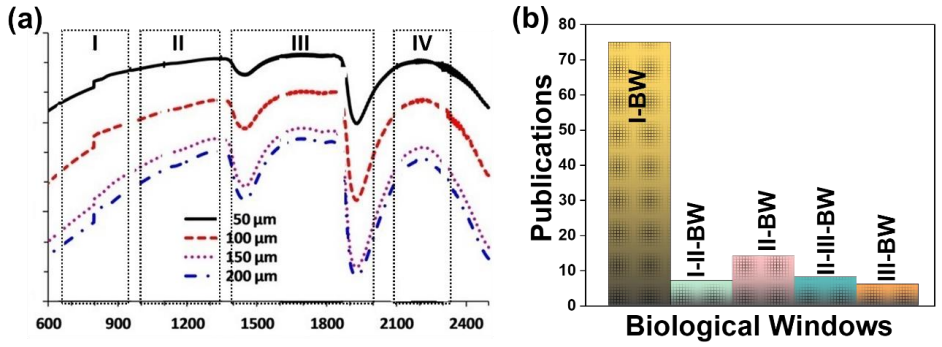

Figure 1.3. (a) Transmittance of brain tissue in the optical tissue windows I, II, III and IV. Adapted with permission.[126] Copyright from Wiley 2016. (b) Number of publications for every biological window, including also the thermometers, whose performance is evaluated by emission lying in two different biological windows.

Within these biological windows (BWs), four distinctive wavelength regions have been establish (see Figure 1.3 (a)):

- First biological window (I-BW) (650-950 nm)
- Second biological window (II-BW) (1000-1350 nm)
- Third biological window (III-BW) or short-wavelength infrared (SWIR) window (1400-2000 nm)
- Fourth biological window (IV-BW) (centered at 2200 nm)

The I-BW is limited at short wavelengths by the absorption of light by oxygenated blood and at long wavelengths by the absorption of water due to the second overtone of its stretching band, a combination of symmetric and antisymmetric stretching modes.[124] This biological window encounters limitations attributed to signal interference by biological tissues autofluorescence, which produces background noise, thus limiting the maximum tissue penetration to 1-2 cm.[125] This biological window is also known as the therapeutic window.[126]

The II-BW provides an improved signal-to-noise ratio by a factor over 100-fold by effectively filtering out autoflorescence from biological tissues.[117] The limits of the II-BW lie in the short wavelength from the second overtone of the stretching band of water and at longer wavelengths by the combination of bending and stretching (symmetric and antisymmetric) modes of water also.[124]

The III-BW or SWIR, despite of the limitation from the absorption bands of water (stretching and bending modes),[124] offers improved image contrast and higher penetration depths compared to the other biological windows due to the reduction of the light scattering.[127]

The IV-BW, centered at 2200 nm, is the least explored one due to the lack of sensitive detectors operating at these wavelengths.[126] The advent of new photodetectors (InSb in single or array photodiodes) and excitation laser sources (supercontinuum lasers operating in the range from 400 nm to 2500 nm), now make the IV-BW a viable spectral domain.[128] The IV-BW shows similar values of light attenuation for skin and other soft tissues comparable with that of the II-BW, lower than the III-BW but better than the I-BW.[126]

Figure 1.3 (a) shows the variation of the transmittance of rat brain tissue as a function of the thickness of the biological sample, covering all four biological windows.[126] The maximum transmittance is located in the III-BW, regardless of their thickness.[126] The transmittance in the II-BW and the IV-BW are close to each other and are much higher than the transmittance in the I-BW, indicating a better potential application for deep imaging.[126] Figure 1.3 (b) presents a summary of the number of publications implementing lanthanide-doped materials as thermometers operating in the different biological window regions. In addition to the main four biological windows, also regions in which the nanothermometers performance is evaluated by emissions lying part on the I-BW and II-BW (named as I-II-BW) and II-BW and III-BW (named as II-III-BW) are presented. The biological window with the highest number of publications is the I-BW, whereas the IV-BW represents up to now, an unexplored region. Recently, however, it has been observed a tendency of increasing the number of publications regarding the II-BW and III-BW, compared to the I-BW, mainly due to the benefits in better image contrast and higher penetration depths. The following sections have been structured according to if the emission lines used for luminescent thermometric purposes lie within any of these biological windows, despite their excitation is provided in a spectral range lying in a different biological window.

2. Lanthanide doped luminescent nanothermometers operating in the I-BW

The I-BW is the most explored biological window related to the performance of the lanthanide doped luminescent thermometers up to now. The most encountered lanthanide active ions are Tm^{3+} and Nd^{3+}, mainly due to their emission bands in the 700-800 nm and 800-950 nm regions, respectively (see Table 1.1). This section and the later ones, will be arranged as follows: the lanthanide ion with the best thermometric performance (only the maximum value of S_{rel} and the

associated minimum value of δT will be given), will appear first. After this, single or dual doped materials, hosts and the excitation wavelength associated to the luminescent thermometers will be presented, providing an overview on how these parameters influence the performance of that specific lanthanide active ion, in order to underline strategies for boosting the thermometric performance.

Table 1.1. Summary of all Ln^{3+} doped luminescent thermometers operating in the I-BW. In the table are shown the activators (A) and sensitizers (S). The excitation (λ_{exc}) and emission (λ_{em}) wavelengths are shown in nanometers (nm), together with the corresponding transition of the emissions. ΔT stands for the temperature range were the thermal reading was investigated. The thermometric parameter (Δ) indicates the luminescent nanothermometry class used in each case: FIR-for band-shape, I-for intensity ratio, $\Delta\lambda$-for spectral, and $\Delta\nu$-for bandwidth thermometry, respectively. VPR stands for valley-to-peak ratio. The maximum relative thermal sensitivity (S_{rel}) and the temperature resolution (δT) are presented at the temperature where these values were obtained. We indicated with an asterisk, the values of S_{rel} or δT calculated by us using the parameters published in the corresponding references. The double line separation between rows stands for different type (single or dual emitting center) of lanthanide doped nanothermometers, as discussed on the corresponding subsections.

A	S	Host	λ_{exc} (nm)	λ_{em} (nm)	Transitions	ΔT (K)	Δ	S_{rel} /T (% K^{-1})/K	δT (K)	Ref.
Tm^{3+}	-	YAP	1210	705, 800	$^3F_{2,3} \rightarrow {}^3H_6$, $^3H_4 \rightarrow {}^3H_6$	324-424	$FIR_{705/800}$	2.61/ 324	0.20*	129
Tm^{3+}	-	$NaNbO_3$	1319	800	$^3H_4 \rightarrow {}^3H_6$	303-453	$FIR_{797/807}$	0.80/303	0.62*	130
Tm^{3+}	Yb^{3+}	Phosphate glass	980	658, 693	$^3F_2 \rightarrow {}^3H_6$, $^1G_4 \rightarrow {}^3H_5$	303-653	I_{693}/I_{658}	3.9/303	0.13*	131
Tm^{3+}	Yb^{3+}	$GdVO_4$@SiO_2	980	700, 800	$^3F_{2,3} \rightarrow {}^3H_6$, $^3H_4 \rightarrow {}^3H_6$	298-333	$FIR_{700/800}$	2/303	0.4	132
Tm^{3+}	Yb^{3+}	$LaPO_4$	975	700, 800	$^3F_{2,3} \rightarrow {}^3H_6$, $^3H_4 \rightarrow {}^3H_6$	293-773	$FIR_{700/800}$	3/293	0.16*	133
Tm^{3+}	Yb^{3+}	S-$LiNbO_3$	980	700, 800	$^3F_{2,3} \rightarrow {}^3H_6$, $^3H_4 \rightarrow {}^3H_6$	323-773	$FIR_{700/800}$	3/323	0.17*	134
Tm^{3+}	Yb^{3+}	$CaWO_4$	980	700, 800	$^3F_{2,3} \rightarrow {}^3H_6$, $^3H_4 \rightarrow {}^3H_6$	303-753	$FIR_{700/800}$	2.79/303	0.17*	135
Tm^{3+}	Yb^{3+}	$NaYF_4$@$NaYF_4$@SiO_2	980	697, 798	$^3F_{2,3} \rightarrow {}^3H_6$, $^3H_4 \rightarrow {}^3H_6$	298-623	$FIR_{697/798}$	2.58/298	0.18*	136
Tm^{3+}	Yb^{3+}	Bi_2TiO_7	980	700, 797	$^3F_{2,3} \rightarrow {}^3H_6$, $^3H_4 \rightarrow {}^3H_6$	300-505	$FIR_{797/700}$	2.41/300	0.20*	137
Tm^{3+}	Yb^{3+}	$LiY_9(SiO_4)_6O_2$	980	695, 789	$^3F_{2,3} \rightarrow {}^3H_6$, $^3H_4 \rightarrow {}^3H_6$	293-553	$FIR_{797/700}$	2.38/293	0.21*	138
Tm^{3+}	Yb^{3+}	$Ca_2Gd_8(SiO_4)_6O_2$	980	700, 790	$^3F_{2,3} \rightarrow {}^3H_6$, $^3H_4 \rightarrow {}^3H_6$	293-553	$FIR_{700/790}$	2.36/293	0.21*	139
Tm^{3+}	Yb^{3+}	YPO_4	975	700, 800	$^3F_{2,3} \rightarrow {}^3H_6$, $^3H_4 \rightarrow {}^3H_6$	293-773	$FIR_{700/800}$	2.33/293	0.21*	133
Tm^{3+}	Yb^{3+}	YAG	976	683, 782	$^3F_{2,3} \rightarrow {}^3H_6$, $^3H_4 \rightarrow {}^3H_6$	333-733	$FIR_{700/800}$	2.31/333	0.22*	140
Tm^{3+}	Yb^{3+}	$BiPO_4$	980	700, 804	$^3F_{2,3} \rightarrow {}^3H_6$, $^3H_4 \rightarrow {}^3H_6$	313-573	$FIR_{700/804}$	2.14*/425	0.23*	141
Tm^{3+}	Yb^{3+}	Bi_2SiO_5@SiO_2	977	650, 700	$^1G_4 \rightarrow {}^3F_4$, $^3F_3 \rightarrow {}^3H_6$	260-400	$FIR_{700/650}$	2.6/260	0.19*	142
Tm^{3+}	Yb^{3+}	Bi_2SiO_5@SiO_2	977	700, 800	$^3F_{2,3} \rightarrow {}^3H_6$, $^3H_4 \rightarrow {}^3H_6$	280-800	$FIR_{700/800}$	2.1/280	0.25	142
Tm^{3+}	Yb^{3+}	P-$LiNbO_3$	980	700, 800	$^3F_{2,3} \rightarrow {}^3H_6$, $^3H_4 \rightarrow {}^3H_6$	323-773	$FIR_{700/800}$	2.04/323	0.25*	134
Tm^{3+}	Yb^{3+}	Sr_2GdF_7	980	650, 700	$^1G_4 \rightarrow {}^3F_4$, $^3F_3 \rightarrow {}^3H_6$	293-563	I_{700}/I_{650}	1.97/353	0.25*	143
Tm^{3+}	Yb^{3+}	$KLuF_4$	980	690, 795	$^3F_{2,3} \rightarrow {}^3H_6$, $^3H_4 \rightarrow {}^3H_6$	303-503	$FIR_{690/795}$	1.36*/503	0.37*	144
Tm^{3+}	Yb^{3+}	YOF	980	801, 806	$^3H_4 \rightarrow {}^3H_6$	12-300	$\Delta\nu_{800.9}$	0.84/300	0.60*	145
Tm^{3+}	Yb^{3+}	PbF_2 in oxyfluoride glass	976	700, 800	$^3F_{2,3} \rightarrow {}^3H_6$, $^3H_4 \rightarrow {}^3H_6$	288-498	I_{700}/I_{800}	0.78/448	0.64*	146
Tm^{3+}	Yb^{3+}	$NaYbF_4$	980	697, 803	$^3F_{2,3} \rightarrow {}^3H_6$, $^3H_4 \rightarrow {}^3H_6$	298-778	I_{697}/I_{803}	0.49*/458	1.02*	147
Tm^{3+}	Yb^{3+}	$NaGdTiO_4$	980	795, 798	$^3H_4 \rightarrow {}^3H_6$	100-300	$FIR_{795/798}$	0.36/100	1.38*	148
Tm^{3+}	Yb^{3+}	$NaGdTiO_4$	980	798, 807	$^3H_4 \rightarrow {}^3H_6$	100-300	$FIR_{807/798}$	0.22/100	2.27*	148

Tm^{3+}	Yb^{3+}	$NaGdTiO_4$	980	798, 812	$^3H_4 \rightarrow {}^3H_6$	100-300	$FIR_{812/798}$	0.21/100	2.38*	148
Tm^{3+}	Yb^{3+}	$NaYF_4@CaF_2$	980	802, 820	$^3H_4 \rightarrow {}^3H_6$	313-373	$FIR_{802/820}$	0.21/313	2.38*	149
Tm^{3+}, Ho^{3+}	Yb^{3+}	YPO_4	980	668 (Ho^{3+}), 699 (Tm^{3+})	$^5F_5 \rightarrow {}^5I_8$ (Ho^{3+}), $^3F_3 \rightarrow {}^3H_6$ (Tm^{3+})	303-563	I_{668}/I_{699}	2.85/563	0.18*	150
Tm^{3+}, Ho^{3+}	-	$KLu(WO_4)_2$	808	696 (Tm^{3+}), 755 (Ho^{3+})	$^3F_{2,3} \rightarrow {}^3H_6$ (Tm^{3+}), $^5S_2,{}^5F_4 \rightarrow {}^5I_7$ (Ho^{3+})	300-333	I_{696}/I_{755}	2.84/303	0.2	151
Tm^{3+}, Ho^{3+}	Yb^{3+}	$Gd_2(WO_4)_3$	980	655 (Ho^{3+}), 700 (Tm^{3+})	$^5F_5 \rightarrow {}^5I_8$ (Ho^{3+}), $^3F_{2,3} \rightarrow {}^3H_6$ (Tm^{3+})	295-595	I_{700}/I_{655}	1.42*/415	0.35*	152
Tm^{3+}, Er^{3+}	Yb^{3+}	$NaLuF_4$	980	660 (Er^{3+}), 695 (Tm^{3+})	$^3F_2 \rightarrow {}^3H_6$ (Tm^{3+}), $^4F_{9/2} \rightarrow {}^4I_{15/2}$ (Er^{3+})	300-600	I_{695}/I_{660}	1.94/300	0.26*	153
Tm^{3+}, Er^{3+}	Yb^{3+}	YF_3:ceramic	980	655 (Er^{3+}), 700 (Tm^{3+})	$^3F_{2,3} \rightarrow {}^3H_6$ (Tm^{3+}), $^4F_{9/2} \rightarrow {}^4I_{15/2}$ (Er^{3+})	298-563	I_{700}/I_{655}	1.89/393	0.27*	154
Tm^{3+}, Er^{3+}	Yb^{3+}	LuF_3	980	656 (Er^{3+}), 701 (Tm^{3+})	$^3F_2 \rightarrow {}^3H_6$ (Tm^{3+}), $^4F_{9/2} \rightarrow {}^4I_{15/2}$ (Er^{3+})	303-543	I_{656}/I_{701}	0.95/363	0.54*	155
Nd^{3+}	-	YAG	590	730-770, 780-840	$^4F_{7/2} \rightarrow {}^4I_{9/2}$, $^4F_{3/2} \rightarrow {}^4I_{9/2}$	77-850	$FIR_{730-770/780-840}$	2.98/200	0.17*	156
Nd^{3+}	-	La_2O_2S	532	818, 897	$^4F_{5/2} \rightarrow {}^4I_{9/2}$, $^4F_{3/2} \rightarrow {}^4I_{9/2}$	270-600	$FIR_{818/897}$	1.95/270	0.26*	157
Nd^{3+}	-	YAP	532	820, 890	$^4F_{5/2} \rightarrow {}^4I_{9/2}$, $^4F_{3/2} \rightarrow {}^4I_{9/2}$	293-611	$FIR_{820/890}$	1.83/293	0.9	158
Nd^{3+}	-	Gd_2O_3	580	820, 892	$^4F_{5/2} \rightarrow {}^4I_{9/2}$, $^4F_{3/2} \rightarrow {}^4I_{9/2}$	288-323	$FIR_{820/892}$	1.75/288	0.14	159
Nd^{3+}	-	$LaPO_4$	690	804, 890	$^4F_{5/2} \rightarrow {}^4I_{9/2}$, $^4F_{3/2} \rightarrow {}^4I_{9/2}$	303-773	$FIR_{804/890}$	1.65/303	0.30*	160
Nd^{3+}	-	Fluorotellurite Glass	514	815, 885	$^4F_{5/2} \rightarrow {}^4I_{9/2}$, $^4F_{3/2} \rightarrow {}^4I_{9/2}$	298-600	$FIR_{815/885}$	1.55*/298	0.32*	161
Nd^{3+}	-	SBN	532	820, 880	$^4F_{5/2} \rightarrow {}^4I_{9/2}$, $^4F_{3/2} \rightarrow {}^4I_{9/2}$	300-700	$FIR_{820/880}$	1.52*/300	0.33*	162
Nd^{3+}	-	YAG	590	780-840, 870-920	$^4F_{5/2} \rightarrow {}^4I_{9/2}$, $^4F_{3/2} \rightarrow {}^4I_{9/2}$	77-850	$FIR_{780-840/870-920}$	1.02/200	0.49*	156
Nd^{3+}	-	$LiLuF_4$	808	862, 866	$^4F_{3/2} \rightarrow {}^4I_{9/2}$	77-575	I_{862}/I_{866}	0.62/77	0.6	163
Nd^{3+}	-	SrF_2	573	800-950	$^4F_{3/2} \rightarrow {}^4I_{9/2}$	293-328	$FIR_{R2/R1}$	0.61/293	2.1	164
Nd^{3+}	-	$LiLuF_4@LiLuF_4$	793	883, 887	$^4F_{3/2} \rightarrow {}^4I_{9/2}$	293-318	I_{887}/I_{883}	0.58/293	3.4	165
Nd^{3+}	-	$LiLaP_4O_{12}$	808	850-900	$^4F_{3/2} \rightarrow {}^4I_{9/2}$	83-600	$\Delta\lambda_{850-900}$	0.47/323	1.05*	166
Nd^{3+}	-	$RbLaP_4O_{12}$	808	850-900	$^4F_{3/2} \rightarrow {}^4I_{9/2}$	83-600	$\Delta\lambda_{850-900}$	0.47/323	1.05*	166
Nd^{3+}	-	$NaLaP_4O_{12}$	808	850-900	$^4F_{3/2} \rightarrow {}^4I_{9/2}$	83-600	$\Delta\lambda_{850-900}$	0.42/323	1.2*	166
Nd^{3+}	-	$LiLaP_4O_{12}$	808	850-900	$^4F_{3/2} \rightarrow {}^4I_{9/2}$	83-600	$\Delta\nu_{850-900}$	0.32/323	1.5*	166
Nd^{3+}	-	Y_2O_3	808	870, 920	$^4F_{3/2} \rightarrow {}^4I_{9/2}$	298-333	I_{870}/I_{820}	0.31/298	1	167
Nd^{3+}	-	$RbLaP_4O_{12}$	808	850-900	$^4F_{3/2} \rightarrow {}^4I_{9/2}$	83-600	$\Delta\nu_{850-900}$	0.28/323	1.1*	166
Nd^{3+}	-	$YNbO_4$	752	880, 890	$^4F_{3/2} \rightarrow {}^4I_{9/2}$	303-473	I_{880}/I_{890}	0.28/303	1.1	168
Nd^{3+}	-	LaF_3	808	865, 885	$^4F_{3/2} \rightarrow {}^4I_{9/2}$	283-333	I_{865}/I_{885}	0.26/283	1.95*	169
Nd^{3+}	-	$NaLaP_4O_{12}$	808	850-900	$^4F_{3/2} \rightarrow {}^4I_{9/2}$	83-600	$\Delta\nu_{850-900}$	0.24/323	2.1*	166

Nd^{3+}	-	$KLaP_4O_{12}$	808	850-900	$^4F_{3/2} \rightarrow {}^4I_{9/2}$	83-600	$\Delta\nu_{850\text{-}900}$	0.20/323	2.5*	166
Nd^{3+}	-	YVO_4	808	879, 887	$^4F_{3/2} \rightarrow {}^4I_{9/2}$	298-333	I_{879}/I_{887}	0.19/298	2.6*	170
Nd^{3+}	-	$KLaP_4O_{12}$	808	850-900	$^4F_{3/2} \rightarrow {}^4I_{9/2}$	83-600	$\Delta\lambda_{850\text{-}900}$	0.47/323	1.05*	166
Nd^{3+}	-	$Gd_3Sc_2Al_3O_{12}$	806	936, 946	$^4F_{3/2} \rightarrow {}^4I_{9/2}$	293-323	$FIR_{936/946}$	0.21/293	2.38*	171
Nd^{3+}	-	YAG	808	938, 945	$^4F_{3/2} \rightarrow {}^4I_{9/2}$	283-343	$FIR_{938/945}$	0.15/283	0.3	172
Nd^{3+}	-	$BiVO_4$	750	872, 902	$^4F_{3/2} \rightarrow {}^4I_{9/2}$	310-523	$FIR_{872/902}$	0.14/310	3	173
Nd^{3+}	-	$NaYF_4$	830	863, 870	$^4F_{3/2} \rightarrow {}^4I_{9/2}$	273-423	$FIR_{863/870}$	0.12/273	0.1	174
Nd^{3+}	-	$KGd(WO_4)_2$	808	883, 895	$^4F_{3/2} \rightarrow {}^4I_{9/2}$	298-333	$FIR_{883/895}$	0.12/298	0.43	175
Nd^{3+}	-	$NaNdF_4$@$NaYF_4$@$NaYF_4$:Nd	808	857, 863	$^4F_{3/2} \rightarrow {}^4I_{9/2}$	293-333	$FIR_{857/863}$	0.11/293	4.5*	176
Nd^{3+}	-	$RbLaP_4O_{12}$	808	850-900	$^4F_{3/2} \rightarrow {}^4I_{9/2}$	83-600	$FIR_{R2/R1}$	0.108/323	4.6*	166
Nd^{3+}	-	$NaLaP_4O_{12}$	808	850-900	$^4F_{3/2} \rightarrow {}^4I_{9/2}$	83-600	$FIR_{R2/R1}$	0.104/323	4.8*	166
Nd^{3+}	-	$KLaP_4O_{12}$	808	850-900	$^4F_{3/2} \rightarrow {}^4I_{9/2}$	83-600	$FIR_{R2/R1}$	0.097/323	5.1*	166
Nd^{3+}	Yb^{3+}	Oxyfluoride Glass	980	750, 863	$^4F_{7/2} \rightarrow {}^4I_{9/2}$ $^4F_{3/2} \rightarrow {}^4I_{9/2}$	303-623	$FIR_{750/863}$	3.27/303	0.15*	177
Nd^{3+}	Yb^{3+}	$SrWO_4$	980	750, 863	$^4F_{7/2} \rightarrow {}^4I_{9/2}$ $^4F_{3/2} \rightarrow {}^4I_{9/2}$	313-453	$FIR_{750/863}$	3.1/313	0.16*	178
Nd^{3+}	Yb^{3+}	$CaWO_4$	980	755, 872	$^4F_{7/2} \rightarrow {}^4I_{9/2}$ $^4F_{3/2} \rightarrow {}^4I_{9/2}$	303-873	$FIR_{750/863}$	3/303	0.16*	179
Nd^{3+}	Yb^{3+}	$Al_4B_2O_9$	977.7	800, 920	$^4F_{5/2} \rightarrow {}^4I_{9/2}$ (Nd^{3+}), $^2F_{5/2} \rightarrow {}^2F_{7/2}$ (Yb^{3+})	298-333	$FIR_{800/920}$	2.6/298	0.19*	180
Nd^{3+}	Yb^{3+}	$NaYF_4$	980	750, 863	$^4F_{7/2} \rightarrow {}^4I_{9/2}$ $^4F_{3/2} \rightarrow {}^4I_{9/2}$	293-333	$FIR_{750/863}$	2.4/293	0.20*	181
Nd^{3+}	Yb^{3+}	Oxyfluoride Glass	980	750, 803	$^4F_{7/2} \rightarrow {}^4I_{9/2}$ $^4F_{5/2} \rightarrow {}^4I_{9/2}$	303-623	$FIR_{750/863}$	2.05/303	0.24*	177
Nd^{3+}	Yb^{3+}	Oxyfluoride Glass	980	803, 863	$^4F_{5/2} \rightarrow {}^4I_{9/2}$ $^4F_{3/2} \rightarrow {}^4I_{9/2}$	303-623	$FIR_{750/863}$	1.95/303	0.25*	177
Nd^{3+}	Yb^{3+}	La_2O_3	980	750, 803	$^4F_{7/2} \rightarrow {}^4I_{9/2}$ $^4F_{3/2} \rightarrow {}^4I_{9/2}$	293-1230	$FIR_{750/803}$	1.6/293	0.1	182
Nd^{3+}	Yb^{3+}	$Al_4B_2O_9$	977.7	864, 920	$^4F_{5/2} \rightarrow {}^4I_{9/2}$ (Nd^{3+}), $^2F_{5/2} \rightarrow {}^2F_{7/2}$ (Yb^{3+})	299-333	$FIR_{800/920}$	1.38/299	0.36*	180
Nd^{3+}, Eu^{3+}	-	Ba_2LaF_7	578.3	699 (Eu^{3+}), 800 (Nd^{3+})	$^5D_0 \rightarrow {}^7F_4$ (Eu^{3+}), $^4F_{3/2} \rightarrow {}^4I_{9/2}$ (Nd^{3+})	290-740	I_{699}/I_{800}	2.2/290	0.22*	183
Nd^{3+}, Eu^{3+}	-	YVO_4	590	696 (Eu^{3+}), 812 (Nd^{3+})	$^5D_0 \rightarrow {}^7F_4$ (Eu^{3+}), $^4F_{3/2} \rightarrow {}^4I_{9/2}$ (Nd^{3+})	299-466	I_{696}/I_{812}	0.79/299	1.4	184
Nd^{3+}, Ti^{4+}	Nd^{3+}, Ti^{4+}	YAG	260	668 (Ti^{4+}), 870 (Nd^{3+})	$^2T_2 \rightarrow O^{2-}$ (Ti^{4+}), $^4F_{3/2} \rightarrow {}^4I_{9/2}$ (Nd^{3+})	123-773	I_{668}/I_{870}	3.70/473	0.13*	185
Nd^{3+}, Cr^{3+}	Nd^{3+}, Cr^{3+}	YAG	590	690 (Cr^{3+}), 890 (Nd^{3+})	$^4T_1 \rightarrow {}^4A_2$ (Cr^{3+}), $^4F_{3/2} \rightarrow {}^4I_{9/2}$ (Nd^{3+})	77-850	I_{690}/I_{890}	3.49/200	0.14*	156
Nd^{3+}, Mn^{4+}	Nd^{3+}, Mn^{4+}	YAG	355	670 (Mn^{4+}), 880 (Nd^{3+})	$^2E \rightarrow {}^4A_2$ (Mn^{4+}), $^4F_{3/2} \rightarrow {}^4I_{9/2}$ (Nd^{3+})	123-823	I_{670}/I_{880}	0.60/475	0.83*	186
Eu^{3+}	-	Y_2O_3	590	690-715	$^5D_0 \rightarrow {}^7F_4$ ($^7F_1$, $^7F_0$)	180-280	$FIR_{690\text{-}714/690\text{-}714}$	1.7/180	0.29*	187
Eu^{3+}	-	Y_2O_3	611	690-715	$^5D_0 \rightarrow {}^7F_4$ ($^7F_2$, $^7F_0$)	283-333	$FIR_{690\text{-}714/690\text{-}714}$	1.55/283	0.29*	187
Er^{3+}	-	SBN	532	800, 850	$^2H_{11/2} \rightarrow {}^4I_{13/2}$	300-700	$FIR_{800/850}$	1.39*/300	0.36*	162

					$^4S_{3/2} \rightarrow {}^4I_{13/2}$					
Er^{3+}	-	$NaErF_4$@$NaGdF_4$	1530	654, 806	$^4F_{9/2} \rightarrow {}^4I_{15/2}$ $^4I_{9/2} \rightarrow {}^4I_{15/2}$	303-593	I_{806}/I_{654}	0.54/303	0.9*	188
Er^{3+}		$NaErF_4$@Yb:$NaYF_4$@Nd:$NaYbF_4$	800	652, 670	$^4F_{9/2} \rightarrow {}^4I_{15/2}$	305-425	$FIR_{652/670}$	0.22/305	2.2*	189
Er^{3+}	-	Y_2O_3	800	654, 660	$^4F_{9/2} \rightarrow {}^4I_{15/2}$	200-1300	$FIR_{654/660}$	0.15/300	3.3*	190
Er^{3+}, Mn^{4+}	Er^{3+}, Mn^{4+}	YAP	980	660 (Er^{3+}), 714 (Mn^{3+})	$^4I_{9/2} \rightarrow {}^4I_{15/2}$ (Er^{3+}), $^2E \rightarrow {}^4A_2$ (Mn^{4+})	300-550	I_{714}/I_{660}	1.95/530	0.25*	191
Er^{3+}, Ho^{3+}	Yb^{3+}	$NaLuF_4$	975	817 (Er^{3+}), 887 (Ho^{3+})	$^4I_{9/2} \rightarrow {}^4I_{15/2}$ (Er^{3+}), $^5I_6 \rightarrow {}^5I_8$ (Ho^{3+})	293-568	I_{887}/I_{817}	1.73/293	0.29*	192
Er^{3+}	Yb^{3+}	YF_3	980	793, 840	$^2H_{11/2} \rightarrow {}^4I_{15/2}$ $^4S_{3/2} \rightarrow {}^4I_{15/2}$	293-473	$FIR_{793/840}$	0.98/293	0.51*	193
Er^{3+}	Yb^{3+}	ZrO_2	980	660, 682	$^4F_{9/2} \rightarrow {}^4I_{15/2}$	293-573	VPR_{660}/ VPR_{682}	0.75/293	0.66*	194
Ho^{3+}, Mn^{4+}	Ho^{3+}, Mn^{4+}	YAP	980	660 (Ho^{3+}), 714 (Mn^{3+})	$^4I_{9/2} \rightarrow {}^4I_{15/2}$ (Er^{3+}), $^2E \rightarrow {}^4A_2$ (Mn^{4+})	300-550	I_{714}/I_{660}	1.17/450	0.42*	191
Ho^{3+}	Yb^{3+}	$KLu(WO_4)_2$	980	650 660	$^5F_5 \rightarrow {}^5I_8$	297-673	$FIR_{650/660}$	0.38/297	1	195
Ho^{3+}	Yb^{3+}	$Ba_2In_2O_5$	980	653 661	$^5F_5 \rightarrow {}^5I_8$	303-573	$FIR_{653/661}$	0.19*/303	2.5	196

2.1. Tm^{3+} doped luminescent thermometers operating in the I-BW

Thulium (Tm^{3+}) ion exhibits an electronic configuration $1s^2\ 2s^2\ 2p^6\ 3s^2\ 3p^6\ 3d^{10}\ 4s^2\ 4p^6\ 4d^{10}\ 5s^2\ 5p^6\ 4f^{12}$, and up to now, represents one of the most investigated active ions for luminescent nanothermometry in the I-BW due to, (among others) NIR-to-NIR upconversion optical properties. Different Tm^{3+} doped luminescent nanothermometers have been developed including single doped Tm^{3+} materials, those using Tm^{3+} as activator and Yb^{3+} as sensitizer, and those that use Tm^{3+} together with another lanthanide ion as activators in the presence or not of Yb^{3+} as sensitizer.

2.1.1. Single Tm^{3+} doped luminescent thermometers operating in the I-BW

Single Tm^{3+} doped luminescent nanothermometers operating in the I-BW, without the presence of Yb^{3+} as a sensitizer, are scarce. In fact, only two examples can be found in literature including orthorhombic yttrium orthoaluminate perovskite ($YAlO_3$, known as YAP),[129] and sodium niobate ($NaNbO_3$),[130] as hosts.

Tm^{3+}:YAP nanothermometers (with grain size of 35 nm) have been developed based on the temperature dependence of its emission lines located at 705 nm and 800 nm, rising from TCLs $^3F_{2,3}$ and $^3H_4$ decaying to the $^3H_6$ ground state, after excitation at 1210 nm.[129] These upconversion emissions can be generated either by sequential absorption of two excitation photons by a single Tm^{3+} ion through excited state absorption (ESA) or by the simultaneous absorption of two photons by two nearby Tm^{3+} ions via energy transfer upconversion (ETU) processes.[129, 197] From these two processes, the $^3F_{2,3}$ excited state is populated. From this state, a radiative decay to the ground state, will generate the emission line at 705 nm. A non-radiative relaxation from the $^3F_{2,3}$ level to the $^3H_4$ level, followed by a radiative decay to the ground state, generates the second emission line at 800 nm (see Figure 1.4 (a)).[129, 197]

For the evaluation of the thermometric performance of the Tm^{3+}:YAP nanothermometers, the fluorescence intensity ratio (FIR),[44] between the emission lines at 705 nm and 800 nm, was used to extract thermal sensing properties over the temperature range from 324 K-424 K. FIR is defined using the emission intensities of the of $|2> \rightarrow |0>$ ($I_{02} \equiv I_2$) and $|1> \rightarrow |0>$ ($I_{01} \equiv I_2$) transitions,

where $|0>$, $|1>$, $|2>$ denote the ground state and the thermally coupled levels 1 and levels 2,[44, 198] respectively, as:

$$FIR = \frac{I_2}{I_1} = \frac{A_{02} h\nu_{02} N_2}{A_{01} h\nu_{01} N_1} \qquad (1.7)$$

where N_2 and N_1 are the populations of the $|2>$ and $|1>$ levels, ν_{02} and ν_{01} are the frequencies of the $|2> \rightarrow |0>$ and $|1> \rightarrow |0>$ transitions, and A_{02} and A_{01} are the total spontaneous emission rates from level $|2>$ and $|1>$ to level $|0>$.

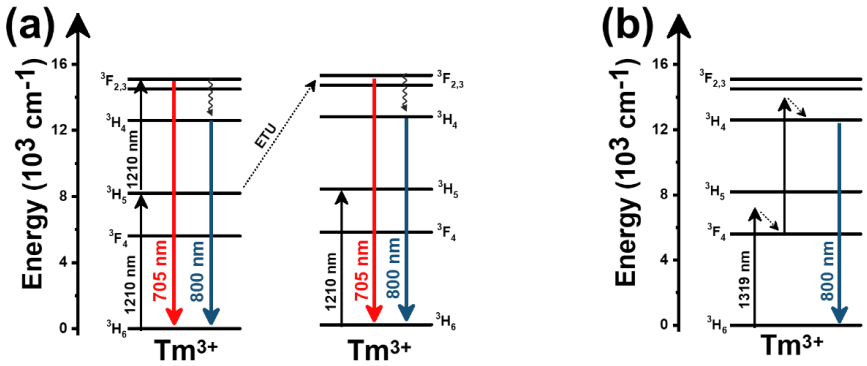

Figure 1.4. Mechanism of the generation of the emission lines for single active Tm^{3+} doped: (a) YAP after excitation at 1210 nm and (b) $NaNbO_3$ material after excitation at 1319 nm. Please note that despite other emission lines can be produced, for sake of simplicity, in this example and what follows for the rest, only the emission lines involved in the luminescence thermometers development are considered.

Since the energy levels 1 and 2 are in thermal equilibrium, the electronic populations can be correlated by the following equation:

$$N_2 = \frac{g_2}{g_1} N_1 \exp\left(-\frac{\Delta E}{k_B T}\right) \qquad (1.8)$$

where g_2 and g_1 are the degeneracies of the two levels, and ΔE is the energy gap between the barycenters of the $|2> \rightarrow |0>$ and $|1> \rightarrow |0>$ emission bands.[47,198] Thus, the expression for FIR can be rewritten as:

$$FIR = \frac{I_2}{I_1} = \frac{g_2 A_{02} h\nu_{02}}{g_1 A_{01} h\nu_{01}} \exp\left(-\frac{\Delta E}{k_B T}\right) = B \exp\left(-\frac{\Delta E}{k_B T}\right) \qquad (1.9)$$

where $B = \frac{g_2 A_{02} h\nu_{02}}{g_1 A_{01} h\nu_{01}}$. By applying the expression of FIR (Equation 1.9) to Equation 1.2 and Equation 1.3, the corresponding expressions for S_{rel} and δT can be obtained as follows:[47]

$$S_{rel} = \left|\frac{\Delta E}{k_B T^2}\right| x\ 100 \qquad (1.10)$$

$$\delta T = \frac{k_B T^2}{\Delta E} \frac{\delta FIR}{FIR} \qquad (1.11)$$

Thus, considering the $|2> \rightarrow |0>$ as the electronic transition forming an emission line at 705 nm and the $|1> \rightarrow |0>$ as the electronic transition forming an emission line at 800 nm, the maximum S_{rel} of the Tm^{3+}:YAP nanothermometer is 2.64% K^{-1} at 324 K, whereas the δT was not reported by the authors.[129] However, knowing the reported value of ΔE=1926 cm^{-1},[129] and applying an experimental setup error $\frac{\delta FIR}{FIR}$ =0.5% that is the most commonly found in literature,[21] δT can be

calculated according to Equation 1.11, with a minimum value of 0.20 K at 324 K and that increased to 0.32 K at 424 K.

Tm^{3+}:$NaNbO_3$, from its side, was based on the change of the FIR of the Stark sub-levels of the $^3H_4 \rightarrow {}^3H_6$ transition with an emission located at around 800 nm, using in particular the emission lines located at 797 nm and 807 nm, after excitation at 1319 nm, in the temperature range 303-453 K.[130] The generation of the 800 nm emission line (among others) is assigned to a multiphonon-assisted excitation from the ground state $^3H_6$ to the $^3H_5$ excited level, a rapid relaxation to the $^3F_4$ level, followed by an excited-state absorption to the $^3H_4$ level, as shown in Figure 1. 4 (b).[130]

Instead of using the expression for FIR, as the thermometric parameter in this case, the authors propose to use the following equation:

$$R = A + B * T \qquad (1.12)$$

where R is the thermometric parameter used in this case (I_{707}/I_{807}), and A and B are parameters determined from the fitting of the experimental data. So that, the authors preferred to use a linear function for this parameter, according to the trend followed by the experimental points obtained in the calibration of the thermometer, without taking into account that the different Stark sub-levels of a particular transition are, of course, under thermal equilibrium, and that the Boltzmann distribution proposed by the model developed with the FIR would be more convenient in this case. As a consequence, S_{rel}, with a maximum value of 0.80% K^{-1} at 303 K, had to be calculated using again a different equation:[130]

$$S_{rel} = \frac{B}{A + B * T}\, 100\% \qquad (1.13)$$

This value is higher than the one that should be obtained when applying strictly the FIR model according to Equation 1.9 (0.25% K^{-1}), and according to that, δT calculated according to Equation 1.11 (0.62 K if the thermal sensitivity given by the authors is used, and 2 K if the thermal sensitivity according to the FIR model is used) is clearly overestimated.

Curiously, the two examples included here are based on upconversion mechanisms with excitation in the II-BW, despite the exploited emissions are within the I-BW, ensuring that both excitation and emission have a good penetration in the biological tissues. The process of upconversion refers to a nonlinear optical phenomenon known as an anti-Stokes emission in which the sequential absorption of two or more low-energy photons leads to high-energy luminescent emission.[199] Upconversion nanomaterials offer the possibility of relative high thermal sensing in combination with high penetration depths and optical tunability.[200] In fact, Pereira *et al*. could demonstrate that the penetration of light by exciting at 1319 nm was twice than the one that can be obtained when exciting at 800 nm.[130] Regardless, the excitation wavelength they used (1319 nm) induced a local heating in the environment where these nanoparticles were used, of up to 8 K for a pump power of 350 mW, due to the fact that this wavelength is not resonant with any of the electronic levels of Tm^{3+}. So, part of the energy of the excitation source is lost in the form of heat, that the nanoparticles dispersed in the surrounding medium.[130]

The only conclusion that can be extracted from these two examples is that to maximize the S_{rel}, and consequently minimize the thermal resolution, the best strategy would be to maximize the separation between the emission lines used in the thermometer, but keeping it below to 2000 cm^{-1} to maintain them inside the defined range of TCLs.[44]

2.1.2. Tm^{3+}, Yb^{3+} codoped luminescent thermometers operating in the I-BW

Lanthanide nanothermometer codoped with Tm^{3+} acting as an activator and Yb^{3+} acting as a sensitizer is, by far, the most explored model for the luminescent thermometers operating in the I-BW. Probably this great interest is due to their NIR-to-NIR upconversion, more efficient than that obtained in Tm^{3+} single doped thermometers.[149] This is a consequence of the bigger absorption cross-section of Yb^{3+} at the pumping wavelength,[201] the lower costs of NIR excitation sources emitting at 980 nm, and the generation of emission lines lying in the I-BW. However, it has to be mentioned the strong effect that this pumping wavelength have in heating biological tissues, due

to the efficient absorption of the wavelength by water.[119] This is why, several authors considered that this approach should be avoided when performing luminescence thermometry for biomedical applications due to its non-discriminating effect to respect the heating of biological tissues.

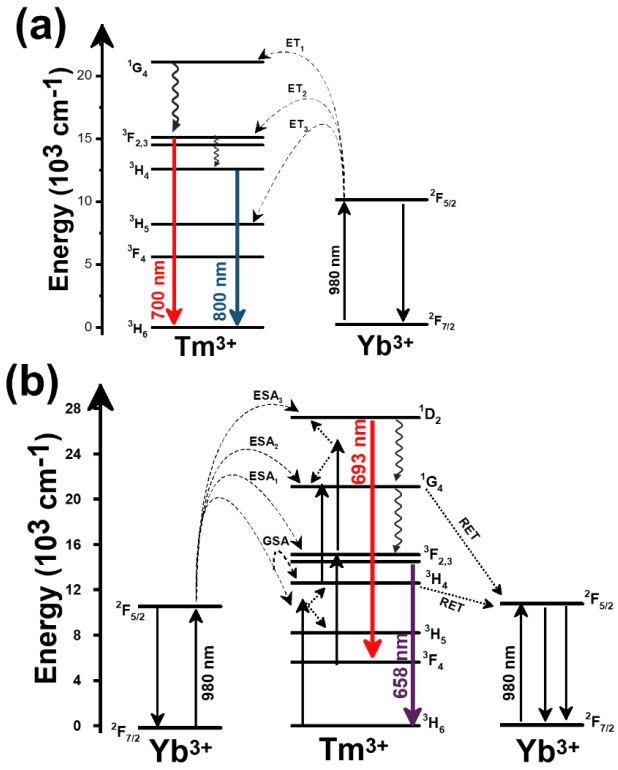

Figure 1.5. Mechanism of the generation of the emission lines for: (a) Tm^{3+}, Yb^{3+}:$GdVO_4$@SiO_2 core@shell nanoparticles (as an illustrative example) after excitation at 980 nm. (b) Tm^{3+}/Yb^{3+} doped phosphate glass material after excitation at 980 nm.

Another characteristic of the Tm^{3+}, Yb^{3+} codoped luminescent thermometers operating in the I-BW is that most of them use the same emission lines to build the luminescent thermometer: the emission at around 700 nm, arising from the $^3F_{2,3} \rightarrow {}^3H_6$ transition, and the emission produced at around 800 nm, arising from the $^3H_4 \rightarrow {}^3H_6$ transition, in both cases of Tm^{3+}, as it was shown in the first example of the previous section. However, in this case, due to the presence of Yb^{3+}, the excitation and emission mechanism is different. Figure 1.5 shows the excitation mechanism used to generate these emission lines after excitation at 980 nm. The 980 nm excitation source is absorbed from Yb^{3+} ion, promoting its electron from the ground state $^2F_{7/2}$ to the excited state $^2F_{5/2}$. From this excited state of Yb^{3+}, via energy transfers (hereafter ET) processes, the excited states of Tm^{3+} are populated. Hence, three ET populates the $^1G_4$, $^2F_{2,3}$ and $^3H_5$ levels of Tm^{3+}. From the $^1G_4$ level, electrons relax at the $^2F_{2,3}$ and fall back at the ground state level $^3H_6$, from which the 700 nm emission arises. From the $^2F_{2,3}$, a relaxation process at $^3H_4$, followed by a radiative decay at the ground state, give rise to the 800 nm emission.[202] It should be emphasized here that other mechanisms and emission lines might be involved in this process, but we are presenting only the emission lines used to determine the thermometric performance.

In all these cases, since the $^3F_{2,3}$ and the $^3H_4$ energy levels can be considered to be thermally coupled since they have a separation of less than 2000 cm^{-1}, the FIR was used as the thermometric parameter. However, despite the big majority of the papers analyzed defined this

FIR as the ratio between the intensity of the emission at 800 nm divided by the intensity of the emission at 700 nm, following the recommendation of Wade *et al.* in their seminal publication,[44] we encountered two recent publications (see reference 137 and 138) in which they defined it in the inverse way. Nevertheless, since Equation 1.9 does not take into account the way in which FIR has been defined, they could be compared to the rest of the luminescent thermometers analyzed in this section. If we analyze the maximum S_{rel} obtained for these kind of luminescent thermometers, it should be between 2-3% K^{-1}, result of having a ΔE between the Tm^{3+} $^3F_{2,3}$ and the $^3H_4$ energy levels around 1785 cm^{-1}. This energy can change slightly from host to host, due to the different crystal field that they can generate, and this would be reflected in the different S_{rel} values reported by the authors and that are listed in Table 1.1. This would provide a δT of the order of 0.2 K, approaching the desired limit of 0.1 K or below for biomedical purposes.[47] The temperatures at which these values are obtained are in all cases around room temperature, and all of them decrease as the temperature increases, as can be seen in Figure 1.6.

We observed that when the FIR model is modified, compared to the equation proposed by Wade *et al.*,[44] to account for the significant overlapping between the two emission bands used in the luminescent thermometer:

$$FIR = B \exp\left(-\frac{\Delta E}{k_B T}\right) + D \qquad (1.14)$$

where D is a fitting parameter, then if S_{rel} is calculated according to Equation 1.10, the value is not correct as it is underestimated, since according to Equation 1.2, the right way to determine S_{rel} should be:

$$S_{rel} = \frac{FIR - D}{FIR}\left|\frac{\Delta E}{k_B T^2}\right| x\ 100 \qquad (1.15)$$

It is important also to note the large variety of materials used to host Tm^{3+} and Yb^{3+} for these kind of thermometers, including vanadates,[103] phosphates,[102,104,112] niobates,[105] tungstates,[106] fluorides,[107,113,114,117,119], oxyfluorides,[115,116] titanates,[108,118], silicates,[109,110] and aluminates.[111]

It is worth to mention here that in some cases the inner active cores have been coated with an inactive shell. This strategy has been used in the case of $GdVO_4$@SiO_2,[202] $NaYF_4$@$NaYF_4$@SiO_2,[136] and Bi_2SiO_5@SiO_2 nanoparticles,[142] using an inert layer constituted by amorphous silica (SiO_2) shell, and in the case of $NaYF_4$@CaF_2 nanoparticles,[149] with an inert layer constituted by cubic CaF_2. The aim of coating the active core with this inert layer was to prevent the thermal degradation of the active core from potential oxidation, and at the same time prevent non-radiative relaxation process of the active ions encountered on the surface of the nanoparticles by their interactions with the surface bound ligands in the case of colloidal dispersions.[136] Also, in the case of $NaYF_4$@$NaYF_4$@SiO_2, the inert $NaYF_4$ interlayer generated, is used for a further protection of the radiative properties of the active ions.[136] Thus, despite it seems evident that these core@shell structures help to increase the quantum yield of the luminescent nanoparticles,[136] no conclusion can be extracted about their thermometric performance, since none of the papers published up to now for Tm^{3+},Yb^{3+} codoped systems operating in the I-BW, reported the comparison between the same material, naked and coated with the inert layer.

Also, by analyzing the data provided in Table 1.1 for the phosphates, it seems that when the phosphate material is based on a metal in the lanthanide series (Y or La), S_{rel} achieved is higher than a material based on a post transition metal. In fact, S_{rel} obtained in Tm^{3+},Yb^{3+}:$LaPO_4$ (S_{rel} =3% K^{-1}) and in Tm^{3+},Yb^{3+}:YPO_4 (S_{rel}=2.33% K^{-1}),[133] are slightly higher than the one obtained in Tm^{3+},Yb^{3+}:$BiPO_4$ (S_{rel} =2.14% K^{-1}).[141] However, other factors, such as the structure can also affect the thermometric performance of these luminescent thermometers, since $LaPO_4$ crystallizes in the monoclinic system, YPO_4 does in the tetragonal system, and $BiPO_4$ is a hexagonal compound.

From another side, Xing *et al.* studied the effect of using a single crystal or a polycrystal on the thermal sensing performance of Tm^{3+},Yb^{3+}:$LiNbO_3$ (labelled as S-$LiNbO_3$ and P-$LiNbO_3$, respectively, on Table 1.1).[203] A higher S_{rel} was obtained for the case of the single crystal (~ 3%

K^{-1}) than for the case of the polycrystal (~ 2% K^{-1}).[203] The authors assigned these differences in the S_{rel} to the effect of the crystallinity of each class of material on the degree of splitting of the upconversion emission spectra.[203] In fact, in Figure 1.7, it can be seen that the spectrum recorded for the single crystal is narrower than the spectrum recorded for the polycrystalline material, and that the spectrum of the polycrystalline material has a rich peak structure.

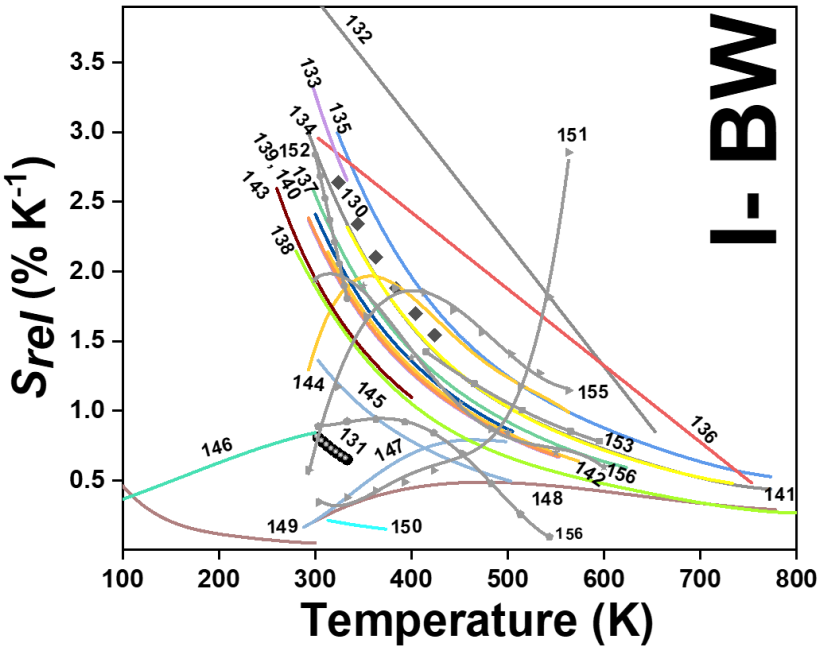

Figure 1.6. Temperature dependence of the relative thermal sensitivity of Tm^{3+} doped luminescent thermometers, operating in the I-BW. In symbols only, in solid lines and in solid lines with symbols, single Tm^{3+}, Tm^{3+}/Yb^{3+} and Tm^{3+}/Ln^{3+} based thermometers, respectively. The numbers represent the corresponding references for each Tm^{3+} based thermometers.

However, as it can be also seen in Figure 1.7, the intensity of the spectrum for the single crystal is much higher than that of the polycrystalline material, which could generate also a saturation effect is the recording of the spectrum has not been made in the optimum conditions that might affect to the thermometric performance of the luminescent thermometer. In fact, the δT and, as a consequence, the S_{rel}, are greatly affected from the signal-to-noise ($\frac{dI}{I}$) ratio of the emission spectrum, from which temperature is estimated.[21,204] At lower signal intensity, the probability of having a high signal-to-noise ratio, is increased, hampering in this way, the thermometric performance of materials.

A few number of examples used the FIR method applied to the thermal evolution of the intensities of different emission lines arising from Stark sublevels of the $^3H_4 \rightarrow {}^3H_6$ transition of Tm^{3+}, lying at around 800 nm, to develop thermometers based on Tm^{3+} and Yb^{3+} codoped materials.[118,119] Since the $^3H_4 \rightarrow {}^3H_6$ transition generates the emission band with the maximum emission in this region by Tm^{3+}, it is logical to use it to develop luminescent thermometers since the optical sensitivity of the detection system is less strict, allowing to use cheaper, and even portable detectors. However, as mention in the previous section, the fact that ΔE in this cases is much smaller (> 300 cm^{-1}), S_{rel} that can be obtained are lower (in the range 0.20-0.40% K^{-1}) than those obtained using other strategies, which gives δT of around 1 K, hence not making these kind of luminescent thermometers competitive enough with other strategies presented.

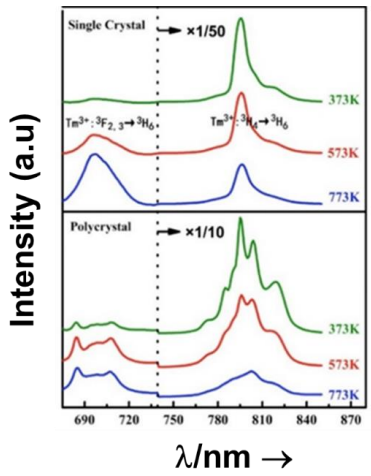

Figure 1.7. Emission spectra of Tm^{3+}/Yb^{3+} codoped $LiNbO_3$ polycrystal and single crystal at different temperatures under 980 nm excitation (1/10 and 1/50 represent 1/10 and 1/50 of actual measured emission intensities for 800 nm in Tm^{3+}/Yb^{3+} codoped $LiNbO_3$ polycrystal and single crystal). Adapted with permission.[203] Copyright from Elsevier.

A different example based on the analysis of the intensity of two different emission lines is that provided by an amorphous Yb^{3+} and Tm^{3+} codoped phosphate glass,[131] and by Tm^{3+},Yb^{3+}:Sr_2GdF_7 glass ceramics.[143] In both cases, the luminescent thermometer developed was based on the intensity ratio between two emissions arising from two different energy levels of Tm^{3+} ($^1G_4$ and $^3F_{2,3}$) that are not thermally coupled, although the population of the $^2F_{2,3}$ level is potentiated as the temperature increases by the non-radiative relaxations generated from the upper excited levels, including the $^1G_4$ level (see Figure 1.5 (b)). In these cases, the authors used two emission bands located at ~700 nm (generated by the $^1G_4 \rightarrow {}^3H_5$ transition) and ~650 nm (generated by the $^3F_{2,3} \rightarrow {}^3H_6$ transition) after excitation at 980 nm, although these two lines exhibited a very low intensity when compared to the 800 nm emission line used in the previous examples. The generation of these emission lines is presented in Figure 1.5 (b). Under 980 nm excitation, Yb^{3+} is excited from the $^2F_{7/2}$ ground state to $^2F_{5/2}$ state. This energy can be transferred to Tm^{3+} that excites its electron from the $^3H_6$ ground state to the $^3H_5$ excited state, that relaxes rapidly and non-radiatively to the $^3F_4$ level. When the energy of a second photon of 980 nm is transferred from Yb^{3+} to the electrons that are in this excited state, they can promote to the $^3F_{2,3}$ level. From here, the radiative $^3F_{2,3} \rightarrow {}^3H_6$ transition can take place, generating the emission at 650 nm. The second emission is generated when part of the energy of the electrons lying in the $^3F_{2,3}$ is dissipated non-radiatively, populating the lower $^3H_4$ energy level. From here, the transfer of the energy of a third photon of 980 nm from Yb^{3+} boosts these electrons to the $^1G_4$ level that can relax radiatively to the ground state, generating the emission at 700 nm.

Despite the two electronic levels from which these emissions arise are not thermally coupled, the authors fitted them to the FIR model, and from it they extracted a ΔE value (2493 cm^{-1} and 2207 cm^{-1},[131,143] respectively) that allowed them to calculate S_{rel} according to Equation 1.10. Since the energy separation between the electronic levels involved in these emissions is of the order of 6000 cm^{-1}, higher than the upper limit defined for TCLs,[44] the Boltzmann model cannot be used, and instead a phenomenological model fitting the experimental data to a conventional exponential curve should be taken into account. One might think that, according to that, the S_{rel} value they provided (3.94% K^{-1} at 303 K and 1.97% K^{-1},[131,143] respectively) should not be considered, since they are based on a wrong model. But, surprisingly, by taking the FIR equation they provided as a phenomenological equation, of the form:

$$\Delta = \frac{I_2}{I_1} = C \exp\left(-\frac{D}{T}\right) \qquad (1.16)$$

where C and D are fitting parameters, and calculating S_{rel} using Equation 1.2, the result is exactly the same, constituting the strategy providing the highest S_{rel} among the different ones proposed for the Tm^{3+},Yb^{3+} codoped systems. However, the low intensity of the emissions used in these luminescent thermometers, will hamper their practical use in real biomedical applications.

To end up this subsection, it is worth to mention a totally different example, based on bandwidth thermometry instead of band-shape thermometry, as are all the luminescent thermometers reported up to now. Lu *et al.* synthesized rhombohedral Tm^{3+},Yb^{3+}:YOF irregular nanoparticles and analyzed their thermal sensing performance via the bandwidth luminescence nanothermometry methodology of the 800 nm emission band of Tm^{3+}, that as we said before is by far the band with the highest emission generated by Tm^{3+} in this region, after exciting the material at 980 nm in the temperature range from 12 to 300 K.[145] The temperature variation of the full width at half maximum (FWHMs) was fitted to a simplified exponential model such as:[205]

$$\Delta\nu = \Delta\nu_0 + A\, e^{R_0 T} \qquad (1.17)$$

where $\Delta\nu_0$ represents the initial FWHM, and A and R_0 are empirical constants to be determined from the fitting model.[205] The corresponding S_{rel} was deduced from the following equation:[205]

$$S_{rel} = \frac{1}{\Delta\nu}\left|\frac{\partial\Delta\nu}{\partial T}\right| x\ 100\ \% \quad (1.18)$$

The maximum S_{rel} obtained was 0.84% K^{-1} at the highest temperature analyzed.[145] Despite this example, strictly speaking, could not be used for biomedical applications since the temperature range analyzed was lower than the biological range of temperatures, the fact that the maximum S_{rel} was obtained at 300 K, might suggest that it would be also useful in this thermal range. This is why we decided to include this example here.

Thus, the conclusion that can be extracted from the examples included in this section is that the most effective strategy to get a high S_{rel} is using the emissions arising from two non-thermally coupled electronic levels that are apart a distance higher than the upper limit defining the thermally coupled range of energies (2000 cm^{-1}). Other strategies, are not as effective as this one to increase S_{rel}. However, the quantum yield of the materials and of the different emissions used has not been taken into account in any of the luminescent thermometers operating in the I-BW reported lying in the category described here. In fact, the low intensity of the emissions considered at ~650 nm and ~700 nm, or the big difference of intensity existing between the two emissions at ~700 nm and at ~800 nm, would imply using highly sensitive (and thus bulky and costly) detectors, or that recording one of the signals in the optimum conditions would affect the collection of the other one in terms of signal-to-noise ratio or saturation of the detector. Thus, other strategies that, *a priori*, have a lower S_{rel}, like those involving different Stark sublevels of the $^3H_4 \rightarrow {}^3H_6$ transition of Tm^{3+}, lying at around 800 nm, might be more effective, due to the high intensity of this emission, that is the consequence of the $^3H_4$ level of Tm^{3+} being electronically fed by different radiative and non-radiative mechanisms. Nevertheless, this would lead to δT of around 1 K, one order of magnitude higher than the ones that are desired nowadays for biomedical applications.

2.1.3. Other Tm^{3+}, Ln^{3+} codoped luminescent thermometers operating in the I-BW

Dual emission centers luminescent nanothermometers, *i.e.* those luminescent thermometers in which there are two activators emitting at different wavelengths,[47] operating in the I-BW, have been based on the emissions arising from Tm^{3+} and another lanthanide ion, acting as activators, with or without Yb^{3+}, acting as sensitizer. Two groups of luminescent thermometers could be identified in this category: (i) those using Tm^{3+} and Ho^{3+} as activators, with the presence or not of Yb^{3+} as sensitizer;[150-152] and (ii) those using Tm^{3+} and Er^{3+} as activators, using always Yb^{3+} as sensitizer.[153-155]

In the case of Ho^{3+}, it has been reported an important temperature-dependence of the emissions arising from the electronically linked energy levels of Ho^{3+} and Tm^{3+}, from which ET and back energy transfer (hereafter BET) processes are possible. Despite the electronic levels of these different ions are not thermally coupled, a relation between their intensities as the temperature changes can be established. Two different strategies have been proposed in this case. Savchuk

et al. doped monoclinic potassium lutetium double tungstate $KLu(WO_4)_2$ nanoparticles with Ho^{3+} and Tm^{3+} and investigated their thermal performance in the physiological range of temperatures (303 K-333 K), after exciting the material at 808 nm.[151] In this case, Tm^{3+} acted both as sensitizer, by absorbing the energy of the 808 nm laser source and transferring part of the energy to Ho^{3+}, and as activator, generating different emission lines, among which one located at ~700 nm attributed to the $^3F_{2,3} \rightarrow {}^3H_6$ transition. The laser radiation at 808 nm excites the Tm^{3+} electrons to the $^3H_4$ level, from where they non-radiatively relax to the $^3F_4$ level. The absorption of a second photon at 808 nm promotes the electrons from the $^3F_4$ level to the $^1G_4$ level, from which they relax radiatively to the $^3H_6$ ground state, generating an emission at 475 nm. Another possibility that can happen is the non-radiative decay from the $^1G_4$ level to the $^3F_{2,3}$ levels, from which a radiative transition to the ground state can occur, generating the emission at 696 nm. The energy levels of Ho^{3+} can be populated through two different ET mechanisms: one between the Tm^{3+} $^3H_4$ level to the Ho^{3+} $^5I_5$ level, and a second one from the $^3F_4$ level of Tm^{3+} to the $^5I_7$ level of Ho^{3+}, from which also a BET process to Tm^{3+} can occur. Besides the direct ET from Tm^{3+}, the $^5I_7$ level of Ho^{3+} can also be populated by the non-radiative relaxation from its $^5I_5$ energy level. The ET of the energy of another photon of 808 nm from Tm^{3+}, promotes the electrons lying in the $^5I_7$ level of Ho^{3+}, the ET from, promotes the electrons of Ho^{3+} to the higher energy levels $^3K_8$ and $^5F_3$. From these levels, non-radiative decay processes populate the $^5S_2$ and $^5F_4$ levels of Ho^{3+} resulting in a radiative transition towards the $^5I_7$ level with emission at 755 nm, and/or towards the $^5I_8$ ground state, with emission at 545 nm. Finally, a radiative transition from the $^5F_5$ level of Ho^{3+}, which is populated from the non-radiative relaxation of the $^3K_8$ and $^5F_3$ energy levels, to the $^5I_8$ ground state, generates an emission at 655 nm.[151] The detailed mechanism for this complex system is depicted in Figure 1.8 (a).

The thermal sensing capacity was estimated from the integrated intensity ratio of the $^3F_{2,3} \rightarrow {}^3H_6$ and the $^5S_2$,$^5F_4 \rightarrow {}^5I_7$ transitions of Tm^{3+} and Ho^{3+}, respectively, corresponding to the emission bands located at 696 nm and 755 nm, arising from non-thermally coupled electronic levels (hereafter NTCLs).[151] Hence, the thermometric parameter (Δ) in this case was fitted to an empirical exponential growing equation of the type:[151]

$$\Delta = \Delta_0 + B\exp(\alpha T) \qquad (1.19)$$

where Δ_0 and B are constants to be determined from the fitting of the experimental data.

Thus, the corresponding S_{rel} was calculated from:

$$S_{rel} = \frac{B\,\alpha\exp(\alpha T)}{\Delta_0 + B\exp(\alpha T)}\ x\ 100 \qquad (1.20)$$

The maximum S_{rel}=2.84% K^{-1} was achieved at 303 K. Savchuk *et al.*, also estimated δT of this luminescent thermometer using the equation:[151]

$$\delta T = \frac{\delta\Delta}{B\exp(\alpha T)} \qquad (1.21)$$

determining a value of 0.2 K at 303 K.[151]

The second strategy developed in Tm^{3+}, Ho^{3+} codoped systems in the presence of Yb^{3+} as sensitizer, is that demonstrated in Tm^{3+}, Ho^{3+}, Yb^{3+}:YPO_4 microplates,[150] and in Tm^{3+}, Ho^{3+}, Yb^{3+}:$Gd_2(WO_4)_3$ nanocrystals.[152] In these two cases, Yb^{3+} acted as a sensitizer to absorb the energy of the 980 nm excitation source and transfer it to Tm^{3+} and Ho^{3+}, to generate an emission line at ~650-660 nm, corresponding to the Ho^{3+} $^5F_5 \rightarrow {}^5I_8$ transition, and another one at ~700 nm, corresponding to the Tm^{3+} $^3F_{2,3} \rightarrow {}^3H_6$ transition. Yb^{3+} ions absorb the 980 nm excition source, and are excited to the $^2F_{5/2}$ state (see Figure 1.8 (b)). Subsequently, the energy of this sensitizer is transferred to the adjacent activators Ho^{3+} and Tm^{3+}, and the sensitizer is relaxed back to the ground state. Ho^{3+} and Tm^{3+} activators are promoted to their excited states (Tm^{3+} to $^3H_5$, $^3F_{2,3}$ and $^1G_4$, and Ho^{3+} to $^5I_6$, $^5F_5$ and $^5S_2$, $^5F_4$). In addition, the excited states involved in the generation of the red emissions ($^3F_{2,3}$ of Tm^{3+} and $^5F_5$ of Ho^{3+}), can be populated from a non-radiative decay from the higher level excited states of the corresponding ions ($^1G_4$ of Tm^{3+} and $^5S_2$, $^5F_4$ of Ho^{3+}).[150,

[152] From these states, decaying back radiatively to the corresponding ground states ($^3F_{2,3} \rightarrow {}^3H_6$ of Tm^{3+} and $^5F_5 \rightarrow {}^5I_8$ of Ho^{3+}), generates the emissions used for thermal sensing.

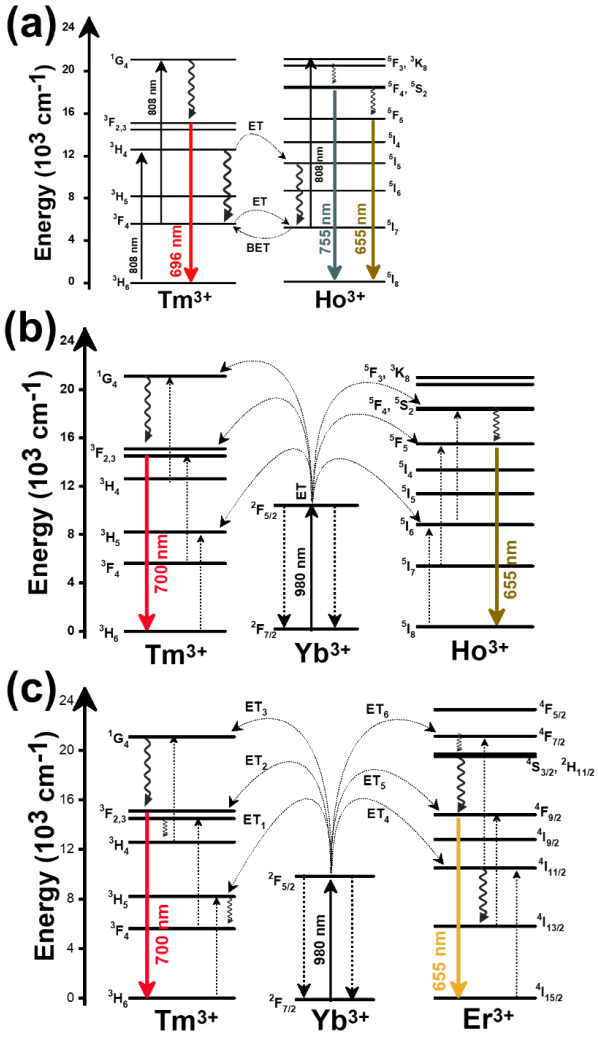

Figure 1.8. Mechanism of the generation of the emission lines for: (a) Tm^{3+}/Ho^{3+} doped $KLu(WO_4)_2$ nanocrystals after excitation at 808 nm, (b) $Tm^{3+}/Ho^{3+}/Yb^{3+}$ doped YPO_4 or $Gd_2(WO_4)_3$ after 980 nm excitation, and (c) $Tm^{3+}/Er^{3+}/Yb^{3+}$ doped YF_3 immersed in a glass ceramic after 980 nm excitation.

Again, these emission bands do not arise from TCLs, hence the thermometric parameter could be deduced from the intensity ratio between these bands, according to a linear equation to which the experimental data fitted of the form:[150]

$$\Delta = X - S * T \qquad (1.22)$$

where *X* and *S* were fitting parameters, or to a polynomial function:[152]

$$\Delta = C_1 + B_1 T + B_2 T^2 + B_3 T^3 \qquad (1.23)$$

where again, C_1, B_1, B_2 and B_3 were the fitting parameters. From these equations the thermal sensitivities could be calculated, depending on the thermometric equation used, as:

$$S_{rel} = \left|\frac{S}{S - ST}\right| x\ 100\% \qquad (1.24)$$

$$S_{rel} = (B_1 + 2B_2T + 3\ B_3T^2)\ x\ 100\% \qquad (1.25)$$

The maximum S_{rel}= 2.86% K^{-1} at 563 K was obtained for Tm^{3+}, Ho^{3+}, Yb^{3+}:YPO_4,[150] that allowed to calculate a δT of 0.2 K. In the case of Ho^{3+}, Yb^{3+}:$Gd_2(WO_4)_3$, the authors reported a substantially lower S_{rel} of 1.43% K^{-1} at 595 K, due to the different phenomenological model used to fit the experimental data.[152]

When the dual emission center consisted on the combination of Tm^{3+} with Er^{3+}, in the presence of Yb^{3+} as sensitizer, the same strategy was always used: the thermal reading was achieved from the temperature dependent intensity ratio between the 700 nm emission line of Tm^{3+} attributed to the $^3F_{2,3} \rightarrow {}^3H_6$ transition, and the 655-660 nm emission line of Er^{3+}, arising from the $^4F_{9/2} \rightarrow {}^4I_{15/2}$ transition.[154] The mechanism of the generation of these emission lines in shown in Figure 1.8 (c).

Shortly, Yb^{3+} acts as sensitizer to absorb the energy of the 980 nm excitation source, and generated three ET processes to Tm^{3+} populating its $^1G_4$ state, between:

- Yb^{3+}: $^2F_{5/2}$ + Tm^{3+}: $^3H_6 \rightarrow Yb^{3+}$: $^2F_{7/2}$ + Tm^{3+}: $^3H_5$ (ET1)
- Yb^{3+}: $^2F_{5/2}$ + Tm^{3+}: $^3H_4 \rightarrow Yb^{3+}$: $^2F_{7/2}$ + Tm^{3+}: $^3F_{2,3}$ (ET2)
- Yb^{3+}: $^2F_{5/2}$ + Tm^{3+}: $^3H_4 \rightarrow Yb^{3+}$: $^2F_{7/2}$ + Tm^{3+}: $^1G_4$ (ET3)

On the other hand, a two-step energy transfer from Yb^{3+} to Er^{3+} can also occur:

- Yb^{3+}: $^2F_{5/2}$ + Er^{3+}: $^4I_{15/2} \rightarrow Yb^{3+}$: $^2F_{7/2}$ + Er^{3+}: $^4I_{11/2}$ (ET4)
- Yb^{3+}: $^2F_{5/2}$ + Er^{3+}: $^4I_{11/2} \rightarrow Yb^{3+}$: $^2F_{7/2}$ + Er^{3+}: $^4F_{7/2}$ (ET5)

followed by a non-radiative relaxation to populate the Er^{3+} $^2H_{11/2}$, $^4S_{3/2}$ and $^4F_{9/2}$ electronic levels.

In addition, the population of the Er^{3+} $^4F_{9/2}$ state can be achieved through another ET process:

- Yb^{3+}: $^2F_{5/2}$ + Er^{3+}: $^4I_{13/2} \rightarrow Yb^{3+}$: $^2F_{7/2}$ + Er^{3+}: $^4F_{9/2}$ (ET6)

Finally, a last ET process between Er^{3+} and Tm^{3+} can occur, populating the $^3F_{2,3}$ level of Tm^{3+} (not presented in Figure 1.8 (c) for clarity reasons):

- Er^{3+}: $^4F_{9/2}$ + Tm^{3+}: $^3H_6 \rightarrow Er^{3+}$: $^4I_{15/2}$ + Tm^{3+}: $^3F_{2,3}$ (ET7)

This strategy was used in Tm^{3+}, Er^{3+}, Yb^{3+}:YF_3 nanoparticles immersed in a glass ceramic,[154] in Tm^{3+}, Er^{3+}, Yb^{3+}:LuF_3 mesocrystals,[155] and in oleic acid capped Tm^{3+}, Er^{3+}, Yb^{3+}:$NaLuF_4$ nanocrystals.[153] It is important to note here that due to the non-resonant energy matching between the Tm^{3+} and Er^{3+} energy levels, the multiphonon assisted energy transfer rate (K_{ET}) can be described by the Mott-Seitz model:[206, 207]

$$K_{ET} \propto \exp\left(-\frac{\Delta E}{k_B T}\right) \qquad (1.26)$$

indicating the temperature dependent behavior and the link between the two emissions involved in this thermometer. ΔE here stands for the energy gap between the excited and de-excited states.

In the case of Tm^{3+}, Er^{3+}, Yb^{3+}:YF_3 nanoparticles immersed in a glass ceramic,[154] the one exhibiting the highest S_{rel} (1.89% K^{-1} at 393 K), the authors fitted the experimental data to a FIR model of the form of Equation 1.14.

However, as discussed previously, since the two energy levels from which the emissions considered are not thermally coupled since they do not belong to the same lanthanide ion, this

model should not be used, and instead a phenomenological one should be implemented, exponential in that case. In the two other cases, phenomenological models were implemented, following polynomial equations in both cases, of second order in the case of oleic acid capped Tm^{3+}, Er^{3+}, Yb^{3+}:$NaLuF_4$ nanocrystals with the form:[153]

$$\Delta = C_1 - B_1T + B_2T^2 \qquad (1.27)$$

And of third order in the case of Tm^{3+}, Er^{3+}, Yb^{3+}:LuF_3 mesocrystals with the form:[155]

$$\Delta = C_1 - B_1T + B_2T^2 - B_3T^3 \qquad (1.28)$$

S_{rel} of these systems were obtained using Equation 1.2, with values of 0.76% K^{-1} at 500 K,[153] and 0.95% K^{-1} at 363 K,[155] respectively. The differences between S_{rel} obtained in these cases can be attributed to the different phenomenological models implemented in each case.

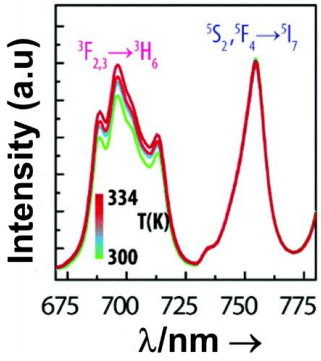

Figure 1.9. Temperature dependence of the emission spectra of Ho, Tm:$KLu(WO_4)_2$ nanocrystals, demonstrating the similar intensity between the $^3F_{2,3} \rightarrow {}^3H_6$ of Tm^{3+} and $^5S_2, {}^5F_4 \rightarrow {}^5I_7$ of Ho^{3+}. Adapted with permission.[151] Copyright from Royal Society of Chemistry.

In general, the strategies to develop luminescent nanothermometers analyzed in this section do not provide higher S_{rel} than those highlighted in the previous sections for Tm^{3+} doped systems, although in some cases they are pretty close. However, they use emission bands with a more similar intensity than those used previously in Tm^{3+},Yb^{3+} codoped systems (see Figure 1.9), which would facilitate recording the two emission bands with enough guaranties with the available detection systems, facilitating their practical use in biomedical applications with δT of ~0.2 K, closer to the ones demanded by the scientific community.

Table 1.1 summarizes all the information regarding Tm^{3+} doped nanothermometers, and Figure 1.6 depicts the evolution of the S_{rel} of every luminescent thermometer based on Tm^{3+} analyzed in this section operating in the I-BW in the range of temperatures studied. From this figure, it can be seen that in the majority of the cases analyzed, S_{rel} has its maximum value at room temperature, and then it decreases as the temperature increases. However, there are three cases in which S_{rel} increases in the biological range of temperatures, decreasing later, and showing maxima at around 350-400 K. These luminescent thermometers, based on Tm^{3+},Yb^{3+}:Sr_2GdF_7,[113] Tm^{3+},Er^{3+},Yb^{3+}:YF_3 nanoparticles embedded in a glass ceramics,[124] and Er^{3+},Yb^{3+}:LuF_3 mesocrystals,[125] would be the best options to perform luminescence thermometry for biological applications in the I-BW, particularly in the two first cases, since their maxima S_{rel} is around 2% K^{-1}, which might allow δT of ~0.2 K, and the emission bands in which they are based have a similar intensity, simplifying the detection setup.

2.2. Nd^{3+} doped luminescent thermometers operating in the I-BW

Nd^{3+} doped luminescent thermometers have attracted significant attention due to their superior luminescent yields in the NIR spectral region.[159, 173, 174] Nd^{3+} ions can be excited with UV, VIS and NIR light to generate emissions in the I-BW,[208,209] with potential advantages for biomedical applications, including large penetration depths, minimal background interference, and little

damage to the targeted samples, especially when excited in the NIR, enhancing their application as luminescent probes for various bioapplications as NIR-to-NIR luminescent nanoprobes.[210-212] Different Nd^{3+} doped luminescent thermometers operating in the I-BW have been designed based on three different pairs of TCL: $^4F_{7/2}/^4F_{3/2}$ (TCL 1), $^4F_{7/2}/^4F_{5/2}$ (TCL 2) and $^4F_{5/2}/^4F_{3/2}$ (TCL 3). In the field of luminescent nanothermometry, Nd^{3+} doped materials have been frequently used as sensitive thermometers in the physiological range of temperatures. An important number of paper has been also devoted to explore luminescent thermometers based on the transitions from different Stark sublevels of the $^4F_{3/2}$ to the ground state $^4I_{9/2}$. Furthermore, other recent references explore the possibilities of developing dual center luminescence thermometers combining Nd^{3+} with other lanthanide ions, such as Eu^{3+} and transition metals like Ti^{4+}. This section will focus first on the temperature sensing properties of single doped Nd^{3+} luminescent thermometers, then on dual center Nd^{3+}/Ln^{3+}codoped luminescent thermometers, and will conclude with dual Nd^{3+}/transition metal codoped luminescent thermometers, all of them operating in the I-BW.

2.2.1. Single Nd^{3+} doped luminescent thermometers operating in the I-BW

Contrary to single Tm^{3+} doped (section 2.1.1), single Nd^{3+} doped thermometers operating in the I-BW, represent the widest explored class of luminescent thermometers operating in the I-BW due to the temperature dependence of the TCLs of Nd^{3+}, lying in this spectral region. The thermometric performance of these thermometers, in general, is based on the FIR model, as can be seen in Table 1.1, because the energy gap between these electronic levels lies in the range 200-2000 cm^{-1}. In single doped Nd^{3+} thermometers operating in this region, the thermally coupled levels $^4F_{7/2}/^4F_{3/2}$ (TCL 1), $^4F_{7/2}/^4F_{5/2}$ (TCL 2) and $^4F_{5/2}/^4F_{3/2}$ (TCL 3), with theoretical energy gaps 1910 cm^{-1}, 1020 cm^{-1} and 960 cm^{-1},[177] respectively, are applied to determine their thermometric performance.

The reported single Nd^{3+} doped luminescent thermometers operating in the I-BW have been excited with VIS and NIR light sources. When single Nd^{3+} doped luminescent thermometers have been excited with VIS light, the three TCLs (TCL 1, TCL 2 and TCL 3), have been used to define the performance of the thermometric parameter. In a typical example of exciting the Nd^{3+} doped particles with green light, the mechanism of the generation of the emission bands (see Figure 1.10 (a)) is as follows: photons of the 580 nm excitation light source are absorbed by Nd^{3+}, promoting its electrons from the $^4I_{9/2}$ ground state to the $^4G_{9/2}$ or $^4G_{7/2}$ excited states, decaying then non-radiatively to the $^4F_{5/2}$ and $^4F_{7/2}$ states. From $^4F_{5/2}$ state, a radiative relaxation decaying back to the ground state generates an emission lying at 780-840 nm. The second emission band at 870-920 nm is generated after the non-radiative relaxation of the electrons from the $^4F_{5/2}$ states to the $^4F_{3/2}$ level, prior to a radiative relaxation to the ground state.[159] A third emission band at the range from 730-770 nm is generated from relaxing back to the ground state from the $^4F_{7/2}$ state.

Nd^{3+} ions were embedded in hosts such as La_2O_2S,[157] YAP,[158] Gd_2O_3,[159] $LaPO_4$,[160] fluorotellurite glass,[161] and strontium barium niobate (SBN) glass ceramic,[162] for this class of luminescent thermometers. In general, the performance of these luminescent thermometers was evaluated by analyzing the intensity ratio of the emissions corresponding to the $^4F_{5/2} \rightarrow {}^4I_{9/2}$ and $^4F_{3/2} \rightarrow {}^4I_{9/2}$ transitions (TCL 3). In general, the performance of these particles was evaluated by the intensity ratio between the TCLs $^4F_{5/2}$ and $^4F_{3/2}$. It should be noted here that for the host La_2O_2S, the FIR model applied is that of Equation 1.14, in which a correction term accounting for the overlapping of the emissions was used although the emission bands where largely apart, whereas for the other cases, the classical FIR model, described by Equation 1.9 is applied. This makes that the S_{rel} of the first example (1.95% K^{-1} at 270 K),[157] can be slightly overestimated to respect the rest. Hence, Nd^{3+} doped hexagonal La_2O_2S particles operated as a luminescent thermometer in the I-BW over the range of the temperatures from 270 K to 600 K, exhibiting a maximum S_{rel} of 1.95% K^{-1} at the lowest temperature analyzed.[157] However, the big size of the particles obtained and the temperature were this maximum value of S_{rel} was obtained, quite often might limit the potential applications of this thermometer.[13] In fact, for this thermometer, by taking into consideration the value of the experimental energy gap reported (ΔE = 987 cm^{-1}),[157] and proper FIR equation to be used (Equation 1.9), the correct value of the S_{rel} that should be considered would be around 1.15% K^{-1} (at 293 K). In the case of the fluorotellurite glass,[161] and SBN glass ceramic,[162] we calculated the values of the S_{rel} (and δT) by considering the energy gap provided by the authors

and the temperature ranges analyzed. From all these results, we can conclude that the maximum S_{rel} of this class of luminescent thermometers would be in the range 1.83-1.15% K^{-1}, in all cases obtained at the lowest temperature analyzed. A higher S_{rel} was reported in Nd^{3+} embedded in YAG, when TCL2 was taken into account.[156] From a comparison between the TCL 2 and TCL 3, revealed that the maximum thermal sensing properties were achieved for the former one, mainly due to the higher experimental energy gap.[156] For TCL 2, the energy gap was 1000 cm^{-1}, whereas for TCL3 was in the range of 900 cm^{-1}. Despite the high S_{rel} at the range of 2.95% K^{-1}, this value was recorded at 200 K, whereas at physiological range, drops down to 0.3% K^{-1}.[156]

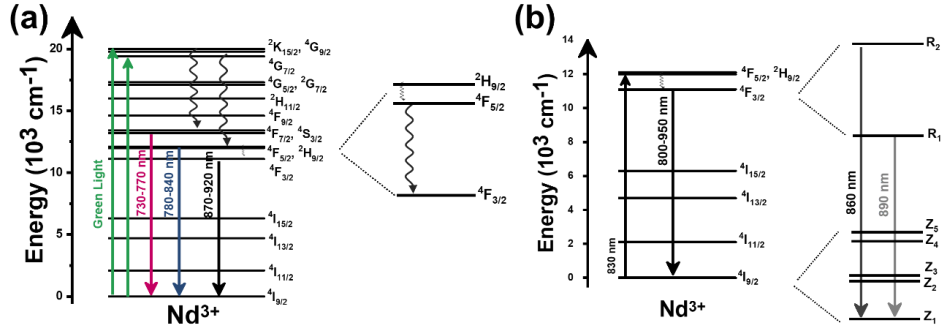

Figure 1.10. Mechanisms of generation of the emission bands in single Nd^{3+} doped nanoparticles after being excited with: (a) visible green light source (the expansion depicts the thermally coupled $^4F_{5/2}$ and $^4F_{3/2}$ levels) and (b) near infrared 830 nm light source.

The performance of the Nd^{3+} doped luminescent thermometers evaluated by considering the Stark-sublevels of the $^4F_{3/2} \rightarrow {}^4I_{9/2}$ transition, resulted in a low S_{rel} (0.11-0.62% K^{-1}) which implied a large δT when determined using Equation 1.3 (> 1 K) independently if the excitation source used was emitting in the VIS or the NIR. Nevertheless, in some cases, in the bibliographic references δT was reported to be smaller, but it was associated to smaller S_{rel} values, that are impossible according to the ΔE associated to the Stark sublevels involved in the emissions used to build the luminescent thermometer, of the order of 50-270 cm^{-1} depending of the host in which Nd^{3+} has been embedded. This energy difference, strictly speaking, does not allow for the application of the FIR model to those emission lines arising from energy levels apart by an energy difference below 200 cm^{-1}, so several reports fit the experimental data to an exponential function of form of that shown in Equation 1.16, which might also explain why in some cases smaller S_{rel} were reported.

Figure 1.10 (b) shows the mechanism of generation of the emission lines associated to the Stark-sublevels of the $^4F_{3/2} \rightarrow {}^4I_{9/2}$ transition after excitation in the NIR. In this way, the electrons in the Nd^{3+} $^4I_{9/2}$ ground state are excited to the $^4F_{5/2}$, $^2H_{9/2}$ state, then, they relax via a non-radiative process, populating the $^4F_{3/2}$ metastable state. If visible light in the green is used to excite the sample, the electrons will be excited to the more energetic $^4G_{9/2}$ or $^4G_{7/2}$ excited states, as shown in Figure 1.10 (a), but from there, they relax non-radiatively to the $^4F_{5/2}$, $^2H_{9/2}$ state, from which the rest of the emission mechanism is the same. The $^4F_{3/2}$ metastable state may be radiatively depopulated, generating emission bands in the I-BW, assigned to the $^4F_{3/2} \rightarrow {}^4I_{9/2}$ transition.[166] Since both levels ($^4F_{3/2}$ and $^4I_{9/2}$) are composed of several Stark sublevels (R_2 and R_1 for $^4F_{3/2}$, and Z_5–Z_1 for $^4I_{9/2}$, as presented in Figure 10 (b)), a plethora of emission bands lying in the 800-950 nm range (see Table 1.1), may be generated, that can be used to define different luminescent thermometers, depending on the host considered. Note that here we focused only on the generation of the emissions lines used to build this class of luminescent thermometers, without taking into account that Nd^{3+} ions can generate other emission lines in different spectral regions, as we will see in the following sections. It should be mentioned here the case of Nd^{3+}:$LiLuF_4$@$LiLuF_4$, where besides the thermalization of R_2 and R_1 levels, it was taken into account the contributions of peak shift and width change of the intensity of the emissions, leading

to higher sensitivity values (if only the thermalization is considered with an energy gap 0f 55 cm^{-1}, a maximum sensitivity value of 0.09% K^{-1} would have been achieved).[165]

Despite of these limitations in this class of thermometers, Marciniak *et al*. investigated the effect of the Nd^{3+} concentrations and the alkali ion in the host on the thermometric performance of Nd^{3+} doped monoclinic tetraphosphates of the form $ALaP_4O_{12}$ where A=Li, K, Na and Rb.[166] The authors investigated the thermometric performance of these compounds, via three different classes of luminescence nanothermometry techniques: band-shape, bandwidth and spectral position.[166]

Regarding the performance of the luminescent thermometer via the band-shape thermometry technique, the experimental data were fitted to an exponential function of form of that shown in Equation 1.16. The authors observed a tendency of the intensity ratio to increase as the temperature increased for all the investigated hosts. However, at higher temperatures, an inversion of this trend could be observed for the hosts containing Li and Na, due to the drastic lowering of the intensity of one of the emissions to respect the other, due to the excited state absorption to higher energy levels (see Figure 1.11 (a)). This effect reduces the usable temperature range for these luminescent thermometers. The highest S_{rel} was obtained for the $LiLaP_4O_{12}$ host while the lowest one was obtained for the $KLaP_4O_{12}$ host, while the other two, $RbLaP_4O_{12}$ and $NaLaP_4O_{12}$ hosts, have similar values (see Table 1.1), following a linear trend with the crystallographic *b* parameter of the materials, coinciding with the direction along which the $(PO_4)^{3-}$ tetrahedral chains characteristic of these compounds run (see Figure 1.11 (b)). [166] Here, the influence of the symmetric P-O-P vibration mode, that shifts towards lower energies as the mass of the alkali ion in the host increases, due to the distance between the alkali ion and the phosphorus ion, seems to play a major role. Also the concentration of Nd^{3+} in the hosts highly influences in the value obtained for the S_{rel} due to the dependence of the energy separation between the two Stark sublevels involved in the generation of the emissions used to build the thermometer (see Figure 1.11 (c)). With the increase of the Nd^{3+} concentration, the position of R_2 and R_1 is shifted (see Figure 1.11 (d)) using $KLaP_4O_{12}$ host as an example. This tendency, with different rates, can be noticed for each of the other hosts. The observed decrease of the ΔE value was the strongest for $RbLaP_4O_{12}$ (decrease by 24 cm^{-1}), compared to $LiLaP_4O_{12}$ (15 cm^{-1}), $NaLaP_4O_{12}$ (6 cm^{-1}) and $KLaP_4O_{12}$ (3 cm^{-1}) (see Figure 1.11 (e)). Since S_{rel} of these nanothermometer is ruled by the Boltzmann distribution, is dependent on ΔE value, it is clear that decreasing ΔE value leads to a decrease in the sensitivity.

Concerning spectral position thermometry, with the increase of the temperature a red-shifting of the emission lines was observed for all the hosts analyzed, with the $RbNdP_4O_{12}$ compound showing the strongest changes, while the $KNdP_4O_{12}$ compound exhibit the smallest ones. This shifting in the position of the emission lines is usually associated with the electron-phonon coupling effect that results from the introduction of random perturbations in the active ion surrounding environment by the host vibration modes at higher temperatures that can be thermally occupied generating stronger electron-host interactions. This fact results in a decrease of the energy of the emitted phonons and thus, a slight shift of the emission band towards higher wavelengths. The spectral change can be described by:[166, 213]

$$\Delta\lambda = \Delta\lambda^S + \Delta\lambda^D + \Delta\lambda^M + \Delta\lambda^R \qquad (1.29)$$

where $\Delta\lambda^S$, $\Delta\lambda^D$, $\Delta\lambda^M$ and $\Delta\lambda^R$ represent the contributions to the spectral shifting of the crystal strain inhomogeneity, single phonon processes, multiphonon processes, and the electron–host interaction effect associated with Raman scattering, respectively. However, the three first parameters can be considered to be temperature independent, and thus, only the electron-host interaction parameter should be considered as the one which controls the emission line shift as the temperature increases.

According to that, the change in the spectral position can be expressed as:[213, 214]

$$\delta\lambda = \delta\lambda_0 + \alpha\left(\frac{T}{\Theta_D}\right)^4 \int_0^{\Theta_D/T} \frac{x^3}{e^x - 1} dx \qquad (1.30)$$

$$x = \frac{\hbar\,\Omega}{k_B\,T}$$

where $\delta\lambda_0$, α, Θ_D and $\hbar\,\Omega$ and represent the initial line position, the electron-host coupling parameter, the effective Debye temperature, and the phonon energy, respectively. The corresponding S_{rel}, thus, can be calculated from the following equation:

$$S_{rel} = \frac{1}{\lambda_2}\frac{\lambda_2 - \lambda_1}{\Delta T}\ 100\% \qquad (1.31)$$

where λ_2 and λ_1 represent the spectral shift at temperatures T_2 and T_1 and ΔT is the result of T_2 - T_1.

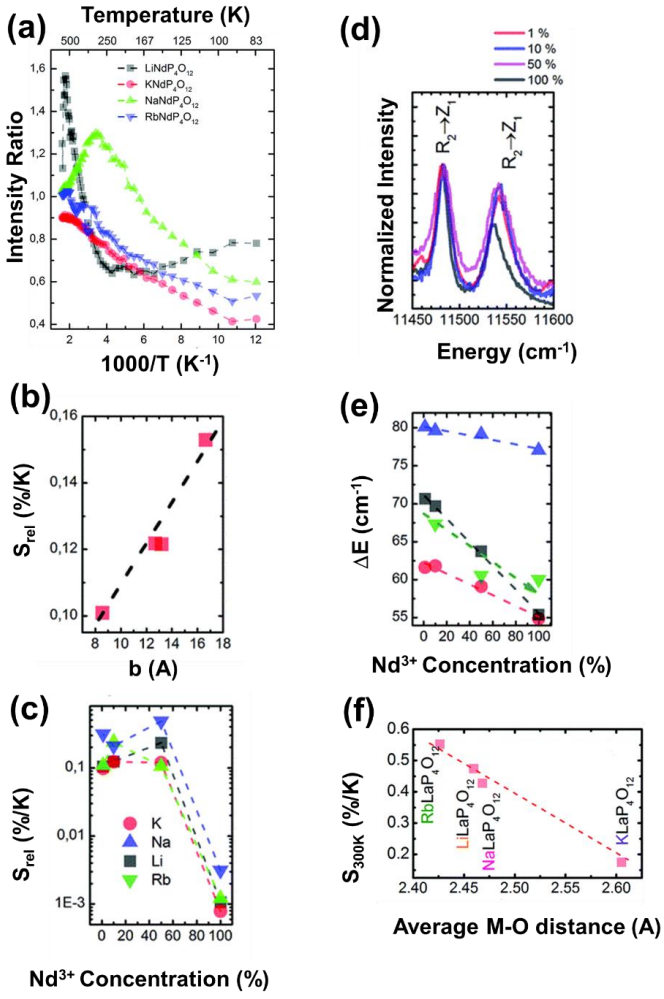

Figure 1.11. (a) The effect of the temperature on the intensity ratio of Nd^{3+} doped AP_4O_{12} nanocrystals, (b) the variation of the relative sensitivity as a function of the cell parameter *b*, (c) the change in the sensitivity as a function of the dopant concentration, (d) comparison of the band position for the $R_2 \rightarrow Z_1$ and $R_1 \rightarrow Z_1$ transition for different concentrations of Nd^{3+} ions in $KLaP_4O_{12}$ host and (e) the effect of the dopant concentration of energy separation between R_1 and R_2 Stark sublevels for AP_4O_{12} nanocrystals and (f) the variation of the relative thermal sensitivity with the average M-O distance in Nd^{3+} doped AP_4O_{12} nanocrystals. Adapted with permission.[166] Copyright The Royal Society of Chemistry 2016.

S_{rel} follows a linear inverse trend with the average distance between the metal and the oxygen host (see Figure 1.11 (f)).[166] After these results, the general conclusion that can be drawn is that the materials exhibiting the shortest metal-oxygen distance exhibited the highest thermometric performance. This is because the electron-host coupling parameter is proportional to the average metal-oxygen distance while the electron-phonon interaction strength increases with the covalence of the bond, which increases proportionally to the shortening of the chemical bond length.[213, 214] These results indicate that to further enhance the thermometric performance of the luminescent thermometers based on Nd^{3+} ions, host types with strong electron-host interaction parameters should be selected.

Using bandwidth luminescence nanothermometry, it was observed that the width of the emission band was broaden as the temperature increased, as a consequence of the electron-phonon interaction. To determine the thermometric performance, the bandwidth of the emission band at a particular temperature could be determined according to:[215]

$$\Delta\nu = \nu_0 \sqrt{coth\left(\frac{\hbar\Omega}{2k_B T}\right)} \qquad (1.32)$$

where ν_0 stand for the full width at half-maximum at the initial temperature. The highest S_{rel} (determined using Equation 1.18) was addressed, yet again, to 1% Nd^{3+} doped $LiLaP_4O_{12}$ for a value of 0.32% K^{-1}.[166] However, in that case, it was not possible to establish a correlation between the structural parameters of the host and S_{rel} for the case of the bandwidth luminescence nanothermometry.

As a final remark, among the three luminescence nanothermometry classes explored to study the thermometric performance of these compounds, the spectral position luminescence nanothermometry technique displayed the best temperature sensing properties (see Table 1.1).[166] Despite this better performance, according to the authors the spectral position is much more difficult to accurately determine and requires high resolution detection systems, which hampers the implementation of this technique to determine the temperature in real biomedical samples.[166]

2.2.2. Dual Nd^{3+}/Ln^{3+} codoped luminescent thermometers operating in the I-BW

Dual Nd^{3+}/Ln^{3+} thermometers operating in the I-BW are mainly based on the incorporation of Yb^{3+} as a sensitizer due to its large absorption cross section at 980 nm, which would lead in brighter emissions.[201] This feature has led this element to be used with Nd^{3+} and other lanthanide ions in photon conversion processes involving ET mechanisms. For the case of Nd^{3+}, the application of Yb^{3+} as sensitizer allows the use of the three TCLs ($^4F_{7/2}$, $^4F_{5/2}$ and $^4F_{3/2}$) for temperature sensing purposes (see Table 1.1). However, as in the case of Tm^{3+}/Yb^{3+} codoped, the overheating problem due to the strong water absorption band around 980 nm, that makes nanothermometers composed of Yb^{3+}, not ideal for biomedical or health applications, as it will cause strong heating up effect and kill normal cells and tissues,[216] should be taken into consideration.

The mechanism of the generation of the emissions in Nd^{3+}/Yb^{3+} codoped thermometers, is based on phonon-assisted energy transfer (hereafter PAET) processes.[180, 182] In a typical process (see Figure 1.12 (a)), under 980 nm excitation, electrons are excited from the Yb^{3+} $^2F_{7/2}$ ground state to the Yb^{3+} $^2F_{5/2}$ excited level. The transfer of energy from this state to the Nd^{3+} states is achieved through PAET processes. This allows the population of the $^4F_{3/2}$, $^4F_{5/2}$ and $^4F_{7/2}$ states of Nd^{3+} if the maximum phonon energy of the host is in the range of assisting the energy gap between these energy levels, of the order of 1750 cm^{-1}, indicating also that they are thermally coupled. Hence, thermal population of the $^4F_{5/2}$ and $^4F_{7/2}$ levels can be achieved from the lower energy level. Also, the PAET process becomes more effective as the temperature increases.[180, 182] From these states, radiative decay to the ground state generates Nd^{3+} emissions in the I-BW window at 863 nm, 803 nm and 750 nm, respectively, as shown in Figure 1.12 (a).

The performance of these Nd^{3+}/Yb^{3+} codoped nanoparticles, was evaluated by the typical FIR model. As can be seen in Table 1.1, the most used TCLs are the $^4F_{3/2}$ and the $^4F_{7/2}$ levels, which when used their emissions to the ground state to calculate the FIR, showed higher thermal

sensing properties compared to the FIR using the emission corresponding to the transition from the $^4F_{5/2}$ level.

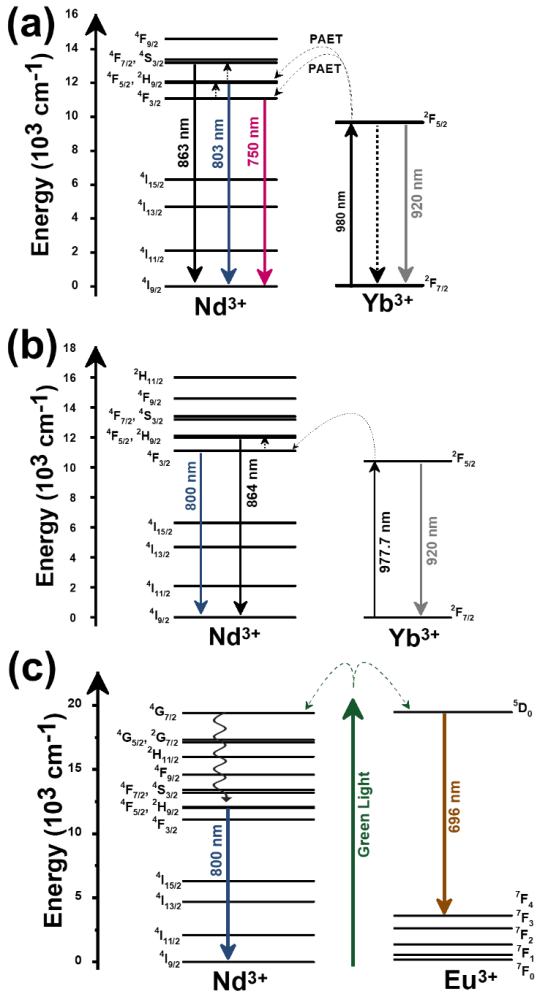

Figure 1.12. Mechanisms of generation of the emission bands of nanoparticles codoped with Nd^{3+} and: (a) Yb^{3+} after 980 nm excitation, (b) Nd^{3+}/Yb^{3+}:$Al_4B_2O_9$, after excitation at 977.7 nm, and (c) Eu^{3+} after excitation in the green.

A full comparison between the temperature sensing performance of the three TCLs in Nd^{3+} with emissions in the I-BW is provided by Nd^{3+}/Yb^{3+} codoped oxyfluoride glass.[177] The results reveal that the best thermometric performance is achieved by using the FIR in the following order: $^4F_{7/2}/^4F_{3/2}$ > $^4F_{7/2}/^4F_{5/2}$ > $^4F_{5/2}/^4F_{3/2}$ (see Figure 1.13 (a)), which is in accordance with the experimental ΔE determined between these levels (2076 cm^{-1}, 1300 cm^{-1} and 1216 cm^{-1}, respectively).[177] The values of S_{rel} obtained by using the $^4F_{3/2}$ and the $^4F_{7/2}$ TCLs allows obtaining a δT of ~0.15-0.2 K, approaching the desired values for biomedical applications,[47] although this low limit is always attained at the minimum temperature analyzed, normally room temperature. The temperature dependence of S_{rel} for these Nd^{3+}, Yb^{3+} codoped luminescent thermometers is presented in Figure 1.14.

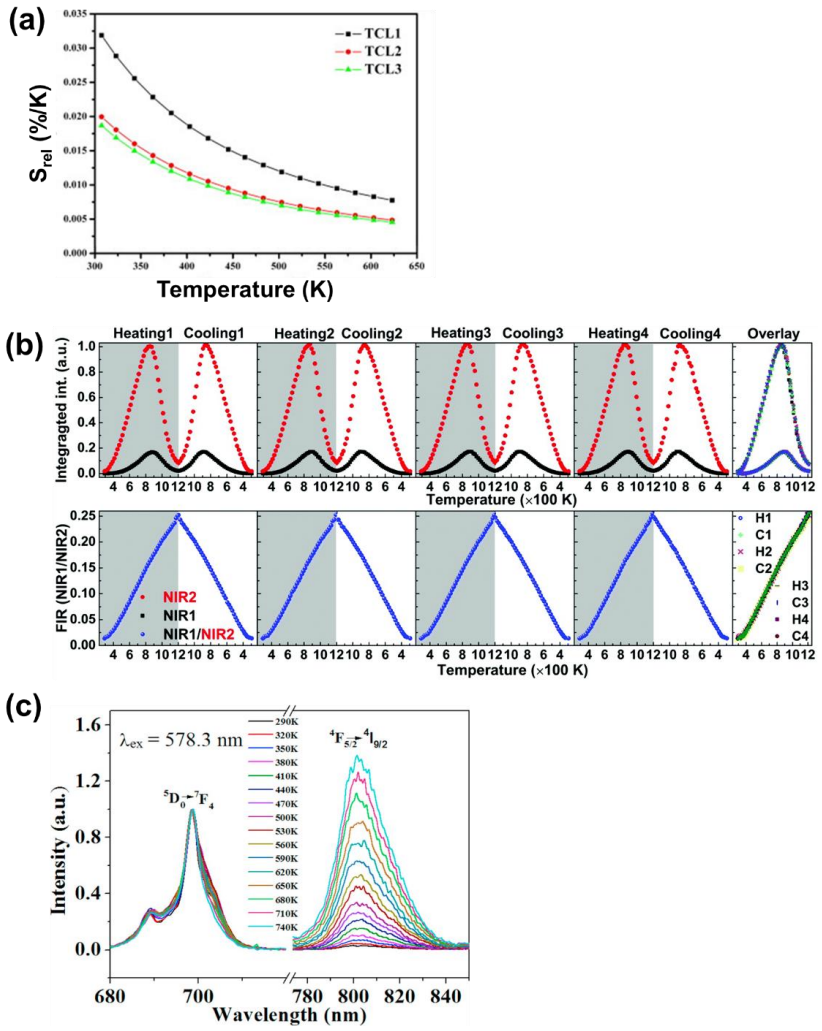

Figure 1.13. (a) Evolution of the relative thermal sensitivity as a function of the three TCLs in Nd^{3+}/Yb^{3+} codoped oxyfluoride glass. The thermally coupled levels are related to $^4F_{7/2}/^4F_{3/2}$ (TCL 1), $^4F_{7/2}/^4F_{5/2}$ (TCL 2) and $^4F_{5/2}/^4F_{3/2}$ (TCL 3).Adapted with permission.[177] Copyright from Elsevier 2012. (b) Repeatability of integrated intensity of 750 nm and 803 nm (upper panels), and FIR of 750/803 (lower panels) over 4 heating and cooling cycles from 293 to 1233 K with a step of 20 K in Nd^{3+}/Yb^{3+} codoped trigonal La_2O_3 microparticles. The last panel shows the overlay of the integrated intensity of 750, 803, and the FIR of 750/803 for the 4 different heating and cooling cycles. H and C represent heating and cooling, respectively. Adapted with permission.[182] Copyright from The Royal Society of Chemistry 2018. (c) Emission spectra of Eu,Nd:Ba_2LaF_7 glass ceramic under the 578.3 nm excitation in the temperature range of 290-740 K. Adapted with permission.[183] Copyright from Elsevier 2017.

Another interesting example here is the luminescent thermometer constituted by Nd^{3+}/Yb^{3+} codoped trigonal La_2O_3 microparticles, in which the thermometric performance was explored in the widest temperature range among this class of thermometers, from room temperature to 1230 K.[182] Here, the repeatability of the measurements was tested via four heating and cooling cycles, revealing excellent agreements (see Figure 1.13 (b)).[182] Also, based on these heating and cooling cycles, the authors could identify the temperature uncertainty expressed as:[49, 182]

$$\Delta T_{min} = \frac{\sigma}{S_{rel}} \quad (1.33)$$

where σ represents the standard deviation of the intensity ratio ($^4F_{7/2}/^4F_{3/2}$ in this case). The value obtained was 0.1 K in the temperature range below 400 K, whereas it increased for higher temperatures, reaching a maximum at 1230 K of ~3 K.[182]

An interesting choice for these dual Nd^{3+}/Ln^{3+} codoped luminescent thermometers operating in this window, is the choice of combining the emissions of Nd^{3+} with emission of Yb^{3+} that besides acting as sensitizer, is also generating an emission line, that can be applied to extract the temperature. Nd^{3+}/Yb^{3+} were used for doping orthorhombic $Al_4B_2O_9$ borate and excited at 977.7 nm wavelength.[180] The generation of the emissions of Nd^{3+} and Yb^{3+} are based on upconversion processes. The excitation laser light, is absorbed from Yb^{3+}, promoting it from the ground state to the $^2F_{5/2}$ excited state. Yb^{3+} can radiative relax back at the ground state, generating the emission line located at 920 nm. From the excited state of Yb^{3+}, via a PAET, the $^4F_{3/2}$ excited state of Nd^{3+} is populated.[180] From this state, a radiative decay at the $^4I_{9/2}$ ground state, generates the 800 nm emission. In the $^4F_{3/2}$ state, a process of annihilation of photons, populates the $^4F_{5/2} + {}^2H_{9/2}$ excited energy level, prior to relaxing at the ground state and generating the emission line at 864 nm (see Figure 1.12 (b)). It should be stated here that the emission of Yb^{3+} changes according to the different hosts where this ion is embedded (see Section 3).

Concerning the thermal sensing, exploring the intensity ratio between the Nd^{3+} emissions versus Yb^{3+} emission, over the physiological range of temperature, lead to the conclusion that the highest S_{rel} was obtained in the case of the 800 nm versus 920 nm (see Table 1.1), with the main reason of the larger energy gap compared to the 864 nm versus 920 nm.[180] The results obtained from this combination are comparable to that of the TCL3, however still lower compared to the TCL1.

Besides Nd^{3+}/Yb^{3+} codoped luminescent thermometers operating in the I-BW, another choice, rarely reported, are Nd^{3+}/Eu^{3+} doped materials. These luminescent thermometers are based on the emissions arising from NTCLs of Eu^{3+} at ~700 nm and Nd^{3+} at ~800 nm.[183, 184] The reason why these Nd^{3+}/Eu^{3+} co-doped thermometers were proposed was to overcome the drawback of the limitation in the maximum value of the S_{rel} that can be achieved operating with TCLs.[217] Thus, the strategy of implementing emission lines generated from two different active centers, was tested.[217] The mechanism of the generation of these emission lines is depicted in Figure 1.12 (c). The excited energy states $^5D_0$ of Eu^{3+} and $^4G_{7/2}$ of Nd^{3+} are very close in energy, therefore they can simultaneously excited at 590 nm. From these excited states, the electrons of Eu^{3+} can fall back to the $^7F_4$ state, generating the emission located at ~700 nm. The electrons of Nd^{3+}, from the $^4G_{7/2}$ level followed a series of non-radiative relaxations that populate the $^4F_{5/2}$ level (among others). From this level, the radiative relaxation back to the ground state generates the emission at ~800 nm.[183, 184]

Two examples that apply this combination of Nd^{3+} and Eu^{3+} ions involve YVO_4,[182] and Ba_2LaF_7,[183] as hosts. One of the interesting characteristics of these thermometers is that the emission that should be expected at around 750 nm for Nd^{3+}, arising from the transition of the $^4F_{7/2}$ level to the ground state is very weak, compared to that observed in Nd^{3+}/Yb^{3+} luminescent thermometers, so it cannot be used for luminescence thermometry in this case. Another interesting feature of this class of thermometers is that while the emission of Eu^{3+} changes slightly with temperature, the emission of Nd^{3+} is highly dependent on the temperature, and its intensity increases as the temperature increases (see Figure 1.13 (c)). In the case of Ba_2LaF_7, S_{rel} reported was calculated with Equation 1.1 corresponding to the absolute thermal sensitivity, thus, It cannot be compared with that of other luminescent thermometers reported in the literature. From the fitting form, the energy gap can be extracted to be 1890.8 cm^{-1} (the authors did not presented any value on the corresponding publication). S_{rel} is however, calculated from the same equation as in TCLs (Equation 1.10). Thus, knowing the temperature range from 290-740 K, the value of S_{rel} is calculated to be 2.2% K^{-1} for a δT of 0.22 K at the lowest temperature under investigation.

From Table 1.1 and Figure 1.14, it can be noted that the purpose of these Nd^{3+}/Eu^{3+} codoped thermometers to achieve better thermal sensing than the one that can be obtained from TCLs, is partially achieved. The performance is better compared to that of the Nd^{3+}/Yb^{3+} luminescent thermometers operating under the TCL 3 scheme, similar to TCL2, however still lower than the TCL 1 scheme. In addition, an important fact to consider is that Nd^{3+}/Eu^{3+} codoped thermometers

are excited in the green, whereas the ones doped with Nd^{3+}/Yb^{3+} are excited in the NIR, thus, another limitation for this class of luminescent thermometers is the penetration depth that can be achieved with them in biological applications.[91]

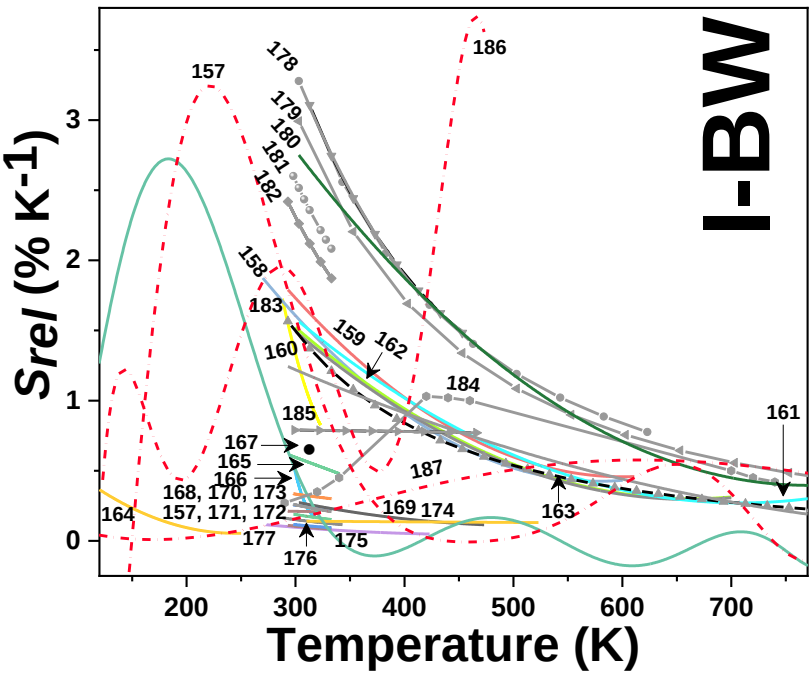

Figure 1.14. Temperature dependence of S_{rel} of Nd^{3+} doped luminescent thermometers, operating in the I-BW. In solid lines, short dash dot and solid lines with symbols, single Nd^{3+}, Nd^{3+}/Ln^{3+} and Nd^{3+}/transition metal doped thermometers, respectively. The numbers represent the corresponding references for each thermometer.

2.2.3. Dual Nd^{3+}/transition metals codoped luminescent thermometers operating in the I-BW

The combination of Ln^{3+} ions with transition metals in the same host lattice, introduces new luminescent properties involving the emissions of both kind of ions.[218] Mixed lanthanide ions/transition metal compounds with luminescent properties from both ions have emerged recently with especial interest for luminescence thermometry, attributable to the fact that the luminescence properties of the transition metals are drastically affected by local symmetry changes and the allowed character of the d-d transitions, which renders these ions as competitive thermal probes to the f-f transition of lanthanide ions.[156, 185, 186] Here, the emissions arising from the Ln^{3+} ions changes barely with temperature, thus, they are considered as reference signals.[156, 185, 186] For the Nd^{3+} doped thermometers operating in the I-BW, the transition metals involved for thermal sensing purposes implicate titanium,[185] chromium,[156] and manganese,[186] all embedded in the yttrium aluminum garnet (YAG) host. To generate the emission lines, however these materials have to be excited with UV (exciting the Ti (IV), Mn (IV)) and VIS (exciting the Cr (III)) light (see Table 1.1), which will hamper their possible biomedical applications.

As an illustrative example, Nd^{3+}/Cr^{3+} co-doped YAG was excited at 590 nm visible light source and the generated emissions are presented in Figure 1.15 (a). Absorption of light at 590 nm allows for the excitation of electrons of Cr^{3+} from the $^4A_2$ ground state to the $^4T_2$ excited state, which was

followed by nonradiative multiphonon relaxation leading to the population of the ^2E state. Radiative relaxation from these two states led to narrow (690 nm) and broad emission bands (710 nm), assigned to the $^2E \rightarrow {}^4A_2$ and $^4T_2 \rightarrow {}^4A_2$ transitions, respectively.[156] In Figure 1.15 (b), the displacement of the $^4T_2$ state parabola with respect to the ground state $^4A_2$ is related to the distortion of the crystal field, leading to the appearance of a crossing point between these parabolas at ΔE energy.[156] Through this crossing point, electrons can be transferred to the ground state via nonradiative multiphonon relaxation, if the thermal energy provided to the system is sufficiently high.[156] For Nd^{3+} emissions, they are generated by absorbing the excitation source and promoting electrons to the $^4G_{5/2}$, $^4G_{7/2}$ excited states, followed by a non-radiative relaxation to the $^4F_{3/2}$ state, where either: (i) radiative relaxation to $^4I_{9/2}$ and $^4I_{11/2}$ states or (ii) thermalization to the higher laying energy levels $^4F_{5/2}$ and $^4F_{7/2}$ can occur, giving rise to emission bands in the I-BW and II-BW.[156] The emission spectra generated by this pair of ions and a simplified mechanism of the generation of these lines, are illustrated in Figure 1.15 (a) and (b).

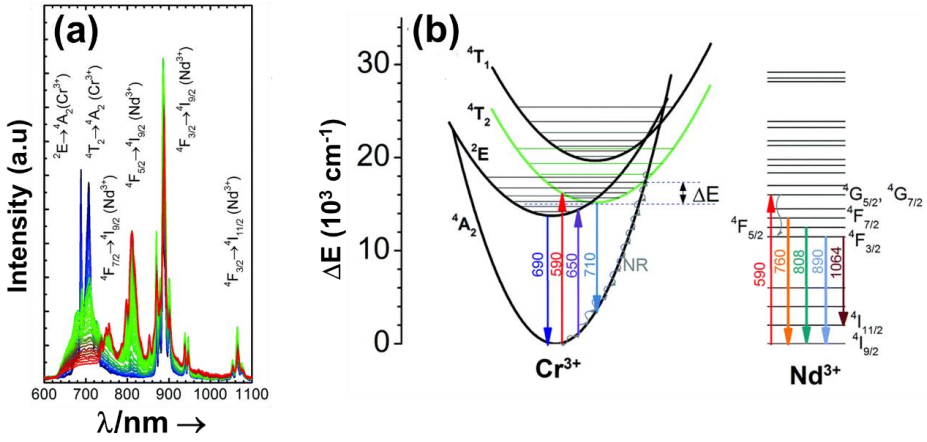

Figure 1.15. (a) Emission and (b) mechanisms of the generation of these emission lines in Nd^{3+}/Cr^{3+} codoped YAG, after being excited at 590 nm. Reproduced with permission.[156] Copyright from Owner Societies.

The performance of this material (and the Nd^{3+}/Ti^{4+} and Nd^{3+}/Mn^{4+} as well) was evaluated through the intensity ratio, defined as:[156]

$$\Delta = \frac{I_{0Cr}}{1 + exp\left(\frac{\Delta E_1}{k_B T}\right)} \frac{1}{I_{0Nd} - \left[1 + exp\left(\frac{\hbar\omega}{k_B T}\right)\right]^p - \left(-exp\left(\frac{\Delta E_2}{k_B T}\right)\right)} \qquad (1.34)$$

This temperature dependence of this intensity ratio involves 3 mechanisms:[156]
(i) The luminescence thermal quenching with a cross-over point, where I_{0Cr} and ΔE_1 represent the initial intensity of the Cr^{3+} emission bands at low temperature, and the energy difference between the bottom of the excited state parabola and the energy of the crossing point of the excited and ground state parabolas.
(ii) The temperature dependence of the $^4F_{3/2}$ luminescence of Nd^{3+}, where I_{0Nd} is the initial intensity of Nd^{3+} emission band corresponding to the $^4F_{3/2} \rightarrow {}^4I_{9/2}$ transition, whose intensity decreased as the temperature increased due to multiphonon depopulation processes, where $\hbar\omega$ and p represent the maximum phonon energy of the host material and the number of phonons involved in the process, respectively.
(iii) The thermal depopulation towards the $^4F_{5/2}$ state of Nd^{3+}, lying ΔE_2=1000 cm^{-1} above the $^4F_{3/2}$ state.
The temperature dependence of the S_{rel} for each Nd^{3+}/transition metal is presented in Figure 1.14, whereas the maximum sensitivity is included in Table 1.1, together with other parameters, such as the excitation wavelength per each case and the emissions used to determine their

performance. A maximum S_{rel} of 3.49% K^{-1} was achieved for this class of thermometer, being higher than the one that can be achieved in Nd^{3+}/Yb^{3+} and single Nd^{3+} doped luminescent thermometers.[156] In fact, this value of sensitivity is approximately 3 times higher when compared to the sensitivity obtained by investigating the intensity ratio of TCL2 or TCL3 in single Nd^{3+} doped in YAG. The reason behind this difference is due to the efficiency $Cr^{3+} \rightarrow Nd^{3+}$ ET.[156]

This class of luminescent thermometers constituted by the combination of the emissions arising from Nd^{3+} and a transition metal, definitely exhibit higher thermal performances, especially in the case of Nd^{3+}/Ti^{4+} and Nd^{3+}/Cr^{3+}, thus their potential application as temperature sensors is attractive. Despite this, as can be observed in Figure 1.14 and in Table 1.1, their maximum S_{rel} are either achieved at low temperatures (Nd^{3+}/Cr^{3+}) or high temperatures (Nd^{3+}/Ti^{4+}). When restricted to physiological range of temperatures, yet again, the value of S_{rel} (for Nd^{3+}/Ti^{4+} is ~3.3% K^{-1},[185] for example) is similar to the one that can be achieved with Nd^{3+}/Yb^{3+} luminescent thermometers. It should be emphasized as well, that these systems are quite complex, and in depth studies to understand the effect of the factors that govern the temperature sensing properties, such as the electron-phonon interaction, the crystal field strength and the physical processes responsible for temperature susceptibility, are highly needed.[185] Last, these materials are excited with UV and VIS light, inducing autofluorescence of the biological tissue, phototoxicity and limited penetration depths when applied in biological tissues.[91] Thus, novel strategies to excite these materials with NIR light sources, generating emissions in the biological windows regimes, need to be developed.

2.3. Eu^{3+} doped luminescent thermometers operating in the I-BW

The application of Eu^{3+} doped materials as luminescent thermometers operating in the I-BW, is based on their emissions located in the deep red regime, around 710 nm, assigned to $^5D_0 \rightarrow {}^7F_4$ transition. These thermometers are rarely reported in the literature, in fact in this regime we could identify only one (Eu^{3+}:Y_2O_3),[187] besides the other two reported in combination with Nd^{3+} emissions (see Section 2.2.1). Eu^{3+}:Y_2O_3 thermometer offer the possibility of predicting the calibration curve of the thermometric parameter independently of the medium in which this thermometer operates, developing in this way primary thermometers. Primary thermometers are defined as thermometers where the temperature is determined based on the knowledge of thermodynamic laws and quantities.[219] In general, to extract the thermometric parameter, the calibration requires independent measurement of the temperature through a thermocouple or an IR camera. But when this thermometer operates in different medium, a new calibration procedure is required. Hence, primary thermometers guarantee a single calibration procedure that is medium-free.

For this Eu^{3+}:Y_2O_3 material, the thermometric parameter, Δ, is determined from the ratio between the emission intensity $^5D_0 \rightarrow {}^7F_4$, when the $^5D_0$ state is excited through the $^7F_2$ and the $^7F_0$, for the physiological range or through the $^7F_1$ and $^7F_0$, for low temperature (down to 180 K).[187] Considering the physiological range as a particular region of interest for biomedical application, Δ is defined as:

$$\Delta = \frac{I_{23}\,(^7F_2)}{I_{23}\,(^7F_0)} = \frac{p\,(^7F_2)}{p\,(^7F_0)} \frac{W_{31}\,(^7F_2)}{W_{31}\,(^7F_0)} \qquad (1.35)$$

where I_{23} is the intensity of the transition from level 3 to level 2 at the steady state regime, p stands for the Boltzmann population factor and W_{31} the absorption rate from state 1 to state 3 (see Figure 1.16 (a)).

Δ is determined by measuring the integrated areas under the emission curves of $^5D_0 \rightarrow {}^7F_4$, excited resonantly through the $^7F_2$ and the $^7F_0$ (Equation 1.36), considering that the excitations towards $^5D_0$ are the same and are dielectric in nature, and the emitting level $^5D_0$ and the ground state $^7F_0$ are nondegenerate:[187]

$$\Delta = \frac{S\,(^5D_0 \rightarrow {}^7F_2)}{S\,(^5D_0 \rightarrow {}^7F_0)} \exp\left(-\frac{\Delta E}{k_B T}\right) \qquad (1.36)$$

where, $S\,(^5D_0 \rightarrow {}^7F_2)$ and $S\,(^5D_0 \rightarrow {}^7F_0)$ represent the area under the red emissions, excited through $^7F_2$ and $^7F_0$, respectively. ΔE stands for the difference among ΔE ($^7F_2$) and ΔE ($^7F_0$). For the performance over the physiological range, the theoretical expression of Δ is:[187]

$$\Delta = 51\ exp\left(-\frac{875}{k_B T}\right) \qquad (1.37)$$

where the $\Delta E = 875$ cm^{-1} is determined from the energy difference between the excitation peak and the emission peak $^5D_0 \rightarrow {}^7F_2$, and the pre-exponential factor 51 is extracted from the values of the areas. The experimental values of Δ are extracted from the integrated intensities of the $^5D_0 \rightarrow {}^7F_4$ transition.[187]

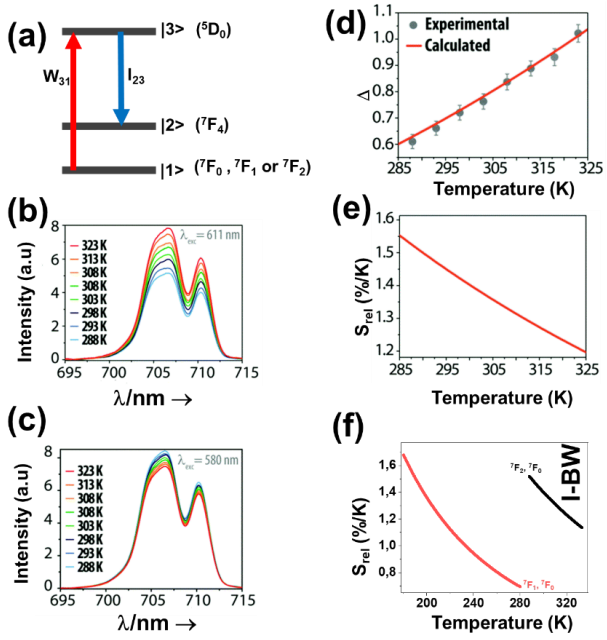

Figure 1.16. (a) Energy level diagram used for stimulating the energy levels of Eu^{3+} ion involved in thermometer operation. Deep red emission spectrum of Eu^{3+}:Y_2O_3 nanocrystals excited at: (b) 611 nm, (c) 580 nm. (d) Thermometric parameter for the physiological range. Points are the experimental values of the Δ parameter obtained from the spectra in (b) and (c) after being corrected for the respective excitation intensity, whereas the line is the calculated curve obtained from Equation 1.38. The error bars in the thermometric parameter are calculated at each temperature. (e) Relative sensitivity in the physiological range. Reproduced with permission.[187] Copyright The Royal Society of Chemistry 2016. (f) The variation of S_{rel} of Eu^{3+} doped nanothermometers operating in the I-BW. Red line is computed using Equation 1.36 and the black line using Equation 1.37.

The thermal sensing was evaluated as a function of the excitation wavelength applied. Hence, two excitation wavelengths were tested, 611 nm and 580 nm. The red emission observed as a function of these two wavelengths, displayed different behavior with the increase of the temperature. For the 611 nm, the intensity increased due to due to the increase of the thermal population of Stark levels of the $^7F_2$ (see Figure 1.16 (b)), whereas for the 580 nm, the opposite is detected, due to the thermal depopulation of the $^7F_0$ ground state (see Figure 1.16 (c)).

Besides the different excitation wavelength applied, the thermometric parameter exhibit the same dependence. Moreover, these experimental values are in excellent agreement with those obtained from the theoretical ones from Equation 1.37, over the physiological range of temperature (see Figure 1.16 (d)), displaying an error of 3%,[187] demonstrating the successful application of Eu^{3+}:Y_2O_3 nanocrystals as a primary thermometer. In terms of S_{rel}, is in the order of 1.55% K^{-1} at the physiological range (see Figure 1.16 (e)). Higher values of the thermal

sensitivity (~1.7% K^{-1} at 180 K) were obtained when considering the performance from the red emission excited through the $^7F_1$ and $^7F_0$. Also for this case, the principles of the primary thermometer can be applied, with a maximum error down to 2%.[187] It should be emphasized that in this case, the thermometric parameter is defined as:

$$\Delta = \left[\frac{n^3\left(\frac{n^2+2}{3}\right)}{n^5}\right]\frac{S\,(^5D_0 \rightarrow {}^7F_1)}{S\,(^5D_0 \rightarrow {}^7F_0)}\exp\left(-\frac{\Delta E}{k_B T}\right) \qquad (1.38)$$

where n stands for the refractive index of the host were Eu^{3+} ions are embedded and is comes from the Lorentz local field correction for electric dipole and magnetic dipole absorption rates (W_{31}) when changing from absorption to spontaneous emission rates. If we compare the performance at the physiological range, the red emission excited through the $^7F_1$ and $^7F_0$, has a performance approximately 2.4 lower compared to the red emission excited through the $^7F_2$ and $^7F_0$ (see Figure 1.16 (f)). If we compare the performance of this single Eu^{3+} nanothermometer with the dual emitting Nd^{3+}/Eu^{3+}, based as well in the red emission of Eu^{3+}, the later ones exhibit better performance is the physiological range (see Table 1.1), illuminated as well in the visible, however, an absolute conclusion cannot be extracted due to the different hosts applied.

Overall, this methodology, provides the ability of predicting the thermometric performance, gives a high reproducibility over the range of 97%, with high thermometric performance. In addition is also versatile, since also Eu^{3+}:Y_2O_3 microcrystals are operative with the same outcomes as the corresponding nanocrystals.[187] One thing that may be regarded as a limitation could be the fact that these materials are illuminated in the visible, which may hamper their penetration depths in biological tissues.

2.4. Er^{3+} doped luminescent thermometers operating in the I-BW

The application of erbium (Er^{3+}) doped materials as luminescent nanothermometers operating in the I-BW are mainly assigned to the presence of the red (~660 nm) and NIR (800 nm and 850 nm) emissions, either in single doped or in combination of these emission lines with other dopants, including other lanthanide ions or transition metals.

2.4.1. Single Er^{3+} doped luminescent thermometers operating in the I-BW

Single Er^{3+} doped materials as nanothermometers in the I-BW are based on the emissions located in the red and NIR. Upon irradiation in the visible or NIR, these emission lines are generated, governed by the cross relaxation (hereafter CR) process ($^4F_{7/2}$, $^4F_{9/2}$) → ($^4F_{9/2}$, $^4F_{11/2}$) (see Figure 17 (a)).[188] Shortly, an Er^{3+} ion via absorption of two photons, is excited from the ground state to the $^4I_{9/2}$ level and further to the $^4F_{7/2}$ excited level. From this level, successive non-radiative decays, leads to the population of the $^4I_{9/2}$ and $^4F_{9/2}$ levels. From these levels, relaxing back to the ground state $^4I_{15/2}$, emissions lying at the red (654 nm) and at the NIR (806 nm), are generated (see Figure 1.17 (a)).[188]

The performance of these thermometers is based on the temperature dependence of the electronic population of the different Stark sublevels located in the red region, intensity ratio of emissions located in the NIR or the ratio between the red and NIR emissions (see Table 1.1). Among these, the performance extracted from the intensity ratio of the NIR emissions represents a promising strategy since demonstrates the highest thermometric performance among them. Hence, Er^{3+} ions embedded in strontium barium niobate (SBN) glass ceramic was investigated as a thermometer in a wide range of temperatures (300-700 K), by studying the ratio in the NIR between the 800 nm and 850 nm emissions, attributed to the $^2H_{11/2} \rightarrow {}^4I_{13/2}$ and $^4S_{3/2} \rightarrow {}^4I_{13/2}$ electronic transitions, respectively.[162] The temperature dependence of this ratio was fitted to the traditional FIR equation (Equation 1.9), achieving a maximum S_{rel} and δT of 1.39% K^{-1} and 0.36 K, at the lowest temperature under investigation. It should be noted here that the authors did not reported these two parameters, but they provided an experimental value of the energy gap (872.3 cm^{-1}),[162] between the thermally coupled $^2H_{11/2}$ and $^4S_{3/2}$ levels, which allowed us to determine their theoretical performance.Regardless of the performance of this thermometer, the excitation wavelength (532 nm) located in the visible region,[162] may hamper their application.

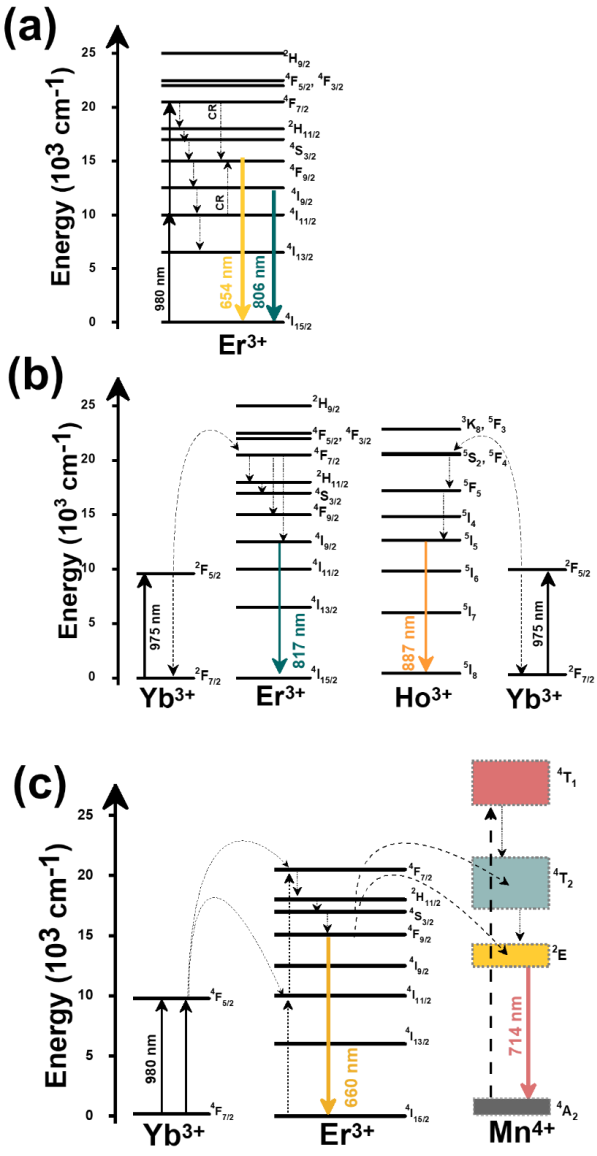

Figure 1.17. Mechanism of the generation of the emission lines of: (a) single Er^{3+} and (b) Er^{3+}/ Ho^{3+}/Yb^{3+} and (c) Er^{3+}/ Mn^{4+}/Yb^{3+} materials.

The performance based on the ratio between the red and NIR emissions is higher compared to that of the Stark sublevels located in the red region.
A typical case is the incorporation of Er^{3+} ion within an active core@inert shell $NaErF_4$@$NaGdF_4$ host.[188] The emissions of these nanocrystals, located at 654 nm and 806 nm, are generated from excitation at either 980 or 1530 nm wavelength.[188] These two emissions are NTCLs, and as expected, the performance was extracted by fitting the intensity ratio in a second order polynomial function, as presented in Equation 1.27. For the fitting assuming TCLs from the emission arising from different Stark sublevel red emissions (654 nm and 660 nm) after excitation with 800 nm light, the performance was up to 9 times lower compared to the performance of thermometers based on the NIR emissions and mixed red, and NIR emissions, respectively (see Table 1.1). The

reason for the poor performance of these thermometers is the relatively low ΔE between the different Stark sublevels.[189, 190] Moreover, the authors, fitted the intensity ratio to a function as presented in Equation 1.14, suffering in this way from the overlap of two emission signals, low discriminability and large detection deviation owing to the requirement of a small thermally coupled states energy gap to realize thermal repopulation.[190] The effect of the small energy gap and the accounting for the overlapping constant parameter (the D constant in Equation 1.14) over S_{rel} of this thermometer in the wide range of temperature from 200 K to 1300 K, are presented in Figure 1.18.

As can be observed, S_{rel} is almost constant with the change of the temperature and the value is among the lowest for all types of Er^{3+} doped thermometers. Regardless of the low performance, is worth mentioning here the idea behind heavily concentrated core@shell@shell Tm^{3+}:$NaErF_4$@Yb^{3+}:$NaYF_4$@Nd^{3+}:$NaYbF_4$, in which Tm^{3+}-mediated transient energy trapping coupled to Nd^{3+}/Yb^{3+} cascade-sensitization is used to efficiently trigger single-band red emission of Er^{3+}, after careful optimization of the doping composition.[189]

2.4.2. Er^{3+}/Yb^{3+} codoped luminescent thermometers operating in the I-BW

Er^{3+} materials codoped with Yb^{3+} as sensitizer, are the most experienced class of Er^{3+} thermometers operating in the I-BW. Yb^{3+} ions, due to the absorption of NIR excitation wavelength, allow for development of NIR-to-NIR based thermometers, besides improving the signal intensity of Er^{3+} emissions.[192-194] Er^{3+}/Yb^{3+} can be applied for luminescent thermometry based on the emissions of Er^{3+}, or in combination of these emissions with other emissions arising from other Ln^{3+} ions or transition metals (see Table 1.1).

A effective strategy is the combination of Er^{3+} and Ho^{3+} emissions in the NIR region, in the presence of Yb^{3+} as sensitizer, doping hexagonal $NaLuF_4$ microcrystals.[192] The emission bands used to determine the thermometric performance of these particles are located at 887 nm and 817 nm, assigned to $^5I_6 \rightarrow {}^5I_8$ of Ho^{3+} and $^4S_{3/2} \rightarrow {}^4I_{13/2}$ of Er^{3+}, respectively.[192] The mechanism of generation of these emissions is presented in Figure 1.17 (b). Shortly, in Er^{3+}, Ho^{3+}, Yb^{3+}:$NaLuF_4$ system, Yb^{3+} absorbs the 975 nm excitation source and transfers the absorbed energy to the emitters Ho^{3+} and Er^{3+}, exciting their excited states via ET mechanisms.[192] From these excited states ($^4F_{7/2}$ for Er^{3+} and $^5S_2$, $^5F_4$ of Ho^{3+}), via non-radiative decays the electronic levels of $^4F_{9/2}$ (Er^{3+}) and $^5I_5$ (Ho^{3+}), are populated and from their radiative decay back to the ground states $^4I_{15/2}$ (Er^{3+}) and $^5I_8$ (Ho^{3+}), the corresponding 817 nm and 887 nm emission lines are generated.[192] Since these two emission lines are arising from different emitting ions, the intensity ratio was fitted to NTCLs model, in the form a second order polynomial function of the form of Equation 1.27. The maximum S_{rel} was in the range of 1.73% K^{-1} at room temperature.[192]

When codoped Er^{3+},Yb^{3+} materials, were investigated alone, without the addition of other ions, based on the emissions of Er^{3+}, the performance is decreased approximately 2 times (see Table 1.1). Two typical examples exploring this strategy, include codoped Er^{3+},Yb^{3+} in ZrO_2,[194] and YF_3.[193] In these cases, the thermal sensing properties were extracted from the emissions located at the red (Er^{3+},Yb^{3+}:ZrO_2) and NIR (Er^{3+},Yb^{3+}:YF_3) regimes, by exciting the particles with NIR wavelength. Here, it is important to note that the performance of codoped Er^{3+},Yb^{3+} in ZrO_2 nanoparticles is derived by a so-called “valley-to-peak” method (VPR).[194]

For emissions that originate from TCLs, if the emissions are close enough, they will overlap and as a consequence, a valley will be formed.[194, 220] As the temperature increases, the linewidth of each emission peak broadens monotonously and, the valley intensity formed by this emission peaks, overlaps also.[220] The VPR is predicted to be a monotonic function of the temperature and is expressed as:[194, 220]

$$VPR = a(T - T_0) + b \qquad (1.39)$$

where a is the slope of the linear fitting, b is a constant, T_0 and T represent the initial and final temperature. S_{rel}, described as the changing rate of the VPR with temperature, is expressed as:[194, 220]

$$S_{rel} = \frac{1}{VPR}\frac{dVPR}{dT} \qquad (1.40)$$

The temperature evolution of S_{rel}, estimated from Equation 1.40, is presented in Figure 1.18. S_{rel} estimated from this methodology, displays a clear tendency of decrease as the temperature is increased.

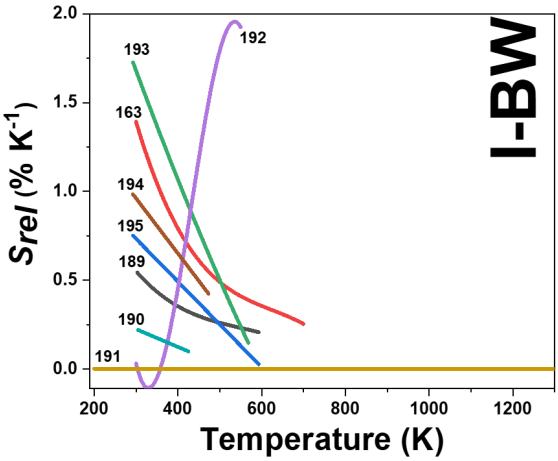

Figure 1.18. Temperature dependence of S_{rel} of Er^{3+} doped luminescent thermometers, operating in the I-BW. Numbers represent the references for each thermometer.

Compared to Er^{3+}, Ho^{3+}, Yb^{3+}:$NaLuF_4$ thermometers, these particles have a performance two times lower, underlying that the combination of the erbium and other lanthanide emission, in the presence of Yb^{3+} as sensitizer is a promising strategy for thermometry. An additional strategy towards better thermal sensing properties compared to the above, is the codoping of Er^{3+} materials with transition metals, such as manganese in the form of Mn^{4+}. Manganese ions generally displays red to NIR photoluminescence assigned to spin forbidden $^2E \rightarrow {}^4A_2$ transition under the excitation of UV or blue light owing to their high effective positive charge and the influence of a strong local crystal-field.[221, 222] Upon proper modification of the crystal-field environment, the spectral position of these ions can be tuned from 620 nm to 723 nm.[223, 224] Hence, since the optical properties of transition metals are highly influence from the medium and often drastically reduces, this makes them highly desirable in nanothermometry, as a codoped material with Ln^{3+} ions, in which the later once act as a reference probe.[156, 185, 186, 191] Contrary to the case of Nd^{3+} codoped with transition metal materials, in which the excitation source was an UV or VIS light (see Section 2.2.3), here, the incorporation of Yb^{3+} as sensitizer has allowed for excitation with excitation sources located at the I-BW and, as well, emissions in the I-BW, overcoming the problems related to the photoxicity and limited penetration depth exhibited by UV and VIS light.

Triple doped $Er^{3+}/Mn^{4+}/Yb^{3+}$:YAP, were investigated as thermal sensors in this regime over the temperature range from 300-550 K. Their performance is based on the intensity ratio of the NTCLs of 714 nm and 660 nm emissions, assigned to the electronic transitions of $^2E \rightarrow {}^4A_2$ and $^4F_{9/2} \rightarrow {}^4I_{15/2}$ of Mn^{4+} and Er^{3+}, respectively.[189] The generation of these emission bands is presented in Figure 1.17 (c). Yb^{3+} absorbs the NIR 980 nm excitation source, and via two photon assisted processes, the excited energy levels ($^4F_{7/2}$ and $^4I_{11/2}$) of Er^{3+} are populated. By decaying non-radiatively, the $^4F_{9/2}$ state is populated, which relaxing back to the $^4I_{15/2}$ ground state, generates the red emission at 660 nm. Via two ET processes, from the $^4F_{7/2}$ and $^4F_{9/2}$ levels of Er^{3+}, $^4T_2$ and ^2E levels of Mn^{4+}, are populated. The ^2E energy level can relax back to the $^4A_2$ ground state generating the emission centered at 714 nm.[191] To extract the dependence of the intensity ratio and the thermometric performance from the temperature, the same models (Equation 1.34) as in

the case of Nd^{3+} codoped with transition metals, were applied. The maximum S_{rel} obtained was 1.95% K^{-1} at 530 K.[191] Despite the relative high thermal sensing properties, it should be emphasized that this value is recorded at high temperature. The same was observed also for Nd^{3+} codoped with transition metals (see Section 2.2.3), except that the highest relative thermal sensitivities were obtained at cryogenic temperatures. At room temperature, the performance of these nanoparticles is highly reduced, and reaches value ~0.003% K^{-1}.[191] The overall temperature dependence of S_{rel} of this material is depicted in Figure 18, together with all other Er^{3+} doped thermometers operating in the I-BW.

To conclude with the section of Er^{3+} doped thermometers operating in the I-BW, the most promising strategy for enhanced thermometric performance involve the dual doping emitting nanoparticles, either with other Ln^{3+} ions or with transition metals. Concerning the choice between the red or NIR emissions, the best choice are the NIR emissions, not only because of the relatively better performance, but also because their location of the wavelength, which ensures better penetration depths.

2.5. Ho^{3+} doped luminescent thermometers operating in the I-BW

Temperature sensors based on holmium (Ho^{3+}) as an activator operating in the I-BW are very limited. The reason for that is because mainly Ho^{3+} is codoped with Tm^{3+}, since this combination is relatively high sensitive to the temperature changes in the I-BW (see section 2.1.3) and III-BW (see section 6.1).

Typical examples involving Ho^{3+} as the main emitting ion, incorporate Yb^{3+} as a sensitizer to enhance the red emission of Ho^{3+}, lying around 660 nm and attributed to the $^5F_5 \rightarrow {}^5I_8$ electronic transition. Typical hosts in which codoped Ho^{3+}/Yb^{3+} are used are the monoclinic $KLu(WO_4)_2$ nanocrystals,[195] and tetragonal $Ba_2In_2O_5$ particles.[196] The red emissions, located at ~650 nm and ~660 nm, were generated after exciting them with 980 nm excitation source. By means of ground state absorption (GSA), Yb^{3+} ions absorb the radiation from the excitation source, exciting their electrons from the $^2F_{7/2}$ ground state to the $^2F_{5/2}$ excited state. Via two ET processes, the electrons are promoted to the $^5I_6$ and $^5S_2$, $^5F_4$ energy levels of Ho^{3+} ion. A nonradiative relaxation from the $^5S_2$, $^5F_4$ energy levels populates the $^5F_5$, from which the radiative process generates the red emissions with two main peaks centered at ~650 nm and ~660 nm (see Figure 1.19 (a)). A second path to explain the population of the $^5F_5$ energy level can also be postulated from a nonradiative process after the first ET transfer process, populating the $^5I_7$ energy level of the Ho^{3+} ion. The second ET from the $^2F_{7/2}$ energy level of Yb^{3+} promotes these electrons to the $^5F_5$ energy level of Ho^{3+}.[195]

From both these hosts, the thermometric performance was evaluated by using the model based on TCLs. Nevertheless, for the case of $KLu(WO_4)_2$ host, the authors considered also the overlapping factor for emission peaks located very close to each other, such as the case of red emissions of Ho^{3+}.[195] Hence, for Ho^{3+}/Yb^{3+}:$KLu(WO_4)_2$ nanocrystals, Equation 1.14 was used to extract the thermal sensing properties, whereas for the case of Ho^{3+}/Yb^{3+}:$Ba_2In_2O_5$ particles, the simple form of FIR equation (Equation 1.9) is applied, which may lead to an overestimation of the performance. Comparing the performance of these particles at room temperature, Ho^{3+}/Yb^{3+}:$KLu(WO_4)_2$ nanoparticles display thermal sensing properties of approximately four times higher compared to the Ho^{3+}/Yb^{3+}:$Ba_2In_2O_5$ particles (see Table 1.1).

Nevertheless, the performance of Ho^{3+}/Yb^{3+}:$KLu(WO_4)_2$ nanoparticles, is lower (~3 times) compared to the performance of $Ho^{3+}/Mn^{4+}/Yb^{3+}$:YAP nanoparticles. The red emission of Ho^{3+} was combined with the 714 nm emission arising from Mn^{4+}, generated after NIR excitation, ensured from the presence of Yb^{3+}. Over the range of 300 K- 550 K, the maximum S_{rel} was achieved at the 530 K.[191] The variation of S_{rel} over the all range is depicted in Figure 1.19 (b). As can be observed, at the physiological range, the thermometric performance of this material, does not differ much from Ho^{3+}/Yb^{3+}:$KLu(WO_4)_2$ nanoparticles. In fact, strictly speaking, the performance of $Ho^{3+}/Mn^{4+}/Yb^{3+}$:YAP nanoparticles at room temperature, is slightly lower compared to the Ho^{3+}/Yb^{3+}:$KLu(WO_4)_2$ nanoparticles.

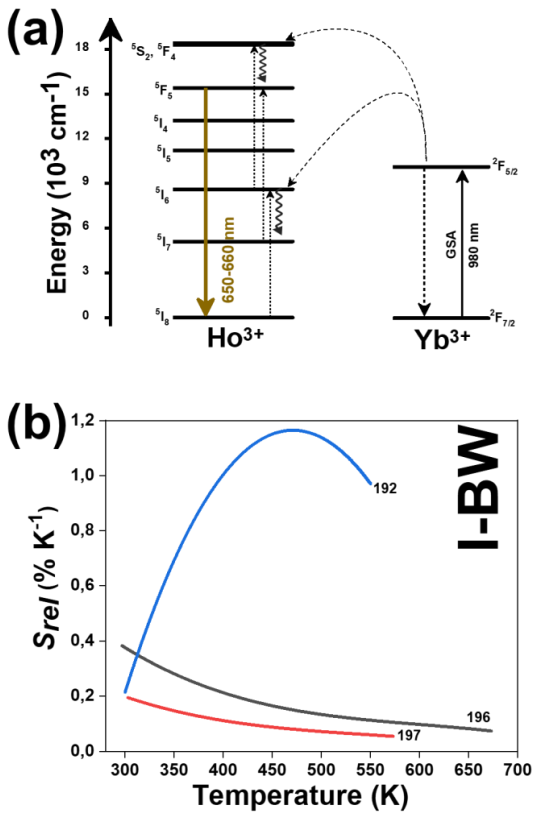

Figure 1.19. (a) Mechanism of the generation of the emission lines of Ho^{3+}/Yb^{3+} materials and (b) Temperature dependence of S_{rel} of Ho^{3+} doped luminescent thermometers, operating in the I-BW. Numbers represent the references for each thermometer.

3. Lanthanide doped luminescent nanothermometers operating in the I and II-BW simultaneously

The emissions of Ln^{3+} ions, upon proper excitation, could be located in a wide range of the electromagnetic spectrum. Besides lying in each of the four biological window regime, the emissions of lanthanide ions used for thermometry, can also be found in two different biological windows. Hence, here, we focus on the luminescent thermometers that use emissions which are placed in the I-BW and the II-BWs. Although the number of publications that report luminescent thermometers working in this mixed region is reduced, the most representative examples are assigned to Nd^{3+} doped materials due to the emissions located at around 850 nm and 1050 nm, covering simultaneously the I-BW and the II-BW by the same material.

3.1. Nd^{3+} doped luminescent thermometers operating in the I-BW and II-BW simultaneously

Nd^{3+} doped materials operating in the I- and II-BWs simultaneously, can be classified in single emitting Nd^{3+} luminescent thermometers, dual emitting luminescent thermometers in combination with other Ln^{3+} ions, and dual emitting luminescent thermometers in combination with transition metals.

Alkali earth fluorides such as CaF_2,[225] and SrF_2[164] have been studied as hosts for single emitting Nd^{3+} luminescent thermometers, due to their low phonon energies that reduce the probability of non-radiative relaxing processes to happen, favoring in this way the luminescence efficiency,[226]

and because they are biocompatible and nanoparticles with sizes below 10 nm can be produced, which makes them attractive for biomedical applications.[164,225] These water dispersible nanocrystals were prepared by hydrothermal synthesis,[227] in which impurities of Gd^{3+} were introduced to enhance the emissions of Nd^{3+}.[164,225]

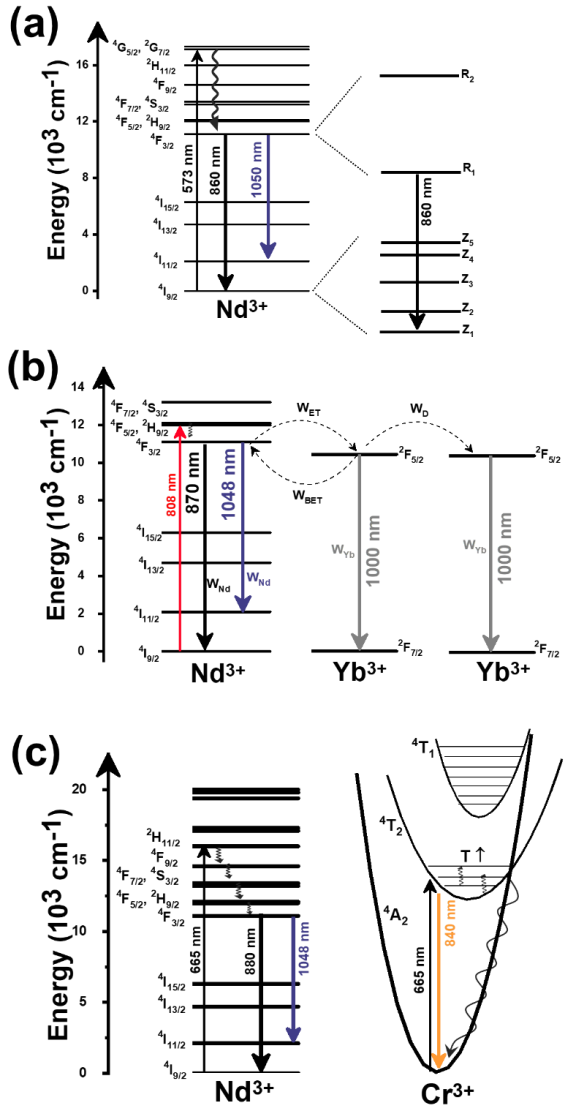

Figure 1.20. Mechanism of the generation of the emission lines of: (a) single Nd^{3+} excited with 573 nm light, (b) dual doped Nd^{3+}/Yb^{3+} excited with 808 nm, and (c) dual doped Nd^{3+}/Cr^{3+} excited with 665 nm, operating in simultaneously on I-BW and II-BW.

Upon excitation at 573 nm, these nanocrystals generate emissions at ~850 nm (I-BW) and ~1050 nm (II-BW), attributed to the $^4F_{3/2} \rightarrow {}^4I_{9/2}$ and $^4F_{3/2} \rightarrow {}^4I_{11/2}$ transitions of Nd^{3+}, respectively.[164, 225] Upon excitation at this wavelength, the $^4G_{5/2}$, $^4G_{7/2}$ energy levels of Nd^{3+} are populated. Then, a non-radiative decay process takes place populating the $^4F_{3/2}$ state. From this energy level, a radiative decay to $^4I_{11/2}$, generates the emission located in the II-BW (see Figure 1.20 (a)). Concerning the emission in the I-BW, from the lower lying Stark sublevels of $^4F_{3/2}$ (R_1 in Figure

1.20 (a)), a radiative decay to the lower lying Stark sublevel of the ground state $^4I_{9/2}$ (Z_1 in Figure 1.20 (a)) generates this emission.

The performance of these luminescent thermometers was based on the fluorescence intensity ratio between the 1050 nm and 850 nm emissions over the physiological range of temperatures, using Equation 1.9. The results, summarized in Table 1.2, show that the highest S_{rel} is assigned to the SrF_2 host with a value of 0.50% K^{-1} and δT of 1.2 K at room temperature.[164] The difference encountered in the thermometric performance of these two materials can be assigned to the lower phonon energy of SrF_2 (366 cm^{-1}) compared to CaF_2 (466 cm^{-1}).[228, 229] Thus, materials with low phonon energies seems to maximize S_{rel} of the luminescence thermometers developed with them. Nevertheless, it should be taken into consideration that the excitation wavelength used for these luminescent thermometers is not located in the biological windows , instead it is located in the VIS, for which the absorption and scattering in the biological tissues is high, resulting in a limited penetration depth, not allowing deep-tissue imaging.[91] Hence, this limitation should be surpassed by employing other ions that are able to absorb excitation sources located within the BWs.

An interesting alternative, was proposed by Marciniak *et al.* through the preparation of dual emitting luminescent thermometers based Nd^{3+} and Yb^{3+} codoped $LiLaP_4O_{12}$, in which, under 808 nm NIR excitation, Nd^{3+} acts as both as sensitizer and acceptor while Yb^{3+} acts only as an acceptor.[207] The reason after this selection is because Nd^{3+} absorption cross section at 800 nm is higher than the one of Yb^{3+} at 980 nm, and the water absorption at ~800 nm is around 25 times lower than that at ~980 nm, overcoming in this way also the overheating problem displayed by the 980 nm excitation.[207] Upon 808 nm excitation, Nd^{3+} absorbs this energy and excites its electrons from the $^4I_{9/2}$ ground state to the $^4F_{5/2}$ excited state. Via a non-radiative process, the $^4F_{3/2}$ state is populated. From this state, two radiative processes towards the $^4I_{9/2}$ and $^4I_{11/2}$ levels, generate the Nd^{3+} emissions at 870 nm and 1060 nm, respectively (see Figure 1.20 (b)). From the $^4F_{3/2}$ state of Nd^{3+}, also an ET process, with W_{ET} probability, can populate the $^2F_{5/2}$ state of Yb^{3+}. A radiative decay from this state, back to the $^2F_{7/2}$ ground state, allows for generation of the 1000 nm emission band of Yb^{3+}.[207]

The thermometric performance of these nanocrystals was tested for the intensity ratio between the emissions at 870 nm (Nd^{3+}) and 1000 nm (Yb^{3+}), as function of the temperature over the range 93-663 K, and as a function of the concentration of Yb^{3+} ions (see Figure 1.21 (a)).[207]

The thermometric performance of these nanocrystals is influenced by three processes: (i) with the increase of the temperature, the electronic population of the Stark sublevels of the $^2F_{5/2}$ manifold of Yb^{3+} increase gradually, leading to a BET process, with probability W_{BET}, towards the $^4F_{3/2}$ state of Nd^{3+} (see Figure 1.20 (b)); (ii) by increasing the concentration of Yb^{3+}, the average distance between these ions decreases, and consequently, the energy diffusion between Nd^{3+} and Yb^{3+} ions, with probability W_D, and among Yb^{3+} ions (W^{Yb}) increases; and (iii) the energy difference between the Nd^{3+} and Yb^{3+} that controls the ET processes between $^4F_{3/2}$ state of Nd^{3+} and the $^2F_{5/2}$ level of Yb^{3+}, with probability W_{ET}, is affected by the changes of temperature and the concentration of Yb^{3+}.[207] Hence, the intensity ratio between these two nonresonant energy matching ions, extracted from the phonon assisted model of energy transfer described by Miyakawa and Dexter,[230] was related to these processes by the following equation:[207]

$$\Delta = \frac{W_{BET} - W_D - W^{Yb}}{W_{ET}} \qquad (1.41)$$

From Equation 1.41, it can be seen that as the doping level of Yb^{3+} increases, the effectiveness of the energy diffusion among the Yb^{3+} network gradually increases, while the impact of the back energy transfer process towards Nd^{3+} decreases, leading to changes in Δ.[207] S_{rel} of these luminescent thermometers is, however, very low, with a maximum of ~0.3% K^{-1} in the physiological range of temperatures (the full variation of the S_{rel} in the interval of temperatures analyzed is presented in Figure 1.21 (b)). The highest concentration of Yb^{3+} ions, achieved the best thermometric performance (see Figure 1.21 (a)), probably because the decrease in the average distance among Nd^{3+}-Yb^{3+} dopants, facilitates the energy diffusion.[207]

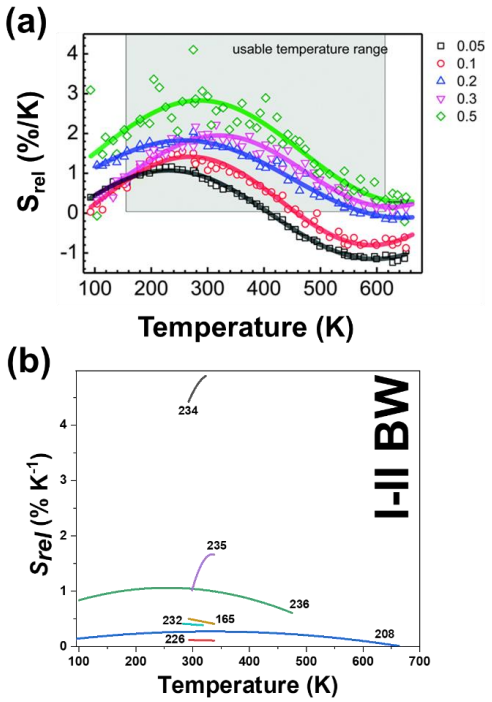

Figure 1.21. (a) S_{rel} of Nd^{3+} and Yb^{3+} doped $LiLaP_4O_{12}$ as a function of Yb^{3+} concentration. Adapted with permission.[207] Copyright from Owner Societies 2015. (b) Temperature dependence of S_{rel} of lanthanide doped luminescent thermometers operating in the I-BW and II-BWs, simultaneously. Numbers correspond to references.

The same strategy was followed for the case of two different active core@active shell nanostructures, one having the core doped with Nd^{3+} ions and the shell with Yb^{3+} ions (Nd^{3+}:LaF_3@Yb^{3+}:LaF_3) and the other constituted by a Yb^{3+} doped core and a Nd^{3+} doped shell (Yb^{3+}:LaF_3@Nd^{3+}:LaF_3).[231] The performance of these two different core@shell structures was also compared with the corresponding nanoparticles containing the two ions in the same layer, revealing a four-fold enhancement of S_{rel}.[231] In addition, the core@shell nanocrystals displayed also an enhanced intensity of the emissions, attributed to the self-quenching effect originating from non-radiative mechanisms such as cross-relaxation, energy migration, and even to energy trap processes occurring between the emitting ions and the OH^- radicals present and the surface of the nanoparticles when the doping ions are located in the same layer.[231] These type of materials, however, where more interesting for the emissions generated by Nd^{3+} in the II-BW (1060 nm and 1350 nm), hence, the will be mentioned again in Section 4.2.

When combining the emissions arising from Nd^{3+} and a transition metal, such as Cr^{3+}, a substantial increase on the thermal sensing is observed (see Table 1.2). The emission of Nd^{3+} located at ~1050 nm in the II-BW, was combined with the emission at 810 nm of Cr^{3+}in the I-BW, both ions being embedded in $LiLaP_4O_{12}$.[233] These emission bands were generated after exciting the nanoparticles at 655 nm, in the lower limit of the I-BW, that allows exciting Cr^{3+} and Nd^{3+} at the same time.[233] To describe the generation of the emission band of Cr^{3+}, a low crystal field assumption for the low symmetry host used, was applied by the authors.[233] Electrons of Cr^{3+} are excited after illumination with the 655 nm light from the $^4A_2$ fundamental state to the $^4T_2$ excited state as can be seen in Figure 1.20 (c). By relaxing back to the $^4A_2$ state, the broad emission line centered at ~810 nm is generated. When temperature increases, the electronic population of the higher vibrational levels of the $^4T_2$ state also increases, and the Cr^{3+} emission can be quenched via non-radiative processes as soon as the thermally excited electrons reach the crossing point

between the $^4T_2$ energy level parabola and the $^4A_1$ energy level parabola (see Figure 1.20 (c)).[233] At the same time, the electrons of Nd^{3+} are pumped from the $^4I_{9/2}$ ground state to the $^2H_{11/2}$ excited state. Then, a non-radiative relaxation to the $^4F_{3/2}$ state happens, from which the 880 nm ($^4F_{3/2} \rightarrow {}^4F_{9/2}$) and the ~1050 nm ($^4F_{3/2} \rightarrow {}^4I_{11/2}$) emissions are produced.[233] The intensity of the emission of Nd^{3+} ion is barely influenced by temperature, so it can be used as reference probe.[233]

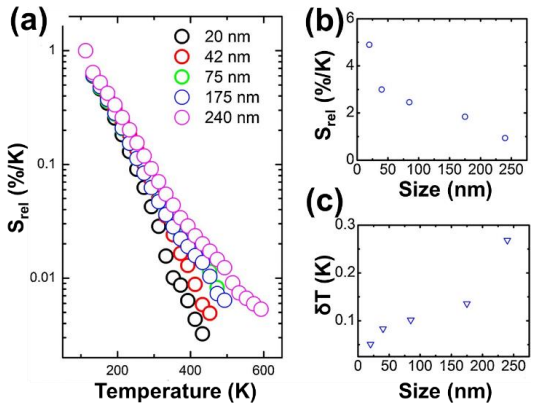

Figure 1.22. The effect of the size of Nd^{3+},Cr^{3+}:$LiLaP_4O_{12}$ nanoparticles on: (a) the intensity ratio between the emissions lines of Cr^{3+} and Nd^{3+} at 810 nm and 1048 nm, respectively, (b) S_{rel}, and (c) δT. Adapted with permission.[232] Copyright from Elsevier 2016.

The intensity ratio between the 810 nm and 1050 nm emission bands of Cr^{3+} and Nd^{3+}, respectively, were used to build the luminescent thermometer, with a maximum S_{rel} of 4.89% K^{-1} at 323 K (see Figure 1.21 (a)).[233] Tuning the concentration of the transition metal ion from 1 at.% and 10 at.%, had no substantial influence on the thermal sensing properties.[233] In Nd^{3+},Cr^{3+} doped $LiLaP_4O_{12}$ nanoparticles, the effect of the size of these nanocrystals on their thermometric performance, was also tested.[232] The conclusion reached was that as the size of the nanocrystals decreases, the intensity ratio of the emissions decreases (~0.81% nm^{-1}, see Figure 1.22 (a)), the emission band positions blue shifted (~0.066 nm grain $size^{-1}$), the temperature sensing regime narrows (from 300 to 600 K for particles with a size of 240 nm to 300-420 K for particles with a size of 20 nm), S_{rel} increases from 1% K^{-1} to 5% K^{-1} (see Figure 1.22 (b)), and δT drops down to 0.03 K (see Figure 1.22 (c)).[232] The reason for that is that with the decrease of the size of the nanoparticles, non-radiative depopulation processes become more important, being the main responsible for the decreasing of the intensity of the emissions. Furthermore, this leads to a faster decrease in the intensity ratio used for the luminescent thermometer, that allows obtaining a higher S_{rel} and a lower δT.[232]

3.2. Yb^{3+} doped luminescent thermometers operating in the I and II-BWs simultaneously

Other than Nd^{3+} doped luminescent thermometers, examples are encountered for Yb^{3+} doped materials acting as luminescent thermometers in the I- and II-BWs simultaneously, based on the ~1000 nm emission of this ion, combined with other emissions arising from other Ln^{3+} ions or transition metal ions.

Only a few cases explore the dual center emitting luminescent thermometers consisting on Yb^{3+} with another Ln^{3+} ion, such as Er^{3+} or a transition metal ion, such as Cr^{3+}. For the Yb^{3+}/Er^{3+} coemitting material, the host is an active core of hexagonal $NaYF_4$ nanorods coated with an amorphous silica shell, synthesized by a hydrothermal method.[234] Under excitation at 975 nm, Yb^{3+} acts as a sensitizer, besides the role of activator, absorbing the energy of the light source and transferring this energy to the other activator Er^{3+} (see Figure 1.23 (a)). By these ET processes, the $^4F_{7/2}$ state of Er^{3+} can be populated, from which a non-radiative decay can take place that can populate the $^4F_{9/2}$ and $^4I_{9/2}$ energy levels of Er^{3+}. From there, by relaxing back to the $^4I_{15/2}$ ground state, from the $^4F_{9/2}$ energy level the red emission at 660 nm is generated, and

from the $^4I_{9/2}$ energy level, the NIR emission located at 810 nm is generated.[234] The 1010 nm emission of Yb^{3+} is generated by simply relaxing back the electrons to the $^2F_{7/2}$ ground state, from the $^2F_{5/2}$ excited energy level.

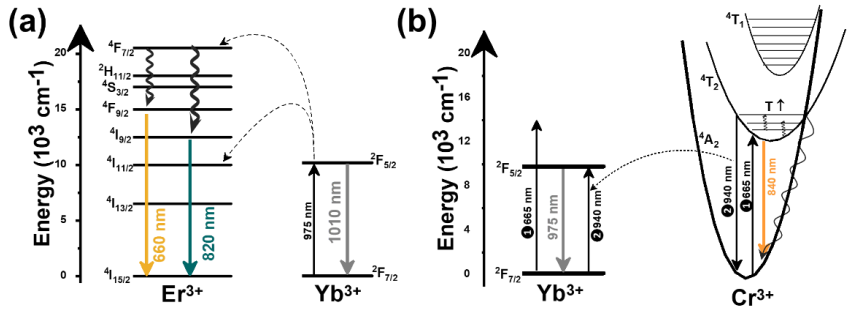

Figure 1.23. Mechanism of the generation of the emission lines of dual doped: (a) Er^{3+}/Yb^{3+} and (b) Cr^{3+}/Yb^{3+} materials operating simultaneously in the I- and II-BWs.

The thermometric performance of this material was extracted by studying the temperature dependence of the intensity ratios 1010 nm/810 nm and 1010 nm/660 nm, both modelled according to a second order polynomial fit, as expected for a luminescent thermometer based on NTCLs (Equation 1.27). Results reveal that the intensity ratio between 1010 nm/810 nm achieves a S_{rel} 2 times higher than the 1010 nm/660 nm intensity ratio.[234] The maximum S_{rel} was 1.64% K^{-1} and the δT 0.76 K, both obtained at 337 K.[234]

For the combination of Yb^{3+}/Cr^{3+} doped $LiLaP_4O_{12}$,[235] the intensity ratio between the emissions of Cr^{3+} located at 840 nm and Yb^{3+} located at 975 nm, the results are not as promising as for the ones obtained for the combination of Nd^{3+}/Cr^{3+}. To generate these emission bands, a first alternative is the excitation with 665 nm light source. The absorption of this visible light allows for the excitation of electrons of Cr^{3+} from the $^4A_2$ ground state to the $^4T_2$ excited state. A radiative relaxation from this level led to a broad emission band, centered at ~840 nm, assigned to the $^4T_2 \rightarrow {}^4A_2$ transition. For the excitation of Yb^{3+}, the authors considered an ET process from Cr^{3+} to Yb^{3+} or a reabsorption process of the 940 nm light generated by Cr^{3+}, that allowed to generate the $^2F_{7/2} \rightarrow {}^2F_{5/2}$ electronic transition of Yb^{3+} (see Figure 1.23 (b)), and its later radiative relaxation generating the emission line at 975 nm used in the luminescent thermometer.

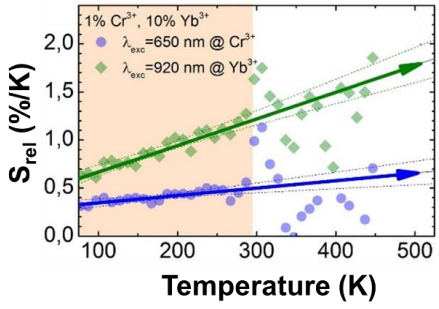

Figure 1.24. S_{rel} of dual doped Cr^{3+}/Yb^{3+} materials operating in the mixed region of I-BW and II-BW, as a function of the excitation wavelength. Adapted with permission.[235] Copyright from Elsevier 2016.

Here, the maximum S_{rel} obtained in the physiological range of temperatures was 0.32% K^{-1}, with δT of 1.6 K.[235] The authors tried to correlate the differences between the sensitivity of Yb^{3+}/Cr^{3+} and Nd^{3+}/Cr^{3+} luminescent thermometers to the population mechanism of the excited states in these ions.[235] For the Nd^{3+}/Cr^{3+} combination, the 655 nm excitation wavelength was chosen to excite simultaneously both ions.[233] For the Yb^{3+}/Cr^{3+} combination, the simple energy diagram of

Yb^{3+} and the lack of high energy levels, prevent the simultaneous excitation of both ions, which concurrently reduces the sensitivity of such luminescent thermometers.[235] A possible solution for the dually doped Yb^{3+}/Cr^{3+} materials would be the use of two excitation beams simultaneously, one for Cr^{3+} (at 650 nm) and another one for Yb^{3+} (~940 nm), which follows a mechanism as presented in Figure 23 (b). In terms of thermometric performance, this last approach achieved a three times higher S_{rel} (see Figure 24), with a value of 1.2% K^{-1}.[235] However, this approach is technically rather complex, exhibits strong fluctuation of sensitivity above 320 K (see Figure 1.24) and is not appropriate for biomedical applications because involves excitation with visible light (650 nm) which is harmful for biological tissues and excitation at around the absorption band of water (920 nm) which results in overheating.[235]

Table 1.2. Summary of all Ln^{3+} doped luminescent thermometers operating simultaneously in the I-BW and II-BW. In the table are shown the activators (A) and sensitizers (S). The excitation (λ_{exc}) and emission (λ_{em}) wavelengths are shown in nanometers (nm), together with the corresponding transition of the emissions ΔT stands for the temperature range were the thermal reading was investigated. The thermometric parameter (Δ) indicates the luminescent nanothermometry class used in each case: FIR-for band-shape and I-for intensity ratio thermometry, respectively. The maximum relative thermal sensitivity (S_{rel}) and the temperature resolution (δT) are presented at the temperature where these values were obtained. We indicated with an asterisk, the values of S_{rel} or δT calculated by us using the parameters published in the corresponding references. The double line separation between rows stands for different type (single or dual emitting center) of lanthanide doped nanothermometers, as discussed on the corresponding subsections.

A	S	Host	λ_{exc} (nm)	λ_{em} (nm)	Transitions	ΔT (K)	Δ	S_{rel}/T (% K^{-1})/K	δT (K)	Ref.
Nd^{3+}	-	Gd^{3+}:SrF_2	573	950, 1150	$^4F_{3/2} \rightarrow {}^4I_{9/2}$ $^4F_{3/2} \rightarrow {}^4I_{11/2}$	293-338	$FIR_{950/1150}$	0.50/293	1.2	164
Nd^{3+}	-	Gd^{3+}:CaF_2	573	867, 1058	$^4F_{3/2} \rightarrow {}^4I_{9/2}$, $^4F_{3/2} \rightarrow {}^4I_{11/2}$	294-338	$FIR_{1058/867}$	0.12/ 294	1.85	225
Nd^{3+} Yb^{3+}	Nd^{3+}	Nd:LaF_3@Yb:LaF_3	790	890 (Nd^{3+}), 1060 (Yb^{3+})	$^2F_{5/2} \rightarrow {}^2F_{7/2}$ (Yb^{3+}), $^4F_{3/2} \rightarrow {}^4I_{13/2}$ (Nd^{3+}),	283-323	I_{890}/I_{1060}	0.41/283	1.2*	231
Nd^{3+} Yb^{3+}	Nd^{3+}	Yb:LaF_3@Nd:LaF_3	790	890 (Nd^{3+}), 1060 (Yb^{3+})	$^2F_{5/2} \rightarrow {}^2F_{7/2}$ (Yb^{3+}), $^4F_{3/2} \rightarrow {}^4I_{13/2}$ (Nd^{3+}),	283-323	I_{890}/I_{1060}	0.36/283	1.4*	231
Nd^{3+} Yb^{3+}	Nd^{3+}	$LiLaP_4O_{12}$	808	870 (Nd^{3+}), 1000 (Yb^{3+})	$^4F_{3/2} \rightarrow {}^4I_{9/2}$, ($Nd^{3+}$) $^2F_{5/2} \rightarrow {}^2F_{7/2}$ (Yb^{3+})	93-663	I_{870}/I_{1000}	0.3/330	1.6*	207
Nd^{3+} Yb^{3+}	Nd^{3+}	Nd, Yb:LaF_3	790	890 (Nd^{3+}), 1060 (Yb^{3+})	$^2F_{5/2} \rightarrow {}^2F_{7/2}$ (Yb^{3+}), $^4F_{3/2} \rightarrow {}^4I_{13/2}$ (Nd^{3+}),	283-323	I_{1300}/I_{1000}	0.1/283	5*	231
Nd^{3+} Cr^{3+}	Nd^{3+} Cr^{3+}	$LiLaP_4O_{12}$	665	810 (Cr^{3+}), 1048 (Nd^{3+})	$^4T_2 \rightarrow {}^4A_2$ (Cr^{3+}) $^4F_{3/2} \rightarrow {}^4I_{11/2}$ (Nd^{3+})	293-323	I_{810}/I_{1048}	4.89/323	0.10*	233
Er^{3+}	Yb^{3+}	$NaYF_4$@SiO_2	975	810 (Er^{3+}), 1010 (Yb^{3+})	$^4I_{9/2} \rightarrow {}^4I_{15/2}$ (Er^{3+}) $^2F_{5/2} \rightarrow {}^2F_{7/2}$ (Yb^{3+})	299-337	I_{1010}/I_{810}	1.64/337	0.76	234
Er^{3+}	Yb^{3+}	$NaYF_4$@SiO_2	975	810 (Er^{3+}), 1010 (Yb^{3+})	$^4I_{9/2} \rightarrow {}^4I_{15/2}$ (Er^{3+}) $^2F_{5/2} \rightarrow {}^2F_{7/2}$ (Yb^{3+})	299-337	I_{1010}/I_{810}	1.64/337	0.76	234
Yb^{3+} Cr^{3+}	Yb^{3+} Cr^{3+}	$LiLaP_4O_{12}$	665+ 920	820 (Cr^{3+}), 975 (Yb^{3+})	$^4T_2 \rightarrow {}^4A_2$ (Cr^{3+}) $^2F_{5/2} \rightarrow {}^2F_{7/2}$ (Yb^{3+})	100-475	I_{820}/I_{975}	1.2/333	0.42*	235
Yb^{3+} Cr^{3+}	Yb^{3+} Cr^{3+}	$LiLaP_4O_{12}$	665	820 (Cr^{3+}), 975 (Yb^{3+})	$^4T_2 \rightarrow {}^4A_2$ (Cr^{3+}) $^2F_{5/2} \rightarrow {}^2F_{7/2}$ (Yb^{3+})	100-475	I_{820}/I_{975}	0.32/333	1.6	235

4. Lanthanide doped luminescent nanothermometers operating in the II-BW

Lanthanide doped luminescent thermometers operating in the II-BW are based on Yb^{3+} and Nd^{3+} doped materials. The explanation for this relies on the ability of these two Ln^{3+} ions to absorb the energy of an excitation source located in the I-BW, and generate emissions in the II-BW, avoiding laser-induced tissue-heating effects,[236, 237] and providing deep penetration depths into biological tissues, while maintaining a high-spatial resolution.[238-240] The thermometric performance of Yb^{3+} is based on the emission at ~1000 nm, either in single doped materials by studying the Stark sublevels of the electronic transition that generate this emission, or combined with other emissions arising from other Ln^{3+} ions, including Tm^{3+} and Nd^{3+}. For Nd^{3+} doped materials, their performance is evaluated in single doped materials by analyzing the Stark sublevels of the 1050 nm and 1330 nm emission bands, or in dual emitting materials composed by co-doping with another Ln^{3+} ion (Ho^{3+}) or combined with the emissions arising from semiconductor quantum dots.

4.1. Yb^{3+} doped luminescent nanothermometers operating in the II-BW

4.1.1. Single Yb^{3+} doped luminescent thermometers operating in the II-BW

The number of reports based on single Yb^{3+} doped materials operating as luminescent thermometers in this spectral region is scarce, and their thermometric performance is relatively poor. For instance, a hybrid compound composed of mesostructured dipyridyl-pyridazine functionalized either with ethenylene bridged mesoporous organosilica (dppz-ePMO) or vinyl silica (vSilica) were both complexed with ytterbium (III) on 2-thenoyltrifluoroacetonate ($Yb(tta)_3$).[241] The diferent peaks in the manifold corresponding to electronic transtions between the different Stark sublevels of the $^2F_{5/2} \rightarrow {}^2F_{7/2}$transition of Yb^{3+} in dppz-ePMO@$Yb(tta)_3$ and dppz-vSilica@ $Yb(tta)_3$ particles, located at 990 nm and 1025 nm or 986 nm and 1015 nm, respectively, were used to determine the temperature through the FIR method. These emission lines have been generated in these materials via excitation with ultraviolet light. In this way, the unique $^4f_{13}$ electronic configuration of Yb^{3+}, can easily gain one electron to reach the more stabilized $^4f_{14}$ configuration of the full shell. This tendency of reduction to Yb^{2+} enables the Yb^{3+} ion in some hosts, such as the case of these organic complexes, to receive an electron from the host's anion under high-energy external excitation, such as the UV light, forming a charge transfer state (CTS) (see Figure 1.25 (a)). The CTS of Yb^{3+} can transfer the excitation energy to the $^2F_{5/2}$ emitting state via a non-radiative relaxation process (see Figure 1.25 (a)), generating the emission bands located at around 980-990 nm (labelled as R_1) and 1015-1025 nm (labelled as R_2). Nevertheless, these hybrids, besides the low S_{rel} they exhibit (0.13-0.17 $\%K^{-1}$) with maximum values at cryogenic temperatures (110 K),[241] as can be seen in Table 1.3, they are excited with UV light, hampering significantly their implementation in possible biomedical applications.

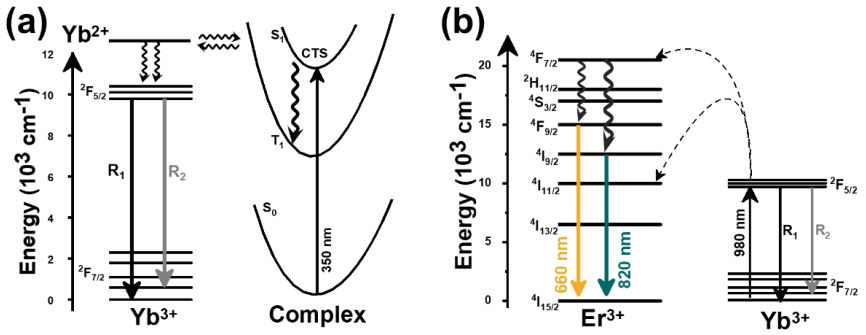

Figure 1.25. Mechanism of generation of Yb^{3+} emissions lines in: (a) organic complexes via charge transfer state (CTS) and (b) in ZrO_2 codoped with Er^{3+}.

Another choice for single Yb^{3+} doped luminescent thermometers operating in the II-BW is the excitation in the NIR using a wavelength of 980 nm.[194] It has been investigated in ZrO_2

nanocrystals codoped with Er^{3+}, in which the authors investigated the performance of the thermometer in the I-BW, II-BW and III-BW, using the different emissions of Er^{3+} and Yb^{3+}.[194] For the luminescent thermometer operating in the II-BW the linear model of VPR (see Equation 1.39) was applied between the different peaks in the manifold corresponding to the $^2F_{5/2} \rightarrow {}^2F_{7/2}$ electronic transition of Yb^{3+}, with peaks located at 1023 nm (label R_1 of Figure 1.25 (b)) and 1036 nm (label R_2 of Figure 1.25 (b))[194] The mechanism of the generation of these emission lines is similar to that reported at Figure 1.23 (a), in which Yb^{3+} not only acts as a sensitizer, but also as an activator. These nanocrystals exhibited a better S_{rel} with a value of 1.1% K^{-1} at room temperature, rendering this approach a better strategy towards the development of single Yb^{3+} doped luminescent thermometers operating in the II-BW. Nevertheless, although excited with NIR source and generating emissions in the II-BW, which should render this material a potential candidate for biomedical applications, one should take into account the strong water absorption band at around 980 nm, that makes Yb^{3+} doped luminescent nanothermometers not ideal for biomedical or biological applications, as this wavelength might cause a strong heating effect in the biological tissues of excessive pumping power densities are applied, which might kill healthy cells and damage biological tissues.[216]

4.1.2. Dual doped Yb^{3+}/Ln^{3+} luminescent thermometers operating in the II-BW

Dual doped Yb^{3+}/Ln^{3+} operating in II-BW are often based on the combination of the 1000 nm emission of Yb^{3+} with either the emission of Tm^{3+} located at 1230 nm or emissions of Nd^{3+} located at 1050 nm and 1300 nm. Here, generally, we underline the differences among incorporating a simple core, a core@shell or a multishell structure in the nanoparticles used for nanothermometry (see Table 1.3). In Table 1.3, as well, it can be observed that Yb^{3+} ions are not performing any more the role of sensitizers, as often reported in the previous sections, but instead they are acting only as an activators. This approach, based on the excitation of these Yb^{3+}/Ln^{3+} materials with wavelengths ranging from 690-808 nm, may lead to a promising strategy to ensure biomedical applications. When Nd^{3+} and Yb^{3+} emissions are combined for thermal sensing, quite often 980 nm is selected as the wavelength for the excitation source (see Table 1.1 for example), a wavelength that, as mentioned before, is not ideal for biomedical or biological applications.[216] Hence, excitations in the wavelength range from 690-808 nm, matching the strong absorptions of Tm^{3+} and Nd^{3+} ions,[242] may provide a good solution to overcome the heating effect caused by the 980 nm laser, and getting deeper penetration depths, since the absorption of water molecules, especially at around 800 nm, is quite weak. This is why for dual doped Yb^{3+}/Ln^{3+} luminescent nanothermometers operating in the II-BW, combinations with Nd^{3+} and Tm^{3+} ions are used.

If we fix our attention on the structure of the nanoparticles, besides their colloidal stability and target abilities in biomedical applications, often exhibit limitations related to the drastic reduction of the luminescence efficiency due to the increase of non-radiative processes due to interactions with other molecules at their surfaces,[243] and difficulty in implementing multifunctionality in these simple nanoparticles.[244] To overcome these limitations, core@shell or multishell nanoparticles have emerged as a very promising strategy. The core@shell or multishell structure allows for flexible designs, incorporating efficient multifunctionality and the facile incorporation of dopants with the desired spatial distribution, allowing the manipulation of ET processes among different ions located in different layers.[245, 246] Hence, here we will highlight the advantages offered by the core@shell nanocrystalline structures when compared to the bare nanocrystals.

First, we focus on luminescent nanothermometers based on the Yb^{3+} and Tm^{3+} emissions located in the II-BW, which display higher S_{rel} than Yb^{3+}/Nd^{3+} thermometers (see Table 1.3). A typical example that explores the differences among the core@shell and the simple particles is the case of Er^{3+}, Yb^{3+}:LaF_3@Tm^{3+}, Yb^{3+}:LaF_3 nanocrystals with sizes ~32 nm, synthesized via wet chemistry methodologies.[247] These active core@active shell nanocrystalline structures were compared, in terms of the intensity of the emissions generated after excitation at either 690 nm or 808 nm, and in terms of the thermometric performance, with their corresponding simple cores.

Upon excitation at 690 nm, the energy is absorbed by Tm^{3+} ions, promoting its electrons from the ground state to the $^3F_3$ excited state. From this state, a CR process $^3F_3$; $^3H_6 \leftrightarrow {}^3F_4$; $^3H_5$ (see Figure 1.26 (a)), takes place leading to the population of the $^3H_5$ energy level, from which a radiative decay to the ground state, generates the 1230 nm emission of Tm^{3+}.

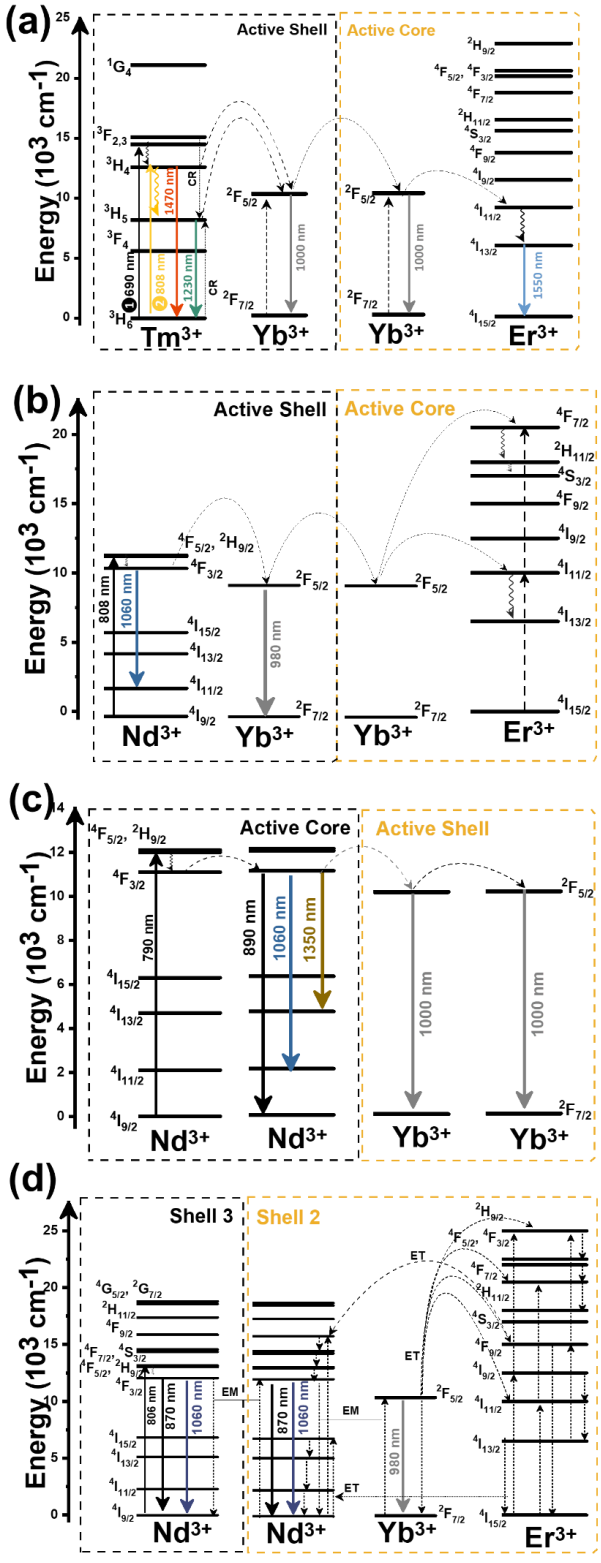
(a)
Active Shell
Active Core
Energy (10³ cm⁻¹)
Tm³⁺
Yb³⁺
Yb³⁺
Er³⁺
1470 nm
808 nm
1230 nm
690 nm
1000 nm
1000 nm
1550 nm
CR
CR
(b)
Active Shell
Active Core
Energy (10³ cm⁻¹)
Nd³⁺
Yb³⁺
Yb³⁺
Er³⁺
808 nm
1060 nm
980 nm
(c)
Active Core
Active Shell
Energy (10³ cm⁻¹)
Nd³⁺
Nd³⁺
Yb³⁺
Yb³⁺
790 nm
890 nm
1060 nm
1350 nm
1000 nm
1000 nm
(d)
Shell 3
Shell 2
Energy (10³ cm⁻¹)
Nd³⁺
Nd³⁺
Yb³⁺
Er³⁺
806 nm
870 nm
1060 nm
870 nm
1060 nm
980 nm
EM
EM
ET
ET
ET

Figure 1.26. (a) Mechanism of the generation of the emission lines on core@shell: (a) Er^{3+}, Yb^{3+}:LaF_3@Tm^{3+},Yb^{3+}:LaF_3 nanocrystals excited either with 690 nm or 808 nm, (b) Er^{3+},Yb^{3+}:$NaYF_4$@Nd^{3+},Yb^{3+}:$NaYF_4$ excited with 808 nm, (c) Nd^{3+}:LaF_3@Yb^{3+}:LaF_3 excited with 790 nm and (d) Tm^{3+},Yb^{3+}:SrF_2@Y^{3+}:SrF_2@Er^{3+},Nd^{3+},Yb^{3+}:SrF_2@Nd^{3+}:SrF_2 nanocrystals excited with 806 nm.

From the $^3H_5$ energy level and from the $^3H_4$ energy level (populated by a non-radiative decay from the $^3F_3$ state), an ET process to the energy resonant $^2F_{5/2}$ state of Yb^{3+} takes place, followed by a radiative relaxation process to the ground state, which leads to the 1000 nm emission of Yb^{3+}. Further ET processes, as presented in Figure 1.26 (a), lead to the population of the $^2F_{5/2}$ and $^4I_{11/2}$ energy levels of Yb^{3+} and Er^{3+}, respectively, present in the active core. The electrons in the $^4I_{11/2}$ state of Er^{3+} can non-radiative decay to the $^4I_{13/2}$ state, prior to relaxing back radiatively to the ground state, leading to the generation of 1550 nm emission of Er^{3+}. The intensity of the 1000 nm, 1230 nm and 1550 nm emissions of Yb^{3+}, Tm^{3+} and Er^{3+} ions in this core@shell structure, were compared to the ones obtained in the Tm^{3+},Er^{3+}, Yb^{3+} bare nanocrystals, revealing that under excitation at 690 nm, brighter emissions is obtained in the core@shell structures (see Figure 1.27 (a)). This big difference between the intensity of the emissions is a direct effect of the core@shell architecture, according to the authors, leading to a spatial separation between Er^{3+} and Tm^{3+} ions in such a way that the $Er^{3+} \rightarrow Tm^{3+}$ ET process, involving the $^4I_{13/2}$ and $^3F_4$ energy levels of Er^{3+} and Tm^{3+}, respectively, is avoided or reduced, as confirmed also from the fluorescence lifetime measurements performed.[247] As can be observed also from Figure 1.27 (a), a significant effect on the signal of the emissions (in the thermometric performance as well, as we will analyze in Section 5) has the application of 808 nm excitation wavelength. Also in this case, the highest intensity of the emissions is generated from the core@shell structures, however the emission of Tm^{3+} is barely detected. The possible explanation about this observation is related to the fact that upon 808 nm excitation, the mechanism of the generation of Tm^{3+} emission, is mainly governed from the de-excitation of the $^3H_4$ state and not through the CR process. Hence, as presented in Figure 1.26 (a) in gold, upon 808 nm excitation, Tm^{3+} ions will absorb the light and excite the electrons towards the $^3H_4$ state, from where due to a direct radiative decay at the ground state, the 1470 nm emission will be generated, For the 1230 nm emission, the corresponding $^3H_5$ energy level is not populated anymore via CR process, but through a simple non-radiative decay from the $^3H_4$ energy level (see Figure 1.26 (a)). The rest of the mechanism for the generation of the other emissions, is the same.

Here, the choice for luminescence nanothermometry, are three intensity ratios that can be created combining the emissions of Yb^{3+} and Tm^{3+}: (i) the 1000 nm emission of Yb^{3+} combined with the 1230 nm emission of Tm^{3+}, located both in the II-BW; (ii) the 1000 nm emission of Yb^{3+} combined with the 1550 nm emission of Er^{3+}, located within the II- and III-BWs and that will be described in Section 5; and (iii) the 1230 nm emission of Tm^{3+} combined with the 1550 nm emission of Er^{3+}, located within the II- and III-BWs (described in Section 5).

For the luminescent thermometer operating exclusively in the II-BW, a maximum S_{rel} of 3.9% K^{-1} was achieved at room temperature, three times higher than the one achieved with the corresponding bare nanoparticles (see Table 1.3), an improvement assigned to the efficient ET and quenching rates in the core@shell structures.[247] In order to extract this S_{rel}, the multiphonon relaxation and energy transfer rates were modelled as a function of the temperature.

Table 1.3. Summary of all Ln^{3+} doped luminescent thermometers operating in the II-BW. In the table are shown the activators (A) and sensitizers (S). The excitation (λ_{exc}) and emission (λ_{em}) wavelengths are shown in nanometers (nm), together with the corresponding transition of the emissions ΔT stands for the temperature range were the thermal reading was investigated. The thermometric parameter (Δ) indicates the luminescent nanothermometry class used in each case: FIR-for band-shape, I-for intensity ratio and $\Delta\nu$-for bandwidth thermometry, respectively. VPR stands for valley-to-peak ratio. The maximum relative thermal sensitivity (S_{rel}) and the temperature resolution (δT) are presented at the temperature where these values were obtained. We indicated with an asterisk, the values of S_{rel} or δT calculated by us using the parameters published in the corresponding references. The double line separation between rows stands for different type (single or dual emitting center) of lanthanide doped nanothermometers, as discussed on the corresponding subsections.

A	S	Host	λ_{exc} (nm)	λ_{em} (nm)	Transitions	ΔT (K)	Δ	S_{rel}/T (% K^{-1})/K	δT (K)	Ref.
Yb^{3+}	-	ZrO_2	980	1023, 1036	$^2F_{5/2} \rightarrow {}^2F_{7/2}$	293-493	$VPR_{1023/1036}$	1.1/293	0.45*	194
Yb^{3+}	-	dppz-ePMO@Yb(tta)$_3$	350	986, 1015	$^2F_{5/2} \rightarrow {}^2F_{7/2}$	110-310	$FIR_{986/1015}$	0.17/110	2.9*	241
Yb^{3+}	-	dppz-vSilica@Yb(tta)$_3$	350	990, 1025	$^2F_{5/2} \rightarrow {}^2F_{7/2}$	110-310	$FIR_{990/1025}$	0.13/110	3.8*	241
Yb^{3+}	Tm^{3+}	Er,Yb:LaF_3@Tm,Yb:LaF_3	690	1000 (Yb^{3+}), 1230 (Tm^{3+})	$^2F_{5/2} \rightarrow {}^2F_{7/2}$ (Yb^{3+}), $^3H_5 \rightarrow {}^3H_6$ (Tm^{3+}),	293-323	I_{1000}/I_{1230}	3.9/ 293	0.3	247
Yb^{3+}	Tm^{3+}	LaF_3	690	1000 (Yb^{3+}), 1230 (Tm^{3+})	$^2F_{5/2} \rightarrow {}^2F_{7/2}$ (Yb^{3+}), $^3H_5 \rightarrow {}^3H_6$ (Tm^{3+})	293-323	I_{1000}/I_{1230}	1.3/ 293	0.38*	247
Yb^{3+}	Nd^{3+}	Er,Yb:$NaYF_4$@Yb,Nd:$NaYF_4$	808	980 (Yb^{3+}), 1060 (Nd^{3+})	$^2F_{5/2} \rightarrow {}^2F_{7/2}$ (Yb^{3+}), $^4F_{3/2} \rightarrow {}^4I_{9/2}$ (Nd^{3+})	103-443	I_{1060}/I_{980}	2.1/370	0.24*	248
Yb^{3+}	Nd^{3+}	Tm,Yb:SrF_2@Y:SrF_2@E:SrF_2@Nd:SrF_2	806	980 (Yb^{3+}), 1060 (Nd^{3+})	$^2F_{5/2} \rightarrow {}^2F_{7/2}$ (Yb^{3+}), $^4F_{3/2} \rightarrow {}^4I_{9/2}$ (Nd^{3+})	293-323	I_{980}/I_{1060}	1.62/323	1.7	249
Nd^{3+}, Yb^{3+}	Nd^{3+}	Nd:LaF_3@Yb:LaF_3	790	1000 (Yb^{3+}), 1300 (Nd^{3+})	$^2F_{5/2} \rightarrow {}^2F_{7/2}$ (Yb^{3+}), $^4F_{3/2} \rightarrow {}^4I_{13/2}$ (Nd^{3+})	283-323	I_{1300}/I_{1000}	0.41/283	1.61	231
Nd^{3+}, Yb^{3+}	Nd^{3+}	Nd:LaF_3@Yb:LaF_3	790	1000 (Yb^{3+}), 1060 (Nd^{3+})	$^2F_{5/2} \rightarrow {}^2F_{7/2}$ (Yb^{3+}), $^4F_{3/2} \rightarrow {}^4I_{11/2}$ (Nd^{3+})	283-323	I_{1060}/I_{1000}	0.41/283	1.61	231
Nd^{3+}, Yb^{3+}	Nd^{3+}	Nd:LaF_3@Yb:LaF_3	790	1000 (Yb^{3+}), 890 (Nd^{3+})	$^2F_{5/2} \rightarrow {}^2F_{7/2}$ (Yb^{3+}), $^4F_{3/2} \rightarrow {}^4I_{9/2}$ (Nd^{3+})	283-323	I_{890}/I_{1000}	0.41/283	1.61	231
Nd^{3+}, Yb^{3+}	Nd^{3+}	Yb:LaF_3@Nd:LaF_3	790	1000 (Yb^{3+}), 1300 (Nd^{3+})	$^2F_{5/2} \rightarrow {}^2F_{7/2}$ (Yb^{3+}), $^4F_{3/2} \rightarrow {}^4I_{13/2}$ (Nd^{3+})	283-323	I_{1300}/I_{1000}	0.36/283	1.61	231
Nd^{3+}, Yb^{3+}	Nd^{3+}	Yb:LaF_3@Nd:LaF_3	790	1000 (Yb^{3+}), 1060 (Nd^{3+})	$^2F_{5/2} \rightarrow {}^2F_{7/2}$ (Yb^{3+}), $^4F_{3/2} \rightarrow {}^4I_{11/2}$ (Nd^{3+})	283-323	I_{1060}/I_{1000}	0.36/283	1.61	231
Nd^{3+}, Yb^{3+}	Nd^{3+}	Yb:LaF_3@Nd:LaF_3	790	1000 (Yb^{3+}), 890 (Nd^{3+})	$^2F_{5/2} \rightarrow {}^2F_{7/2}$ (Yb^{3+}), $^4F_{3/2} \rightarrow {}^4I_{9/2}$ (Nd^{3+}),	283-323	I_{890}/I_{1000}	0.36/283	1.61	231
Nd^{3+}, Yb^{3+}	Nd^{3+}	PDC	808	1005 (Yb^{3+}), 1052 (Nd^{3+})	$^2F_{5/2} \rightarrow {}^2F_{7/2}$ (Yb^{3+}), $^4F_{3/2} \rightarrow {}^4I_{11/2}$ (Nd^{3+})	298-368	I_{1005}/I_{1052}	0.48/298	0.08	250
Nd^{3+}, Yb^{3+}	Nd^{3+}	PDC	808	1005 (Yb^{3+}), 1065 (Nd^{3+})	$^2F_{5/2} \rightarrow {}^2F_{7/2}$ (Yb^{3+}), $^4F_{3/2} \rightarrow {}^4I_{11/2}$ (Nd^{3+})	298-368	I_{1005}/I_{1052}	0.17/318	0.35	250
Nd^{3+}, Yb^{3+}	Nd^{3+}	Yb,Nd:LaF_3	790	1000 (Yb^{3+}), 890 (Nd^{3+})	$^2F_{5/2} \rightarrow {}^2F_{7/2}$ (Yb^{3+}), $^4F_{3/2} \rightarrow {}^4I_{9/2}$ (Nd^{3+})	283-323	I_{890}/I_{1000}	0.1/283	1.61	231
Nd^{3+}, Yb^{3+}	Nd^{3+}	Yb,Nd:LaF_3	790	1000 (Yb^{3+}), 1060 (Nd^{3+})	$^2F_{5/2} \rightarrow {}^2F_{7/2}$ (Yb^{3+}), $^4F_{3/2} \rightarrow {}^4I_{11/2}$ (Nd^{3+}),	283-323	I_{1300}/I_{1000}	0.1/283	1.61	231
Nd^{3+}, Yb^{3+}	Nd^{3+}	Yb,Nd:LaF_3	790	1000 (Yb^{3+}), 1300 (Nd^{3+})	$^2F_{5/2} \rightarrow {}^2F_{7/2}$ (Yb^{3+}), $^4F_{3/2} \rightarrow {}^4I_{13/2}$ (Nd^{3+})	283-323	I_{1300}/I_{1000}	0.1/283	1.61	231
Nd^{3+}	-	YAP	532	1348	$^4F_{3/2} \rightarrow {}^4I_{13/2}$	293-370	$\Delta\nu_{1348}$	3.3/293	0.37	158

Nd^{3+}	-	$LiLuF_4$@$LiLuF_4$	793	1316, 1328	$^4F_{3/2} \rightarrow {}^4I_{13/2}$	293-318	$FIR_{1316}/_{1328}$	0.49/293	1.02	165
Nd^{3+}	-	$LiLuF_4$@$LiLuF_4$	793	1045, 1055	$^4F_{3/2} \rightarrow {}^4I_{11/2}$	293-318	$FIR_{1045}/_{1055}$	0.48/293	1.05	165
Nd^{3+}	-	YVO_4@SiO_2	808	1064, 1066	$^4F_{3/2} \rightarrow {}^4I_{11/2}$	297-331	$FIR_{1064}/_{1066}$	0.45/331	0.50	251
Nd^{3+}	-	Y_2O_3	532	1053, 1075	$^4F_{3/2} \rightarrow {}^4I_{11/2}$	298-333	$FIR_{1053}/_{1075}$	0.43/293	0.2	167
Nd^{3+}	-	YVO_4	808	1064, 1066	$^4F_{3/2} \rightarrow {}^4I_{11/2}$	297-331	$FIR_{1064}/_{1066}$	0.35/331	0.44	251
Nd^{3+}	-	Y^{3+}:CaF_2	808	1053, 1062	$^4F_{3/2} \rightarrow {}^4I_{11/2}$	300-333	$FIR_{1053}/_{1062}$	0.18/300	2.7*	252
Nd^{3+}	-	PDC	808	1054, 1065	$^4F_{3/2} \rightarrow {}^4I_{11/2}$	298-368	$FIR_{1054}/_{1065}$	0.18/318	0.3	250
Nd^{3+}	-	$KGd(WO_4)_2$	808	1067, 1075	$^4F_{3/2} \rightarrow {}^4I_{11/2}$	298-333	$FIR_{1067}/_{1075}$	0.16/298	3*	175
Nd^{3+}, QDs	Nd^{3+}, QDs	Nd:NaGdF$_4$@ QD@PGLA	808	1060 (Nd^{3+}), 1300 (QDs)	$^4F_{3/2} \rightarrow {}^4I_{11/2}$ (Nd^{3+}) First exciton (QDs)	283-323	I_{1060}/I_{1300}	2.5/303	0.2	253
Nd^{3+}, Ho^{3+}	Nd^{3+}	Er,Ho,Yb:NaGdF$_4$@Yb: NaGdF$_4$@Nd, Yb: NaGdF$_4$@ NaGdF$_4$	806	1180 (Ho^{3+}), 1340 (Nd^{3+})	$^5I_6 \rightarrow {}^5I_8$ (Ho^{3+}), $^4F_{3/2} \rightarrow {}^4I_{13/2}$ (Nd^{3+})	293-323	I_{1180}/I_{1340}	1.17/293	1.2	254

Returning to the case of Yb^{3+} and Nd^{3+} emissions located in the II-BW, a hexagonal $NaYF_4$ core co-doped with Er^{3+} and Yb^{3+} and a hexagonal $NaYF_4$ shell co-doped with Nd^{3+} and Yb^{3+}, was tested as temperature sensor. Here, to determine the temperature, the emissions generated by Yb^{3+} and Nd^{3+} located in the outer shell were used (the inner core was used for sensing in the visible, which is out of the scope of this chapter).[248] By exciting the nanocrystals at 808 nm, the electrons are optically excited from the ground state of Nd^{3+} ions up to its $^4F_{5/2}$ excited state, followed by a fast non-radiative decay to populate the $^4F_{3/2}$ metastable state. At this stage, different radiative and non-radiative processes can take place (see Figure 1.26 (b)), starting from the generation of the Nd^{3+} emission at 1060 nm, corresponding to the $^4F_{3/2} \rightarrow {}^4I_{11/2}$ electronic transition, and the energy transfer between Nd^{3+} and Yb^{3+} in the shell, ruled by the Miyakava–Dexter model.[230] From here, the emission of Yb^{3+} located at 980 nm, assigned to $^2F_{5/2} \rightarrow {}^2F_{7/2}$ transition, is generated. Also, the energy migration from the Yb^{3+} ions in the shell to the Yb^{3+} ions in the core, followed by energy migration between Yb^{3+} and Er^{3+} can take place, leading finally to the green emission of Er^{3+} in the visible.[248] The mechanisms for the generation of the green emissions of Er^{3+} are out of the scope of this chapter, thus, will not be presented here.

The intensity ratio between the 1060 nm emission of Nd^{3+} and the 980 nm emission of Yb^{3+} was studied as a function of the temperature, over the range from 103-443 K and the concentration of Nd^{3+} in the outer shell, tuned from 1, 3, 10 and 15 at.% with respect to the concentration of Yb^{3+}.[248] Results reveal that the maximum S_{rel} is 2.1% K^{-1} at 370 K.[248] In addition, this S_{rel} is proportional to the content of Nd^{3+} in the outer shell. This effect is related to the shortening of the average Nd^{3+}-Yb^{3+} distance, and hence facilitating the Nd^{3+} to Yb^{3+} ET.[248]

The thermal sensing properties of simple Nd^{3+}, Yb^{3+} doped LaF_3 nanoparticles and two different active core@active shell nanostructures, one having the core doped with Nd^{3+} ions and the shell with Yb^{3+} ions (Nd^{3+}:LaF_3@Yb^{3+}:LaF_3) and the other constituted by a Yb^{3+} doped core and a Nd^{3+} doped shell (Yb^{3+}:LaF_3@Nd^{3+}:LaF_3),[231] were also studied. In these structures, Nd^{3+} ions display two additional emission bands at 890 nm (located in the I-BW) and 1350 nm (located in the II-BW), assigned to the $^4F_{3/2} \rightarrow {}^4I_{9/2}$ and $^4F_{3/2} \rightarrow {}^4I_{13/2}$ electronic transitions, respectively. The 790 nm excitation source is absorbed from Nd^{3+} ions, promoting its electrons to the $^4F_{5/2}$ excited state. Then, a rapid phonon-assisted relaxation to the metastable $^4F_{3/2}$ state takes place. From this state, possible ion-to-ion ET lead to the population of the $^4F_{3/2}$ state of Nd^{3+} ion, from which three radiative decays at $^4I_{9/2}$, $^4I_{11/2}$ and $^4I_{13/2}$ produce emissions at 890 nm, 1060 nm and 1350 nm, respectively (see Figure 1.26 (c)). Further ET process can lead to the excitation of Yb^{3+} ions from their ground state up to the $^2F_{5/2}$ state, from which infrared emission at 1000 nm is produced.

Here, all the possible intensity ratios (considering the emissions of Nd^{3+} versus the emission of Yb^{3+}, which obey to a linear fitting function) were explored for temperature sensing. The same S_{rel} was found for all the three intensity ratios, either in the simple nanoparticles or in the core@shell structures (see Table 1.3). Comparing the performance of the simple nanoparticles with that of the core@shell structures, a four-fold improvement in their S_{rel} was observed. Besides this improvement, the values of S_{rel} are relatively low with a maximum of ~0.41% K^{-1} in the physiological range of temperatures.

The performance of these Nd^{3+}, Yb^{3+} doped LaF_3 nanoparticles is comparable with that of Nd^{3+} and Yb^{3+} codoped lanthanide complex with pyridine-3,5-dicarboxylate (hereafter PDC).[250] Here, Nd^{3+} emission peaks at 1054 nm and 1065 nm are generated from the transitions between the different Stark sublevels in the $^4F_{3/2} \rightarrow {}^4I_{11/2}$ electronic transition, whereas the Yb^{3+} emission at 1005 nm is assigned to the $^2F_{5/2} \rightarrow {}^2F_{7/2}$ transition, after exaction with 808 nm light source. The intensity ratios among the three combination (the combination of Nd^{3+} emissions is presented in Section 4.2.1) of these emissions were tested for temperature sensing. Here, Nd^{3+} emissions at 1054 nm and 1065 nm are generated from the different Stark sublevels of the $^4F_{3/2} \rightarrow {}^4I_{11/2}$ transition, whereas the Yb^{3+} emission at 1005 nm is assigned to the $^2F_{5/2} \rightarrow {}^2F_{7/2}$ transition. The temperature dependence of the 1065 nm/1005 nm intensity ratio, were modelled using Equation 1.14, while the 1054 nm/1005 nm intensity ratio was fitted to a linear equation, with the argument that the variation of this ratio with temperature obeys a linear dependency. The highest S_{rel} was obtained, in fact, for the 1054 nm/1005 nm ratio with a value of 0.48% K^{-1} and a δT of 0.08 K.[250] It should be underlined here, that the uncertainty in the determination of the intensity ratio here was taken as 0.033%,[250] clearly lower than the one generally accepted (0.5%),[21] which of course, will imply a lower δT.

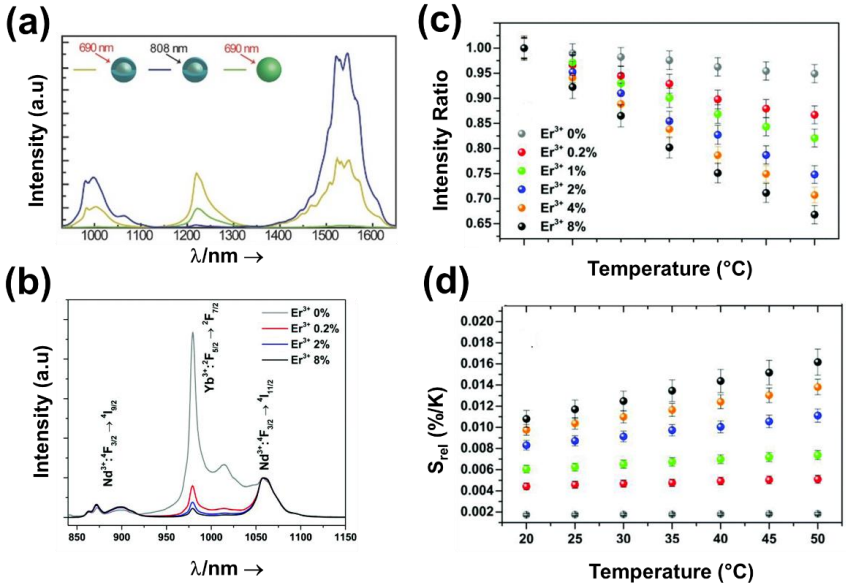

Figure 1.27. (a) Room temperature emission spectra of simple core under 690 nm excitation (green) and of active core@active shell (concentration of lanthanide ions Tm^{3+}, Yb^{3+} and Er^{3+} are 10 mol%, 10 mol% and 2 mol%, respectively) under 690 (yellow) and 808 nm (blue) laser excitations. The green sphere and the grey core covered with blue sphere, represent the simple core and the active core@active shell, respectively. Adapted with permission.[247] Copyright from Wiley 2017. Effect of Er^{3+} concentration on: (b) intensity of the emissions, (c) intensity ratio, (d) relative thermal sensitivity on Tm^{3+},Yb^{3+}:SrF_2 @Y^{3+}:SrF_2@Er^{3+},Nd^{3+},Yb^{3+}:SrF_2 @Nd^{3+}:SrF_2 nanocrystals. Adapted with permission.[249] Copyright The Royal Journal of Chemistry 2018.

Cortelletti *et al*. reported the thermometric performance of a complex system in the form of a core@multishell nanostructure, composed by Tm^{3+},Yb^{3+}:SrF_2 (core)@Y^{3+}:SrF_2 (shell 1)@Er^{3+},Nd^{3+},Yb^{3+}:SrF_2 (shell 2)@Nd^{3+}:SrF_2 (shell 3) nanomaterial,[249] based on the intensity ratio between the emissions of Yb^{3+} at 980 nm and of Nd^{3+} located at 1060 nm (another emission of Nd^{3+} is generated at 870 nm, but the authors investigated only the 1060 nm for thermal sensing due to higher intensity of emission).[249] The performance of this nanothermometer was closely related to the amount of Er^{3+} ions in shell 2. In this structure, the excitation source 806 nm, is absorbed by the Nd^{3+} ions present in shell 3. This energy allows the promotion of the Nd^{3+} electrons to the $^4F_{5/2}$ excited state, from which a non-radiative decay will populate the lower $^4F_{3/2}$ excited state. From here, radiative decays to the $^4I_{11/2}$ and $^4I_{9/2}$ states, generate the emissions located at 870 nm and 1060 nm, respectively. From the $^4F_{5/2}$ excited state of Nd^{3+}, first an ET process can lead to the population of the other Nd^{3+} ions located in shell 2 (see Figure 1.26 (d)). Then, from this shell, another ET process can lead to the population of the excited state of Yb^{3+}, prior to a radiative decay to the ground state, generating the 980 nm emission.[249] Hence, between Nd^{3+} ions and Yb^{3+} ions, ET and BET processes may exist. However, this is true only when no Er^{3+} ions in shell 2 are found. With the addition of Er^{3+} ions, several ET processes with Yb^{3+} ions in shell , may occur, influencing in this way not only the intensity of the emissions generated, but also the thermometric performance.

In terms of the intensity of the emissions, with the increase of the concentration of Er^{3+} ions, the intensity of the emission of Yb^{3+} clearly decreases (see Figure 1.27 (b)), due to a prominent increase of the probability of the $Yb^{3+} \rightarrow Er^{3+}$ ET process. This ET process quenches the emission of Yb^{3+}, which is favorable for luminescence nanothermometry means. When considering the intensity ratio between the emission of Yb^{3+} with the emission of Nd^{3+}, its slope in the evolution with temperature increases as the concentration of Er^{3+} increases (see Figure 1.27 (c)), and thus, the S_{rel} also increases (see Figure 1.27 (d)), generating better luminescent thermometers. From these figures it can be extracted that the thermometric performance of the nanomaterials with the highest Er^{3+} concentration is approximately 5 times better compared to the material without this ion. Thus, it can be concluded that efficient $Yb^{3+} \rightarrow Er^{3+}$ ET processes are beneficial for the thermometric performance, although it is difficult to predict the effect of these processes in complex systems. Nevertheless, the maximum S_{rel} achieved (1.62% K^{-1} in the physiological range of temperatures) is still lower when compared to the one achieved in Er^{3+},Yb^{3+}:LaF_3@Tm^{3+},Yb^{3+}:LaF_3,[231] and Er^{3+},Yb^{3+}:$NaYF_4$@Nd^{3+},Yb^{3+}:$NaYF_4$ [248] nanostructures.

To conclude, core@shell and core@multishell nanoarchitectures offer a boost in the brightness of the emissions generated and in addition, in a significant enhancement on their temperature sensing performance. Regardless of their high thermometric performance, it should be admitted that these structures do offer very complex systems either from the synthetic or spectroscopic point of view. Additionally, most of them are hydrophobic, hence, for biomedical applications further functionalization of their surfaces are needed to make them water dispersible.

4.2. Nd^{3+} doped luminescent nanothermometers operating in the II-BW

4.2.1. Single Nd^{3+} doped luminescent thermometers operating in the II-BW

Luminescent thermometers based on single Nd^{3+} doped nanoparticles operating in the II-BW are mainly based on the emissions generated by the Stark sublevels of the $^4F_{3/2} \rightarrow {}^4I_{11/2}$ electronic transition emission located at ~1064 nm. Hence, to determine the performance of these thermometers, the fitting model based on the FIR was applied (Equation 1.9). Another option for temperature sensing relies in the use of the emission at the borderline of the II-BW spectral region located at ~1350 nm.

For the choice of the 1064 nm emission, the S_{rel} obtained is relative very low, ranging from 0.16% K^{-1} to 0.45% K^{-1} (see Table 1.3). Despite this, from these 1064 nm based luminescent thermometers, some useful strategies can be extracted. Hence, the incorporation of amorphous silica coating can tailor the performance of luminescent nanothermometers. Such strategy has been explored for the case of Nd^{3+} doped YVO_4@SiO_2 nanoparticles.[251] The performance of this material was tested as a function of the silica thickness and compared to that of the uncoated corresponding material. Results show a proportional relationship between S_{rel} and the thickness of the silica shell (see Figure 1.28 (a)).

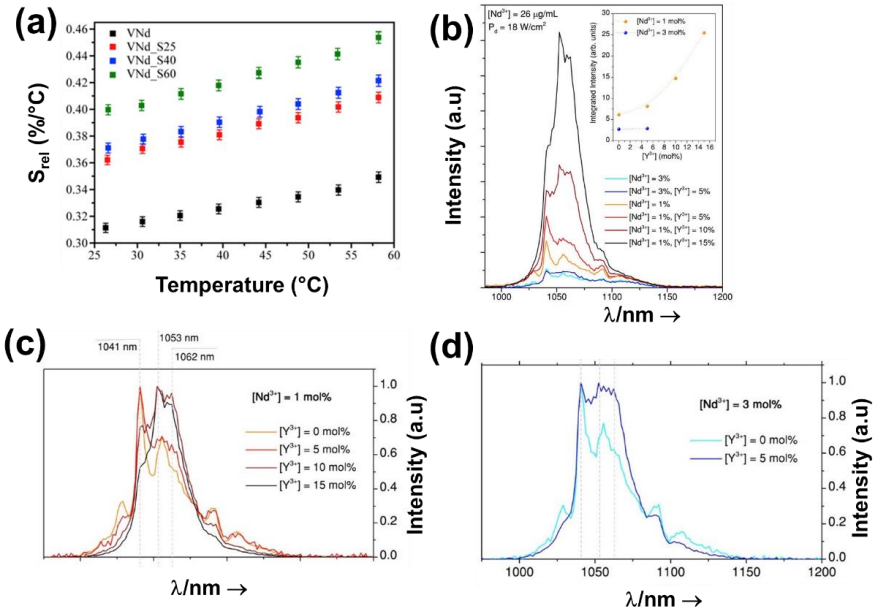

Figure 1.28. Effect of the thickness of the silica shell on the thermal performance of Nd^{3+} doped $YVO_4@SiO_2$, where S25, S40, S60 stand for the thickness of the silica in nm. Adapted with permission.[251] Copyright from Elsevier 2017. Effect of Y^{3+} impurities in Nd^{3+} doped CaF_2, (b) intensity of $^4F_{3/2} \rightarrow {}^4I_{11/2}$ emissions and (c), (d), spectral line shape of $^4F_{3/2} \rightarrow {}^4I_{11/2}$ emissions. Adapted with permission.[252] Copyright from American Chemical Society 2018.

When using the 1350 nm emission for temperature sensing, Nd^{3+} doped YAP nanoparticles were used to explore the full width at half maximum (Δv) of the emission located at 1348 nm as a function of the temperature, from room temperature to 370 K.[158] Upon green light excitation, Nd^{3+} promotes its electrons from the $^4I_{9/2}$ ground state to the $^4G_{9/2}$ or $^4G_{7/2}$ excited states, followed by non-radiatively decay to the $^4F_{5/2}$ and $^4F_{7/2}$ states. $^4F_{5/2}$ can populate the $^4F_{3/2}$ using another non-radiative decay. From this state, a radiative decay to the $^4I_{13/2}$, generates the emission located at 1348 nm (see Figure 1.29 (a)). As the temperature increased, Δv became broader and its relation with temperature could be fitted to a second order polynomial function of the form:[158]

$$\Delta v = a + bT + cT^2 \quad (1.42)$$

where a, b and c are constants to be determined from the fitting of the experimental data. S_{rel} of this thermometer is 3.3% K^{-1} and δT of 0.37 K at room temperature.[158]

An additional strategy towards tuning the performance of these thermometers is the intentional introduction of impurities in the host, such as the case of the incorporation of Y^{3+} ions in Nd^{3+} doped CaF_2 cubic nanoparticles.[252] The presence of Y^{3+} avoids the formation of clusters of Nd^{3+} ions in these nanoparticles, and thus, it prevents the quenching of their emissions, leading to a brighter luminescence upon using the proper doping ratio (see Figure 1.28 (b)).[252] A brighter emission lead to a more accurate and reliable performance of the thermometer.[21, 204] Nevertheless, the S_{rel} of these nanocrystals, tested as a function of the amount of the impurity on the structure, is relative low.[252] Besides the generation of brighter emissions, the introduction of impurities lead to changes in the shape of the emission band (see Figure 1.28 (c) and (d)). These changes are assigned to a modification of the direct environment around Nd^{3+} ions and to a different distribution of the optical centers among the different nanoparticles.[252] Besides tuning the optical and thermometric performance of these nanocrystals via the introduction of impurities, their relatively low thermal sensitivity arise also from the emission used being generated by TCLs with a low energy gap between them in the range of 49-98 cm^{-1}, depending on the Y^{3+} content.[252]

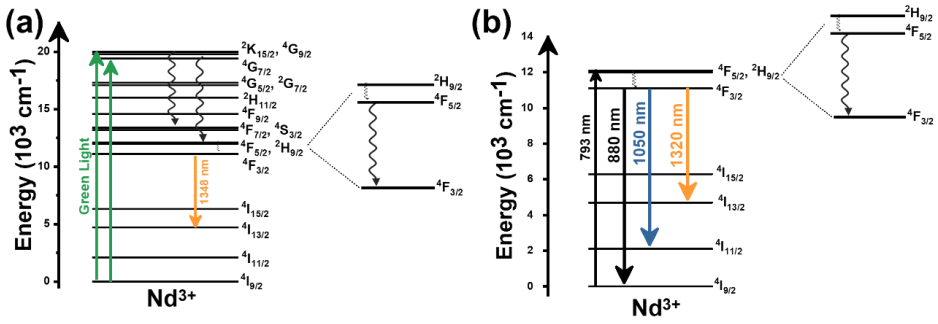

Figure 1.29. Mechanism of the generation of the: (a) 1348 nm emission in Nd^{3+} doped YAP nanoparticles, under green light excitation and (b) 1050 nm and 1320 nm emissions in Nd^{3+} doped $LiLuF_4$@$LiLuF_4$ nanoparticle under 793 nm excitation.

Further, Skripka *et al.* demonstrated that upon intermixing and discriminating different factors such as the absolute intensity, the spectral shift and the line broadening, contributing to the emission changes of Nd^{3+}, better thermometric performance can be extracted when compared to the nanothermometers based only on the thermalization of the Stark sublevels.[165] Hence, upon 793 nm, the Nd^{3+} ions embedded in a core@shell structure $LiluF_4$@$LiLuF_4$, can absorb the energy and excite the electrons to the $^4F_{5/2}$ state, from which due to non-radiative decays, the $^4F_{3/2}$ state can be populated (see Figure 1.29 (b)). From here, successive radiative decays can lead to the generation of emissions lines located at 880 nm (described in Section 2.2.1), 1050 nm and 1320 nm. The corresponding FIR between different emission peaks coming from differentStark sublevels of each of these emissions, were extracted to determine the thermometric performance of these nanomaterials. Hence, the FIR from the 1050 nm emissions, generates a relatively higher S_{rel} compared to the 1320 nm emissions, for values of 0.49% K^{-1} and 0.48% K^{-1} at the physiological range of temperatures, respectively. The authors emphasized that if taken into account only the temperature dependence of the emissions coming only from the thermalization of the corresponding energy states for each emission, the performance of these nanothermometers would have been in the range of 0.09 $\%K^{-1}$ (the energy gap was around 55 cm^{-1}). Thus, by spectrally resolve the fine Stark structure of the Nd^{3+} with the adequate detector systems (InGaAs NIR sensors in this case) and proper choice and design of the host material, an improvement on the thermal sensitivity based on singled Nd^{3+} nanothermometers, can be achieved.

Overall, concerning the thermometric performance of single Nd^{3+} doped luminescent thermometers, the use of the 1350 nm emission results in a higher S_{rel}, however, if advanced detector system and proper host material are chosen, the 1050 nm emission, can stand as a promising alternative. Further, the thermometers based on the 1350 nm emissions, rely on the excitation in the visible, which will, of course, limit the biomedical applications of this thermal sensor.[162] On the other hand, most of the 1050 nm are mostly excited within the I-BW, which besides their low S_{rel}, facilitates their use in biological experiments.

4.2.2. Dual doped Nd^{3+} luminescent thermometers operating in the II-BW

Although there are not too many examples of dual emitting luminescent thermometers combining Nd^{3+} with other materials or Ln^{3+} apart from Yb^{3+}, the ones reported exhibit a high S_{rel}.

For example, Cerón *et al*. developed a high-resolution temperature sensor consisting on Nd^{3+} doped $NaGdF_4$ dielectric nanoparticles and semiconductor PbS/CdS/ZnS quantum dots (QDs) combined in a poly(lactic-co-glycolic acid) (PLGA) hybrid nanostructure, excited within the I-BW (808 nm) and emitting in the II-BW.[253] This thermometer worked on the basis of the different temperature responses of its components. While the emission of Nd^{3+}, located at 1060 nm, remained unchanged in the physiological range of temperatures, the 1300 nm emission of the

QDs, assigned to their first exciton, decreased linearly due to photon-assisted processes (see Figure 1.30 (a)).[253] Hence, they developed a highly sensitive thermometer based on the change in the emission of the quantum dots and using the emission of the Ln^{3+} ion as a reference probe. The value of S_{rel} and the corresponding δT, achieved at 303 K, are 2.5% K^{-1} at 0.2 K, respectively.[253]

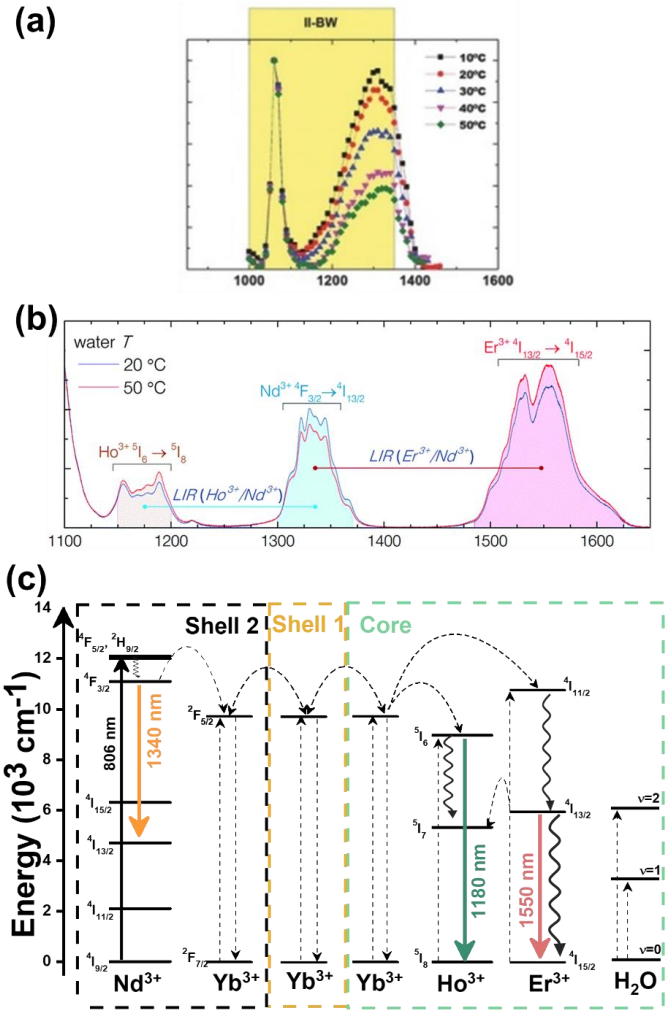

Figure 1.30. (a) Evolution of the emissions of Nd^{3+} and QDs in Nd:$NaGdF_4$@ PbS/CdS/ZnS coated with PGLA. Adapted with permission.[253] Copyright from Wiley-WCH 2015. (a) Emissions and (c) mechanism of the generation of the emission lines on Er^{3+}, Ho^{3+}, Yb^{3+}@Yb^{3+}@Nd^{3+},Yb^{3+}@$NaGdF_4$ multishell nanocrystals. Figure (b) is adapted with permission.[254] Copyright from The Royal Society of Chemistry 2017.

A water soluble multishell complex nanostructure based on hexagonal $NaGdF_4$ has been also proposed as a thermal probe in the II-BW (and in the mixed II- III BW region, as will be discussed in Section 5). This multishell nanostructure, composed of an active core Er^{3+}, Ho^{3+}, Yb^{3+}:$NaGdF_4$@inert shell Yb^{3+}:$NaGdF_4$ (shell 1)@active shell Nd^{3+},Yb^{3+}:$NaGdF_4$ (shell 2)@inert shell $NaGdF_4$ (shell 3) (hereafter Er^{3+},Ho^{3+}, Yb^{3+}@Yb^{3+}@Nd^{3+},Yb^{3+}@$NaGdF_4$), was synthesized via a thermal decomposition process, leading to oleate capped nanoparticles.[254] To render this nanostructure water dispersible, an encapsulation process using polyethylene glycol-grafted

phospholipid (PEG-DOPE) micelles was performed. The 806 nm energy of the excitation source lead to emissions located in the II-BW and III-BW (see Figure 1.30 (b)).

The excitation source is absorbed by the Nd^{3+} ions in shell 2 that subsequently generate the emission at 1340 nm, after a non-radiative decay to the $^4F_{3/2}$ level. This energy is also transferred via several ET processes through Yb^{3+} ions in shell 1 to the core, leading to the population of the $^5I_6$ and $^4I_{11/2}$ levels of Ho^{3+} and Er^{3+}, respectively (see Figure 1.30 (c)). The 1180 nm emission of Ho^{3+} is generated after a radiative decay to the ground state $^5I_8$. From the excited $^4I_{11/2}$ level of Er^{3+}, a non-radiative decay leads to the population of the lower excited level $^4I_{13/2}$, prior to relaxing to the ground state, were the 1550 nm emission located in the III-BW, is produced.[254] Therefore, the role of the shell 1 is to suppress the interionic quenching of Er^{3+} and Ho^{3+} emissions by Nd^{3+} ions, while the presence of Yb^{3+} in the core, shell 1 and shell 2, facilitates the energy migration across the multiple layers.[254] Hence, from this nanostructure, three emissions are generated, from which two of them are located at the II-BW (1180 nm of Ho^{3+} and 1340 nm of Nd^{3+}) and one in the III-BW (1550 nm of Er^{3+}). In this section, we will explore the possibility of the emissions located in the II-BW for thermal sensing.

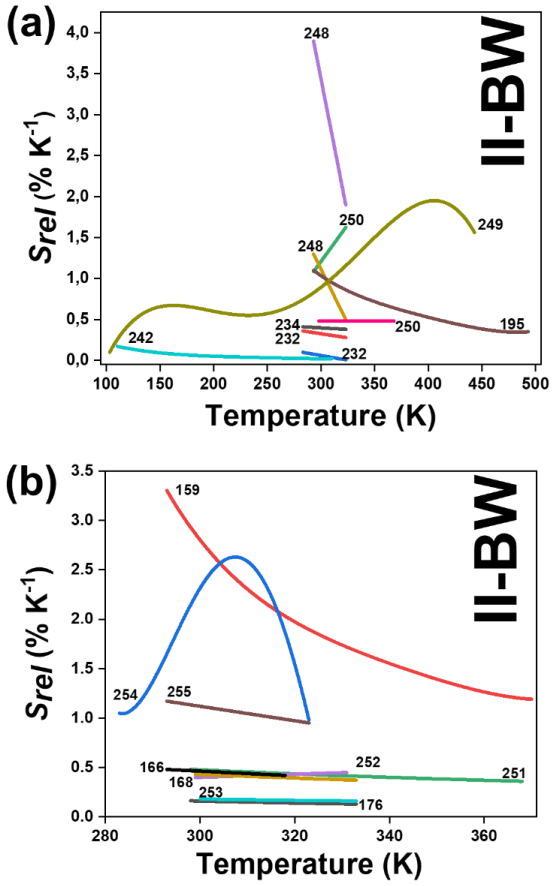

Figure 1.31. Temperature dependence of the relative thermal sensitivity of: (a) Yb^{3+} and (b) Nd^{3+} doped luminescent thermometers operating in the II-BW region. Numbers represent the corresponding references.

The temperature determination from this luminescent thermometer is done by studying the temperature dependence over the physiological range of the intensity ratio between the emission at 1180 nm of Ho^{3+} (located at the core) and the 1340 nm emission of Nd^{3+} (located in shell 2).

With the increase of the temperature, the intensity of the emission of Ho^{3+} increases, due to the phonon-assisted Yb^{3+} ($^2F_{5/2}$) → Ho^{3+} ($^5I_6$) process,[255] whereas the emission of Nd^{3+} decreases, due to the phonon-assisted energy transfer Nd^{3+} ($^4F_{3/2}$) → Yb^{3+} ($^2F_{5/2}$) process (see Figure 1.30 (b) and (c)).[207, 254]

These multishell nanocrystals are dispersible in water, hence, additional de-excitation channels related to the presence of water molecules on the surface of these nanocrystals, should be expected. In order to prevent these channels, the third passivating undoped shell was introduced. In terms of the generation of the emissions lines, Nd^{3+} ions located in shell 2, absorbs the laser source and subsequently is excited at the $^4F_{5/2}$, from which a radiative decay at the $^4I_{13/2}$ energy level, generates the emission line at 1340 nm (see Figure 1.30 (c)). Part of the excitation energy is transfer from Yb^{3+} ions in shell 2 through the shell 1 to the core via successive ET processes, leading to the population of $^5I_6$ state of Ho^{3+} and $^4I_{11/2}$ state of Er^{3+} ions. From these levels, successive non-radiative decays can lead to the population of $^5I_7$ state of Ho^{3+} and $^4I_{13/2}$ state of Er^{3+} ions. In addition, $^5I_7$ state of Ho^{3+} ions can be populated also from the $^4I_{13/2}$ state of Er^{3+} ions via ET (see Figure 1.30 (c)). The maximum S_{rel} achieved for the intensity ratio 1180 nm/1340 nm is 1.17% K^{-1} in the physiological range of temperatures. These nanocrystals represent a good choice for biomedical application due to high S_{rel} in the physiological range of temperature, they are water dispersible and operate in the II-BW.

Besides its relatively good temperature sensing performance, these core@shell and multishell materials, introduced during this spectral regime, are based on fluoride doped hosts synthesized (mostly) through the thermal decomposition of trifluoroacetate precursors to control the size and morphology, which is accompanied by high toxicity of the by-product and final products of the reactions.[256] Nevertheless, in terms of the thermometric performance, clearly complex nanoarchitectures, such as core@shell and multishell materials, exhibit high relative thermal sensing compared to the other forms of materials (see Figure 1.31 (a) and (b)) and fulfill the conditions to be applied for biomedical applications. They can be excited in the biological windows and generated highly temperature dependent emissions, also located within the biological windows regimes.

5. Lanthanide doped luminescent nanothermometers operating in the II and III-BW simultaneously

Based on the emission at 1550 nm, Er^{3+} ions represent one of the most explored lanthanide luminescent ions for thermometry operating in the II-BW and III-BW simultaneously, by combining this emission with other emissions located at the II-BW arising either from other Ln^{3+} ions, or transition metals. Concerning the combination of Er^{3+} with lanthanide ions, typical examples involve Er^{3+} codoped with Yb^{3+}, Nd^{3+} and Ho^{3+} emissions. For the combination with transition metals, only one example involves the application of the Er^{3+} emission with the emission of nickel (II), located at the II-BW. A few cases explore also single center emitting Ln^{3+} ions (Nd^{3+} and Tm^{3+}) as potential thermometers operating in this region.

Table 1.4. Summary of all Ln^{3+} doped luminescent thermometers operating simultaneously in the II-BW and III-BW regions. In the table are shown the activators (A) and sensitizers (S). The excitation (λ_{exc}) and emission (λ_{em}) wavelengths are shown in nanometers (nm), together with the corresponding transition of the emissions. ΔT stands for the temperature range were the thermal reading was investigated. The thermometric parameter (Δ) indicates the luminescent nanothermometry class used: I-for intensity ratio thermometry. The maximum relative thermal sensitivity (S_{rel}) and the temperature resolution (δT) are presented at the temperature where these values were obtained. We indicated with an asterisk, the values of S_{rel} or δT calculated by us using the parameters published in the corresponding references. The double line separation between rows stands for different type of lanthanide doped nanothermometers, as discussed on the corresponding subsections.

A	S	Host	λ_{exc} (nm)	λ_{em} (nm)	Transitions	ΔT (K)	Δ	S_{rel}/T (% K^{-1})/K	δT (K)	Ref.
Er^{3+}, Yb^{3+}	Tm^{3+}	Er, Yb:LaF_3@Tm, Yb:LaF_3	690	1000 (Yb^{3+}), 1550	$^2F_{5/2}$ → $^2F_{7/2}$ (Yb^{3+}), $^4I_{13/2}$ → $^4I_{15/2}$	293-323	I_{1000}/I_{1550}	5/293	0.3	247

				(Er^{3+})	(Er^{3+})					
Er^{3+}, Yb^{3+}	Yb^{3+}	$Na_2K(Lu_3Si_6O_{18})$	903	1125 (Yb^{3+}), 1640 (Er^{3+})	$^2F_{5/2} \rightarrow {}^2F_{7/2}$ (Yb^{3+}), $^4I_{13/2} \rightarrow {}^4I_{15/2}$ (Er^{3+})	12-450	I_{1125}/I_{1640}	2.6/26.8	0.08	257
Er^{3+}, Yb^{3+}	Tm^{3+}	Er, Yb:LaF_3@Tm, Yb:LaF_3	808	1000 (Yb^{3+}), 1550 (Er^{3+})	$^2F_{5/2} \rightarrow {}^2F_{7/2}$ (Yb^{3+}), $^4I_{13/2} \rightarrow {}^4I_{15/2}$ (Er^{3+})	293-323	I_{1000}/I_{1550}	0.80/293	0.62*	247
Er^{3+}, Yb^{3+}	Tm^{3+}	Er, Tm, Yb:LaF_3	690	1000 (Yb^{3+}), 1550 (Er^{3+})	$^2F_{5/2} \rightarrow {}^2F_{7/2}$ (Yb^{3+}), $^4I_{13/2} \rightarrow {}^4I_{15/2}$ (Er^{3+})	293-323	I_{1000}/I_{1550}	0.7/293	0.71*	247
Er^{3+}, Ho^{3+}	Yb^{3+}	$NaYF_4$	980	1150 (Ho^{3+}), 1550 (Er^{3+})	$^5I_6 \rightarrow {}^5I_8$ (Ho^{3+}), $^4I_{13/2} \rightarrow {}^4I_{15/2}$ (Er^{3+})	299-319	I_{1150}/I_{1550}	2.17/319	0.23*	258
Er^{3+}, Ho^{3+}	Yb^{3+}	$NaYF_4$	980	1150 (Ho^{3+}), 1550 (Er^{3+})	$^5I_6 \rightarrow {}^5I_8$ (Ho^{3+}), $^4I_{13/2} \rightarrow {}^4I_{15/2}$ (Er^{3+})	298-319	I_{1150}/I_{1550}	1.87/298	0.2	259
Er^{3+}, Ho^{3+}	Yb^{3+}	Gd_2O_3	980	1149 (Ho^{3+}), 1545 (Er^{3+})	$^5I_6 \rightarrow {}^5I_8$ (Ho^{3+}), $^4I_{13/2} \rightarrow {}^4I_{15\%2}$ (Er^{3+})	313-573	I_{1550}/I_{1149}	0.82/498	0.61*	260
Er^{3+}, Ho^{3+}	Yb^{3+}	Y_2O_3	980	1149 (Ho^{3+}), 1545 (Er^{3+})	$^5I_6 \rightarrow {}^5I_8$ (Ho^{3+}), $^4I_{13/2} \rightarrow {}^4I_{15/2}$ (Er^{3+})	313-573	I_{1550}/I_{1149}	0.80/523	0.62*	260
Er^{3+}, Ho^{3+}	Yb^{3+}	YAG	980	1149 (Ho^{3+}), 1545 (Er^{3+})	$^5I_6 \rightarrow {}^5I_8$ (Ho^{3+}), $^4I_{13/2} \rightarrow {}^4I_{15/2}$ (Er^{3+})	313-573	I_{1550}/I_{1149}	0.48/573	1.05*	260
Er^{3+}, Ho^{3+}	Yb^{3+}	$BaTiO_3$	980	1149 (Ho^{3+}), 1545 (Er^{3+})	$^5I_6 \rightarrow {}^5I_8$ (Ho^{3+}), $^4I_{13/2} \rightarrow {}^4I_{15/2}$ (Er^{3+})	313-573	I_{1550}/I_{1149}	0.40/573	1.25*	260
Er^{3+}, Ho^{3+}	Yb^{3+}	$NaLuF_4$	975	1177 (Ho^{3+}), 1545 (Er^{3+})	$^5I_6 \rightarrow {}^5I_8$ (Ho^{3+}), $^4I_{13/2} \rightarrow {}^4I_{15/2}$ (Er^{3+})	298-568	I_{1177}/I_{1545}	0.21/298	2.38*	192
Er^{3+}, Ho^{3+}	Yb^{3+}	YVO_4	980	1149 (Ho^{3+}), 1545 (Er^{3+})	$^5I_6 \rightarrow {}^5I_8$ (Ho^{3+}), $^4I_{13/2} \rightarrow {}^4I_{15/2}$ (Er^{3+})	313-573	I_{1550}/I_{1149}	0.17/573	2.9*	260
Er^{3+}, Nd^{3+}	Nd^{3+}	Er,Ho,Yb:NaGdF_4@Yb:NaGdF_4 @Nd,Yb:NaGdF_4@NaGdF_4	806	1340 (Nd^{3+}), 1550 (Er^{3+})	$^4F_{3/2} \rightarrow {}^4I_{13/2}$ (Nd^{3+}), $^4I_{13/2} \rightarrow {}^4I_{15/2}$ (Er^{3+})	293-323	I_{1550}/I_{1340}	1.1/293	0.8	254
Er^{3+}, Ni^{2+}	Er^{3+}, Ni^{2+}	$SrTiO_3$	375	1245 (Ni^{2+}), 1540 (Er^{3+})	$^3T_{2g} \rightarrow {}^3A_{2g}$ (Ni^{2+}), $^4I_{13/2} \rightarrow {}^4I_{15/2}$ (Er^{3+})	123-483	I_{1540}/I_{1245}	5.8/483	0.08*	261
Tm^{3+}	-	LaF_3	690	1230, 1470	$^3H_5 \rightarrow {}^3H_6$ $^3H_4 \rightarrow {}^3F_4$	297-361	I_{1470}/I_{1230}	1.90/297	0.26*	262
Nd^{3+}	-	Gd_2O_3	808	1315, 1350	$^4F_{3/2} \rightarrow {}^4I_{13/2}$	303-393	I_{1315}/I_{1350}	0.23/303	2.17*	263

5.1. Er^{3+} doped luminescent nanothermometers operating in the II-BW and III-BW simultaneously

Several luminescent nanothermometers have been reported using the 1550 nm emission of Er^{3+} together with the emission of another Ln^{3+} ion, including Yb^{3+}, Ho^{3+} and Nd^{3+}, operating in this way in the II-BW and III-BW simultaneously.

Among these combinations, pairing it with the 1000 nm emission of Yb^{3+}, stands out as one of the most promising strategies to develop highly sensitive thermometers, especially when sensitized via Tm^{3+} (see Table 1.4). For example, Er^{3+}, Yb^{3+}:LaF_3@Tm^{3+}, Yb^{3+}:LaF_3 nanocrystals (also explored in the II-BW) display an outstanding S_{rel} with a value of 5% K^{-1} at room temperature.[247]

This high thermal sensitivity was extracted from the intensity ratio between the 1000 nm emission of Yb^{3+} and the 1550 nm emission of Er^{3+}, generated after the core@shell nanocrystals have been excited at 690 nm (the mechanism of generation of the emission lines is presented in Figure 1.26 (a)). Compared to the performance of the core-only Er^{3+}, Tm^{3+},Yb^{3+}:LaF_3 nanoparticles, the active core@active shell nanocrystals have a 7-fold higher S_{rel} (see Table 1.4).[247]

Furthermore, the authors investigated the effect of the excitation laser wavelength (690 nm and 808 nm) applied on the thermal sensing properties of these nanocrystals. The results suggests that the high value of S_{rel} achieved when exciting the nanoparticles at 690 nm, is a result of the $^3H_5$ level of Tm^{3+} ions contributing to the overall emission spectrum generated by the nanoparticles and/or when the $^3H_5$ (Tm^{3+}), $^2F_{5/2}$ (Yb^{3+}) $\rightarrow$ $^3H_5$ (Tm^{3+}), $^2F_{5/2}$ (Yb^{3+}) ET process is involved, implying that the 690 nm, contrary to the 808 nm, highly favors this ET process.[247] For the case of 808 nm emission, the maximum S_{rel} was only ~0.80% K^{-1}. Hence, an important conclusion drawn from this reference, is that engineering core@shell is not always a key feature on producing highly sensitive nanothermometers, but one has to properly select the most suitable excitation wavelength.

Er^{3+} and Yb^{3+} codoped lanthanide silicate host $Na_2K(Lu_3Si_6O_{18})$ with triclinic crystalline structure, synthesized by an autoclave assisted hydrothermal process, was also tested as luminescent nanothermometer over a wide range of temperatures (12-450 K).[257] The emission lines, located at 930-1125 nm corresponding to electronic transitions of Yb^{3+} and 1425-1640 nm corresponding to electronic transitions of Er^{3+}, were generated after excitation at 903 nm. Yb^{3+} acted here also as sensitizer, by absorbing the energy of the excitation source and promoting its electrons to the $^2F_{5/2}$ level. From here, an ET process can populate the $^4I_{11/2}$ level of Er^{3+}. From this level, a non-radiative decay can populate the $^4I_{13/2}$ level, prior to radiatively decay at the ground state, generating the emission of this ion. From this level, the $^4I_{9/2}$ can be populated, followed by an ET to the upper Stark sublevel of the $^2F_{5/2}$ state of Yb^{3+}. From here the lower Stark sublevel of the $^2F_{5/2}$ state can be populated via non-radiative processes, prior to relax radiatively to the ground state, where the emission of Yb^{3+} can be generated. The mechanism of the generation of these lines are similar to the ones presented in Figure 1.23 (a) or 1.25 (b), except a non-radiative process take place from $^4I_{11/2}$ level of Er^{3+} towards its $^4I_{13/2}$ level.

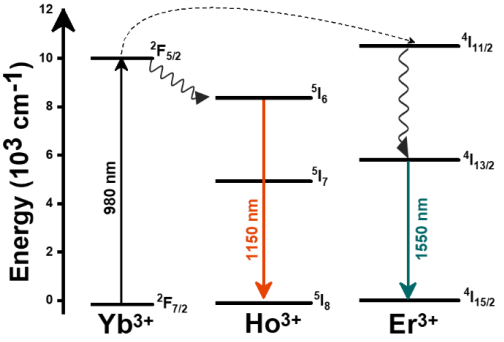

Figure 1.32. Mechanism of the generation of emissions lines in Er^{3+}, Ho^{3+}, Yb^{3+}:$NaYF_4$ material under 980 nm excitation.

To extract the intensity ratio and eventually the S_{rel}, the authors related the total transition probabilities to the inverse of the lifetime using the classic Mott-Seitz model.[264, 265] Besides this, this lifetime, considered as the sum of radiative (assumed to be temperature independent) and non-radiative lifetime (expressing an Arrhenius type of temperature dependence), is considered by the authors, to be proportional to the intensity of the emissions, as follows:[264, 265]

$$\frac{I\,(T)}{I_0} = \frac{\tau\,(T)}{\tau_0} \qquad (1.43)$$

where $I\,(T)$ and I_0 stand for the intensity at temperature T and 0 K, respectively, whereas $\tau\,(T)$ and τ_0 stands for the lifetime at temperature T and 0 K (the radiative lifetime), respectively. Taking into account two deactivation channels arising from two different emissions, from which one dominates over the other, such as the case of this thermometer, the thermometric parameter, related to the ratios between two intensities, is expressed as:

$$\Delta = \frac{I_1}{I_2} = \frac{\Delta_0}{1 + \alpha_1 \exp\left(-\frac{\Delta E_1}{k_B T}\right) + \alpha_2 \exp\left(-\frac{\Delta E_2}{k_B T}\right)} \qquad (1.44)$$

where Δ_0 is the thermometric parameter at 0 K, α is the ratio between the radiative and non-radiative rates, and ΔE_1 and ΔE_2 are the activation energies of the two deactivation channels. For the case of Er^{3+},Yb^{3+} codoped $Na_2K(Lu_3Si_6O_{18})$ these two channels, responsible for thermal sensing due to Er^{3+}-to-Yb^{3+} energy transfer associated with ΔE_1 and ΔE_2, are, respectively, the Er^{3+}-to-Yb^{3+} energy transfer through the resonant excited levels, and the energy migration between the two distinct neighboring Yb^{3+} sites.[257] The S_{rel} calculated over the temperature range from 12 K to450 K reached the maximum of 2.6% K^{-1} at 26.8 K.[257] Despite of this high value, if we observe the temperature dependence of S_{rel} in the physiological range of temperatures, the value is close to zero (see Figure 1.33).

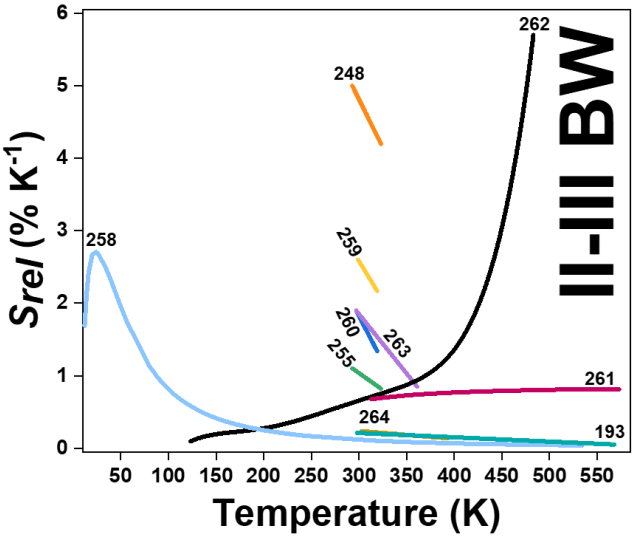

Figure 1.33. Temperature dependence of S_{rel} of all nanothermometers operating simultaneously in the II and III-BW regions. Numbers represent the corresponding literature references for each thermometer.

A second combination of emissions for luminescent thermometers operating simultaneously in the II and III-BWs is that formed by the emissions of Er^{3+} and Ho^{3+} ions, located at ~1550 nm and ~1150 nm, respectively. These emission lines are generated in the presence of Yb^{3+} ion as sensitizer, hence special attention should be payed to the overheating problem when pumping at 980 nm.

For Er^{3+},Ho^{3+}, Yb^{3+}:$NaYF_4$ nanothermometers operating within these spectral regions, we would like to stress that by using Yb^{3+} as sensitizer, which has to be excited at 980 nm, and Er^{3+} as emitter at 1550 nm,[258, 259] an overlap with the water absorption bands, especially at around 1500 nm, is produced, together with heat induced by the absorption of NIR photons by water, which

would hamper their potential biomedical applications.[266, 267] For thermal sensing, the intensity ratio between the 1150 nm emission of Ho^{3+} and 1550 nm of Er^{3+} was used. These emissions lines are generated after the absorbance of the 980 nm excitation source from Yb^{3+}, which promotes its electrons to the $^2F_{5/2}$ excited state. From here, the $^4I_{11/2}$ level of Er^{3+} and the $^5I_6$ level of Ho^{3+}, can be populated by ET or photon assisted ET processes (see Figure 1.32), respectively. From the $^4I_{11/2}$ level, Er^{3+} ion can be relaxed non-radiatively to the $^4I_{13/2}$, prior to decaying radiatively to the ground state $^4I_{15/2}$, generating the emission at 1550 nm.[258, 259] From the 1150 nm emission of Ho^{3+}, it can be generated from direct relaxation from the $^5I_6$ level to the ground state $^5I_8$ level (see Figure 1.32).

In terms of thermal sensitivity, Er^{3+},Ho^{3+}, Yb^{3+}:$NaYF_4$ nanocrystals,[258, 259] show a 9-fold higher sensitivity than Er^{3+},Ho^{3+}, Yb^{3+}:$NaLuF_4$ nanocrystals,[192] being both based on the intensity ratio between the 1150 nm emission of Ho^{3+} and 1550 nm of Er^{3+} and operative in the physiological range of temperatures (see Figure 1.33 for a comparison of the evolution of the S_{rel} of these materials and Table 1.4 for maximum values of sensitivity). Nevertheless, the thermometric parameter of the Er^{3+},Ho^{3+}, Yb^{3+}:$NaYF_4$ nanocrystals was fitted to a simple linear function (as in Equation 1.22),[254] whereas for $NaLuF_4$, nanocrystals it was fitted according to a second order polynomial function (as in Equation 1.23).[191] In the former case, an overestimation of S_{rel} might have been produced due to the fitting model used.

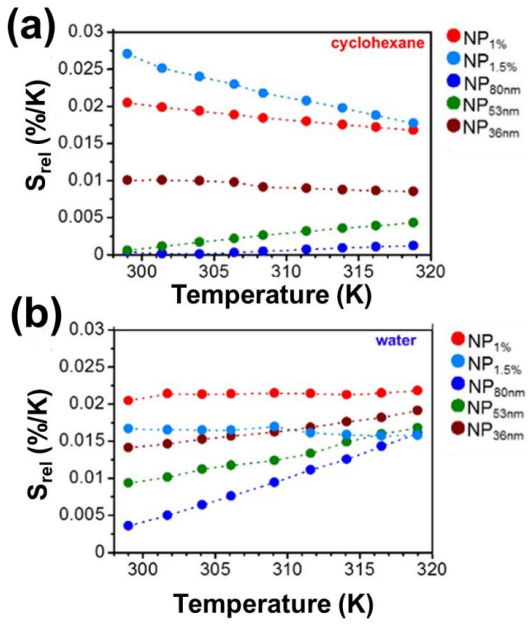

Figure 1.34. The thermal sensing properties of Er^{3+}/Ho^{3+}/ Yb^{3+}:$NaYF_4$ nanocrystals as a function of dispersing agents: (a) cyclohexane and (b) distilled water. Also the effect of the concentration of the emitting Ho^{3+} content (1.5 mol% and 3 mol%) and the size of the nanocrystals (36 nm, 53 nm and 83 nm) can be observed. Adapted with permission.[258] Copyright from Elsevier 2018.

Similar S_{rel} for Er^{3+},Ho^{3+}, Yb^{3+}:$NaYF_4$ nanocrystals was also achieved by Wortmann *et al.*[258] The authors evaluated the performance of these nanocrystals by tuning their sizes, dispersing agent (distilled water versus apolar organic solvent such as cyclohexane) and concentration of the emitting ions. Three trends were observed: (i) S_{rel} is increasing with the decrease of the size of the nanocrystals (see Figure 1.34 (a) and (b)), attributed to the increase of the surface ions due to increase of the surface-to-volume ratio with the decrease of size, (ii) S_{rel} is higher when the nanocrystals are dispersed in water than in cyclohexane (see Figure 1.34 (a) and (b)), attributed to the O–H vibrational stretching mode of water molecules, (iii) S_{rel} is dependent from the concentration of emitting ions (tuned only for Ho^{3+} ions for 1.5 mol% and 3 mol%), governed by

CR and quenching processes (see Figure 1.34 (a) and (b)).[258] Nevertheless, the maximum S_{rel} for a value of 2.17% K^{-1} was obtained for nanoparticles with size around 48 nm, dispersed in cyclohexane and concentration of Ho^{3+} ions for 1.5 mol%.[258] The authors did not provide any explanation about this value of S_{rel}. Please note that for every tuned parameter, the authors have reported the value of S_{rel} at the highest temperature under investigation (319 K), but in some cases, especially when the particles are dispersed in cyclohexane (see Figure 1.34 (a)), S_{rel} exhibits the maximum value at room temperature.

Continuing the combination between the emissions of Er^{3+} and Ho^{3+}, a novel strategy is reported by Jia *et al*. exploring a new type of phonon-assisted nanothermometry.[260] The authors reasoned that phonons can play an essential role in allocation of harvested excited energy into the two emitting ions (Er^{3+} and Ho^{3+}) via two type of phonon-assisted processes, mainly multi-phonon relaxation (MPR) and phonon-assisted energy transfer (PAT) processes.[260] By doing so, these processes greatly influence the nanothermometric performance of the nanocrystals. Hence, by excitation at 980 nm, Yb^{3+} can absorb this energy to promote its electrons from the fundamental to the excited state, from where a part of the energy is then transferred to the $^4I_{11/2}$ state of Er^{3+} via an ET process. From there, the downshifting emission corresponding to the $^4I_{13/2} \rightarrow {}^4I_{15/2}$ transition, located at 1550 nm, takes place via a MPR process. Part of the energy of the Yb^{3+} ions is also transferred via a PAT process to the $^5I_6$ state of Ho^{3+}, from which, a radiative decay back to the ground state, leads to the 1190 nm emission (see Figure 1.35 (a)).[260] The electronic population of the energy states of Er^{3+} and Ho^{3+} is governed by MPR and PAT processes. It should be stated here that additional PAT processes take place between Er^{3+} and Ho^{3+} but they do not influence the thermometric performance of these materials. The temperature dependence of the probability rates of these processes to happen can be described as:[260, 268]

$$WPR_{MPR} = WPR_{MPR}(0)\left[\frac{\exp(\frac{hv}{k_BT})}{\exp\left(\frac{hv}{k_BT}\right)-1}\right]^{\frac{\Delta E_1}{hv}} \qquad (1.45)$$

$$WPR_{PAT} = WPR_{PAT}(0)\left[\frac{\exp(\frac{hv}{k_BT})}{\exp\left(\frac{hv}{k_BT}\right)-1}\right]^{\frac{\Delta E_2}{hv}} \qquad (1.46)$$

where $WPR_{MPR}(0)$, $WPR_{PAT}(0)$, hv, $\Delta E_1$and ΔE_2 represent the MPR rate at 0 K, the PAT rate at 0 K, the phonon energy of the host, the energy gap between the $^4I_{11/2}$ and $^4I_{13/2}$ states of Er^{3+}, and the energy gap between the $^2F_{5/2}$ electronic level of Yb^{3+} and the $^5I_6$ electronic state of Ho^{3+},respectively. The thermometric parameter, defined as the intensity ratio between the emissions of Er^{3+} and Ho^{3+}, and the corresponding S_{rel} can be defined as:

$$\Delta = \frac{I_{Er}}{I_{Yb}} = \frac{N_{Yb}W_RW_{MPR}A_1}{N_{Yb}W_{PAT}A_2} = a\left[\frac{\exp\left(\frac{hv}{k_BT}\right)}{\exp\left(\frac{hv}{k_BT}\right)-1}\right]^b \qquad (1.47)$$

$$S_{rel} = \left|\frac{1}{\Delta}\frac{d\Delta}{dT}\right| = \frac{\Delta E_1 - \Delta E_2}{k_BT^2}\frac{1}{\exp\left(\frac{hv}{k_BT}\right)-1} \qquad (1.48)$$

where $a=\frac{W_RW_{MPR}(0)A_1}{W_{PAT}(0)A_2}$, $b=\frac{\Delta E_1-\Delta E_2}{hv}$, N_{Yb} represents specifically the electronic population of the $^2F_{5/2}$ state of Yb^{3+},W_R is the probability rate of the ET process, and A_1 and A_2 represent the spontaneous emission rate of the corresponding emission transitions.

For temperature sensing purposes, the effect of these two novel mechanisms was tested as a function of the matrices used to host the Ln^{3+} ions. Thus, Er^{3+}, Ho^{3+}, and Yb^{3+} were embedded in five different hosts, including $BaTiO_3$, Gd_2O_3, Y_2O_3, YAG and YVO_4.[260] Theoretically, the different phonon modes of the host would contribute differently to the MPR and PAT processes, however one of them should play a major role.[269] In this study, the authors investigated the effect of the

dominant and cutoff phonons on the thermometric performance of these luminescent thermometers, and determined that the dominant phonons have a major contribution on the MPR and PAT processes, and as a consequence, also on their temperature sensing performance. Hence, the term hv in Equation 1.47 and Equation 1.48 was assigned to the dominant phonons presented in each of the tested hosts.[260] The ability to sense temperature by these nanomaterials will be reversely proportional to the dominant phonon energy (see Figure 1.35 (b), assuming identical $\Delta E_1 - \Delta E_2$ in the different hosts by ignoring the small differences that can be produced.[260] The highest S_{rel} was obtained for Er^{3+},Ho^{3+}, Yb^{3+}:Gd_2O_3 nanoparticles, which displayed the lowest dominant phonon energy. It can be noticed that the maximum S_{rel} of these materials was usually obtained at the maximum temperature investigated (see Table 1.4), contrary to the general trend observed in the other luminescence thermometers considered. In Table 1.4, however, it can be also observed that this phonon-assisted luminescent thermometers do not offer an improvement of the thermal sensitivity, when compared to the other thermometers (see for example Er^{3+},Ho^{3+}, Yb^{3+}:$NaYF_4$,[258,259]). In fact, their S_{rel} are relatively low, although for the case of Er^{3+}/Ho^{3+}/ Yb^{3+}:$NaLuF_4$,[192] S_{rel} is similar, regardless of the fact that the better performance of the later is achieved at room temperature.

For the combination of the emissions arising from Er^{3+} and Nd^{3+} ions, located at 1550 nm and 1340 nm, respectively, we recall the water soluble Er^{3+},Ho^{3+}, Yb^{3+}@ Yb^{3+}@Nd^{3+},Yb^{3+}@$NaGdF_4$ in PEG-DOPE micelles seen previously in Section 4.2.2, as the only example that could be find in the literature.[254] The mechanism of the generation of these emission lines is presented in Figure 1.30 (c). S_{rel}, extracted from the ratio of the emission intensity at 1550 nm versus the emission intensity at 1340 nm is 1.1% K^{-1} at room temperature.[254] This value is relatively low compared to other type of active core@active shell nanoparticles, such as the case of Er^{3+}, Yb^{3+}:LaF_3@Tm^{3+}, Yb^{3+}:LaF_3 nanocrystals, but still higher compared to the major part of the luminescent nanothermometers based on the combination of emissions arising from Er^{3+} and Ho^{3+} ions (see Table 1.4). Despite this, the temperature sensing properties of this multishell structure are acceptable for biomedical applications since they are water dispersible and are excited within the biological windows regime.

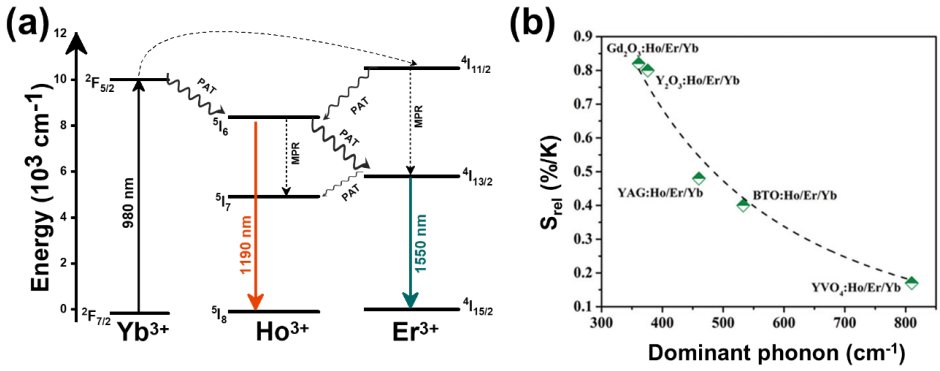

Figure 1.35. (a) Schematic representation of the mechanism of the generation of the emission bands in Er^{3+},Ho^{3+}, Yb^{3+} co-doped materials after 980 nm excitation. (b) Relative thermal sensitivity of Er^{3+},Ho^{3+}, Yb^{3+} co-doped materials as a function of the dominant phonon energy. Adapted with permission.[260] Copyright from Wiley 2020.

Combining the emission of Er^{3+} with Ni^{2+} resulted in a S_{rel} slightly higher than the one obtained with the highly sensitive Er^{3+}, Yb^{3+}:LaF_3@Tm^{3+}, Yb^{3+}:LaF_3 nanocrystals. The Er^{3+}, Ni^{2+} doped $SrTiO_3$ nanocrystals were excited at 375 nm, and two emission bands were generated at 1540 nm, generated by Er^{3+}, and at 1240 nm, generated by Ni^{2+}, respectively.[261]

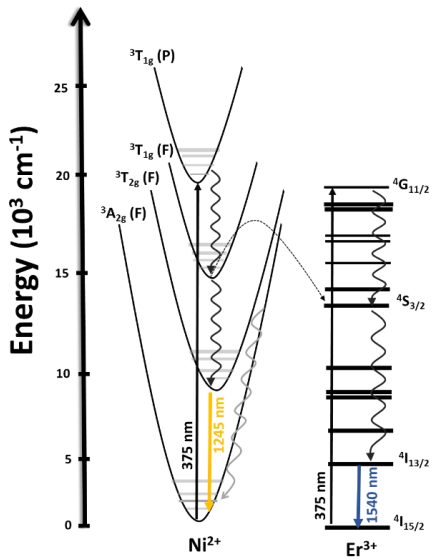

Figure 1.36. Mechanism of the generation of emissions lines in Ni^{2+}, Er^{3+}:$SrTiO_3$ under 375 nm excitation.

Upon excitation at 375 nm, Er^{3+} ions are excited from the ground state to the $^4G_{11/2}$ state. From here, non-radiative decay processes can populate the $^4S_{3/2}$ and $^4I_{13/2}$ states. From the later, a radiative relaxation to the ground state results in the generation of the 1540 nm emission band. Similarly, the 1240 nm emission of Ni^{2+} ion is generated from the absorption of the 375 nm source, promoting its electrons to the $^3T_{1g}$ (P) excited state. From here, non-radiative decay processes can populate the $^3T_{1g}$ (P) and $^3T_{2g}$ (F) metastable states, prior of relaxing radiatively to the ground state which results in the generation of the corresponding emission band of this transition metal ion. [261] In addition, from the $^3T_{1g}$ (P), an ET process to the $^4S_{3/2}$ state of Er^{3+}, can take place (see Figure 1.36), which eventually will lead to the generation of the emission band at 1540 nm. The emission located at 1540 nm is temperature insensitive, serving as reference, whereas the emission at 1240 nm, drastically changes as the temperature increases.[261]

The maximum S_{rel} from this luminescent thermometer was 5.8% K^{-1}, obtained at the highest temperature under investigation (483 K).[261] This value is comparable with that reported for Er^{3+}, Yb^{3+}:LaF_3@Tm^{3+}, Yb^{3+}:LaF_3 nanocrystals, despite the significant differences in terms of excitation wavelength. However, to have a proper comparison with other luminescent thermometers as potential temperature sensors for biomedical applications, the S_{rel} in the physiological range of temperature should be compared. By doing so, the value of S_{rel} in the physiological range for this luminescent thermometer is ~0.80% K^{-1} (see Figure 1.33).[261] In addition, another significant limitation for the luminescent thermometers based on the combination of Er^{3+} and Ni^{2+}, is the need of excitation in the UV at 375 nm, which reduces significantly the penetration depth that can be achieved, and more important, this light induces phototoxicity in biological tissues.[91]

5.2. Other Ln^{3+} doped luminescent nanothermometers operating in the II-BW and III-BW simultaneously

Single doped lanthanide materials based on the emission of Tm^{3+} and Nd^{3+} are reported as luminescent thermometers operating simultaneously in the II- and III-BWs.

For the Tm^{3+} doped thermometers, their performance is based on the intensity ratio between the 1230 nm and 1470 nm emissions, generated after excitation either at 690 nm or 790 nm, as reported in the case when embedded in hexagonal LaF_3.[262] The mechanism of the generation of these emission bands is based on cross-relaxation processes (CR) and multiphonon decay processes (see Figure 1.37 (a)). The population of the $^3H_5$ level is favored by the CR2 process, whereas the population of the $^3H_4$ level is attributed to the relaxation of the absorbed phonons at

690 nm that have been excited to the $^3F_3$ level.[262] From the $^3H_5$ level, a radiative decay to the $^3H_6$ ground state, generates the emission located at 1230 nm, whereas through the $^3H_4 \rightarrow {}^3F_4$ transition, the emission band located at 1470 nm, is generated.

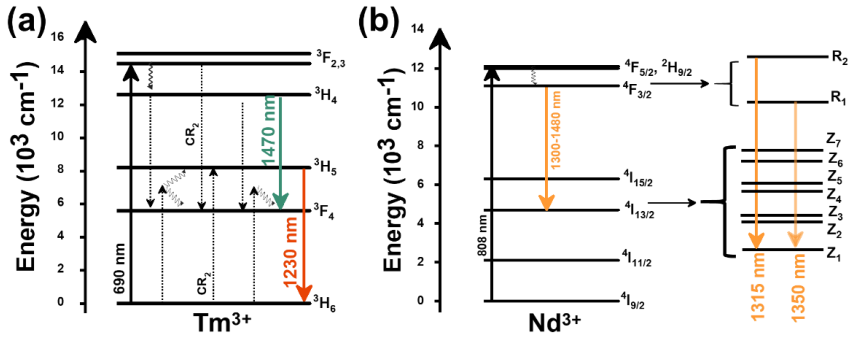

Figure 1.37. Mechanism of the generation of the emission lines on: (a) Tm^{3+} doped LaF_3 nanocrystals, and (b) Nd^{3+} doped Gd_2O_3 nanospheres, operating in the II-BW and III-BW regions simultaneously.

Concerning the temperature sensing properties of this Tm^{3+} doped thermometer, they were extracted from a linear temperature dependence of the intensity ratio between the 1230 nm and the 1470 nm emission bands of Tm^{3+}. However, several parameters were tested before determining the optimal S_{rel}. First, two different excitation wavelengths (690 nm and 790 nm) were tested with the goal of determining which one generates brighter emissions. Upon 690 nm excitation, both emissions exhibited a higher intensity when compared to the 790 nm excitation (see Figure 1.38 (a)), demonstrating a more efficient excitation path. In fact, when excited at 790 nm, the 1230 nm emission band shows a considerably lower luminescence intensity compared to the other emission band, mainly due to inefficient population of the $^3H_5$ level due to the small branching ratio of the $^3H_4 \rightarrow {}^3H_5$ transition and the low phonon energy of the LaF_3 host (<400 cm^{-1}),[270] that hampers multiphonon decay processes in this large energy gap.

For the case of 690 nm excitation, this level is populated through a CR process ($^3F_3$; $^3H_6 \leftrightarrow {}^3F_4$; $^3H_5$) that can be demonstrated by the increase of the intensity of the 1230 nm emission band when the concentration of Tm^{3+} increased.[262] Second, by tuning the concentration of Tm^{3+} from 1 mol% to 5 mol% the concentration that displays the highest change in the intensity of the emissions as the temperature increased was selected. It can be observed in Figure 1.38 (b) that the intensity of the 1230 nm emission band changes substantially as a function of the concentration of Tm^{3+}, whereas the band at 1470 nm is almost insensitive, upon increasing the temperature from 297 K to 361 K. The intensity ratio increases as the temperature increases for all the Tm^{3+} concentrations explored (see Figure 1.38 (c)). In terms of S_{rel}, values of 0.90% K^{-1}, 1.65% K^{-1} and 1.5% K^{-1},[262] where obtained for 1 mol%, 3 mol% and 5 mol% Tm^{3+}, respectively, (see Figure 1.38 (d)).These values are quite high and comparable to the performance of dual emitting luminescent thermometers operating in these spectral regions. These results, combined with an estimation of the δT of ~0.2 K, deduced by considering the generally accepted uncertainty in the determination of the intensity ratio (0.5%),[21] clearly underlines the potential of this thermometer for biomedical applications.

For the Nd^{3+} doped thermometers operating in these spectral regions, the only example that could be found in the literature consider the ions are embedded in cubic Gd_2O_3 in the shape of nanospheres with a mean diameter 108 nm ± 21 nm, synthesized via a precipitation method.[263] The performance of this material as temperature sensor is based on the FIR from the emission lines of the Stark sublevels of the $^4F_{3/2} \rightarrow {}^4I_{13/2}$ transition, located in the region 1300 nm-1480 nm, while excited at 808 nm.[263] This excitation source promotes Nd^{3+} electrons from the ground state to the $^4F_{5/2}$ excited state. From there, the $^4F_{3/2}$ level is populated through a non-radiative decay process (see Figure 1.37 (b)). The different Stark sublevels of $^4F_{3/2}$ state are populated via non-

radiative decay processes among them. Radiative decays from these Stark sublevels to the lower Stark sublevel of the $^4I_{13/2}$ state generate the two emissions located at 1315 nm and 1350 nm used for temperature sensing in this particular case.These nanospheres exhibit a S_{rel} of 0.23% K^{-1}.[263] The authors also detected that this value is independent of the concentration of Nd^{3+} ions and is exclusively governed by the energy gap (ΔE=150 ± 20 cm^{-1}),[263] which, since it corresponds to the energy separation between Stark sublevels, is relative low.

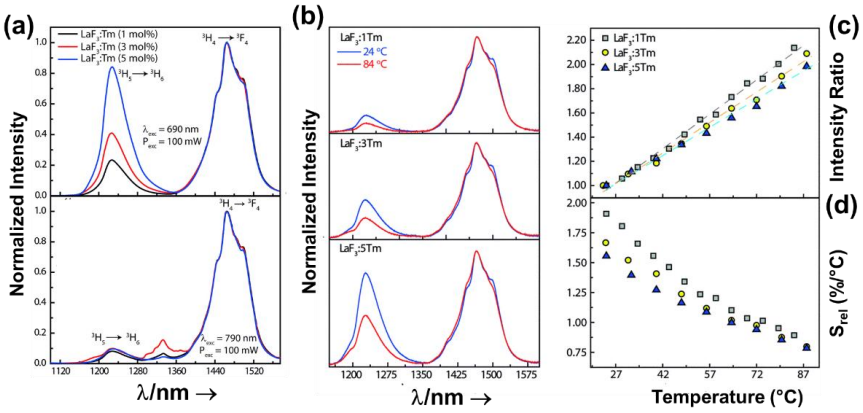

Figure 1.38. (a) Emission spectra in Tm^{3+} doped LaF_3 nanocrystals as a function of the concentration of the Tm^{3+} ions (1, 3, 5 mol%) and the excitation source (690 nm and 790 nm). (b) Variation of the intensity of the emissions in Tm^{3+} doped LaF_3 nanocrystals (1, 3, 5 mol%) with the change of the temperature. Variation of the: (c) intensity ratio and (d) relative thermal sensitivity of Tm^{3+} doped LaF_3 nanocrystals as a function of the concentration of Tm^{3+} ions and temperature. Adapted with permission.[262] Copyright from The Royal Society of Chemistry 2019.

6. Lanthanide doped luminescent nanothermometers operating in the III-BW

The third biological window (III-BW), or the short wavelength infrared (SWIR) region as it was originally named,[127] started gaining the attention of the researchers when Naczynski *et al*. reported that longer wavelengths than those lying in the I- and II-BWs transmitted up to three times more efficiency through oxygenated-blood and melanin containing tumors, and as a consequence for luminescent thermometry this would allow for a deeper thermal reading in biological samples due to the reduction of tissue scattering and absorption, compared to the other BWs.[127] Moreover, up to now, the luminescent thermometers reported operating in the III-BW are all excited at wavelengths lying in the I-BW (see Table 1.5), providing an important advantage for their possible applications in biomedicine. Typical Ln^{3+} ions applied for thermal sensing in the III-BW are mainly based on the emissions arising from Tm^{3+} located at ~1450 nm and ~1800 nm, the emission of Er^{3+} ions located at ~1550 nm, and the emission of Ho^{3+} ions located at ~1960 nm. For the case of Tm^{3+} based luminescent thermometers operating in this spectral region, their performance is determined by the temperature dependence of the intensity ratio of two emissions, or as more often encountered, combined with the emission of Ho^{3+} ions, using or not Yb^{3+} as a sensitizer. For the case of Er^{3+} doped thermometers, the performance is entirely based on the temperature dependence of emissions arising from TCLs constituted by the Stark sublevels of the $^4I_{13/2} \rightarrow {}^4I_{15/2}$ transition, using as a sensitizer Yb^{3+}.

Table 1.5. Summary of all Ln^{3+} doped luminescent thermometers operating in the III-BW. In the table are shown the activators (A) and sensitizers (S). The excitation (λ_{exc}) and emission (λ_{em}) wavelengths are shown in nanometers (nm), together with the corresponding electronic transition producing these emissions. ΔT stands for the temperature range were the temperature reading was investigated. The thermometric parameter (Δ) indicates the luminescent nanothermometry class used in each case: FIR-for band-shape and

I-for intensity ratio thermometry, respectively. The maximum relative thermal sensitivity (S_{rel}) and the temperature resolution (δT) are presented at the temperature where these values were obtained. Marked by asterisk are the values of S_{rel} or δT calculated by us, using the parameters published in the corresponding references in Ref. column. The double line separation between rows stands for different type of lanthanide doped nanothermometers, as discussed on the corresponding subsections.

A	S	Host	λ_{exc} (nm)	λ_{em} (nm)	Transitions	ΔT (K)	Δ	S_{rel}/T (% K^{-1})/K	δT (K)	Ref.
Tm^{3+}	-	$KLu(WO_4)_2$	808	1470, 1740	$^3H_4 \rightarrow {}^3F_4$, $^3F_4 \rightarrow {}^3H_6$	298-333	I_{1470}/I_{1740}	0.08/298	6.2 *	271
Tm^{3+}	Yb^{3+}	$NaYF_4$	980	1470, 1740	$^3H_4 \rightarrow {}^3F_4$, $^3F_4 \rightarrow {}^3H_6$	298-333	I_{1470}/I_{1740}	0.6/298	0.8 *	271
Tm^{3+}	Yb^{3+}	$KLu(WO_4)_2$	980	1470, 1960	$^3H_4 \rightarrow {}^3F_4$, $^3F_4 \rightarrow {}^3H_6$	298-333	I_{1470}/I_{1960}	0.22/298	2.2 *	271
Tm^{3+}	Yb^{3+}	$KLu(WO_4)_2$	808	1470, 1740	$^3H_4 \rightarrow {}^3F_4$, $^3F_4 \rightarrow {}^3H_6$	298-333	I_{1470}/I_{1740}	0.06/298	8.3 *	271
Tm^{3+}, Ho^{3+}	Yb^{3+}	$KLu(WO_4)_2$	980	1480 (Tm^{3+}), 1960 (Ho^{3+})	$^3H_4 \rightarrow {}^3F_4$ (Tm^{3+}), $^5I_7 \rightarrow {}^5I_8$ (Ho^{3+})	298-333	I_{1480}/I_{1960}	0.52/298	0.9 *	271
Er^{3+}	Yb^{3+}	$LuVO_4$	980	1637, 1660	$^4I_{13/2} \rightarrow {}^4I_{15/2}$	298-523	$FIR_{1637}/_{1660}$	0.54/523	0.92*	272
Er^{3+}	Yb^{3+}	$LuVO_4$@SiO_2	915	1469, 1527	$^4I_{13/2} \rightarrow {}^4I_{15/2}$	298-523	$FIR_{1469}/_{1527}$	0.18/298	2.7 *	273
Er^{3+}	Yb^{3+}	NaY_2F_5O	980	1535, 1554	$^4I_{13/2} \rightarrow {}^4I_{15/2}$	298-333	$FIR_{1535}/_{1554}$	0.15/298	3.3 *	271
Er^{3+}	Yb^{3+}	$BaMoO_4$	980	1521, 1531	$^4I_{13/2} \rightarrow {}^4I_{15/2}$	293-553	$FIR_{1521}/_{1531}$	0.13/293	3.8 *	274
Er^{3+}	Yb^{3+}	$BaMoO_4$	980	1504, 1531	$^4I_{13/2} \rightarrow {}^4I_{15/2}$	293-553	$FIR_{1504}/_{1531}$	0.095/293	5.2 *	274
Er^{3+}	Yb^{3+}	$KLu(WO_4)_2$	980	1535, 1554	$^4I_{13/2} \rightarrow {}^4I_{15/2}$	298-333	$FIR_{1535}/_{1554}$	0.095/298	5.2 *	271
Er^{3+}	Yb^{3+}	Lu_2O_3	980	1535, 1554	$^4I_{13/2} \rightarrow {}^4I_{15/2}$	298-333	$FIR_{1535}/_{1554}$	0.09/298	5.5 *	271
Er^{3+}	Yb^{3+}	$NaYF_4$	980	1535, 1554	$^4I_{13/2} \rightarrow {}^4I_{15/2}$	298-333	$FIR_{1535}/_{1554}$	0.06/298	8.3 *	271

6.1. Tm^{3+} doped luminescent nanothermometers operating in the III-BW

Tm^{3+} doped luminescent thermometers operating in the III-BW, are either excited at 980 nm or 808 nm, as a function of whether Yb^{3+} has been used as sensitizer or not.

When Yb^{3+} is used as sensitizer, Tm^{3+} doped thermometers are excited at 980 nm (see Table 1.5). These thermometers can be formed by nanoparticles single doped with Tm^{3+} or co-doped with Ho^{3+} ions, using Yb^{3+} to absorb the energy of the excitation source. Upon 980 nm excitation, the luminescence of the single Tm^{3+} doped nanoparticles is composed of two emissions at ~1450 nm and ~1800 nm, whereas when also Ho^{3+} is present, a third emission band at ~1960 nm is observed. Yb^{3+} ions acting as sensitizer, absorb the 980 nm excitation light, promoting their electrons from the $^2F_{7/2}$ ground stated to the $^2F_{5/2}$ excited state. Due to the energy resonance between this level of Yb^{3+} and the $^3H_5$ level of Tm^{3+}, an ET process takes place, populating this level of Tm^{3+}. From the $^3H_5$ level, electrons can relax non-radiatively to the $^3F_4$ level. From this state, a second ET transfer process from Yb^{3+} can take place, promoting Tm^{3+} electrons to the $^3F_4$ excited state. Then, a second non-radiative relaxation process takes place towards the $^3H_4$ energy level, from which the emission band located at 1450 nm is generated through the $^3H_4 \rightarrow {}^3F_4$ electronic transition (see Figure 1.39 (a)). Finally, a radiative relaxation of the electrons from the $^3F_4$ level to the ground state gives rise to the second emission of Tm^{3+} located at 1800 nm.[271] With the addition of Ho^{3+}, an additional ET process can take place from Yb^{3+} to the $^5I_6$ level of Ho^{3+} that is resonant in energy with the $^2F_{5/2}$ excited state of Yb^{3+}. From this state, the $^5I_7$ level of Ho^{3+} can be populated through a non-radiative relaxation process, prior to a radiative transition to the ground state of this ion ($^5I_8$), generating the emission at 1960 nm.[271] Another less probable alternative for the generation of the Ho^{3+} emission band, is a direct ET process from the $^3H_5$ level of Tm^{3+} to the resonant $^5I_6$ level of Ho^{3+} (see Figure 1.39 (a)). This mechanism is less probable to

occur due to the high number of concentration of Yb^{3+} in the nanoparticles, up to ten times higher than that of Tm^{3+}.[271]

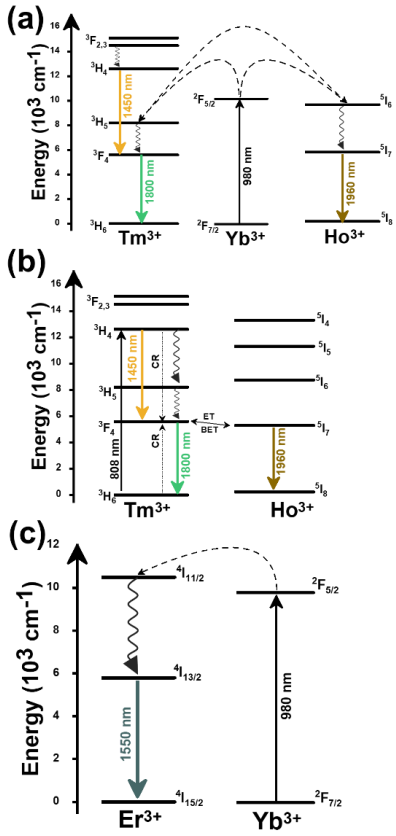

Figure 1.39. Mechanism of the generation of the emission lines in: (a) Ho^{3+},Tm^{3+},Yb^{3+}:$KLu(WO_4)_2$, (b) Ho^{3+},Tm^{3+}:$KLu(WO_4)_2$, and (c) Er^{3+},Yb^{3+} doped materials operating as luminescent thermometers in the III-BW.

The addition of Ho^{3+} provided positive effects not only in the intensity of the luminescence, that was improved, but also in their temperature sensing properties. Hence, the presence of Ho^{3+} plays an important role in transferring additional energy towards Tm^{3+} ions through the $^5I_6$ and $^3H_5$ levels of Ho^{3+} and Tm^{3+} (see Figure 1.39 (a)), respectively, apart from that already transferred from Yb^{3+}.[271] Hence, this outcome should be underlined as a beneficial strategy to enhance the intensity of the emissions of these ions in the III-BW. We underline here that three emissions (1450 nm, 1800 nm of Tm^{3+} and 1960 nm of Ho^{3+}) are generated, hence, two out of three of them can be used for thermal sensing. Nevertheless, in this case the intensity ratio among only the emissions of Tm^{3+} ions, were considered, and S_{rel} of $KLu(WO_4)_2$ nanoparticles codoped with Ho^{3+} and Tm^{3+} ions, exhibited a two-fold higher sensitivity when compared to single Tm^{3+} doped nanoparticles (see Table 1.5).[271]

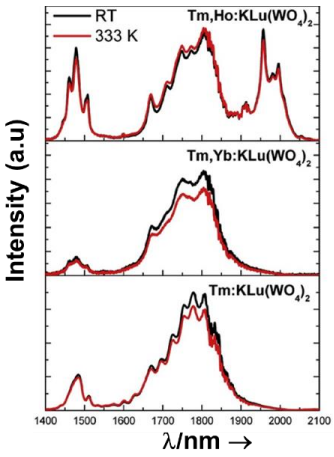

Figure 1.40. Effect of temperature in the III-BW emissions for the $KLu(WO_4)_2$ nanoparticles doped with Tm^{3+}; Tm^{3+}, Yb^{3+} and Ho^{3+}, Tm^{3+} ions after pumping at 808 nm. Adapted with permission.[271] Copyright from Elsevier 2018.

Besides the benefits demonstrated by these kinds of luminescent thermometers, one thing that should be considered is the fact that they are excited at 980 nm, so being probed that a heating up effect takes place, hampering their potential biomedical applications.[216] To surpass this drawback, the possibility of exciting these materials at 808 nm through the direct absorption of energy by Tm^{3+} was considered as a solution.

Hence, in the absence of Yb^{3+} ions, an illustrative example are the Ho^{3+} and Tm^{3+} codoped $KLu(WO_4)_2$ nanocrystals. Upon 808 nm excitation, Tm^{3+} promotes its electrons from the $^3H_6$ ground state to the $^3H_4$ excited state. The electrons decay radiatively to the $^3F_4$ manifold, generating the emission line at 1.45 µm. From the $^3F_4$ level, a second radiative relaxation to the $^3H_6$ ground state generates the emission line at 1.8 µm. Tm^{3+} might undergo a CR process like $^3H_4$, $^3H_6 \leftrightarrow {}^3F_4$, $^3F_4$, which contributes to the higher intensity observed for the emission band at 1.8 µm. Also, due to the energy resonance between the $^3F_4$ level of Tm^{3+} and the $^5I_7$ level of Ho^{3+}, ET and BET processes might take place between these electronic levels, promoting the electrons of Ho^{3+} to this excited state from the ground state. Then, the electrons of Ho^{3+} relax radiatively to the $^5I_8$ ground state, giving rise to the emission band at 1.96 µm (see Figure 1.39 (b)).[275]

The temperature sensing properties of Tm^{3+}:$KLu(WO_4)_2$, Tm^{3+},Yb^{3+}:$KLu(WO_4)_2$ and Ho^{3+}, Tm^{3+}:$KLu(WO_4)_2$ nanocrystals where compared upon excitation at 808 nm in the physiological range of temperatures.[275] It was observed that when the temperature increased, the intensity of the 1450 nm band remained unchanged, while the intensity of the 1800 nm band decreased for Tm^{3+} and Tm^{3+},Yb^{3+} particles. Instead, for Tm^{3+},Ho^{3+} codoped nanoparticles, the intensity of both 1450 nm and 1960 nm bands decreased as the temperature increased, while the intensity of the 1800 nm band increased (see Figure 1. 40), indicating that the BET mechanism (see Figure 1.39 (b)) between these two ions is promoted as the temperature increased.[271] As a consequence, the S_{rel} of Ho^{3+},Tm^{3+}:$KLu(WO_4)_2$ nanoparticles is approximately 5 times higher than that of Tm^{3+}: $KLu(WO_4)_2$ and Tm^{3+},Yb^{3+}: $KLu(WO_4)_2$ nanoparticles, by considering either the 1450 nm/1800 nm or the 1800 nm/1960 nm intensity ratio.[271] We underline as important conclusion from this section the combination of Tm^{3+} and Ho^{3+} emissions, mainly the ones located at 1800 nm and 1960 nm, respectively, to generate highly sensitive thermometers.

6.2. Er^{3+} doped luminescent nanothermometers operating in the III-BW

Er^{3+} doped luminescent nanothermometers operating in the III-BW exhibit, in general, a very low S_{rel} (see Table 1.5). Their performance, based entirely on the Stark sublevels of the $^4I_{13/2} \rightarrow {}^4I_{15/2}$ transition, has been evaluated through the FIR model (see Equation 1.9), being strictly related to ΔE of the Stark sublevels involved in the generation of the emissions in which these luminescent thermometers are based (50-130 cm^{-1}), that in general are very small.

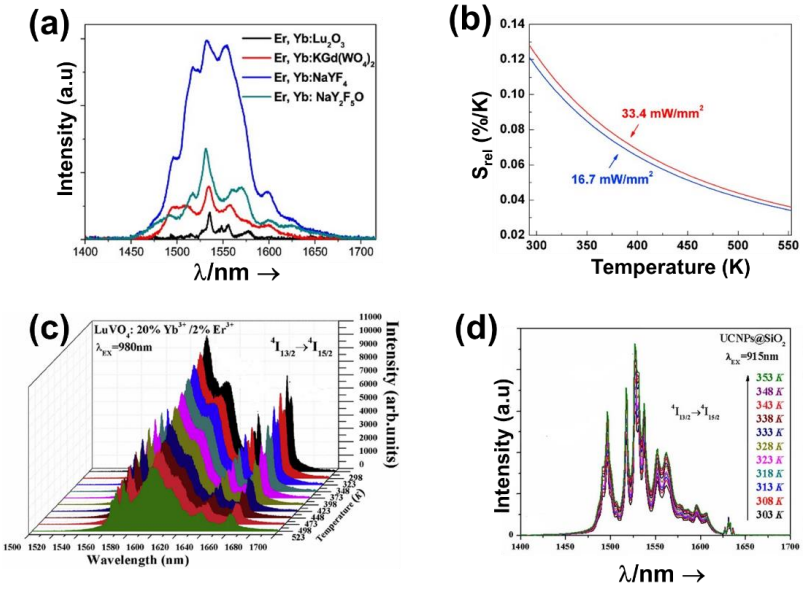

Figure 1.41. (a) Er^{3+} 1550 nm emission in different hosts. Adapted with permission.[271] Copyright from Elsevier 2018. (b) Effect of the excitation power density at 980 nm in the relative thermal sensitivity of Er^{3+}, Yb^{3+}:$BaMoO_4$ nanoparticles. Adapted with permission.[274] Copyright from Elsevier 2018. (c) Temperature dependence of the Er^{3+} 1550 nm emission in uncoated $LuVO_4$ nanoparticles, excited at 980 nm. Adapted with permission.[272] Copyright from Elsevier 2018. (d) Temperature dependence of Er^{3+} 1550 nm emission in uncoated $LuVO_4$@SiO_2, excited at 915 nm. Adapted with permission.[273] Copyright from American Chemical Society 2019.

Er^{3+} doped luminescent thermometers operating in the III-BW, use Yb^{3+} as sensitizer which implies excitation at 980 nm. The mechanism of generation of this emission band is depicted in Figure 1.39 (c). After the absorption of a photon at 980 nm by Yb^{3+}, the electrons of Yb^{3+} are promoted to the excited $^2F_{5/2}$ energy level. Then, an ET from the excited $^5F_{5/2}$ energy level of Yb^{3+} to Er^{3+} ions occurs, populating the $^4I_{11/2}$ energy level of this ion. After, a multiphonon relaxation from the $^4I_{11/2}$ to the $^4I_{13/2}$ energy level allows generating the radiative $^4I_{13/2} \rightarrow {}^4I_{15/2}$ transition, whose emission is centered at 1550 nm.[271-273]

The intensity of the emission generated and the thermometric performance of different Er^{3+} based luminescent thermometers operating the III-BW, was analyzed by Savchuk *et al*. as a function of the different hosts in which this ion was embedded, including oxyfluorides (NaY_2F_5O), fluorides ($NaYF_4$), rare-earth sesquioxides (Lu_2O_3) and double tungstates ($KLu(WO_4)_2$).[271] In terms of intensity, the fluoride host exhibited the highest one, mainly attributed to its low phonon energy (see Figure 1.41 (a)).[271] Comparing their temperature sensing properties, deduced from Equation 1.9, over the physiological range of temperature, the oxyfluoride host (NaY_2F_5O) exhibited the highest S_{rel}, with a value of 0.15% K^{-1} at room temperature.[271] Compared to the other hosts, this value is approximately 3 times higher.

In another study, exploring $BaMoO_4$ as host for Er^{3+}, the authors demonstrated that the performance of these Er^{3+} doped luminescent thermometers is influenced by the excitation power density.[274] The authors tested two different intensity ratios from the Stark sublevels of the $^4I_{13/2} \rightarrow {}^4I_{15/2}$ transitions (1504 nm/1531 nm and 1521 nm/1531 nm) under two different excitation power densities (16.7 mW/mm^2 and 33.4 mW/mm^2) . The 1504 nm/1531 nm intensity ratio was almost insensitive to the variation of the excitation power density, whereas the 1521 nm/1531 nm intensity ration performed slightly better at higher excitation power densities (see Figure 1.41 (b)).

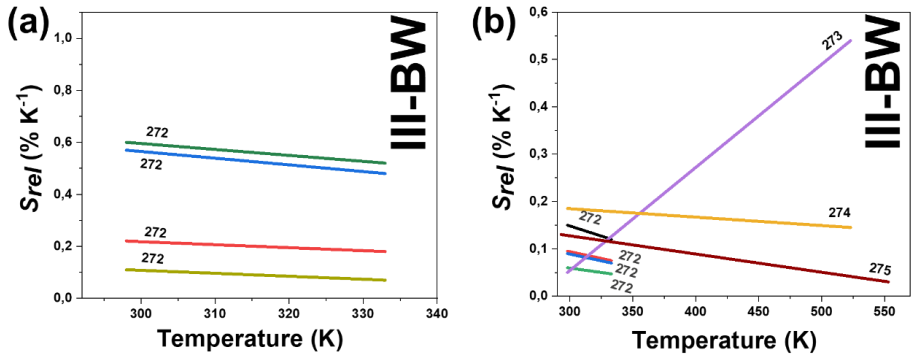

Figure 1.42. Temperature dependence of S_{rel} of: (a) Ho^{3+}/Tm^{3+} and (b) Er^{3+} doped thermometers operating in the III-BW. Numbers represent the corresponding references.

All the thermometers mentioned above, have extracted their performance based on the Boltzmann model of Equation 1.9, however, in some other references a new fitting model was applied. This is the case of Er^{3+}, Yb^{3+} embedded in $LuVO_4$,[272] or $LuVO_4@SiO_2$.[273] Here, the thermometric parameter was fitted to the phenomenological form:

$$\Delta = B\, exp(a + bT + cT^2) \qquad (1.49)$$

where B, a, b and c are all constants to be determined from the fitting.

According to that, S_{rel} can be calculated by:

$$S_{rel} = \left|\frac{1}{\Delta}\frac{d\Delta}{dT}\right| x\ 100\% = \left|\frac{B\ (b + cT)\ \exp(a + bT + cT^2)}{B\ \exp(a + bT + cT^2)}\right| x\ 100\% = |b + cT|\ x\ 100\% \qquad (1.50)$$

The maximum value obtained for S_{rel} in the case of uncoated $LuVO_4$ was around 0.54% K^{-1} at the highest temperature under study (523 K).[272] For the silica coated nanoparticles, S_{rel} obtained was lower, ~0.18% K^{-1}, obtained at room temperature, although it was excited at a different wavelength than the uncoated nanoparticles.[273] An additional difference between these two materials was observed in the evolution of the intensity of the emissions as the temperature increased. For the uncoated nanoparticles, excited at 980 nm, the intensity of the emissions decreased as the temperature increased (see Figure 1.41 (c)). On the opposite, for the SiO_2 coated nanoparticles a general increase of the intensity of the emission band as the temperature increased was observed (see Figure 1.41 (d)), assigned, according to the authors, to the improvement of the multiphonon relaxation process from the $^4I_{11/2}$ level to the $^4I_{13/2}$ level at high temperature.

Final remarks about this section, should be devoted to the fact that the excitation wavelength used for these luminescent thermometers has the drawback of causing overheating and probably killing healthy tissues in biomedical applications.[216] Even though for the case of Er^{3+}, Yb^{3+} embedded $LuVO_4@SiO_2$, excitation at 915 nm was applied to overcome this problem, the absorption cross section of Yb^{3+} ions at this wavelength is only half of that at 980 nm, which generates weaker emissions that can inhibit their applicability as luminescent thermometers.[21, 204, 276]

In summary, the variation of S_{rel} with the increase of the temperature for the luminescent thermometers operating in the III-BW is presented in Figure 1.42 (a) and (b). In general, for these thermometers a decrease of S_{rel} is observed as the temperature increases, with the exception of the thermometer based on Er^{3+}, Yb^{3+}:$LuVO_4$, due to the different model to which the experimental data were fitted. In addition, the sensitivity of the Er^{3+} doped thermometers operating within the III-BW is relatively low compared to Tm^{3+} doped ones. When compared to the thermometers operating in the other BWs regimes, the sensitivity of the thermometers operating in the III-BW, are lower, implying that additional strategies to boost their performances are needed.

7. Applications of lanthanide doped luminescent nanothermometers operating within the biological windows

The development of highly sensitive lanthanide doped luminescent nanothermometers by means of tunable synthetic strategies and the characterization of their thermometric performance, has accelerated their application as potential tools for thermal sensing in *ex-vivo*, *in-vitro* and *in-vivo* trials, including 2D subcutaneous dynamic thermal imaging, as well as controlled photothermal therapy experiments. This section covers most of the examples published up to now devoted to the applications of these lanthanide doped luminescent nanothermometers operating within the different biological windows spectral ranges. It concludes with some other applications, distinct from biomedical/biological fields, in which these luminescent thermometers have also been used.

7.1. Biological/biomedical applications of lanthanide doped luminescent nanothermometers operating within the biological windows.

7.1.1. *Ex-vivo* thermometry using lanthanide doped luminescent nanothermometers operating in the biological windows.

Lanthanide doped luminescent nanothermometers, upon laser irradiation, can sense the temperature within biological tissues. Upon the proper selection of the excitation wavelength, followed by de-excitation processes, radiative processes can take place, as presented in the previous sections, which are the main responsible for the production of luminescence. The temperature dependence properties of the luminescence of the lanthanide materials, allows their applicability as nanothermometers, despite the fact that recalibration of the thermometer is required when embedded in a new medium. Thereby, with these properties, lanthanide doped nanothermometers have the potential of being implemented as biological thermal sensors. Here, we cover the examples published in the literature of lanthanide doped luminescence nanothermometers acting as thermal sensing agents in *ex-vivo* experiments. *Ex-vivo* refers to experimentation or measurements done in or on tissue from a biological organism in an external environment with minimal alteration of natural conditions.[277]

The lanthanide ion most used in biological/biomedical applications is Nd^{3+}, and because of good reasons. First, this ion can be excited with cost-effective laser diodes (NIR energy sources), which, more importantly rely in the I-BW. Possible choices for excitation are 790 nm and 808 nm. Among these, 808 nm represent the best choice, as it has been demonstrated to be a risk-free wavelength for biological applications.[204, 278] Additionally, all the characteristic emission bands of Nd^{3+}, located at ~890 nm, ~1060 nm and ~1350 nm, lie within the biological windows, respectively at the I, II- and III-BWs. Hence, excitation and emissions within the biological windows, will allow to go for higher penetration depths and get a deeper temperature sensing.

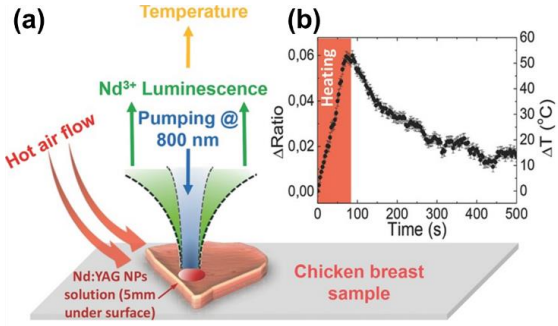

Figure 1.43. *Ex-vivo* temperature sensing in the I-BW with Nd^{3+} doped YAG nanoparticles: (a) Scheme of the experimental setup used to measure the time evolution of the subtissue temperature of a chicken tissue sample injected with an aqueous dispersion of the nanothermometers and externally heated by a flow of hot air. (b) Time evolution of the subtissue temperature determined from the ratio between the intensities of the 938 nm and 945 nm emissions of Nd^{3+}.[172] Adapted with permission. Copyright from Wiley-VCH 2015.

Benayas *et al*.[172] reported the ability of Nd^{3+}:YAG nanothermometers for *ex-vivo* temperature monitoring, based on their emissions located in the I-BW (see Table 1.1). The temperature

sensing properties of these nanothermometers were based on the emission lines from different Stark sublevels of the emitting state located at around 938 nm and 945 nm ($^4F_{3/2} \rightarrow {}^4I_{11/2}$ transition), after pumping at 808 nm with a power of 100 mW. To verify the temperature sensing ability of these nanothermometers in biological tissues, an *ex-vivo* experimental setup was designed (see Figure 1.43 (a)). Briefly, 100 µL of a 0.1 wt% water dispersion of Nd^{3+}:YAG nanoparticles were injected in a chicken breast tissue with a thickness of 5 mm. The biological tissue was externally heated using a hot air flow (343 K) for 90 s, prior to cooling it down naturally. The luminescence and the intensity ratio of the particles during the heating/cooling cycles was monitored for a period of more than 8 min. The time evolution of the intensity ratio between the two emission lines and the corresponding subtissue heating determined from the same intensity ratio revealed that during the heating process a linear increase of the subtissue temperature with time was produced, reaching a maximum temperature change of about 328 K (see Figure 1.43 (b)).[172] When the hot air flow was turned off, an exponential decrease of the temperature due to thermal diffusion was observed (see Figure 1.43 (b)).

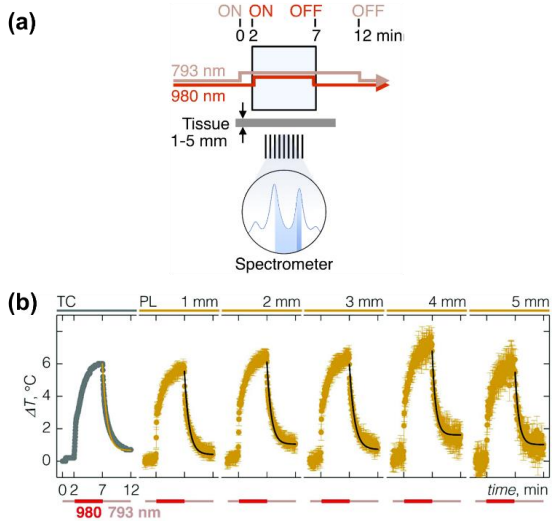

Figure 1.44. (a) Setup for heating-cooling measurements through pork fat tissue (reported on the Supporting Information of the corresponding reference). (b) Heating-cooling cycles of aqueous dispersion of Nd:$LiLuF_4$@$LiLuF_4$ nanocrystals measured with a thermocouple (TC) and via the intensity ratio among the Stark sublevels of the 1050 nm emissions of Nd^{3+} ion, as a function of the tissue thickness (1-5 mm) of the pork fat. Adapted with permission.[165] Copyright from The Royal Society of Chemistry 2019.

Based on heating-cooling cycle dynamics, Skripka *et al*. explored water dispersible Nd^{3+}:$LiLuF_4$@$LiLuF_4$ nanocrystals as *ex-vivo* thermal sensors.[165] These nanocrystals, in principle, can work as *ex-vivo* thermal sensors in three biological windows (they generate emissions involving Stark sublevels located at 880 nm, 1050 nm and 1320 nm), however, the authors selected the emission located at the II-BW ($^4F_{3/2} \rightarrow {}^4I_{11/2}$ transition, 1050 nm emission) due to the higher intensity of this emission band when compared to the other two. The heating-cooling cycles of an aqueous dispersion of these nanocrystals with concentration 5 mg/mL were measure by irradiating the sample with 793 nm (power density ~ 49 W cm^{-2}) and 980 nm light source (power density ~ 37 W cm^{-2}) light, and placing the pork fat tissue of various thicknesses (1 to 5 mm) in front of the emission collecting lens (see Figure 1.44 (a)). The 793 nm laser is used to generate the emission of the nanoparticles, whereas the 980 nm laser, is absorbed by water and converted into heat.[165] The nanoparticles were continuously excited with the 793 nm for a period of 12 min. The recorded photoluminescence and the calculated intensity ratio based on the Stark sublevels of the 1050 nm emission of Nd^{3+} ions, were used to calculate the temperature. Temperature increase was induced by simultaneously turning ON the 980 nm laser at the 2 min mark thereby heating the solution for 5 min after which it was switched OFF (see Figure 1.44 (a)). After switching OFF the 980 nm, the cooling profile measured with the emission generated by the nanoparticles

was recorded over the next 5 min with the 793 nm laser still ON. In addition, a thermocouple was used for contact measurement of temperature change inside the cuvette. Based on these heating-cooling cycles, the heat dissipation time constant of the nanoparticles into the surrounding medium, δT and the temporal uncertainty of the nanothermometers were determined at different biological tissue thicknesses. The results revealed that as the biological tissue becomes thicker, the values for the heat dissipation time constant determined from the spectra collected with the nanoparticles began to deviate from those measured with the thermocouple. Also, a significant error was observed in the determination of the temperature difference induced solely by the 980 nm light, and calculated between the OFF point of the 980 nm laser and the end of the cycle, attributed to the photoluminescence extinction of the biological tissue.[165] With the increase of the thickness of the biological tissue from 1 to 5 mm, the δT of the luminescent thermometer changed from 0.19 to 1.23 K, while the temporal uncertainty changed from 0.52 ± 0.37 to 4.26 ± 6.60 s for.[165] As a conclusion, and as it can be observed in Figure 1.44 (b), the reliability of these nanothermometers is highly compromised for a tissue thickness above 2 mm.

Another example of a luminescent nanothermometer applied in an *ex-vivo* experiment is that of water dispersible hybrid Nd^{3+} doped $NaGdF_4$ nanoparticles and semiconductor PbS/CdS/ZnS QDs in PGLA, operating in the II-BW using the intensity ratio between the 1060 nm emission of Nd^{3+} and the 1220 nm emission of QDs (see Table 1.3).[62] The ability of these particles to sense the temperature in biological tissues was tested through a setup based on the scheme presented in Figure 1.45 (a). Shortly, around 100 µL of a 1 mg/mL dispersion of these particles in distilled water were subcutaneously injected into a chicken breast sample at a depth of ~2 mm. The biological tissue was externally heated using a hot air current (323 K) for 20 s, prior to letting it to cool down naturally. The emissions of the Nd^{3+} and QDs generated within the tissue, after excitation at 808 nm with a 1 W cm^{-2} power density, were collected by an optical fiber and spectrally analyzed by a high-resolution spectrometer. The temperature profile of the 1060 nm emission of Nd^{3+} and the 1220 nm emission of the QDs, displayed a different behavior during heating/cooling cycles (see Figure 1.45 (b)). During the heating cycle (shadowed area), the emission of Nd^{3+} remains unchanged, while the emission of the QDs drastically decreased due to thermal quenching effects. During the cooling process, the emission of the QDs recovered its initial value due to thermal relaxation processes. The variation of the temperature of the tissue during the heating/cooling cycles was determined by calculating the intensity ratio between these two emissions (shown in Figure 1.45 (c)).[62] Results showed a temperature increase of approximately 6 K at the end of the heating pulse. During the cooling cycle, a pseudo-exponential decreasing profile was observed during two minutes, until the initial room temperature was recovered. From the magnitude of the random fluctuations in the temperature profile (see Figure 1.45 (c)), an estimation of δT of 0.2 K (see Table 1.3).

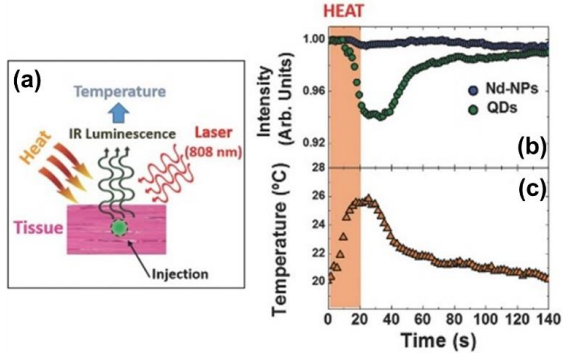

Figure 1.45. *Ex-vivo* temperature sensing in the II-BW with hybrid Nd^{3+} doped $NaGdF_4$ and QDs in PGLA particles: (d) Experimental setup. (e) Evolution of the 1060 nm (Nd^{3+} emission) and 1220 nm (QDs emission) injected in chicken breast tissue during a heating/cooling cycle of the tissue. The intensity values have been normalized to their room temperature value. (f) Temperature evolution of the tissue during the heating/cooling cycle. The temperatures have been calculated based on the ratio of the of the emission

intensity of the (Nd^{3+} emission) and 1220 nm (QDs emission). Adapted with permission. Copyright from Wiley 2015.

Ex-vivo lanthanide nanothermometers operating in the III-BW have been also reported. Savchuk *et al.* investigated the intensity ratio between the 1470 nm versus the 1711 nm emissions of Tm^{3+} in Ho, Tm:KLuW particles to sense temperature inside a chicken breast piece of meat with a thickness of 2 mm, after being excited at 808 nm with a power of 200 mW.[271] For the experiment, the nanoparticles were deposited on a microscope glass slide, on top of which a slice of chicken breast was placed. A heating gun, with a power of 1 W and fixed to a horizontal moving stage to control its movement, was used to induce the heating of the chicken breast. The heating gun was moved away from its initial position, close to the chicken breast sample, to generate a decrease of temperature in the biological tissue. The maximum temperature reached in the chicken breast, was maintained below 318 K to avoid overpassing the denaturalization temperature. The excitation beam was focused on the nanoparticles by using a 40x microscope objective with a numerical aperture of 0.6. The photoluminescence generated by the Ho, Tm:KLuW particles was collected with a Yokogawa AQ6375 optical spectrum analyzer detector and the temperature was determined through the intensity ratio indicated above. In addition, close to the nanoparticles and inside the chicken breast sample, a digital multimeter connected to a small Pt-100 thermocouple, was placed to record the changes of temperature (see the setup in Figure 1.46 (a)). The temperature profile resulting from moving the heating gun away is shown in Figure 1.46 (b). Moving the heating gun results in a temperature drop of 1.5 K cm^{-1}. The temperature determined by the nanoparticles displayed a difference of 0.8 K compared to the one determined by the Pt-100 thermocouple. This difference could be assigned to the different thermal conductivity of the two materials (nanoparticles and thermocouple) or also to the different location of the thermal probes.

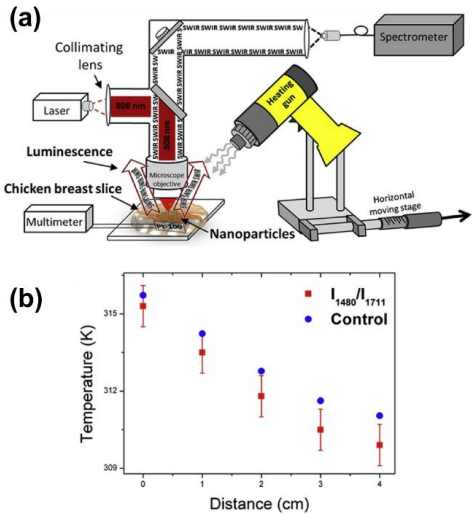

Figure 1.46. *Ex-vivo* temperature sensing in the III-BW with Ho, Tm:KLu$(WO_4)_2$ nanoparticles: (a) Experimental setup and (b) The temperature recorded from the intensity ratio of 1480 nm vs 1711 nm of Tm^{3+} emissions in Ho, Tm:KLu$(WO_4)_2$ particles (in red squares) and from the thermocouple (in blue spheres). Adapted with permission.[271] Copyright from Elsevier 2018.

7.1.2. *Ex-vivo* photothermal experiments combined with thermometry using lanthanide doped luminescent nanothermometers operating in the biological windows

Lanthanide doped luminescent nanothermometers, upon laser irradiation, not only can sense temperature, but they can also generate heat under special conditions. These two processes are generated due to the peculiar electronic configuration of the Ln^{3+} ions, which give rise to radiative and non-radiative processes, upon the proper selection of the excitation source. These two processes are the main responsible for the production of luminescence and heat in lanthanide doped materials, respectively. Thus, lanthanide doped materials have the potential of being

implemented as photothermal agents within biological/biomedical media. Photothermal therapy, that employs light-absorbing agents to convert photoenergy into heat to achieve local hyperthermia, is regarded as a minimally invasive and highly efficient methodology for targeted cancer treatment.[279-282] Typical conditions that have to be fulfilled by a material to act as a potential photothermal agent include high light-to-heat conversion efficiency, sizes in the nanometric range, excitation and emission within the biological window spectral ranges, and real-time temperature feedback.[282] Here, we cover the examples published in the literature which involve the application of lanthanide doped luminescence as nanothermometers combined with materials that can generate heat, and the so-called self-assessed lanthanide doped nanothermometers, which can simultaneously sense the temperature but also generate heat generated within the medium where they are embedded.

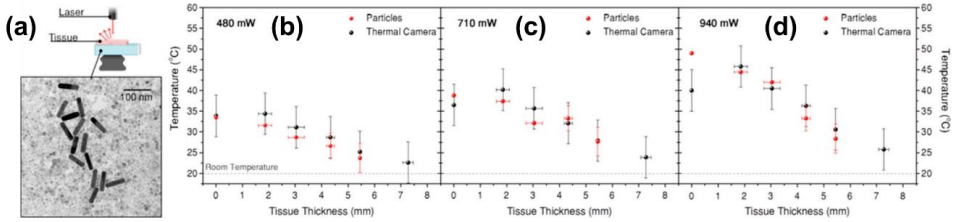

Figure 1.47. (a) *Ex-vivo* photothermal experiment in chicken breast using a colloidal solution containing gold nanorods as photothermal agents and Nd^{3+},Y^{3+}:CaF_2 nanoparticles as luminescent thermometers (a TEM image of the mixed colloid is presented as well). Temperature recorded from the particles by using the intensity ratio of the Stark sublevels of the 1050 nm emission of Nd^{3+} (in red) and from the thermal camera (in black) as a function of the power of the 808 nm laser applied: (b) 480 mW, (c) 710 mW and (d) 940 mW. Adapted with permission.[252] Copyright from American Chemical Society 2018.

Nd^{3+},Y^{3+}:CaF_2 nanoparticles, combined with Au nanorods have been used in *ex-vivo* photothermal experiments. [252] Nanoparticles that sense the temperature (Nd^{3+},Y^{3+}:CaF_2) are combined with nanoparticles that generate heat (Au nanorods), It must be emphasized that the Nd^{3+} doped particles alone would have the ability to generate heat upon NIR excitation due to their ladder-like electronic configuration.[20, 209] In fact, the heat generated by Nd^{3+} doped nanoparticles is a consequence of both the increase in the absorbed pump power when illuminated at 808 nm, since the absorption coefficient of these nanoparticles is proportional to the Nd^{3+} concentration, and the reduction in the fluorescence quantum yield due to Nd^{3+}-Nd^{3+} interactions, such as C and energy migrations when the distance among these ions is short enough. Therefore, it would be possible to tailor the balance between light and heat generation through an appropriate choice of the Nd^{3+} content inside the nanoparticles. Nevertheless, the authors opted to choose Au nanorods as photothermal agents because the use of lanthanide doped nanoparticles would require higher illumination doses to achieve the target temperature.[252, 283] Au nanorods, upon excitation on their longitudinal plasmon mode can efficiently generate heat.[20, 284] Hence, nanorods with a local surface plasmon resonance maximum at ~810 nm were used in order to meet with the requirements for biomedical applications, that is being excited and emitting within biological windows regimes, and efficiently absorb the 808 nm excitation source. Concerning the Nd^{3+},Y^{3+}:CaF_2 temperature sensors, they operated in the II-BW using different emission pics of the band located at 1050 nm, through the FIR model (see Table 1.3). For the *ex-vivo* experiment, 1 mol% Nd^{3+} and 10 mol% Y^{3+} co-doped CaF_2 nanoparticles were chosen due to their S_{rel} and good emission intensity. These nanoparticles with concentration 1.6 mg/mL were combined with Au nanorods with a concentration 1.3 × 10^{-3} mM by simply mixing within a cuvette.[252] A TEM image of the combined nanoparticles dispersion is presented in Figure 1.47 (a). The nanoparticles suspension was introduced in a cuvette, on top of which a chicken breast sample with different thicknesses was placed. On the bottom of the cuvette, a thermal camera was used to monitor the generation of heat (see Figure 1.47 (a)). The luminescence generated by the Nd^{3+},Y^{3+}:CaF_2 nanoparticles, after 808 nm illumination, was recorded by a InGaAs spectrometer, and then the temperature was determined by calculating the corresponding intensity ratio. For the experiment, the power of the excitation laser was kept below 0.94 W to avoid overheat of the biological tissue. Also, a low concentration of Nd^{3+} in the nanoparticles was

used to avoid the generation of heat by them, thus, the generated heat could be only attributed to the Au nanorods.[20, 284] Under these conditions, the generated heat recorded by the thermal camera and the temperature determined by the intensity ratio between the emission lines coming from different Stark sublevels of the emitting state in the 1050 nm emission ($^4F_{3/2} \rightarrow {}^4I_{11/2}$ transition) of the Nd^{3+},Y^{3+}:CaF_2 nanoparticles, were compared as a function of the power of the laser applied (see Figure 1.47 (b)-(d)), showing a good agreement for thicknesses of the chicken breast below 5.5 mm.[252] For a thickness of 2 mm, a δT of 0.2 K was obtained, fulfilling the requirements for a nanothermometer to be operative in biomedical applications.[13] This δT was determine using Equation 1.3 after recalibrating the nanothermometry (determining the value of B of Equation 1.9 from power dependence experiments) at the new embedded medium.[252] Above this thickness, the δT increased, reaching a value of 3.5 K for a thickness of 5.5 mm, clearly jeopardizing the reliability of this luminescent thermometer, and indicated also that a recalibration of the luminescence thermometer was required inside chicken breast.[219, 252]

7.1.3. *In-vitro* thermometry using lanthanide doped luminescent nanothermometers operating in the biological windows.

Lanthanide doped luminescent nanothermometers can operate also in *in-vitro* media. *In-vitro* stands for investigation performed with microorganisms, cells, or biological molecules outside their normal biological context.[285] *In-vitro* nanothermometry (also known as cellular nanothermometry) is more often experienced in the visible regime. Possible explanations could be attributed to the sufficient penetration depth achieved from VIS light in *in-vitro* cell culture to analyze the whole thickness of the sample, and this light is easily visualized using conventional optical microscopes, which renders a more easy location of the nanoparticles and recording of their luminescence spectra within the cell culture. Typical examples of lanthanide doped *in-vitro* luminescent nanothermometers operating within the VIS regime involve Er^{3+},Yb^{3+} co-doped particles pumped in the NIR region,[23, 286] and Eu^{3+} complexes with organic molecules excited with UV light.[287-290] Clearly, these examples are out of the scope of this chapter. For a more comprehensive understanding of *in-vitro* luminescent nanothermometry operating in the VIS region, the reader is pleased to refer to other references.[291]

By working with luminescent thermometers operating within the biological windows spectral regions, higher thermal sensitivities can be achieved when compared to those operating in the VIS,[271] and thermal maps with higher spatial resolution can be recorded, due to the lower scattering at these wavelengths.[127] Nevertheless, the number of lanthanide doped nanoparticles operating within the biological windows as *in-vitro* luminescent nanothermometers is very limited. In fact, we could identify only one *in-vitro* luminescent nanothermometer based on a hybrid nanostructure that combines plasmonic Au nanoparticles as an efficient optical heater with Nd^{3+},Y^{3+}:CaF_2 nanoparticles acting as luminescent thermometers.[283] These materials can be both excited with the same wavelength, 808 nm, located in the I-BW, while the emissions of the lanthanide nanoparticles used to determine the temperature are located within the II-BW. Hence, both functionalities (heating and thermal sensing) can be triggered by using a single excitation source. The luminescent thermometer constituted by the Nd^{3+},Y^{3+}:CaF_2 nanoparticles is based on the FIR of different emission lines generated by different Stark sublevels of the $^4F_{3/2} \rightarrow {}^4I_{11/2}$ transition of Nd^{3+}, located at ~1050 nm. Y^{3+} ions were intentionally added to break energy migration paths between Nd^{3+} ions, which would otherwise quench the emission intensity. Concerning to the nanoheater, the authors chose Au nanostars, which exhibited a higher light-to-heat conversion capacity when compared to the Au nanorods used previous in *ex-vivo* thermometry (see Section 7.1.1).[284] To properly prepare the combination of these nanoparticles for *in-vitro* luminescence nanothermometry, the Nd^{3+},Y^{3+}:CaF_2 nanoparticles and Au nanostars were co-assembled into hybrid structures by using polysterene beads with diameter around 500 nm as the colloidal support that were finally coated with a silica shell (~7 nm thick) to prevent their dissociated when used in biological environments.[283] TEM images of the hybrid structures can be seen in Figures 1.48 (a) and (b). Finally, these hybrids were internalized into a 3D spheroids tumor cell model prepared using a U-87MG human glioblastoma cell line.[283]

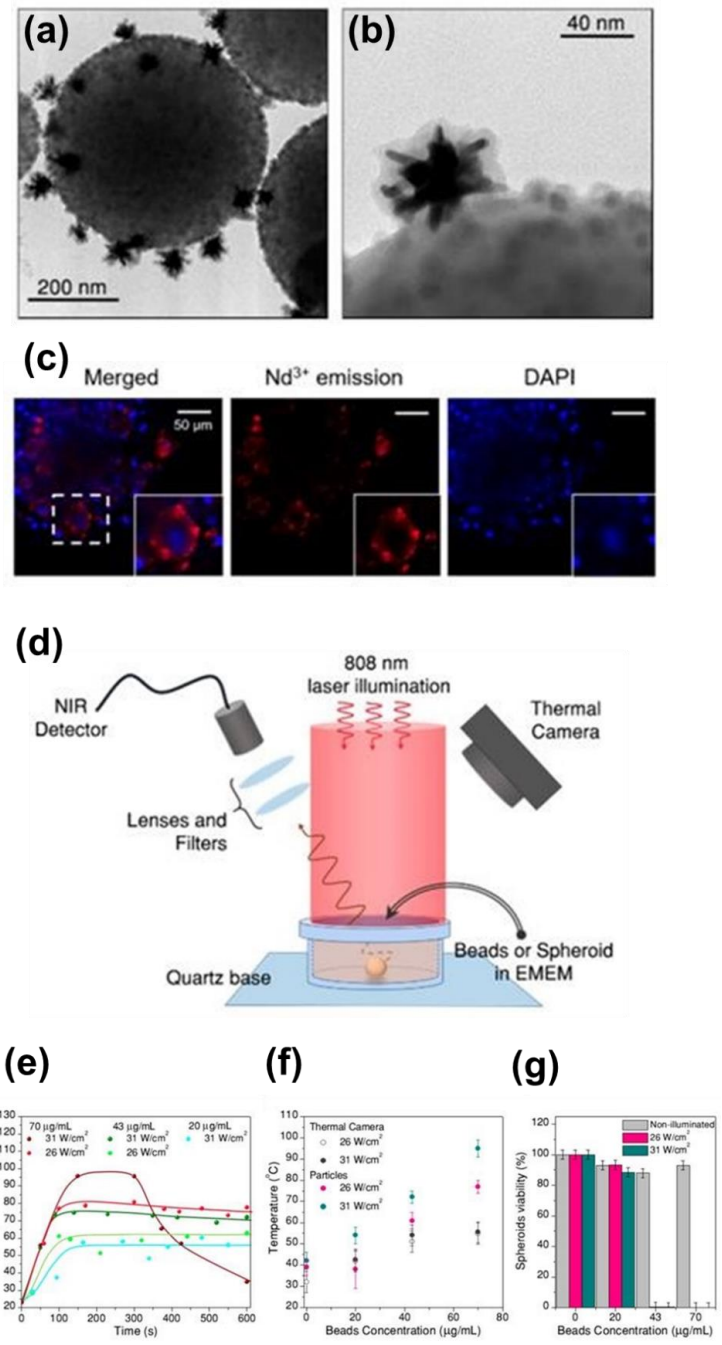

Figure 1.48. *In-vitro* thermal sensing using Nd^{3+},Y^{3+}:CaF_2 nanoparticles and Au nanostars, combined in polysterene beads, coated with silica shell, forming a hybrid structure. (a) and (b) TEM images of the hybrid nanostructures combining Nd^{3+},Y^{3+}:CaF_2 nanoparticles and Au nanostars, polysterene beads and silica shell. (c) Images of the surface of a treated spheroid (150 µg/mL), showing Nd^{3+} emission apparently located in the cytoplasm. (d) Experimental setup used to illuminate the samples and record their photoluminescence while monitoring the change of the temperature of the solution with a thermal camera. (e) Temperature measurements inside spheroids during photothermal treatment as a function of time, using different excitation powers and different concentrations of hybrid beads. (f) Average temperature at thermal

equilibrium compared to the temperature determined by a thermal camera. (g) Viability of the spheroids at 24 h after photothermal treatment. Adapted with permission.[283] Copyright from IvySpring 2019.

The hybrids with a concentration of 100 µg/mL, dispersed in water, were added to the cell culture medium and incubated to allow internalization for 48 hours at room temperature. The location of the hybrids inside the 3D tumor model could be monitored through the observation of the Nd^{3+} luminescence, using a modified Lightsheet microscope to properly record the emissions band at 1050 nm. As can be seen in Figure 1.48 (c), the emission of Nd^{3+} (presented in red color) was observed surrounding DAPI (4′,6-diamidino-2-phenylindole, used to label cell nuclei) emission, indicating the location of the hybrid beads in the cell cytoplasm.

The ability of these hybrids to emit light and generate heat was monitored in their cell medium (1 mL, 0.02 wt.%), using the experimental setup shown in Figure 1.48 (d). The hybrids were illuminated at 808 nm with a fiber-coupled laser diode using different powers and the beam collimated to a 3 mm diameter spot. The emissions were collected with a lens, filtered with a longpass filter cut-off at 850 nm to remove the laser signal, and finally recorded by an InGaAs spectrometer. The generated heat was monitored also by a thermal camera. From Equation 1.9, ΔE is independent of the external environment due to electrical shielding of 4f orbitals. Nevertheless, the pre-exponential factor B is a correction parameter related to detected differences in the intensity of the emissions when embedded in different mediums. It is clear that when the Nd^{3+},Y^{3+}:CaF_2 nanoparticles, combined in the hybrid structures or immersed in the tumor cell culture, the intensity of the emission will drastically change, as the medium changes. To correct the value of this parameter, fortunately a full calibration is not needed,[283] instead it is sufficient to measure several spectra at different excitation powers.[219] By doing so, a linear fit to the data then allows to calculate the intensity ratio at zero power, which can be assumed to be the value of FIR (following Equation 1.9) at room temperature.[219, 252] Accordingly, the value of B can be deduced using Equation1.9. The results obtained are in accordance with the temperature recorded from the thermal camera (differences below 1.5 K),[283] demonstrating successful recalibration of the nanothermometer within the new medium.

In the *in-vitro* experiment, the local temperature inside the 3D spheroids was investigated as a function of the different concentration of the hybrids (no hybrids, 20 µg mL^{-1}, 43 µg mL^{-1} and 70 µg mL^{-1} of hybrids) and different excitation power densities (26 W cm^{-2} and 31 W cm^{-2}), during a period of time of 10 min to maintain the spheroids alive.[283] The recorded temperature data, after transforming each of the intensity ratios of the emissions of the Nd^{3+},Y^{3+}:CaF_2 nanoparticles into temperatures, are shown in Figure 49 (e). The evolution of the temperature with time follows an initial fast increase until thermal equilibrium is reached at around 100 s. After 100 s, the temperature remained stable for all the samples, with the only exception of the hybrids excited at 31 W cm^{-2} and loaded with a concentration of 70 µg mL^{-1}, for which, according to the authors, the boiling point of water was likely reached prior to cooling due to the expansion and dead of the 3D spheroids. δT was found to be between 3 K and 4 K, although it could reach up to 9 K for the sample with the lowest concentration of the hybrids, excited at the lowest power density.[283] The average temperature at equilibrium increased proportionally to the increase of the concentration of the hybrids and the laser power density (see Figure 1.48 (f)). It was also observed that the temperature measured by the hybrids was higher than that recorded by the thermal camera, in agreement with the fact that the particles measure the temperature in the local proximity of the Au nanostars, while the thermal camera monitors the temperature at the surface of the cell medium. A final cell viability test in the spheroids (see Figure 1.48 (g)) revealed that when the local temperature surpassed 328 K, cells were almost completely dead, with viability below 1% for a treatment reaching 334 K, and 0.3% above this temperature.[283]

Despite the positive results obtained in this *in-vitro* experiment, there are, however, some aspects to be improved for proper operation of these particles in *in-vitro* environments. One would be the size of the hybrids used there, with a diameter of 830 ± 30 nm, clearly above the desired dimensions of nanometers in the biomedical fields.[13, 20] Additionally, the number of the lanthanide doped temperature sensors per Au nanoparticle should be increased, to favor a higher intensity of the emission of Nd^{3+} in order to improve the signal-to-noise ratio and to reduce the time required to record the spectra. Also the distance between the Au nanoparticles and the Ln^{3+} ions, should

be larger than 5 nm, in order to avoid quenching of the Nd^{3+} emissions. Another issue to take into consideration is the low S_{rel} of these luminescent thermometers, 0.18% K^{-1} at room temperature (see Table 1.3).

7.1.4. *In-vivo* thermometry using lanthanide doped luminescent nanothermometers operating in the biological windows.

Lanthanide doped luminescent nanothermometers can be implemented also in *in-vivo* mediums. *In-vivo* stands for investigations performed on whole living organisms, basically mice in this chapter.[292]

Nd^{3+}:LaF_3 nanoparticles have been used as a luminescent nanothermometer for *in-vivo* applications operating in the I-BW. In addition, these nanoparticles can release heat under excitation at 808 nm at a power of 4 W cm^{-2} when the doping level inside the nanoparticles is high, such as 5.6%.[169] As described in Section 7.1.1, it is possible to tailor the balance between light and heat generation through an appropriate choice of the Nd^{3+} content inside the nanoparticles. Carrasco *et al*. used these Nd^{3+}:LaF_3 nanoparticles for *in-vivo* photothermal treatment with continuous temperature monitoring in a mouse model.[169] The authors chose the intensity ratio between the emission lines at 865 and 885 nm, assigned to two Stark sublevels of the $^4F_{3/2} \rightarrow {}^4I_{9/2}$ transition of Nd^{3+} (see Table 1.1).

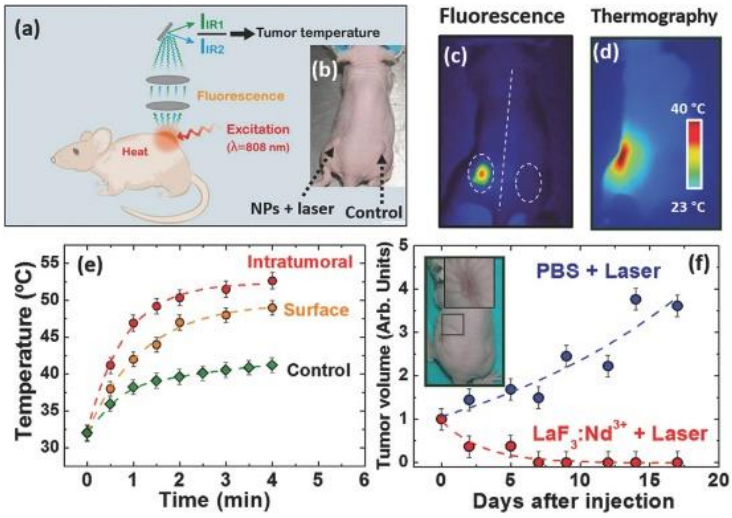

Figure 1.49. Temperature-controlled photothermal therapy in living mice with Nd^{3+}:LaF_3 nanoparticles operating in the I-BW. (a) Schematic representation of the dynamically controlled photothermal treatment of tumors in mice by using Nd^{3+} doped LaF_3 nanoparticles. (b) Optical image of a tumor-bearing mouse. The left tumor was treated with Nd^{3+}:LaF_3 nanoparticles and laser, while the one on the right was used as control. (c) Luminescent and (d) thermal images collected immediately after a 4 min long irradiation treatment. (e) Time evolution of the intratumoral temperature determined from the analysis of the luminescence of the Nd^{3+}:LaF_3 nanoparticles, and tumor surface temperature (both treated and control tumor) as measured by infrared thermal imaging. (f) Post-treatment size evolution of both treated and control tumors. The inset shows the optical image of the surface scar left at the tumor site 15 days after the therapy. Adapted with permission.[169] Copyright 2015, Wiley-VCH.

Figure 1.49 (a) shows a schematic representation of the experimental setup applied in this investigation. Tumor-bearing mice, with one tumor per flank, were injected with a dispersion of Nd^{3+}:LaF_3 nanoparticles in phosphate-buffered saline (PBS) at a concentration of 10% in mass in one of the tumors, while the other one was used as control (see Figure 1.49 (b)). The injected volume was equal to ½ of the estimated tumor volume, from which it was estimated that around 7×10^{13} nanoparticles were injected. Intratumor injection was chosen to avoid the preferential taken up of the nanoparticles by liver and spleen observed in intravenous injection. Only the tumor containing the nanoparticles exhibited luminescence within the I-BW (see Figure 50 (c)), and heating capability (see Figure 1.49 (d)) recorded with a thermographic camera. During the

photothermal therapy experiment, the intratumoral temperature was monitored (see Figure 1.49 (e)), together with the temperature determined at the surface of the skin of the mouse (being obtained by infrared thermographic imaging) in the treated tumor and the control tumor (injected only with the equivalent amount of pure PBS and illuminated also with the 808 nm laser). The photothermal treatment lasted for 4 min. This figure reveals the discrepancy between the intratumoral temperature, determined with the luminescent nanothermometers internalized in the tumor, and the surface temperature, determined by thermographic imaging, revealing the importance of an accurate temperature control at the injection site to minimize collateral damages due to overheating. The photothermal therapy treatment resulted successful, with a decrease of the size of the tumor after treatment to finally leave only a surface scar behind, as can be seen in Figure 1.49 (f). Meanwhile, the growth of the control tumor was not stopped.

Real-time subcutaneous thermal sensing has been proposed as a powerful tool for the study of the thermal dynamics of biological tissues during *in-vivo* experiments. Such studies would, in turn, provide access to the basic properties of biological tissues from which possible alterations related to incipient diseases could be detected.[293] Ximendes *et al*. used Nd^{3+}:LaF_3@Yb^{3+}:LaF_3 core@shell nanoparticles to measure subcutaneous thermal transients as a potential theranostics tool.[231] The core@shell nanoparticles were excited at 790 nm, and by using the intensity ratio between the emissions of Nd^{3+} at 1.3 μm ($^4F_{3/2} \rightarrow {}^4I_{13/2}$) and Yb^{3+} at around 1 μm ($^2F_{5/2} \rightarrow {}^2F_{7/2}$), the temperature could be determined (see Table 1.2). The authors used these luminescent nanothermometers to measure subcutaneous thermal transients, since the cooling dynamics strongly depend on the biological tissue properties. By measuring these cooling relaxation profiles it was possible to determine the characteristic thermal relaxation time that is unequivocally related to the fundamental properties of a particular biological tissue, and that additionally can provide information about the tissue status. The detection of small variations in the subcutaneous tissue relaxation times would allow for the identification of possible alterations of its thermal diffusivity, specific heat, thermal conductivity and density associated to diseases and, hence, could be used to detect anomalies caused by incipient diseases, such as dehydration, inflammation, ischemia or, even, tumor growth.

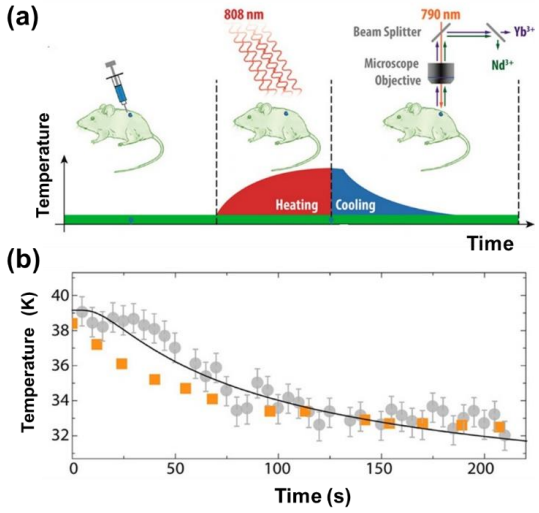

Figure 1.50. Measurement of *in-vivo* subcutaneous thermal transients in biological tissues using luminescence thermometry within the biological windows. (a) Schematic representation of the subcutaneous thermal relaxation experiments. (b) Time evolution of the temperature measured by the subcutaneous luminescent thermometer (grey and orange) and the IR camera (blue). Dots correspond to experimental subcutaneous (circles) and skin (squares) temperatures. Adapted with permission.[231] Copyright 2016, American Chemical Society.

To do that, the authors injected subcutaneously 200 µL of Nd^{3+}:LaF_3@Yb^{3+}:LaF_3 core@shell nanoparticles dispersed in PBS with a concentration of 1% in mass over the right flank of a CD1 mouse at a depth of 2 mm approximately. The mouse was anesthetized by isoflurane inhalation, and placed in a small animal imaging chamber equipped with a body temperature controller so that the mouse temperature was kept at 307 K ± 1 K. A moderate temperature increment was induced at the injection site by illuminating the mouse with a 808 nm laser beam with a power density of 0.7 W cm^{-2} during 4 min that activated the release of heat from the nanoparticles. After that, a low power 790 nm laser diode at a power of 30 mW was also focused on the subcutaneously injected nanoparticles through an infrared long working distance microscope objective to generate the luminescence of the nanoparticles from which temperature could be determined. After 4 min of irradiation, the 808 nm laser was turned off and the mouse tissues gradually recovered their initial temperature. Figure 1.50 (a) shows a schematic representation of the experimental setup used for this experiment. The luminescence of the nanoparticles was used to monitor the dynamics of the subcutaneous thermal relaxation. Just after the end of the heating cycle, the subcutaneous temperature was determined to be 312 K ± 1 K. The authors could reveal clear differences between the thermal relaxation curves corresponding to the subcutaneous and skin temperatures (see Figure 1.50 (b)). According to the authors, those differences arise mainly due to the different physical mechanisms responsible for heat dissipation: whereas for the skin the dissipation may be essentially convective, for the subcutaneous tissues it could be assumed to be mainly conductive, due to the lack of any physical contact with air. Another reason for these different thermal relaxation curves is the minimum blood flow in the hypodermis, several orders of magnitude lower than in internal organs.

Through the analysis subcutaneous thermal relaxation dynamics, which allows access to the characteristic thermal relaxation time of a given subcutaneous tissue, it was possible to compute the thermal diffusivity of the mouse tissue, resulting in a value of 0.13 ± 0.04 mm^2 s^{-1}, which is similar to that reported for chicken breast tissue determined.[294] Additionally, the subcutaneous thermal monitoring allowed the quantification of the local thermal dose administrated in a hyperthermia treatment that in that case was 54 ± 8 J. This parameter is considered nowadays one of the most important factors which influence the efficiency of hyperthermia treatments. Since the total energy given by the 808 nm laser in the tissue was 560 ± 63 J, the biological tissue absorbed only a 10 % of this energy. Thus, the absorption coefficient of the biological tissue was 0.23 ± 0.05 cm^{-1}, also in agreement with previous reported data in the literature.[294] This parameter was determined by relating the thermal energy dose, that is the required heat to cause a temperature increment in a tissue of mass,[231] with the Lambert−Beer law.

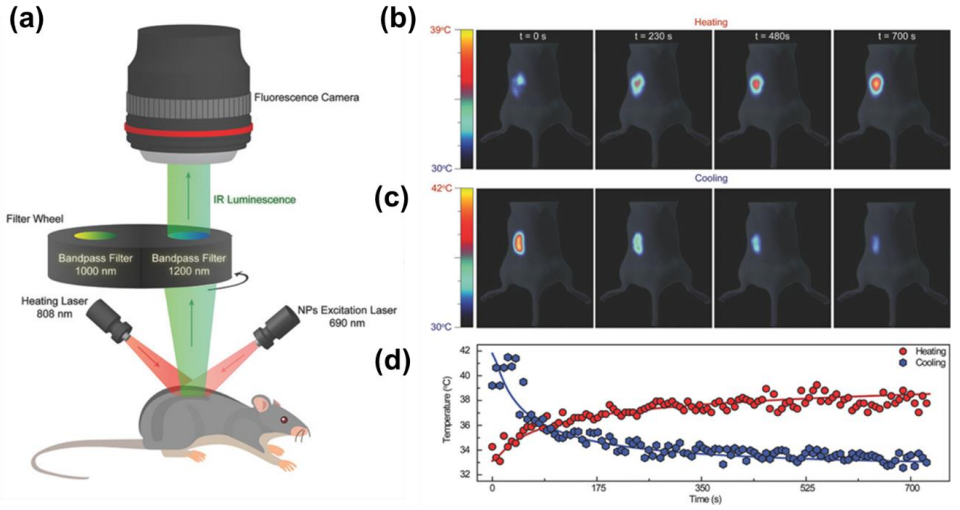

Figure 1.51. (a) Schematic representation of the *in-vivo* experiment to extract 2D subcutaneous thermal images. (b) Thermal images obtained during the heating and relaxation (cooling) cycles. (c) Time evolution

of the average temperature in the injection area as measured by the subcutaneous lanthanide nanothermometers during heating and thermal relaxation cycles. Adapted with permission.[247] Copyright 2017, Wiley CH.

Despite this big advance, accurate thermal-based diagnosis would require, at least, the dynamical acquisition of 2D subcutaneous thermal images. To do that it is necessary to acquire low-noise luminescence thermal images with commercially available shortwave infrared cameras, and therefore, to reconstruct accurate bidimensional thermal images. For this purpose, Ximendes *et al.* designed and synthesized Er^{3+},Yb^{3+}:LaF_3@Yb^{3+},Tm^{3+}:LaF_3 core@shell nanoparticles capable of 2D subcutaneous dynamic thermal imaging when excited at 690 nm (in the I-BW), emitting in the II and III-BWs.[247] In these lanthanide-doped nanoparticles, Tm^{3+} and Er^{3+} ions are spatially separated, with Tm^{3+} acting as the sensitizer, while Er^{3+} and Yb^{3+} were used as activators. The emissions used for the luminescent thermometer in this case were those of Er^{3+} at 1550 nm (III-BW), and Yb^{3+} at 1000 nm (II-BW) (see Table 1.4). The authors used these core@shell nanoparticles for the acquisition of 2D thermal videos unveiling heat diffusion at the subcutaneous level. These videos allowed the acquisition of 2D patterns of tissue thermal properties that, in turn, could be used to identify and localize damaged (or non-healthy) biological tissues *in-vivo*. Moreover, this analysis made possible the quantification of the thermal dose administered in the whole area of injection during a hyperthermia treatment. For that, the authors subcutaneously injected 200 µL of a dispersion of the Er^{3+},Yb^{3+}:LaF_3@Yb^{3+},Tm^{3+}:LaF_3 core@shell nanoparticles in PBS in a CD1 mouse model. Then, the temperature at the injection site was increased by illuminating at 808 nm with an excitation density of 0.7 W cm^{-2}, and it was measured through the luminescence of the nanoparticles excited at 690 nm with a power density of 0.1 W cm^{-2}, low enough to avoid additional heating. A schematic representation of the experimental setup used can be seen in Figure 1.51 (a). From the videos recorded, the authors extracted thermal images at different time delays after the beginning and cooling cycles (see Figure 1.51 (b)-(c)), providing detailed 2D images of the subcutaneous spatial distribution of temperature with a time resolution better than 1 s, from which the authors computed the time evolution of the subcutaneous temperature during both heating and cooling cycles (see Figure 1.51 (d)). The thermal diffusivity of the tissue was determined to be 0.15 ± 0.02 mm^2 s^{-1} for the heating process, and 0.12 ± 0.02 mm^2 s^{-1} for the cooling one.[294]

7.2. Other applications of lanthanide doped luminescent nanothermometers operating within the biological windows.

7.2.1. Microwire nanothermometry using lanthanide doped luminescent materials operating in the biological windows.

Lanthanide doped luminescent materials can be used as nanothermometers also outside the biological/biomedical fields. A typical example involves the application of lanthanide doped luminescent materials as thermal probes in microwires, for the evaluation of the Joule induced heating effect in a copper microwire.[172] Nd^{3+} doped YAG luminescent nanothermometers, operating in the I-BW based on the thermally coupled Stark sublevels of the $^4F_{3/2} \rightarrow {}^4I_{9/2}$ electronic transition of of Nd^{3+}, located at 940 nm (see Table 1.1), constitute a potential nanothermometer for temperature readings in microwires.

In order to sense the temperature in a copper microwire, a drop of an aqueous dispersion of these nanoparticles (1 wt.%), was deposited onto a 100 µm thick wire, which was fixed on a glass plate. After the evaporation of water, a 808 nm laser diode was focused onto the wire using a 10x magnification and a microscope objective with numerical aperture of 0.55, that produced a laser spot of approximately 1.8 µm in diameter on the wire. Using the same microscope objective, the luminescence arising from the Nd^{3+} doped YAG nanoparticles was collected (see Figure 1.52 (a) for the experimental setup used). The increase of the temperature caused by the ohmic heating in the microwire was monitored by an infrared thermographic camera and also by the intensity ratio of the luminescent particles. The temperature calculated from the intensity ratio of the emission generated by the nanoparticles, presented a parabolic dependence with the different electrical currents applied (see Figure 53 (b)). This dependence was the expected one since the Joule heating effect is directly proportional to the square of the electrical current applied.[172] To validate the results obtained from the thermal readings of the nanoparticles, the data recorded with the infrared thermographic camera, were also considered. The results obtained, shown in Figure 1.52 (b)), reveal good agreement between the two methodologies. Furthermore, the thermal images recorded by the infrared camera, display a maximum microwire temperature

increase of around 13 K (see Figure 1.52 (c)), in very good agreement to the maximum temperature determined by the luminescent thermometers (see Figure 1.52 (b)).

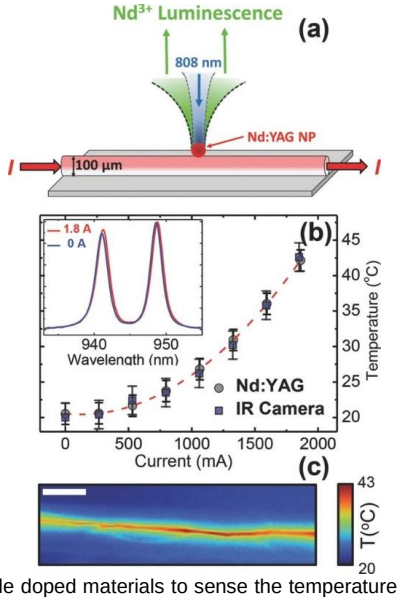

Figure 1.52. Applying lanthanide doped materials to sense the temperature in a microwire: (a) Scheme of the experimental setup used to determine the temperature in a copper microwire. (b) Temperature of the microwire as a function of the applied current, obtained from the intensity ratio of the emissions generated by the nanoparticles and from the infrared thermographic camera. The emission spectra generated by the nanoparticles placed on the wire obtained at the two extreme values of the electrical current (0 and 1.8 A) can be seen in the inset. (c) Thermal image of the microwire when conducting the maximum electrical current applied (1.8 A), as obtained with a thermographic camera, scale bar is 2 cm long. Adapted with permission.[172] Copyright from Wiley 2015.

7.2.2. Microfluidic nanothermometry using lanthanide doped luminescent materials operating in the biological windows.

Continuing with the applicability of lanthanide doped luminescent materials as nanothermometers outside the biological/biomedical field, we provide an example of Nd^{3+} doped YAG nanoparticles used as thermal probes in microfluidics.[172] The working principle of these nanoparticles is based on the thermally coupled Stark sublevels of the $^4F_{3/2} \rightarrow {}^4I_{9/2}$ electronic transition of Nd^{3+}, located at 940 nm in the I-BW (see Table 1.1). Taking advantage of the water dispersibility of these Nd^{3+} doped YAG nanoparticles, thermal imaging of a simple optofluidic device consisting of a 100 µm thick microchannel was recorded. In this microchannel, a single-mode fiber-coupled 1480 nm diode laser with maximum power of 200 mW, was used as a heating source. This laser was focused on the channel containing the dispersion of the nanoparticles in water, via a microscope objective with a magnification of 10x and numerical aperture of 0.25. To extract the temperature pattern generated by the 1480 nm laser irradiation, strongly absorbed by water, the microfluidic channel was filled with 0.1 wt.% aqueous dispersion of the nanoparticles, while being monitored with a thermal camera (see Figure 1.53 (a) for the experimental setup). Concerning the excitation and luminescence of the nanoparticles, they were excited with a 808 nm laser, which was focused onto the optofluidic device using a microscope objective with 10x magnification and numerical aperture of 0.55, that produced a laser spot of approximately 1.8 µm in diameter on the channel, whereas the luminescence was collected using the same microscope objective. Figure 1.53 (b) shows the temperature increment at the focus of the 1480 nm heating laser, represented as a function of the 1480 nm laser power. The measurements of temperature were performed by overlapping both the focused heating and probe (808 nm) laser beams. It can be extracted that for laser powers below 60 mW, the “on-focus” temperature increased linearly, whereas above this value the relationship does not obey to a linear function.[172] The authors reasoned this behavior so that at high laser powers additional heating is produced, which can lead to the creation of

relevant convection currents and the formation of bubbles.[172] By applying a power of 60 mW, a 2D thermal image of the microchannel in the surroundings of the 1480 nm laser spot was recorded by scanning the 808 nm laser along a 900 × 900 μm^2 area around the heating laser spot. It was observed that the laser-induced heating caused an increase of the temperature in a large area around the laser spot (see Figure 1.53 (c)) well far from the microchannel itself, due to thermal diffusion.[172]

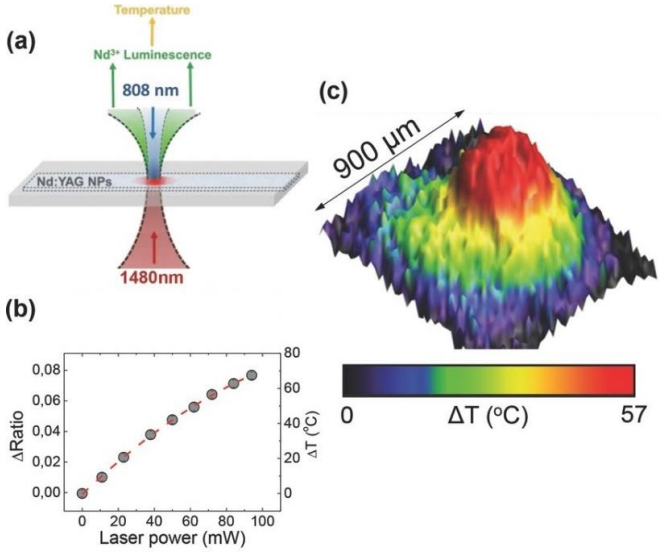

Figure 1.53. Temperature sensing in optofluidics. (a) Scheme of the experimental setup used to record the temperature distribution within an optical trap created by a 1480 nm focalized laser beam on a microchannel filled with an aqueous dispersion of Nd^{3+}:YAG nanothermometers. (b) Temperature increment as a function of power of the 1480 nm laser. (c) All-optical thermal imaging (temperature distribution 2D map) of the area under pumping from the 1480 nm laser where the optical trap is created. Adapted with permission.[172] Copyright from Wiley 2015.

7.2.3. Measuring thermal resistance of nanoparticles through lanthanide nanothermometers

Luminescence nanothermometers can be also used as a tool for the unveiling of the thermal properties of the particles themselves, such as the determination of their thermal resistance. Thermal resistance is a key parameter to model the heat transfer at the nanoscale.[151] In order to achieve this, Savchuk *et al.*[151] applied Ho,Tm doped $KLu(WO_4)_2$ nanoparticles, excited with 808 nm laser source, as upconversion materials based on the 696 nm emission of Tm^{3+} and the 755 nm emission of Ho^{3+}, located in the I-BW (see Table 1.1).

In a typical experiment, the 808 nm laser is focused on the surface of the nanoparticles, generating, simultaneously, upconversion emissions and heat, due to radiative and non-radiative processes, respectively. A beam splitter was used to redirect a part of the emitted signal to a portable spectrophotometer that records the upconversion emission generated from the nanoparticles (see Figure 1.54 (a) for the experimental setup). These emissions were recorded as a function of time and the later converted into temperature by the intensity ratio between emissions of Ho^{3+} and Tm^{3+}, following Equation 1.19. The temperature increment ($\Delta T\ (t)$) from the nanoparticles (see Figure 1.54 (b)) is tested as a function of the concentration of the emitting ions within the host (1 at.% Ho^{3+}, 5 at.% Tm^{3+} (black squares) and 1 at.% Ho^{3+}, 15 at.% Tm^{3+} (green circles)). Results demonstrated that the $\Delta T\ (t)$ generated is smaller for the host with the smallest amount of Tm^{3+} ions, suggesting a positive correlation between the heat generated due to non-radiative Tm^{3+}-to-Ho^{3+} ET and Ho^{3+}-to-Tm^{3+} BET (see Figure 1.8 (a)) and the Tm^{3+} concentration. In addition, the plateau discerned for high power densities above 300 x 10^6 W m^{-2} and not observed for power ranges studied for the sample with higher Tm^{3+} ions content, is related to a saturation effect on the Tm^{3+} absorption at 808 nm.

The heat dissipation follows the classical Fourier law, resulting in a temperature increase given by:[295, 296]

$$\Delta T\ (t) = \Delta T_m \left[1 - exp\left(-\frac{hA}{mc}t\right)\right] = \Delta T_m \left[1 - exp\left(-\frac{t}{RC}\right)\right] = \Delta T_m \left[1 - exp\left(-\frac{t}{\tau}\right)\right] \qquad (1.51)$$

where ΔT_m is the temperature increase in the steady-state regime (see Figure 1.54 (c)), h is the convective heat transfer coefficient, A is the thermal contact area, $R = 1/hA$ is the convective thermal resistance and $\tau = RC$ stands for the system's thermal time constant.[151]
Fitting this equation to the heating curve of the 1 at.% Ho^{3+}, 5 at.% Tm^{3+}:$KLu(WO_4)_2$ particles in contact with air, presented in Figure 1.54 (c), is was obtained ΔT_m=18.3 ± 0.2 K and τ=0.223 ± 0.004 s, corresponding to R=(9.50 ± 0.17) x 10^7 K W^{-1}.[151] In addition, the extraction of τ, allows for the determination of the δT of the nanothermometers, calculated by Equation 1.5. The δT exhibit a value of 0.0033 ± 0.0007 s, which is 2-4 order of magnitude better than the thermometers based on scanning thermal microscopy (0.1 s,[297] and 1.5 s),[298, 299] and Raman spectroscopy (90 s).[300]

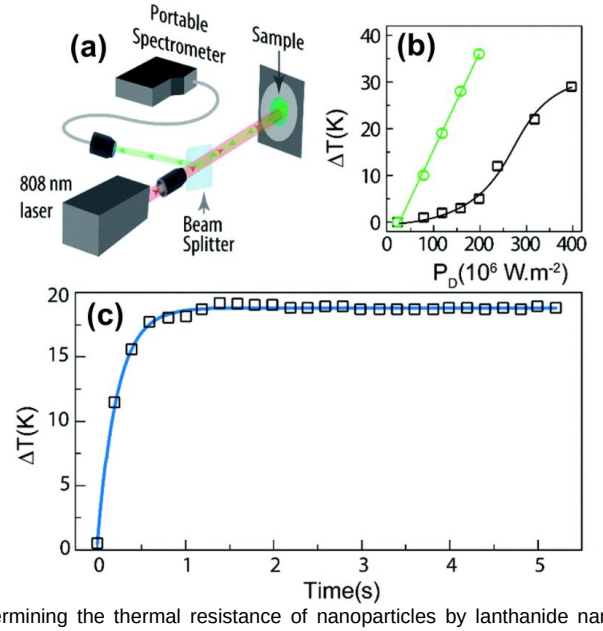

Figure 1.54. Determining the thermal resistance of nanoparticles by lanthanide nanothermometers: (a) Scheme of the experimental setup used under 808 nm excitation. (b) Temperature increase induced as a function of the different power of the laser applied, and as concentration of the two emitting ions: 1 at.% Ho^{3+}, 5 at.% Tm^{3+} (black squares) and 1 at.% Ho^{3+}, 15 at.% Tm^{3+} (green circles), embedded in $KLu(WO_4)_2$ host. (c) Heating curve of 1 at.% Ho^{3+}, 5 at.% Tm^{3+} doped $KLu(WO_4)_2$ nanoparticles excited with 808 nm laser operating with a power of 318 x 10^6 W m^{-2}. The blue line corresponds to the best fit to experimental data using Equation 51, (r^2=0.997). Adapted with permission.[151] Copyright from The Royal Society of Chemistry 2018.

8. Aims of the thesis

After reviewing the literature, several strategies to enrich the field of the applications of luminescent lanthanide doped materials have been underlined in the present thesis. The applicability of these materials as thermal sensors in the third biological window is aimed due to the reduction of scattering and absorption within biological systems, which implies deep penetration depths.
In this thesis, it has been decided to apply as energy source, the near infrared light due to its advantages upon biological matter. These light sources do not generate autofluorescence or

phototoxicity in the biological tissues. These light sources do not suffer from photobleaching, autofluorescence and photoxicity and in addition allow for deep-tissue penetration within the biological windows spectral regions.

A careful selection of the lanthanide ions, focusing on holmium (III) and thulium (III) was done. These ions, allow to generate self-assessed photothermal agents, *i.e.* the same particle releases heat and emit light that allows determining the temperature *in situ*. These lanthanide ions were used as doping ions in monoclinic double tungstates ($KRE(WO_4)_2$) and simple cubic rare-earth sesquioxides (RE_2O_3, RE=rare-earth). These hosts offer photochemical stability, large values of absorption and emission cross sections for lanthanide ions, and the possibility of doping without fluorescence quenching.

We extended our objectives furthermore, by investigating the role of the size and shape of these materials on their applications. To meet with our objectives, we developed novel synthetic methodologies for the preparation of monoclinic ($KRE(WO_4)_2$) crystalline particles and cubic rare-earth sesquioxides colloidal nanoarchitectures, with nanodimensional or submicrometer sizes, and with well-defined shapes.

Furthermore, we have also explored if these nanoparticles might present additional functionalities. The generation of white light emission by lanthanide doped colloidal rare-earth sesquioxide nanocrystals has been explored and we analyzed the possibility of applying the white light generated by these nanoparticles for temperature sensing. We finally explored the applicability of these nanocrystals as antioxidant agents and analyzed the key factors that might influence this behavior.

9. Structure of the thesis

Apart from the introduction, which highlights the current status of luminescent lanthanide doped materials operating within the biological windows spectral regions and their applications, the thesis has been designed in the following way:
Chapter II describes the synthetic methodologies for the preparation of the luminescent lanthanide doped materials and the characterization techniques applied.

Chapter III underlines the applicability of holmium (III) and thulium (III) doped monoclinic $KRE(WO_4)_2$) particles as self-assessed photothermal agents operating in the III-BW. In addition, we present two novel synthetic methodologies (solvothermal and thermal decomposition synthesis) for the preparation of monoclinic $KRE(WO_4)_2$ hosts.

Chapter IV focuses on the wet chemical synthesis of cubic rare-earth sesquioxides (RE_2O_3, RE = rare-earth). It is further extended in doping these hosts with lanthanide ions, either in simple core, core@shell or layer-by-layer nanoarchitectures. Finally, the role of their morphological characteristics on their ability to sense temperature within the III-BW and to act as photothermal agents has been analyzed.

Chapter V explores the application of Y_2O_3 (doped with Ho^{3+} and Tm^{3+} lanthanide ions or undoped, depending on the application) as white light emitters and antioxidant agents. The possibility of applying white light emission for luminescent nanothermometry is presented. Finally, these nanocrystals can also act as antioxidant nanoagents even in biological environments.

The thesis ends by extracting the main conclusions of this work.

10. References

1. Allison, S.; Gillies, G., Remote thermometry with thermographic phosphors: Instrumentation and applications. *Review of Scientific Instruments* **1997,** 68, (7), 2615-2650.
2. Khalid, A. H.; Kontis, K., Thermographic phosphors for high temperature measurements: Principles, current state of the art and recent applications. *Sensors* **2008,** 8, (9), 5673-5744.
3. Uchiyama, S.; Gota, C.; Tsuji, T.; Inada, N., Intracellular temperature measurements with fluorescent polymeric thermometers. *Chemical Communications* **2017,** 53, (80), 10976-10992.
4. Jaque, D.; Maestro, L. M.; Del Rosal, B.; Haro-Gonzalez, P.; Benayas, A.; Plaza, J.; Rodriguez, E. M.; Sole, J. G. J. n., Nanoparticles for photothermal therapies. **2014,** 6, (16), 9494-9530.
5. McCabe, K. M.; Hernandez, M., Molecular thermometry. *Pediatric Research* **2010,** 67, (5), 469.
6. Wolfbeis, O. S., Sensor paints. *Advanced Materials* **2008,** 20, (19), 3759-3763.
7. Childs, P. R.; Greenwood, J.; Long, C., Review of temperature measurement. *Review of Scientific Instruments* **2000,** 71, (8), 2959-2978.
8. Grand View Research, I., Temperature sensor market by product type (Bimetallic, Thermistor, IC, RTD, Thermocouple, IR, Fiber Optic), End-User Industry (Oil & Gas, Chemicals, Automotive, Consumer Electronics, Healthcare), and Geography-Global Forecast to 2023. **2018**.
9. Brites, C. D.; Lima, P. P.; Silva, N. J.; Millán, A.; Amaral, V. S.; Palacio, F.; Carlos, L. D., A luminescent molecular thermometer for long-term absolute temperature measurements at the nanoscale. *Advanced Materials* **2010,** 22, (40), 4499-4504.
10. Jaque, D.; Vetrone, F., Luminescence nanothermometry. *Nanoscale* **2012,** 4, (15), 4301-4326.
11. Laha, S. S.; Naik, A. R.; Kuhn, E. R.; Alvarez, M.; Sujkowski, A.; Wessells, R. J.; Jena, B. P., Nanothermometry measure of muscle efficiency. *Nano Letters* **2017,** 17, (2), 1262-1268.
12. Wang, X.; Wolfbeis, O. S.; Meier, R. J., Luminescent probes and sensors for temperature. *Chemical Society Reviews* **2013,** 42, (19), 7834-7869.
13. Quintanilla, M.; Liz-Marzan, L. M., Guiding rules for selecting a nanothermometer. *Nano Today* **2018,** 19, 126-145.
14. Albers, A. E.; Chan, E. M.; McBride, P. M.; Ajo-Franklin, C. M.; Cohen, B. E.; Helms, B. A., Dual-emitting quantum dot/quantum rod-based nanothermometers with enhanced response and sensitivity in live cells. *Journal of the American Chemical Society* **2012,** 134, (23), 9565-9568.
15. Rocha, U.; Jacinto da Silva, C.; Ferreira Silva, W.; Guedes, I.; Benayas, A.; Martínez Maestro, L.; Acosta Elias, M.; Bovero, E.; van Veggel, F. C. J. M.; García Solé, J. A.; Jaque, D., Subtissue thermal sensing based on neodymium-doped LaF_3 nanoparticles. *ACS Nano* **2013,** 7, (2), 1188-1199.
16. Okabe, K.; Inada, N.; Gota, C.; Harada, Y.; Funatsu, T.; Uchiyama, S., Intracellular temperature mapping with a fluorescent polymeric thermometer and fluorescence lifetime imaging microscopy. *Nature Communications* **2012,** 3, (1), 705.
17. Childs, P. R. N., Chapter 1-Nanoscale Thermometry and Temperature Measurement. In *Thermometry at the Nanoscale: Techniques and Selected Applications*, The Royal Society of Chemistry: 2016; pp 1-22.
18. DeBerardinis, R. J.; Lum, J. J.; Hatzivassiliou, G.; Thompson, C. B., The biology of cancer: metabolic reprogramming fuels cell growth and proliferation. *Cell Metabolism* **2008,** 7, (1), 11-20.
19. Karnebogen, M.; Singer, D.; Kallerhoff, M.; Ringert, R. H., Microcalorimetric investigations on isolated tumorous and non-tumorous tissue samples. *Thermochimica Acta* **1993,** 229, 147-155.
20. Jaque, D.; Martínez Maestro, L.; del Rosal, B.; Haro-Gonzalez, P.; Benayas, A.; Plaza, J. L.; Martín Rodríguez, E.; García Solé, J., Nanoparticles for photothermal therapies. *Nanoscale* **2014,** 6, (16), 9494-9530.
21. Brites, C.; Millán, A.; Carlos, L., Handbook on the Physics and Chemistry of Rare Earths. In Amsterdam: Elsevier: 2016.
22. Carlos, L. D.; Palacio, F., Thermometry at the nanoscale:techniques and selected applications. **2016**.
23. Vetrone, F.; Naccache, R.; Zamarrón, A.; Juarranz de la Fuente, A.; Sanz-Rodríguez, F.; Martinez Maestro, L.; Martín Rodriguez, E.; Jaque, D.; García Solé, J.; Capobianco, J. A., Temperature sensing using fluorescent nanothermometers. *ACS Nano* **2010,** 4, (6), 3254-3258.
24. Gota, C.; Okabe, K.; Funatsu, T.; Harada, Y.; Uchiyama, S., Hydrophilic fluorescent nanogel thermometer for intracellular thermometry. *Journal of the American Chemical Society* **2009,** 131, (8), 2766-2767.
25. Cahill, D. G., Analysis of heat flow in layered structures for time-domain thermoreflectance. *Review of Scientific Instruments* **2004,** 75, (12), 5119-5122.
26. Löw, P.; Kim, B.; Takama, N.; Bergaud, C., High-spatial-resolution surface-temperature mapping using fluorescent thermometry. *Small* **2008,** 4, (7), 908-914.
27. Kim, S. H.; Noh, J.; Jeon, M. K.; Kim, K. W.; Lee, L. P.; Woo, S. I., Micro-Raman thermometry for measuring the temperature distribution inside the microchannel of a polymerase chain reaction chip. *Journal of Micromechanics and Microengineering* **2006,** 16, (3), 526-530.
28. Childs, P. R. N.; Greenwood, J. R.; Long, C. A., Review of temperature measurement. *Review of Scientific Instruments* **2000,** 71, (8), 2959-2978.
29. Corke, M.; Kersey, A. D.; Jackson, D. A.; Jones, J. D. C., All-fibre 'michelson' thermometer. *Electronics Letters* **1983,** 19, (13), 471-473.

30. Kim, K.; Jeong, W.; Lee, W.; Reddy, P., Ultra-high vacuum scanning thermal microscopy for nanometer resolution quantitative thermometry. *ACS Nano* **2012,** 6, (5), 4248-4257.
31. Greenwood, J. R.; Childs, P. R. N.; Chaloner, P., Gold leads to PRTs for monitoring high temperatures. *Gold Bulletin* **1999,** 32, (3), 85-89.
32. Gao, Y.; Bando, Y., Carbon nanothermometer containing gallium. *Nature* **2002,** 415, (6872), 599-599.
33. Klinkert, B.; Narberhaus, F., Microbial thermosensors. *Cellular and Molecular Life Sciences* **2009,** 66, (16), 2661-2676.
34. Mills, G.; Zhou, H.; Midha, A.; Donaldson, L.; Weaver, J. M. R., Scanning thermal microscopy using batch fabricated thermocouple probes. *Applied Physics Letters* **1998,** 72, (22), 2900-2902.
35. Hammiche, A.; Reading, M.; Pollock, H. M.; Song, M.; Hourston, D. J., Localized thermal analysis using a miniaturized resistive probe. *Review of Scientific Instruments* **1996,** 67, (12), 4268-4274.
36. Tovee, P. D.; Pumarol, M. E.; Rosamond, M. C.; Jones, R.; Petty, M. C.; Zeze, D. A.; Kolosov, O. V., Nanoscale resolution scanning thermal microscopy using carbon nanotube tipped thermal probes. *Physical Chemistry Chemical Physics* **2014,** 16, (3), 1174-1181.
37. Kortmann, J.; Sczodrok, S.; Rinnenthal, J.; Schwalbe, H.; Narberhaus, F., Translation on demand by a simple RNA-based thermosensor. *Nucleic Acids Research* **2011,** 39, (7), 2855-2868.
38. Narberhaus, F.; Waldminghaus, T.; Chowdhury, S., RNA thermometers. *FEMS Microbiology Reviews* **2006,** 30, (1), 3-16.
39. Chowdhury, S.; Maris, C.; Allain, F. H. T.; Narberhaus, F., Molecular basis for temperature sensing by an RNA thermometer. *The EMBO Journal* **2006,** 25, (11), 2487-2497.
40. Brites, C. D.; Lima, P. P.; Silva, N. J.; Millán, A.; Amaral, V. S.; Palacio, F.; Carlos, L. D., Thermometry at the nanoscale. *Nanoscale* **2012,** 4, (16), 4799-4829.
41. Ananias, D.; Brites, C. D. S.; Carlos, L. D.; Rocha, J., Cryogenic nanothermometer based on the MIL-103 (Tb,Eu) metal-organic framework. *European Journal of Inorganic Chemistry* **2016,** 2016, (13-14), 1967-1971.
42. Omary, M. A.; Patterson, H. H., Luminescence, Theory. In *Encyclopedia of Spectroscopy and Spectrometry (Third Edition)*, Lindon, J. C.; Tranter, G. E.; Koppenaal, D. W., Eds. Academic Press: Oxford, 2017; pp 636-653.
43. DeLuca, J. A., An introduction to luminescence in inorganic solids. *Journal of Chemical Education* **1980,** 57, (8), 541.
44. Wade, S. A.; Collins, S. F.; Baxter, G. W., Fluorescence intensity ratio technique for optical fiber point temperature sensing. *Journal of Applied Physics* **2003,** 94, (8), 4743-4756.
45. Dong, B.; Cao, B.; He, Y.; Liu, Z.; Li, Z.; Feng, Z., Temperature sensing and in vivo imaging by molybdenum sensitized visible upconversion luminescence of rare-earth oxides. *Advanced Materials* **2012,** 24, (15), 1987-1993.
46. Hu, F.; Cao, J.; Wei, X.; Li, X.; Cai, J.; Guo, H.; Chen, Y.; Duan, C. K.; Yin, M., Luminescence properties of Er^{3+}-doped transparent $NaYb_2F_7$ glass-ceramics for optical thermometry and spectral conversion. *Journal of Materials Chemistry C* **2016,** 4, (42), 9976-9985.
47. Brites, C. D. S.; Millán, A.; Carlos, L. D., Chapter 281-Lanthanides in Luminescent Thermometry. In *Handbook on the Physics and Chemistry of Rare Earths*, Jean-Claude, B.; Vitalij K, P., Eds. Elsevier: 2016; Vol. 49, pp 339-427.
48. Ishiwada, N.; Fujioka, S.; Ueda, T.; Yokomori, T., Co-doped Y_2O_3:Tb^{3+}/Tm^{3+} multicolor emitting phosphors for thermometry. *Optics Letters* **2011,** 36, 760-762.
49. Quintanilla, M.; Benayas, A.; Naccache, R.; Vetrone, F., Chapter 5-Luminescent nanothermometry with lanthanide-doped nanoparticles. In *Thermometry at the Nanoscale:Techniques and Selected Applications*, The Royal Society of Chemistry: 2016; pp 124-166.
50. He, X.; Gao, J.; Gambhir, S. S.; Cheng, Z., Near-infrared fluorescent nanoprobes for cancer molecular imaging: status and challenges. *Trends in Molecular Medicine* **2010,** 16, (12), 574-583.
51. Donner, J. S.; Thompson, S. A.; Kreuzer, M. P.; Baffou, G.; Quidant, R., Mapping intracellular temperature using green fluorescent protein. *Nano Letters* **2012,** 12, (4), 2107-2111.
52. Nazarenko, V. V.; Remeeva, A.; Yudenko, A.; Kovalev, K.; Dubenko, A.; Goncharov, I. M.; Kuzmichev, P.; Rogachev, A. V.; Buslaev, P.; Borshchevskiy, V.; Mishin, A.; Dhoke, G. V.; Schwaneberg, U.; Davari, M. D.; Jaeger, K. E.; Krauss, U.; Gordeliy, V.; Gushchin, I., A thermostable flavin-based fluorescent protein from chloroflexus aggregans: A framework for ultra-high resolution structural studies. *Photochemical & Photobiological Sciences* **2019,** 18, (7), 1793-1805.
53. Savchuk, O. A.; Silvestre, O. F.; Adão, R. M. R.; Nieder, J. B., GFP fluorescence peak fraction analysis based nanothermometer for the assessment of exothermal mitochondria activity in live cells. *Scientific Reports* **2019,** 9, (1), 7535-7546.
54. Kiyonaka, S.; Kajimoto, T.; Sakaguchi, R.; Shinmi, D.; Omatsu-Kanbe, M.; Matsuura, H.; Imamura, H.; Yoshizaki, T.; Hamachi, I.; Morii, T.; Mori, Y., Genetically encoded fluorescent thermosensors visualize subcellular thermoregulation in living cells. *Nature Methods* **2013,** 10, (12), 1232-1238.
55. Nakano, M.; Arai, Y.; Kotera, I.; Okabe, K.; Kamei, Y.; Nagai, T., Genetically encoded ratiometric fluorescent thermometer with wide range and rapid response. *Plos One* **2017,** 12, (2), 172344-172358.
56. Gota, C.; Okabe, K.; Funatsu, T.; Harada, Y.; Uchiyama, S., Hydrophilic fluorescent nanogel thermometer for intracellular thermometry. *Journal of the American Chemical Society* **2009,** 131, 2766-2767.

57. Hayashi, T.; Kawamoto, K.; Inada, N.; Uchiyama, S., Cationic fluorescent nanogel thermometers based on thermoresponsive poly(N-isopropylacrylamide) and environment-sensitive benzofurazan. *Polymers* **2019,** 11, (8), 1305-1317.
58. Uchiyama, S.; Tsuji, T.; Kawamoto, K.; Okano, K.; Fukatsu, E.; Noro, T.; Ikado, K.; Yamada, S.; Shibata, Y.; Hayashi, T.; Inada, N.; Kato, M.; Koizumi, H.; Tokuyama, H., A cell-targeted non-cytotoxic fluorescent nanogel thermometer created with an imidazolium-containing cationic radical initiator. *Angewandte Chemie International Edition* **2018,** 57, (19), 5413-5417.
59. Borisov, S. M.; Wolfbeis, O. S., Temperature-sensitive europium(III) probes and their use for simultaneous luminescent sensing of temperature and oxygen. *Analytical Chemistry* **2006,** 78, (14), 5094-5101.
60. Tan, C.; Wang, Q., Photophysical studies of novel lanthanide (Eu^{3+} and Tb^{3+}) luminescent hydrogels. *Inorganic Chemistry Communications* **2011,** 14, (4), 515-518.
61. Peng, H.; Stich, M. I. J.; Yu, J.; Sun, L.; Fischer, L. H.; Wolfbeis, O. S., Luminescent europium(III) nanoparticles for sensing and imaging of temperature in the physiological range. *Advanced Materials* **2010,** 22, (6), 716-719.
62. Cerón, E. N.; Ortgies, D. H.; del Rosal, B.; Ren, F.; Benayas, A.; Vetrone, F.; Ma, D.; Sanz-Rodríguez, F.; Solé, J. G.; Jaque, D.; Rodríguez, E. M., Hybrid nanostructures for high-sensitivity luminescence nanothermometry in the second biological window. *Advanced Materials* **2015,** 27, (32), 4781-4787.
63. Zhu, X.; Feng, W.; Chang, J.; Tan, Y.-W.; Li, J.; Chen, M.; Sun, Y.; Li, F., Temperature-feedback upconversion nanocomposite for accurate photothermal therapy at facile temperature. *Nature Communications* **2016,** 7, (1), 10437.
64. Sekiguchi, T.; Sotoma, S.; Harada, Y., Fluorescent nanodiamonds as a robust temperature sensor inside a single cell. *Biophysics and Physicobiology* **2018,** 15, 229-234.
65. Tzeng, Y. K.; Tsai, P. C.; Liu, H. Y.; Chen, O. Y.; Hsu, H.; Yee, F. G.; Chang, M. S.; Chang, H. C., Time-resolved luminescence nanothermometry with nitrogen-vacancy centers in nanodiamonds. *Nano Letters* **2015,** 15, (6), 3945-3952.
66. Kucsko, G.; Maurer, P. C.; Yao, N. Y.; Kubo, M.; Noh, H. J.; Lo, P. K.; Park, H.; Lukin, M. D., Nanometre-scale thermometry in a living cell. *Nature* **2013,** 500, 54-58.
67. Wang, Z.; Ananias, D.; Carné-Sánchez, A.; Brites, C. D. S.; Imaz, I.; Maspoch, D.; Rocha, J.; Carlos, L. D., Lanthanide-organic framework nanothermometers prepared by spray-drying. *Advanced Functional Materials* **2015,** 25, (19), 2824-2830.
68. Zhao, D.; Rao, X.; Yu, J.; Cui, Y.; Yang, Y.; Qian, G., Design and synthesis of an MOF thermometer with high sensitivity in the physiological temperature range. *Inorganic Chemistry* **2015,** 54, (23), 11193-11199.
69. Rocha, J.; Brites, C. D. S.; Carlos, L. D., Lanthanide organic framework luminescent thermometers. *Chemistry An European Journal* **2016,** 22, (42), 14782-14795.
70. Engeser, M.; Fabbrizzi, L.; Licchelli, M.; Sacchi, D., A fluorescent molecular thermometer based on the nickel(II) high-spin/low-spin interconversion. *Chemical Communications* **1999**, (13), 1191-1192.
71. Köse, M. E.; Carroll, B. F.; Schanze, K. S., Preparation and spectroscopic properties of multiluminophore luminescent oxygen and temperature sensor films. *Langmuir* **2005,** 21, (20), 9121-9129.
72. Chandrasekharan, N.; Kelly, L. A., A dual fluorescence temperature sensor based on perylene/exciplex interconversion. *Journal of the American Chemical Society* **2001,** 123, (40), 9898-9899.
73. Feng, J.; Tian, K.; Hu, D.; Wang, S.; Li, S.; Zeng, Y.; Li, Y.; Yang, G., A triarylboron-based fluorescent thermometer: sensitive over a wide temperature range. *Angewandte Chemie International Edition* **2011,** 50, (35), 8072-8076.
74. Samy, R.; Glawdel, T.; Ren, C. L., Method for microfluidic whole-chip temperature measurement ssing thin-film poly(dimethylsiloxane)/rhodamine B. *Analytical chemistry* **2008,** 80, (2), 369-375.
75. Victor, R.; Woisel, P.; Hoogenboom, R., Supramolecular control over thermoresponsive polymers. *Materials Today* **2016,** 19, (1), 44-55.
76. Pietsch, C.; Schubert, U. S.; Hoogenboom, R., Aqueous polymeric sensors based on temperature-induced polymer phase transitions and solvatochromic dyes. *Chemical Communications* **2011,** 47, (31), 8750-8765.
77. Vlaskin, V. A.; Janssen, N.; van Rijssel, J.; Beaulac, R.; Gamelin, D. R., Tunable dual emission in doped semiconductor nanocrystals. *Nano Letters* **2010,** 10, (9), 3670-3674.
78. Maestro, L. M.; Rodríguez, E. M.; Rodríguez, F. S.; la Cruz, M. C. I.; Juarranz, A.; Naccache, R.; Vetrone, F.; Jaque, D.; Capobianco, J. A.; Solé, J. G., CdSe quantum dots for two-photon fluorescence thermal imaging. *Nano Letters* **2010,** 10, (12), 5109-5115.
79. Jorge, P.; Martins, M. A.; Trindade, T.; Santos, J. L.; Farahi, F., Optical fiber sensing using quantum dots. *Sensors* **2007,** 7, (12), 3489-3534.
80. Maestro, L. M.; Jacinto, C.; Silva, U. R.; Vetrone, F.; Capobianco, J. A.; Jaque, D.; Solé, J. G., CdTe quantum dots as nanothermometers: towards highly sensitive thermal imaging. *Small* **2011,** 7, (13), 1774-1778.
81. Herrera, A. P.; Rodríguez, M.; Torres-Lugo, M.; Rinaldi, C., Multifunctional magnetite nanoparticles coated with fluorescent thermo-responsive polymeric shells. *Journal of Materials Chemistry* **2008,** 18, (8), 855-858.
82. Walker, G. W.; Sundar, V. C.; Rudzinski, C. M.; Wun, A. W.; Bawendi, M. G.; Nocera, D. G., Quantum-dot optical temperature probes. *Applied Physics Letters* **2003,** 83, (17), 3555-3557.

83. Haro-González, P.; Ramsay, W. T.; Maestro, L. M.; Del Rosal, B.; Santacruz-Gomez, K.; del Carmen Iglesias-de la Cruz, M.; Sanz-Rodríguez, F.; Chooi, J. Y.; Sevilla, P. R.; Bettinelli, M., Quantum dot-based thermal spectroscopy and imaging of optically trapped microspheres and single cells. *Small* **2013,** 9, (12), 2162-2170.
84. Li, S.; Zhang, K.; Yang, J. M.; Lin, L.; Yang, H., Single quantum dots as local temperature markers. *Nano Letters* **2007,** 7, (10), 3102-3105.
85. Brites, C.; Lima, P.; Silva, N.; Millán, A.; Amaral, V.; Palacio, F.; Carlos, L., Lanthanide-based luminescent molecular thermometers. *New Journal of Chemistry* **2011,** 35, 1177-1183.
86. Brites, C. D. S.; Balabhadra, S.; Carlos, L. D., Lanthanide-based thermometers: At the cutting-edge of luminescence thermometry. *Advanced Optical Materials* **2019,** 7, (5), 1801239-1801269.
87. Wang, X.; Liu, Q.; Bu, Y.; Liu, C. S.; Liu, T.; Yan, X., Optical temperature sensing of rare-earth ion doped phosphors. *RSC Advances* **2015,** 5, (105), 86219-86236.
88. Kiyonaka, S.; Sakaguchi, R.; Hamachi, I.; Morii, T.; Yoshizaki, T.; Mori, Y., Validating subcellular thermal changes revealed by fluorescent thermosensors. *Nature Methods* **2015,** 12, (9), 801-802.
89. Baffou, G.; Rigneault, H.; Marguet, D.; Jullien, L., A critique of methods for temperature imaging in single cells. *Nature Methods* **2014,** 11, (9), 899-901.
90. Soni, K. S.; Desale, S. S.; Bronich, T. K., Nanogels: An overview of properties, biomedical applications and obstacles to clinical translation. *Journal of Controlled Release* **2016,** 240, 109-126.
91. Hemmer, E.; Benayas, A.; Légaré, F.; Vetrone, F., Exploiting the biological windows: Current perspectives on fluorescent bioprobes emitting above 1000 nm. *Nanoscale Horizons* **2016,** 1, (3), 168-184.
92. Rassamesard, A.; Huang, Y. F.; Lee, H. Y.; Lim, T. S.; Li, M. C.; White, J. D.; Hodak, J. H.; Osotchan, T.; Peng, K. Y.; Chen, S. A.; Hsu, J. H.; Hayashi, M.; Fann, W., Environmental effect on the fluorescence lifetime and quantum yield of single extended luminescent conjugated polymers. *Journal of Physical Chemistry C* **2009,** 113, (43), 18681-18688.
93. Bohara, R. A., Chapter 1-Introduction and Types of Hybrid Nanostructures for Medical Applications. In *Hybrid Nanostructures for Cancer Theranostics*, Ashok Bohara, R.; Thorat, N., Eds. Elsevier: 2019; pp 1-16.
94. Jaque, D.; Rosal, B. d.; Rodríguez, E. M.; Maestro, L. M.; Haro-González, P.; Solé, J. G., Fluorescent nanothermometers for intracellular thermal sensing. *Nanomedicine* **2014,** 9, (7), 1047-1062.
95. del Rosal, B.; Ximendes, E.; Rocha, U.; Jaque, D., In Vivo luminescence nanothermometry: From materials to applications. *Advanced Optical Materials* **2017,** 5, (1), 1600508-1600522.
96. Alkahtani, M. H.; Alghannam, F.; Jiang, L.; Almethen, A.; Rampersaud, A. A.; Brick, R.; Gomes, C. L.; Scully, M. O.; Hemmer, P. R., Fluorescent nanodiamonds: Past, present, and future. *Nanophotonics* **2018,** 7, (8), 1423-1453.
97. Jaque, D.; Del Rosal, B.; Martín Rodríguez, E.; Martinez Maestro, L.; Haro-González, P.; Solé, J., Fluorescent nanothermometers for intracellular thermal sensing. *Nanomedicine* **2014,** 9, 1047-1062.
98. Cui, Y.; Zhu, F.; Chen, B.; Qian, G., Metal-organic frameworks for luminescence thermometry. *Chemical Communications* **2015,** 51, (35), 7420-7431.
99. Petryayeva, E.; Algar, W. R.; Medintz, I. L., Quantum dots in bioanalysis: A review of applications across various platforms for fluorescence spectroscopy and imaging. *Applied Spectroscopy* **2013,** 67, (3), 215-252.
100. Qiu, X.; Zhu, X.; Su, X.; Xu, M.; Yuan, W.; Liu, Q.; Xue, M.; Liu, Y.; Feng, W.; Li, F., Near-infrared upconversion luminescence and bioimaging in vivo based on quantum dots. *Applied Science* **2019,** 6, (5), 1801834-1801842.
101. Teitelboim, A.; Oron, D., Broadband near-infrared to visible upconversion in quantum dot-quantum well heterostructures. *ACS Nano* **2016,** 10, (1), 446-452.
102. Jaque García, D.; García Solé, J., Chapter 4-Quantum Dot Fluorescence Thermometry. In *Thermometry at the Nanoscale: Techniques and Selected Applications*, The Royal Society of Chemistry: 2016; pp 83-123.
103. Buenzli, J. C. G.; Eliseeva, S. V., Intriguing aspects of lanthanide luminescence. *Chemical Science* **2013,** 4, (5), 1939-1949.
104. Carlos, L. D.; Ferreira, R. A.; Bermudez, V. d. Z.; Ribeiro, S. J., Lanthanide-containing light-emitting organic-inorganic hybrids: a bet on the future. *Advanced Materials* **2009,** 21, (5), 509-534.
105. Zhou, J.; Leano Jr, J. L.; Liu, Z.; Jin, D.; Wong, K. L.; Liu, R. S.; Bünzli, J. C. G., Impact of lanthanide nanomaterials on photonic devices and smart applications. *Small* **2018,** 14, (40), 1801882-1801911.
106. Chen, G.; Yang, C.; Prasad, P. N., Nanophotonics and nanochemistry: Controlling the excitation dynamics for frequency up-and down-conversion in lanthanide-doped nanoparticles. *Accounts of Chemical Research* **2013,** 46, (7), 1474-1486.
107. Gnach, A.; Lipinski, T.; Bednarkiewicz, A.; Rybka, J.; Capobianco, J. A., Upconverting nanoparticles: Assessing the toxicity. *Chemical Society Reviews* **2015,** 44, (6), 1561-1584.
108. Anderson, R. R.; Parrish, J. A., The Optics of Human Skin. *Journal of Investigative Dermatology* **1981,** 77, (1), 13-19.
109. Smith, A. M.; Mancini, M. C.; Nie, S., Second window for in vivo imaging. *Nature Nanotechnology* **2009,** 4, (11), 710-711.
110. Santos, P. V. d.; Araujo, M. T. d.; Gouveia-Neto, A. S.; Neto, J. A. M.; Sombra, A. S. B., Optical temperature sensing using upconversion fluorescence emission in Er^{3+}/Yb^{3+}-codoped chalcogenide glass. *Applied Physics Letters* **1998,** 73, (5), 578-580.

111. Collins, S.; Baxter, G.; Wade, S.; Sun, T.; Grattan, K.; Zhang, Z.; Palmer; AW, Comparison of fluorescence-based temperature sensor schemes: theoretical analysis and experimental validation. *Journal of Applied Physics* **1998,** 84, (9), 4649-4654.
112. Brites, C. D. S.; Lima, P. P.; Silva, N. J. O.; Millán, A.; Amaral, V. S.; Palacio, F.; Carlos, L. D., Thermometry at the nanoscale. *Nanoscale* **2012,** 4, (16), 4799-4829.
113. Baker, S. N.; McCleskey, T. M.; Baker, G. A., An ionic liquid-based optical thermometer. In *Ionic Liquids IIIB: Fundamentals, Progress, Challenges, and Opportunities*, American Chemical Society: 2005; Vol. 902, pp 171-181.
114. Savchuk, O. A.; Carvajal, J. J.; Cascales, C.; Aguiló, M.; Díaz, F., Benefits of silica core-shell structures on the temperature sensing properties of Er,Yb:$GdVO_4$ up-conversion nanoparticles. *ACS Applied Materials & Interfaces* **2016,** 8, (11), 7266-7273.
115. Bartlett, J. W.; Frost, C., Reliability, repeatability and reproducibility: Analysis of measurement errors in continuous variables. *Ultrasound in Obstetrics & Gynecology* **2008,** 31, (4), 466-475.
116. Taylor, B. N.; Kuyatt, C. E., Guidelines for evaluating and expressing the uncertainty of NIST measurement results. **1994**.
117. Lim, Y. T.; Kim, S.; Nakayama, A.; Stott, N. E.; Bawendi, M. G.; Frangioni, J. V., Selection of quantum dot wavelengths for biomedical assays and imaging. *Molecular Imaging* **2003,** 2, (1), 50-64.
118. Zonios, G.; Bykowski, J.; Kollias, N., Skin melanin, hemoglobin, and light scattering properties can be quantitatively assessed in vivo using diffuse reflectance spectroscopy. *Journal of Investigative Dermatology* **2001,** 117, (6), 1452-1457.
119. Hale, G. M.; Querry, M. R., Optical constants of water in the 200-nm to 200-μm wavelength region. *Applied Optics* **1973,** 12, (3), 555-563.
120. Prahl, S., Optical absorption of hemoglobin. http://omlc.ogi.edu/spectra/hemoglobin **1999**.
121. Jacques, S. L.; McAuliffe, D. J., The melanosome: Threshold temperature for explosive vaporization and internal absorption coefficient during pulsed laser irradiation. *Photochemistry and Photobiology* **1991,** 53, (6), 769-775.
122. Wang, L. V.; Wu, H., *Biomedical optics: Principles and imaging*. John Wiley & Sons: 2012.
123. Jacques, S., Optical Properties of Biological Tissues: A Review. *Physics in Medicine and Biology* **2013,** 58, R37-R61.
124. Chaplin, M., Water Structure and Science. London South Bank University. http://www1.lsbu.ac.uk/water/water_structure_science.html.
125. del Rosal, B.; Villa, I.; Jaque, D.; Sanz-Rodríguez, F., In vivo autofluorescence in the biological windows: The role of pigmentation. *Journal of Biophotonics* **2016,** 9, (10), 1059-1067.
126. Shi, L.; Sordillo, L. A.; Rodríguez-Contreras, A.; Alfano, R., Transmission in near-infrared optical windows for deep brain imaging. *Journal of Biophotonics* **2016,** 9, (1-2), 38-43.
127. Naczynski, D. J.; Tan, M. C.; Zevon, M.; Wall, B.; Kohl, J.; Kulesa, A.; Chen, S.; Roth, C. M.; Riman, R. E.; Moghe, P. V., Rare-earth-doped biological composites as in vivo shortwave infrared reporters. *Nature Communications* **2013,** 4, (1), 2199-2209.
128. Sordillo, L.; Pu, Y.; Pratavieira, S.; Budansky, Y.; Alfano, R., Deep optical imaging of tissue using the second and third near-infrared spectral windows. *Journal of Biomedical Optics* **2014,** 19, (5), 56004-56010.
129. Hernandez-Rodriguez, M. A.; Lozano-Gorrin, A. D.; Lavin, V.; Rodriguez-Mendoza, U. R.; Martin, I. R., Yttrium orthoaluminate nanoperovskite doped with Tm^{3+} ions as upconversion optical temperature sensor in the near-infrared region. *Optics Express* **2017,** 25, (22), 27845-27856.
130. Pereira, A. F.; Ferreira, J.; Gouveia-Neto, A. S.; Jacinto, C., 1.319μm excited thulium doped nanoparticles for subtissue thermal sensing with deep penetration and high contrast imaging. *Sensors and Actuators B: Chemical* **2017,** 238, 525-531.
131. Chen, Y.; Chen, G.; Liu, X.; Xu, J.; Zhou, X.; Yang, T.; Yuan, C.; Zhou, C., Upconversion luminescence, optical thermometric properties and energy transfer in Yb^{3+}/Tm^{3+} co-doped phosphate glass. *Optical Materials* **2018,** 81, 78-83.
132. Savchuk, O.; Carvajal Marti, J. J.; Cascales, C.; Haro-Gonzalez, P.; Sanz-Rodríguez, F.; Aguilo, M.; Diaz, F., Bifunctional Tm^{3+},Yb^{3+}:$GdVO_4$@SiO_2 core-shell nanoparticles in HeLa cells: upconversion luminescence nanothermometry in the first biological window and biolabelling in the visible. *Nanomaterials* **2020,** 10, (5), 993.
133. Runowski, M.; Shyichuk, A.; Tymiński, A.; Grzyb, T.; Lavín, V.; Lis, S., Multifunctional optical sensors for nanomanometry and nanothermometry: high-pressure and high-temperature upconversion luminescence of lanthanide-doped phosphates-$LaPO_4$/YPO_4:Yb^{3+}-Tm^{3+}. *ACS Applied Materials & Interfaces* **2018,** 10, (20), 17269-17279.
134. Xing, L.; Xu, Y.; Wang, R.; Xu, W.; Zhang, Z., Highly sensitive optical thermometry based on upconversion emissions in Tm^{3+}/Yb^{3+} codoped $LiNbO_3$ single crystal. *Optics Letters* **2014,** 39, (3), 454-457.
135. Li, L.; Qin, F.; Zhou, Y.; Zheng, Y.; Zhao, H.; Zhang, Z., Using the upconversion luminescence of the $CaWO_4$:Yb^{3+}-X^{3+} (X =Er/Ho/Tm) phosphors for ratiometric thermal sensing. *Journal of Luminescence* **2018,** 202, 301-308.
136. Bu, Y.; Yan, X. H., Controlled synthesis and temperature-dependent spectra of $NaYF_4$:Yb^{3+}, Re^{3+}@$NaYF_4$@SiO_2 (RE =Er, Tm) core-shell-shell nanophosphors. *Applied Physics B* **2017,** 123, 59-69.
137. Ge, W.; Xu, M.; Shi, J.; Zhu, J.; Li, Y., Highly temperature-sensitive and blue upconversion luminescence properties of $Bi_2Ti_2O_7$:Tm^{3+}/Yb^{3+} nanofibers by electrospinning. *Chemical Engineering Journal* **2019**, 391,123546-123553.

138. Zhang, J.; Jin, C., Structure, morphology and upconversion luminescence of rare earth ions doped $LiY_9(SiO_4)_6O_2$ for temperature sensing. *Industrial & Engineering Chemistry Research* **2019,** 58, (8), 3490-3498.
139. Zhang, J.; Chen, G.; Zhai, Z.; Chen, H.; Zhang, Y., Optical temperature sensing using upconversion luminescence in rare-earth ions doped $Ca_2Gd_8(SiO_4)_6O_2$ phosphors. *Journal of Alloys and Compounds* **2019,** 771, 838-846.
140. Yu, L.; Ye, L.; Bao, R.; Zhang, X.; Wang, L.G., Sensitivity-enhanced Tm^{3+}/Yb^{3+} co-doped YAG single crystal optical fiber thermometry based on upconversion emissions. *Optics Communications* **2018,** 410, 632-636.
141. Wang, N.; Fu, Z.; Wei, Y.; Sheng, T., Investigation for the upconversion luminescence and temperature sensing mechanism based on $BiPO_4$:Yb^{3+}, RE^{3+} (RE^{3+}=Ho^{3+}, Er^{3+} and Tm^{3+}). *Journal of Alloys and Compounds* **2019,** 772, 371-380.
142. Casagrande, E.; Back, M.; Cristofori, D.; Ueda, J.; Tanabe, S.; Palazzolo, S.; Rizzolio, F.; Canzonieri, V.; Trave, E.; Riello, P., Upconversion-mediated Boltzmann thermometry in double-layered Bi_2SiO_5:Yb^{3+},Tm^{3+}@SiO_2 hollow nanoparticles. *Journal of Materials Chemistry C* **2020**, 8, 7828-7836.
143. Chen, W.; Cao, J.; Hu, F.; Wei, R.; Chen, L.; Guo, H., Sr_2GdF_7:Tm^{3+}/Yb^{3+} glass ceramic: A highly sensitive optical thermometer based on FIR technique. *Journal of Alloys and Compounds* **2018,** 735, 2544-2550.
144. Min, Q.; Bian, W.; Qi, Y.; Lu, W.; Yu, X.; Xu, X.; Zhou, D.; Qiu, J., Temperature sensing based on the up-conversion emission of Tm^{3+} in a single $KLuF_4$ microcrystal. *Journal of Alloys and Compounds* **2017,** 728, 1037-1042.
145. Lu, H.; Yang, J.; Huang, D.; Zhou, Q.; Yang, M.; Zhang, X.; Wang, Y.; Zhu, H., Ultranarrow NIR bandwidth and temperature sensing of YOF:Yb^{3+}/Tm^{3+} phosphor in low temperature range. *Journal of Luminescence* **2018,** 206, 613-617.
146. Fu, Y.; Zhao, L.; Guo, Y.; Yu, H., Highly sensitive optical thermometers based on unconventional thermometric coupled levels of Tm^{3+} following a Boltzmann-type distribution in oxyfluoride glass ceramics. *New Journal of Chemistry* **2019,** 43, (42), 16664-16669.
147. Luo, L.; Yu, J., Controlled synthesis and upconversion luminescence of Tm^{3+}-doped $NaYbF_4$ nanoparticles for non-invasion optical thermometry. *Journal of Alloys and Compounds* **2018,** 739, 926-933.
148. Zhou, A.; Song, F.; Song, F.; Feng, M.; Adnan, K.; Ju, D.; Wang, X., Optical thermometry using fluorescence intensities multi-ratios in $NaGdTiO_4$:Yb^{3+}/Tm^{3+} phosphors. *Optical Materials* **2018,** 78, 438-444.
149. Wu, R.; Zhou, J.; Lei, L.; Zhang, S.; Xiao, Z.; Zhang, J.; Xu, S., α-$NaYF_4$:Yb^{3+}-Tm^{3+}@CaF_2 nanocrystals for NIR-to-NIR temperature sensing. *Chemical Physics Letters* **2017,** 667, 206-210.
150. Ding, M.; Zhang, M.; Lu, C., $Yb^{3+}/Tm^{3+}/Ho^{3+}$ tri-doped YPO_4 submicroplates: A promising optical thermometer operating in the first biological window. *Materials Letters* **2017,** 209, 52-55.
151. Savchuk, O. A.; Carvajal, J. J.; Brites, C. D. S.; Carlos, L. D.; Aguilo, M.; Diaz, F., Upconversion thermometry: a new tool to measure the thermal resistance of nanoparticles. *Nanoscale* **2018,** 10, (14), 6602-6610.
152. Lu, H.; Haoyue, H.; Gao, Y.; Li, D.; Shi, G.; Song, Y.; Wang, Y.; Zhang, X., Optical sensing of temperature based on non-thermally coupled levels and upconverted white light emission of a $Gd_2(WO_4)_3$ phosphor co-doped with in Ho(III), Tm(III), and Yb(III). *Microchimica Acta* **2017,** 184, 641–646
153. Lu, H.; Hao, H.; Shi, G.; Gao, Y.; Wang, R.; Song, Y.; Wang, Y.; Zhang, X., Optical temperature sensing in β-$NaLuF_4$: $Yb^{3+}/Er^{3+}/Tm^{3+}$ based on thermal, quasi-thermal and non-thermal coupling levels. *RSC Advances* **2016,** 6, (60), 55307-55311.
154. Chen, D.; Liu, S.; Li, X.; Yuan, S.; Huang, P., Upconverting luminescence based dual-modal temperature sensing for $Yb^{3+}/Er^{3+}/Tm^{3+}$: YF_3 nanocrystals embedded glass ceramic. *Journal of the European Ceramic Society* **2017,** 37, (15), 4939-4945.
155. Ding, M.; Chen, D.; Lu, C.; Xi, J.; Ji, Z.; Xu, Z., Lanthanide-doped LuF_3 mesocrystals for optical thermometry. *Materials Letters* **2017,** 189, 5-8.
156. Marciniak, L.; Bednarkiewicz, A.; Drabik, J.; Trejgis, K.; Strek, W., Optimization of highly sensitive YAG:Cr^{3+},Nd^{3+} nanocrystal-based luminescent thermometer operating in an optical window of biological tissues. *Physical Chemistry Chemical Physics* **2017,** 19, (10), 7343-7351.
157. Jiang, G.; Wei, X.; Zhou, S.; Chen, Y.; Duan, C.; Yin, M., Neodymium doped lanthanum oxysulfide as optical temperature sensors. *Journal of Luminescence* **2014,** 152, 156-159.
158. Hernández-Rodríguez, M. A.; Lozano-Gorrín, A. D.; Martín, I. R.; Rodríguez-Mendoza, U. R.; Lavín, V., Comparison of the sensitivity as optical temperature sensor of nano-perovskite doped with Nd^{3+} ions in the first and second biological windows. *Sensors and Actuators B: Chemical* **2018,** 255, 970-976.
159. Balabhadra, S.; Debasu, M. L.; Brites, C. D. S.; Nunes, L. A. O.; Malta, O. L.; Rocha, J.; Bettinelli, M.; Carlos, L. D., Boosting the sensitivity of Nd^{3+}-based luminescent nanothermometers. *Nanoscale* **2015,** 7, (41), 17261-17267.
160. Suta, M.; Antić, Ž.; Đorđević, V.; Kuzman, S.; Dramićanin, M. D.; Meijerink, A., Making Nd^{3+} a sensitive luminescent thermometer for physiological temperatures-an account of pitfalls in Boltzmann thermometry. *Nanomaterials* **2020,** 10, (3), 543-563.
161. Lalla, E. A.; León-Luis, S. F.; Monteseguro, V.; Pérez-Rodríguez, C.; Cáceres, J. M.; Lavín, V.; Rodríguez-Mendoza, U. R., Optical temperature sensor based on the Nd^{3+} infrared thermalized emissions in a fluorotellurite glass. *Journal of Luminescence* **2015,** 166, 209-214.

162. Haro-González, P.; Martín, I. R.; Martín, L. L.; León-Luis, S. F.; Pérez-Rodríguez, C.; Lavín, V., Characterization of Er^{3+} and Nd^{3+} doped Strontium Barium Niobate glass ceramic as temperature sensors. *Optical Materials* **2011,** 33, (5), 742-745.
163. Huang, P.; Zheng, W.; Tu, D.; Shang, X.; Zhang, M.; Li, R.; Xu, J.; Liu, Y.; Chen, X., Unraveling the electronic structures of neodymium in $LiLuF_4$ nanocrystals for ratiometric temperature sensing. *Advanced Science* **2019,** 6, (10), 1802282-1802289.
164. Pedroni, M.; Cortelletti, P.; Cantarelli, I. X.; Pinna, N.; Canton, P.; Quintanilla, M.; Vetrone, F.; Speghini, A., Colloidal nanothermometers based on neodymium doped alkaline-earth fluorides in the first and second biological windows. *Sensors and Actuators B: Chemical* **2017,** 250, 147-155.
165. Skripka, A.; Morinvil, A.; Matulionyte, M.; Cheng, T.; Vetrone, F., Advancing neodymium single-band nanothermometry. *Nanoscale* **2019,** 11, (23), 11322-11330.
166. Marciniak, Ł.; Bednarkiewicz, A.; Hreniak, D.; Strek, W., The influence of Nd^{3+} concentration and alkali ions on the sensitivity of non-contact temperature measurements in $ALaP_4O_{12}:Nd^{3+}$ (A =Li, K, Na, Rb) nanocrystalline luminescent thermometers. *Journal of Materials Chemistry C* **2016,** 4, (47), 11284-11290.
167. Kolesnikov, I. E.; Kalinichev, A. A.; Kurochkin, M. A.; Mamonova, D. V.; Kolesnikov, E. Y.; Kurochkin, A. V.; Lähderanta, E.; Mikhailov, M. D., $Y_2O_3:Nd^{3+}$ nanocrystals as ratiometric luminescence thermal sensors operating in the optical windows of biological tissues. *Journal of Luminescence* **2018,** 204, 506-512.
168. Đačanin Far, L.; Lukić-Petrović, S. R.; Đorđević, V.; Vuković, K.; Glais, E.; Viana, B.; Dramićanin, M. D., Luminescence temperature sensing in visible and NIR spectral range using Dy^{3+} and Nd^{3+} doped $YNbO_4$. *Sensors and Actuators A: Physical* **2018,** 270, 89-96.
169. Carrasco, E.; del Rosal, B.; Sanz-Rodríguez, F.; de la Fuente, Á. J.; Gonzalez, P. H.; Rocha, U.; Kumar, K. U.; Jacinto, C.; Solé, J. G.; Jaque, D., Intratumoral thermal reading during photo-thermal therapy by multifunctional fluorescent nanoparticles. *Advanced Functional Materials* **2015,** 25, (4), 615-626.
170. Kolesnikov, I. E.; Golyeva, E. V.; Kurochkin, M. A.; Lähderanta, E.; Mikhailov, M. D., Nd^{3+}-doped YVO_4 nanoparticles for luminescence nanothermometry in the first and second biological windows. *Sensors and Actuators B: Chemical* **2016,** 235, 287-293.
171. Dantelle, G.; Matulionyte, M.; Testemale, D.; Cantarano, A.; Ibanez, A.; Vetrone, F., Nd^{3+} doped $Gd_3Sc_2Al_3O_{12}$ nanoparticles: towards efficient nanoprobes for temperature sensing. *Physical Chemistry Chemical Physics* **2019,** 21, (21), 11132-11141.
172. Benayas, A.; del Rosal, B.; Pérez-Delgado, A.; Santacruz-Gómez, K.; Jaque, D.; Hirata, G. A.; Vetrone, F., Nd:YAG near-infrared luminescent nanothermometers. *Advanced Optical Materials* **2015,** 3, (5), 687-694.
173. Gschwend, P. M.; Starsich, F. H. L.; Keitel, R. C.; Pratsinis, S. E., Nd^{3+}-doped $BiVO_4$ luminescent nanothermometers of high sensitivity. *Chemical Communications* **2019,** 55, (50), 7147-7150.
174. Wawrzynczyk, D.; Bednarkiewicz, A.; Nyk, M.; Strek, W.; Samoc, M., Neodymium (iii) doped fluoride nanoparticles as non-contact optical temperature sensors. *Nanoscale* **2012,** 4, (22), 6959-6961.
175. Savchuk, O.; Carvajal, J. J.; De la Cruz, L. G.; Haro-González, P.; Aguiló, M.; Díaz, F., Luminescence thermometry and imaging in the second biological window at high penetration depth with $Nd:KGd(WO_4)_2$ nanoparticles. *Journal of Materials Chemistry C* **2016,** 4, (31), 7397-7405.
176. Marciniak, L.; Pilch, A.; Arabasz, S.; Jin, D.; Bednarkiewicz, A., Heterogeneously Nd^{3+} doped single nanoparticles for NIR-induced heat conversion, luminescence, and thermometry. *Nanoscale* **2017,** 9, (24), 8288-8297.
177. Xu, W.; Zhao, H.; Zhang, Z.; Cao, W., Highly sensitive optical thermometry through thermally enhanced near infrared emissions from Nd^{3+}/Yb^{3+} codoped oxyfluoride glass ceramic. *Sensors and Actuators B: Chemical* **2013,** 178, 520-524.
178. Song, H.; Han, Q.; Tang, X.; Zhao, X.; Ren, K.; Liu, T., Nd^{3+}/Yb^{3+} codoped $SrWO_4$ for highly sensitive optical thermometry based on the near infrared emission. *Optical Materials* **2018,** 84, 263-267.
179. Xu, W.; Song, Q.; Zheng, L.; Zhang, Z.; Cao, W., Optical temperature sensing based on the near-infrared emissions from Nd^{3+}/Yb^{3+} codoped $CaWO_4$. *Optics Letters* **2014,** 39, 4635-4638.
180. Silva, A. F.; Elan, F.; Falcão-Filho, E. L.; Maia, L. J. Q.; de Araújo, C. B., Thermal sensitivity of frequency upconversion in $Al_4B_2O_9:Yb^{3+}/Nd^{3+}$ nanoparticles. *Journal of Materials Chemistry C* **2017,** 5, (5), 1240-1246.
181. Xu, W.; Qi, H.; Zheng, L.; Zhang, Z.; Cao, W., Multifunctional nanoparticles based on the Nd^{3+}/Yb^{3+} codoped $NaYF_4$. *Optics Letters* **2015,** 40, (23), 5678-5681.
182. Gao, G.; Busko, D.; Kauffmann-Weiss, S.; Turshatov, A.; Howard, I. A.; Richards, B. S., Wide-range non-contact fluorescence intensity ratio thermometer based on Yb^{3+}/Nd^{3+} co-doped La_2O_3 microcrystals operating from 290 to 1230 K. *Journal of Materials Chemistry C* **2018,** 6, (15), 4163-4170.
183. Zhao, Z.; Hu, F.; Cao, Z.; Chi, F.; Wei, X.; Chen, Y.; Duan, C.; Yin, M., Self-crystallized $Ba_2LaF_7:Nd^{3+}/Eu^{3+}$ glass ceramics for optical thermometry. *Ceramics International* **2017,** 43, (17), 14951-14955.
184. Kolesnikov, I.; Mamonova, D.; Kalinichev, A.; Kurochkin, M.; Medvedev, V.; Kolesnikov, E.; Lahderanta, E.; Manshina, A., Constructing of efficient dual activating ratiometric $YVO_4:Nd^{3+}/Eu^{3+}$ nanothermometer: co-doping or mixture. *Nanoscale* **2020**,12, (10), 5953-5960.
185. Drabik, J.; Cichy, B.; Marciniak, L., New type of nanocrystalline luminescent thermometers based on Ti^{3+}/Ti^{4+} and Ti^{4+}/Ln^{3+} (Ln^{3+}= Nd^{3+}, Eu^{3+}, Dy^{3+}) luminescence intensity ratio. *Journal of Physical Chemistry C* **2018,** 122, (26), 14928-14936.

186. Trejgis, K.; Marciniak, L., The influence of manganese concentration on the sensitivity of bandshape and lifetime luminescent thermometers based on $Y_3Al_5O_{12}$:Mn^{3+},Mn^{4+},Nd^{3+} nanocrystals. *Physical Chemistry Chemical Physics* **2018,** 20, (14), 9574-9581.
187. Souza, A. S.; Nunes, L. A. O.; Silva, I. G. N.; Oliveira, F. A. M.; da Luz, L. L.; Brito, H. F.; Felinto, M. C. F. C.; Ferreira, R. A. S.; Júnior, S. A.; Carlos, L. D.; Malta, O. L., Highly-sensitive Eu^{3+} ratiometric thermometers based on excited state absorption with predictable calibration. *Nanoscale* **2016,** 8, (9), 5327-5333.
188. Lu, K.; Yi, Y.; Xu, L.; Sun, X.; Liu, L.; Li, H., Temperature-independent lifetime and thermometer operated in a biological window of upconverting $NaErF_4$ nanocrystals. *Nanomaterials* **2020***,* 10 (1)*,* 24-36*.*
189. Lu, K.; Sun, X.; Xu, L.; Jiang, B.; Ren, J.; Carvajal, J. J.; Zhao, E.; Liu, L.; Zhang, J., Self-monitored biological nanoheaters operating in the first biological window based on single-band red upconversion nanoparticles fabricated through architectural design. *Journal of Alloys and Compounds* **2020**, 842,155602-155610.
190. Brandão-Silva, A. C.; Gomes, M. A.; Macedo, Z. S.; Avila, J. F. M.; Rodrigues, J. J.; Alencar, M. A. R. C., Multiwavelength fluorescence intensity ratio nanothermometry: High sensitivity over a broad temperature range. *Journal of Physical Chemistry C* **2018,** 122, (35), 20459-20468.
191. Chen, D.; Xu, W.; Yuan, S.; Li, X.; Zhong, J., Ln^{3+}-Sensitized Mn^{4+} near-infrared upconverting luminescence and dual-modal temperature sensing. *Journal of Materials Chemistry C* **2017,** 5, (37), 9619-9628.
192. Runowski, M.; Bartkowiak, A.; Majewska, M.; Martín, I. R.; Lis, S., Upconverting lanthanide doped fluoride $NaLuF_4$:Yb^{3+}-Er^{3+}-Ho^{3+}-optical sensor for multi-range fluorescence intensity ratio (FIR) thermometry in visible and NIR regions. *Journal of Luminescence* **2018,** 201, 104-109.
193. Ćirić, A.; Aleksić, J.; Barudžija, T.; Antić, Ž.; Đorđević, V.; Medić, M.; Periša, J.; Zeković, I.; Mitrić, M.; Dramićanin, M. D., Comparison of three ratiometric temperature readings from the Er^{3+} upconversion emission. *Nanomaterials* **2020,** 10, (4), 627-637.
194. Zhou, J.; Lei, R.; Wang, H.; Chen, C.; Chen, B.; Pan, E.; Zhao, S.; Xu, S., Er^{3+}/Yb^{3+}-codoped ZrO_2 nanocrystals as ratiometric luminescence nanothermometers that cover three biological windows. *ACS Applied Nano Materials* **2020,** 3, (1), 186-194.
195. Savchuk, O. A.; Carvajal, J. J.; Pujol, M. C.; Barrera, E. W.; Massons, J.; Aguilo, M.; Diaz, F., Ho,Yb:$KLu(WO_4)_2$ nanoparticles: a versatile material for multiple thermal sensing purposes by luminescent thermometry. *Journal of Physical Chemistry C* **2015,** 119, (32), 18546-18558.
196. Wang, Z.; Jiao, H.; Fu, Z., Investigating the luminescence behaviors and temperature sensing properties of rare-earth-doped $Ba_2In_2O_5$ phosphors. *Inorganic Chemistry* **2018,** 57, (15), 8841-8849.
197. Rodríguez-Rodríguez, H.; Imanieh, S.; Lahoza, F.; Martin, I., Analysis of the upconversion process in Tm^{3+} doped glasses for enhancement of the photocurrent in silicon solar cells. *Solar Energy Materials and Solar Cells* **2016,** 144, 29-32.
198. Shinn, M.; Sibley, W.; Drexhage, M.; Brown, R., Optical transitions of Er^{3+} ions in fluorozirconate glass. *Physical Review B* **1983,** 27, (11), 6635-6649.
199. Auzel, F., Upconversion and anti-stokes processes with f and d ions in solids. *Chemical Reviews* **2004,** 104, (1), 139-174.
200. Haase, M.; Schäfer, H., Upconverting nanoparticles. *Angewandte Chemie International Edition* **2011,** 50, (26), 5808-5829.
201. Boulon, G., Why so deep research on Yb^{3+}-doped optical inorganic materials? *Journal of Alloys and Compounds* **2008,** 451, (1), 1-11.
202. Ol. A. Savchuk, J. J. Carvajal, C. Cascales, P. Haro-Gonzalez, F. Sanz-Rodriguez, M. Aguilo, F. Diaz, Tm^{3+},Yb^{3+}:$GdVO_4$@SiO_2 core-shell nanoparticles upconversion luminescence nanothermometry in the first biological window and their internalization in HeLa cells for biolabelling in the visible. *Nanomaterials,* **2020**, 10, (5), 993-1010.
203. Xing, L.; Yang, W.; Ma, D.; Wang, R., Effect of crystallinity on the optical thermometry sensitivity of Tm^{3+}/Yb^{3+} codoped $LiNbO_3$ crystal. *Sensors and Actuators B: Chemical* **2015,** 221, 458-462.
204. Rocha, U.; Jacinto, C.; Kumar, K. U.; López, F. J.; Bravo, D.; Solé, J. G.; Jaque, D., Real-time deep-tissue thermal sensing with sub-degree resolution by thermally improved Nd^{3+}:LaF_3 multifunctional nanoparticles. *Journal of Luminescence* **2016,** 175, 149-157.
205. Kolesnikov, I. E.; Kalinichev, A. A.; Kurochkin, M. A.; Golyeva, E. V.; Kolesnikov, E. Y.; Kurochkin, A. V.; Lähderanta, E.; Mikhailov, M. D., YVO_4:Nd^{3+} nanophosphors as NIR-to-NIR thermal sensors in wide temperature range. *Scientific Reports* **2017,** 7, (1), 18002-18010.
206. Zheng, S.; Chen, W.; Tan, D.; Zhou, J.; Guo, Q.; Jiang, W.; Xu, C.; Liu, X.; Qiu, J., Lanthanide-doped $NaGdF_4$ core-shell nanoparticles for non-contact self-referencing temperature sensors. *Nanoscale* **2014,** 6, (11), 5675-5679.
207. Marciniak, Ł.; Bednarkiewicz, A.; Stefanski, M.; Tomala, R.; Hreniak, D.; Strek, W., Near infrared absorbing near infrared emitting highly-sensitive luminescent nanothermometer based on Nd^{3+} to Yb^{3+} energy transfer. *Physical Chemistry Chemical Physics* **2015,** 17, (37), 24315-24321.
208. Chen, Y.; Lin, X.; Luo, Z.; Huang, Y., Spectroscopic properties of Nd^{3+} ions in $La_2(WO_4)_3$ crystal. *Chemical Physics Letters* **2003,** 381, (5), 598-604.
209. Yu, Z.; Chan, W. K.; Tan, T. T. Y., Neodymium-sensitized nanoconstructs for near-infrared enabled photomedicine. *Small* **2020,** 16, (1), 1905265-1905286.

210. Wang, R.; Li, X.; Zhou, L.; Zhang, F., Epitaxial seeded growth of rare-earth nanocrystals with efficient 800 nm near-infrared to 1525 nm short-wavelength infrared downconversion photoluminescence for in vivo bioimaging. *Angewandte Chemie* **2014,** 53, (45), 12086-12090.
211. Fan, Y.; Wang, P.; Lu, Y.; Wang, R.; Zhou, L.; Zheng, X.; Li, X.; Piper, J. A.; Zhang, F., Lifetime-engineered NIR-II nanoparticles unlock multiplexed in vivo imaging. *Nature Nanotechnology* **2018,** 13, (10), 941-946.
212. Shao, W.; Chen, G.; Kuzmin, A.; Kutscher, H. L.; Pliss, A.; Ohulchanskyy, T. Y.; Prasad, P. N., Tunable narrow band emissions from dye-eensitized core/shell/shell nanocrystals in the second near-infrared biological window. *Journal of the American Chemical Society* **2016,** 138, (50), 16192-16195.
213. Sardar, D. K.; Yow, R. M., Inter-Stark energy levels and effects of temperature on sharp emission lines of Nd^{3+} in $LiYF_4$. *Physica Status Solidi (a)* **1999,** 173, (2), 521-534.
214. Sardar, D. K.; Yow, R. M., Optical characterization of inter-Stark energy levels and effects of temperature on sharp emission lines of Nd^{3+} in $CaZn_2Y_2Ge_3O_{12}$. *Optical Materials* **1998,** 10, (3), 191-199.
215. Solé, J. G., Bausá, L. and Jaque, D., Fundamentals. In *An Introduction to the Optical Spectroscopy of Inorganic Solids*, 2005; pp 1-38.
216. Wang, Y. F.; Liu, G. Y.; Sun, L. D.; Xiao, J. W.; Zhou, J. C.; Yan, C. H., Nd^{3+}-sensitized upconversion nanophosphors: efficient in vivo bioimaging probes with minimized heating effect. *ACS Nano* **2013,** 7, (8), 7200-7206.
217. Cheng, Y.; Gao, Y.; Lin, H.; Huang, F.; Wang, Y., Strategy design for ratiometric luminescence thermometry: circumventing the limitation of thermally coupled levels. *Journal of Materials Chemistry C* **2018,** 6, (28), 7462-7478.
218. Suijver, J. F., Upconversion Phosphors. In *Luminescence: From Theory to Applications*, 2007; pp 133-177.
219. Balabhadra, S.; Debasu, M. L.; Brites, C. D. S.; Ferreira, R. A. S.; Carlos, L. D., Upconverting nanoparticles working as primary thermometers in different media. *Journal of Physical Chemistry C* **2017,** 121, (25), 13962-13968.
220. Zhou, Y.; Qin, F.; Zheng, Y.; Zhang, Z.; Cao, W., Fluorescence intensity ratio method for temperature sensing. *Opt. Lett.* **2015,** 40, 4544-4547.
221. Peng, M.; Yin, X.; Tanner, P. A.; Brik, M. G.; Li, P., Site occupancy preference, enhancement mechanism, and thermal resistance of Mn^{4+} red luminescence in $Sr_4Al_{14}O_{25}$: Mn^{4+} for warm WLEDs. *Chemistry of Materials* **2015,** 27, (8), 2938-2945.
222. Wang, B.; Lin, H.; Huang, F.; Xu, J.; Chen, H.; Lin, Z.; Wang, Y., Non-rare-earth $BaMgAl_{10-2x}O_{17}$:xMn^{4+},xMg^{2+}: a narrow-band red phosphor for use as a high-power warm w-LED. *Chemistry of Materials* **2016,** 28, (10), 3515-3524.
223. Brik, M. G.; Camardello, S. J.; Srivastava, A. M., Influence of covalency on the Mn^{4+} $^2E_g \rightarrow {}^4A_{2g}$ emission energy in crystals. *ECS Journal of Solid State Science and Technology* **2014,** 4, (3), 39-43.
224. Chen, D.; Zhou, Y.; Zhong, J., A review on Mn^{4+} activators in solids for warm white light-emitting diodes. *RSC Advances* **2016,** 6, (89), 86285-86296.
225. Cortelletti, P.; Facciotti, C.; Cantarelli, I. X.; Canton, P.; Quintanilla, M.; Vetrone, F.; Speghini, A.; Pedroni, M., Nd^{3+} activated CaF_2 NPs as colloidal nanothermometers in the biological window. *Optical Materials* **2017,** 68, 29-34.
226. Chen, G.; Qiu, H.; Prasad, P. N.; Chen, X., Upconversion nanoparticles: design, nanochemistry, and applications in theranostics. *Chemical Reviews* **2014,** 114, (10), 5161-5214.
227. Pedroni, M.; Piccinelli, F.; Passuello, T.; Polizzi, S.; Ueda, J.; Haro-González, P.; Martinez Maestro, L.; Jaque, D.; García-Solé, J.; Bettinelli, M.; Speghini, A., Water (H_2O and D_2O) dispersible NIR-to-NIR upconverting Yb^{3+}/Tm^{3+} doped MF_2 (M =Ca, Sr) colloids: influence of the host crystal. *Crystal Growth & Design* **2013,** 13, (11), 4906-4913.
228. Richman, I., Longitudinal optical phonons in CaF_2, SrF_2, and BaF_2. *The Journal of Chemical Physics* **1964,** 41, (9), 2836-2837.
229. Bogdan, N.; Vetrone, F.; Ozin, G. A.; Capobianco, J. A., Synthesis of ligand-free colloidally stable water dispersible brightly luminescent lanthanide-doped upconverting nanoparticles. *Nano Letters* **2011,** 11, (2), 835-840.
230. Miyakawa, T.; Dexter, D. L., Cooperative and stepwise excitation of luminescence: trivalent rare-earth ions in Yb^{3+} sensitized crystals. *Physical Review B* **1970,** 1, (1), 70-80.
231. Ximendes, E. C.; Santos, W. Q.; Rocha, U.; Kagola, U. K.; Sanz-Rodríguez, F.; Fernández, N.; Gouveia-Neto, A. d. S.; Bravo, D.; Domingo, A. M.; del Rosal, B.; Brites, C. D. S.; Carlos, L. D.; Jaque, D.; Jacinto, C., Unveiling in vivo subcutaneous thermal dynamics by infrared luminescent nanothermometers. *Nano Letters* **2016,** 16, (3), 1695-1703.
232. Marciniak, L.; Bednarkiewicz, A.; Strek, W., The impact of nanocrystals size on luminescent properties and thermometry capabilities of Cr, Nd doped nanophosphors. *Sensors and Actuators B: Chemical* **2017,** 238, 381-386.
233. Marciniak, L.; Bednarkiewicz, A.; Kowalska, D.; Strek, W., A new generation of highly sensitive luminescent thermometers operating in the optical window of biological tissues. *Journal of Materials Chemistry C* **2016,** 4, (24), 5559-5563.
234. Runowski, M.; Stopikowska, N.; Szeremeta, D.; Goderski, S.; Skwierczyńska, M.; Lis, S., Upconverting lanthanide Fluoride core@shell nanorods for luminescent thermometry in the first and second biological windows: β-$NaYF_4$:Yb^{3+}-Er^{3+}@SiO_2 temperature sensor. *ACS Applied Materials & Interfaces* **2019,** 11, (14), 13389-13396.

235. Marciniak, L.; Bednarkiewicz, A., Nanocrystalline NIR-to-NIR luminescent thermometer based on Cr^{3+},Yb^{3+} emission. *Sensors and Actuators B:Chemical* **2017,** 243, 388-393.
236. Maestro, L. M.; Haro-González, P.; del Rosal, B.; Ramiro, J.; Caamaño, A. J.; Carrasco, E.; Juarranz, A.; Sanz-Rodríguez, F.; Solé, J. G.; Jaque, D., Heating efficiency of multi-walled carbon nanotubes in the first and second biological windows. *Nanoscale* **2013,** 5, (17), 7882-7889.
237. Zou, X.; Liu, Y.; Zhu, X.; Chen, M.; Yao, L.; Feng, W.; Li, F., An Nd^{3+}-sensitized upconversion nanophosphor modified with a cyanine dye for the ratiometric upconversion luminescence bioimaging of hypochlorite. *Nanoscale* **2015,** 7, (9), 4105-4113.
238. Hong, G.; Robinson, J. T.; Zhang, Y.; Diao, S.; Antaris, A. L.; Wang, Q.; Dai, H., In Vivo fluorescence imaging with Ag_2S quantum dots in the second near-infrared region. *Angewandte Chemie International Edition* **2012,** 51, (39), 9818-9821.
239. Hemmer, E.; Venkatachalam, N.; Hyodo, H.; Hattori, A.; Ebina, Y.; Kishimoto, H.; Soga, K., Upconverting and NIR emitting rare earth based nanostructures for NIR-bioimaging. *Nanoscale* **2013,** 5, (23), 11339-11361.
240. Zhang, Y.; Hong, G.; Zhang, Y.; Chen, G.; Li, F.; Dai, H.; Wang, Q., Ag_2S quantum dot: A bright and biocompatible fluorescent nanoprobe in the second near-infrared window. *ACS Nano* **2012,** 6, (5), 3695-3702.
241. Kaczmarek, A. M.; Esquivel, D.; Ouwehand, J.; Van Der Voort, P.; Romero-Salguero, F. J.; Van Deun, R., Temperature dependent NIR emitting lanthanide-PMO/silica hybrid materials. *Dalton Transactions* **2017,** 46, (24), 7878-7887.
242. Han, S.; Deng, R.; Xie, X.; Liu, X., Enhancing luminescence in lanthanide-doped upconversion nanoparticles. *Angewandte Chemie International Edition* **2014,** 53, (44), 11702-11715.
243. Wang, F.; Liu, X., Recent advances in the chemistry of lanthanide-doped upconversion nanocrystals. *Chemical Society Reviews* **2009,** 38, (4), 976-989.
244. Mahalingam, V.; Vetrone, F.; Naccache, R.; Speghini, A.; Capobianco, J. A., Colloidal Tm^{3+}/Yb^{3+}-doped $LiYF_4$ nanocrystals: multiple luminescence spanning the UV to NIR regions via low-energy excitation. *Advanced Materials* **2009,** 21, (40), 4025-4028.
245. Wen, H.; Zhu, H.; Chen, X.; Hung, T. F.; Wang, B.; Zhu, G.; Yu, S. F.; Wang, F., Upconverting near-infrared light through energy management in core-shell-shell nanoparticles. *Angewandte Chemie International Edition* **2013,** 52, (50), 13419-13423.
246. Xie, X.; Gao, N.; Deng, R.; Sun, Q.; Xu, Q. H.; Liu, X., Mechanistic investigation of photon upconversion in Nd^{3+}-sensitized core-shell nanoparticles. *Journal of the American Chemical Society* **2013,** 135, (34), 12608-12611.
247. Ximendes, E. C.; Rocha, U.; Sales, T. O.; Fernández, N.; Sanz-Rodríguez, F.; Martín, I. R.; Jacinto, C.; Jaque, D., In vivo subcutaneous thermal video recording by supersensitive infrared nanothermometers. *Advanced Functional Materials* **2017,** 27, (38), 1702249-1702259.
248. Marciniak, L.; Prorok, K.; Francés-Soriano, L.; Pérez-Prieto, J.; Bednarkiewicz, A., A broadening temperature sensitivity range with a core-shell YbEr@YbNd double ratiometric optical nanothermometer. *Nanoscale* **2016,** 8, (9), 5037-5042.
249. Cortelletti, P.; Skripka, A.; Facciotti, C.; Pedroni, M.; Caputo, G.; Pinna, N.; Quintanilla, M.; Benayas, A.; Vetrone, F.; Speghini, A., Tuning the sensitivity of lanthanide-activated NIR nanothermometers in the biological windows. *Nanoscale* **2018,** 10, (5), 2568-2576.
250. Zhou, X.; Wang, Y.; Wang, H.; Xiang, L.; Yan, Y.; Li, L.; Xiang, G.; Li, Y.; Jiang, S.; Tang, X.; Zhou, X., Nd^{3+} and Nd^{3+}/Yb^{3+}-incorporated complexes as optical thermometer working in the second biological window. *Sensing and Bio-Sensing Research* **2020,** 29, 100345-100354.
251. Kolesnikov, I. E.; Kurochkin, M. A.; Kalinichev, A. A.; Mamonova, D. V.; Kolesnikov, E. Y.; Kurochkin, A. V.; Lähderanta, E.; Mikhailov, M. D., Effect of silica coating on luminescence and temperature sensing properties of Nd^{3+} doped nanoparticles. *Journal of Alloys and Compounds* **2018,** 734, 136-143.
252. Quintanilla, M.; Zhang, Y.; Liz-Marzán, L. M., Subtissue plasmonic heating monitored with CaF_2:Nd^{3+},Y^{3+} nanothermometers in the second biological window. *Chemistry of Materials* **2018,** 30, (8), 2819-2828.
253. Cerón, E. N.; Ortgies, D. H.; del Rosal, B.; Ren, F.; Benayas, A.; Vetrone, F.; Ma, D.; Sanz-Rodríguez, F.; Solé, J. G.; Jaque, D.; Rodríguez, E. M., Hybrid nanostructures for high-sensitivity luminescence nanothermometry in the second biological window. *Advanced Materials* **2015,** 27, (32), 4781-4787.
254. Skripka, A.; Benayas, A.; Marin, R.; Canton, P.; Hemmer, E.; Vetrone, F., Double rare-earth nanothermometer in aqueous media: opening the third optical transparency window to temperature sensing. *Nanoscale* **2017,** 9, (9), 3079-3085.
255. Martín-Rodríguez, R.; Meijerink, A., Infrared to near-infrared and visible upconversion mechanisms in $LiYF_4$:Yb^{3+}, Ho^{3+}. *Journal of Luminescence* **2014,** 147, 147-154.
256. Naccache, R.; Yu, Q.; Capobianco, J. A., The fluoride host: nucleation, growth, and upconversion of lanthanide-doped nanoparticles. *Advanced Optical Materials* **2015,** 3, (4), 482-509.
257. Ananias, D.; Almeida Paz, F. A.; Carlos, L. D.; Rocha, J., Near-infrared ratiometric luminescent thermometer based on a new lanthanide silicate. *Chemistry A European Journal* **2018,** 24, (46), 11926-11935.
258. Wortmann, L.; Suyari, S.; Ube, T.; Kamimura, M.; Soga, K., Tuning the thermal sensitivity of β-$NaYF_4$:Yb^{3+}, Ho^{3+}, Er^{3+} nanothermometers for optimal temperature sensing in OTN-NIR (NIR II/III) biological window. *Journal of Luminescence* **2018,** 198, 236-242.

259. Sekiyama, S.; Umezawa, M.; Kuraoka, S.; Ube, T.; Kamimura, M.; Soga, K., Temperature sensing of deep abdominal region in mice by using over-1000 nm near-infrared luminescence of rare-earth-doped $NaYF_4$ nanothermometer. *Scientific Reports* **2018,** 8, (1), 16979-16991.
260. Jia, M.; Fu, Z.; Liu, G.; Sun, Z.; Li, P.; Zhang, A.; Lin, F.; Hou, B.; Chen, G., NIR-II/III luminescence ratiometric nanothermometry with phonon-tuned sensitivity. *Advanced Optical Materials* **2020,** 8, (6), 1901173-1901180.
261. Matuszewska, C.; Elzbieciak-Piecka, K.; Marciniak, L., Transition metal ion-based nanocrystalline luminescent thermometry in $SrTiO_3:Ni^{2+},Er^{3+}$ nanocrystals operating in the second optical window of biological tissues. *Journal of Physical Chemistry C* **2019,** 123, (30), 18646-18653.
262. Ximendes, E. C.; Pereira, A. F.; Rocha, U.; Silva, W. F.; Jaque, D.; Jacinto, C., Thulium doped LaF_3 for nanothermometry operating over 1000 nm. *Nanoscale* **2019,** 11, (18), 8864-8869.
263. Balabhadra, S.; Debasu, M. L.; Brites, C. D. S.; Rocha, J.; Carlos, L. D., Implementing luminescence thermometry at 1.3 μm using $(GdNd)_2O_3$ nanoparticles. *Journal of Luminescence* **2016,** 180, 25-30.
264. Seitz, F., An interpretation of crystal luminescence. *Transactions of the Faraday Society* **1939,** 35, (0), 74-85.
265. Mott, N. F., On the absorption of light by crystals. **1938,** 167, (930), 384-391.
266. Thimsen, E.; Sadtler, B.; Berezin, M. Y., Shortwave-infrared (SWIR) emitters for biological imaging: a review of challenges and opportunities. *Nanophotonics* **2017,** 6, (5), 1043-1054.
267. Labrador-Páez, L.; Pedroni, M.; Speghini, A.; García-Solé, J.; Haro-González, P.; Jaque, D., Reliability of rare-earth-doped infrared luminescent nanothermometers. *Nanoscale* **2018,** 10, (47), 22319-22328.
268. Suo, H.; Guo, C.; Wang, W.; Li, T.; Duan, C.; Yin, M., Mechanism and stability of spectrally pure green up-conversion emission in Yb^{3+}/Ho^{3+} co-doped $Ba_5Gd_8Zn_4O_{21}$ phosphors. *Dalton Transactions* **2016,** 45, (6), 2629-2636.
269. Yamada, N.; Shionoya, S.; Kushida, T., Phonon-assisted energy transfer between trivalent rare earth ions. *Journal of the Physical Society of Japan* **1972,** 32, (6), 1577-1586.
270. Xiaoting, Z.; Hayakawa, T.; Ishikawa, Y.; Liushuan, Y.; Nogami, M., Structural investigation and Eu^{3+} luminescence properties of $LaF_3:Eu^{3+}$ nanophosphors. *Journal of Alloys and Compounds* **2015,** 644, 77-81.
271. Savchuk, O. A.; Carvajal, J. J.; Haro-Gonzalez, P.; Aguiló, M.; Díaz, F., Luminescent nanothermometry using short-wavelength infrared light. *Journal of Alloys and Compounds* **2018,** 746, 710-719.
272. Ma, Y.; Xiang, G.; Zhang, J.; Liu, Z.; Zhou, P.; Liu, W.; Tang, X.; Jiang, S.; Zhou, X.; Li, L.; Luo, Y.; Jin, Y., Upconversion properties and temperature sensing behaviors in visible and near-infrared region based on fluorescence intensity ratio in $LuVO_4$: Yb^{3+}/Er^{3+}. *Journal of Alloys and Compounds* **2018,** 769, 325-331.
273. Xiang, G.; Liu, X.; Zhang, J.; Liu, Z.; Liu, W.; Ma, Y.; Jiang, S.; Tang, X.; Zhou, X.; Li, L.; Jin, Y., Dual-mode optical thermometry based on the fluorescence intensity ratio excited by a 915 nm wavelength in $LuVO_4:Yb^{3+}/Er^{3+}@SiO_2$ nanoparticles. *Inorganic Chemistry* **2019,** 58, (12), 8245-8252.
274. Lei, R.; Liu, X.; Huang, F.; Deng, D.; Zhao, S.; Xu, H.; Xu, S., Optical thermometry based on anomalous temperature-dependent 1.53 μm infrared luminescence of Er^{3+} in $BaMoO_4$: Er^{3+}/Yb^{3+} phosphor. *Optical Materials* **2018,** 86, 278-285.
275. Jambunathan, V.; Mateos, X.; Pujol, M. C.; Carvajal, J. J.; Massons, J.; Aguiló, M.; Díaz, F., Near-infrared photoluminescence from Ho^{3+}-doped monoclinic $KLu(WO_4)_2$ crystal codoped with Tm^{3+}. *Journal of Luminescence* **2009,** 129, (12), 1882-1885.
276. Zhan, Q.; Qian, J.; Liang, H.; Somesfalean, G.; Wang, D.; He, S.; Zhang, Z.; Andersson-Engels, S., Using 915 nm laser excited $Tm^{3+}/Er^{3+}/Ho^{3+}$-doped $NaYbF_4$ upconversion nanoparticles for in vitro and deeper in vivo bioimaging without overheating irradiation. *ACS Nano* **2011,** 5, (5), 3744-3757.
277. Wikipedia Contributors, *Ex-vivo*.
278. Koenig, K.; Liang, H.; Berns, M. W.; Tromberg, B. J., Cell damage in near infrared multimode optical traps due to multi-photon absorption. *Optics Letters* **1996,** 21, 1090-1092.
279. Dickerson, E. B.; Dreaden, E. C.; Huang, X.; El-Sayed, I. H.; Chu, H.; Pushpanketh, S.; McDonald, J. F.; El-Sayed, M. A. J. C. l., Gold nanorod assisted near-infrared plasmonic photothermal therapy (PPTT) of squamous cell carcinoma in mice. *Cancer Letters* **2008,** 269, (1), 57-66.
280. Cheng, L.; Wang, C.; Feng, L.; Yang, K.; Liu, Z., Functional nanomaterials for phototherapies of cancer. *Chemical Reviews* **2014,** 114, (21), 10869-10939.
281. Shao, J.; Xie, H.; Huang, H.; Li, Z.; Sun, Z.; Xu, Y.; Xiao, Q.; Yu, X. F.; Zhao, Y.; Zhang, H., Biodegradable black phosphorus-based nanospheres for in vivo photothermal cancer therapy. *Nature Communications* **2016,** 7, (1), 1-13.
282. Jaque, D.; Martinez Maestro, L.; Del Rosal, B.; Haro-González, P.; Benayas, A.; Plaza, J.; Martín Rodríguez, E.; Solé, J., Nanoparticles for photothermal therapies. *Nanoscale* **2014,** 6, (16), 9494-9530.
283. Quintanilla, M.; García, I.; de Lázaro, I.; García-Alvarez, R.; Henriksen-Lacey, M.; Vranic, S.; Kostarelos, K.; Liz-Marzán, L. M., Thermal monitoring during photothermia:hybrid probes for simultaneous plasmonic heating and near-infrared optical nanothermometry. *Theranostics* **2019,** 9, (24), 7298-7312.
284. Maestro, L. M.; Haro-González, P.; Sánchez-Iglesias, A.; Liz-Marzán, L. M.; García Solé, J.; Jaque, D., Quantum dot thermometry evaluation of geometry dependent heating efficiency in gold nanoparticles. *Langmuir* **2014,** 30, (6), 1650-1658.

285. Wikipedia Contributors, *In vitro*.
286. Fischer, L. H.; Harms, G. S.; Wolfbeis, O. S., Upconverting nanoparticles for nanoscale thermometry. *Angewandte Chemie International Edition* **2011,** 50, (20), 4546-4551.
287. Zohar, O.; Ikeda, M.; Shinagawa, H.; Inoue, H.; Nakamura, H.; Elbaum, D.; Alkon, D. L.; Yoshioka, T., Thermal imaging of receptor-activated heat production in single cells. *Biophysical Journal* **1998,** 74, (1), 82-89.
288. Oyama, K.; Takabayashi, M.; Takei, Y.; Arai, S.; Takeoka, S.; Ishiwata, S.; Suzuki, M., Walking nanothermometers: spatiotemporal temperature measurement of transported acidic organelles in single living cells. *Lab on a Chip* **2012,** 12, (9), 1591-1593.
289. Takei, Y.; Arai, S.; Murata, A.; Takabayashi, M.; Oyama, K.; Ishiwata, S.; Takeoka, S.; Suzuki, M., A nanoparticle-based ratiometric and self-calibrated fluorescent thermometer for single living cells. *ACS Nano* **2014,** 8, (1), 198-206.
290. Suzuki, M.; Tseeb, V.; Oyama, K.; Ishiwata, S., Microscopic detection of thermogenesis in a single HeLa cell. *Biophysical Journal* **2007,** 92, (6), 46-48.
291. Uchiyama, S.; Inada, N., Chapter 12-Cellular thermometry. In *Thermometry at the Nanoscale: Techniques and Selected Applications*, The Royal Society of Chemistry: 2016; pp 353-382.
292. Wikipedia Contributors, *In vivo*.
293. Ozerdem, U.; Hargens, A. R., A simple method for measuring interstitial fluid pressure in cancer tissues. *Microvascular Research* **2005,** 70, (1), 116-120.
294. Tromberg, B. J.; Coquoz, O.; Fishkin, J. B.; Pham, T.; Anderson, E. R.; Butler, J.; Cahn, M.; Gross, J. D.; Venugopalan, V.; Pham, D., Non-invasive measurements of breast tissue optical properties using frequency-domain photon migration. *Philosophical Transactions of the Royal Society B: Biological Sciences* **1997,** 352, (1354), 661-668.
295. Lienhard, J. H., A heat transfer textbook. *Courier Corporation* **2013**.
296. F. P. Incropera , D. P. D., T. L. Bergman and A. S. Lavine, Introduction to heat transfer. *Wiley, New York* **2006**.
297. Saïdi, E.; Babinet, N.; Lalouat, L.; Lesueur, J.; Aigouy, L.; Volz, S.; Labéguerie-Egéa, J.; Mortier, M., Tuning temperature and size of hot spots and hot-spot arrays. *Small* **2011,** 7, (2), 259-264.
298. Tetienne, J. P.; Lombard, A.; Simpson, D. A.; Ritchie, C.; Lu, J.; Mulvaney, P.; Hollenberg, L. C. L., Scanning nanospin ensemble microscope for nanoscale magnetic and thermal imaging. *Nano Letters* **2016,** 16, (1), 326-333.
299. Sedmak, I.; Urbančič, I.; Štrancar, J.; Mortier, M.; Golobič, I., Transient submicron temperature imaging based on the fluorescence emission in an Er/Yb co-doped glass-ceramic. *Sensors and Actuators A: Physical* **2015,** 230, 102-110.
300. Deshpande, V. V.; Hsieh, S.; Bushmaker, A. W.; Bockrath, M.; Cronin, S. B., Spatially resolved temperature measurements of electrically heated carbon nanotubes. *Physical Review Letters* **2009,** 102, (10), 105501-105505.

Chapter II

Experiments

This chapter will be devoted to the synthetic methodologies used to synthesize lanthanide doped luminescent materials and their techniques used for their structural, morphological, thermal, surface and optical characterizations.

Related to the synthetic methodologies, modified sol-gel Pechini, solvothermal methodologies (microwave-assisted and conventional autoclave) and wet chemical synthesis (thermal decomposition and digestive ripening methodologies), will be described in details.

X-ray Powder diffraction (XRPD) and Raman scattering were employed to identify the crystalline structure of the synthesized luminescent materials. The size and shape of the crystal particles was investigated via transmission electron microscopy (TEM) and high resolution transmission electron microscopy (HRTEM). Electron diffraction in the HRTEM equipment was used to orient crystallographically the nanocrystals with special morphologies and assemblies. The crystalline phase transformation of the precursors and seeds with temperature was explored via differential thermal analysis (DTA) and thermogravimetric analysis (TGA). Via Fourier Transform Infrared (FT-IR) and Proton Nuclear Magnetic Resonance (^{1}H NMR), the presence or absence of functional groups on the surface of the synthesized luminescent materials, was inspected. Spectroscopic characterization techniques combining the measurements of absorbance, transmittance, photoluminescence lying on the visible and third (III-BW) biological window regime and the ability to convert the absorbed light into heat, were carried out to highlight the multifunctionalities of these luminescent lanthanide doped particles.

2.1. Theory of the nucleation and crystal growth in a liquid phase

2.1.1. Nucleation

Nucleation refers to the process of generation of the first nuclei, which act as templates for the crystal growth.[1, 2] There exist two types of nucleation: homogeneous and heterogeneous nucleation. The homogeneous nucleation consist on the formation of uniform nuclei throughout the parent phase, whereas, heterogeneous nucleation forms at structural inhomogeneities (impurities, grain boundaries, dislocations).[1, 2]

In the classical nucleation theory, a nucleus is considered as a spherical particle and its total free energy is defined by thermodynamics terms.[2, 3] The total free energy ΔG of a particle with radius r is expressed as:

$$\Delta G = 4\pi r^2\gamma + \frac{4}{3}\pi r^3 \Delta G_v \quad (2.1)$$

where γ and ΔG_v are the surface free energy per unit area and the free energy per unit volume of a crystal, respectively. ΔG_v is dependent upon the absolute temperature T, Boltzmann's contant k_B, the supersaturation of the solution S and its molar volume v of the monomer (the units from which the nucleus are formed):[4, 5]

$$\Delta G_v = -\frac{k_B T \ln(S)}{v} \quad (2.2)$$

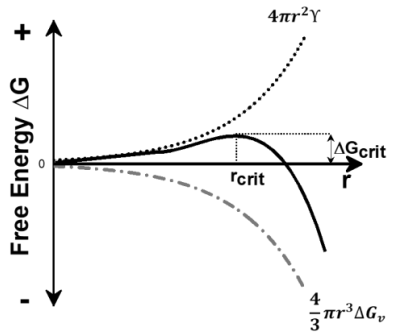

Figure 2.1. Dependence of the total free energy ΔG versus particle radius r. The contributions from the surface free energy (short dot line) and bulk free energy (short dash dot line) are also depicted. r_{crit} and ΔG_{crit} represent the critical radius and free energy.

Supersaturation represents the driving force for the crystallization and is a prerequisite before a solid phase will appear in a saturated solution.[1, 2] The variation of the total free energy from the radius of the particles and the two terms (volume and surface) are presented in Figure 2.1. From the volume term, the formation of the nuclei is favored as long as the supersaturation S levels are higher than 1.[2] From the surface term, an extra free energy is required for the formation of the nuclei.[2] As a consequence, nucleus with radius smaller than the so-called "critical radius" cannot grow further, but only dissolve back into the solution, as it is the only way to decrease back their free energy.[2] Thus, the critical radius r_{crit} represents the minimum size of the nuclei that can survive in solution and grow further. Due to the surface term that is always positive and the volume term always negative, a maximum free energy which allows the formation and growth of nucleus, *i.e* critical free energy is deduced by differentiating $\Delta G/\Delta r$ =0.

$$\Delta G_{crit} = \frac{4}{3}\pi\gamma r_{crit}^2 = \Delta G_{crit}^{homo} \quad (2.3)$$

To this critical free energy corresponds a critical radius:

$$r_{crit} = -\frac{2\gamma}{\Delta G_v} = \frac{2\gamma v}{k_B T \ln(S)} \qquad (2.4)$$

In addition, a reaction rate ($\frac{dN}{dt}$) for the formation of the nuclei can be deduced using the Arrhenius equation:

$$\frac{dN}{dt} = A \exp\left(-\frac{\Delta G_{crit}}{k_B T}\right) = A\, exp\left(\frac{16\pi\gamma^3 v^2}{3{k_B}^3 T^3 N_A^2 (lnS)^2}\right) \qquad (2.5)$$

where N, A, N_A, γ, v, T, S and k_B are the number of nuclei, pre-exponential factor, Avogadro's number, the surface free energy, the molar volume of the monomer, the absolute temperature, the supersaturation and the Boltzmann constant, respectively.

Hence, from Equation 5, there are three experimental parameters that can be varied for the control of the nucleation rate: the level of supersaturation, the temperature of the reaction and the surface free energy. Kwon and Hyeon investigated the variation of the nucleation rate as a function of these three parameters.[2] The largest effect on the nucleation rate was assigned to the level of supersaturation. As the level of supersaturation increased from 2 to 4, the nucleation rate was increased about ≈10^{70} times.[2] The nucleation rate can be adjusted by changing the surface free energy. In the synthesis, modifying the nature and concentration of the surfactant in the solution can change the surface free energy, so as to control the nucleation rate.[2]

2.1.2. Growth

The growth of the nanocrystals depends on two mechanisms: the surface reaction and the monomer's diffusion to the surface.[6] The growth of the nanocrystals by diffusion is modeled by Fick's first law:

$$J = 4\pi r^2 D \frac{dC}{dr} \qquad (2.6)$$

where J, r, D and C present the total flux of monomers passing through a spherical plane with radius particle radius r, the diffusion coefficient and the concentration at a distance r. Fick's law can be tuned to the expression:

$$J = \frac{4\pi D r\ (r + \delta)}{\delta}(C_b - C_i) \qquad (2.7)$$

in the case of a nanoparticle within solution where δ is the distance from the particle surface to the bulk concentration of monomers within solution, C_b is the bulk concentration of monomers within the solution, C_i is the concentration of monomers at the solid/liquid interface. As the total flux is constant irrespective of x due to the steady state of the solute diffusion, integration of $C(x)$ from $(r + \delta)$ to r leads to:

$$J = 4\pi D r\ (C_b - C_i) \qquad (2.8)$$

For the case of the surface reaction, a similar expression can be formulated:

$$J = 4\pi r^2 k(C_i - C_r) \qquad (2.9)$$

where k and C_r represent the rate of the surface reaction and solubility of the monomers, respectively.

Thus, from Equation 8 and Equation 9, there are two limiting factors affecting the growth: either the diffusion of monomers to the surface or the rate of the surface reaction of these monomers. If diffusion is the limiting factor then the change in the particle size with time is represented from Equation 2.10:

$$\frac{dr}{dt} = \frac{Dv}{r}(C_b - C_r) \qquad (2.10)$$

If the surface reaction is the limiting factor, then the change in the particle size with time is as follows:

$$\frac{dr}{dt} = kv(C_b - C_r) \qquad (2.11)$$

When the growth of nanoparticles is neither attributed to diffusion nor surface reaction controlled, the increase in the particle's radius with time is written as:

$$\frac{dr}{dt} = \frac{Dv\,(C_b - C_r)}{r + \frac{D}{k}} \qquad (2.12)$$

For a diffusion coefficient D <<1, the diffusion rate dominates over the surface reaction.[7]

2.1.3. Formation of a size distribution

Up to now, based on the classical nucleation theory, above some critical radius, the particles will form and grow whereas below this radius, the particles will redissolve. However, this conclusion does not explain the difference in the sizes of the particles during growth. To explain this observations, a size focusing effect should be taken into account. Considering r^* as the particle radius in equilibrium within the bulk solution and if the process of the diffusion is responsible for the growth, the rate of change of the particle size with time is expressed:[7, 8]

$$\frac{dr}{dt} = \frac{K_D}{r}\left(\frac{1}{r^*} - \frac{1}{r}\right) \qquad (2.13)$$

where K_D (constant of diffusion) is defined as follows:

$$K_D = \frac{2\gamma D v^2 C_b}{k_B T} \qquad (2.14)$$

If the size distribution is narrow, the change in the standard deviation Δr for a given particle radius at equilibrium, is given by:

$$\frac{d(\Delta r)}{dt} = \frac{K_D \Delta r}{\bar{r}^2}\left(\frac{2}{\bar{r}} - \frac{1}{r^*}\right) \qquad (2.15)$$

where $\bar{r}$ is the mean particle radius.

According to this equation, there are two regimes depending on the supersaturation. If the supersaturation is high such that $\frac{\bar{r}}{r^*} \geq 2$, then $\frac{d(\Delta r)}{dt} \leq 0$ and the growth of the system is self-sharpening of the size distribution. On the contrary, if $\frac{\bar{r}}{r^*} < 2$ then $\frac{d(\Delta r)}{dt} > 0$, the size distribution tends to broaden even within the diffusion controlled growth.

Similar, when the growth is controlled by the surface, the rate of change of the particle size with time, the constant of the surface and the change in the standard deviation for a give particle radius at equilibrium, are given by:[7, 8]

$$\frac{dr}{dt} = K_R\left(\frac{1}{r^*} - \frac{1}{r}\right) \qquad (2.16)$$

$$K_R = \frac{2\gamma k v^2 C_b}{RT} \qquad (2.17)$$

$$\frac{d(\Delta r)}{dt} = \frac{K_R \Delta r}{\bar{r}^2} \qquad (2.18)$$

In the case where the surface reaction dominates, the size distribution will always be within the broadening regime, this is as for any value of $\bar{r}$, $\frac{d(\Delta r)}{dt}$ will always be positive.[7, 8]

2.1.4. Theories of nucleation and growth

On the literature, there exist different theories regarding the nucleation and growth of colloidal nanocrystals. The most used and important theories rely on the LaMer mechanism, [9, 10] Ostwald[11] and digestive ripening, [12] coalescence[13] and oriented attachment[14] and intraparticle growth.[15, 16]

The most widely used mechanism is the LaMer mechanism, in which the conceptual difference between the nucleation and growth of nanocrystals. Nucleation and growth of the nanocrystals was achieved by studying the formation of sulfur sols from the decomposition of sodium thiosulfate. The process consisted in two steps: first, formation of free sulfur from the thiosulfate, and the second, formation of sulfur sols in solution.[9, 10] A general diagram for the LaMer mechanism is depicted in Figure 2.2 (a). The process of nucleation and growth according to the LaMer mechanism can be divided into three sections: (I) A rapid increase in the concentration of free monomers in solution, (II) the monomers with concentration C_m undergoes "burst nucleation" which reduces the concentration of free monomers in solution and generates the first nuclei appearing in the solution at the region between C_{min} and C_{max}, and (III) growth occurring under the control of the diffusion or surface reaction of the monomers through the solution.[9, 10]

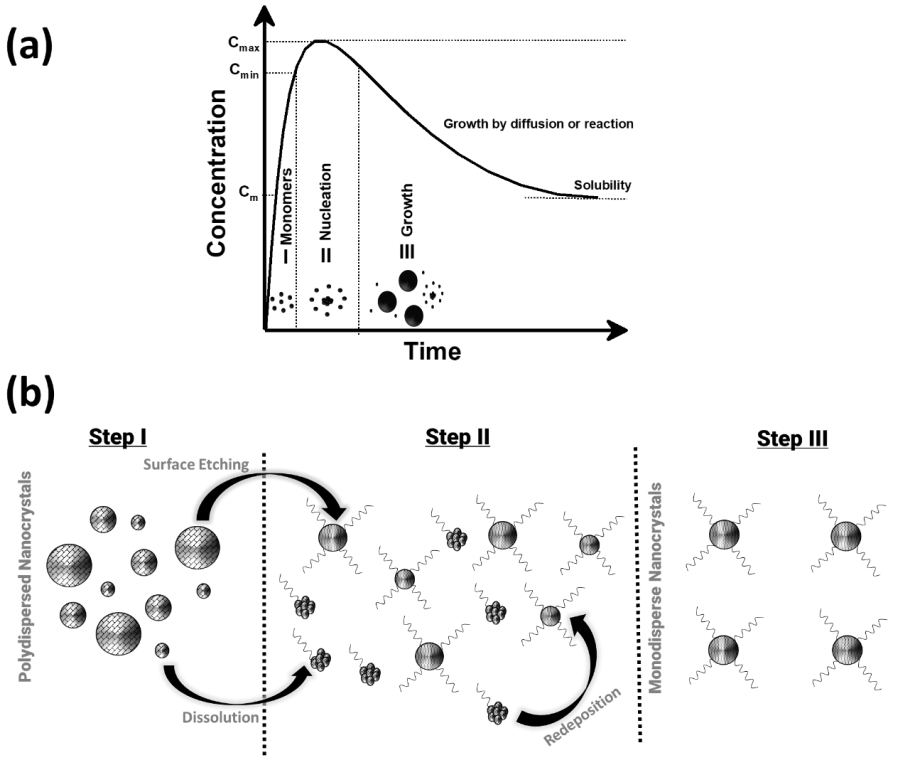

Figure 1.2. Schematic diagram for the: (a) LaMer mechanism of nucleation and growth of sulfur sols, and (b) digestive ripening mechanism for the formation of monodisperse nanocrystals.

Ostwald ripening[11] growth mechanism is based on the change of the solubility of nanoparticles and the surface energy. Due to high solubility and the surface energy of smaller particles within solution, these particles resdissolve, and in turn, allow the larger particles to grow even more.

Digestive ripening is effectively the inverse of the Ostwald ripening. Smaller particles grow at expense of the larger ones. Digestive ripening process converts the polydispersed nanocrystals with crystalline defects into nearly monodisperse ones without resorting to any size separation.[12] The formation of these monodisperse nanocrystals through the digestive ripening mechanism involves the following steps (Figure 2.2 (b)):[12]

Step I: Replacing the existing weakly bounded ligands/surfactants/solvent molecules and binding the newly added ligands to the nanocrystals surface.
Step II: Breaking the larger nanocrystals present in the as-prepared state, leading to the narrowing of the size distribution due to the surface etching of these nanocrystals and the formation of ligand-metal complex species on the nanocrystals surface due to redeposition.
Step III: Size focusing of the nanocrystals when they are refluxed in a relatively high boiling point solvent in the presence of the surface-active ligands, resulting in formation of monodisperse nanocrystals.

2.2. Synthesis of nanocrystals: Wet chemical methodologies

Synthesis of the nanomaterials is a vital component in the development of nanoscience and nanotechnology. Advances in the field of nanoscience and nanotechnology, largely depend on the ability to precisely control the size and shape of the synthesized nanomaterials. Development of new synthetic strategies for the synthesis of nanocrystals with controllable size and shape, are of paramount importance in understanding and tuning the chemical, physical and optical properties of the synthesized nanocrystals.[17, 18] Tailoring the size and shape of these colloidal nanocrystals, not only provides new properties which cannot be achieved by their bulk counterparts,[19-21] but also enables design of nanocrystals optimized for applications in nanoscience and nanotechnology.[22-27]

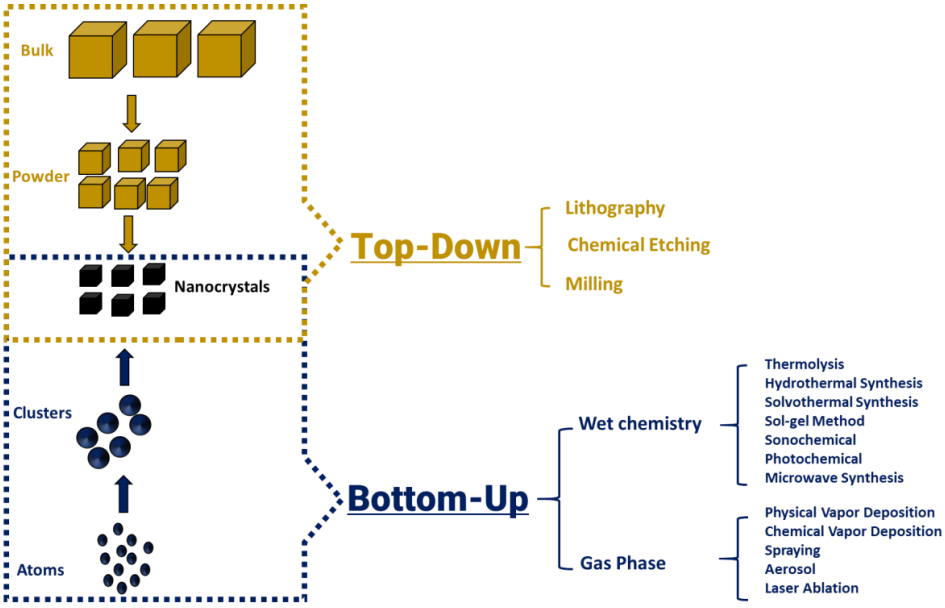

Figure 2.3. Schematic illustration of the synthetic methods to produce nanomaterials.

Therefore, various approaches have been developed to control these parameters and, hence, meet the requirements for various applications. The fabrication of nanocrystals can be divided into two methodologies: the top-down and the bottom-up (check Figure 2.3).[28,29] Top-down approach refers to size reduction or successive cutting of a bulk material to get nano-sized particle. Traditional examples of top-down approaches for the synthesis of nanostructures involve milling, chemical etching and lithography. However, this methodology induces surface-defects of the final product and cannot provide large scale production.[28,29] Bottom-up methodology provides an accurate route for the atomically precise fabrication of nanomaterials based on the rational design of precursor and manipulation of the reactions.[28,29] Depending on the medium in which the nanomaterials are formed, the bottom-up techniques are classified as gas phase and wet chemical methods. The gas phase method involve the preparation of the nanomaterials based on physical or chemical vapor deposition (PVD and CVD), laser ablation, aerosol and spraying.[28, 29] Wet chemical synthesis have attracted great interest for the production of the nanostructures,

assigned to the fabricating of low-dimensional structures with an accurate control on the dimensions and composition. The aim of wet chemical methodologies is to synthesize colloidal crystals with sub-nanometer sizes over a broad range of dimensional-morphological regimes by careful regulation of the nucleation and growth parameters in liquid media under the assistance of selected surfactants, solvents or catalyst additives.[2,22,30,31] Wet chemical techniques can be classified in different synthetic reactions involving thermal decomposition methods (thermolysis), hydrothermal or solvothermal based, microwave-assisted, sol-gel based methods, sonochemical and photochemical methods.

In this thesis, we will focus on the production of the nanomaterials based on the wet chemical synthesis, devoted mostly on the sol-gel methods, solvothermal based and thermal decomposition type of methods.

2.2.1. The modified sol-gel Pechini methodology for $KLu(WO_4)_2$ nanocrystals synthesis

Sol-gel chemistry refers to the preparation of inorganic polymers or ceramics via a transformation from liquid precursors to a sol and finally to a network structure called a *"*gel*"*.[32] A sol is traditionally formed through the hydrolysis and polycondensation of metal alkoxide precursors and is generally defined as a colloidal system. A colloidal system is described as *"*the molecules or polymolecular particles dispersed in a medium that have at least in one direction a dimension roughly between 1 nm and 1 μm*"*. The *"*gel*"* is simply defined as a non-fluid 3D network that extends through a fluid phase.

Scheme 2.2. Proposed mechanism of the sol-gel Pechini methodology.

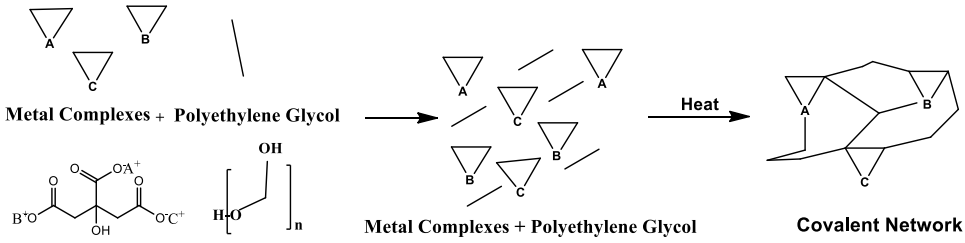

The Pechini methodology, named after the author Maggio P. Pechini, was first implemented to synthesize lead and alkaline earth titanates and niobates by using resin intermediates.[33] This methodology relies on the principle of the sol-gel chemistry and as a first step, involves the incorporation of small organic chelating ligands to form a homogeneous metal/organic ligand complex solution. The Pechini methodology, in contrary to the traditional sol-gel chemistry, convert the metal/organic ligand complex into a covalent polymeric network to entrap the metal ions (Scheme 2.1). A possible explanation for the formation of this network is to delay the thermal decomposition or the organic matrix in order to gain more control over the growing product.[34] A typical synthetic approach would involve the dissolution of metal salts in water and citric acid or EDTA to form a homogeneous precursor solution containing metal-citrate/EDTA chelate complexes. Via thermal treatment, the key reaction in the Pechini methodology, the polyesterification, between the citrate and an added poly/ethylene glycol, is produced, leading to an extended covalent network polymer. This polymer is later calcined to form the desired final product.[34] A significant advantage of the Pechini method is the ability to form a polymeric precursor where two or more metals may be dispersed homogeneously throughout the network.

Developments to enhance the range of materials synthesized via the sol-gel Pechini method have led to tuning of the experimental parameters.[35-37] Thus, focus on the substitution of citric acid with chelating agents with di-, tri-, tetra-carboxylic acids with higher thermal decomposition temperature and poly/ethylene glycol with other polyols, have highly enhanced the range of synthesized materials.[35, 36, 38, 39] These developments have emerged into a so-called modified sol-gel Pechini methodology.

The nucleation and growth of nanocrystals with the sol-gel methodology is governed by the presence of the small organic molecules, including citric acid, tartaric acid, glyocolic acid and oxalic acid.[34] The role of these small molecules is to ensure the homogeneity and stability of the metal complexes formed. This stability and homogeneity is controlled by the pH, thus reports underlie the addition of ammonia or ethylene diamine to modify the pH and enhance cation binding to the citrate.[34, 40] However, in addition to traditional sol-gel approaches, in which the growth of the desired nanocrystals is achieved by the pyrolysis in air of the formed "gel",[34] in modified sol-gel Pechini the sacrificial "gel" is formed after transesterification between citrate and ethylene glycol, prior to air pyrolysis.[34]

In this thesis, we performed the modified sol-gel Pechini methodology to synthesize undoped and lanthanide doped monoclinic potassium lutetium double tungstate ($KLu(WO_4)_2$) nanoparticles using ethylenediaaminetetracetic acid (EDTA) as a chelating agent and polyethylene glycol as the esterification agent, inspired also from the work of Galceran *et al*.[39] $KLu(WO_4)_2$ as a host, offers a high chemical stability, large value of absorption and emission cross section for the dopant ions and the possibility to dope the host independent of the concentration level, without fluorescence quenching effect.[41, 42]

In general, the modified sol-gel Pechini methodology for the synthesis of undoped $KLu(WO_4)_2$ nanoparticles implies:

- Dissolution of lutetium (III) nitrate hydrate ($Lu(NO_3)_3{\cdot}5H_2O$) in a mixture of distilled water and EDTA
- Addition of tungstate precursors (K_2CO_3 + $(NH_4)_2WO_4$), taking into account an equimolar ratio of metal precursors (Lu and K, please note that W is part of the anion $(WO_4)^{2-}$, so is not countable) and EDTA, followed by a heating process at 353 K to ensure complete homogenization of the mixture
- Esterification process via addition of polyethylene glycol (PEG, MW=400 g/mol) with half of the amount of the molar ratio of EDTA, followed by a heating process at 373 K to generate the polymeric gel and evaporate completely the water
- Precalcination at 573 K for 2 h to form the precursor powder composition
- The final calcination step at 1023 K for 2 h provides the desired final product of the combustion, *i.e.* the monoclinic $KLu(WO_4)_2$ nanoparticles.

The synthetic methodology for the synthesis of Ho^{3+} and Tm^{3+} doped $KLu(WO_4)_2$ nanoparticles is identical to the undoped $KLu(WO_4)_2$, with the difference of addition of holmium (III) nitrate pentahydrate ($Ho(NO_3)_3{\cdot}5H_2O$) and thulium (III) nitrate pentahydrate ($Tm(NO_3)_3{\cdot}5H_2O$), during the dissolution step in distillated water and EDTA.

2.2.2. Solvothermal methodologies for the synthesis of $KLu(WO_4)_2$ nanocrystals

The modified sol-gel Pechini methodology suffers from agglomeration of the nanocrystals formed and as a consequence from no control of the size and shape of the final product of the reaction partially due to the high temperature treatment (calcination process) employed. To achieve a certain degree of control on the morphology of the $KLu(WO_4)_2$ crystals and no presence of agglomerates, we implemented the wet chemical route of solvothermal method in the presence of multiple organic coating surfactants. Solvothermal synthesis is generally is defined as a chemical reaction taking place in a solvent at temperatures above the boiling point and pressures above 1 bar. The medium used in a solvothermal synthesis can be anything from water (hydrothermal) to alcohol or any other organic or inorganic solvent.[43] Solvothermal synthesis can be often assisted by microwave irradiation or conventional heating reactions.[43] Contrary to the modified sol-gel Pechini method, in this approach, the introduction of organic surfactants with the capping ability on the surface of the product, prevents produced nanocrystals from aggregation by dispersing them in organic or aqueous media.[44] The incorporation of organic surfactants into wet chemical routes allows for thermodynamic or kinetic control over the nucleation and growth of nanocrystals. These surfactants adsorb on metal surfaces, subsequently modify the surface energy and affect the thermodynamic equilibrium of nanocrystal shapes.[45-47]

In addition, these solvothermal techniques allow for potential large-scale production, lower reaction temperatures and shorter reaction times, compared to the modified sol-gel Pechini method, reducing the production cost of these materials.[44] The incorporation of the organic surfactants for the preparation of colloidal nanocrystals through the wet solution-phase colloidal chemistry approach has shown great success in controlling the size and morphology of the nanocrystals.[48-50] In order to achieve the control of size and shape of the nanocrystals, organic compounds such as oleic acid (OLAC), oleylamine (OLAM) acting both as surfactants and capping agents, alone, combined or mixed with 1-octadecene (ODE) or trioctylphosphine oxide (TOPO) have allowed precise control over the synthesis of the inorganic colloidal nanocrystals (oxides, sulfides, tellurides, chalcogenides (binary, ternary and quaternary), and metallic nanocrystals.[1, 8, 30, 50, 51]

In the field of lanthanide doped materials, the combinatory effect of OLAC and OLAM has been already explored in the preparation of sesquioxides,[52-54] fluorides[55-58] and tetragonal double tungstates.[59, 60] The preparation of these materials is quite often concentrated into the wet chemical routes such as thermal decomposition methodologies or the digestive ripening mechanisms, whereas the use of the combinatory effect of OLAC and OLAM in solvothermal-assisted methods is scarce. A typical example of exploring OLAC and OLAM as organic surfactants via the solvothermal-assisted methods is the preparation of tetragonal bipyramids of $NaLa(MoO_4)_2$ nanocrystals using heating via autoclave at 413 K during 6 h.[61]

Inspired from this work, we incorporated the solvothermal synthesis (microwave and conventional autoclave-assisted) to prepare undoped and doped $KLu(WO_4)_2$ nanocrystals. In a typical microwave-assisted solvothermal synthesis, an equimolar ratio of organic surfactants (OLAC and OLAM, 6 mmol each) and 18 mL of ethanol were prepared until homogenization (solution A). In solution A, solution B made of 0.3 mmol lutetium (III) precursor ($Lu(NO_3)_3{\cdot}H_2O$ or $Lu(Ac)_3{\cdot}H_2O$) dispersed in 4 mL distillated water and solution C made of 0.6 mmol K_2WO_4 dispersed in 4 mL distillated water, were added dropwise, filling 38% of the microwave vial. The mixture was heated at 453 K for 3 h using a Milestone ETHOS One reactor equipped with a temperature sensor and a stirring bar. After the reaction was finished, the mixture was allowed to cool down naturally to room temperature. The product of the reaction was collected after purifying the mixture with an excess of ethanol to extract the precipitate, centrifuged at 6000 rpm for 5 min, and redispersed in n-hexane. This purification step was repeated until the supernatant was colorless and transparent, removing in this way the excess of organic surfactants. Finally, the purified precipitate was dried at 353 K for approximately 1 h. A part of the dried product, (hereafter the seeds) was collected for structural and morphological characterizations. The other part of the product was calcined in a conventional furnace at a specific temperature and time to obtain KLuW as the final product. In terms of the molar ratios used, it is important to maintain an equimolar ratio of OLAC and OLAM, and a ratio between the lutetium (III) precursor and organic surfactants of 1:40 and between the lutetium (III) precursor and K_2WO_4 of 1:2. Deviation from these ratios may lead in impurities of the final product and also generation of different products.

The conventional autoclave-assisted solvothermal method synthesis of $KLu(WO_4)_2$ was performed using the same experimental parameters as in the microwave-assisted synthesis, but changing the solution holder (here it is used an autoclave metallic reactor) and the heating was provided by a conventional heating furnace.

To synthesize the Ho, Tm:$KLu(WO_4)_2$ nanocrystals, the same synthetic methodologies were applied (either microwave-assisted or conventional autoclave solvothermal method), except for the incorporation of the holmium (III) and thulium (III) precursors in the solution B.

2.2.3. Wet chemical synthesis based on thermal decomposition

Thermal decomposition or thermolysis is a reaction of chemical decomposition under the action of heat.[50] In reactions employing this methodology, all reagents, including precursors and high boiling point solvents, are mixed into a reaction vessel and heated controllably to induce the nucleation and growth of the nanocrystals. At the mixing temperature, the reaction solution is comprised largely of precursors. With the increase of the temperature, the precursors experience an increased thermodynamic driving force, converting them into monomers. The heating process

eventually triggers the nucleation of crystallites, with continued heating required to grow these nuclei into mature and final product nanocrystals.[50] The thermal decomposition synthesis strongly depend on the level of the reactivity of the precursors and the ligands employed. Thus, control over the reactivity of these components allows for a rapid nucleation to guarantee a large quantity of nuclei with relative short period of time and decoupling of the nucleation and growth stages to reduce particle polydispersity.[50]

For the thermal decomposition in lanthanide-based nanocrystals, organometallic precursors are lanthanide-based organic salts, such as benzoylacetones,[62] acetylacetonates,[52,63] acetates,[53,64-66] and trifluoroacetates.[67] With the increase of the temperature, the organometallic precursor is chemically decomposed so that breaking and nucleation of C-O bond could happen toward targeted nanoproducts. Oleic acid and oleylamine with polar capping groups have the ability to act as capping reagents to control the size and morphology of nanocrystals by selective adsorption on specific facets.[47] The control over the size and shape of the final product can be tuned by controlling the crystal nucleation and growth process via adjustment of the synthetic parameters, including temperature, time, heating rate or the molar ratio between the organic surfactants and the precursors.

2.2.3.1. Thermolysis-assisted synthesis of monoclinic $KLu(WO_4)_2$ sub-micrometric rods

Monoclinic $KLu(WO_4)_2$ with precise morphology were synthesized by a thermolysis method in the presence of organic surfactants OLAC and OLAM (Scheme 2.2). In a typical synthesis, a 2 mL 0.2 M of lutetium (III) acetate tetrahydrate was added into a mixture of 12 mmol OLAC, 12 mmol OLAM and 24 mmol ODE. The mixture was heated up to 423 K for 1 h to ensure the complexation of the Lu^{3+} with the organic surfactants. After cooled down to room temperature, a 2 mL 0.4 M of K_2WO_4 was added drop wise. The mixture was heated at 323 K for 0.5 h and 373 K for 0.5 h under vacuum to removal the residual oxygen. After switching to an inert atmosphere, the temperature was raised at 573 K for 2 h to ensure the nucleation and growth of material. The final product was collected after performing purification at the cooled down reaction mixture. The purification includes washing the final reaction solution with ethanol or acetone, centrifugation at 5000 rpm for 10 min, prior to dispersion in apolar solvent (n-hexane, cyclohexane or chloroform). This purification cycle has repeated until transparent color solution of the supernatant. The obtained product of the purification (the seeds) was calcined at 1023 K for 2 h to form the desired monoclinic $KLu(WO_4)_2$ sub-micrometric rods.

By introducing holmium (III) and thulium (III) dopants into the 2 mL 0.2 M of lutetium (III) acetate tetrahydrate solution and following the same synthetic strategy, Ho, Tm: $KLu(WO_4)_2$ sub-micrometric rods could be synthesized.

Scheme 2.2. Synthesis of monoclinic $KLu(WO_4)_2$ rods by thermal decomposition

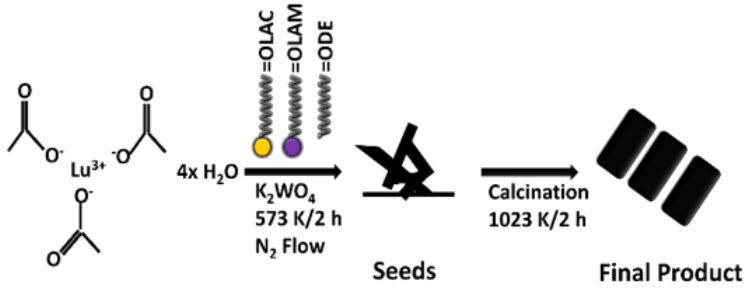

2.2.3.2. Synthesis of sesquioxide nanocrystals by thermal decomposition

The control over the size and shape of the final product of the thermal decomposition for the synthesis of sesquioxides was achieved via tuning the time of growth of the nanocrystals.

In a typical procedure for the synthesis of yttrium sesquioxide colloidal nanocrystals with a nanotriangle shape and a lateral length of 23 ± 0.3 nm, 2.5 mmol of $Y(Ac)_3 \cdot H_2O$ and 4 mmol of $NaNO_3$ were dissolved in a mixture of 25 mmol OLAC, 25 mmol OLAM and 15 mmol ODE. The

reaction mixture was heated at 393 K under vacuum and held at this temperature for 0.5 h. The reaction mixture was then heated to 583 K and kept at this temperature for 0.5 h. After the reaction, the reaction mixture was cooled to room temperature naturally and was purified by washing with an excess of ethanol, followed by centrifugation at 5000 rpm for 10 minutes and redispersed in n-hexane. The purification cycle (the same as in the case of $KLu(WO_4)_2$ sub-micrometric rods) was repeat for three times and the final desired product was either stored in a solution dispersed with n-hexane or stored as a solid powder product after drying it an oven at 333 K for 4 h.

Upon tuning the reaction time, different morphological characteristics of the yttrium oxide colloidal nanocrystals, can be obtained. Thus, keeping the same parameters as in the case of nanotriangles, for a reaction time of 1 h, a mixture of nanotriangles and flower-like type morphologies was obtained as final product. At 2 h of reaction time, the morphology of the final product resembles the nanohearts with average lateral length of 32 ± 0.5 nm.

2.2.3.3. Synthesis of crystalline core@shell sesquioxide nanostructures by thermal decomposition

For the synthesis of colloidal crystalline active core@inert shell Ho, Tm:Y_2O_3@Y_2O_3 nanostructures, the core material Ho, Tm:Y_2O_3 with the nanotriangle morphology was selected. The core materials was synthesized using the same approach as the undoped Y_2O_3, with the exception of the addition of 3 mol% Ho^{3+} and 5 mol% Ho^{3+} as dopants to substitute the Y^{3+} ion in the Y_2O_3 host.

Scheme 2.3. Synthesis of core, core@shell and layer-by-layer colloidal nanocrystals by thermal decomposition. A) The experimental setup used to synthesize the colloidal nanocrystals. Synthesis of the: B) core Ho, Tm:Y_2O_3, C) core@shell and D) layer-by-layer nanoarchitectures.

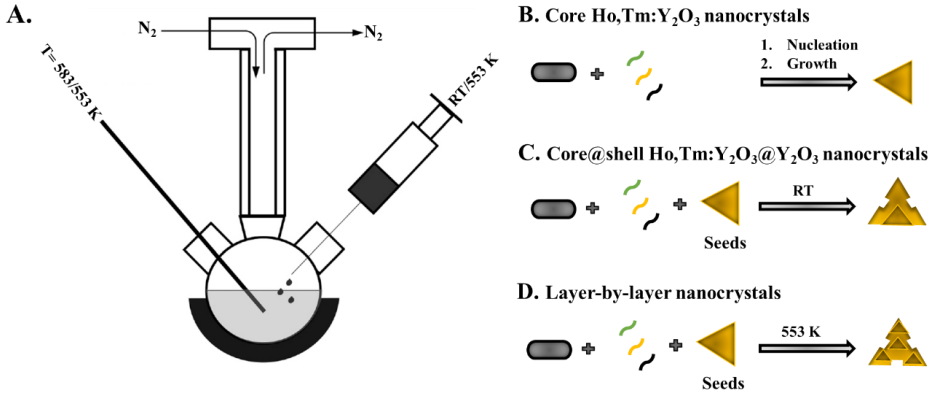

For the synthesis of the core@shell colloidal nanocrystals**,** 2.5 mmol of $Y(Ac)_3 \cdot H_2O$, 4 mmol of $NaNO_3$ and 0.25 g/mL of the already prepared Ho, Tm:Y_2O_3 nanotriangles (dispersed in n-hexane), were mixed at room temperature and dissolved into a solution containing 25 mmol of OLAC, 25 mmol of OLAM and 15 mmol of ODE under vigorous stirring. The reaction mixture was heated at 353 K for 30 min to remove the n-hexane. The mixture was heated under vacuum at 413 K for 30 min to remove the residual water and oxygen. After switching to a nitrogen flow, the reaction temperature was increased to 583 K and held at this temperature for 30 min. After the reaction was completed, the final solution was cooled down to room temperature naturally. A three time purification cycle extracted the final desired product, stored either in a powder or solution form.

Additionally, the core materials predissolved in OLAM, were seeded-growth hot injected at the mixture of the synthesis of the undoped material. In a typical experiment, 2.5 mmol of $Y(Ac)_3 \cdot H_2O$ and 4 mmol of $NaNO_3$ were dissolved into a solution containing 25 mmol of OLAC, 17.5 mmol of OLAM and 15 mmol of ODE with vigorous stirring. The mixture was heated under vacuum at 413 K for 30 min to remove oxygen. After switching to nitrogen flow, the reaction temperature was

increased to 583 K. At this point, predissolved in 12.5 mmol OLAM 0.3 g/mL of the Ho^{3+}, Tm^{3+}:Y_2O_3 nanotriangles, were added at the mixture with a rate of 0.5 mL/min. The rate of the injection was controlled using a syringe pump. After complete injection of the Ho^{3+}, Tm^{3+}:Y_2O_3, which lasted approximately 10 min, the reaction was continued for another 30 min. After the reaction was completed, the final solution was naturally cooled down to room temperature. A three time purification cycle extracted the final desired product, finally stored either in a powder or solution form. The morphology of these nanocrystals resembles that of a layer-by-layer nanostructure with the core material on top of the shell.

A general scheme explaining the thermal decomposition synthesis methodologies that is applied for the synthesis of shell or core, core@shell and layer-by-layer colloidal nanocrystals is depicted in Scheme 2.3.

2.2.4. Digestive ripening of sesquioxide colloidal nanocrystals

In a typical digestive ripening reaction, 0.2 mmol of $Y(Ac)_3 \cdot H_2O$ and 0.1 mmol of NaCl were mixed and dissolved in 45 mmol of OLAM under nitrogen atmosphere. The solution was heated at 553 K using a ramp of 15 K/min. Once the temperature reached 553 K, 15 mmol of OLAC were swiftly injected into the reaction flask. The solution temperature was held at 553 K for 1 h. After the reaction, the solution was naturally cooled down to room temperature. The product of the reaction was extracted by adding excess of ethanol to the solution, followed by centrifugation at 4500 rpm for 10 min, after which the supernatant was discarded and the precipitate was redissolved in n-hexane. This separation step was repeat three times. The rare earth oxide colloidal nanocrystals can be either stored in n-hexane or dried in an oven at 333 K for 4 h to form a solid product.

The same methodology can be applied for the synthesis of other lanthanide oxides, for example, substituting $Y(Ac)_3 \cdot H_2O$ with $Gd(Ac)_3$ and $Yb(Ac)_3$, one can achieve the synthesis of Gd_2O_3 and Yb_2O_3, respectively.

2.3. Characterization Techniques

2.3.1. Structural Characterizations

2.3.1.1. X-Ray Powder Diffraction

Max von Laue, in 1912, discovered that crystalline substances act as three-dimensional diffraction gratings for X-ray wavelengths similar to the spacing of planes in a crystal lattice. X-ray diffraction is now a common technique to analyze crystal structures and atomic spacing.[68] X-ray diffraction is based on constructive interference of monochromatic X-rays and in a crystalline sample. These X-rays are generated by a cathode ray tube, filtered to produce monochromatic radiation, collimated to concentrate, and directed toward the sample. Constructive interference is achieved when the incident beam and the sample obey the Bragg's law condition:[68]

$$n\lambda = 2d\ sin\theta \qquad (2.19)$$

where n, λ, d and θ are the order of the diffracted beam, the wavelength of the incident beam, the interplanar distance in the atomic planes in a crystal and the angle of the incident or scattered beam, respectively. Thus, the Bragg's law correlates the wavelength of the electromagnetic radiation with the diffraction angle and as a consequence, with the lattice spacing in a crystal. Figure 2.4 presents the principles of the X-ray diffraction technique.

The diffracted irradiation is then detected, processed and its intensity counted. Scanning the sample through a range of 2θ, all possible diffraction directions of the lattice are attained due to the random orientation of the powdered material. Conversion of the diffraction peaks to interplanar distance d allows for the identification of the crystal or the structural family where it belongs, because each crystal (or structural family) has a set of unique interplanar distance. Typically, this is achieved by the comparison of the interplanar distance d with standard reference patterns. In this thesis, the Joint Committee on Powder Diffraction Standards (JCPDS) database[69] was used for the identification of the crystal or the structural family.

In this thesis, powder X-ray diffraction measurements were made using a Siemens D5000 diffractometer (Bragg-Brentano parafocusing geometry and vertical θ-θ goniometer) fitted with a curved graphite diffracted-beam monochromator, incident and diffracted-beam Soller slits, a 0.06° receiving slit and scintillation counter as a detector. The angular 2θ diffraction range used was between 5 and 70°. The data were collected with an angular step of 0.05° at 3s per step and sample rotation to increase the probability of diffraction of all possible atomic planes. Cu K_α radiation was obtained from a copper X-ray tube operated at 40 kV and 30 mA.

In addition, we implemented X-ray powder diffraction studies to investigate the effect of the temperature on the crystalline structure when needed. For that, the temperature dependent X-ray powder diffraction measurements were recorded using a Bruker-AXS D8-Discover diffractometer equipped with parallel incident beam (Göbel mirror), vertical θ-θ goniometer, XYZ motorized stage and a GADDS (General Area Detector Diffraction System). Samples were placed directly on the sample holder and the area of interest was selected with the aid of a video-laser focusing system. An X-ray collimator system allows to analyse areas of 500 μm. The X-ray diffractometer was operated at 40 kV and 40 mA to generate Cu K_α radiation. The GADDS detector was a HI-STAR (multiwire proportional counter of 30 × 30 cm with 1024 × 1024 pixels). We collected one frame (2D XRD patterns) covering 2θ= 12-45º with a detector-sample distance of 15 cm. The exposition time was 300 s per frame. The resulting frames were both gamma integrated to obtain a 2θ diffractogram. Identification of the different crystalline phases was achieved by comparison of the XRD pattern with the ICDD data base[69] (release 2007) using Diffrac^{plus} Evaluation software (Bruker 2007). The temperature was controlled with a MRI BTS-Solid temperature sample stage (Pt heating ribbon heating stage). The X-ray diffraction patterns were collected from room temperature up to 1273 K with heating at a rate of 10 K/min. The sample was maintained during 60 s at the desired temperature before starting the measurement. The temperature stage was covered with a beryllium (Be) dome and an air static atmosphere was used throughout the measurement.

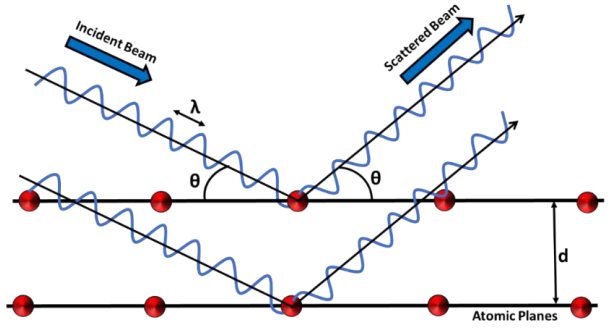

Figure 2.4. Principle of X-ray diffraction technique.

2.3.1.2. Raman Spectroscopy

When a monochromator laser light with energy $E_1=hv_1$ and corresponding wavelength λ_1, it excites molecules and transforms them into oscillating dipoles. These dipoles emit light of three different modes (Figure 2.5): (i) elastic Rayleigh scattering mode (Figure 2.5 (b)), when a molecule absorbs a photon with frequency v_1 or wavelength λ_1 and emit light with the same frequency and wavelength as the excitation source ($v_1=v_2$ and $\lambda_1=\lambda_2$) when relaxing back to the ground state, (ii) Raman scattering:Stokes shift mode (Figure 2.5 (a)), when a molecule absorbs a photon with frequency v_1 or wavelength λ_1, after a non-radiative relaxation process to the excited state 2 with a loss of a part of the energy, the following emissive transition from the excited state 2 back to the ground state 0 will generate photon emission with less energy (higher frequency $v_1>v_2$ and lower wavelength $\lambda_1<\lambda_2$) than the excitation source, due to the law of energy conservation,[70] and (iii) Raman scattering: Anti-Stokes shift mode (Figure 2.5 (c)), when a molecule is excited from the ground state to a higher energy level by two-photon absorption, hot band absorption or upconversion processes,[70] then jumps back to the ground state by generating one photon with

higher energy energy (lower frequency $v_1<v_2$ and higher wavelength $\lambda_1>\lambda_2$) than either of the absorbed photons.

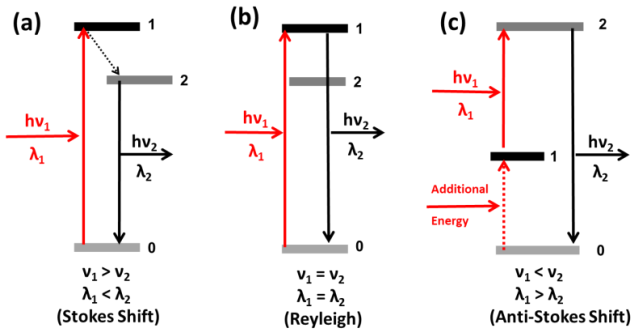

Figure 2.5. Scattering of light by molecule.

The Raman scattering modulations are specific to molecular vibration and phonon in crystal, thus, it is possible to analyze composition of material or crystal lattice information by analyzing spectrum of Raman scattered light. This analysis method is Raman spectroscopy. In the Raman spectrum, the Anti-Stokes peaks are weaker than the Stokes peaks and both peaks intensities are proportional to the fourth of the frequency of the energy of the laser used to excite them. The Raman spectrum is recorded via absorptions of the photons provide from the excitation laser source and reemission. The frequency of the emitted photons is shifted up or down in comparison with original frequency provided from the laser source, due to the Raman effect. This shifting in frequency provides information about vibrational, rotational and other low frequency transitions in the crystals.

The Raman spectroscopy was used in this thesis to reveal the role of the phonon energy values in the multiphonon non-radiative decay processes, which will be related to the ability of the crystals to convert the absorbed light into heat. In addition, the vibrational modes observed were used to confirm the formation of desired crystalline phases. In this thesis, a micro-Raman analysis was performed, using a Renishaw inVia Reflex microscope with the unpolarized light from a 514 nm argon laser focused on the sample by a 50x Leica objective. Analysis were performed from the range of 200–2000 cm^{-1}, using a grating with 2400 lines per mm and an exposure time of 10 s.

2.3.2. Morphological Characterizations

2.3.2.1. Transmission electron microscopy

Transmission electron microscopy (TEM) is a technique in which high an energy electron beam, generated from an electron gun, is allowed to strike a very thin sample. The electron beam is transmitted through the sample and generates an image providing information about the size and shape of the sample.[71] The TEM operates in the same principle as a light microscope, but uses electron radiation, with a much shorter wavelength, instead of visible light.

In this thesis, TEM images were acquired using a JEOL JEM-1011 electron microscope operating at an accelerating voltage of 100 kV. For the preparation of the TEM grids, 7-15 µL of nanocrystals dispersed in apolar or polar solvents, were placed on the surface of a copper grid covered by a holey carbon film (HD200 Copper Formvar/carbon). Thus, nanocrystals such as $KLu(WO_4)_2$ obtained after a calcination process, were dispersed either in distilled water or ethanol, whereas the colloidal nanocrystals synthesized by the thermolysis or the digestive ripening processes, were dispersed in apolar solvents such as n-hexane, toluene or cyclohexane.

2.3.2.2. High resolution transmission electron microscopy

High resolution transmission electron microscopy (HRTEM) is a TEM imaging mode that allows the imaging of the crystallographic structure of a sample at an atomic level.[72] HRTEM uses the transmitted and the scattered electron beam to create an interference image. The outgoing-

modulated electron waves at very low angles interfere with themselves during propagation through the objective lens. All electrons emerging from the specimen are combined at a point in the image plane. HRTEM has been extensively and successfully used for analyzing crystal structures and lattice imperfections in various kinds of advanced materials on an atomic resolution scale. It can be used for the characterization of point defects, stacking faults, dislocations, interferences, precipitates, grain boundaries, and surface structures. Difference between TEM and HRTEM rely on the spatial resolution of the image generated. TEM resolution is limited by spherical and chromatic aberrations of the magnetic lenses used and reaches a limit of 0.5 Å. In the contrary, HRTEM resolution reaches below 0.5 Å due to the incorporation of monochromator and a Cs corrector.[72] With this high resolution, it is possible to image crystal structures, defects in the crystal, and individual atoms.[72]

In this thesis, a JEM-2100 high resolution transmission electron microscopy (HRTEM) operating at 300 kV was used to identify the shape of yttrium oxide colloidal nanocrystals synthesized via the thermal decomposition method and digestive ripening mechanism.

2.3.3. Thermal Characterizations

Thermogravimetric Analysis (TGA) is a technique in which the mass of a material is monitored as a function of temperature or time as the sample specimen is subjected to a controlled temperature program in a controlled atmosphere.[73] Traditionally, TGA is used in combination with Differential Thermal Analysis (DTA). In DTA, the material under study and a reference material undergo identical thermal cycles, (*i.e.* same cooling or heating cycles) while recording any temperature difference between the sample and the reference material.[73] The detected temperature difference is plotted against time or temperature, providing information about oxidation, decomposition, melting, crystallization or phase transition, leading to endothermic or exothermic processes in the sample. Figure 2.6 presents a scheme of the setup of DTA.

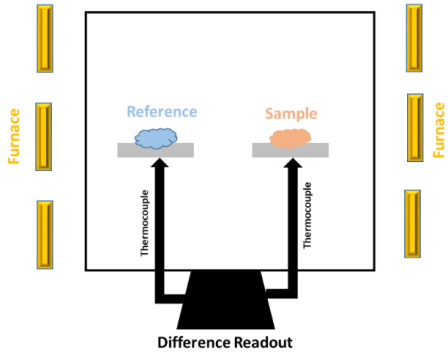

Figure 2.6. Setup of Differential Thermal Analysis technique.

In this thesis, DTA and TGA were used to study the thermal evolution of the seeds and final products obtained from the solvothermal methodologies, with the temperature, by using a TA Instruments SDT 2960 simultaneous differential scanning calorimetry−thermogravimetric analysis system. The heating rate was at 10 $Kmin^{-1}$ with an air flux of 90 cm^3min^{-1} and the Al_2O_3 was used as a reference.

2.3.4. Surface Characterization

2.3.4.1. Fourier Transform-Infrared Spectroscopy

To confirm the presence of organic surfactants onto the surface of formed colloidal nanocrystals, we investigated the functional groups present on their surface by Fourier Transform-Infrared Spectroscopy (FT-IR). FTIR is an analytical technique used to identify organic (and in some cases inorganic) materials. This technique measures the absorption of infrared radiation by the sample

material versus the wavelength of the excitation radiation. The infrared absorption bands identify molecular components and/or vibrations in a crystal. When a material is irradiated with infrared radiation, absorbed IR radiation usually excites the matter into a higher vibrational state. The wavelength of light absorbed corresponds to the energy difference between the at-rest and excited vibrational states.

The FT-IR spectrometer uses an interferometer to modulate the wavelength from a broadband infrared source. A detector measures the intensity of the transmitted or reflected light as a function of its wavelength. The signal obtained from the detector is an interferogram, which must be analyzed by a computer using Fourier transforms to obtain the infrared spectrum. The FT-IR spectra are usually presented as plots of intensity versus wavenumber (in cm^{-1}).

In this thesis, the infrared spectra were recorded in the range of 400-4000 cm^{-1} with a resolution of 2 cm^{-1} on a FT-IR IluminatIR II, Smith spectrophotometer, to investigate the presence of different functional groups on the surface of the synthesized nanomaterials.

2.3.4.2. Proton Nuclear Magnetic Resonance (^{1}H NMR) Spectroscopy

An additional technique for the detection of the organic surfactants on the surface of the synthesized colloidal nanocrystals is proton nuclear magnetic resonance (^{1}H NMR). In general, ^{1}H NMR is a technique is quite often applied in organic chemistry to study hydrogen-containing molecules. Protons, when exposed to a magnetic field, can spin and this will induce a magnetic dipole moment. When exposed to this magnetic field, the protons will orient themselves along the field. However, protons have two magnetic dipole moment orientations, hence when exposed to the magnetic field, they can align with the same direction as the field, known as spin-up (+1/2), or align opposite to the field, known as spin-down (-1/2). The spin-up state has lower in energy and is a more stable spin state.

If an electromagnetic wave with a precise frequency is directed towards the spin-up state, the spin-up proton will absorb the energy and transition to the spin-down state. At this stage, it is said that these protons undergo resonance and this frequency is known as the resonance frequency or chemical shift. Different hydrogens in molecules can have different chemical shift values. These values can be determined by acquiring ^{1}H NMR analysis.

Within this thesis, pure colloidal nanocrystals were prepared for ^{1}H NMR analysis by dissolving 5 mg of the nanocrystals in 0.5 mL of deuterated chloroform, provided from Sigma Aldrich. ^{1}H NMR measurements were measured at room temperature and recorded on a Bruker Avance Neo spectrometer operating at a ^{1}H frequency of 400 MHz and featuring a broadband-inverse (BBI) probe.

2.3.5. Spectroscopic Characterization

When light interacts with a material, light can be absorbed, transmitted, scattered or reflected. When part of the light is absorbed, in the case of lanthanide doped materials, it can be converted simultaneously into photoluminescence and heat generation, due to existence of the radiative and non-radiative depopulation processes. Here, we describe shortly the experiments based on the measurements of the optical absorbance for the evaluation of the antioxidant properties of lanthanide doped materials. In addition, also for the ex-vivo experiments carried under Ho, Tm doped KLuW particles, related to the recording of the transmittance of the chicken breast piece of meat. In addition, we underline the techniques used to measure the photoluminescence (either visible or III-BW), temperature-dependence of the photoluminescence ((either visible or III-BW), and heat generation from the lanthanide doped particles.

2.3.5.1. Optical absorption and transmittance

Absorption spectroscopy portrays a spectroscopic technique that measures the absorption of light from a sample as a function of the wavelength. The variation of the intensity of the absorption varies as a function of the wavelength. This variation is represent with the absorption spectrum. This spectroscopy technique is employed as a tool to determine the presence of a particles substance in a sample, and in addition can quantify the amount of the substance present. This quantification follows the Lambert-Beer law. This law relates the optical attenuation of a material

containing a single attenuating species of uniform concentration to the optical path length through the sample and absorptivity of the species by the following equation:

$$A = \varepsilon C l \qquad (2.20)$$

where A is the absorbance of the sample, ε is the molar attenuation coefficient or absorptivity of the attenuating species, l is the optical path length, and C is concentration of the attenuating species.

From the absorbance, also the transmittance T of the same material sample can be correlated by using the equation:

$$T = 10^{-A} \qquad (2.21)$$

The optical absorption or transmission within this thesis, were measured an Agilent Cary 5000 UV-Vis-NIR spectrophotometer. This spectrophotometer is operative in the spectral range from 350 to 2500 nm with a limiting spectral resolution of <0.05 nm in the UV-Vis range and of <0.2 nm in the NIR range. The UV light source is a deuterium flash lamp and the Vis-IR light source a quartz halogen lamp. The UV-Vis light is detected by a silicon photodetector and the IR light is detected by a lead sulphide detector called PbSmart.

2.3.5.2. Photoluminescence

A general scheme of the setup used to measure the photoluminescence of the lanthanide doped materials during this thesis, is presented in Figure 2.7. In a typical photoluminescence measurement for Ho, Tm doped nanoparticles operating in the III-BW, the emission spectra were recorded in a Yokogawa AQ6375 optical spectrum analyzer in the range from 1350 nm to 2200 nm, with a resolution of 2 nm and an integration time of 1 s. The nanoparticles were excited by a 808 nm fiber-coupled diode laser (Thorlabs) with a power range from 0.2 mW to 1 W, and the beam was focused on the sample using a 20× microscope objective (numerical aperture 0.4) and bringing a spot diameter of around 1 μm in the sample. The excitation density is around 100 W/cm^2. The scattered excitation radiation was eliminated by using a 850 nm longpass dichroic filter (Thorlabs).

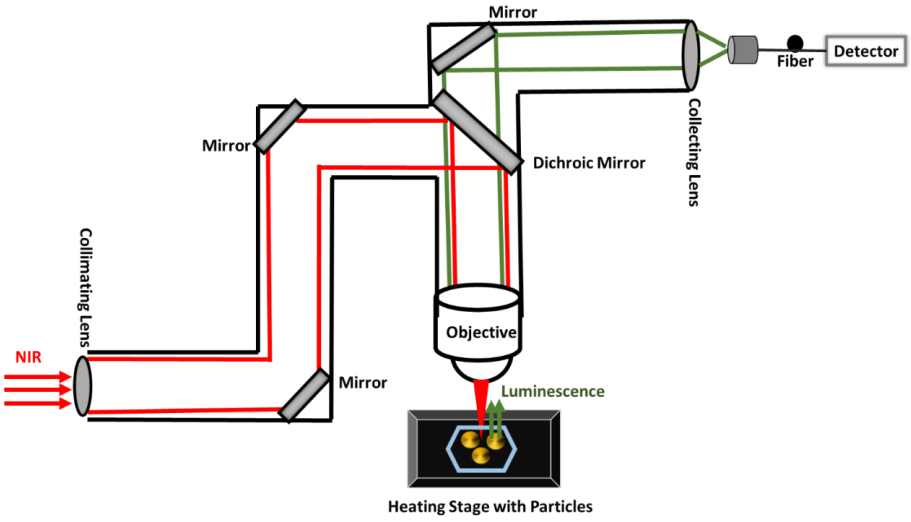

Figure 2.7. General scheme of the setup used to measure the photoluminescence of the lanthanide doped materials. In red line the NIR excitation source, in green the generated luminescence.

Additionally, these lanthanide doped materials have been investigated as thermal sensors in the visible and in the III-BW. To deduce their ability to sense temperature changes, the variation of the photoluminescence with the change of temperature (either in the physiological range or up to

473 K) was investigated. For this analysis, the methodology was the same, except that the doped materials were introduced inside a heating stage (Linkam, THMS 600) equipped with a boron disk for improved temperature distribution. The temperature accuracy of the heating stage was in the range of ± 0.3 K.

The experimental setup to measure the photoluminescence and the temperature-dependence of the photoluminescence for Ho, Tm doped yttrium oxide (cores, core@shell and layer-by-layer nanoarchitectures) was similar, except the change in the power of the laser used and the temperature at which the particles were exposed to.

In addition for Ho, Tm doped yttrium oxide, the same experimental setup was used to record the white light generated upon high 808 nm laser power from 0.6 W to 1 W. The white emission spectra were recorded in a range from 400 nm to 2200 nm, where the recorded emissions were separated in three regions: 400 nm-800 nm, using a 750 nm shortpass dichroic filter (Thorlabs), 850 nm-1200 nm using a 850 nm longpass dichroic filter (Thorlabs) and a Yokogawa AQ6373 optical spectrum analyzer, and 1200 nm-2200 nm using a 850 nm longpass dichroic filter (Thorlabs) using a Yokogawa AQ6375 optical spectrum analyzer, operative with resolution 2 nm and integration time of 1 s.

2.3.5.3. Photothermal conversion efficiency

In this thesis, we measured the ability of the lanthanide doped materials to convert the absorbed NIR light into heat via the integrated sphere methodology.[74]

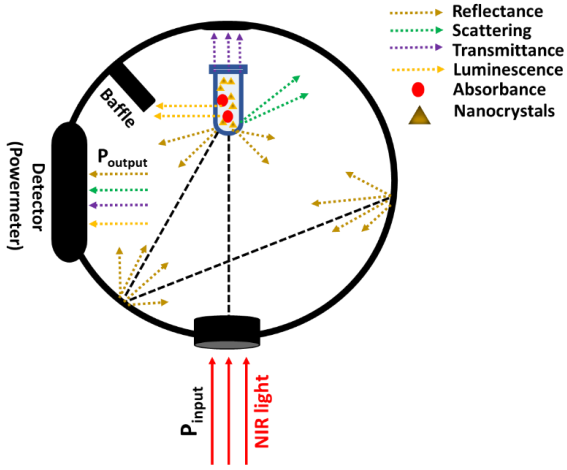

Figure 2.8. The principle of the integrated sphere method to determine the photothermal conversion efficiency.

A general scheme of the integrated sphere and the phenomena taking place, are presented in Figure 2.8. In general, a glass cuvette containing lanthanide doped materials dispersed in water or apolar organic solvents with a concentration of around 100 mg/mL, is placed inside the integrating sphere, aligned to the NIR laser irradiation with different powers. The NIR irradiation is achieved by a diode laser in the NIR wavelength region (808 nm) with different laser powers ranging from 0.2 W to 3 W. This NIR laser from the fiber tip generates a circular spot size of 5 mm in diameter on the sample. A baffle was introduced in the integrating sphere, between the sample and the detector, in order to prevent the direct reflections from the sample to the detector. The signal was collected using a powermeter Ophir Nova II.

Using the integrated sphere method, the photothermal conversion efficiency η is calculated from the expression:[74]

$$\eta = \left| \frac{P_{blank} - P_{sample}}{P_{empty} - P_{sample}} \right| x\ 100\% \qquad (2.22)$$

where P_{blank}, P_{empty} and P_{sample} are the power values measured for the solvent (distilled water or apolar solvents), the empty sample holder and the nanomaterials doped with Ho^{3+} and Tm^{3+}, respectively.

2.4. References

1. Kwon, S. G.; Hyeon, T., Colloidal chemical synthesis and formation kinetics of uniformly sized nanocrystals of metals, oxides, and chalcogenides. *Accounts of Chemical Research* **2008,** 41 (12), 1696-1709.
2. Kwon, S. G.; Hyeon, T., Formation mechanisms of uniform nanocrystals via hot-Injection and heat-up methods. *Small* **2011,** 7 (19), 2685-2702.
3. Strey, R.; Wagner, P. E.; Viisanen, Y., The problem of measuring homogeneous nucleation rates and the molecular contents of nuclei: progress in the form of nucleation pulse measurements. *Journal of Physical Chemistry* **1994,** 98 (32), 7748-7758.
4. Erdemir, D.; Lee, A. Y.; Myerson, A. S., Nucleation of crystals from solution:classical and two-step models. *Accounts of Chemical Research* **2009,** 42 (5), 621-629.
5. Polte, J., Fundamental growth principles of colloidal metal nanoparticles-a new perspective. *CrystEngComm* **2015,** 17 (36), 6809-6830.
6. Sugimoto, T., Chapter 8-Control of particle characteristics. In *Monodispersed Particles*, Sugimoto, T., Ed. Elsevier: Amsterdam, **2001**; pp 368-452.
7. R. Viswanatha, D. D.Sarma, Growth of nanocrystals in solution. In *Nanomaterials Chemistry*, **2007**, pp 139-170.
8. Thanh, N. T. K.; Maclean, N.; Mahiddine, S., Mechanisms of nucleation and growth of nanoparticles in solution. *Chemical Reviews* **2014,** 114 (15), 7610-7630.
9. Mer, V. K. L., Nucleation in Phase Transitions. *Industrial & Engineering Chemistry* **1952,** 44 (6), 1270-1277.
10. LaMer, V. K.; Dinegar, R. H., Theory, production and mechanism of formation of monodispersed hydrosols. *Journal of the American Chemical Society* **1950,** 72 (11), 4847-4854.
11. Ostwald, W., ÜBer Die Vermeintliche isomerie des roten und gelben quecksilberoxyds und die oberflächenspannung fester köRper. *Zeitschrift für Physikalische Chemie* **1900,** 34, 495-503.
12. Shimpi, J. R.; Sidhaye, D. S.; Prasad, B. L. V., Digestive ripening: a fine chemical machining process on the nanoscale. *Langmuir* **2017,** 33 (38), 9491-9507.
13. Zheng, H.; Smith, R. K.; Jun, Y.; Kisielowski, C.; Dahmen, U.; Alivisatos, A. P., Observation of single colloidal platinum nanocrystal growth trajectories. *Science* **2009,** *324* (5932), 1309-1312.
14. Niederberger, M.; Cölfen, H., Oriented attachment and mesocrystals: Non-classical crystallization mechanisms based on nanoparticle assembly. *Physical Chemistry Chemical Physics* **2006,** 8 (28), 3271-3287.
15. Peng, X.; Manna, L.; Yang, W.; Wickham, J.; Scher, E.; Kadavanich, A.; Alivisatos, A. P., Shape control of CdSe nanocrystals. *Nature* **2000,** 404 (6773), 59-61.
16. Peng, Z. A.; Peng, X., Mechanisms of the shape evolution of CdSe nanocrystals. *Journal of the American Chemical Society* **2001,** 123 (7), 1389-1395.
17. Murphy, C. J.; Sau, T. K.; Gole, A. M.; Orendorff, C. J.; Gao, J.; Gou, L.; Hunyadi, S. E.; Li, T., Anisotropic metal nanoparticles: synthesis, assembly, and optical applications. *Journal of Physical Chemistry B* **2005,** 109 (29), 13857-13870.
18. Xia, Y.; Xiong, Y.; Lim, B.; Skrabalak, S. E., Shape-controlled synthesis of metal nanocrystals: simple chemistry meets complex physics? *Angewandte Chemie International Edition* **2009,** 48 (1), 60-103.
19. Li, X.; Wang, M.; Shen, H.; Zhang, Y.; Wang, H.; Li, L. S., Inorganic SnX-complex-induced 1D, 2D, and 3D copper sulfide superstructures from anisotropic hexagonal nanoplate building blocks. *Chemistry An European Journal* **2011,** 17 (37), 10357-10364.
20. Li, X.; Si, H.; Niu, J. Z.; Shen, H.; Zhou, C.; Yuan, H.; Wang, H.; Ma, L.; Li, L. S., Size-controlled syntheses and hydrophilic surface modification of Fe_3O_4, Ag, and Fe_3O_4/Ag heterodimer nanocrystals. *Dalton Transactions* **2010,** 39 (45), 10984-10989.
21. Li, X.; Niu, J. Z.; Shen, H.; Xu, W.; Wang, H.; Li, L. S., Shape controlled synthesis of tadpole-like and heliotrope seed-like $AgInS_2$ nanocrystals. *CrystEngComm* **2010,** 12 (12), 4410-4415.
22. Talapin, D. V.; Lee, J. S.; Kovalenko, M. V.; Shevchenko, E. V., Prospects of colloidal nanocrystals for electronic and optoelectronic applications. *Chemical Reviews* **2010,** 110 (1), 389-458.
23. Kamat, P. V., Quantum Dot Solar Cells. Semiconductor nanocrystals as light harvesters. *Journal of Physical Chemistry C* **2008,** 112 (48), 18737-18753.
24. Algar, W. R.; Susumu, K.; Delehanty, J. B.; Medintz, I. L., Semiconductor quantum dots in bioanalysis: crossing the valley of death. *Analytical Chemistry* **2011,** 83 (23), 8826-8837.
25. Nozik, A. J.; Beard, M. C.; Luther, J. M.; Law, M.; Ellingson, R. J.; Johnson, J. C., Semiconductor quantum dots and quantum dot arrays and applications of multiple exciton generation to third-generation photovoltaic solar cells. *Chemical Reviews* **2010,** 110 (11), 6873-6890.
26. Konstantatos, G.; Sargent, E. H., Nanostructured materials for photon detection. *Nature Nanotechnology* **2010,** *5* (6), 391-400.

27. Labrador-Páez, L.; Ximendes, E. C.; Rodríguez-Sevilla, P.; Ortgies, D. H.; Rocha, U.; Jacinto, C.; Martín Rodríguez, E.; Haro-González, P.; Jaque, D., Core-shell rare-earth-doped nanostructures in biomedicine. *Nanoscale* **2018,** 10 (27), 12935-12956.
28. Qiao, S. Z.; Liu, J.; Max Lu, G. Q., Chapter 21-Synthetic Chemistry of Nanomaterials. In *Modern Inorganic Synthetic Chemistry (Second Edition)*, Xu, R.; Xu, Y., Eds. Elsevier: Amsterdam, 2017; pp 613-640.
29. Wu, Y.; Wang, D.; Li, Y., Understanding of the major reactions in solution synthesis of functional nanomaterials. *Science China Materials* **2016,** 59 (11), 938-996.
30. Jun, Y.; Choi, J.; Cheon, J., Shape control of semiconductor and metal oxide nanocrystals through nonhydrolytic colloidal routes. *Angewandte Chemie International Edition* **2006,** 45 (21), 3414-3439.
31. Park, J.; Lee, E.; Hwang, N. M.; Kang, M.; Kim, S. C.; Hwang, Y.; Park, J. G.; Noh, H. J.; Kim, J. Y.; Park, J. H.; Hyeon, T., One-nanometer-scale size-controlled synthesis of monodisperse magnetic iron oxide nanoparticles. *Angewandte Chemie* **2005,** 44 (19), 2872-2877.
32. Zha, J.; Roggendorf, H., Sol-gel science, the physics and chemistry of sol-gel processing, Ed. by C. J. Brinker and G. W. Scherer. *Academic Press, Boston* **1991,** 3 (10), 522-522.
33. Pechini, M. P. Method of preparing lead and alkaline earth titanates and niobates and coating method using the same to form a capacitor. US Patent No. 3330697, 1967.
34. Danks, A. E.; Hall, S. R.; Schnepp, Z., The evolution of 'sol-gel' chemistry as a technique for materials synthesis. *Materials Horizons* **2016,** 3 (2), 91-112.
35. Rudisill, S. G.; Shaker, S.; Terzic, D.; Le Maire, R.; Su, B. L.; Stein, A., Generalized approach to the microstructure direction in metal oxide ceramics via polymerization-induced phase separation. *Inorganic Chemistry* **2015,** 54 (3), 993-1002.
36. Rudisill, S. G.; Hein, N. M.; Terzic, D.; Stein, A., Controlling microstructural evolution in Pechini gels through the interplay between precursor complexation, step-growth polymerization, and template confinement. *Chemistry of Materials* **2013,** *25* (5), 745-753.
37. Motta, M.; Deimling, C. V.; Saeki, M. J.; Lisboa-Filho, P. N., Chelating agent effects in the synthesis of mesoscopic-size superconducting particles. *Journal of Sol-Gel Science and Technology* **2008,** 46 (2), 201-207.
38. Motta, M.; Deimling, C.; Saeki, M.; Lisboa-Filho, P., Chelating agent effects in the synthesis of mesoscopic-size superconducting particles. *Journal of Sol-Gel Science and Technology* **2008,** 46, 201-207.
39. Galceran, M.; Pujol, M.; Aguiló, M.; Díaz, F., Sol-gel modified Pechini method for obtaining nanocrystalline $KRE(WO_4)_2$ (RE=Gd and Yb). *Journal of Sol-Gel Science and Technology* **2007,** 42, 79-88.
40. Xu, G.; Ma, H.; Zhong, M.; Zhou, J.; Yue, Y.; He, Z., Influence of pH on characteristics of $BaFe_{12}O_{19}$ powder prepared by sol-gel auto-combustion. *Journal of Magnetism and Magnetic Materials* **2006,** 301 (2), 383-388.
41. Jambunathan, V.; Mateos, X.; Pujol, M. C.; Carvajal, J. J.; Massons, J.; Aguiló, M.; Díaz, F., Near-infrared photoluminescence from Ho^{3+}-doped monoclinic $KLu(WO_4)_2$ crystal codoped with Tm^{3+}. *Journal of Luminescence* **2009,** 129 (12), 1882-1885.
42. Petrov, V.; Cinta Pujol, M.; Mateos, X.; Silvestre, Ò.; Rivier, S.; Aguiló, M.; Solé, R. M.; Liu, J.; Griebner, U.; Díaz, F., Growth and properties of $KLu(WO_4)_2$, and novel ytterbium and thulium lasers based on this monoclinic crystalline host. *Laser & Photonics Reviews* **2007,** 1 (2), 179-212.
43. Demazeau, G., Solvothermal reactions: an original route for the synthesis of novel materials. *Journal of Materials Science* **2008,** 43 (7), 2104-2114.
44. Park, J.; An, K.; Hwang, Y.; Park, J. G.; Noh, H. J.; Kim, J. Y.; Park, J. H.; Hwang, N. M.; Hyeon, T., Ultra-large-scale syntheses of monodisperse nanocrystals. *Nature Materials* **2004,** 3 (12), 891-895.
45. Chen, M.; Wu, B.; Yang, J.; Zheng, N., Small adsorbate-assisted shape control of Pd and Pt nanocrystals. *Advanced Materials* **2012,** 24 (7), 862-879.
46. Lohse, S. E.; Murphy, C. J., The quest for shape control: a history of gold nanorod synthesis. *Chemistry of Materials* **2013,** 25 (8), 1250-1261.
47. Yin, Y.; Alivisatos, A. P., Colloidal nanocrystal synthesis and the organic-inorganic interface. *Nature* **2005,** *437* (7059), 664-670.
48. Fan, L.; Guo, R., Growth of dendritic silver crystals in CTAB/SDBS mixed-surfactant solutions. *Crystal Growth & Design* **2008,** 8 (7), 2150-2156.
49. Warner, J. H.; Cao, H., Shape control of PbS nanocrystals using multiple surfactants. *Nanotechnology* **2008,** 19 (30), 305605.
50. van Embden, J.; Chesman, A. S. R.; Jasieniak, J. J., The heat-up synthesis of colloidal nanocrystals. *Chemistry of Materials* **2015,** 27 (7), 2246-2285.
51. Pileni, M. P., Control of the size and shape of inorganic nanocrystals at various scales from nano to macrodomains. *The Journal of Physical Chemistry C* **2007,** 111 (26), 9019-9038.
52. Si, R.; Zhang, Y. W.; Zhou, H. P.; Sun, L. D.; Yan, C. H., Controlled-synthesis, self-assembly behavior, and surface-dependent optical properties of high-quality rare-earth oxide nanocrystals. *Chemistry of Materials* **2007,** 19 (1), 18-27.
53. Wang, D.; Kang, Y.; Ye, X.; Murray, C. B., Mineralizer-assisted shape-control of rare earth oxide nanoplates. *Chemistry of Materials* **2014,** 26 (22), 6328-6332.
54. Jeong, J.; Kim, N.; Kim, M. G.; Kim, W., Generic synthetic route to monodisperse sub-10 nm lanthanide oxide nanodisks: a modified digestive ripening orocess. *Chemistry of Materials* **2016,** 28 (1), 172-179.

55. Boyer, J. C.; Vetrone, F.; Cuccia, L. A.; Capobianco, J. A., Synthesis of colloidal upconverting $NaYF_4$ nanocrystals doped with Er^{3+}, Yb^{3+} and Tm^{3+}, Yb^{3+} via thermal decomposition of lanthanide trifluoroacetate precursors. *Journal of the American Chemical Society* **2006,** 128 (23), 7444-7445.
56. Ye, X.; Collins, J. E.; Kang, Y.; Chen, J.; Chen, D. T. N.; Yodh, A. G.; Murray, C. B., Morphologically controlled synthesis of colloidal upconversion nanophosphors and their shape-directed self-assembly. *Proceedings of the National Academy of Sciences* **2010,** 107 (52), 22430-22435.
57. Na, H.; Woo, K.; Lim, K.; Jang, H. S., Rational morphology control of β-$NaYF_4$:Yb,Er/Tm upconversion nanophosphors using a ligand, an additive, and lanthanide doping. *Nanoscale* **2013,** 5 (10), 4242-4251.
58. Wang, J.; Deng, R.; MacDonald, M. A.; Chen, B.; Yuan, J.; Wang, F.; Chi, D.; Andy Hor, T. S.; Zhang, P.; Liu, G.; Han, Y.; Liu, X., Enhancing multiphoton upconversion through energy clustering at sublattice level. *Nature Materials* **2014,** 13 (2), 157-162.
59. Wang, Z. J.; Zhang, Y. L.; Zhong, J. P.; Yao, H. H.; Wang, J.; Wu, M. M.; Meijerink, A., One-step synthesis and luminescence properties of tetragonal double tungstates nanocrystals. *Nanoscale* **2016,** 8 (34), 15486-15489.
60. Cascales, C.; Paíno, C. L.; Bazán, E.; Zaldo, C., Ultrasmall, water dispersible, TWEEN80 modified Yb:Er:$NaGd(WO_4)_2$ nanoparticles with record upconversion ratiometric thermal sensitivity and their internalization by mesenchymal stem cells. *Nanotechnology* **2017,** 28 (18), 185101.
61. Bu, W.; Chen, Z.; Chen, F.; Shi, J., Oleic acid/oleylamine cooperative-controlled crystallization mechanism for monodisperse tetragonal bipyramid $NaLa(MoO_4)_2$ nanocrystals. *Journal of Physical Chemistry C* **2009,** 113 (28), 12176-12185.
62. Si, R.; Zhang, Y. W.; You, L. P.; Yan, C. H., Rare-Earth oxide nanopolyhedra, nanoplates, and nanodisks. *Angewandte Chemie International Edition* **2005,** 44 (21), 3256-3260.
63. Paek, J.; Lee, C. H.; Choi, J.; Choi, S. Y.; Kim, A.; Lee, J. W.; Lee, K., Gadolinium oxide nanoring and nanoplate: anisotropic shape control. *Crystal Growth and Design* **2007,** 7 (8), 1378-1380.
64. Huo, Z.; Tsung, C. K.; Huang, W.; Fardy, M.; Yan, R.; Zhang, X.; Li, Y.; Yang, P., Self-organized ultrathin oxide nanocrystals. *Nano Letters* **2009,** 9 (3), 1260-1264.
65. Zhang, Q.; Yan, B., Salt-effect-based synthesis and anomalous magnetic properties of rare-earth oxide nanosheets with sub-1 nm thickness. *Chemistry A European Journal* **2012,** 18 (17), 5150-5154.
66. Cao, Y. C., Synthesis of square gadolinium oxide nanoplates. *Journal of the American Chemical Society* **2004,** 126 (24), 7456-7457.
67. Naccache, R.; Yu, Q.; Capobianco, J. A., The fluoride host: nucleation, growth, and upconversion of lanthanide-doped nanoparticles. *Advanced Optical Materials* **2015,** 3 (4), 482-509.
68. Bashir, S.; Liu, J., Chapter 3-Nanocharacterization. In *Advanced Nanomaterials and their Applications in Renewable Energy*, Liu, J. L.; Bashir, S., Eds. Elsevier: Amsterdam, 2015; pp 117-180.
69. The International Centre for Diffraction Data..
70. Lakowicz, J., *Principles of Fluorescence Spectroscopy*. 2006; Vol. 1.
71. Goodhew, P., General Introduction to Transmission Electron Microscopy (TEM). 2011; pp 1-19.
72. Titus, D.; James Jebaseelan Samuel, E.; Roopan, S. M., Chapter 12-Nanoparticle characterization techniques. In *Green Synthesis, Characterization and Applications of Nanoparticles*, Shukla, A. K.; Iravani, S., Eds. Elsevier: 2019; pp 303-319.
73. Groenewoud, W. M., Chapter 2-Thermogravimetry. In *Characterisation of Polymers by Thermal Analysis*, Groenewoud, W. M., Ed. Elsevier Science B.V.: Amsterdam, 2001; pp 61-76.
74. Savchuk, O. A.; Carvajal, J. J.; Massons, J.; Aguiló, M.; Díaz, F., Determination of photothermal conversion efficiency of graphene and graphene oxide through an integrating sphere method. *Carbon* **2016,** 103, 134-141.

Chapter III

Self-assessing photothermal properties of Ho, Tm:KLuW materials in the III-BW

Doping monoclinic $KLu(WO_4)_2$ (hereafter KLuW) with holmium (Ho^{3+}) and thulium (Tm^{3+}) ions, allows for the application of these materials as self-assessed photothermal agents, *i.e.* these materials can simultaneously act as thermal sensors and photothermal agents, due to the presence of radiative and non-radiative processes, when excited with light, developing multifuctional nanoparticles in which the release of heat and the determination of the temperature *in situ* through the light emitted by them are combined in a single nanoparticle. The advantage of these self-assessed photothermal agents is the ability to self-determine the temperature of a system using luminescence nanothermometry, without the need of an external thermal probe.

Monoclinic KLuW is chosen as a host due to the high chemical stability, high absorption and emission cross section for lanthanide ions and the ability of incorporating high concentration of doping ions without fluorescence quenching.

The self-assessing photothermal properties of these materials were tested and compared as a function of the method of synthesis of these materials. Ho, Tm:KLuW nanocrystals and microcrystals were synthesized via four different synthetic methodologies: (i) the modified sol-gel Pechini, (ii) the conventional heating assisted solvothermal method, (iii) the microwave-assisted solvothermal method, and (iv) thermolysis assisted method. The modified sol-gel Pechini method, was applied using ethylenediaminetetraacetic acid as the chelating agent and polyethyleneglycol as the esterification agent. In the other methods, which represent three novel methods for the synthesis of monoclinic KLuW, oleic acid and oleylamine, acting as organic coordinating agents, were introduced to achieve the desire crystalline compound. In terms of morphology, the modified sol-gel Pechini method produced nanocrystals with irregular shapes and a tendency of agglomeration, with sizes ranging from 150 nm to 2 μm. The solvothermal methods (microwave-assisted and conventional heating) produced nanocrystals with irregular shapes with sizes of 12 nm and 16 nm, respectively. The products of the microwave-assisted solvothermal methodology exhibited a more defined shape and a closer morphology to the spherical form. In the thermal decomposition assisted method, the final product of the reaction displayed a rod-like morphology in the range of micrometers.

The temperature sensing properties of these nanoparticles were tested considering their emissions in the third biological window (III-BW), after excitation with a light source lying as well in the biological window regime, in particular in the first biological window (I-BW). In the III-BW, light transmits more effectively (up to three times) through specific biological tissues like those containing melanin, achieving deeper light penetration depths, which is an advantage for the practical use of these luminescent thermometers in real *in vivo* applications. Additionally, scattering is reduced in this spectral range, as it is commonly accepted that the scattering coefficient decreases with increasing wavelength from the visible into the near-infrared. On the

other hand, excitation in the first biological window, precisely at 808 nm wavelength, allows to overcome the problems of inducing phototoxicity with ultraviolet light, as it was done with several luminescent thermometers developed previously, and the heat-induced effect from the 980 nm excitation, which overlaps with the absorption band of water molecules. Upon testing different doping levels of Ho^{3+} and Tm^{3+} in these nanoparticles, the optimal doping ratio for maximizing the intensity of the emissions in the III-BW and their temperature sensing abilities, was determined. The temperature sensing properties were investigated by analyzing the temperature dependence, in the physiological range of temperatures (293-333 K), of the intensity ratios between the emissions generated at 1.45 μm and 1.8 μm by Tm^{3+} and at 1.96 μm by Ho^{3+}. The best temperature sensing properties were observed by the nanocrystals synthesized from the modified sol-gel Pechini method with 1 mol% Ho^{3+}, 10 mol% Tm^{3+} doping ratio with a value of relative thermal sensitivity of 0.90% K^{-1}, which induced a temperature resolution of 0.55 K at 293 K.

As photothermal agents, the ability of these materials to convert the 808 nm excitation light into heat, was tested by using the integrated sphere method. The photothermal conversion efficiency of these nanocrystals was tested also as a function of the power of the laser applied. The results reveal that the particles with a rod-like morphology and with 3 mol% Ho^{3+}, 5 mol% Tm^{3+} doping ratio, act as the best photothermal agent among them, with a photothermal conversion efficiency value of 66 ± 2%, comparable to that obtained in gold nanorods.

To proof the self-assessed photothermal properties of these particles, they were embedded in chicken breast, at a depth of 2 mm, and after illuminating them with the 808 nm excitation light source, they released heat that increased the temperature of the environment, and at the same time emitted light that allowed determining the temperature *in situ* without the requirement of an external thermal probe. The temperature measured from the Ho, Tm:KLuW nanoparticles is in agreement with that recorded from a thermocouple embedded also in the chicken breast, as close as possible to the position of the Ho, Tm:KLuW nanoparticles, demonstrating the potentiality of these materials as multifunctional agents.

Paper II

Short-wavelength infrared self-assessed photothermal agents based on Ho, Tm:KLu$(WO_4)_2$ nanocrystals operating in the third biological window (1.45-1.96 μm wavelength range)

Albenc Nexha, Joan J. Carvajal,* Maria Cinta Pujol, Francesc Díaz and Magdalena Aguiló
Universitat Rovira i Virgili, Departament Química Física i Inorgànica,
Física i Cristal·lografia de Materials i Nanomaterials (FiCMA-FiCNA)-EMaS, Campus Sescelades, E-43007, Tarragona, Spain
**joanjosep.carvajal@urv.cat*

Abstract

$KLu_{1-x-y}Ho_xTm_y(WO_4)_2$ nanocrystals with different atomic concentrations (x=0.01, 0.03, 0.05, 0.075, 0.1, 0.15 and y=0.05, 0.1, 0.2) were synthesized via the modified sol-gel Pechini method, using ethylenediaminetetraacetic acid as the chelating agent, and polyethylenglycol as the esterification agent. Different doping levels were implemented with the goal to determine the optimal ratio for maximizing the intensity of their optical emission in the short-wavelength infrared (SWIR) region, their thermal sensitivity as luminescent thermometers and the photothermal conversion efficiency to act as photothermal agents. The obtained $KLu_{1-x-y}Ho_xTm_y(WO_4)_2$ nanocrystals exhibit a monoclinic structure and an irregular shape, with a size of around 150 nm. The photoluminescence spectrum in the SWIR region of the obtained nanocrystals, excited at 808 nm, shows three main bands attributed to the electronic transitions: $^3H_4 \rightarrow {}^3F_4$ (1.45 μm) and $^3F_4 \rightarrow {}^3H_6$ (1.8 μm) of Tm^{3+} and $^5I_7 \rightarrow {}^5I_8$ (1.96 μm) of Ho^{3+}.
The temperature dependency of the three emission bands was recorded in the physiological range of temperatures from 293 K to 333 K, displaying a relative thermal sensitivity (S_{rel}) of 0.90% K^{-1} at 293 K for the doping level of 1 at.% Ho^{3+} and 10 at.% Tm^{3+} , representing the highest reported up to now in the SWIR region. The photothermal conversion efficiency (η) of the $KLu_{1-x-y}Ho_xTm_y(WO_4)_2$ nanocrystals is 40 ± 2% for the same doping levels, being competitive with other photothermal agents reported before, like metallic and semiconductor nanocrystals. The simultaneous ability of these nanocrystals to combine photothermal conversion efficiency and thermal sensing in the SWIR is demonstrated through an *ex-vivo* experiment.

1. Introduction

Photothermal therapy refers to the process of generation of heat from the absorbance of light with the ultimate goal of inducing cellular hyperthermia. This is a process applied for the treatment of tumoral diseases between 314 K (41 ºC) and 321 K (48 ºC) that leads to protein aggregation, long term cell inactivation, and cell death.[1] This therapy is achieved through the incorporation of the so-called photothermal agents,[2] which absorb light and convert it efficiently into heat. Additionally, the photothermal agents should exhibit tumor-homing ability to improve the efficiency of the photothermal therapy without rendering toxic side effects.[3]

Photoabsorber nanomaterials such as gold nanostructures (nanoparticles,[4] nanorods,[5-8] nanoshells,[9] nanocages[10] and hollow nanospheres[11]), carbon nanomaterials,[12] palladium nanosheets,[13] copper sulfide nanoparticles,[14] and polymers[15] have been reported as examples of efficient photothermal agents. However, besides efficient absorbance features, good photo-stability and excellent photothermal conversion efficiency have been reported for these structures, none of these materials allows for the reading of temperature by themselves. Thus, external temperature control is required. This is especially important when the real temperature inside the tumor is substantially different from the one that can be determined from outside the body.[16] So,

multifunctional thermal agents that combine photothermal conversion ability and thermal sensing are highly desired, as pointed out by Quintanilla and Liz-Marzán in their excellent and recent review about the guiding rules for selecting a nanothermometer, in which they discuss the specific case of multifunctional probes combining photothermal activity and thermometry applied to the biomedical field.[17] In this context, recently, some approaches have been developed. For instance, PbS/CdS/ZnS quantum dots have been demonstrated to show heating and thermometric behavior.[16] Other approaches involve thermosensitive polymer-capped gold nanorods, which combine plasmonic heating, and use the temperature-dependent local surface plasmon resonance spectra due to the submolecular conformational change of the thermosensitive polymer (pNIPAAm) to measure the temperature, with a thermal precision of 80 mK, and a temporal response as fast as <4 ms.[18] Another example are the magnetoplasmonic (Co/Au or Fe/Au) nanodomes developed by Li *et al.*, that merge exceptionally efficient plasmonic heating and temperature detection by measuring the magnetic-induced rotation of the nanodomes in solution, with a precision of 0.05 K.[19]

Lanthanide based nanomaterials can also provide these two functions in a single material. The peculiar electronic configuration of lanthanide ions gives rise to a rich electronic energy level structure that can be excited with light, leading to radiative and non-radiative processes. Radiative processes emit light that can be used for thermal sensing purposes through luminescence nanothermometry, while non-radiative processes result in heat generation that can make of these materials potential photothermal agents.[20, 21] Lanthanide based nanomaterials can operate in a very broad range of the electromagnetic spectrum, covering from the UV to the NIR, depending on the ion chosen, and only limited by the transparency of the host in which they are embedded. This is a clear advantage when compared to other types of photothermal agents developed up to now. In fact, by embedding neodymium in some hosts and operating above certain doping ranges, it is possible to develop multifunctional nanoparticles that can be used as both photothermal agents and luminescent thermometers.[22-24]

Biological windows are the spectral ranges where biological tissues become partially transparent due to a simultaneous reduction in both absorption and scattering of light.[25] In biological tissues, the extinction coefficient of optical radiation is determined by the absorbance of the different components of the tissue and their optical scattering. These characteristics give rise to the different biological windows in which the biological tissues are more transparent: (i) the first biological window (I-BW) lying in the range 650-950 nm, (ii) the second biological window (II-BW) extending from 1000 to 1350 nm, and (iii) the third biological window (III-BW), also called short wavelength infrared region (SWIR), that goes from 1350 nm to 2400 nm.[26, 27] The III-BW, or SWIR, is important because light transmits more effectively (up to three times) through specific biological tissues like those containing melanine, achieving higher light penetration depths.[28] Also, scattering is reduced in this spectral range, as it is commonly accepted that the scattering coefficient decreases with increasing wavelength into near-infrared (NIR).[27]

In this paper, we analyze the SWIR emission of the Ho, Tm: $KLu(WO_4)_2$ nanocrystals for temperature sensing and light-to-heat conversion after near infrared (NIR) excitation. In particular, for temperature sensing, we analyzed the emission bands at 1.45 μm and 1.8 μm of Tm^{3+} and the 1.96 μm emission band of Ho^{3+}, excited at 808 nm, and we evaluated their photothermal conversion at this particular excitation wavelength. Monoclinic potassium lutetium double tungstate ($KLu(WO_4)_2$) offers a high chemical stability, large values of absorption and emission cross sections for lanthanide ions, and the possibility to dope the material, regardless of the concentration level, without fluorescence quenching.[29, 30] We optimized the concentration of the doping ions to maximize their performance for these two functionalities. In this way we develop multifunctional nanoparticles that can be used as self-assessed photothermal agents, in which the same nanoparticle releases heat and emits light that allows determining the temperature *in situ*.

2. Experiments

2.1. Materials

Lutetium nitrate hydrate ($Lu(NO_3)_3 \cdot H_2O$, 99.99%), holmium nitrate pentahydrate ($Ho(NO_3)_3 \cdot 5H_2O$, 99.9%), potassium carbonate (K_2CO_3, 99.99%) and ethylenediaminetetraacetic acid (EDTA, 99%) were purchased from Alfa Aesar. Thulium nitrate pentahydrate ($Tm(NO_3)_3 \cdot 5H_2O$, 99.9%) and poly(ethyleneglycol) (PEG, MW= 400 g/mol) were purchased from Sigma Aldrich. Ammonium tungstate ($(NH_4)_2WO_4$, 99.99%) was purchased from American Elements.

2.2. Synthesis of $KLu_{1-x-y}Ho_xTm_y(WO_4)_2$ nanocrystals

$KLu_{1-x-y}Ho_xTm_y(WO_4)_2$ (hereafter Ho,Tm:KLuW) nanocrystals with atomic concentrations x=0.01, 0.03, 0.05, 0.075, 0.1, 0.15 at.% and y=0.05, 0.1, 0.2 at.% were synthesized using the modified sol-gel Pechini method.[31] Lutetium (III) nitrate hydrate, holmium (III) nitrate pentahydrate and thulium (III) nitrate pentahydrate used as starting reagents, were dissolved completely under stirring in distilled water, followed by the addition of EDTA as the chelating agent, in a molar ratio [EDTA]/[metals]=1. Ammonium tungstate and potassium carbonate were added to the aqueous mixture, subsequently heated at 353 K under magnetic stirring during a day until the complete dissolution of the reagents. Poly(ethyleneglycol) acting as the esterification agent, was added to the mixture in a molar ratio [PEG]/[EDTA]=2. The solution was heated at 373 K to evaporate water and generate the polymeric gel. The polymeric gel was then precalcined at 573 K for 3 hours to obtain the precursor powders that were finally calcined at 1023 K for 2 hours to eliminate the organic compounds and crystallize the desired nanocrystals.

2.3. Characterization

Powder X-ray diffraction (XRD) measurements were made using a Siemens D5000 diffractometer (Bragg-Brentano parafocusing geometry and vertical θ-θ goniometer) fitted with a curved graphite diffracted-beam monochromator, incident and diffracted-beam Soller slits, a 0.06º receiving slit and a scintillation counter as a detector. The angular 2θ diffraction range was between 5 and 70º. The data were collected with an angular step of 0.05º at 3s per step and sample rotation. Cu K_α radiation was obtained from a copper X-ray tube operated at 40 kV and 30 mA.

For the morphological characterization, transmission electron microscopy (TEM) images were recorded using a JEOL JEM-1011 electron microscope operating at an accelerating voltage of 100 kV. For the preparation of the TEM grids, the nanocrystals were dispersed in ethanol using ultrasounds and around 15 µL of diluted ethanol dispersion were placed on the surface of a copper grid covered by a holey carbon film (HD200 Copper Formvar/carbon).

To characterize the vibrational modes of the nanocrystals, a micro-Raman analysis was performed, using a Renishaw inVia Reflex microscope with the unpolarized light from a 514 nm argon laser focused on the sample by a 50X Leica objective. Analysis were performed from the range of 200-2000 cm^{-1}, using a grating with 2400 lines/mm and an exposure time of 10 s.

For the photoluminescence analysis of the nanocrystals, the emission spectra were recorded in a Yokogawa AQ6375 optical spectrum analyzer in the range from 1350 nm to 2200 nm, with a resolution of 2 nm and an integration time of 1 s. The nanoparticles were excited by a 808 nm fiber-coupled diode laser with a power of 200 mW and the beam was focused on the sample using a 20X microscope objective (numerical aperture 0.4) and bringing a spot diameter of around 1 µm in the sample. The excitation density is around 100 W/cm^2. The scattered excitation radiation was eliminated by using a 850 nm longpass dichroic filter (Thorlabs). For the temperature-photoluminescence dependence analysis, the methodology was the same, except that the nanocrystals were introduced inside a heating stage (Linkam, THMS 600) equipped with a boron disk for improved temperature distribution.

The photothermal conversion efficiency was investigate by applying the method of the integrating sphere.[32] A glass cuvette containing an aqueous solution of the $KLu_{1-x-y}Ho_xTm_y(WO_4)_2$ nanocrystals with a concentration of 1 g/L was placed inside the integrating sphere, perpendicular to the laser irradiation provided by the 808 nm fiber-coupled diode laser with a power of 200 mW.

The laser from the fiber tip was collimated with a spot size of 5 mm in diameter on the sample. The signal was collected using a powermeter Ophir Nova II.

For the self-assessed photothermal conversion proof of concept, the methodology was exactly the same as in the photoluminescence analysis of the nanocrystals, with the addition of a digital multimeter equipped with a platinium and platinium-10% rhodium thermocouple to monitor the temperature, covered with a 2 mm thick chicken breast slice, and placed close to the injected nanoparticles.

3. Results and Discussion

3.1. Structural and Morphological Characterizations

All Ho,Tm:KLuW nanocrystals synthesized with different molar concentrations crystallize in the monoclinic system with the *C*2/*c* spatial group, confirmed by powder X-ray diffraction (XRD) according to the reference XRD pattern of $KLu(WO_4)_2$ (JCPDS file 54-1204),[33] as presented in Figure 1 for some representative samples. The XRD patterns of all the samples are shown in Figure S1 (Supporting Information).

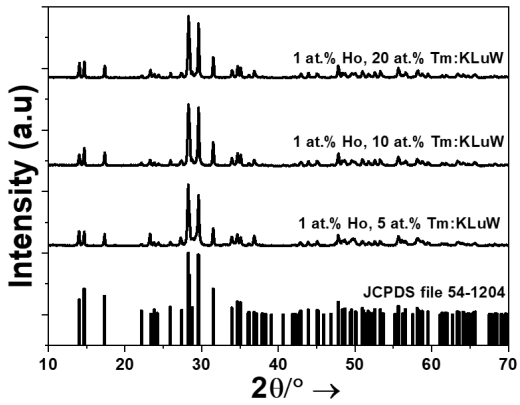

Figure 1. XRD pattern of the Ho,Tm:KLuW nanocrystals synthesized by the modified sol-gel Pechini method containing different dopant concentrations (1 at.% Ho and 5, 10 and 20 at.% Tm). The reference pattern of $KLu(WO_4)_2$ (JCPDS file 54-1204)[26] is included for comparison.

By using the Debye-Scherrer equation,[34] we estimated an average crystallite value of 43 ± 2 nm.

TEM micrographs reveal the irregular shape of the Ho,Tm:KLuW nanocrystals, as can be seen in Figure 2, with the presence of aggregates with sizes up to 1.8 µm. The use of high temperature annealing to achieve the desired crystalline monoclinic phase favors the aggregation of the nanocrystals and the wide size distribution ranging from 150 ± 25 nm to 1.8 µm, as can be observed in the size distribution plot obtained after the analysis of the TEM pictures, and shown in Figure 2(d). This behavior, however is a typical observation in the modified sol-gel Pechini method, as reported elsewhere.[21, 31] No differences in terms of size distribution were observed as a function of the dopant concentrations.

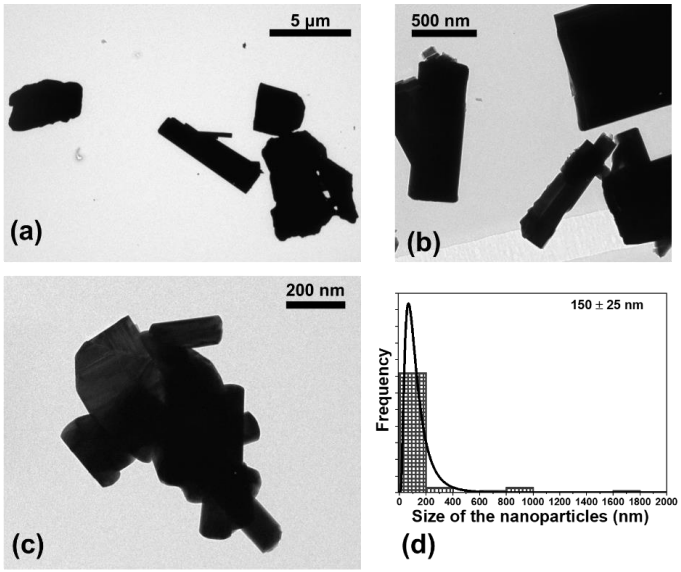

Figure 2. TEM images of the $KLu_{1-x-y}Ho_xTm_y(WO_4)_2$ nanoparticles with different dopant concentrations: (a) 1 at.% Ho, 5 at.% Tm, (b) 1 at.% Ho, 10 at.% Tm and (c) 1 at.% Ho, 20 at.% Tm. (d) Lognomal size distribution of the $KLu_{1-x-y}Ho_xTm_y(WO_4)_2$ nanoparticles. No variations in size distribution was observed as a function of the dopant concentrations.

Due to the role of the phonon energy values in the multiphonon non-radiative decay processes, which will be related to the photothermal conversion efficiency of our nanocrystals, we have determined the optical phonons of the synthesized samples as shown in Figure 3. The vibrational modes observed in the obtained nanocrystals are the expected ones for the monoclinic $KLu(WO_4)_2$ compound,[30] taking as an example the Ho,Tm:KLuW nanoparticles (1 at.% Ho, 10 at.% Tm), as shown in Figure 3. The strongest peak, observed at around 902 cm^{-1}, is attributed to the stretching mode of (W-O). The second most intense peak, observed at around 746 cm^{-1}, is the coupling between the stretching mode of (W-O) and the oxygen-doubled bridged (WOOW).[29] The range between 270-400 cm^{-1} is attributed to the bending modes and the 400-1000 cm^{-1} range is related to the stretching modes of the WO_6 group in the double tungstates.[30] The phonons below 270 cm^{-1} are associated to the translational modes of the cations (K^{+1}, Lu^{3+} and W^{6+}) and rotational motion of WO_6 groups in the unit cell.[30]

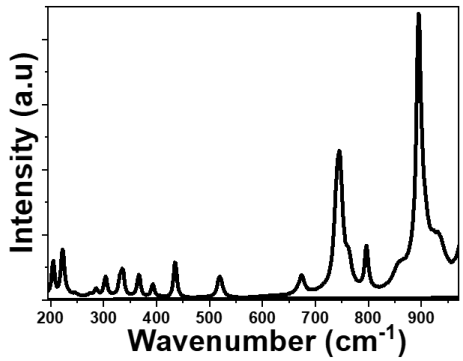

Figure 3. Unpolarized Raman spectra of the obtained $KLu_{1-x-y}Ho_xTm_y(WO_4)_2$ nanocrystals (1 at.% Ho, 10 at.% Tm) by the modified Pechini method.

3.2. Photoluminescence characterizations

The emission spectra of the Ho,Tm:KLuW nanocrystals, regardless of the dopant concentrations while excited at 808 nm, show three main peaks assigned to the: $^3H_4 \rightarrow {}^3F_4$ (1.45 μm) and $^3F_4 \rightarrow {}^3H_6$ (1.8 μm) electronic transitions of Tm^{3+} and $^5I_7 \rightarrow {}^5I_8$ (1.96 μm) electronic transition of Ho^{3+}.[29] The mechanisms of generation of these bands are depicted in Figure 4. Tm^{3+} absorbs a photon at 808 nm and promotes its electrons from the $^3H_6$ ground state to the $^3H_4$ excited state. The electrons decay radiatively to the $^3F_4$ manifold, generating the emission line at 1.45 μm. From the $^3F_4$ level to the $^3H_6$ ground state, the emission line at 1.8 μm is generated. Tm^{3+} ions undergo cross-relaxation (CR) process into the $^3F_4$ excited state, when one of the ions is initially excited into the upper $^3H_4$ excited state and then it relaxes non-radiatively to the $^3F_4$ level while this energy is used to promote an electron in the $^3H_6$ ground state to the $^3F_4$ level, due to the energy resonance between these two processes. Also, due to the energy resonance between the $^3F_4$ level of Tm^{3+} and the $^5I_7$ level of Ho^{3+}, an energy transfer (ET) and a back energy transfer (BET) process might take place, promoting the electrons of Ho^{3+} to this excited state from the ground state. Then, the electrons of Ho^{3+} relax radiatively to the $^5I_8$ ground state, giving rise to the emission band at 1.96 μm.[29]

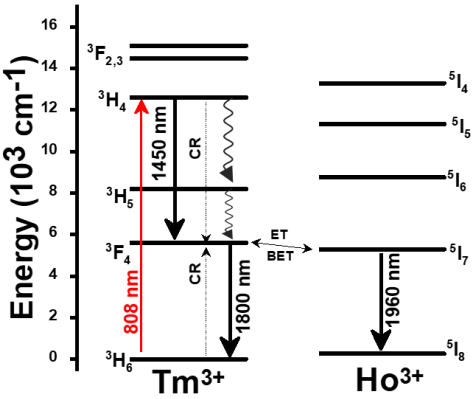

Figure 4. Energy level diagram of Ho^{3+} and Tm^{3+} ions in Ho,Tm:KLuW and the mechanisms of generation of their SWIR emission lines. Solid arrows indicate radiative processes. The red arrow indicate the absorption process excited by the 808 nm laser. The black arrows indicate the three radiative emissions: $^3H_4 \rightarrow {}^3F_4$, $^3F_4 \rightarrow {}^3H_6$ and $^5I_7 \rightarrow {}^5I_8$. Curved arrows indicate non-radiative multiphonon decays processes. The dashed arrows stands for the cross relaxation (CR) process in Tm^{3+} ($^3H_6$,$^3H_4$) $\leftrightarrow$ ($^3F_4$,$^3F_4$).

These SWIR emissions of the Ho,Tm:KLuW nanocrystals with 1, 3, 5, 7.5, 10, 15 at.% concentrations of Ho, and 5, 10, 20 at.% concentration of Tm, recorded by exciting the nanoparticles with the 808 nm laser and 200 mW of power, are shown in Figure 5 (a) and (b). When the concentration of Ho^{3+} was kept constant at 1 at.% and the concentration of Tm^{3+} increased from 5 to 20 at.% (Figure 5 (a)), the intensities of the bands at 1.45 μm and 1.96 μm decreased, while the peak at 1.8 μm increased until reaching saturation. By increasing the amount of Tm^{3+}, the cross relaxation (CR) process is promoted, favoring the electronic population of the $^3F_4$ level versus the $^4H_4$ level in the same ion. This would explain why the intensity of the 1.45 μm band decreased, while that of the 1.8 μm band increased when the Tm^{3+} concentration increased until a value of 10 at.% of Tm^{3+}. The intensity of this emission seems not increase further for higher Tm^{3+} concentrations, as can be seen for the sample containing 20 at.% of Tm^{3+}. This fact could be related to the appearance of some concentration quenching effects. In fact, in the bulk crystal singly doped with Tm^{3+}, the concentration quenching effect for the emission located at 1.8 μm (indicated by the decrease of the measured lifetime) has been already observed at doping

levels of 5 at.% of Tm^{3+}.[30] This migration of energy among the Tm^{3+} ions could also contribute to the decrease observed in the intensity of the 1.45 µm emission. Also, the increase of the Tm/Ho concentration ratio will shift the electronic population balance between the $^3F_4$ level of Tm^{3+} and the $^5I_7$ level of Ho^{3+} towards the Tm^{3+} level (*i.e.* favoring the BET versus ET process[35]) favoring the emission located at 1.8 µm versus that located at 1.9 µm.

When the concentration of Tm^{3+} was kept constant at 5 at.%, the intensity of the Tm^{3+} bands (1.45 µm and 1.8 µm) increased as the concentration of Ho^{3+} increased from 1 at.% to 3 at.%, but then decreased as the Ho^{3+} concentration increased from 3 to 15 at.% (Figure 5 (b)). For the 1.96 µm emission band of Ho^{3+} from its side, it may be observed that its maximum of intensity can be seen for the sample containing 3 at.% of Ho^{3+}, and it decreases as the Ho^{3+} concentration increases. However, for the sample containing a 10 at.% of Ho^{3+} an increase of intensity is observed again, without having a clear reason that could explain this behavior, since for higher Ho^{3+} concentration a clear concentration quenching effect is observed.

So, from these figures, it can be deduced that the sample with concentrations of Ho^{3+} 3 at.% and of Tm^{3+} of 5 at.% shows, in the three emission bands simultaneously, the maximum intensity that allows its further applications for luminescent thermometry.

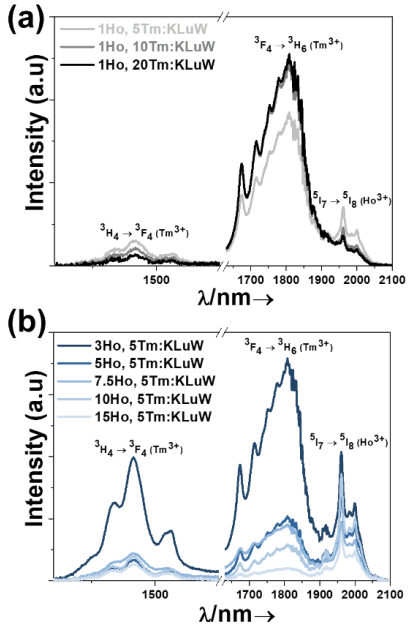

Figure 5. SWIR emissions recorded at room temperature of Ho,Tm:KLuW nanocrystals excited at 808 nm: (a) 1 at.% Ho^{3+}; 5, 10, 20 at.% Tm^{3+}, (b) 5 at.% Tm^{3+}; 3, 5, 7.5, 10, 15 at.% Ho^{3+}. Please note that the part of the graph from 1580 nm to 1630 nm was removed due to the presence of the second harmonic of the 808 nm laser source.

3.3. Luminescent thermometric characterizations

We studied the temperature dependence of the intensity of the emission bands generated by $KLu_{1-x-y}Ho_xTm_y(WO_4)_2$ nanocrystals after pumping at 808 nm in the physiological range of temperatures between 293 K and 333 K. In general, as the temperature increases, the intensity of the emissions decreases. This behavior is related to the thermal activation of the luminescence quenching mechanisms, such as the increase of the non-radiative decay rates.[20] Figure 6 (a) shows the evolution of the intensity of the three bands when the temperature is gradually increased from room temperature to 333 K, taking as an example the $KLu_{0.92}Ho_{0.03}Tm_{0.05}(WO_4)_2$ nanocrystals.

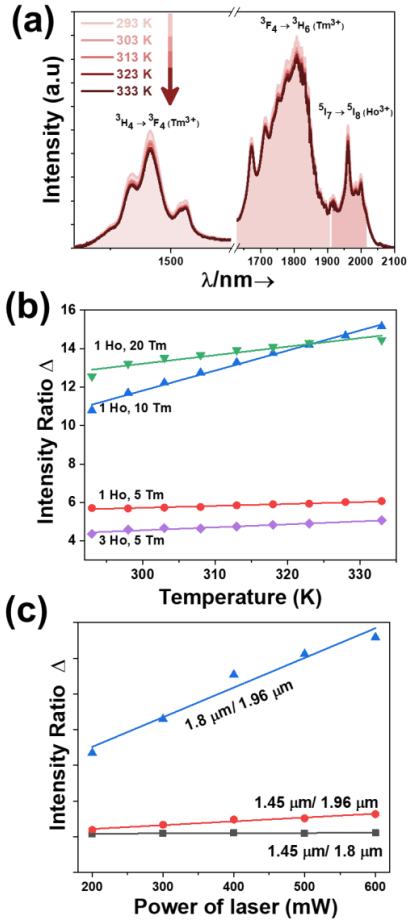

Figure 6. (a) Temperature dependence of the intensity of the SWIR emissions of the $KLu_{0.92}Ho_{0.03}Tm_{0.05}(WO_4)_2$ nanocrystals excited at 808 nm. Please note that the part of the graph from 1580 nm to 1630 nm was removed due to the presence of the second harmonic of the 808 nm laser source. (b) Temperature dependence of the intensity ratio Δ (experimental data and linear fitting according to Equation 2 for 1.8 μm/1.96 μm for different Ho,Tm:$KLu(WO_4)_2$ nanocrystals with different Ho^{3+} and Tm^{3+} concentrations. (c) Variation of the intensity ratio Δ, calculated for the $KLu_{0.89}Ho_{0.01}Tm_{0.1}(WO_4)_2$ sample, with the excitation power.

To determine the luminescence thermometric performance of our nanocrystals, we calculated four different parameters: (i) the integrated intensity ratio ($\Delta = I_i/I_j$, being I_i and I_j the integrated intensities of two of the three bands observed, defined as the thermometric parameter); (ii) the absolute thermal sensitivity (S_{abs}); (iii) the relative thermal sensitivity (S_{rel}); and (iv) the temperature uncertainty (δT), which will be described later.

We calculated the evolution of the thermometric parameter Δ by using the ratio between the integrated intensity area of the emission bands centered at 1.45 μm versus 1.8 μm, 1.45 μm versus 1.96 μm, and 1.8 μm versus 1.96 μm. In general, we observed that Δ doesn't show a significant temperature dependence (see Figure S2 at Supporting Information), excluding the ratio between the 1.8 μm versus 1.96 μm for the $KLu_{0.85}Ho_{0.1}Tm_{0.05}(WO_4)_2$, $KLu_{0.92}Ho_{0.03}Tm_{0.05}(WO_4)_2$, $KLu_{0.89}Ho_{0.01}Tm_{0.1}(WO_4)_2$, $KLu_{0.79}Ho_{0.01}Tm_{0.2}(WO_4)_2$ samples, in which Δ changes significantly with the increase of the temperature, as presented in Figure 6 (b). In general, the intensity ratio between the 1.8 μm versus the 1.96 μm emission bands, compared to the other two ratios, was more influenced by the temperature changes.

The temperature dependence of Δ, can be modelled by following the approach reported by Brites *et al.* for dual center emission lanthanide based thermometers. [36] This model is based on the fact that the total transition probability of an emitting level is the sum of the radiative and non-radiative transition probabilities [37] and relating the integrated luminescence intensity to the inverse of the total transition probability,[38] the temperature dependence of the intensity ratio can be expressed by:

$$\Delta = \frac{I_1}{I_2} = \Delta_0 \frac{1+\sum_i \alpha_{2i}\, exp\left(-\frac{\Delta E_{2i}}{k_B T}\right)}{1+\sum_i \alpha_{1i}\, exp\left(-\frac{\Delta E_{1i}}{k_B T}\right)} \qquad (1)$$

where 1 and 2 are the two emissions whose intensities are used to estimate the thermometric performance; Δ_0 stands for the ratio between the I_{01}/I_{02} at 0 K for 1 and 2 emissions; α_{2i} and α_{1i} stands for the ratio between the non-radiative and radiative probabilities for the emitting level of the electronic transitions 1 and 2, respectively; and the sum sign extends from i= 1 to n, being n all possible non-radiative process deactivation channels of transitions with intensities I_1 and I_2. Finally, ΔE_{2i} and ΔE_{1i} are the activation energies for the thermally quenched processes of transitions 1 and 2.

If the exponential term dominates in the intensities of the transitions involved, as it is our case, and assuming a single deactivation channel ($1 << \alpha_j \exp(-\Delta E_j/k_B T)$), Equation 1 could be transformed into:

$$\Delta = \Delta_0 \frac{\alpha_{2i}}{\alpha_{1i}} \frac{exp\left(-\frac{\Delta E_2}{k_B T}\right)}{exp\left(-\frac{\Delta E_1}{k_B T}\right)} = B \exp\left(\frac{\Delta E_1 - \Delta E_2}{k_B T}\right) = B \exp\left(\frac{-C}{T}\right) \qquad (2)$$

where $B=\Delta_0 \frac{\alpha_{2i}}{\alpha_{1i}}$ is an empirical constant to be determined by fitting and $C = \frac{\Delta E_1 - \Delta E_2}{k_B}$ is the energy difference between the two activation energies for the thermally quenched processes, while k_B is the Boltzmann constant expressed in cm^{-1} (k_B=0.695 cm^{-1}).

By fitting Equation 2 to the experimental emission-temperature dependence for each sample (shown in Figure 6 (b)), we estimated the values of B and C. The results are summarized in Table 1.

We also determined the variation of the integrated intensity ratio with the excitation power, since it is a very important point when envisaging the application of these luminescent nanothermometers in biomedical fields. Figure 6 (c) shows that the relationship between the integrated intensity ratio and the excitation power can be assimilated to be linear for the three different intensity ratios considered in this work concerning the 1.45 µm, the 1.8 µm and the 1.96 µm emissions, calculated for the $KLu_{0.89}Ho_{0.01}Tm_{0.1}(WO_4)_2$ sample. As can be seen in the figure, the intensity ratio that exhibits the highest change, and that also deviates the most from the linear behavior is the ratio between the emissions located at 1.8 µm and 1.96 µm. This is important, since during biological application there is no real control on the power actually reaching the nanoparticles, and this might become a source of inaccuracy. Thus, having a linear relationship, this inaccuracy source is minimized.

By using Equation 2 and the calculated values of the constants B and C for each Ho,Tm:KLuW nanocrystals, we can estimate the thermometric performance of our nanocrystals by calculating the absolute thermal sensitivity S_{abs} and the relative thermal sensitivity S_{rel}. The absolute thermal sensitivity was introduced by dos Santos *et al.*[39] and it is expressed by:

$$S_{abs} = \frac{\partial \Delta}{\partial T} \qquad (3)$$

The sample exhibiting the highest S_{abs} is $KLu_{0.89}Ho_{0.01}Tm_{0.1}(WO_4)_2$. Its S_{abs} is more than double, or more than five times higher than the rest of the samples exhibiting a significant S_{abs}. Furthermore, while S_{abs} increases for this sample when the temperature increases, it decreases for the rest of the samples.

Usually S_{rel} is used as a figure of merit to compare the performance of different thermometers, independently of their nature, whereas S_{abs} cannot be used to compare the performance of different luminescent thermometers because it depends on the experimental setup and characteristics of the sample such as the absorption and lifetimes.[36]

The relative thermal sensitivity expresses the maximum change in the intensity ratio Δ for each temperature degree and it is defined, according to Brites *et al.* by:[36]

$$S_{rel} = \frac{1}{\Delta} \left|\frac{\partial \Delta}{\partial T}\right| x\ 100\ \% \qquad (4)$$

Considering Equation 2 and 4, we deduce the final expression for S_{rel} for our $KLu_{1-x-y}Ho_xTm_y(WO_4)_2$ nanocrystals:

$$S_{rel} = \left|\frac{\Delta E}{k_B T^2}\right| x\ 100\ \% \qquad (5)$$

where $\Delta E = \Delta E_2 - \Delta E_1$ is determined by the fitting and T represents the temperature in kelvin (K).

Besides S_{rel}, the temperature resolution δT is also another parameter to determine the thermometer's performance. The temperature resolution (or temperature uncertainty) is defined as the smallest temperature change that can be resolved in a given measurement and it is estimated according to Brites *et al.*: [36]

$$\delta T = \frac{1}{S_{rel}} \frac{\delta \Delta}{\Delta} = \left|\frac{k_B T^2}{\Delta E}\right| \frac{\delta \Delta}{\Delta} \qquad (6)$$

where $\frac{\delta \Delta}{\Delta}$ is the relative error in the determination of the thermometric parameter. This parameter depends on the acquisition setup, and a typical value that can be used is 0.5%.[21]

Figure 7 (a)-(c) and Table 1 give the values of S_{abs}, S_{rel} and δT and all the fitting parameters for the selected nanocrystals operating in the SWIR regime. The maximum S_{rel} for the 1.8 µm/1.96 µm of all the synthesized nanocrystals are shown in Figure S3 and Table S1 in the Supporting Information section.

$KLu_{0.89}Ho_{0.01}Tm_{0.1}(WO_4)_2$ nanocrystals showed the highest relative thermal sensitivity reported so far in the literature for the SWIR regime, with a value of 0.90% K^{-1} and the smallest temperature resolution of 0.55 K at 293 K. For this sample, the highest S_{rel}=0.90% K^{-1} at 293 K decreased to 0.70% K^{-1} when the temperature increased up to 333 K, while δT increased to 0.72 K. Thus, they are excellent thermal probes to operate in the biological range of temperatures, with temperature resolutions always below one degree.

Another interesting observation is that S_{rel} calculated for the same sample, considering Δ calculated with the two integrated intensity ratios 1.45 µm/1.96 µm and 1.8 µm/1.96 µm, gives the same value. This is due to the fact that S_{rel} is calculated by using the $\Delta E_1 - \Delta E_2$ obtained from the fitting, which was the same in both cases (see Table 1), and it is related to the difference of energy of the two thermal activation energy values for the non-radiative quenching process related to each emission. Pandey *et al.*[40] assumed that this difference of energy can be correlated to the energy gap between the two emitting levels of the two transitions used to calculate the intensity ratio (despite they are non-thermally coupled levels), so, in parallel, we can assume that this difference of energy, 537 cm^{-1}, corresponds to the energy gap between the levels $^5I_7$ of Ho^{3+} and $^3F_4$ of Tm^{3+}. The reported value of this energy gap in Ho,Tm:KLuW bulk single crystals is 660 cm^{-1}, [41] close to the one determined by our fitting. The electronic population equilibrium between these two resonant emitting levels determines the thermometric behavior of our samples. Our hypothesis is that the electronic populations of the two emitting levels of Tm^{3+} are linked by the efficient cross relaxation (CR) process $^3H_4$, $^3H_6 \leftrightarrow {}^3F_4$,$^3F_4$ thus favoring the occupation of the $^3F_4$ level, and the corresponding energy transfer (ET) and back-energy transfer (BET) processes with the $^5I_7$ level of Ho^{3+}, marked as dashed arrows in Figure 4. Thus, apparently, the thermal sensing performance of our nanocrystals is governed by these energy transfer and back transfer processes, and this is why S_{rel} is the same in these two cases.

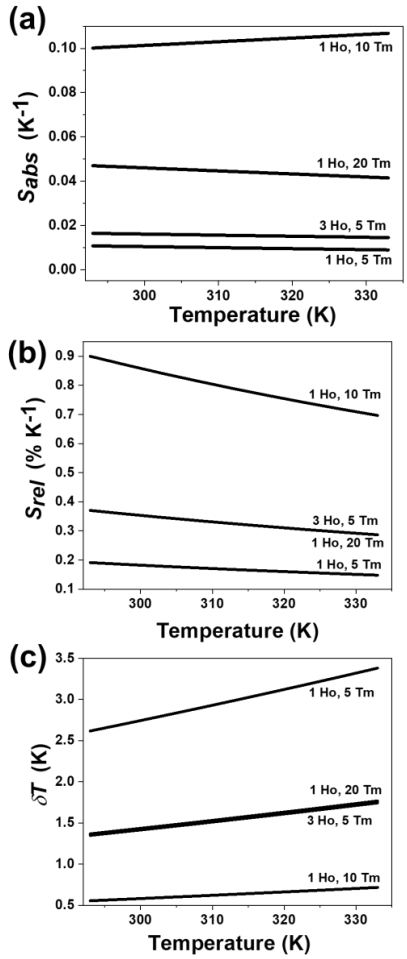

Figure 7. Determination of the: (a) absolute thermal sensitivity (S_{abs}), (b) relative thermal sensitivity (S_{rel}), and (c) temperature resolution (δT) for selected Ho,Tm:KLuW nanocrystals.

The reason why the nanocrystals with a doping level of 1 at.% Ho and 20 at.% Tm or 3 at.% Ho and 5 at.% Tm exhibit lower experimental values of $\Delta E_1 - \Delta E_2$ might be related to the fact that other thermally activated processes such as diffusion among lanthanide (Ln^{3+}) ions are happening, and also multiphonon non-radiative decays might become more important, thus affecting the electronic population balance between the $^3F_4$ and $^5I_7$ levels. As described in the Equation 3 and 6, the values of S_{rel} and δT are calculated directly from the $(\Delta E_1 - \Delta E_2)$ obtained by the fitting, so the variation of the temperature resolution for the different samples follows the same trend that the thermal relative sensitivity.

Table 1. Fitting parameters, S_{abs}, S_{rel} and δT of the most representative $KLu_{1-x-y}Ho_xTm_y(WO_4)_2$ nanocrystals analyzed in this work.

Sample (intensity ratio considered)	***B***	***C***	**$\Delta E_1 - \Delta E_2$ (cm^{-1})**	**R^2**	**S_{abs} (K^{-1}) 293 K**	**S_{rel} (% K^{-1}) 293 K**	**δT (K) 293 K**
1 at.% Ho, 10 at.% Tm (1.45 μm/1.96 μm)	4.4	773	537	0.99	0.0027	0.90	0.55
1 at.% Ho, 5 at.% Tm (1.8 μm/1.96 μm)	9.9	165	114	0.95	0.011	0.19	2.62
3 at.% Ho, 5 at.% Tm (1.8 μm/1.96 μm)	13	318	221	0.95	0.016	0.37	1.34

1 at.% Ho, 10 at.% Tm (1.8 μm/1.96 μm)	155	773	537	0.99	0.097	0.90	0.55
1 at.% Ho, 20 at.% Tm (1.8 μm/1.96 μm)	37	313	218	0.92	0.046	0.37	1.36

Table 2 compares the performance of different lanthanide based luminescent thermometers operating in the SWIR region. As can be seen Ho,Tm:KLuW nanocrystals exhibit the highest S_{rel} reported up to now, indicating that they would allow for the smallest temperature resolution when used as thermal probes. We also demonstrated that by optimizing the concentration of dopants in the nanocrystals, S_{rel} can be increased by 50%, when compared to previous reported values for the same material.[42]

Table 2. Comparison of the performance of Ln^{3+} doped systems used in luminescence nanothermometry operating in the SWIR region. The temperature range (ΔT), the excitation wavelength (λ_{exc}), transitions and emission wavelengths (λ_{em}) used to define Δ, and S_{rel} values are presented for comparison.

Material	**ΔT (K)**	**λ_{exc} (nm)**	**λ_{em} (nm)**	**Transitions**	**Δ**	**S_{rel} (% K^{-1})**	**Ref.**
$KLu_{0.89}Ho_{0.01}Tm_{0.1}(WO_4)_2$	293-333	808	1450 1800 1960	$^3H_4 \rightarrow {}^3F_4$ $^3F_4 \rightarrow {}^3H_6$, $^5I_7 \rightarrow {}^5I_8$	I_{1450}/I_{1960} I_{1800}/I_{1960}	0.90	This work
$KLu_{0.975}Ho_{0.01}Tm_{0.015}(WO_4)_2$	293-333	808	1480 1780	$^3H_4 \rightarrow {}^3F_4$, $^3F_4 \rightarrow {}^3H_6$	I_{1480}/I_{1780}	0.61	42
$Tm,Yb:NaYF_4$	298-333	980	1470 1740	$^3H_4 \rightarrow {}^3F_4$, $^3F_4 \rightarrow {}^3H_6$	I_{1470}/I_{1740}	0.6	42
$Tm,Yb,Ho:KLu(WO_4)_2$	298-333	980	1480 1780	$^3H_4 \rightarrow {}^3F_4$, $^3F_4 \rightarrow {}^3H_6$	I_{1480}/I_{1780}	0.57	42
$Er,Yb:LuVO_4$	298-523	980	1637 1660	$^4I_{13/2} \rightarrow {}^4I_{15/2}$	I_{1637}/I_{1660}	0.54	43
$Tm,Yb,Ho:KLu(WO_4)_2$	298-333	980	1780 1960	$^3F_4 \rightarrow {}^3H_6$, $^5I_7 \rightarrow {}^5I_8$	I_{1780}/I_{1960}	0.45	42
$Tm,Yb:KLu(WO_4)_2$	298-333	980	1480 1780	$^3H_4 \rightarrow {}^3F_4$, $^3F_4 \rightarrow {}^3H_6$	I_{1480}/I_{1780}	0.22	42
$Er,Yb:LuVO_4@SiO_2$	298-523	915	1496, 1527	$^4I_{13/2} \rightarrow {}^4I_{15/2}$	I_{1496}/I_{1527}	0.18	44
$Er,Yb:NaY_2F_5O$	298-333	980	1535, 1554	$^4I_{13/2} \rightarrow {}^4I_{15/2}$	I_{1535}/I_{1554}	0.15	42
$Er,Yb:KLu(WO_4)_2$	298-333	980	1535, 1553	$^4I_{13/2} \rightarrow {}^4I_{15/2}$	I_{1535}/I_{1553}	0.095	42
$Er,Yb:Lu_2O_3$	298-333	980	1535, 1556	$^4I_{13/2} \rightarrow {}^4I_{15/2}$	I_{1535}/I_{1556}	0.09	42
$Er,Yb:NaYF_4$	298-333	980	1535, 1554	$^4I_{13/2} \rightarrow {}^4I_{15/2}$	I_{1535}/I_{1554}	0.06	42

3.4. Photothermal conversion efficiency

To determine the photothermal conversion efficiency, *i.e.* the ability of our nanocrystals to convert the absorbed light into heat, we used the integrating sphere method.[21, 32]

In this method, the photothermal conversion efficiency (η) is calculated from the following expression:

$$\eta = \left|\frac{P_{blank} - P_{sample}}{P_{empty} - P_{sample}}\right| x\ 100\% \qquad (7)$$

where P_{blank}, P_{empty} and P_{sample} are the power values measured for the solvent (distilled water in this case), the empty sample holder and the dispersion of $Ho,Tm:KLu(WO_4)_2$ nanocrystals in water, respectively.

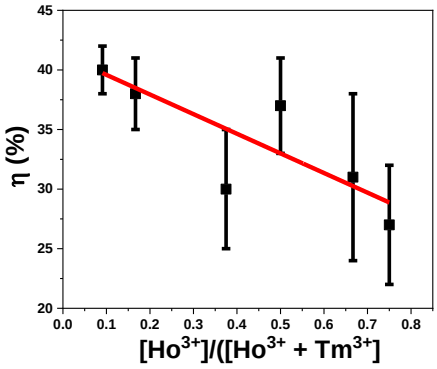

Figure 8. Variation of photothermal conversion efficiency with the concentration ratio of Ho^{3+} versus all doping ions. The red line is included as an eye guide for the reader.

The photothermal conversion efficiency for all synthesized samples is reported in Table S1 of the Supporting Information section. The $KLu_{0.94}Ho_{0.01}Tm_{0.05}(WO_4)_2$ and $KLu_{0.89}Ho_{0.01}Tm_{0.1}(WO_4)_2$ nanocrystals exhibited the highest photothermal conversion efficiency, with values of 38 ± 3% and 40 ± 2%, respectively. These results are in agreement with the ones obtained previously from Savchuk *et al.* for the photothermal conversion efficiency of $KLu_{0.84}Ho_{0.01}Tm_{0.15}(WO_4)_2$ nanocrystals. [21] The photothermal conversion is favored by the increase of probability of multiphonon decay transitions to happen and also to the appearance of some quenching processes due to impurities attached to the surface of the nanocrystals.[45] The increase of concentration of the active lanthanide ion is usually related to the increase of the probability of these mentioned processes to happen.[46] Figure 8 shows the efficiency of the photothermal conversion versus the concentration ratio of $Ho^{3+}/(Ho^{3+} + Tm^{3+})$. As shown in the figure, there is a tendency to increase the photothermal conversion in our nanocrystals when the Ho^{3+} doping versus the total doping concentrations is decreased, so this could be related with the fact that the main deactivation non radiative channels are present in the Tm^{3+} ions, as shown in Figure 4. However, Tm^{3+} ions are not only responsible for this behavior. In fact, when plotting the efficiency of the photothermal conversion versus the Tm^{3+} concentration, no apparent tendency is observed (see Figure S4 in the Supporting Information). From these results it is evident that the energy transfer processes between Tm^{3+} and Ho^{3+}, and the energy difference between the $^3F_4$ level of Tm^{3+} and the $^5I_7$ electronic level of Ho^{3+} are responsible for the photothermal conversion of these nanocrystals.

Additionally, we measured the dependence of the photothermal conversion efficiency with the power of the excitation source for the $KLu_{0.89}Ho_{0.01}Tm_{0.1}(WO_4)_2$ sample, excited at 808 nm. η shows no change when the pumping power is changed (see Figure S5 in the Supporting Information). Table 3 shows a comparison of the values of the photothermal conversion efficiency of different materials in which this property has been analyzed, together with the method used for the determination of η, and the excitation wavelengths used.

Table 3. Comparison of photothermal conversion efficiency (η) in different materials. The excitation wavelength (λ_{exc}) of the laser and the method used to extract η are included for comparison.

Material	Method	λ_{exc} (nm)	η (%)	Ref.
Au nanostars	Double Beam Fluorescence Thermometry	808	102	47
Au nanorods	Double Beam Fluorescence Thermometry	808	95	47
$NaNdF_4$@$NaYF_4$@ Nd:$NaYF_4$	Thermal Relaxation	808	72.7	48
$NdVO_4$ in water	Thermal Relaxation	808	72.1	49
Au nanoshells	Double Beam Fluorescence Thermometry	808	68	47
Graphene in DMF	Integrating Sphere	808	67	32
Au nanorods	Double Beam Fluorescence Thermometry	808	63	47

Au nanorods	Thermal Relaxation	815	61	50
Au/AuS nanoshells	Thermal Relaxation	815	59	50
Graphene Oxide in water	Integrating Sphere	808	58	32
Ho, Tm:$KLu(WO_4)_2$	Integrating Sphere	808	40	This work
Au/SiO_2 nanoshells	Thermal Relaxation	815	34	50
FePt nanoparticles	$P_{converted\ to\ heat}/P_{excitation}$	800	30	51
Cu_9S_5	Thermal Relaxation	980	25.7	52
Au nanoshells	Thermal Relaxation	808	25	53

Ho,Tm:$KLu(WO_4)_2$ nanocrystals show a lower photothermal conversion efficiency values when compared to others Ln^{3+} doped systems such as $NaNdF_4$@$NaYF_4$@ Nd:$NaYF_4$,[48] and $NdVO_4$ nanoparticles,[49] and also graphene materials,[32] and gold nanostructures,[47, 50] as can be seen in Table 2. However, they exhibit a higher photothermal conversion efficiency than other metallic and semiconductor nanocrystals also reported as photothermal agents, as they are also listed in Table 2.

3.5. Self-assessed nanocrystals: proof of concept

However, the main benefit of using Ho,Tm:$KLu(WO_4)_2$ nanocrystals as photothermal conversion agents compared to other types of materials is the ability to self-determine the temperature reached by the system, through luminescence thermometry, generating self-assessed photothermal agents. It should be noted here that although $NaNdF_4$@$NaYF_4$@Nd:$NaYF_4$ [48] and $NdVO_4$ [49] nanoparticles should have the same potentiality, the reading of temperature in these cases has been done using an external thermal probe and not by using the emissions generated by the nanoparticles. Even, Rocha *et al*.[54], that reported Nd^{3+} doped LaF_3 as self-monitored photothermal agents, compared only the temperature measured at the surface of the biological tissue with the temperature determined by the nanoparticles inside the tissue, without validating this last temperature with an external thermal probe.

To proof the self-assessed ability of our nanocrystals, we prepare a dispersion of the nanocrystals in distilled water using a concentration of 1 g/L. This water dispersion was used to fill a glass vial, inside of which we introduced a Pt-Pt/Rh thermocouple to monitor the temperature, at the same time that the dispersion was excited at 808 nm with a power of 0.2 W and a beam spot diameter of 10 μm on the external surface of the vial, and its photoluminescence spectrum was recorded.

Figure 9 (a) shows the temperature evolution in the water dispersion achieved by different Ho,Tm:$KLu(WO_4)_2$ nanoparticles with different doping concentrations. Also, the temperature reached in pure distilled water is included in the figure for comparison. When comparing with the water only behavior, it can be affirmed that mainly the temperature increase is attributed to the light-to-heat conversion of the nanocrystals. The general tendency observed is a fast increase in the temperature in the first 25-30 s and then a more slow tendency until reaching a saturation temperature after around 100 s.

The three selected samples $KLu_{0.89}Ho_{0.01}Tm_{0.1}(WO_4)_2$ (high η), $KLu_{0.92}Ho_{0.03}Tm_{0.05}(WO_4)_2$ (medium η) and $KLu_{0.875}Ho_{0.075}Tm_{0.05}(WO_4)_2$ (low η), achieve an increase of temperature of 17 K, 13.5 K and 10 K, respectively. As expected, the sample with the highest photothermal conversion efficiency ($KLu_{0.89}Ho_{0.01}Tm_{0.1}(WO_4)_2$) shows the highest temperature increase. Thus, to prove the concept of the self-assessed photothermal agents in real biological samples in an *ex-vivo* experiment, we selected this sample. For the *ex-vivo* experiment, the measurement scheme-methodology applied for the temperature determination was adapted from a previous article from our group with slight modifications, as is shown in Figure 9 (b). [55] For that a piece of chicken breast meat was cut in two pieces. On the top of the first piece, a small amount of $KLu_{0.89}Ho_{0.01}Tm_{0.1}(WO_4)_2$ luminescent nanoparticles were deposited. Close to the nanoparticles, a thermocouple was located also on this piece of chicken breast. Then, the second piece of chicken breast, 2 mm thick, was placed on the top of these nanoparticles, covering both the luminescent nanoparticles and the thermocouple, so that the nanoparticles (and the reference thermocouple, of course) are wrapped by the same medium in all directions. The $KLu_{0.89}Ho_{0.01}Tm_{0.1}(WO_4)_2$ nanoparticles where then illuminated with the 808 nm laser with a power of 200 mW and a spot size of 10 μm on the surface of the chicken breast. The power of the

excitation laser beam was set to the maximum value that the chicken breast can hold showing no degradation or burning on its surface. This laser beam crossed the chicken breast piece of meat before exciting the luminescent nanoparticles.

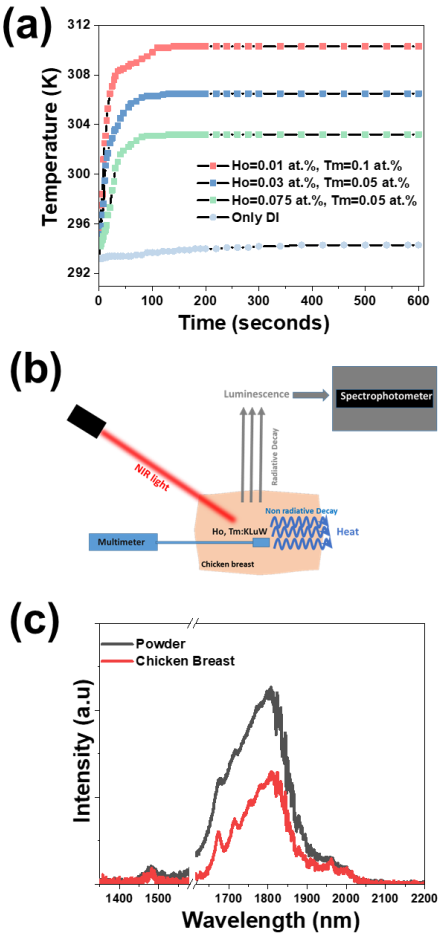

Figure 9. (a) Time-dependent temperature profiles achieved in the aqueous dispersion of different doping levels of Ho,Tm:KLuW nanocrystals with different doping concentrations when illuminated with the 808 nm laser. (b) Schematic representation of the setup for *ex-vivo* temperature determination. (c) SWIR emission of 1 at.% Ho, 10 at.% Tm:KLuW nanocrystals in air and covered by a 2 mm thick chicken breast piece of meat.

Finally, the spectrum generated by the luminescent nanoparticles was recorded from the exterior of the chicken breast piece of meat. This spectrum was recorded when, according to Figure 9 (a) and Figure S7 in the Supporting Information, the temperature was stabilized. Furthermore, we confirmed that the temperature was not fluctuating any longer through the reading of the temperature performed with the thermocouple located close to the nanoparticles. With this spectrum we extracted the thermometric parameter Δ, and by comparing its value against the calibration curve shown in Figure 6 (b) and its expression according to Equation 2, we determined the temperature inside the chicken breast piece of meat. This temperature was compared with the one measured by the thermocouple located close to the nanoparticles.

The SWIR emission of our nanocrystals transmitted through the 2 mm chicken breast is shown in Figure 9 (c), together with the spectrum of the same nanoparticles not covered by the chicken

breast piece of meat, to show the attenuation of the signal caused by the biological tissue. This was the maximum thickness that allowed us to record a spectra with appropriate intensities ratios among the three emission bands in order to determine the temperature. It is worth to mention that the excitation beam is also going through the chicken piece of meat so the level of laser power reaching the nanocrystals has also been reduced by the scattering and absorption of the tissue (the transmittance of the chicken breast is shown in Figure S6 at Supporting Information).

We determined the 1.8 μm/1.96 μm thermometric parameter from the spectrum recorded and shown in Figure 9 (c), and then, by using the calibration curve shown in Figure 6 (b) and its mathematical expression according to Equation 2, we calculated a temperature of 312.8 K. The thermocouple, from its side, indicated a temperature value of 312 K (the graph of temperature evolution with time in that case is shown in Figure S7, Supporting Information). Thus, the difference between the temperature determined with the emission of our nanocrystals and that of the thermocouple is 0.8 K. This difference might be assigned to the different thermal conductivity of our nanoparticles (dielectric material) and that of the thermocouple (metal). Another possibility for this difference might be that the calibration of the luminescent thermometer has been done in air, and not directly inside the chicken breast, thus, the medium in which the nanoparticles are embedded can also affect to the determination of temperature by luminescence means. A solution to avoid this problem would be to perform a recalibration of the thermometer in the new medium.[56] Another possibility is determining the relationship between the intensity ratio and the excitation power inside of the new medium and adjust the B parameter in Equation 2, as suggested by Quintanilla *et al*.[57] However, up to the moment this approach has been proved to be effective only for single center emitting luminescent thermometers, in which the emissions considered to calculate the thermometric parameter are generated only by the same lanthanide ion. Still, another possibility is generating a primary thermometer with these luminescence nanoparticles, as pointed out by Balabhadra *et al.*[58] However, again, all the theory developed to generate these primary thermometers concerns only single center emitting luminescent thermometers. In our case, however, we assessed the temperature determined by the luminescent thermometer by comparing it with the temperature read with a thermocouple. Obviously, for practical applications in the future, the thermocouple should be removed, and any one of the solutions proposed to mitigate the differences between the temperature determined by the luminescent thermometer and the thermocouple should be applied. Despite of this, we consider that with the approach presented in the present manuscript, we demonstrated that Ho,Tm:KLuW nanoparticles can be used as self-assessed photothermal conversion agents.

4. Conclusions

Monoclinic $KLu_{1-x-y}Ho_xTm_y(WO_4)_2$ nanocrystals synthesized via the modified sol-gel Pechini method were analyzed as candidates for luminescence nanothermeters in the SWIR region. Exciting the $KLu_{1-x-y}Ho_xTm_y(WO_4)_2$ nanocrystals with a 808 nm laser diode, produced three emission peaks located at 1.45 μm, 1.8 μm and 1.96 μm attributed to the $^3H_4 \rightarrow {}^3F_4$, $^3F_4 \rightarrow {}^3H_6$ transitions of Tm^{3+} and the $^5I_7 \rightarrow {}^5I_8$ transition of Ho^{3+}, respectively. The emission intensity ratio between 1.45 μm/1.96 μm or 1.8 μm/1.96 μm produced the highest relative thermal sensitivity S_{rel} reported so far in the SWIR region, reaching a value of 0.90% K^{-1} at 293 K and a temperature resolution δT of 0.55 K for the $KLu_{0.89}Ho_{0.01}Tm_{0.1}(WO_4)_2$ nanocrystals. The ability to convert light into heat for these nanocrystals was also analyzed, achieving a photothermal conversion efficiency on the range of 40 ± 2% for the same nanocrystals. We probed that these nanocrystals can be used as self-assessed photothermal agents: the same nanoparticle releases heat that will increase the temperature of the environment in which it is embedded, and emits light that allows determining the temperature *in situ* without the addition of an external thermal probe.

Despite the penetration depth at which this probe of concept could be performed was restricted to 2 mm in the present experiments to avoid damages in the biological tissues, it has been probed that the SWIR region, or third biological window, is the most suitable one for deep tissue imaging.[27] In this spectral region the penetration power of light is higher than the one that can be achieved in the second biological windows, and much higher than the one that can be achieved

in the first biological window. In fact, by an appropriate dispersion of the nanoparticles in biological compatible fluids, a penetration depth of 1 cm has been demonstrated when operating in the second biological window.[59] Thus, we are convinced that by optimizing the measurement conditions similar or higher penetration depths can be achieved for this kind of self-assessed photothermal agents.

5. Acknowledgements

This work was supported by the Spanish Government under projects MAT2016-75716-C2-1-R (AEI/FEDER, UE) and by the Generalitat de Catalunya under project 2017SGR755. A.N acknowledges financial support from the Generalitat de Catalunya under grant 2017FI_B00620 and 2018FI_B100161.

6. References

1. Jaque, D.; Martínez Maestro, L.; del Rosal, B.; Haro-Gonzalez, P.; Benayas, A.; Plaza, J. L.; Martín Rodríguez, E.; García Solé, J., Nanoparticles for photothermal therapies. *Nanoscale* **2014,** 6, (16), 9494-9530.
2. Day, E. S.; Morton, J. G.; West, J. L., Nanoparticles for thermal cancer therapy. *Journal of Biomechanical Engineering* **2009,** 131, (7), 074001-074006.
3. Key, J.; Park, K., Multicomponent, tumor-homing chitosan nanoparticles for cancer imaging and therapy. *International Journal of Molecular Sciences* **2017,** 18, (3), 594-613.
4. Giljohann, D. A.; Seferos, D. S.; Daniel, W. L.; Massich, M. D.; Patel, P. C.; Mirkin, C. A., Gold nanoparticles for biology and medicine. *Angewandte Chemie International Edition* **2010,** 49, (19), 3280-3294.
5. Jain, P. K.; Huang, X.; El-Sayed, I. H.; El-Sayed, M. A., Noble metals on the nanoscale: optical and photothermal properties and some applications in imaging, sensing, biology, and medicine. *Accounts of Chemical Research* **2008,** 41, (12), 1578-1586.
6. Alkilany, A. M.; Thompson, L. B.; Boulos, S. P.; Sisco, P. N.; Murphy, C. J., Gold nanorods: Their potential for photothermal therapeutics and drug delivery, tempered by the complexity of their biological interactions. *Advanced Drug Delivery Reviews* **2012,** 64, (2), 190-199.
7. Kennedy, L. C.; Bickford, L. R.; Lewinski, N. A.; Coughlin, A. J.; Hu, Y.; Day, E. S.; West, J. L.; Drezek, R. A., A new era for cancer treatment: gold-nanoparticle-mediated thermal therapies. *Small* **2011,** 7, (2), 169-183.
8. von Maltzahn, G.; Park, J. H.; Agrawal, A.; Bandaru, N. K.; Das, S. K.; Sailor, M. J.; Bhatia, S. N., Computationally guided photothermal tumor therapy using long-circulating gold nanorod antennas. *Cancer Research* **2009,** 69, (9), 3892-3900.
9. Loo, C.; Lowery, A.; Halas, N.; West, J.; Drezek, R., Immunotargeted nanoshells for integrated cancer imaging and therapy. *Nano Letters* **2005,** 5, (4), 709-711.
10. Skrabalak, S. E.; Au, L.; Lu, X.; Li, X.; Xia, Y., Gold nanocages for cancer detection and treatment. *Nanomedicine* **2007,** 2, (5), 657-668.
11. Zhang, J. Z., Biomedical applications of shape-controlled plasmonic nanostructures: A case study of hollow gold nanospheres for photothermal ablation therapy of cancer. *Journal of Physical Chemistry Letters* **2010,** 1, (4), 686-695.
12. Yang, K.; Feng, L.; Shi, X.; Liu, Z., Nano-graphene in biomedicine: theranostic applications. *Chemical Society Reviews* **2013,** 42, (2), 530-547.
13. Huang, X.; Tang, S.; Mu, X.; Dai, Y.; Chen, G.; Zhou, Z.; Ruan, F.; Yang, Z.; Zheng, N., Freestanding palladium nanosheets with plasmonic and catalytic properties. *Nature Nanotechnology* **2011,** 6, (1), 28-32.
14. Tian, Q.; Tang, M.; Sun, Y.; Zou, R.; Chen, Z.; Zhu, M.; Yang, S.; Wang, J.; Wang, J.; Hu, J., Hydrophilic flower-like CuS superstructures as an efficient 980 nm laser-driven photothermal agent for ablation of cancer cells. *Advanced Materials* **2011,** 23, (31), 3542-3547.
15. Cheng, L.; Yang, K.; Chen, Q.; Liu, Z., Organic stealth nanoparticles for highly effective in vivo near-infrared photothermal therapy of cancer. *ACS Nano* **2012,** 6, (6), 5605-5613.
16. del Rosal, B.; Carrasco, E.; Ren, F.; Benayas, A.; Vetrone, F.; Sanz-Rodríguez, F.; Ma, D.; Juarranz, Á.; Jaque, D., Infrared-Emitting QDs for Thermal therapy with real-time subcutaneous temperature feedback. *Advanced Functional Materials* **2016,** 26, (33), 6060-6068.
17. Quintanilla, M.; Liz-Marzán, L. M., Guiding rules for selecting a nanothermometer. *Nano Today* **2018,** 19, 126-145.
18. Chen, X.; Xia, Q.; Cao, Y.; Min, Q.; Zhang, J.; Chen, Z.; Chen, H. Y.; Zhu, J. J., Imaging the transient heat generation of individual nanostructures with a mechanoresponsive polymer. *Nature Communications* **2017,** 8, (1), 1498-1508.

19. Li, Z.; Lopez-Ortega, A.; Aranda-Ramos, A.; Tajada, J. L.; Sort, J.; Nogues, C.; Vavassori, P.; Nogues, J.; Sepulveda, B., Simultaneous local heating/thermometry based on plasmonic magnetochromic nanoheaters. *Small* **2018,** 14, (24), 1800868-1800878.
20. Riseberg, L. A.; Moos, H. W., Multiphonon orbit-lattice relaxation of excited states of rare-earth ions in crystals. *Physical Review* **1968,** 174, (2), 429-438.
21. Savchuk, O. A.; Carvajal, J. J.; Brites, C. D. S.; Carlos, L. D.; Aguilo, M.; Diaz, F., Upconversion thermometry: a new tool to measure the thermal resistance of nanoparticles. *Nanoscale* **2018,** 10, (14), 6602-6610.
22. Bednarkiewicz, A.; Wawrzynczyk, D.; Nyk, M.; Strek, W. J. A. P. B., Optically stimulated heating using Nd^{3+} doped NaYF4 colloidal near infrared nanophosphors. *Applied Physics B* **2011,** 103, (4), 847-852.
23. Suo, H.; Zhao, X.; Zhang, Z.; Guo, C., 808 nm light-triggered thermometer-heater upconverting platform based on Nd^{3+}-sensitized yolk-shell GdOF@SiO_2. *ACS Applied Materials & Interfaces* **2017,** 9, (50), 43438-43448.
24. Carrasco, E.; del Rosal, B.; Sanz-Rodríguez, F.; de la Fuente, Á. J.; Gonzalez, P. H.; Rocha, U.; Kumar, K. U.; Jacinto, C.; Solé, J. G.; Jaque, D., Intratumoral thermal reading during photo-thermal therapy by multifunctional fluorescent nanoparticles. *Advanced Functional Materials* **2015,** 25, (4), 615-626.
25. Weissleder, R., A clearer vision for in vivo imaging. *Nature Biotechnology* **2001,** 19, (4), 316-317.
26. Hemmer, E.; Benayas, A.; Légaré, F.; Vetrone, F., Exploiting the biological windows: current perspectives on fluorescent bioprobes emitting above 1000 nm. *Nanoscale Horizons* **2016,** 1, (3), 168-184.
27. Shi, L.; Sordillo, L. A.; Rodríguez-Contreras, A.; Alfano, R., Transmission in near-infrared optical windows for deep brain imaging. *Journal of Biophotonics* **2016,** 9, (1-2), 38-43.
28. Naczynski, D. J.; Tan, M. C.; Zevon, M.; Wall, B.; Kohl, J.; Kulesa, A.; Chen, S.; Roth, C. M.; Riman, R. E.; Moghe, P. V., Rare-earth-doped biological composites as in vivo shortwave infrared reporters. *Nature Communications* **2013,** 4, (1), 2199.
29. Jambunathan, V.; Mateos, X.; Pujol, M. C.; Carvajal, J. J.; Massons, J.; Aguiló, M.; Díaz, F., Near-infrared photoluminescence from Ho^{3+}-doped monoclinic $KLu(WO_4)_2$ crystal codoped with Tm^{3+}. *Journal of Luminescence* **2009,** 129, (12), 1882-1885.
30. Petrov, V.; Cinta Pujol, M.; Mateos, X.; Silvestre, Ò.; Rivier, S.; Aguiló, M.; Solé, R. M.; Liu, J.; Griebner, U.; Díaz, F., Growth and properties of $KLu(WO_4)_2$, and novel ytterbium and thulium lasers based on this monoclinic crystalline host. *Laser & Photonics Reviews* **2007,** 1, (2), 179-212.
31. Galceran, M.; Pujol, M.; Aguiló, M.; Díaz, F., Sol-gel modified Pechini method for obtaining nanocrystalline $KRE(WO_4)_2$ (RE=Gd and Yb). *Journal of Sol-Gel Science and Technology* **2007,** 42, 79-88.
32. Savchuk, O. A.; Carvajal, J. J.; Massons, J.; Aguiló, M.; Díaz, F., Determination of photothermal conversion efficiency of graphene and graphene oxide through an integrating sphere method. *Carbon* **2016,** 103, 134-141.
33. Pujol, M. C.; Aznar, A.; Mateos, X.; Solans, X.; Massons, J.; Suriñach, S.; Díaz, F.; Aguiló, M., Structural redetermination, thermal expansion and refractive indices of $KLu(WO_4)_2$. *Journal of Applied Crystallography* **2006,** 39, (2), 230-236.
34. Patterson, A. L., The Scherrer formula for X-Ray particle size determination. *Physical Review* **1939,** 56, (10), 978-982.
35. Payne, S. A.; Smith, L. K.; Kway, W. L.; Tassano, J. B.; Krupke, W. F., The mechanism of Tm to Ho energy transfer in $LiYF_4$. *Journal of Physics: Condensed Matter* **1992,** 4, (44), 8525-8542.
36. Brites, C. D. S.; Millán, A.; Carlos, L. D., Chapter 281-Lanthanides in Luminescent Thermometry. In *Handbook on the Physics and Chemistry of Rare Earths*, Jean-Claude, B.; Vitalij K, P., Eds. Elsevier: 2016; Vol. 49, pp 339-427.
37. Mott, N. F., On the absorption of light by crystals. *Proceedings of the Royal Society A* **1938,** 167, (930), 384-391.
38. Duarte, M.; Martins, E.; Baldochi, S. L.; Vieira, N. D.; Vieira, M. M. F., De-excitation mechanisms of $BaLiF_3$:Co^{2+} crystals. *Optics Communications* **1999,** 159, (4), 221-224.
39. Santos, P. V. d.; Araujo, M. T. d.; Gouveia-Neto, A. S.; Neto, J. A. M.; Sombra, A. S. B., Optical temperature sensing using upconversion fluorescence emission in Er^{3+}/Yb^{3+}-codoped chalcogenide glass. *Applied Physics Letters* **1998,** 73, (5), 578-580.
40. Pandey, A.; Rai, V., Optical thermometry using FIR of two close lying levels of different ions in Y_2O_3:Ho^{3+}-Tm^{3+}-Yb^{3+} phosphor. *Applied Physics B* **2013,** 113, 221-225.
41. Jambunathan, V.; Schmidt, A.; Mateos, X.; Pujol, M. C.; Griebner, U.; Petrov, V.; Zaldo, C.; Aguiló, M.; Díaz, F., Crystal growth, optical spectroscopy, and continuous-wave laser operation of co-doped (Ho,Tm):$KLu(WO_4)_2$ monoclinic crystals. *Journal of the Optical Society of America B* **2014,** 31, (7), 1415-1421.
42. Savchuk, O. A.; Carvajal, J. J.; Haro-Gonzalez, P.; Aguiló, M.; Díaz, F., Luminescent nanothermometry using short-wavelength infrared light. *Journal of Alloys and Compounds* **2018,** 746, 710-719.
43. Ma, Y.; Xiang, G.; Zhang, J.; Liu, Z.; Zhou, P.; Liu, W.; Tang, X.; Jiang, S.; Zhou, X.; Li, L.; Luo, Y.; Jin, Y., Upconversion properties and temperature sensing behaviors in visible and near-infrared region based on fluorescence intensity ratio in $LuVO_4$: Yb^{3+}/Er^{3+}. *Journal of Alloys and Compounds* **2018,** 769, 325-331.
44. Xiang, G.; Liu, X.; Zhang, J.; Liu, Z.; Liu, W.; Ma, Y.; Jiang, S.; Tang, X.; Zhou, X.; Li, L.; Jin, Y., Dual-Mode Optical Thermometry Based on the Fluorescence Intensity Ratio Excited by a 915 nm Wavelength in $LuVO_4$:Yb^{3+}/Er^{3+}@SiO_2 Nanoparticles. *Inorganic Chemistry* **2019,** 58, (12), 8245-8252.

45. del Rosal, B.; Rocha, U.; Ximendes, E. C.; Martín Rodríguez, E.; Jaque, D.; Solé, J. G., Nd^{3+} ions in nanomedicine: Perspectives and applications. *Optical Materials* **2017,** 63, 185-196.
46. Kolesnikov, I. E.; Kalinichev, A. A.; Kurochkin, M. A.; Mamonova, D. V.; Kolesnikov, E. Y.; Lähderanta, E.; Mikhailov, M. D., Bifunctional heater-thermometer Nd^{3+}-doped nanoparticles with multiple temperature sensing parameters. *Nanotechnology* **2019,** 30, (14), 145501-145513.
47. Maestro, L. M.; Haro-González, P.; Sánchez-Iglesias, A.; Liz-Marzán, L. M.; García Solé, J.; Jaque, D., Quantum dot thermometry evaluation of geometry dependent heating efficiency in gold nanoparticles. *Langmuir* **2014,** 30, (6), 1650-1658.
48. Marciniak, L.; Pilch, A.; Arabasz, S.; Jin, D.; Bednarkiewicz, A., Heterogeneously Nd^{3+} doped single nanoparticles for NIR-induced heat conversion, luminescence, and thermometry. *Nanoscale* **2017,** 9, (24), 8288-8297.
49. del Rosal, B.; Pérez-Delgado, A.; Carrasco, E.; Jovanović, D. J.; Dramićanin, M. D.; Dražić, G.; de la Fuente, Á. J.; Sanz-Rodriguez, F.; Jaque, D., Neodymium-based stoichiometric ultrasmall nanoparticles for multifunctional deep-tissue photothermal therapy. *Advanced Optical Materials* **2016,** 4, (5), 782-789.
50. Cole, J. R.; Mirin, N. A.; Knight, M. W.; Goodrich, G. P.; Halas, N. J., Photothermal efficiencies of nanoshells and nanorods for clinical therapeutic applications. *Journal of Physical Chemistry C* **2009,** 113, (28), 12090-12094.
51. Chen, C. L.; Kuo, L. R.; Lee, S. Y.; Hwu, Y. K.; Chou, S. W.; Chen, C. C.; Chang, F. H.; Lin, K. H.; Tsai, D. H.; Chen, Y. Y., Photothermal cancer therapy via femtosecond-laser-excited FePt nanoparticles. *Biomaterials* **2013,** 34, (4), 1128-1134.
52. Tian, Q.; Jiang, F.; Zou, R.; Liu, Q.; Chen, Z.; Zhu, M.; Yang, S.; Wang, J.; Wang, J.; Hu, J., Hydrophilic Cu_9S_5 nanocrystals: A photothermal agent with a 25.7% heat conversion efficiency for photothermal ablation of cancer cells in vivo. *ACS Nano* **2011,** 5, (12), 9761-9771.
53. Pattani, V. P.; Tunnell, J. W., Nanoparticle-mediated photothermal therapy: A comparative study of heating for different particle types. *Lasers in Surgery and Medicine* **2012,** 44, (8), 675-684.
54. Rocha, U.; Kumar, K. U.; Jacinto, C.; Ramiro, J.; Caamaño, A. J.; Solé, J. G.; Jaque, D., Nd^{3+} doped LaF_3 nanoparticles as self-monitored photo-thermal agents. *Applied Physics Letters* **2014,** 104, (5), 53703-53709.
55. Savchuk, O. A.; Carvajal, J. J.; Cascales, C.; Aguiló, M.; Díaz, F., Benefits of silica core-shell structures on the temperature sensing properties of Er,Yb:$GdVO_4$ up-conversion nanoparticles. *ACS Applied Materials & Interfaces* **2016,** 8, (11), 7266-7273.
56. Souza, A. S.; Nunes, L. A. O.; Silva, I. G. N.; Oliveira, F. A. M.; da Luz, L. L.; Brito, H. F.; Felinto, M. C. F. C.; Ferreira, R. A. S.; Júnior, S. A.; Carlos, L. D.; Malta, O. L., Highly-sensitive Eu^{3+} ratiometric thermometers based on excited state absorption with predictable calibration. *Nanoscale* **2016,** 8, (9), 5327-5333.
57. Quintanilla, M.; Zhang, Y.; Liz-Marzán, L. M., Subtissue plasmonic heating monitored with CaF_2:Nd^{3+},Y^{3+} nanothermometers in the second biological window. *Chemistry of Materials* **2018,** 30, (8), 2819-2828.
58. Balabhadra, S.; Debasu, M. L.; Brites, C. D. S.; Ferreira, R. A. S.; Carlos, L. D., Upconverting nanoparticles working as primary thermometers in different media. *Journal of Physical Chemistry C* **2017,** 121, (25), 13962-13968.
59. Savchuk, O.; Carvajal, J. J.; De la Cruz, L. G.; Haro-González, P.; Aguiló, M.; Díaz, F., Luminescence thermometry and imaging in the second biological window at high penetration depth with Nd:$KGd(WO_4)_2$ nanoparticles. *Journal of Materials Chemistry C* **2016,** 4, (31), 7397-7405.

Supporting Information

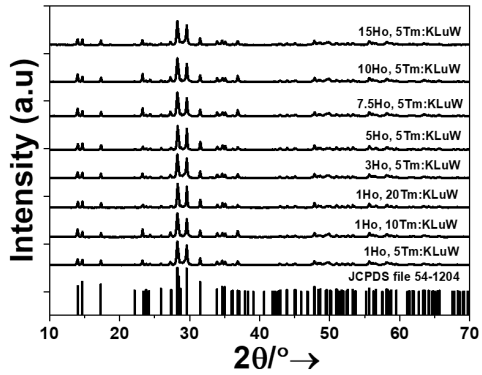

Figure S1. XRD patterns of the all Ho,Tm:KLuW nanocrystals synthesized by the modified sol-gel Pechini method containing different dopant concentrations. The reference pattern of $KLu(WO_4)_2$ (JCPDS file 54-1204) is included for comparison.

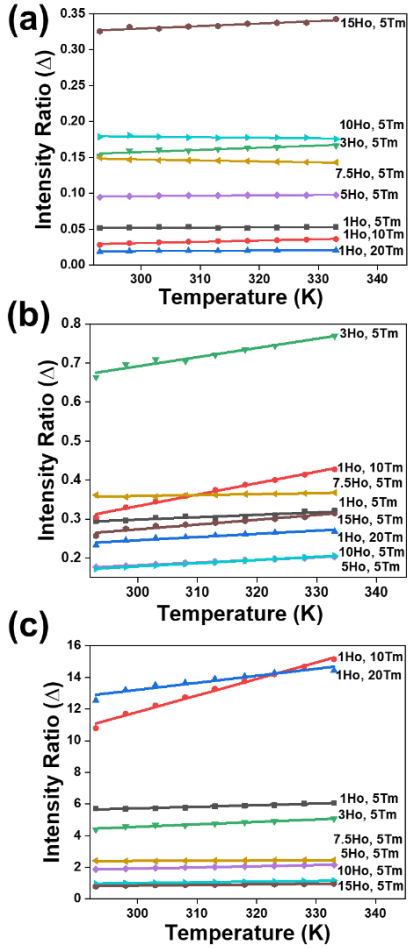

Figure S2. The variation of the thermometric parameter Δ with temperature: (a) 1.45 μm/1.8 μm, (b) 1.45 μm/1.96 μm, and (c) 1.8 μm/1.96 μm.

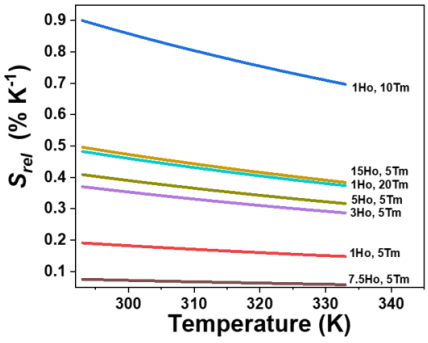

Figure S3. The relative thermal sensitivity of the $KLu_{1-x-y}Ho_xTm_y(WO_4)_2$ nanocrystals operating in the SWIR regime for the emission intensity ratio 1.8 μm/1.96 μm

Table S1. Photothermal conversion efficiency and relative thermal sensitivity of all the synthesized $Ho,Tm:KLu(WO_4)_2$ nanocrystals

Ho^{3+} (at.%)	**Tm^{3+} (at.%)**	**S_{rel} (% K^{-1})**	**η (%)**
0.01	0.05	0.19	38 ± 3
0.01	0.1	0.90	40 ± 2
0.01	0.2	0.37	17 ± 2
0.03	0.05	0.37	30 ± 5
0.05	0.05	0.40	37 ± 4
0.075	0.05	0.075	14 ± 2
0.1	0.05	0.49	31 ± 4
0.15	0.05	0.48	27 ± 5

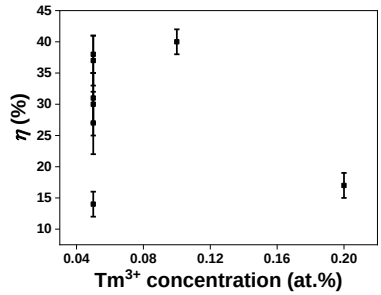

Figure S4. Variation of the photothermal conversion efficiency with the concentration of Tm^{3+}.

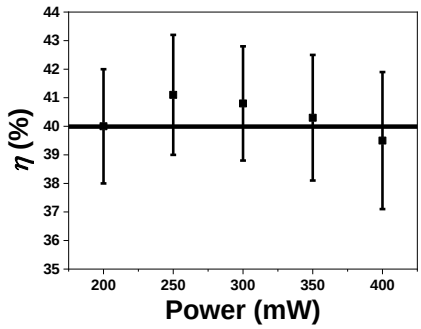

Figure S5. Variation of the photothermal conversion efficiency of the $KLu_{1-x-y}Ho_xTm_y(WO_4)_2$ (x=0.01 at.%, y=0.1 at.%) nanocrystals with the laser pumping power.

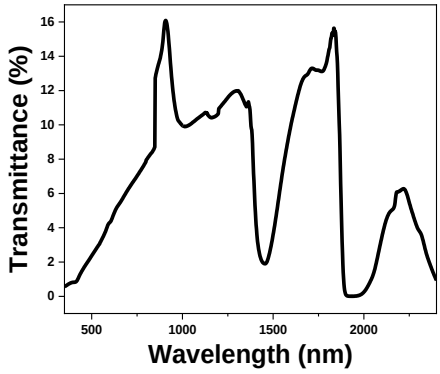

Figure S6. Transmittance of the chicken breast piece of meat used in the *ex-vivo* experiment.

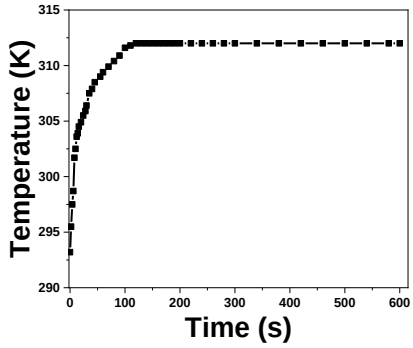

Figure S7. Evolution of the temperature with time when the $KLu_{1-x\,y}Ho_xTm_y(WO_4)_2$ (x=0.01 at.%, y=0.1 at.%) nanocrystals are covered with a 2 mm thick chicken breast piece of meat, recorded with the reference thermocouple.

Paper III

Effect of size and shape of Ho, Tm:$KLu(WO_4)_2$ nanocrystals in the performance as simultaneous luminescent nanothermometers operating in the third biological window and as photothermal agents

Albenc Nexha, Maria Cinta Pujol,* Joan J. Carvajal, Francesc Díaz and Magdalena Aguiló
Universitat Rovira i Virgili, Departament Química Física i Inorgànica,
Física i Cristal·lografia de Materials i Nanomaterials (FiCMA-FiCNA)-EMaS, Campus Sescelades, E-43007, Tarragona, Spain
*mariacinta.pujol@urv.cat

Abstract

The incorporation of oleic acid and oleylamine, acting as coating organic surfactants for the novel solvothermal synthesis, resulted in the formation of monoclinic $KLu(WO_4)_2$ nanocrystals. The formation of this crystalline phase was confirmed structurally from X-ray powder diffraction patterns and Raman vibrational modes, and thermally from the differential thermal analysis. The transmission electron microscopy images confirm the nanodimensional size (~12 nm and ~16 nm for microwave-assisted and conventional autoclave solvothermal synthesis, respectively) of the particles and no agglomeration, contrary to the traditional modified sol-gel Pechini methodology. Upon doping with holmium (III) and thulium (III) lanthanide ions, these nanocrystals can generate simultaneously photoluminescence and heat, acting as nanothermometers and as photothermal agents in the third biological window, *i.e.* self-assessed photothermal agents, upon excitation with 808 nm near infrared, lying in the first biological window. The emissions of these nanocrystals, regardless of the solvothermal synthetic methodology applied to synthesize them, are located at 1.45 μm, 1.8 μm and 1.96 μm, attributed to the $^3H_4 \rightarrow {}^3F_4$ and $^3F_4 \rightarrow {}^3H_6$ electronic transition of Tm^{3+} and $^5I_7 \rightarrow {}^5I_8$ electronic transition of Ho^{3+}, respectively. The self-assessing properties of these nanocrystals are studied as a function of their size and shape and compared to the modified sol-gel Pechini methodology, revealing that small nanocrystals generate more heat and sense the temperature less. The self-assessing ability of these nanocrystals in the third biological window is proven *via* an *ex-vivo* experiment, achieving thermal knowledge and heat generation at a maximum penetration depth of 2 mm.

1. Introduction

Photothermal therapy, that employs light-absorbing agents to convert photoenergy into heat, achieving local hyperthermia, is regarded as a minimally invasive and highly efficient methodology for targeted cancer treatment.[1-4] Efficient photothermal agents require high light-to-heat conversion efficiency, small size, and working under excitation and generated emission wavelengths operating in the optical biological windows. To this, it can be added real-time temperature feedback to monitor treatment.[4]

A high light-to-heat conversion efficiency allows performing effective hyperthermia with low laser powers and suppresses any overheating effect.[4] Small sizes for the photothermal agents guarantee successful intracellular studies and applications, and the effective excretion of the nanoparticles after the photothermal treatment, avoiding *in vivo* toxicity.[5, 6]

Regarding the excitation wavelength, it should exhibit deep biological tissue penetration possibilities to trigger these agents inside the human body by pumping from outside or through

laparoscopic approaches. Energy dissipation in biological tissues arise from light absorption and scattering by biological tissue components (mainly water, fat, hemoglobin, and melanin).[7] Thus, this energy dissipation should be minimized. High penetration depths are achieved when the light used (both for excitation and from generated emissions) lies in the so-called optical biological windows. Biological windows are the spectral ranges where biological tissues become partially transparent due to a simultaneous reduction in both absorption and scattering of light.[7] They are split in four different spectral ranges, apart mainly by the different absorption bands of water: (i) the first biological window (I-BW) extending from 650 nm to 950 nm; (ii) the second biological window (II-BW) extending from 1000 nm to 1350 nm; (iii) the third biological window (III-BW) extending from 1350 nm to 2000 nm; and (iv) the fourth biological window (IV-BW), centered at 2200 nm.[8] Among these biological windows, the III-BW achieves the highest light penetration depth in specific biological tissues like those containing melanin and oxygenated blood tissues, due to a maximum reduction of the scattering coefficient,[9] and effective light transmission.[8]

Laser-triggered photothermal therapy using near infrared excitation sources (NIR, λ=700-1100 nm) is highly attractive due to higher penetration depth in biological tissues, compared to ultraviolet (UV) or visible (VIS) light sources.[10, 11] Hence, photothermal agents that respond strongly to light excitation within the NIR excitation wavelengths and generate emissions within the biological windows, are of paramount value.[12, 13] For these reasons, noninvasive sensing of the real-time temperature *in situ* feedback is crucial.[14-16]

Materials including gold nanostructures (nanostars,[17] nanorods,[17, 18] nanoshells,[19] and nanocages[20]), carbon,[21-24] palladium,[25-28] and copper[29-31] based nanomaterials, have been reported as potential photothermal agents. Despite their considerable high light-to-heat conversion efficiency, particularly for the gold nanostructures, these photothermal agents require additional components able to measure temperature due to the lack of self-assessment feedback.[32] This feedback is especially important when the real temperature inside the tumor is substantially different from the one that can be determined from outside the body.[33] Hence, multifunctional agents that combine photothermal conversion efficiency and thermal sensing, are highly desirable.

Lanthanide doped nanomaterials offer these two properties in one single material due to their peculiar electronic configuration, giving rise to radiative and non-radiative processes, responsible for the generation of luminescence and heat, respectively.[34-36] These two properties are exhibited simultaneously in a material doped with lanthanide ions, after excitation with the suitable wavelength, rendering this material the potential to be self-assessed photothermal agents, *i.e.* the same material releases heat and emits light that allows determining the temperature *in situ*. Holmium (Ho^{3+}) and thulium (Tm^{3+}) doped potassium lutetium double tungstates $KLu(WO_4)_2$ (hereafter Ho, Tm:KLuW) after being illuminated with NIR light exhibit this self-assessed photothermal property.[36] Previous results have confirmed that this material exhibit potential thermal sensing properties in the III-BW and light-to-heat conversion efficiency ~40%.[36] The multifunctionality of Ho, Tm:KLuW nanoparticles was demonstrated by determining the temperature *in situ* in an *ex-vivo* experiment increasing the temperature of the biological sample by 17 K.[36] However, the dual functionality of Ho, Tm:KLuW as thermal sensing and photothermal conversion agents was demonstrated on nanocrystals synthesized by the modified sol-gel Pechini method. This methodology often suffers from morphological irregularities and wide size particles distribution up to several microns.[35-37] Hence, engineering and developing this material to control their morphology and size dispersion as potential self-assessed photothermal conversion agents, is important. A possibility to do this is by synthesizing non-aggregated, well-shaped and nanodimensional Ho,Tm:KLuW particles by applying novel microwave-assisted and conventional autoclave solvothermal methodologies in the presence of organic surfactants, oleic acid (OLAC) and oleylamine (OLAM), to control their nucleation and growth.

The incorporation of OLAC and OLAM acting as surfactants, alone, combined or mixed with 1-octadecene (ODE) or trioctylphosphine oxide (TOPO) allowed a good control on the synthesis of the inorganic colloidal nanocrystals (oxides, sulfides, tellurides, chalcogenides (binary, ternary and quaternary), and metallic nanocrystals,[38] via wet chemical methodologies. The combinatory effect of OLAC-OLAM has also been used in the synthesis of Ln^{3+} doped materials

(sesquioxides,[39] tetragonal double tungstates,[40, 41] and fluorides[42]). However, the major part of the methodologies with this binary combination are applied in heat up (or thermal decomposition) methodologies, whereas reports in the application of this combination in microwave-assisted or solvothermal synthesis methodologies are scarce, especially when dealing with Ln^{3+} doped materials. To the best of our knowledge, the only report so far for the implementation of the combinatory effect of oleic acid and oleylamine organic surfactants in microwave-assisted or hydrothermal/solvothermal approaches in a Ln^{3+}-doped material is attributed to the preparation of tetragonal bipyramids of Eu^{3+}:$NaLa(MoO_4)_2$. An equimolar ratio of OLAC-OLAM was incorporated into this solvothermal approach at 413 K during 6 h.[43]

Here, undoped KLuW and Ho, Tm doped KLuW nanocrystals with sizes below 20 nm have been synthesized via novel solvothermal methodologies (microwave-assisted and conventional autoclave). The successful formation of the monoclinic crystalline phase was confirmed by X-ray powder diffraction (XRPD), Raman vibrational modes and differential thermal analysis (DTA). A possible mechanism underlying the combined effect of OLAC and OLAM organic surfactants is proposed. The effect of the nanodimensional size and ellipsoidal shape of Ho, Tm;KLuW nanocrystals synthesized by these methodologies on their self-assessed photothermal properties with temperature reading in the third biological window by luminescence thermometry is investigated. The emissions of these nanocrystals lying in the III-BW are generated after excitation with 808 nm NIR light, lying in the I-BW. For thermal sensing, the intensity ratio between the 1.45 μm and 1.8 μm emission bands of Tm^{3+} and the 1.96 μm emission band of Ho^{3+} is analyzed in the physiological range of temperatures (293 K-333 K). The photothermal conversion efficiency, determined by the integrated sphere method,[44] was also investigated using the 808 nm energy source. The multifunctional properties of these nanocrystals, was demonstrated in an *ex-vivo* experiment, confirming the ability of these materials to simultaneously sense temperature and generate heat through NIR excitation.

2. Experiments

2.1. Materials

Lutetium nitrate hydrate ($Lu(NO_3)_3 \cdot H_2O$, 99.99%), holmium nitrate pentahydrate ($Ho(NO_3)_3 \cdot 5H_2O$, 99.9%), potassium tungstate (K_2WO_4, 99.5%), oleylamine (OLAM, 70%), potassium carbonate (K_2CO_3, 99.99%) and n-hexane (99%) were purchased from Alfa Aesar. Thulium nitrate pentahydrate ($Tm(NO_3)_3 \cdot 5H_2O$, 99.9%) and oleic acid (OLAC, 90%) was purchased from Sigma Aldrich. Absolute ethanol was purchased from VWR.

2.2. Synthesis of nanocrystals

2.2.1. Microwave-assisted solvothermal synthesis of undoped and doped $KLu(WO_4)_2$ nanocrystals

The microwave-assisted solvothermal reaction was carried out in a Milestone ETHOS One reactor equipped with temperature sensor and a stirring bar. The stoichiometric ratio of the precursors and the ratio of the precursors versus the organic surfactants, have been chosen taking as reference the work of Bu *et al.*[43] in which they prepared nanocrystals of double molybdates $NaLa(MoO_4)_2$. The initial stoichiometric ratio of the precursors and the ratio of the precursors versus the organic surfactants, were inspired in the above mentioned work. In the present work, we studied the effects on the products of the reduction of the reaction temperature and time in the microwave-assisted solvothermal approach, with the aim to develop a green approach for the synthesis of $KLu(WO_4)_2$. Other parameters, such as the different cation precursors used, the OLAC-OLAM molar ratio, and the calcination temperature and time were also explored.

In a typical microwave-assisted solvothermal synthesis (hereafter MW) of the undoped KLuW nanoparticles with the optima conditions, OLAC (6×10^{-3} mol) and OLAM (6×10^{-3} mol) were mixed in 18 mL of ethanol and were magnetically stirred for 20 min until a homogeneous transparent solution was obtained. The starting OLAC:OLAM molar ratio was 1:1, as used in the work of Bu *et al*.[43] Two different solutions in 4 mL of water were prepared containing 0.3×10^{-3}

mol of $Lu(NO_3)_3{\cdot}H_2O$ and 0.6 x 10^{-3} mol of K_2WO_4, respectively. K_2WO_4 was used as the K^+ cation and WO_4^{2-} anion precursor, simultaneously, implying an initial stoichiometry between the cations of K:Lu:W=4:1:2. The aqueous solution of $Lu(NO_3)_3{\cdot}H_2O$ was added slowly to the organic-based surfactant solution while stirring, which turned from a transparent homogeneous solution to a milky one. When the K_2WO_4 precursor aqueous solution was added dropwise, the milky mixture's color was slightly attenuated, mainly by the addition of water. All the mixture was transferred to a microwave vial with a total volume of 70 mL, equipped with a stirring bar, which was filled up to 38 % of its total volume. The reaction was performed at 453 K for 3 h with stirring. This reaction temperature was reached in 10 min. After the reaction, the system was cooled down to room temperature naturally. The products of this reaction (hereafter the seeds) were collected after purifying the mixture with an excess of ethanol to extract the precipitate, centrifuged at 6000 rpm for 5 min, and redispersed in n-hexane. This purification step was repeated until the supernatant was colorless and transparent, removing in this way the excess of organic surfactants. The seeds were obtained in powder form after treatment at 353 K for 1 h, approximately. The seeds were calcined in a conventional furnace at 1023 K for 2 h to obtain KLuW as the final product. For the synthesis of Ho, Tm doped KLuW, the methodology was the same, except the addition of 3 mol% Ho^{3+}, 5 mol% Tm^{3+} or 1 mol% Ho^{3+}, 10 mol% Tm^{3+}, as dopants substituting the Lu^{3+} ions in the KLuW host. These doping ratios ratio represent the maximum brightness of both emissions in the III-BW and the best self-assessing properties, as presented in our previous work.[36]

2.2.2. Conventional autoclave solvothermal synthesis of undoped and doped $KLu(WO_4)_2$ nanocrystals

The conventional autoclave solvothermal synthesis of undoped and doped KLuW was performed using the same experimental parameters as in the microwave-assisted synthesis, but changing the solution container (here it is used an autoclave metallic reactor) and the heating was provided by a conventional heating furnace. In this methodology, the reaction time and temperature were also optimized.

In a typical conventional autoclave solvothermal synthesis (hereafter CA) of the undoped KLuW with the optima conditions, the autoclave metallic reactor, which has a total volume of 60 mL, was filled up to 38 % of the total volume, in order to keep the same conditions as in the microwave-assisted reaction. The purification process applied to the product obtained in the reaction of conventional heating solvothermal synthesis was the same than that used in the microwave assisted synthesis. The calcination process was set at 1023 K and 2 h.

2.3. Characterizations

X-ray powder diffraction (XRPD) measurements were made using a Siemens D5000 diffractometer (using Bragg-Brentano parafocusing geometry and a vertical θ-θ goniometer) fitted with a curved graphite diffracted-beam monochromator, incident and diffracted-beam Soller slits, a 0.06° receiving slit and scintillation counter as detector. The angular 2θ diffraction range was set between 5 and 70°. The data were collected with an angular step of 0.05° at 3s per step while sample was rotated to gain statistics. Cu K_α radiation was obtained from a Copper X-ray tube operated at 40 kV and 30 mA. The temperature-dependent X-ray powder diffraction measurements were made using a Bruker-AXS D8-Discover diffractometer equipped with parallel incident beam (Göbel mirror), vertical θ-θ goniometer, XYZ motorized stage and a GADDS (General Area Diffraction System) as detector. Samples were placed directly on the sample holder and the area of interest was selected with the aid of a video-laser focusing system. An X-ray collimator system allows to analyse areas of 500 μm. The X-ray diffractometer was operated at 40 kV and 40 mA to generate Cu K_α radiation. The GADDS detector was a HI-STAR (multiwire proportional counter of 30 × 30 cm with a 1024 × 1024 pixel). We collected one frame (2D XRD patterns) covering 2θ=12-45° with a detector-sample distance of 15 cm. The exposition time was 300 s per frame and it was γ-integrated to generate the conventional 2θ vs. intensity diffractogram. Identification of the crystal phases was achieved by comparison of the XRD diffractogram with the ICDD data base (release 2007) using Diffrac^{plus} Evaluation software (Bruker 2007). The temperature was controlled with a MRI BTS-Solid temperature sample stage (Pt heating ribbon heating stage). The patterns were collected from room temperature up to 1273 K, heating at a

rate of 10 K/min. The sample was maintained during 60 s at the desired temperature before starting the measurement. The temperature stage was covered with a beryllium (Be) dome and an air static atmosphere was used throughout the measurement.

For the morphological characterization, transmission electron microscopy (TEM) images were acquired using a JEOL JEM-1011 electron microscope operating at an accelerating voltage of 100 kV. For the preparation of the TEM grids, the seeds dispersed in n-hexane and the final products in distilled water, were placed on the surface of a Copper grid covered by a holey carbon film (HD200 Copper Formvar/carbon).

Fourier Transform Infrared (FT-IR) spectra were recorded in the range of 400-4000 cm^{-1} on a FT-IR IluminatIR II, Smith spectrophotometer, to investigate the presence of the different functional groups on the surface of the samples.

Differential thermal analysis (DTA) and thermal gravimetric analysis (TGA) were used to study the thermal evolution of the seeds and final products with the temperature by using a TA Instruments SDT 2960 simultaneous differential scanning calorimetry-thermogravimetric analysis system. The heating rate was set at 10 K min^{-1} with an air flux of 90 cm^3 min^{-1}. Al_2O_3 was used as the reference material.

To characterize the vibration modes of the nanocrystals, a micro-Raman analysis was performed, using a Renishaw inVia Reflex microscope equipped with unpolarized light coming from a 514 nm argon laser, and focused through a 50× Leica objective. The analysis were performed in the range of 200-2000 cm^{-1}, using a grating with 2400I mm^{-1} to disperse the spectra and an exposure time of 10 s.

For the photoluminescence analysis of the nanocrystals, the emission spectra were recorded in a Yokogawa AQ6375 optical spectrum analyzer in the range from 1350 nm to 2200 nm, with a resolution HIGH3 and an integration time of 1 s. The nanoparticles were excited by the 808 nm emission fiber-coupled diode laser with a power of 200 mW and the beam was focused on the sample using a 20× microscope objective (numerical aperture 0.4) and a spot size of ~10^{-6} m. The excitation density was around 100 W cm^{-2}. The scattered excitation radiation was eliminated by using a 850 nm longpass dichroic filter (Thorlabs). For analyzing the temperature-photoluminescence dependence, the methodology was the same, except that the nanocrystals were located inside a heating stage (Linkam, THMS 600) equipped with a boron disk for improved temperature distribution.

The photothermal conversion efficiency was investigate by applying the method of the integrating sphere.[44] A glass cuvette containing an aqueous solution of the Ho, Tm doped KLuW nanoparticles with a concentration of 1 g L^{-1} was placed inside the integrating sphere, in a position perpendicular to the laser irradiation provide by the 808 nm fiber-coupled diode laser with a power of 200 mW. The laser from the fiber tip was collimated to a spot size of 5 mm in diameter on the sample. A baffle was introduced in the integrating sphere, between the sample and the detector, in order to prevent the direct reflections from the sample to the detector. The generated signals, such as the scattered, reflected, transmitted light and part of the light that is absorbed and converted into another light wavelength, were collected by an Ophir Nova II powermeter.[44]

For the *ex-vivo* experiment, the methodology applied was exactly the same as in the photoluminescence analysis of the nanocrystals, with the addition of a digital multimeter equipped with a platinum and platinum-10% rhodium thermocouple to monitor the temperature, covered with a 2 mm thick chicken breast slice, and placed close to the injected nanoparticles. A thermal camera was also coupled to this optical system to monitor the temperature increase at the surface of the chicken breast.

3. Results and Discussion

3.1. Characterization of the nanocrystals

The synthesis of the undoped KLuW and Ho, Tm doped KLuW nanocrystals, was achieved via microwave-assisted (MW) and conventional autoclave (CA) solvothermal methodologies in the presence of an equimolar ratio of OLAC and OLAM, and the precursors $Lu(NO_3)_3{\cdot}H_2O$ and K_2WO_4, at 453 K for 3 h. This resulted in the formation of the first initial product, that we called seeds, followed by a calcination post treatment at 1023 K during 2 h to form the desired compound. The synthesis conditions were analyzed to optimize the different parameters. The results of this optimization process can be found in the Supporting Information (summarized in Table S1 and Section S1 and Section S2). X-ray powder diffraction (XRPD) data reveal that the synthesized nanocrystals crystallize in the monoclinic system with the *C*2/*c* spatial group, as confirmed by the comparison with the reference pattern of $KLu(WO_4)_2$ (JCPDS file 54-1204),[45] presented in Figure 1 (a) for the undoped nanocrystals and in Figure S16 at the Supporting Information under Section S3 for the doped nanocrystals. The presence of the dopants displays no significant effect on the purity of the crystalline phase obtained.

To understand in more detail the physical process that take place during the calcination step, transforming the seeds into the monoclinic KLuW crystalline phase, a Differential Thermal Analysis (DTA) and Thermal Gravimetric Analysis (TGA) of the seeds obtained by the MW solvothermal method, were performed. The thermograms of the seeds are provided in Figure 1 (b). The seeds were heated from room temperature to 1273 K. During the heating process from room temperature to 800 K, two peaks in the DTA curve were observed, associated to two weight losses in the TGA curve. The broad peak at 543 K and the less intense peak at 673 K are most probably attributed to the degradation of the organic surfactants,[46] which have the ability to bind to the surface of the seeds to prevent their aggregation. In this range of temperatures, the major loss of weight (~ 4%) is observed, as can be seen in the TGA signal. Similar results are reported for nanoparticles coated with oleic acid, in which these two distinct peaks observed in the DTA curve are related to either the number of layers (bilayer or quasi-two-layers) of oleic acid coating the surface of the nanocrystals or the type of bonding that oleic acid forms with the metal ions.[47-49] Instead, if the organic surfactant would be coating the nanoparticles with a monolayer, a single weight loss should be observed, as previously described in the literature.[50] Hence, these results confirm that the seeds are coated with a bilayer or quasi-two-layers of oleic acid. A more complex peak structure appears in the region of 823-933 K, which can be attributed to different transformations of the seeds. The formation of the monoclinic KLuW phase is observed by the appearance of a sharp peak at 1013 K.

To confirm the hypothesis expressed in the previous paragraph we analyzed the evolution of the diffraction pattern of the seeds as a function of temperature in the range from RT to 1273 K. From the XRPD data (Figure 1 (c)) obtained when applying a thermal treatment to the seeds obtained by the MW solvothermal reaction, we can observe that the XRD patterns recorded from room temperature (see Figure S2 at Supporting Information) to 673 K, exhibit no significant changes. Instead of analyzing the whole 2θ range, we focused to the 2θ range from 22° to 39°, since it represents the region in which the most intense peaks of both, seeds and final products appear. The XRD pattern obtained at 973 K, show peaks that can be attributed to the starting seeds and peaks of KLuW, which gradually increased their intensity as the temperature increased. Monoclinic KLuW seems to form at 1013 K, as confirmed from the DTA exothermic peak at this temperature, and it remains as the only crystalline phase present in the diffraction patterns until at least 1173 K, as presented from Figure 1 (c). At 1273 K, the orthorhombic phase of KLuW is observed, corresponding to the high temperature crystalline phase of this compound.[51, 52] This phase would start to form at 1218 K, according to the DTA analysis (see Figure 1 (b)).

As a final confirmation for the successful formation of monoclinic KLuW phase, we performed a DTA analysis of the nanoparticles obtained by the MW solvothermal synthesis. The obtained data are compared with the DTA analysis of a bulk monoclinic KLuW crystal, presented in Figure 1 (d). The two samples have a similar behavior, showing an intense endothermic peak at around 1311-1316 K. As Kletsov *et al.*[54] indicated the polymorphous transformation in double tungstates takes

place at temperatures near the melting point. Hence the transformation from the low temperature crystalline phase (monoclinic) to a higher temperature crystalline phase (orthorhombic) and the melting process are responsible for the appearance of these peaks around 1311-1316 K. These processes are reversible, because KLuW melts congruently, and the crystalline transformation is also reversible.[54, 55] The slight difference between the two samples lies on that the peaks of the sample prepared by the MW solvothermal method appear to be slightly shifted to lower temperatures. For example, the endothermic sharp peak observed for the sample coming from the bulk single crystal appears at 1316 K, whereas for the MW solvothermal sample, it appears at 1311 K. Also, during the cooling process the peak observed at 1293 K for the bulk sample, appears at 1273 K for the MW solvothermal sample. These differences may be attributed to the size of the particles in each case (microsize for the bulk crystal sample and nanosize for the MW solvothermal sample).

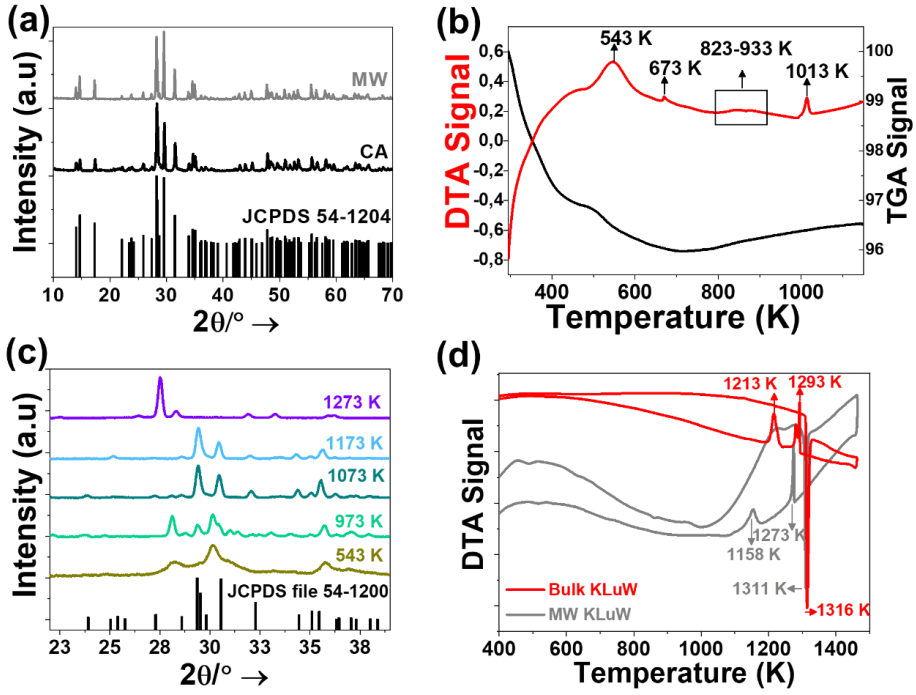

Figure 1. (a) XRPD patterns of undoped KLuW nanoparticles synthesized by the MW and CA solvothermal methodologies. The reference pattern of $KLu(WO_4)_2$ (JCPDS file 54-1204) is included for comparison. (b) DTA-TGA analysis of the seeds obtained from the MW solvothermal reaction at 453 K and 3 h. (c) Evolution of the XRPD pattern of the seeds with temperature. (d) DTA analysis of KLuW final product obtained from the MW solvothermal method and a bulk KLuW crystal obtained by the high temperature top-seeded solution method.[53]

Unpolarized Raman spectra were recorded to investigate the vibrational modes of doped KLuW materials. Regardless of the doping ratio used, the observed vibrational modes for all materials, are the expected ones for the monoclinic KLuW phase (see Figure 2).[55] In general, the most intense peak is observed at around 900 cm^{-1} which is attributed to the stretching mode of (W-O), followed by the second most intense peak at around 750 cm^{-1} is the coupling between the stretching mode of (W-O) and oxygen-doubled bridges (WOOW).[55] The range between 270-400 cm^{-1} is attributed to the WOOW and W-O bending modes,[55] and the 400-1000 cm^{-1} range is related to the stretching modes of the WO_6 group in the double tungstates.[55] The phonons below 270 cm^{-1} are associated to the translational modes of the cations (K^{+1}, Lu^{3+} and W^{6+}) and the rotational motion of the WO_6 groups in the unit cell.[55]

The size and shape of these nanocrystals was investigated by transmission electron microscopy (TEM). The synthesized particles exhibit an ellipsoidal (see Figure 3 (a)) and an irregular shape (see Figure 3 (b)) for the MW and CA based methodologies, respectively. In terms of the size, the nanocrystals synthesized by MW methodology are smaller compared to the ones produced by the CA methodology, with an average diameter of 12 nm (see Figure 3 (c)) for the particles produced by the MW method and a length of 16 nm (see Figure 3 (d)) for the particles synthesized by the CA method, respectively. These sizes are similar to the ones determined by applying the Debye-Scherrer equation,[56] (19 nm and 28 nm for MW and CA, respectively).

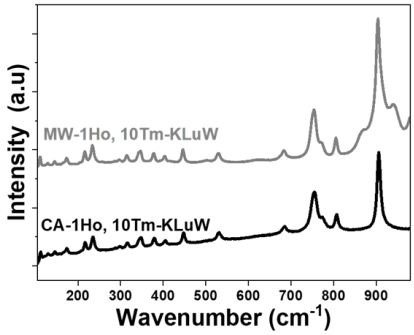

Figure 2. Unpolarized Raman spectra of 1 mol% Ho, 10 mol% Tm:KLuW nanoparticles synthesized by the MW and CA solvothermal methodologies.

Overall, these solvothermal methodologies not only surpass the limitation exhibited by the traditional modified sol-gel Pechini method regarding the agglomeration and wide size distribution,[35-37] but in addition offer time and power-effective methods for the synthesis of monoclinic KLuW. In terms of time, the Pechini approach requires approximately one day and a half to prepare the KLuW particles (one day to have the lanthanide precursors completely dissolved in an aqueous solution of EDTA, K_2CO_3, and $(NH_4)_2WO_4$, 2-3 h to evaporate the water after the addition of PEG, followed by 3 h of precalcination process, and finally 2 h of calcination at 1023 K).[35-37] For the solvothermal methodologies, the maximum time needed to prepare the nanocrystals is approximately 6 h, considering here a reaction time of 3 h, the purification process of 20 min, the complete evaporation of the organic apolar solvent (n-hexane) of around 1 h, and the final step of calcination of 1.5-2 h. This time can be reduced even at only 3 h, by considering a reaction in which the sacrificial seeds are obtained in a reaction time of only 0.08 h. However, the final KLuW product obtained for a reaction time of 0.08 h suffers from agglomeration and relatively large particle sizes (see Figure S15 (f) at Supporting Information), not fulfilling the basic requirements for photothermal agents used in biomedical applications.[4]

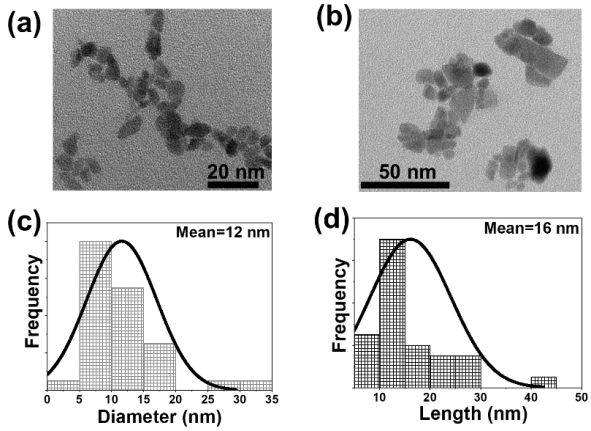

Figure 3. TEM images and lognormal size distribution of undoped KLuW nanoparticles synthesized via: (a), (c) MW and (b), (d) CA solvothermal methodologies.

In terms of power, to achieve the final product, through the Pechini method the reaction mixture has to pass through four different heating processes: dissolution of the lanthanide precursors at 353 K, evaporation of water at 373 K, precalcination process at 573 K, and final calcination at 1023 K. For the MW and CA solvothermal methodologies, only three steps are required: reaction at 453 K, solvent evaporation at 353 K and calcination at 1023 K.

Lately, another microwave-assisted hydrothermal synthesis method for the preparation of monoclinic $KY(WO_4)_2$ nanocrystals without using organic surfactants, has been proposed.[57] This reaction involves preheating at 388 K for 0.5 h, a reaction at 523 K for 3 h, a purification process with deionized water, and a drying process at 353 K for 20 h, after calcination at 1023 K for 1 h. The final product of the reaction shows a tendency towards agglomeration and irregular morphological habits. Nevertheless, the ability of MW and CA solvothermal methods to generate discrete nanoparticles with no agglomerations, close-to-regular shapes and through a time and energy-effective method, offers significant advantages in the synthesis of these nanoparticles.

The two solvothermal based methodologies reported here, display differences among them, especially in the size and shape of the seeds and final products obtained. The seeds obtained by these two methods, exhibit a similar XRD pattern (see Figure S1 (a) and Figure S12 (a) at Supporting Information), but a significant different morphology (see Figure S2 (a) and Figure S13 (a) at Supporting Information). The seeds obtained by the MW method are nanorods (see Figure S2 (a) at Supporting Information)) with an average length of 322 nm, whereas the seeds obtained by the CA solvothermal method exhibit an urchin-like morphology ((see Figure S12 (a) at Supporting Information)) with an average length of 585 nm. The differences between these two approaches should be attributed to the different heating mechanisms to achieve the desired reaction temperature and the way in which the precursors behave exposed to these mechanisms, affecting hence, the kinetics of the reaction and as a consequence, the nucleation and growth mechanisms of the seeds. The MW solvothermal method drives chemical reactions by taking advantage of the ability of the used reagents and solvents to transform microwave irradiation into heat. Therefore, chemical reactions become more efficient and can be performed in a shorter time due to the selective absorption of microwave energy by polar molecules, in most of the cases, leading to an uniform heating in the reaction mixture.[58] The CA solvothermal reaction, from its side, involves the use of a furnace as the heating system, which heats the walls of the reactor by thermal convection or conduction, leading to longer times for the reaction mixture to reach a homogenous distribution of the desired temperature, and as a consequence the reaction mixture is not uniformly heated while part of the energy is wasted by dissipation.[58]

3.2. Mechanism of formation of KLuW nanocrystals via MW or CA solvothermal methods

Taking into account all the parameters that affect to the size, shape and formation of KLuW nanocrystals in the solvothermal synthesis, an insight to the possible formation mechanism is attempted. We believe that in the synthesis of the monoclinic KLuW nanocrystals takes place a so-called “cooperative-controlled crystallization mechanism”, which was introduced by Bu *et al.,* for the synthesis of uniform bipyramidal tetragonal $NaLa(MoO_4)_2$ nanocrystals.[43] In this mechanism, the role of the organic surfactants was to control the nucleation and growth of $NaLa(MoO_4)_2$ nanocrystals by selectively binding to a specific crystal facet. The main difference between the synthesis of the two compounds is that while tetragonal $NaLa(MoO_4)_2$ can be obtained directly from the solvothermal reaction, monoclinic KLuW could not be obtained as a direct product of the MW or CA solvothermal method, but a calcination step was crucial to achieve the desired KLuW phase. Hence, here the cooperative-controlled crystallization mechanism would affect the formation of the seeds, having a critical role in defining the final size of the KLuW nanocrystals.

Scheme 1 summarizes the proposed possible formation mechanism of the monoclinic KLuW nanocrystals via the MW (or CA) solvothermal methods. When OLAC and OLAM are mixed in an equimolar ratio in ethanol, a mixture of deprotonated OLAC containing carboxylate anions ($C_{17}H_{33}COO^-$, plotted in the scheme as OLAC-), protonated OLAM ($C_{18}H_{35}NH_3^+$, plotted in the

scheme as $OLAM^+$) and the corresponding acid-base complex ($C_{17}H_{33}COO^-$:$C_{18}H_{35}NH_3^+$, plotted in the scheme as $OLAM^+$ $OLAC^-$) are present. In fact, as stated by *Bu et al.* OLAM helps enhancing the deprotonation of OLAC and forms an acid-base complex with OLAC molecules. OLAM also contributes to keep the pH values stable to 8.7,[43] which was confirmed experimentally in both MW and CA solvothermal methods.

By adding the $Lu(NO_3)_3{\cdot}H_2O$ aqueous solution, a lutetium-OLAC complex, i.e. $Lu(NO_3)_{3-x}(C_{17}H_{33}COO)_x$ would form via anion exchange. Proof of the complexation between the lanthanide cation and the OLAC anion is the change of the aspect of the solution from a homogeneous transparent solution to a milky one. After the addition of the aqueous solution of K_2WO_4, an ion exchange and substitution among NO_3^-, OLAC- and WO_4^2, as well as Lu^{3+} and K^+ takes place, leading to the formation of the primitive nucleus precursors.[43, 59] During the solvothermal reaction, the precursor's nucleuses reach a critical size leading to the formation of stable nucleus of the precursor compound. Later on, solvothermal growth and ripening processes result in the production of the initial anisotropic carboxylate anions caped seeds. The enhanced deprotonation of OLAC, having a superior electron-donating ability than OLAM, facilitates the binding to metal ions on the facets of the seeds.[60] It is worth to mention that in the case of the MW reaction, this binding process seems to be more anisotropic, and the OLAC capping groups shows a preferential binding, observed by an enhanced XRPD intensity of the angle at around 10° (see Figure S1 (a) at Supporting Information) starting the formation of the nanorod morphology. Since the crystalline nature of the seeds could not be identified, it is not possible to identify to which crystal faces, these deprotonated OLAC molecules would bind preferentially.

After the solvothermal treatment, the formed seeds coated with oleic acid, sediment at the bottom of the Teflon microwave or autoclave vial after centrifugation because of the effect of gravity and their hydrophobic surfaces. Free OLAC dimers, OLAM, protonated OLAM, acid-base complexes and the excess of organic surfactants would not bind to the seed surfaces and would be washed away during the purification steps with ethanol and hexane. Finally, to achieve the desired crystalline phase, the seeds were calcined at 1023 K for 2 h at ambient atmosphere. Apparently, the OLAC-OLAM system acts like a media-regulator, maintaining a stable pH value in the mixture, which is a key feature for the formation of seeds that will be later calcined to obtain the monoclinic KLuW phase. When excess of OLAM or no organic surfactants were used, the final product of the synthesis was a mixture of compounds (see Figure S5 at the Supporting Information) instead of pure KLuW. OLAM contributes to keep the pH values stable to 8.7,[43] which was confirmed experimentally in both MW and CA solvothermal methods. This value of the pH is highly important for the formation of the desired seed precursors and pure monoclinic phase. Thus, tuning the value of the pH would greatly influence the degree of the hydrolysis and the state of the cations and tungsten ions present in this liquid phase chemical reaction. Since the organic surfactants maintain these stable pH values, upon removing them (reaction MW-10), the pH value dropped to 7.55, as a consequence the XRD patterns of the seeds and the corresponding final product is highly different that the reactions with pH 8.7 (see Figure S6 (a) and (b) at Supporting Information). At pH 7.55, the final product obtained was a mixture between K_2WO_4 and Lu_2O_3 (see Figure S6 (b) at Supporting Information). On the other hand, the increase of the value of the pH to 10.2, when excess of OLAM (4 times) in comparison with OLAC was added (reaction MW-9), additional low intensity peaks are observed in the XRD pattern of the final product (see Figure S6 (b) at Supporting Information).

Further surface FT-IR characterization of the dried seeds (see Figure S17 at Supporting Information) confirms that they are coated with oleic acid. These results confirm the adsorption of the oleyl group on their surfaces, by the presence of the peaks related to the $-CH_2$ asymmetric and symmetric stretching vibrations of this group, observed at 2930 cm^{-1} and 2850 cm^{-1}, respectively.[47, 61] The characteristic peaks of OLAC (1709 cm^{-1}) and OLAM (1593 and 3300 cm^{-1}) could not be identified in the spectrum, indicating that no free OLAC or OLAM are present on the samples.[62] The broad band observed at 3440 cm^{-1}, can be attributed to the stretching vibration modes of the O-H bonds, generated by the adsorption of oleic acid on the surface of the seeds. Finally, the two strong peaks observed at 1625 and 1460 cm^{-1} indicate the bidentate coordination of OLAC to the metal atoms.[63] OLAM is not observed on the FT-IR spectrum of the seeds, confirming that OLAM helps to the formation of an acid base complex with OLAC, and

consequently, more OLAC molecules present dissociated hydroxyl groups that facilitate the adsorption of OLAC on the surface of the seeds. This observation is in agreement with other papers published previously,[47, 64] and also with the case when only OLAM was used as organic surfactant.[65] After calcination at 1023 K, there is no presence of the capping surfactants, as confirmed by the FT-IR spectrum corresponding to the KLuW nanocrystals (see Figure S6 at Supporting Information), and also by the DTA results (see Figure 1 (d)). Another factor that confirms the successful elimination of the organic coating is the dispersibility of the final nanocrystals in water (see Figure S18 at Supporting Information). If the hydrophobic organic surfactants would be present on the surface of the KLuW nanocrystals, they would not be dispersible in water due to their hydrophobic nature.

Scheme 1. Proposed mechanism for the formation of monoclinic KLuW nanocrystals via the MW solvothermal method as an example.

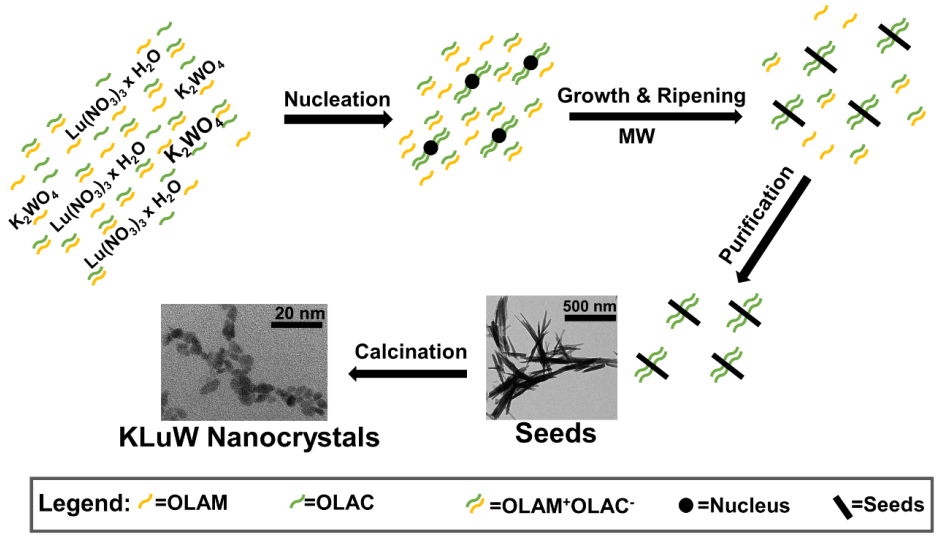

3.3. Photoluminescence characterizations

The emissions of the Ho, Tm:KLuW nanoparticles synthesized via MW and CA solvothermal methodologies, lying in the third biological window (III-BW), were recorded at room temperature after excitation at 808 nm with a power of 200 mW. The emission spectra, regardless of the doping ratio applied, consist of three emission bands: 1.45 µm and 1.8 µm, corresponding to the $^3H_4 \rightarrow {}^3F_4$ and $^3F_4 \rightarrow {}^3H_6$ electronic transitions of Tm^{3+}, and 1.96 µm, corresponding to the $^5I_7 \rightarrow {}^5I_8$ electronic transition of Ho^{3+} (see Figure 4 (a) for 3 mol% Ho, 5 mol% Tm:KLuW and Figure S19 at Supporting Information for 1 mol% Ho, 10 mol% Tm:KLuW), respectively.[11] These doping ratios were selected according to a previous work achieved from our group in which these doping ratios, among others, exhibited the highest photoluminescence intensity in the III-BW (3 mol% Ho^{3+}, 5 mol% Tm^{3+}) and the highest photothermal conversion efficiency (1 mol% Ho^{3+}, 10 mol% Tm^{3+}).[36] Comparing the intensity of the emission generated, the nanocrystals synthesized by the MW method, produce a brighter emission. The mechanisms of generation of these emission bands is depicted in Figure 4 (b). Tm^{3+} absorbs a photon at 808 nm and promotes its electrons from the $^3H_6$ ground state to the $^3H_4$ excited state. From there, the electrons decay radiatively to the $^3F_4$ manifold, generating the emission line at 1.45 µm. With another radiative decay from the $^3F_4$ level to the $^3H_6$ ground state, the emission line at 1.8 µm is generated. Tm^{3+} ions also undergoes cross-relaxation (CR) process into the $^3F_4$ excited state, when one of the ions is initially excited into the upper $^3H_4$ excited state and then it relaxes non-radiatively to the $^3F_4$ level while this energy is used to promote an electron in the $^3H_6$ ground state to the $^3F_4$ level, due to the energy resonance between these two processes. Due that the $^3F_4$ level of Tm^{3+} and the $^5I_7$ level of Ho^{3+} are resonant in energy, energy transfer (ET) and back energy transfer (BET) processes might take place,

promoting the electrons of Ho^{3+} from the ground state to this excited state. Then, the electrons of Ho^{3+} relax back radiatively to the $^5I_8$ ground state, giving rise to the emission band at 1.96 μm.[36]

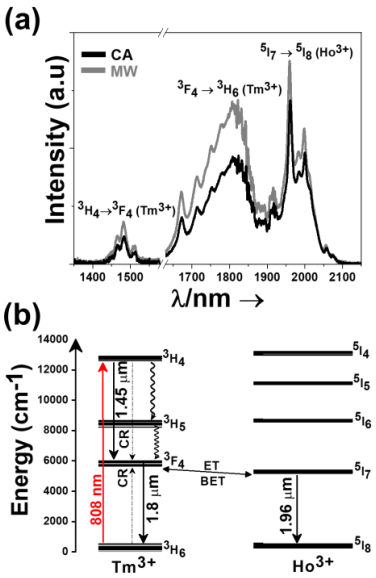

Figure 5. (a) Third biological window emissions recorded at room temperature for 3 mol% Ho, 5 mol% Tm:KLuW nanocrystals excited at 808 nm. Please note that part of the spectrum from 1580 nm to 1630 nm was removed due to the presence of the second harmonic of the 808 nm laser source. (b) Energy level diagram of Ho^{3+} and Tm^{3+} in KLuW nanoparticles and the mechanism of generation of their emission lines in the III-BW. Solid arrows indicate radiative processes, the red arrow indicates the absorption process, the three radiative emissions are indicated by black arrows, curved arrows indicate non-radiative multiphonon decay processes. The dashed arrows stands for the cross relaxation (CR) process in Tm^{3+} ($^3H_6$,$^4H_4$) ↔ ($^3F_4$,$^3F_4$).

3.4. Ho, Tm:KLuW nanocrystals as luminescent thermal sensors in the third biological window

The thermal sensing capacity in the III-BW spectral region of Ho, Tm doped KLuW nanoparticles synthesized via MW and CA solvothermal methodologies for the doping concentration of 1 mol% Ho, 10 mol% Tm and 3 mol% Ho, 5 mol% Tm, has been evaluated and compared to the performance of other thermal sensors, by studying the dependence of the intensity ratio (Δ), the absolute (S_{abs}) and relative (S_{rel}) thermal sensitivities,, and the temperature resolution (δT), in the physiological range of temperatures between 293 K and 333 K after 808 nm excitation using 200 mW laser power.

With the increase of the temperature, the intensity of the Ho^{3+} emission band decreases (see Figure 6 (a)) due to the thermal activation of luminescence quenching mechanisms,[34] while the intensity of the Tm^{3+} emission bands remains almost unchanged, hence they can be used as a reference for thermal sensing. The temperature dependence of the intensity ratio, can be modelled through the approach for dual center emission lanthanide based thermometers.[66] This model is based on the fact that the total transition probability of a particular emitting level is the sum of the radiative and non-radiative transition probabilities, [67] and the integrated luminescence intensity can be correlated to the inverse of the total transition probability.[68] The dependence of the intensity ratio vs. temperature can be expressed by:

$$\Delta = \frac{I_1}{I_2} = \Delta_0 \frac{1+\sum_i \alpha_{2i}\, exp\left(-\frac{\Delta E_{2i}}{k_B T}\right)}{1+\sum_i \alpha_{1i}\, exp\left(-\frac{\Delta E_{1i}}{k_B T}\right)} \qquad (1)$$

where 1 and 2 are the two emissions whose intensities are used to estimate the thermometric performance; Δ_0 stands for the ratio between the I_{01}/I_{02} at 0 K for the 1 and 2 emissions; α_{2i} and α_{1i} stands for the ratio between the non-radiative and radiative probabilities for the emitting level of the electronic transitions 1 and 2, respectively; and the sum sign extends from I= 1 to n, being n all the possible non-radiative deactivation channels of the electronic starting levels for the transitions with intensities $I_1$and I_2. Finally, ΔE_{2i} and ΔE_{1i} are the activation energies for the thermally quenched processes of the transitions 1 and 2, and k_B is the Boltzmann constant expressed in cm^{-1} (k_B=0.695 cm^{-1}).

If the exponential term dominates in the intensities of the transitions involved and assuming a single deactivation channel (1<<α_i exp (-$\Delta E_i/k_B$T), Equation 1 could be converted to:

$$\Delta = \Delta_0 \frac{\alpha_{2i}}{\alpha_{1i}} \frac{exp\left(-\frac{\Delta E_2}{k_B T}\right)}{exp\left(-\frac{\Delta E_1}{k_B T}\right)} = B \exp\left(\frac{\Delta E_1 - \Delta E_2}{k_B T}\right) = B \exp\left(\frac{-C}{T}\right) \quad (2)$$

where B=$\Delta_0 \frac{\alpha_{2i}}{\alpha_{1i}}$ is an empirical constant to be determined by experimental fitting, and $C = \frac{\Delta E_1 - \Delta E_2}{k_B}$ is the energy difference between the two activation energies for the thermally quenched processes divided by the Boltzmann's constant.

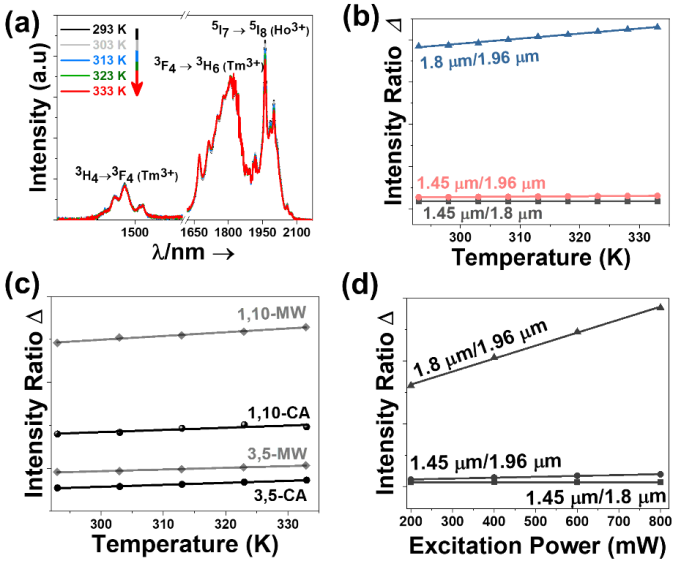

Figure 6. (a) Temperature dependence of the intensity of the emission bands lying in the III-BW for 3 mol% Ho, 5 mol% Tm:KLuW nanocrystals synthesized via the MW-assisted methodology, as an illustrative example. Please note that part of the spectra from 1580 nm to 1620 nm was removed due to the presence of the second harmonic of the 808 nm laser source. (b) Temperature-dependence of the intensity ratios for 3 mol% Ho, 5 mol% Tm:KLuW, as an example. (c) Evolution of the intensity ratio 1.8 μm/1.96 μm for all the Ho, Tm:KLuW nanocrystals synthesized by solvothermal methodologies with temperature (experimental scattered data and linear fitting according to Equation 2). (d) Dependence of the intensity ratio with the power of the excitation source for 3 mol% Ho, 5 mol% Tm:KLuW nanoparticles synthesized via MW solvothermal synthesis, as an illustrative example.

Compared to the other two intensity ratios that can be calculated (the 1.45 μm/1.8 μm and 1.45 μm/1.96 μm), the intensity ratio between the bands at 1.8 μm and 1.96 μm, is the one that results affected the most by the increase of temperature (see Figure 6 (b) and Figure S20 at Supporting Information). This is in agreement with the results obtained previously for Ho, Tm:KLuW nanoparticles synthesized by the modified sol-gel Pechini method.[36] For this intensity ratio, by fitting Equation 2 to the experimental emission-temperature dependence for each Ho,Tm:KLuW sample (see Figure 6 (c)), we determined the values of B and C. The results are summarized in

Table S3 at Supporting Information. In addition, we explored the power dependence of the intensity ratio for the three emission bands. This relation is of paramount interest when investigating the application of these lanthanide doped luminescent thermometers in biomedical fields.[69] This relation is linear: with the increase of the excitation power, the intensity ratio increases (see Figure 6 (c)). The intensity ratio that exhibits the highest change with the increase of the excitation power is the one between the emissions located at 1.8 μm and 1.96 μm.[36] This linear relation is important during biological application of these lanthanide doped luminescent thermometers where is no real control on the power reaching the particles and this might rise imprecision during measurements. Thus, having a linear relation, this imprecision source is reduced.

Knowing the value of B and C for each Ho, Tm doped KLuW materials, we can estimate their thermometric performance by calculating S_{abs}, S_{rel} and δT.

The absolute thermal sensitivity depends on the experimental setup used to record the spectra and the characteristics of the sample (absorption and lifetimes).[66] Hence, S_{abs} will allow the comparison of only Ho, Tm:KLuW analyzed using the experimental setup applied here, but not allow the comparison with different classes of thermometers. The absolute thermal sensitivity is expressed by:[66]

$$S_{abs} = \frac{\partial \Delta}{\partial T} \qquad (3)$$

The samples with the highest absolute thermal sensitivity are the ones synthesized by the MW solvothermal methodology, with 1 mol% Ho and 10 mol% Tm dopant concentrations (see Figure 7 (a) and Table S3 at Supporting Information).

To compare different classes of thermometers, the relative thermal sensitivity is used as a figure of merit and expresses the maximum change in the intensity ratio for each temperature degree.[66] The relative thermal sensitivity is defined as:[66]

$$S_{rel} = \frac{1}{\Delta}\left|\frac{\partial \Delta}{\partial T}\right| x\ 100\% = \left|\frac{\Delta E}{k_B T^2}\right| x\ 100\% \qquad (4)$$

where $\Delta E = \Delta E_2 - \Delta E_1$ is determined by experimental fitting and T is the absolute temperature.

In general, the intensity of the emissions generated by the Ho, Tm:KLuW nanocrystals synthesized by the CA solvothermal method is more sensitive to the changes of temperature when compared to the nanocrystals synthesized by the MW method. The 3 mol% Ho, 5 mol% Tm doping concentrations showed the highest relative thermal sensitivity with a value of 0.33% K^{-1} at room temperature (see Figure 7 (b) and Table S3 at Supporting Information). The lowest S_{rel} is obtained for the 1 mol% Ho, 10 mol% Tm: KLuW nanocrystals synthesized by the MW-assisted methodology. A general trend in the temperature dependence of the relative thermal sensitivity with the temperature is its decrease as the temperature increased (see Figure 7 (b)).

The temperature resolution is defined as the smallest temperature change that can be detected in a given measurement and it is estimated by:[66]

$$\delta T = \frac{1}{S_{rel}} \frac{\delta \Delta}{\Delta} = \left|\frac{k_B T^2}{\Delta E}\right| \frac{\delta \Delta}{\Delta} \qquad (5)$$

where $\frac{\delta \Delta}{\Delta}$ = 0.5% is the relative error in the determination of the thermometric parameter, determined by the acquisition setup used.[35] The variation of the temperature resolution with the increase of the temperature follows the inverse trend of the relative thermal sensitivity. Hence, the better is the relative thermal sensitivity, the lowest is the temperature resolution (see Figure 7 (c) and Table S3 at Supporting Information). The lowest δT corresponds to 3 mol% Ho, 5 mol% Tm: KLuW synthesized by the CA methodology with a value of 1.5 K at 293 K. As the temperature increases, this value increases up to a maximum of 1.94 K at 333 K.

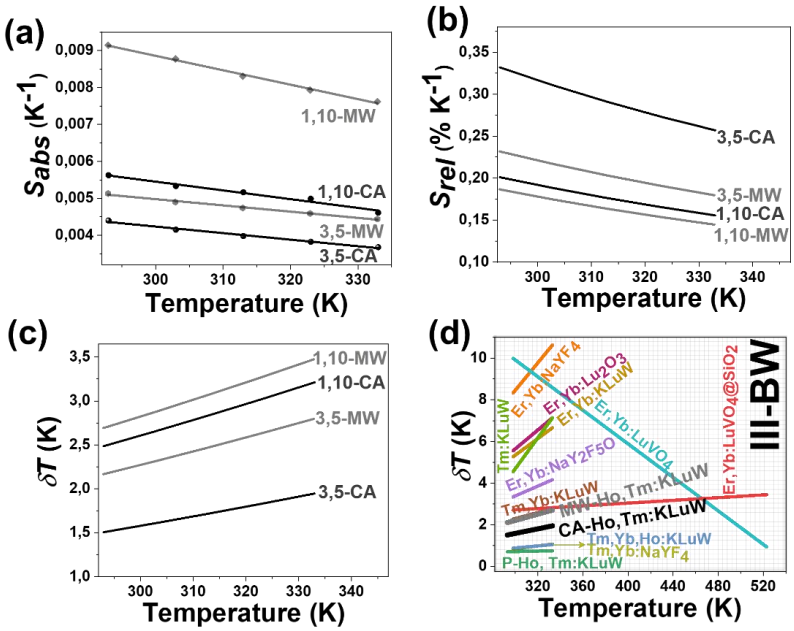

Figure 7. (a) Absolute thermal sensitivity (S_{abs}) (experimental scattered data and linear fitting using Equation 3); (b) relative thermal sensitivity (S_{rel}); and (c) temperature resolution (δT) of Ho, Tm:KLuW nanoparticles synthesized by conventional autoclave (CA in solid black lines) and microwave-assisted (MW in dot black lines) solvothermal methods. Numbers, 3, 5 and 1, 10 represent the doping concentration in mol% of Ho^{3+} and Tm^{3+}, respectively. (d) Comparison of the thermometric performance of lanthanide doped materials operating in the III-BW. Ho, Tm:KLuW nanoparticles synthesized by conventional autoclave (CA in solid black line for the 3 mol% Ho, 5 mol% Tm doping ratio as the best nanothermometer) and microwave-assisted (MW in solid gray lines for the 3 mol% Ho, 5 mol% Tm doping ratio as the best nanothermometer) solvothermal methods. The Ho, Tm:KLuW nanoparticles synthesized by the modified sol-gel Pechini methodology is included for comparison ((MW in solid green line for the 1 mol% Ho, 10 mol% Tm doping ratio as the best nanothermometer).

Furthermore, we compared the thermometric performance of these nanocrystals with the corresponding Ho, Tm:KLuW synthesized from the modified sol-gel Pechini methodology. Hence, Ho, Tm:KLuW from this methodology exhibit higher thermometric performance compared to the solvothermal methodologies. Being recorded with the exact same experimental setup, the S_{abs} in both doping ratios from the modified sol-gel Pechini methodology are relative high compared to the corresponding ratios from the MW and CA solvothermal methodology (see Figure 7 (a)). The trend is furthermore extended also for the case of the relative thermal sensitivity (see Figure 7 (b)). It should be noted here that the doping ratio 1 mol% Ho and 10 mol% Tm:KLuW synthesized by the modified sol-gel Pechini methodology, displays one of the most sensitive thermometers operating in the III-BW.[36] The temperature resolution, being reverse proportional to the relative thermal sensitivity, exhibited the lowest value for the product of the sol-gel Pechini methodology (see Figure 7 (c)). Apparently, the thermometric performance of Ho, Tm:KLuW nanocrystals decreases with the decrease of their sizes. So, Ho,Tm:KLuW sensors synthesized by the modified sol-gel Pechini methodology, CA and MW, have sizes ranging from 150 nm,[36] 16 nm and 12 nm, respectively, and their corresponding maximum S_{rel} are in the range of 0.90% K^{-1}, 0.33% K^{-1} and 0.23% K^{-1}, respectively. Similar results are obtained in the case of Er^{3+}, Yb^{3+}:$NaYF_4$,[70] Er^{3+}:Y_2O_3,[71] Pr^{3+}:LaF_3 and Pr^{3+}:$LiYF_4$ sensors.[72] It was argued that as the size of the particles decreases, the amount of the luminescent active ions close to their surfaces is increased due to higher surface to volume ratio. These ions can interact with the ligands attached to the surface of the nanoparticles, leading to quenching processes that would affect negatively their thermal sensitivity.[70-71]

Having determined S_{rel} and δT, now we can compare the performance of these nanocrystals with other sensors operating in the III-BW. The performance of 1 mol% Ho and 10 mol% Tm:KLuW synthesized by MW and CA is comparable to that of Tm,Yb:KLuW,[73] and Er,Yb:$LuVO_4$@SiO_2,[74] (see Figure 7 (d)). Nevertheless, the performance of MW and CA nanocrystals is lower compared to the Tm, Yb, Ho:KLuW, and Tm,Yb:$NaYF_4$.[73]

3.5. Ho, Tm:KLuW nanocrystals as photothermal conversion agents

When a material is illuminated with light, it can be absorbed, scattered, reflected and/or transmitted. The part of the light which is absorbed can be converted in photoluminescence and heat. In lanthanide-doped materials, this transformation into heat is due to the non-radiative processes that can occur in the relaxation of the electrons of the ion. The photothermal conversion efficiency, *i.e.* the ability of the nanocrystals to convert the absorbed light into heat, was determined using the integrating sphere methodology.[44]

In this method, the photothermal conversion efficiency (η) is calculated from the expression:

$$\eta = \left|\frac{P_{blank} - P_{sample}}{P_{empty} - P_{sample}}\right| x\ 100\% \qquad (6)$$

where P_{blank}, P_{empty} and P_{sample} are the power values measured for the solvent (distilled water in this case), the empty sample holder and the doped Ho,Tm:KLuW nanoparticles synthesized via the solvothermal methodologies, respectively.

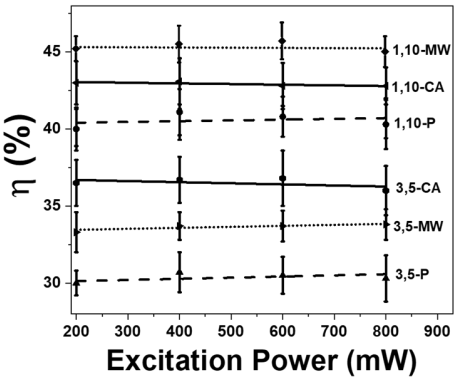

Figure 8. Power dependence of the photothermal conversion efficiency of all Ho, Tm doped KLuW nanoparticles synthesized via solvothermal methods (conventional autoclave (CA in solid black lines) and microwave-assisted (MW in dot black lines)) and modified sol-gel Pechini method (P in dashed black lines). Numbers, 3, 5 and 1, 10 represent the doping concentration in mol% of Ho^{3+} and Tm^{3+}.

The photothermal conversion efficiency of the Ho,Tm:$KLu(WO_4)_2$ nanoparticles was measured by illuminating a sample of the Ho,Tm:$KLu(WO_4)_2$ nanoparticles dispersed in distilled water with a concentration of 1 g L^{-1} with a laser emitting at 808 nm with a power of 200 mW. Figure 8 summarizes the photothermal conversion efficiencies obtained. The highest light-to-heat conversion efficiency was obtained by the nanoparticles with the smallest sizes, synthesized by the MW solvothermal method with a value of η=45 ± 2% for the 1 mol% Ho, 10 mol% Tm doped KLuW nanoparticles. The same material, synthesized by the CA approach and with slightly larger sizes, displays a light-to-heat conversion efficiency slightly lower, of 43 ± 3%. Instead, when the doping levels were3 mol% Ho, 5 mol% Tm, the highest photothermal conversion efficiency was obtained for the nanocrystals synthesized by the CA methodology with a value of 36 ± 3%. This is not surprising since the corresponding 3 mol% Ho, 5 mol% Tm KLuW nanocrystals synthesized by the MW-assisted method present the highest emission intensity among all the nanocrystals analyzed (see Figure 5 (a)).

In addition, we explored the excitation power dependence of the photothermal conversion efficiency. The results obtained reveal that the change of the pumping power has no influence on the photothermal conversion efficiency (see Figure 8). The increase of the concentration of Tm^{3+} favors the increase of the probability of multiphonon decay transitions, which in turn favors the generation of heat.[36] Also, it seems that the decrease of materials's size enhances the non-radiative processes to happen, which are responsible for the generation of heat. So, smaller sizes imply a higher photothermal conversion efficiency. Up to date, there are no reports concerning a size and shape dependence study on the photothermal conversion efficiency of lanthanide-doped materials. So, we have checked in literature the effect of the size on the photothermal conversion efficiency for different photothermal agents. Gold nanomaterials are the most studied compounds for photothermal therapy. Thus, there are reports that have studied the dependence of the photothermal conversion efficiency with the size of different gold nanostructures, such as gold nanobipyramids or spherical materials.[75-76] Both publications state that as the size of the gold nanocrystals increases, the light-to-heat ability decreases because the fraction of the light that is scattered becomes larger. This larger scattering implies that light is absorbed less by the nanocrystals, and as stated above, to produce an efficient light-to-heat conversion, a material should first, efficiently absorb light. Coming back to the lanthanide doped materials, Ho, Tm:KLuW nanoparticles synthesized by the sol-gel Pechini method are bigger, so the light-to-heat efficiency should be lower when compared to that of the nanoparticles synthesized by the MW solvothermal method (see Figure 8), that is the method that produces smaller nanoparticles. Baffou *et al.*[77] used the Green' dyadic method (GDM)[78] to investigate quantitatively how the photothermal conversion efficiency depended on the shape of gold nanostructures. The conclusion they reached was that small, flat, elongated or sharp nanoparticles appear to be much more efficient heaters than massive or bulk structures with the argument that the light source field penetrates more easily inside a thin nanostructure when compared to a thick one. The Ho, Tm:KLuW nanoparticles synthesized by the MW-assisted solvothermal method are thinner and smaller and as a consequence should be better heaters than the Ho, Tm:KLuW materials produced by sol-gel Pechini or CA assisted solvothermal method.

Compared to other classes of photothermal conversion agents, the Ho, Tm:KLuW nanocrystals synthesized by solvothermal methods exhibit a higher photothermal conversion efficiency than FePt nanoparticles,[79] Cu_9S_5,[29] graphene oxide,[44] Au/AuS or Au/SiO_2 nanoshells (see Table 1).[80] The photothermal conversion efficiency reported here is of the same order of magnitude than that reported for graphene in DMF,[44] and Au nanoshells or Au nanorods.[17] However, the ability of Au nanostars,[17] or core@shell@shell $NaNdF_4$@$NaYF_4$@Nd:$NaYF_4$,[81] to generate heat is still higher compared to the Ho, Tm doped KLuW nanocrystals reported here (see Table 1).

Table 1. Comparison of photothermal conversion efficiency (η) in different materials. The excitation wavelength (λ_{exc}) of the laser and the method used to extract η are included for comparison.

Material	**Method**	**λ_{exc} (nm)**	**η (%)**	**Ref.**
Au nanostars	Double Beam Fluorescence Thermometry	808	102	17
Au nanorods	Double Beam Fluorescence Thermometry	808	95	17
$NaNdF_4$@$NaYF_4$@ Nd:$NaYF_4$	Thermal Relaxation	808	72.7	81
$NdVO_4$ in water	Thermal Relaxation	808	72.1	82
Au nanoshells	Double Beam Fluorescence Thermometry	808	68	17
Graphene in DMF	Integrating Sphere	808	67	44
Au nanorods	Double Beam Fluorescence Thermometry	808	63	17
Au nanorods	Thermal Relaxation	815	61	80
Au/AuS nanoshells	Thermal Relaxation	815	59	80
Graphene Oxide in water	Integrating Sphere	808	58	44
Ho, Tm:$KLu(WO_4)_2$-MW	**Integrating Sphere**	**808**	**45**	**This work**
Ho, Tm:$KLu(WO_4)_2$-CA	**Integrating Sphere**	**808**	**43**	**This work**
Ho, Tm:$KLu(WO_4)_2$-Pechini	Integrating Sphere	808	40	36
Au/SiO_2 nanoshells	Thermal Relaxation	815	34	80
FePt nanoparticles	$P_{converted\ to\ heat}/P_{excitation}$	800	30	79
Cu_9S_5	Thermal Relaxation	980	25.7	29
Au nanoshells	Thermal Relaxation	808	25	83

3.6. Ho, Tm:KLuW nanocrystals as self-assessed photothermal agents

Ho,Tm:KLuW nanocrystals exhibit the ability to self-determine the temperature achieved by the system when releasing heat by using luminescence thermometry, generating self-assessed photothermal agents. This ability was proved by monitoring the temperature generated by a dispersion of these nanoparticles with a concentration of 1 g L^{-1}, after excitation at 808 nm with a power of 200 mW and a beam spot diameter of approximately 10 μm on the external surface of the vial, while recording the photoluminescence spectrum.

Figure 9 (a) illustrates the temperature evolution in the water dispersion of the Ho, Tm doped KLuW nanocrystals synthesized by the solvothermal methodologies. The nanocrystals with a doping concentration of 1 mol% Ho and 10 mol% Tm allows achieving the maximum temperature of 316.8 K in 100 s. In addition, the temperature evolution of pure distilled water is included for comparison. From the data it can be concluded that the temperature increase of more than 20 K achieved has to be attributed to the light-to-heat conversion ability of these nanocrystals. The general tendency observed, independently of the doping concentration in the nanocrystals, is a fast increase of the temperature in the first 25-30 s and then a slower increase of temperature until reaching the thermal equilibrium after approximately 100 s, in which, despite the water dispersion of nanocrystals is still illuminated with the 800 nm laser, the temperature does not increase further. Further, we compared also the temperature profile of modified sol-gel Pechini methodology, and the increase of the temperature are in accordance with the data obtained from the photothermal conversion efficiency (see Figure 9 (a)). Results reconfirm that the smaller and non-aggregated nanoparticles synthesized from the solvothermal methodologies, have higher temperature increase compared to the Pechini ones. This trend is observed for both doping ratios studied (1 mol% Ho, 10 mol% Tm and 3 mol% Ho, 5 mol% Tm).

Further, we tested the sedimentation time of the nanocrystals synthesized from these different morphologies. It is generally accepted that large and heavy nanoparticles can sediment quickly, causing the dose of nanoparticles on biological applications to vary.[84-85] In such cases, the actual concentration of nanoparticles in biomedical systems, could be significantly different from the initial provided value. And since, the reliability of these biological systems is strictly related to the concentration of the nanoparticles, these variations in the concentration of nanoparticles, may be a source of inaccuracies and misleading.[84-85] To test sedimentation properties, the nanocrystals with a concentration of 1 g/L were dispersed in distilled water, and different photographs of the vials were acquired as function of the time (see Figure S21 at Supporting Information). It can be observed that the nanocrystals synthesized from the solvothermal methodology (MW approach as an illustrative example) are stable for longer times compared to the aggregated nanoparticles achieved from the modified sol-gel Pechini methodology. Precisely speaking, the modified sol-gel Pechini methodology start to sediment at the bottom of the vial after 2 h, whereas the MW solvothermal methodology are stable up to 4.5 h. These results indicate that the nanocrystals produced from the solvothermal methodologies are more stable in biological compatible fluids, such as distilled water, which increases their potential to be applied for temperature determination in biomedical applications.

To prove the concept of the self-assessed photothermal agents in real biological samples in an *ex-vivo* experiment, 1 mol% Ho and 10 mol% Tm:KLuW materials synthesized via MW assisted solvothermal method (the particles with the highest photothermal conversion efficiency) were injected into a chicken breast piece of meat and the temperature reached was measured. When illuminated with the 808 nm light, the nanoparticles will generate photoluminescence in the III-BW, simultaneously, heat will be also released.[36] Hence, the goal of the self-assessing properties of these nanocrystals is to use the generated photoluminescence to determine how much the temperature increases inside the chicken breast piece of meat. This temperature is also measured by a thermocouple located near the injected nanoparticles to verify that the temperature determined by luminescence means is correct. In addition, we implemented to the optical setup an infrared camera with the goal to record the temperature of tissue's surface. In this way, we monitor the temperature inside the tissue and also at the surface of the chicken breast. As can be noted from Figure 9 (b), the temperature recorded at these two positions is remarkable different. The temperature measured inside the chicken breast from the thermocouple is 313.4 K,

whereas the one at the surface of the tissue is around 305.2 K, leading to a difference of 9.2 K (22%) among them. These large differences are in accordance with other reports dealing with *ex-vivo* and *in-vivo* photothermal therapies based on heating nanoparticles,[86-87] and are assigned to the heat diffusion processes taking place at the surface of the tissue.[86-87]

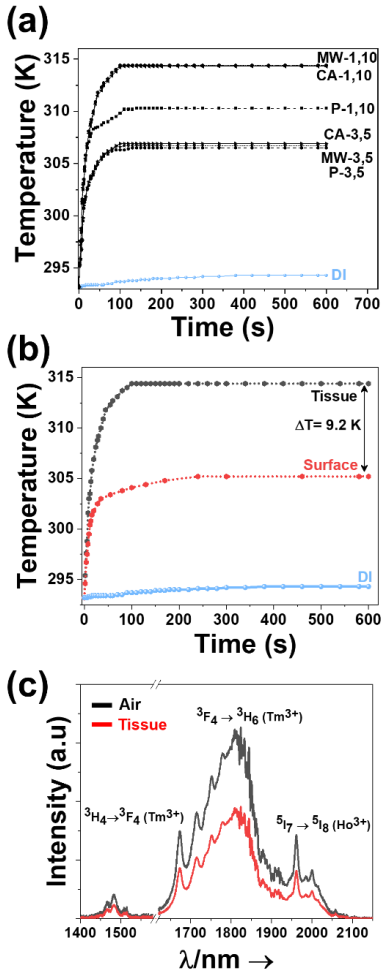

Figure 9. (a) Time-dependent temperature profile of Ho, Tm doped KLuW nanoparticles synthesized by the solvothermal (conventional autoclave (CA in solid black lines) and microwave-assisted (MW in dot black lines)) and modified sol-gel Pechini method (P in dashed black lines) achieved in an aqueous dispersion when illuminated with the 808 nm laser. Numbers, 3, 5 and 1, 10 represent the doping concentration in mol% of Ho^{3+} and Tm^{3+} ions. (b) Time-dependent temperature profile of 1 mol% Ho, 10 mol% Tm doped KLuW nanocrystals produced from MW solvothermal method, measured at the surface and inside the tissue of chicken breast, after irradiation with 808 nm wavelength. Symbols and lines stand for experimental data and solid lines, respectively. (c) Emissions in the III-BW of 1 mol% Ho, 10 mol% Tm doped KLuW nanocrystals in air and inside a 2 mm thick chicken breast piece of meat. Please note that part of the graph from 1580 nm to 1620 nm was removed due to the presence of the second harmonic of the 808 nm laser.

Hence, having established that the proper temperature read-out is achieved inside the chicken breast, we placed around 25 mg of the nanoparticles and a thermocouple, in between two pieces of chicken breast, 2 mm thick, ensuring the same medium in all directions. The nanoparticles were then irradiated with the 808 nm laser, using a power of 200 mW and a spot size of ~10 μm on the surface of the chicken breast. This value of the power of the laser was the maximum power

showing no degradation or burning of the surface of the chicken breast. It has to be taken into account that the power of the beam reaching the Ho, Tm:KLuW particles inside the chicken breast is reduced by the scattering and the absorption of the biological tissue.

The luminescence generated by the nanoparticles was recorded when the temperature measured by the thermocouple was stabilized (after around 100-120 s from the beginning of the experiment). From this spectrum, the 1.8 μm/1.96 μm intensity ratio could be extracted and by using the calibration curve shown in Figure 6 (c) the temperature inside the chicken breast was determinate. This temperature was then compared with the one measured by the thermocouple located close to the nanoparticles. Figure 9 (c) presents the III-BW emissions generated by the nanocrystals, transmitted through the 2 mm thick chicken breast, together with the spectrum of the same nanoparticles not covered by the chicken breast, recorded in open air, showing that the biological tissue does not affect the measurements of the temperature by attenuating one of these emission bands more than the others.

The temperature determined by the luminescent thermometer was 313.1 K, whereas the thermocouple indicated a temperature of 313.4 K (see Figure S22 at Supporting Information). Hence, the difference between the temperature determined by the luminescent thermometer and the thermocouple is only 0.3 K. Typical temperature difference was reported also in the case of the implementation of Ho, Tm doped KLuW nanocrystals synthesized via the modified sol-gel Pechini methodology,[36] however in this case, the difference is slightly lower. In addition, for the Pechini method, the maximum temperature. For the modified sol-gel Pechini methodology, the difference in temperature is in the range of 0.7 K.[36] The smaller difference exhibited by the products of the solvothermal methodology might rely to their smaller size and shape which ensures better distribution of the nanoparticles in the medium. Possible explanations for the small difference between the temperature determined by the luminescence thermometer and the thermocouple might rely on: i) the different thermal conductivity of the dielectric material and the metallic thermocouple, and ii) the fact that the calibration of the luminescent thermometer was performed in air and not directly inside the biological tissue. In fact, it has been reported that the medium in which the nanoparticles are embedded highly affects the determination of the temperature by luminescent thermometry.[88-91] However, the small difference observed shows that in preliminary experiments it is not necessary to perform this calibration if care is taken to verify that the thermal equilibrium has been reached.

The approach presented here demonstrates the potential applicability of Ho, Tm doped KLuW nanocrystals as multifunctional materials which can act simultaneously as luminescent nanothermeters operating in the III-BW and as photothermal agents, regardless of their size and shape. Furthermore, compared to the traditional modified sol-gel Pechini methodology, the products of the solvothermal methodology offer smaller sizes and no agglomeration, which in turn results in no sedimentation for longer times compared to agglomerated Ho, Tm:KLuW synthesized from Pechini methodology. The sedimentation data reveal that Ho, Tm doped KLuW nanocrystals achieved from solvothermal methodologies can be dispersed for longer times in solvents for temperature determination in biomedical applications. In addition, as a benefit of their smaller sizes, a lower temperature difference recorded from the nanocrystals and an external thermocouple in an *ex-vivo* experiment, is determined.

4. Conclusions

Monoclinic $KLu(WO_4)_2$ nanocrystals with sizes below 20 nm were synthesized via microwave-assisted and conventional autoclave solvothermal methods, in the presence of organic surfactants (oleic acid and oleylamine). The formation of the monoclinic crystalline phase was confirmed from X-ray powder diffraction pattern, Raman vibrational modes and differential thermal characterizations. These solvothermal methodologies introduced here, offer final product with defined shape and no agglomeration, in addition they are time and energy-effective when compared to other methods of synthesizing monoclinic $KLu(WO_4)_2$ particles, such as the modified sol-gel Pechini method. These two methodologies may provide some guidance in the preparation of other type of nanomaterials including vanadates, carbonates, molybdates and phosphates.

These nanocrystals, act as self-assessed photothermal agents in the third biological window, upon doping with Ho^{3+} and Tm^{3+} ions and excitation with near infrared light, such as the 808 nm, lying in the first biological window. These doped nanocrystals can simultaneously generate luminescence and heat, which are the sources of their applications as nanothermometers and photothermal agents, respectively. The III-BW emissions located at 1.45 μm, 1.8 μm and 1.96 μm, are attributed to the $^3H_4 \rightarrow {}^3F_4$ and $^3F_4 \rightarrow {}^3H_6$ electronic transition of Tm^{3+} and $^5I_7 \rightarrow {}^5I_8$ electronic transition of Ho^{3+}. Upon doping with 1 mol% Ho, 10 mol% Tm and 3 mol% Ho, 5 mol% Tm for both microwave-assisted and conventional autoclave synthesis, the highest thermometric performance among these nanothermometers, studied at the physiological range of temperature (293 K-333 K), was assigned to the 3 mol% Ho, 5 mol% Tm nanoparticles synthesized from the conventional autoclave method, for a value of the relative thermal sensitivity of 0.33% K^{-1} and temperature resolution of 1.4 K at room temperature. Related to their photothermal conversion efficiency, the 1 mol% Ho, 10 mol% Tm nanoparticles synthesized from the microwave-assisted method, exhibit the highest efficiency for a value of 45 ± 2%. These results underline that smaller size of particles generates more heat, but sense the temperature less, compared to agglomerated nanocrystals achieved from modified sol-gel Pechini methodology. In addition, these nanocrystals were probed as self-assessed photothermal agents: the same nanocrystals, upon excitation, released heat that will increase the temperature of the medium in which they are embedded, and luminescence, which allows the determination of the temperature in situ without the addition of an external thermal probe. The Ho, Tm:KLuW nanocrystals achieved temperature reading at a penetration depth of 2 mm inside a chicken breast.

5. Acknowledgements

This work was supported by the Spanish Government under projects MAT2016-75716-C2-1-R (AEI/FEDER, UE) and by the Generalitat de Catalunya under project 2017SGR755. A.N acknowledges financial support from the Generalitat de Catalunya under grant 2017FI_B00620, 2018FI_B100161 and 2019 FI_B200154.

6. References

1. Dickerson, E. B.; Dreaden, E. C.; Huang, X.; El-Sayed, I. H.; Chu, H.; Pushpanketh, S.; McDonald, J. F.; El-Sayed, M. A., Gold nanorod assisted near-infrared plasmonic photothermal therapy (PPTT) of squamous cell carcinoma in mice. *Cancer Letters* **2008,** 269, (1), 57-66.
2. Cheng, L.; Wang, C.; Feng, L.; Yang, K.; Liu, Z., Functional nanomaterials for phototherapies of cancer. *Chemical Reviews* **2014,** 114, (21), 10869-10939.
3. Shao, J.; Xie, H.; Huang, H.; Li, Z.; Sun, Z.; Xu, Y.; Xiao, Q.; Yu, X. F.; Zhao, Y.; Zhang, H., Biodegradable black phosphorus-based nanospheres for in vivo photothermal cancer therapy. *Nature Communications* **2016,** 7, (1), 1-13.
4. Jaque, D.; Martinez Maestro, L.; Del Rosal, B.; Haro-González, P.; Benayas, A.; Plaza, J.; Martín Rodríguez, E.; Solé, J., Nanoparticles for photothermal therapies. *Nanoscale* **2014,** 6, (16), 9494-9530
5. Gnach, A.; Lipinski, T.; Bednarkiewicz, A.; Rybka, J.; Capobianco, J. A., Upconverting nanoparticles: assessing the toxicity. *Chemical Society Reviews* **2015,** 44, (6), 1561-1584.
6. Zhang, F., *Photon upconversion nanomaterials*. Springer: 2015; Vol. 416.
7. Weissleder, R., A clearer vision for in vivo imaging. *Nature Biotechnology* **2001,** 19, (4), 316-317.
8. Shi, L.; Sordillo, L. A.; Rodríguez-Contreras, A.; Alfano, R., Transmission in near-infrared optical windows for deep brain imaging. *Journal of Biophotonics* **2016,** 9, (1-2), 38-43.
9. Naczynski, D. J.; Tan, M. C.; Zevon, M.; Wall, B.; Kohl, J.; Kulesa, A.; Chen, S.; Roth, C. M.; Riman, R. E.; Moghe, P. V., Rare-earth-doped biological composites as in vivo shortwave infrared reporters. *Nature Communications* **2013,** 4, (1), 2199-2209.
10. Chen, W. R.; Adams, R. L.; Carubelli, R.; Nordquist, R. E., Laser-photosensitizer assisted immunotherapy: a novel modality for cancer treatment. *Cancer Letters* **1997,** 115, (1), 25-30.
11. Chen, W. R.; Adams, R. L.; Higgins, A. K.; Bartels, K. E.; Nordquist, R. E., Photothermal effects on murine mammary tumors using indocyanine green and an 808 nm diode laser: an in vivo efficacy study. *Cancer Letters* **1996,** 98, (2), 169-173.
12. Kolesnikov, I.; Golyeva, E.; Kalinichev, A.; Kurochkin, M.; Lähderanta, E.; Mikhailov, M., Nd^{3+} single doped YVO_4 nanoparticles for sub-tissue heating and thermal sensing in the second biological window. *Sensors Actuators B: Chemical* **2017,** 243, 338-345.

13. Savchuk, O.; Carvajal, J.; De la Cruz, L.; Haro-Gonzalez, P.; Aguilo, M.; Diaz, F., Luminescence thermometry and imaging in the second biological window at high penetration depth with Nd:$KGd(WO_4)_2$ nanoparticles. *Journal of Materials Chemistry C* **2016,** 4, (31), 7397-7405.
14. Takei, Y.; Arai, S.; Murata, A.; Takabayashi, M.; Oyama, K.; Ishiwata, S. i.; Takeoka, S.; Suzuki, M., A nanoparticle-based ratiometric and self-calibrated fluorescent thermometer for single living cells. *ACS Nano* **2014,** 8, (1), 198-206.
15. Vetrone, F.; Naccache, R.; Zamarrón, A.; Juarranz de la Fuente, A.; Sanz-Rodríguez, F.; Martinez Maestro, L.; Martín Rodriguez, E.; Jaque, D.; García Solé, J.; Capobianco, J. A., Temperature Sensing Using Fluorescent Nanothermometers. *ACS Nano* **2010,** 4, (6), 3254-3258.
16. Martín Rodríguez, E.; López-Peña, G.; Montes, E.; Lifante, G.; García Solé, J.; Jaque, D.; Diaz-Torres, L. A.; Salas, P., Persistent luminescence nanothermometers. *Applied Physics Letters* **2017,** 111, (8), 81901-81907.
17. Maestro, L. M.; Haro-González, P.; Sánchez-Iglesias, A.; Liz-Marzán, L. M.; García Solé, J.; Jaque, D., Quantum dot thermometry evaluation of geometry dependent heating efficiency in gold nanoparticles. *Langmuir* **2014,** 30, (6), 1650-1658.
18. Huang, X.; Neretina, S.; El-Sayed, M. A., Gold nanorods: from synthesis and properties to biological and biomedical applications. *Advanced Materials* **2009,** 21, (48), 4880-4910.
19. Oldenburg, S.; Averitt, R.; Westcott, S.; Halas, N., Nanoengineering of optical resonances. *Chemical Physics Letters* **1998,** 288, (2-4), 243-247.
20. Chen, J.; Wang, D.; Xi, J.; Au, L.; Siekkinen, A.; Warsen, A.; Li, Z. Y.; Zhang, H.; Xia, Y.; Li, X., Immuno gold nanocages with tailored optical properties for targeted photothermal destruction of cancer cells. *Nano Letters* **2007,** 7, (5), 1318-1322.
21. Yang, K.; Feng, L.; Shi, X.; Liu, Z., Nano-graphene in biomedicine: theranostic applications. *Chemical Society reviews* **2013,** 42, (2), 530-547.
22. Moon, H. K.; Lee, S. H.; Choi, H. C., In vivo near-infrared mediated tumor destruction by photothermal effect of carbon nanotubes. *ACS Nano* **2009,** 3, (11), 3707-3713.
23. Zhu, X.; Feng, W.; Chang, J.; Tan, Y.W.; Li, J.; Chen, M.; Sun, Y.; Li, F., Temperature-feedback upconversion nanocomposite for accurate photothermal therapy at facile temperature. *Nature Communications* **2016,** 7, 10437-10447.
24. Yang, K.; Zhang, S.; Zhang, G.; Sun, X.; Lee, S. T.; Liu, Z., Graphene in mice: ultrahigh in vivo tumor uptake and efficient photothermal therapy. *Nano Letters* **2010,** 10, (9), 3318-3323.
25. Huang, X.; Tang, S.; Mu, X.; Dai, Y.; Chen, G.; Zhou, Z.; Ruan, F.; Yang, Z.; Zheng, N., Freestanding palladium nanosheets with plasmonic and catalytic properties. *Nature Nanotechnology* **2011,** 6, (1), 28-32.
26. Xiao, J. W.; Fan, S. X.; Wang, F.; Sun, L. D.; Zheng, X. Y.; Yan, C. H., Porous Pd nanoparticles with high photothermal conversion efficiency for efficient ablation of cancer cells. *Nanoscale* **2014,** 6, (8), 4345-4351.
27. Liu, Y.; Wang, D. D.; Zhao, L.; Lin, M.; Sun, H. Z.; Sun, H. C.; Yang, B., Polypyrrole-coated flower-like Pd nanoparticles (Pd NPs@PPy) with enhanced stability and heat conversion efficiency for cancer photothermal therapy. *RSC Advances* **2016,** 6, (19), 15854-15860.
28. Rubio-Ruiz, B.; Pérez-López, A. M.; Bray, T. L.; Lee, M.; Serrels, A.; Prieto, M.; Arruebo, M.; Carragher, N. O.; Sebastián, V.; Unciti-Broceta, A., High-precision photothermal ablation using biocompatible palladium nanoparticles and laser scanning microscopy. *ACS Applied Materials & Interfaces* **2018,** 10, (4), 3341-3348.
29. Tian, Q.; Jiang, F.; Zou, R.; Liu, Q.; Chen, Z.; Zhu, M.; Yang, S.; Wang, J.; Wang, J.; Hu, J., Hydrophilic Cu_9S_5 nanocrystals: A photothermal agent with a 25.7% heat conversion efficiency for photothermal ablation of cancer cells in vivo. *ACS Nano* **2011,** 5, (12), 9761-9771.
30. Li, Y.; Lu, W.; Huang, Q.; Li, C.; Chen, W., Copper sulfide nanoparticles for photothermal ablation of tumor cells. *Nanomedicine* **2010,** 5, (8), 1161-1171.
31. Lakshmanan, S. B.; Zou, X.; Hossu, M.; Ma, L.; Yang, C.; Chen, W. J., Local field enhanced Au/CuS nanocomposites as efficient photothermal transducer agents for cancer treatment. *Journal of Biomedical Nanotechnology*, **2012,** 8, (6), 883-890.
32. Zhang, Z.; Suo, H.; Zhao, X.; Guo, C., 808 nm laser triggered self-monitored photo-thermal therapeutic nano-system Y_2O_3: Nd^{3+}/Yb^{3+}/Er^{3+}@SiO_2@Cu_2S. *Photonics Research* **2020,** 8, (1), 32-38.
33. del Rosal, B.; Carrasco, E.; Ren, F.; Benayas, A.; Vetrone, F.; Sanz-Rodríguez, F.; Ma, D.; Juarranz, Á.; Jaque, D., Infrared-emitting QDs for thermal therapy with real-time subcutaneous temperature feedback. *Advanced Functional Materials* **2016,** 26, (33), 6060-6068.
34. Riseberg, L. A.; Moos, H. W., Multiphonon orbit-lattice relaxation of excited states of rare-earth ions in crystals. *Physical Review* **1968,** 174, (2), 429-438.
35. Savchuk, O. A.; Carvajal, J. J.; Brites, C. D. S.; Carlos, L. D.; Aguilo, M.; Diaz, F., Upconversion thermometry: a new tool to measure the thermal resistance of nanoparticles. *Nanoscale* **2018,** 10, (14), 6602-6610.
36. Nexha, A.; Carvajal, J. J.; Pujol, M. C.; Díaz, F.; Aguiló, M., Short-wavelength infrared self-assessed photothermal agents based on Ho,Tm: $KLu(WO_4)_2$ nanocrystals operating in the third biological window (1.45-1.96 μm wavelength range). *Journal of Materials Chemistry C* **2020,** 8, (1), 180-191.
37. Galceran, M.; Pujol, M.; Aguiló, M.; Díaz, F., Sol-gel modified Pechini method for obtaining nanocrystalline $KRE(WO_4)_2$ (RE=Gd and Yb). *Journal of Sol-Gel Science and Technology* **2007,** 42, 79-88.

38. van Embden, J.; Chesman, A. S. R.; Jasieniak, J. J., The heat-up synthesis of colloidal nanocrystals. *Chemistry of Materials* **2015,** 27, (7), 2246-2285.
39. Si, R.; Zhang, Y. W.; Zhou, H. P.; Sun, L. D.; Yan, C. H., Controlled-synthesis, self-assembly behavior, and surface-dependent optical properties of high-quality rare-earth oxide nanocrystals. *Chemistry of Materials* **2007,** 19, (1), 18-27.
40. Wang, Z. J.; Zhang, Y. L.; Zhong, J. P.; Yao, H. H.; Wang, J.; Wu, M. M.; Meijerink, A., One-step synthesis and luminescence properties of tetragonal double tungstates nanocrystals. *Nanoscale* **2016,** 8, (34), 15486-15489.
41. Cascales, C.; Paíno, C. L.; Bazán, E.; Zaldo, C., Ultrasmall, water dispersible, TWEEN80 modified Yb:Er:NaGd$(WO_4)_2$ nanoparticles with record upconversion ratiometric thermal sensitivity and their internalization by mesenchymal stem cells. *Nanotechnology* **2017,** 28, (18), 185101-185113.
42. Ma, L.; Liu, Y.; Liu, L.; Jiang, A.; Mao, F.; Liu, D.; Wang, L.; Zhou, J., Simultaneous activation of short-wave infrared (SWIR) light and paramagnetism by a functionalized shell for high penetration and spatial resolution theranostics. *Advanced Functional Materials* **2018,** 28, (6), 1705057-1705068.
43. Bu, W.; Chen, Z.; Chen, F.; Shi, J., Oleic Acid/oleylamine cooperative-controlled crystallization mechanism for monodisperse tetragonal bipyramid NaLa$(MoO_4)_2$ nanocrystals. *The Journal of Physical Chemistry C* **2009,** 113, (28), 12176-12185.
44. Savchuk, O. A.; Carvajal, J. J.; Massons, J.; Aguiló, M.; Díaz, F., Determination of photothermal conversion efficiency of graphene and graphene oxide through an integrating sphere method. *Carbon* **2016,** 103, 134-141.
45. Pujol, M. C.; Aznar, A.; Mateos, X.; Solans, X.; Massons, J.; Suriñach, S.; Díaz, F.; Aguiló, M., Structural redetermination, thermal expansion and refractive indices of KLu$(WO_4)_2$. *Journal of Applied Crystallography* **2006,** 39, (2), 230-236.
46. Seyhan, M.; Kucharczyk, W.; Yarar, U. E.; Rickard, K.; Rende, D.; Baysal, N.; Bucak, S.; Ozisik, R., Interfacial surfactant competition and its impact on poly(ethylene oxide)/Au and poly(ethylene oxide)/Ag nanocomposite properties. *Nanotechnology, Science and Applications* **2017,** 10, 69-77.
47. Zhang, L.; He, R.; Gu, H. C., Oleic acid coating on the monodisperse magnetite nanoparticles. *Applied Surface Science* **2006,** 253, (5), 2611-2617.
48. Sahoo, Y.; Pizem, H.; Fried, T.; Golodnitsky, D.; Burstein, L.; Sukenik, C. N.; Markovich, G., Alkyl phosphonate/phosphate coating on magnetite nanoparticles:A comparison with fatty acids. *Langmuir* **2001,** 17, (25), 7907-7911.
49. Araújo-Neto, R. P.; Silva-Freitas, E. L.; Carvalho, J. F.; Pontes, T. R. F.; Silva, K. L.; Damasceno, I. H. M.; Egito, E. S. T.; Dantas, A. L.; Morales, M. A.; Carriço, A. S., Monodisperse sodium oleate coated magnetite high susceptibility nanoparticles for hyperthermia applications. *Journal of Magnetism and Magnetic Materials* **2014,** 364, 72-79.
50. Shen, L.; Laibinis, P. E.; Hatton, T. A., Bilayer surfactant stabilized magnetic fluids: Synthesis and interactions at interfaces. *Langmuir* **1999,** 15, (2), 447-453.
51. Kaminskii, A. J. I. M., Preparation and Luminescence-generation properties of KLu$(WO_4)_2$-Nd^{3+}. *Inorganic Materials* **1983,** 19, (6), 885-894.
52. Yudanova, L.; Potapova, O.; Pavlyuk, A. J. I. M., Phase-diagram of the system KLu$(WO_4)_2$-KNd$(WO_4)_2$ and growth of KLu$(WO_4)_2$ single-crystals. *Inorganic Materials* **1987,** 23, (11), 1657-1660.
53. Kifle, E.; Mateos, X.; de Aldana, J. R. V.; Ródenas, A.; Loiko, P.; Choi, S. Y.; Rotermund, F.; Griebner, U.; Petrov, V.; Aguiló, M.; Díaz, F., Femtosecond-laser-written Tm:KLu$(WO_4)_2$ waveguide lasers. *Opt. Lett.* **2017,** 42, (6), 1169-1172.
54. Klevtsov, P.; Kozeeva, L. In Synthesis X-ray and thermographic study of potassium-rare earth tungstatcs, KLn$(WO_4)_2$; Ln-rare-earth elements, *Doklady Akademii Nauk*, **1969**, 571-574.
55. Petrov, V.; Cinta Pujol, M.; Mateos, X.; Silvestre, Ò.; Rivier, S.; Aguiló, M.; Solé, R. M.; Liu, J.; Griebner, U.; Díaz, F., Growth and properties of KLu$(WO_4)_2$, and novel ytterbium and thulium lasers based on this monoclinic crystalline host. *Laser & Photonics Reviews* **2007,** 1, (2), 179-212.
56. Patterson, A. L., The Scherrer formula for X-ray particle size determination.*Physical Review* **1939,** 56, (10), 978-982.
57. Ropuszyńska-Robak, P.; Tomaszewski, P. E.; Kępiński, L.; Macalik, L., Alkali metal impact on structural and phonon properties of Er^{3+} and Tm^{3+} co-doped MY$(WO_4)_2$ (M =Li, Na, K) nanocrystals. *RSC Advances* **2018,** 8, (5), 2632-2641.
58. Bilecka, I.; Niederberger, M., Microwave chemistry for inorganic nanomaterials synthesis. *Nanoscale* **2010,** 2, (8), 1358-1374.
59. Mai, H. X.; Zhang, Y. W.; Sun, L. D.; Yan, C. H., Orderly aligned and highly luminescent monodisperse rare-Earth orthophosphate nanocrystals synthesized by a limited anion-exchange reaction. *Chemistry of Materials* **2007,** 19, (18), 4514-4522.
60. Li, Y.; Liu, J.; Wang, Y.; Wang, Z. L., Preparation of Monodispersed Fe-Mo Nanoparticles as the catalyst for CVD synthesis of carbon nanotubes. *Chemistry of Materials* **2001,** 13, (3), 1008-1014.
61. Ahrenstorf, K.; Heller, H.; Kornowski, A.; Broekaert, J. A. C.; Weller, H., Nucleation and growth mechanism of Ni_xPt_{1-x} nanoparticles. *Advanced Functional Materials* **2008,** 18, (23), 3850-3856.
62. Shukla, N.; Liu, C.; Jones, P. M.; Weller, D., FTIR study of surfactant bonding to FePt nanoparticles. *Journal of Magnetism and Magnetic Materials* **2003,** 266, (1), 178-184.
63. Bronstein, L. M.; Huang, X.; Retrum, J.; Schmucker, A.; Pink, M.; Stein, B. D.; Dragnea, B., Influence of iron oleate complex structure on iron oxide nanoparticle formation. *Chemistry of Materials* **2007,** 19, (15), 3624-3632.

64. Klokkenburg, M.; Hilhorst, J.; Erné, B. H., Surface analysis of magnetite nanoparticles in cyclohexane solutions of oleic acid and oleylamine. *Vibrational Spectroscopy* **2007,** 43, (1), 243-248.
65. Smolensky, E. D.; Park, H. Y.; Berquo, T. S.; Pierre, V. C., Surface functionalization of magnetic iron oxide nanoparticles for MRI applications-effect of anchoring group and ligand exchange protocol. *Contrast Media & Molecular Imaging* **2011,** 6, (4), 189-99.
66. Brites, C. D. S.; Millán, A.; Carlos, L. D., Chapter 281-Lanthanides in Luminescent Thermometry. In *Handbook on the Physics and Chemistry of Rare Earths*, Jean-Claude, B.; Vitalij K, P., Eds. Elsevier: 2016; Vol. 49, pp 339-427.
67. Mott, N. F., On the absorption of light by crystals. *Proceedings of the Royal Society A* **1938,** 167, (930), 384-391.
68. Duarte, M.; Martins, E.; Baldochi, S. L.; Vieira, N. D.; Vieira, M. M. F., De-excitation mechanisms of $BaLiF_3:Co^{2+}$ crystals. *Optics Communications* **1999,** 159, (4), 221-224.
69. Bednarkiewicz, A.; Marciniak, L.; Carlos, L. D.; Jaque, D., Standardizing luminescence nanothermometry for biomedical applications. *Nanoscale* **2020**, 12, 14405-14421
70. Savchuk, O. A.; Carvajal, J. J.; Cesteros, Y.; Salagre, P.; Nguyen, H. D.; Rodenas, A.; Massons, J.; Aguiló, M.; Díaz, F., Mapping temperature distribution generated by photothermal conversion in graphene film using Er,Yb:$NaYF_4$ nanoparticles prepared by microwave-assisted solvothermal method. **2019,** 7, 88-99.
71. Brandão-Silva, A. C.; Gomes, M. A.; Novais, S. M. V.; Macedo, Z. S.; Avila, J. F. M.; Rodrigues, J. J.; Alencar, M. A. R. C., Size influence on temperature sensing of erbium-doped yttrium oxide nanocrystals exploiting thermally coupled and uncoupled levels' pairs. *Journal of Alloys and Compounds* **2018,** 731, 478-488.
72. Pudovkin, M. S.; Korableva, S. L.; Koryakovtseva, D. A.; Lukinova, E. V.; Lovchev, A. V.; Morozov, O. A.; Semashko, V. V., The comparison of Pr^{3+}:LaF_3 and Pr^{3+}:$LiYF_4$ luminescent nano- and microthermometer performances. *Journal of Nanoparticle Research* **2019,** 21, (12), 266.
73. Savchuk, O. A.; Carvajal, J. J.; Haro-Gonzalez, P.; Aguiló, M.; Díaz, F., Luminescent nanothermometry using short-wavelength infrared light. *Journal of Alloys and Compounds* **2018,** 746, 710-719.
74. Xiang, G.; Liu, X.; Zhang, J.; Liu, Z.; Liu, W.; Ma, Y.; Jiang, S.; Tang, X.; Zhou, X.; Li, L.; Jin, Y., Dual-mode optical thermometry based on the fluorescence intensity ratio excited by a 915 nm wavelength in $LuVO_4:Yb^{3+}/Er^{3+}@SiO_2$ nanoparticles. *Inorganic Chemistry* **2019,** 58, (12), 8245-8252.
75. Chen, H.; Shao, L.; Ming, T.; Sun, Z.; Zhao, C.; Yang, B.; Wang, J., Understanding the photothermal conversion efficiency of gold nanocrystals. *Small* **2010,** 6, (20), 2272-2280.
76. Jiang, K.; Smith, D. A.; Pinchuk, A., Size-dependent photothermal conversion efficiencies of plasmonically heated gold nanoparticles. *Journal of Physical Chemistry C* **2013,** 117, (51), 27073-27080.
77. Baffou, G.; Quidant, R.; Girard, C., Heat generation in plasmonic nanostructures: Influence of morphology. *Applied Physics Letters* **2009,** 94, (15), 153109.
78. Martin, O. J. F.; Girard, C.; Dereux, A., Generalized field propagator for electromagnetic scattering and light confinement. *Physical Review Letters* **1995,** 74, (4), 526-529.
79. Chen, C. L.; Kuo, L. R.; Lee, S. Y.; Hwu, Y. K.; Chou, S. W.; Chen, C. C.; Chang, F. H.; Lin, K. H.; Tsai, D. H.; Chen, Y. Y., Photothermal cancer therapy via femtosecond-laser-excited FePt nanoparticles. *Biomaterials* **2013,** 34, (4), 1128-1134.
80. Cole, J. R.; Mirin, N. A.; Knight, M. W.; Goodrich, G. P.; Halas, N. J., Photothermal efficiencies of nanoshells and nanorods for clinical therapeutic applications. *Journal of Physical Chemistry C* **2009,** 113, (28), 12090-12094.
81. Marciniak, L.; Pilch, A.; Arabasz, S.; Jin, D.; Bednarkiewicz, A., Heterogeneously Nd^{3+} doped single nanoparticles for NIR-induced heat conversion, luminescence, and thermometry. *Nanoscale* **2017,** 9, (24), 8288-8297.
82. del Rosal, B.; Pérez-Delgado, A.; Carrasco, E.; Jovanović, D. J.; Dramićanin, M. D.; Dražić, G.; de la Fuente, Á. J.; Sanz-Rodriguez, F.; Jaque, D., Neodymium-based stoichiometric ultrasmall nanoparticles for multifunctional deep-Tissue Photothermal Therapy. *Advanced Optical Materials* **2016,** 4, (5), 782-789.
83. Pattani, V. P.; Tunnell, J. W., Nanoparticle-mediated photothermal therapy: A comparative study of heating for different particle types. *Lasers in Surgery and Medicine* **2012,** 44, (8), 675-684.
84. Cho, E. C.; Zhang, Q.; Xia, Y., The effect of sedimentation and diffusion on cellular uptake of gold nanoparticles. *Nature Nanotechnology* **2011,** 6, (6), 385-391.
85. Xu, C.; Tung, G. A.; Sun, S., Size and concentration effect of gold nanoparticles on X-ray attenuation as measured on computed tomography. *Chemistry of Materials* **2008,** 20, (13), 4167-4169.
86. Ximendes, E. C.; Rocha, U.; Jacinto, C.; Kumar, K. U.; Bravo, D.; López, F. J.; Rodríguez, E. M.; García-Solé, J.; Jaque, D., Self-monitored photothermal nanoparticles based on core-shell engineering. *Nanoscale* **2016,** 8, (5), 3057-3066.
87. Carrasco, E.; del Rosal, B.; Sanz-Rodríguez, F.; de la Fuente, Á. J.; Gonzalez, P. H.; Rocha, U.; Kumar, K. U.; Jacinto, C.; Solé, J. G.; Jaque, D., Intratumoral thermal reading during photo-thermal therapy by multifunctional fluorescent nanoparticles. *Advanced Functional Materials* **2015,** 25, (4), 615-626.
88. Rocha, U.; Kumar, K. U.; Jacinto, C.; Ramiro, J.; Caamaño, A. J.; Solé, J. G.; Jaque, D., Nd^{3+} doped LaF_3 nanoparticles as self-monitored photo-thermal agents. *Applied Physics Letters* **2014,** 104, (5), 053703.
89. Wortmann, L.; Suyari, S.; Ube, T.; Kamimura, M.; Soga, K., Tuning the thermal sensitivity of β-$NaYF_4$: Yb^{3+}, Ho^{3+}, Er^{3+} nanothermometers for optimal temperature sensing in OTN-NIR (NIR II/III) biological window. *Journal of Luminescence* **2018,** 198, 236-242.

90. Skripka, A.; Benayas, A.; Marin, R.; Canton, P.; Hemmer, E.; Vetrone, F., Double rare-earth nanothermometer in aqueous media: opening the third optical transparency window to temperature sensing. *Nanoscale* **2017,** 9, (9), 3079-3085.
91. Huang, B.; Bergstrand, J.; Duan, S.; Zhan, Q.; Widengren, J.; Ågren, H.; Liu, H., Overtone vibrational transition-induced lanthanide excited-state quenching in Yb^{3+}/Er^{3+}-doped upconversion nanocrystals. *ACS Nano* **2018,** 12, (11), 10572-10575.

Supporting Information

Table S1. Summary of all the experimental parameters applied in the microwave assisted and conventional heating solvothermal method for the synthesis of $KLu(WO_4)_2$ nanocrystals. Under the column "Label", the text "MW" or "CA" refers to the type of reaction applied, "MW" stands for microwave assisted and "CA" for conventional autoclave heating solvothermal method. OLAC:OLAM presents the molar ratio between the organic surfactants. T_R, t_R, T_C and t_C represent the reaction temperature, reaction time, calcination temperature and calcination time of the reaction methodology applied, respectively.

Label	Precursors	OLAC:OLAM	K:Lu:W	T_R (K)	t_R (h)	T_C(K)	t_C (h)	Product
MW-1	$Lu(NO_3)_3{\cdot}H_2O$, K_2WO_4	1:1	4:1:2	453	3	1023	2	KLuW
MW-2	$Lu(NO_3)_3{\cdot}H_2O$,K_2WO_4	1:1	4:1:2	423	3	1023	2	KLuW
MW-3	$Lu(NO_3)_3{\cdot}H_2O$,K_2WO_4	1:1	4:1:2	393	3	1023	2	KLuW
MW-4	$Lu(NO_3)_3{\cdot}H_2O$,K_2WO_4	1:1	4:1:2	453	2	1023	2	KLuW
MW-5	$Lu(NO_3)_3{\cdot}H_2O$,K_2WO_4	1:1	4:1:2	453	1	1023	2	KLuW
MW-6	$Lu(NO_3)_3{\cdot}H_2O$,K_2WO_4	1:1	4:1:2	373	0.5	1023	2	KLuW
MW-7	$Lu(NO_3)_3{\cdot}H_2O$,K_2WO_4	1:1	4:1:2	343	0.5	1023	2	KLuW
MW-8	$Lu(NO_3)_3{\cdot}H_2O$,K_2WO_4	1:1	4:1:2	303	0.5	1023	2	KLuW
MW-9	$Lu(NO_3)_3{\cdot}H_2O$,K_2WO_4	1:4	4:1:2	453	3	1023	2	KLuW
MW-10	$Lu(NO_3)_3{\cdot}H_2O$,K_2WO_4	-	4:1:2	453	3	1023	2	K_2WO_4 + Lu_2O_3
MW-11	$Lu(Ac)_3{\cdot}H_2O$,K_2WO_4	1:1	4:1:2	453	3	1023	2	KLuW
MW-12	$Lu(NO_3)_3{\cdot}H_2O$,K_2WO_4	1:1	1:1:1/2	453	3	1023	2	Lu_2O_3
MW-13	$Lu(NO_3)_3{\cdot}H_2O$,K_2WO_4	1:1	1:1:2	453	3	1023	2	Unknown
MW-14	$Lu(NO_3)_3{\cdot}H_2O$,K_2WO_4	1:1	4:1:2	453	3	973	2	KLuW
MW-15	$Lu(NO_3)_3{\cdot}H_2O$,K_2WO_4	1:1	4:1:2	453	3	923	2	KLuW + Others
MW-16	$Lu(NO_3)_3{\cdot}H_2O$,K_2WO_4	1:1	4:1:2	453	3	873	2	KLuW + Others
MW-17	$Lu(NO_3)_3{\cdot}H_2O$,K_2WO_4	1:1	4:1:2	453	3	1023	1.5	KLuW
MW-18	$Lu(NO_3)_3{\cdot}H_2O$,K_2WO_4	1:1	4:1:2	453	3	1023	1	KLuW + Others
MW-19	$Lu(NO_3)_3{\cdot}H_2O$,K_2WO_4	1:1	4:1:2	453	3	1023	0.5	KLuW + Others
CA-1	$Lu(NO_3)_3{\cdot}H_2O$,K_2WO_4	1:1	4:1:2	453	3	1023	2	KLuW
CA-2	$Lu(NO_3)_3{\cdot}H_2O$,K_2WO_4	1:1	4:1:2	423	3	1023	2	KLuW
CA-3	$Lu(NO_3)_3{\cdot}H_2O$,K_2WO_4	1:1	4:1:2	393	3	1023	2	KLuW
CA-4	$Lu(NO_3)_3{\cdot}H_2O$,K_2WO_4	1:1	4:1:2	453	12	1023	2	K_2WO_4 + Lu_2O_3
CA-5	$Lu(NO_3)_3{\cdot}H_2O$,K_2WO_4	1:1	4:1:2	453	6	1023	2	KLuW
CA-6	$Lu(NO_3)_3{\cdot}H_2O$,K_2WO_4	1:1	4:1:2	453	2	1023	2	KLuW
CA-7	$Lu(NO_3)_3{\cdot}H_2O$,K_2WO_4	1:1	4:1:2	453	1	1023	2	KLuW
CA-8	$Lu(NO_3)_3{\cdot}H_2O$,K_2WO_4	1:1	4:1:2	453	0.5	1023	2	KLuW
CA-9	$Lu(NO_3)_3{\cdot}H_2O$,K_2WO_4	1:1	4:1:2	453	0.25	1023	2	KLuW
CA-10	$Lu(NO_3)_3{\cdot}H_2O$,K_2WO_4	1:1	4:1:2	453	0.16	1023	2	KLuW
CA-11	$Lu(NO_3)_3{\cdot}H_2O$,K_2WO_4	1:1	4:1:2	453	0.08	1023	2	KLuW

Table S2. Average size of the most relevant final products obtained from the MW and CA solvothermal synthesis, calculated from TEM images and Debye-Scherrer equation.

Label	Size from TEM images (nm)	Size from Debye-Scherrer equation (nm)
MW-1	12	19
MW-2	82	53
MW-3	164	68
MW-4	33	37
MW-5	111	67
MW-9	275	77
MW-11	41	48
CA-1	16	28
CA-2	132	64
CA-3	145	67
CA-5	1167	80
CA-6	142	60
CA-7	171	60
CA-8	212	68
CA-9	215	68
CA-10	221	71
CA-11	416	80

Section 1. Microwave-assisted solvothermal synthesis of $KLu(WO_4)_2$ nanocrystals

1.1. The effect of the reaction temperature on the microwave-assisted solvothermal synthesis of $KLu(WO_4)_2$ nanocrystals.

The influence of the reaction temperature in the microwave-assisted (hereafter MW) solvothermal synthesis of the monoclinic KLuW was analyzed in terms of crystalline phase and morphology of the obtained seeds and the final products. Keeping constant the molar ratio of OLAC:OLAM=1:1, the precursors $Lu(NO_3)_3{\cdot}H_2O$ and K_2WO_4, and the reaction time, first, we tested the effect of the reaction temperature, setting it in successive experiments at 453 K, 423 K and 393 K, labeled as MW-1, MW-2 and MW-3. Table S1 summarizes all the experimental parameters used for each synthesis. Figure S1 (a) and (b) shows the XRD pattern of the seeds and the final products obtained as described.

As shown in Figure S1 (a), the seeds are crystalline, but they are not the monoclinic crystalline KLuW, because the diffraction pattern does not match. The X-ray patterns of the seeds exhibit just a few significant broaden peaks in all of the three reaction temperatures which difficult its identification. We believe that they might be formed by a mixture of different compounds, among which KLuW can also be present with a low degree of crystallinity, as some of the more prominent peaks observed in the patterns almost coincide with the position of the most intense peaks for this compound in the reference pattern included also in this Figure (JCPDS file 54-1204).

The XRD patterns of the final products obtained at all reaction temperatures (Figure S1 (b)) are attributed to the monoclinic crystalline phase of KLuW (JCPDS file 54-1204), space group *C*2/*c*. The temperature of the reaction has not a significant influence on the crystalline structure of the final products obtained. However, the X-ray diffraction of the product obtained at the lowest temperature analyzed, shows one additional extra diffraction peak with a very low intensity, indicated in the Figure S1 (b) with asterisk. Since only one peak was observed with a very low intensity, it was impossible to identify to which compound it would belong, testing reaction precursors and the composition of the seeds.

Apparently, the seeds obtained at 453 K show a more homogeneous and defined morphology as shown in the histogram of the length of the nanorods. The nanorods have a wide length distribution ranging from 100 nm up to 800 nm, with a higher concentration of nanorods with a length around 320 nm and a diameter around 36 nm. By decreasing the reaction temperature to 423 K, it resulted in an increase of the average diameter of the seeds, in the range of 100 nm (see Figure S2 (b)). Further decrease of the reaction temperature to 393 K, produced an aggregation of the particles and the appearance of some particles with a new morphological habit consisting of spheres (see Figure S2 c).

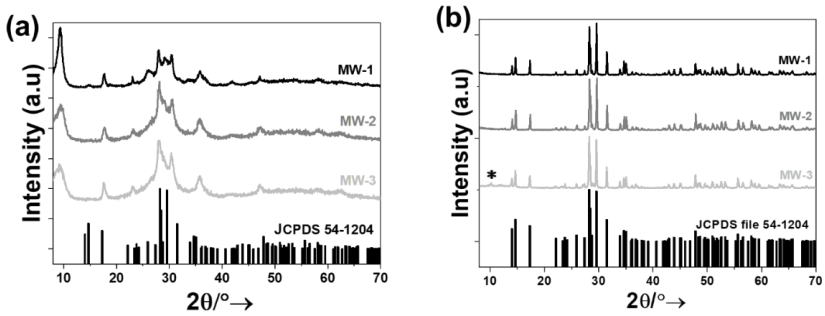

Figure S1. XRD patterns of the products obtained by the MW solvothermal method for the synthesis of KLuW nanocrystal performed at different reaction temperatures for 3 h: (a) seeds and (b) final products obtained by the calcination of the seeds at 1023 K during 2 h (Refer to Table S1 for full experimental details). The reference pattern of KLuW (JCPDS 54-1204) is included for comparison. The diffraction peaks that do not belong to the KLuW phase in the final products are marked with *.

Figure S2 (d)-(f) shows the TEM images obtained of the final products. As it can be observed, the final product (see Figure S2 d) originated from the calcination of the seeds with a more defined morphology obtained at 453 K (see Figure S2 (a)), show a narrower size distribution and smaller particles than the final products derived from the seeds obtained at other reaction temperatures. The size of the nanocrystals increased drastically with the decrease of the temperature of the reaction. Thus, the final product obtained at 453 K, had an average size distribution of 12 nm (see Table S2), the product obtained at 423 K had an average size of 82 nm and the product obtained at 393 K has the largest average size with a value of 164 nm (see Table S2). In addition, the calculation of the average crystallite sizes with the Debye-Scherrer equation, confirms the size of monoclinic KLuW nanocrystals (see Table S2). The crystalline habit for the final products shown in Figure S2, is irregular, with no defined crystalline faces and a tendency to be ellipsoids.

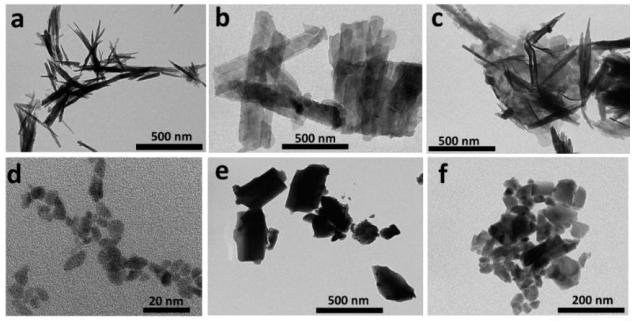

Figure S2. TEM images of the seeds and the final products, respectively obtained by the MW solvothermal method, synthesized at different reaction temperatures during 3 h: (a) and (d) MW-1, (b) and (e) MW-2, (c) and (f) MW-3. In all cases, the final product is obtained by the calcination of the seeds at 1023K during 2h.

1.2. Effect of the time of the reaction on the microwave-assisted solvothermal synthesis of $KLu(WO_4)_2$ nanocrystals

We also analyzed the effect of the time of the reaction on the MW solvothermal synthesis. For that, the MW reaction temperature was set to 453 K and the time of the reaction was tuned, keeping the other parameters unchanged (experiments summarized in Table S1). The seeds and the final products of the reactions at 3 h (labeled as MW-1), 2 h (labeled as MW-4) and 1 h (labeled as MW-5) were analyzed via XRD and TEM. The XRD patterns obtained are shown in Figure S3 (a) and (b).

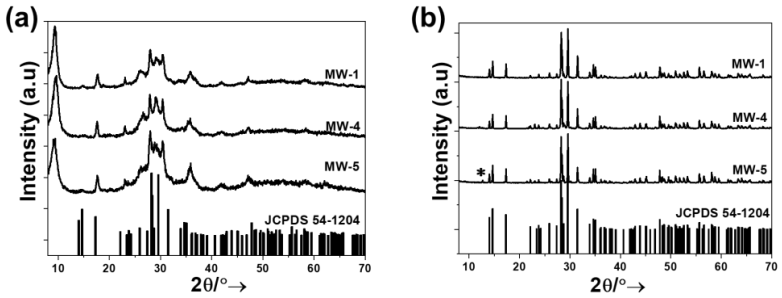

Figure S3. XRD patterns of the products obtained by the MW solvothermal synthesis method performed at 453 K and at different times:(a) seeds and (b) final products. The reference pattern of KLuW (JCPDS 54-1204) is included for comparison.

As in the previous case, the seeds show a similar XRD patterns, with no important effect of the reaction time on them. Again, it is difficult to define the compound that forms the seeds, although KLuW cannot be disregarded, as can be seen from the reference diffraction pattern. The final products obtained, are all formed basically by KLuW. However, as the reaction time decreases, some additional peaks with a low intensity appear, although it was impossible to determine at which crystalline phase they belong.

Figure S4 (a)-(f) shows the TEM images of the seeds and the final products obtained by the MW solvothermal method setting the reaction temperature at 453 K and changing the reaction time. Decreasing the reaction time from 3 h to 1 h, implies changes in the morphology of the seeds in the sequence of nanorods-rectangular plates-aggregated nanorods and nanoplates. As can be seen by the contrast in color in the images, the nanorods obtained at 3 h (see Figure S4 (a)) are thicker than the rectangular plates obtained after 2 h of reaction (see Figure S4 (b)). Finally, at 1 h, in the mixture obtained of nanorods and nanoplates (see Figure S4 (c)), it can be seen that the nanorods are thicker than the nanoplates. Taking into account the pure morphological habits of the reaction time of 3 h and 2 h (excluding here the morphological mixture of the 1 h reaction), the length and the width of the seeds increases with the decrease of the reaction time. The effect of the time of the reaction influences also the morphology and the size of the final products. They exhibit morphology close to a sphere and their sizes range from 12 nm up to 111 nm with the decrease of the reaction time from 3 h to 1 h (see Table S2).

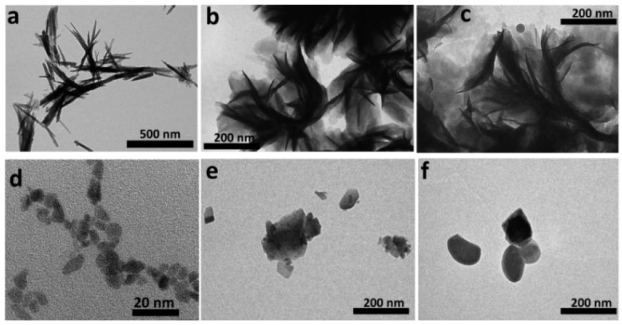

Figure S4. TEM images of the seeds and the final products for the KLuW synthesized via MW solvothermal method at 453 K and different reaction times: (a) and (d) MW-1, (b) and (e) MW-4,(c) and (f) MW-5.

Additionally, other synthesis were performed and analyzed structurally via XRD (only the final products) using lower temperatures of the reaction, such as 373 K, 343 K and 303 K at 0.5 h as the reaction time, labeled as MW-6, MW-7 and MW-8, respectively. The patterns of the final products of the synthesis when the temperature of the reaction was 373 K, 343 K and 303 K are shown in Figure S5.

Although the major part of the peaks of pattern for all final products obtained at 373 K, 343 K and 303 K can be attributed to the KLuW, the final product obtained at 303 K show a large number of

additional diffraction peaks indicated by an asterisk. As we have seen discussed up to now, using as reaction temperature 453 K and as reaction time 3 h, the final products correspond to KLuW crystalline phase, without additional peaks and with a narrower size distribution. Therefore, we established these two parameters as optimum for the synthesis of KLuW via MW solvothermal method.

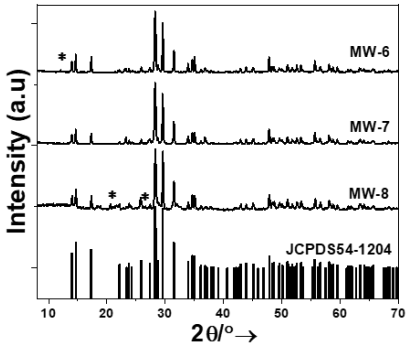

Figure S5. XRD patterns of final products for the KLuW synthesized via MW solvothermal method using MW-6, MW-7 and MW-8 reaction conditions. The reference pattern of the m-KLuW (JCPDS 54-1204) is included for comparison. We have marked with *, peaks that do not belong to the KLuW monoclinic crystalline phase.

1.3. The effect of the organic surfactants on the microwave-assisted solvothermal synthesis of $KLu(WO_4)_2$ nanocrystals

We wanted to analyze the effect of the ratio of organic surfactants on the morphology and the crystalline structure of the seeds and the final products. When an excess amount of OLAM (labeled as MW-9), respect to OLAC (4 times) was provided to the reaction mixture, the XRD pattern of the seeds and of the final product does not exhibit significant changes in comparison with those obtained in a reaction with equimolar ratio of surfactants (Figure S6 (a)). Additional low intensity peaks are observed in the case of the XRD pattern of final product (Figure S6 (b)).

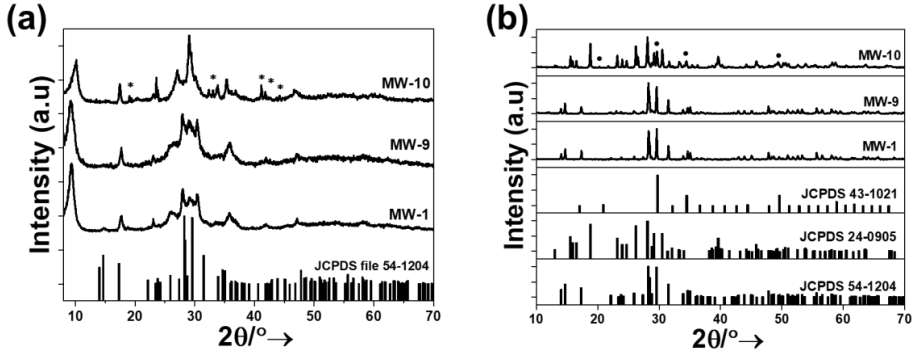

Figure S6. XRD pattern of the products obtained via MW solvothermal method by varying the ratio of the organic surfactants: (a) seeds and (b) final products. The XRD reference patterns of the KLuW (JCPDS file 54-1204), K_2WO_4 (JCPDS file 24-0905), and Lu_2O_3 (JCPDS file 43-1021) are included for comparison. Marked in asterisk, the new diffraction peaks that appeared on the seeds and final product when no organic surfactants were used in the reaction. Marked with black spheres, the diffraction peaks assigned to the cubic Lu_2O_3 phase for the final product.

However, the morphology of the seeds obtained by using an excess of OLAM in the reaction (shown in Figure S7 (a)), changed significantly comparing with the nanorods obtained from an equimolar ratio of OLAC:OLAM (see Figure S2 (a)). They exhibit a flower-like type morphology composed of curved nanorods with a smaller width of approximately 20 nm, compared to the seeds obtained in the equimolar ratio reaction. The final product obtained with an excess of OLAM (see Figure S7 (b)),

does not exhibit a regular morphology and shows particles with sizes in the range of 275 nm (see Table S2). To verify the significant role of the surfactants in the synthesis reaction, we tested the reaction without the presence of these organic surfactants (labeled as MW-10).

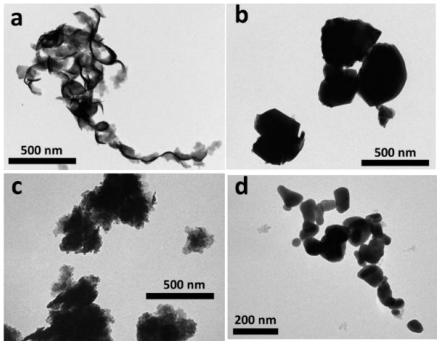

Figure S7. TEM images of seeds and final products synthesized via MW solvothermal method, modifying the concentration of the organic surfactants in the reaction solution: (a) and (b) MW-9, and (c) and (d) MW-10, used.

Figure S6 (a) and (b) show the XRD patterns of the seeds and the final products obtained when oleic acid and oleylamine were not introduced in the reaction solution, respectively, whereas the morphological features are presented in Figure S7 (c) and (d). As can be seen in Figure S6 (b), in the absence of the organic surfactants, a mixture between monoclinic K_2WO_4 (JCPDS file 24-0905) and cubic Lu_2O_3 (JCPDS file 43-1021) was obtained. An even more complex trend is observed in the XRD patterns of the seeds (Figure 6 (a)), apparently there is a mixture of compounds, taking into account all the diffraction peaks observed in all the seeds obtained until now. The TEM images revealed that both, the seeds (Figure S7 (c)) and the final products (Figure S7 (d)), obtained without the presence of organic surfactants in the reaction, exhibited an irregular morphology, with agglomerated nanoparticles and in the case of the seeds, very different from the nanorods or nanoplates observed in the previous experiments and discrete nanoparticles in the case of the final product.

1.4. The effect of the precursors on the microwave-assisted solvothermal synthesis of $KLu(WO_4)_2$ nanocrystals

In this section, the aim is to test the effect of reagents used for the synthesis of KLuW and their concentration in the seeds and final products crystalline phases of the MW solvothermal reaction. Our synthetic approach is built of three types of precursors: the lutetium precursors, the potassium precursors and the tungsten precursors.

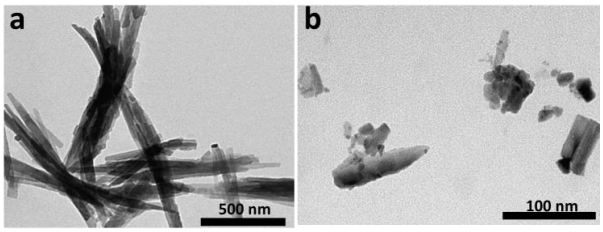

Figure S8. TEM images of the: (a) seeds and (b) final product synthesized via the MW solvothermal method using lutetium (III) acetate hydrate (reaction MW-11).

Initially, the lutetium precursor was changed from lutetium (III) nitrate hydrate to lutetium (III) acetate hydrate (labelled as MW-11), keeping the other parameters unchanged, including here the K:Lu:W ratio set at 4:1:2 (as in the case of lutetium (III) nitrate). The morphology of the seeds resembles the nanorods synthesized using lutetium (III) nitrate hydrate as precursor (see Figure S8 (a)), with similar lengths, except that they show an increase in their widths to approximately 100 nm. The TEM image

of the final product reveal an irregular morphology with an average size distribution of around 41 nm (see Table S2).

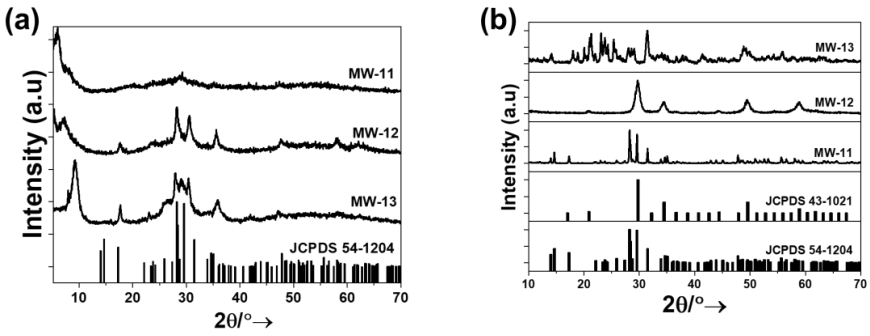

Figure S9. XRD patterns of: (a) the seeds and (b) the final products obtained by changing or tuning the precursor reagents and their concentrations.

The XRD pattern of the seeds is similar to that one obtained from the lutetium (III) nitrate reaction (see Figure S1 (a) and Figure S9 (a)) and the final product's crystalline phase was still attributed to the monoclinic KLuW (see Figure S9 (b)). Thus, the change of lutetium precursor has no effect on the formation of monoclinic KLuW phase. The next step was to check the influence of the K_2WO_4 precursor, thus, using 0.15 mmol K_2WO_4 and 0.3 mmol of Lu(III) precursor (either nitrate or acetate), we check what effect would have introducing into our reaction a lower amount of K_2WO_4, applying a ratio of K:Lu:W=1:1:1/2 (labelled as MW-12). The XRD results for the seeds and final product are shown in Figure S9 (a) and (b). The results obtained for this K:Lu:W ratio reveal that the seeds are amorphous and the final product do not match with KLuW, but with the cubic Lu_2O_3 (JCPDS file 43-1021).

In a last experiment, following the stoichiometry of the desired final product $KLu(WO_4)_2$, we applied a ratio of K:Lu:W=1:1:2 (labeled as MW-13). To apply this stoichiometry, it is needed to use a different precursor for K and for W. Thus, we incorporated 0.3 mmol of Lu (III) precursor, 0.15 mmol of K_2CO_3 and 0.6 mmol of $(NH_4)_2WO_4$, having the desired ratio K:Lu:W=1:1:2. The introduction of K_2CO_3 and $(NH_4)_2WO_4$ is a typical combination used to synthesize monoclinic KLuW via the modified sol-gel Pechini method Clearly, the XRD pattern of the seeds (see Figure S9 (a)) significantly changed from that of the K:Lu:W=4:1:2 ratio. The XRD pattern of the final product does not match also with the KLuW crystalline phase and due to its complexity it was impossible to deduce to which compound/compounds it corresponds (see Figure S9 (b)).

A possible explanation to why the initial reagent ratios K:Lu:W=1:1:2 and K:Lu:W=1:1:1/2 did not form the desired monoclinic KLuW phase, could be related to the fact that in order to allow the organic surfactants (OLAC, OLAM) to control the nucleation and growth of the nanocrystals, one should form a supersaturated solution, a critical condition for the formation of the first nucleus and as a consequence also of the final product. Since we are providing a lower amount of K^+ and W into our reaction mixture, this would imply no reactivity and block of the supersaturation conditions and formation of the desired crystalline phases for the seeds and final product. From this section, we conclude that the optimal precursor ratio for the synthesis of KLuW via the MW solvothermal method is K:Lu:W=4:1:2, using a single combined potassium and tungsten precursor (K_2WO_4).

1.5. Optimization of the calcination post treatment

We observed the effect of the calcination temperature on the crystalline phase formed in the final product of MW solvothermal reaction synthesis. To describe in more detail, the physical process that take place during the calcination step, transforming the seeds into the monoclinic KLuW crystalline phase, a careful Differential Thermal Analysis (DTA) and Thermal Gravimetric Analysis (TGA) of the seeds obtained by the MW solvothermal method was performed. The DTA and TGA analysis of the seeds and their interpretations, are presented in Figure 1 (b) of the manuscript.

The transformation from the unknown crystalline phase of the seeds to the monoclinic KLuW is covering the range of temperatures from around 973 K to 1173 K, so, to better define the appropriate calcination temperature, several experiments were performed applying different calcination

temperatures during a constant time of 2 h. The calcination temperature was tuned from 1023 K (labeled as MW-1), 973 K (labeled as MW-14), 923 K (labeled as MW-15) and 873 K (labeled as MW-16). All experimental details assigned to the tuning of the calcination temperature are presented in Table S1. The XRD patterns of the final products obtained are shown in Figure S10. At 1023 K, we obtained pure KLuW (see Figure S1 (b)), but when the calcination temperature is lower, the diffraction patterns resemble to that offered in Figure S1 (c), corresponding to the transition from the seeds to KLuW, and curiously the structure is almost identical to the temperature analyzed, proofing that these phases are formed below 973 K. According to these results, we established the optimal calcination temperature as 1023 K.

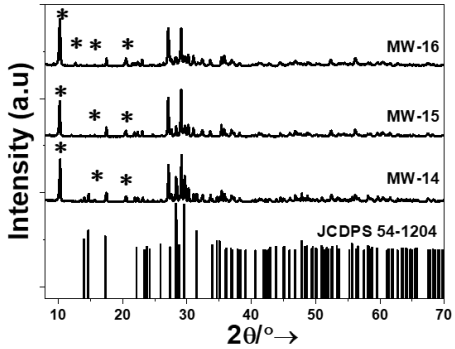

Figure S10. XRD pattern of the products obtained via the MW solvothermal method on the synthesis of KLuW using different calcination temperatures.

Having established the calcination temperature, now we can tune the calcination time keeping the calcination temperature constant at 1023 K. The crystalline structure of the obtained products are shown in Figure S11. For the calcination times at 2 h (MW-1) and 1.5 h (labeled as MW-17), the phase obtained belongs to monoclinic KLuW. However, for shorter calcination times (1 h (labeled as MW-18) and 0.5 h (labeled as MW-19)), a mixture between monoclinic KLuW and an unknown compound is observed. According to these results, we establish the optimal calcination time in between 1.5 h and 2 h for a calcination temperature of 1023 K.

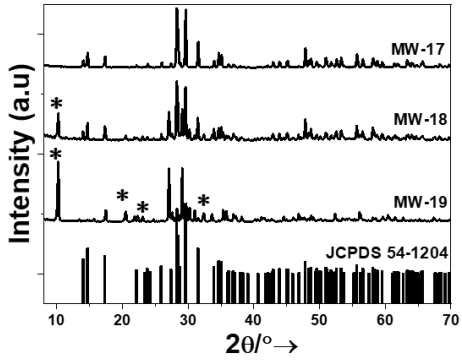

Figure S11. XRD pattern of the products obtained by the MW solvothermal method for the synthesis of KLuW obtained at different calcination times when the calcination temperature was set at 1023 K. In asterix, marked the additional peaks not assigned to monoclinic KLuW.

All the experiments performed to optimize the synthesis of KLuW nanocrystals through the MW solvothermal method are summarized in Table S1. According to these results, the optima parameters for the synthesis of KLuW through this method are: use of $Lu(NO_3)_3 \cdot H_2O$ and K_2WO_4 as precursors for Lu^{3+}, K^+ and WO_4^{2-}, use of an equimolar ratio of the organic surfactants OLAC and

OLAM, perform the reaction at 453 K during 3 h and perform the calcination at 1023 K during 1.5 h to 2 h calcination temperature and time.

Section 2. Conventional autoclave solvothermal synthesis of $KLu(WO_4)_2$ nanocrystals

2.1. Effect of the conventional heating using metallic autoclave solvothermal synthesis of $KLu(WO_4)_2$ nanocrystals

We tested which is the effect of the reaction temperature in the conventional heating autoclave (CA) starting from the optimum temperature for the MW solvothermal method (453 K) (labeled as CA-1) and reducing it to 423 K (labeled as CA-2) and 393 K (labeled as CA-3). All the other parameters for the CA solvothermal method are summarized in Table S1. We tested if there is any effect of the use of the conventional heating autoclave (CA) in the solvothermal synthesis of the KLuW nanocrystals in comparison with the MW heating. The reaction temperatures analyzed were 453 K as the optimum one in the MW assisted method, and also lower temperatures were tested, as 423 K and 393 K. The other experimental parameters of the synthesis were the same as the optimized ones in the MW solvothermal approach. The obtained results were structurally and morphologically investigated, as in the previous sections.

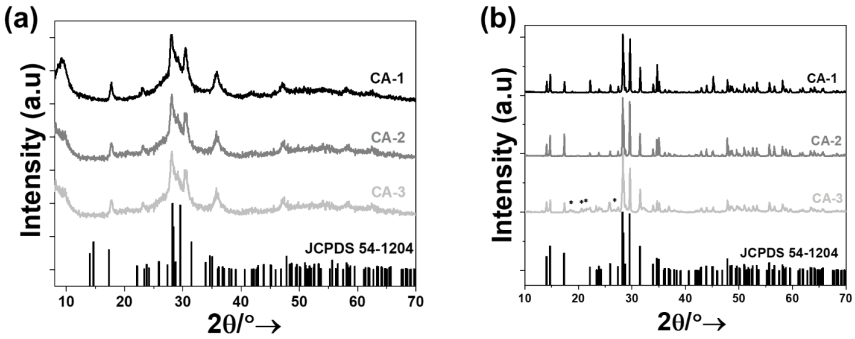

Figure S12. XRD patterns obtained via the CA solvothermal method for the synthesis of KLuW performed at different reaction temperatures for 3 h: (a) seeds, and (b) final products. In all cases, the final product is obtained by the calcination of the seeds at 1023 K during 2 h. The reference pattern of KLuW (JCPDS 54-1204) is included for comparison. Marked with asterisk the diffraction peaks observed in the patterns that could not be attributed to monoclinic KLuW.

The XRD patterns of the seeds and the final products for the CA approach were similar to those obtained via the MW solvothermal method. The XRD pattern of the seeds obtained through the CA solvothermal method at different reaction temperatures do no differ one from another, they exhibit the same XRD pattern, the same broadening behavior, and we could not assign the XRD pattern to any crystalline phase (see Figure S12 (a)). The XRD pattern of the final products obtained at these different reaction temperatures could be identified as pure monoclinic KLuW in all cases, regardless of the reaction temperature applied (see Figure S12 (b)). However, some additional XRD diffraction peaks that do not belong to the monoclinic KLuW could be observed in the XRD pattern of the product obtained at 393 K.

From the morphological point of view (see Figure S13), almost all the seeds obtained, exhibited an irregular shape and tendency to aggregation. The seeds of the reaction at 453 K, show a better defined and homogeneous morphology with an urchin-like shape with an average length of 585 nm. By decreasing the temperature down to 423 K and 393 K, it resulted in an increase of the tendency to aggregation with lengths approximately of 4.5 μm (see Figure S13 (b)) and the formation of structures with no defined shape (see Figure S13 (c)).

KLuW nanoparticles obtained via the CA reaction at 453 K show a small size and a more regular shape with an average size distribution of 16 nm (see Table S2). By decreasing the reaction temperature, it had the same effect on the final products, as it was discussed in the case of the seeds. Thus, when the reaction was performed at 423 K, it produced nanoparticles in the range of 132 nm, and when the reaction was performed at 393 K, the nanoparticles obtained had an average size of 326 nm (see Table S2).

According to these results, we established the 453 K as the optimal temperature for the preparation of the pure monoclinic KLuW by the CA solvothermal method, because we obtained smaller and more discrete nanoparticles then in the other temperatures.

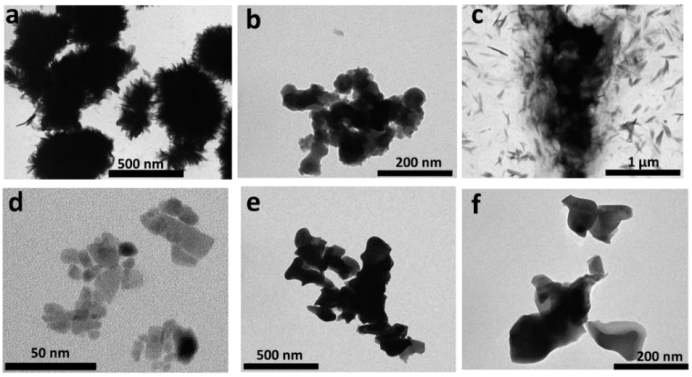

Figure S13. TEM images of the seeds and the final products obtained by the CA solvothermal method for the synthesis KLuW at different reaction temperatures during 3 h: (a) and (d) CA-1, b) and (e) CA-2, (c) and (f) CA-3, respectively. In all cases, the final products are obtained by the calcination of the seeds at 1023 K during 2 h, (g) Lognormal length distribution of the final product presented in (d).

2.2. Effect of the reaction time on the CA solvothermal synthesis of $KLu(WO_4)_2$ nanocrystals. Taking into account the results of the reaction obtained previously at 453 K and 3 h, we tuned the reaction time from 12 h to 0.08 h (5 min), while keeping the other experimental parameters constant. Every final product of the reaction was structurally and morphologically analyzed. All the details of the experimental parameters of the reactions are summarized in Table S1.
All final products obtained are assigned to the monoclinic KLuW (Figure S14). However, when the time of the reaction was increased furthermore to 12 h, the crystalline phase of the obtained product is assigned to a mixture of monoclinic K_2WO_4 (JCPDS 24-0905) and cubic Lu_2O_3 (JCPDS file 43-1021). The same result was also obtained in the MW assisted solvothermal method when no organic surfactants were included in the reaction solution (reaction MW-10).

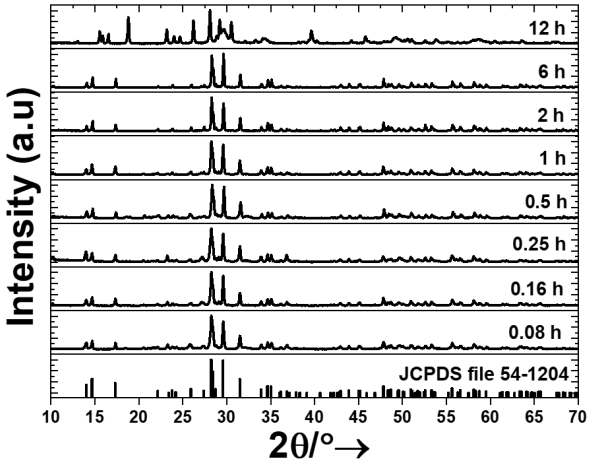

Figure S14. XRD patterns of the final products obtained by the CA solvothermal at different reaction times. The reference pattern of monoclinic KLuW (JCPDS 54-1204) is included for comparison.

All the morphological features of the final products obtained via the CA solvothermal synthesis tuning the reaction time, are presented in Figure S15 (a)-(h).

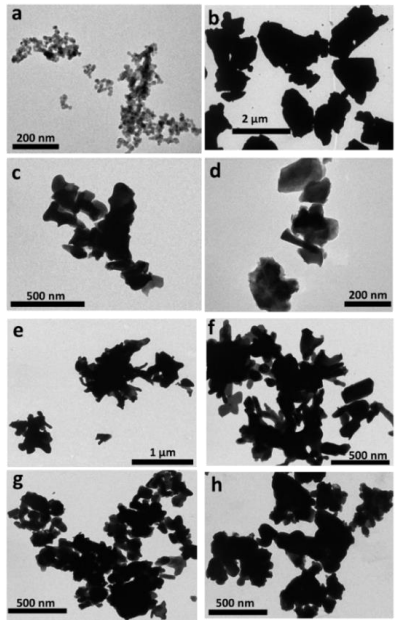

Figure S15. TEM images of the final products obtained by the CA solvothermal at different reaction times: (a) 12 h, (b) 6 h, c) 2 h, (d) 1 h, (e) 0.5 h, (f) 0.25 h, (g) 0.16 h and (f) 0.08 h.

When KLuW is obtained as a product, in general it exhibits an irregular morphology (see Figure 15b-h) and a tendency to increase its size when the reaction time was different from 3 h (check Table S1). Thus, for the reaction performed during 6 h (see Figure S15 (b)), an average size distribution in the range of 1.2 µm was detected. The reactions performed during 2 h (see Figure S15 (c)) and 1 h (see Figure S15 (d)), produced particles with an average size of 142 nm and 171 nm (see Table S2), respectively. Further decrease of the reaction time, resulted in a further increase of the average size of the particles. For example, the reactions at 0.5 h (see Figure S15 (e)) and 0.25 h (see Figure S15 (f)) resulted in 212 nm and 215 nm average size (see Table S2), respectively. An additional decrease of the reaction time to 0.16 h (see Figure S15 (g)), produced particles with an average size of 221 nm (see Table S2). The highest increase of size of the final products, was obtained at the lowest reaction time tested (0.08 h) (see Figure S15 (h)), giving an average size of 416 nm (see Table S2). Thus, the optima conditions for the synthesis of KLuW nanocrystals involve using a reaction temperature of 453 K during 3 h, followed by a calcination at 1023 K during 2 h.

Section 3. Other characterizations of Ho, Tm doped $KLu(WO_4)_2$ nanocrystals

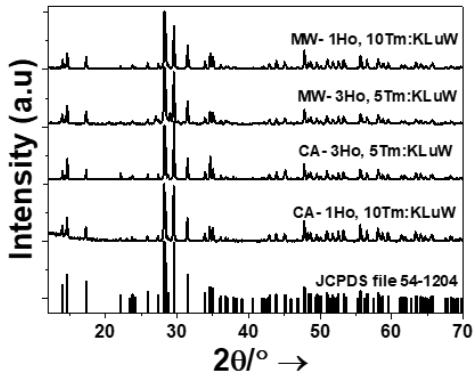

Figure S16. XRD patterns of 1 mol% Ho, 10 mol% Tm and 3 mol% Ho, 5 mol% Tm:KLuW synthesized via MW and CA solvothermal based methodologies.

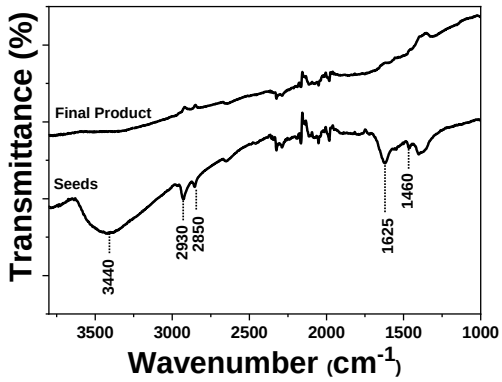

Figure S17. FT-IR spectra of the seeds and KLuW nanocrystals synthesized via the MW solvothermal method.

Figure S18. Monoclinic KLuW nanocrystals dispersed in distilled water.

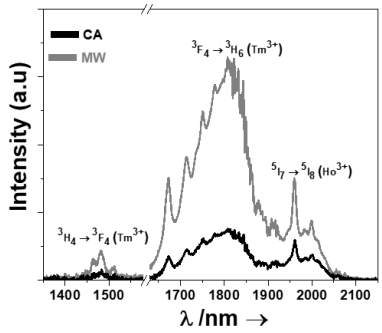

Figure S19. Third biological window emissions recorded at room temperature for 1 mol% Ho, 10 mol% Tm:KLuW materials excited at 808 nm. Please note that part of the graph from 1580 nm to 1630 nm was removed due to the second harmonic of the 808 nm laser source.

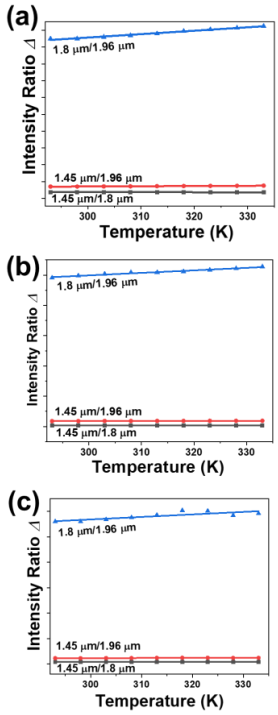

Figure S20. Temperature dependence of the three emission bands in: (a) 3 mol% Ho, 5 mol% Tm:KLuW of MW, (b) 1 mol% Ho, 10 mol% Tm:KLuW of MW, and (c) 1 mol% Ho, 10 mol% Tm:KLuW of CA solvothermal synthesis.

Table S3. Fitting parameters and thermometric performance extracted from the intensity ratio 1.8 μm/1.96 μm for Ho, Tm:KLuW materials synthesized via the solvothermal methodologies

Doping level (mol %)	Synthetic Methodology	B	C	ΔE_1-ΔE_2 (cm^{-1})	R^2	S_{abs} (K^{-1})	S_{rel} (% K^{-1})	δT (K)
1 Ho, 10 Tm	MW	8 ± 0.3	159 ± 10	111	0.98	0.0091	0.18	2.6
1 Ho, 10 Tm	CA	5 ± 0.7	173 ± 45	120	0.99	0.0056	0.20	2.4
3 Ho, 5 Tm	MW	4 ± 0.1	199 ± 11	138	0.98	0.0044	0.23	2.1
3 Ho, 5 Tm	CA	4 ± 0.1	285 ± 10	198	0.99	0.0051	0.33	1.5

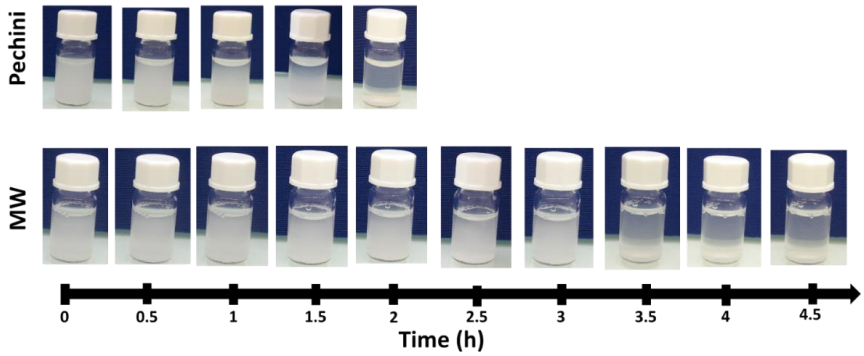

Figure S21. Sedimentation test of Ho, Tm:KLu(WO_4)$_2$ nanocrystals synthesized from the modified sol-gel Pechini and solvothermal (MW as an example) methodologies

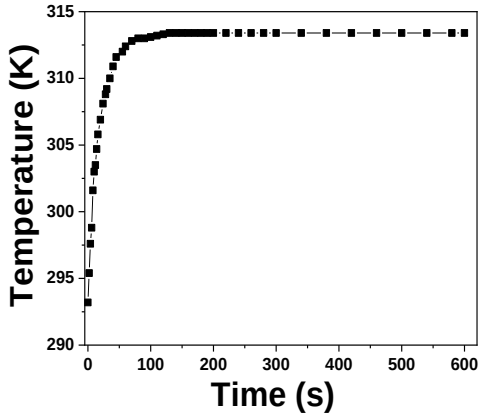

Figure S22. Evolution of the temperature with time for 1 mol% Ho, 10 mol% Tm:KLuW nanocrystals embedded in a 2 mm thick chicken breast piece of meat, recorded with the reference thermocouple.

Paper IV

Synthesis of monoclinic Ho, Tm:KLu$(WO_4)_2$ microrods with high photothermal conversion efficiency via thermal decomposition-assisted method

Albenc Nexha, Joan J. Carvajal,* Maria Cinta Pujol, Francesc Díaz and Magdalena Aguiló
Universitat Rovira i Virgili, Departament de Química Física i Inorgànica,
Física i Cristal·lografia de Materials i Nanomaterials (FiCMA-FiCNA)-EMaS, Campus Sescelades, E-43007, Tarragona, Spain
*joanjosep.carvajal@urv.cat

Abstract

Monoclinic potassium lutetium double tungstate (KLu$(WO_4)_2$) microcrystals with precise rod shape were synthesized using a novel thermal decomposition-assisted method. The formation of the monoclinic crystalline phase was confirmed by X-ray powder diffraction and unpolarized Raman spectroscopy. The potential applications of the KLu$(WO_4)_2$ microrods were confirmed by properly doping with lanthanide ions (Ho^{3+} and Tm^{3+}) and recording their emissions in the visible and near-infrared (NIR), after excitation with a 808 nm near infrared laser source. The temperature sensing properties of these rods by using the different emission lines lying in the NIR were analyzed, and compared to those exhibited by other Ho, Tm:KLuW particles synthesized through different methods (modified sol-gel Pechini, microwave-assisted and conventional autoclave solvothermal methodologies). The photothermal conversion efficiency of Ho^{3+}, Tm^{3+}:KLu$(WO_4)_2$ microrods was also analyzed and established in the range of 66 ± 2%, higher than that of Ho, Tm:KLu$(WO_4)_2$ nanoparticles synthesized by other methods, and comparable to that of gold nanorods.

1. Introduction

Monoclinic potassium lutetium double tungstate (KLu$(WO_4)_2$, hereafter KLuW) is a key material with a plethora range of applications. KLuW has been developed as a promising solid state laser material,[1-3] and also for waveguide applications.[4, 5] Recently, a growing interest has been devoted to the implementation of KLuW as a potential host for applications in temperature nanosensors,[6-8] and as photothermal agent.[7, 8] The boost of the applications of KLuW is attributed to its high photo-chemical stability, high concentration doping possibilities with lanthanide (Ln^{3+}) ions without fluorescence quenching effects, and high absorption and emission cross sections exhibited by these dopants due to the strong anisotropy of the KLuW host.[9]

Traditionally, monoclinic KLuW used for solid state lasers or waveguides, was based in bulk-sized single crystals obtained via Top Seeded Solution Growth Slow Cooling method (TSSG-SC).[10, 11] However, the dimensions of these bulk single crystals represent a serious drawback when applying this material at lower scales where size and shape are of paramount importance, and thus are not compatible for temperature sensing and photothermal conversion applications with the ultimate goal of generating heat and determine the temperature reached, especially important in biomedical applications.

To expand the applications of KLuW materials in the nanoscale, attempts have been devoted to the preparation of doped KLuW nanocrystals. These nanocrystals upon doping with Ho^{3+} and Tm^{3+} ions (hereafter Ho, Tm:KLuW), exhibit self-assessed photothermal properties, meaning they can simultaneously generate photoluminescence and heat due to the radiative and non-radiative processes that happen within the electronic structure of the dopants, upon excitation with near infrared (NIR) light.[8] This property is highly desirable, especially if the emissions generated from

these lanthanide ions are located within the biological windows for biomedical applications.[12, 13, 14, 15] Another potential application for this kind of materials is in optoelectronics, and more specifically optical communications which are governed by NIR excited sources, where photothermal conversion efficiency plays a crucial role.[16-18] In light emitting diodes (LED), for example, the light-to-heat conversion efficiency can be applied to manage the heat generated by the device in order to avoid efficiency losses as the LED lifetimes is highly dependent on the junction temperature.[19] Hence, Ho, Tm:KLuW can heat the medium where they are embedded, and simultaneously sense this temperature increase due to the temperature-dependence of their photoluminescence, acting as luminescent thermometers.[8] Different morphologies of the same material, can exhibit a different performance as nanothermometers and as photothermal agents, due to the effect of their sizes and shapes on the radiative and non-radiative mechanisms among the luminescent centers.[20, 21]

The use of the modified sol-gel Pechini methodology for the synthesis of these materials resulted in the formation of nanocrystals with sizes of approximately 150 nm.[6-8, 22] The synthesis mechanism consists in the formation of organic-inorganic composite materials, formed at relative low temperatures by the hydrolysis of the constituent molecular precursors, and subsequent polycondensation, and a last process of calcination at 1023 K.[6-8, 22] Regardless of the potential of this methodology to produce these nanoparticles with good applicability in thermal sensing, photothermal conversion efficiency and self-assessed photothermal agents, this synthetic approach suffers from irregularly shaped final products characterized by a high degree of aggregation with sizes up to 2 μm.[6-8, 22] A possible way to address this drawback is by silane functionalization of the surface of the nanoparticles that allows its desaggregation.[23] However, this implies adding an additional step to the synthesis of these nanoparticles.

Recently, we reported a novel solvothermal synthetic methodology based on the implementation of organic surfactants (oleic acid (OLAC) and oleylamine (OLAM)) as coating agents to control the growth of sacrificial seeds, which upon calcination, allowed the formation of discrete nanocrystals with average sizes below 20 nm.[24] This methodology, although representing a cost-effective way in terms of time and energy to synthesize KLuW nanoparticles compared to the modified sol-gel Pechini method, still exhibit the drawback of producing nanoparticles with shapes that are not properly defined.

In this work, we address the morphological limitations exhibited by the modified sol-gel Pechini and the solvothermal synthesis methodologies by implementing an innovative thermal decomposition-assisted synthesis method for the preparation of monoclinic KLuW crystals. Further, upon doping with Ho^{3+} and Tm^{3+} ions, we explored the self-assessing photothermal ability of these crystals and compared their performance with the nanoparticles synthesized by the other methods. These crystalline particles produced by the thermal decomposition-assisted method exhibit higher photothermal conversion efficiency, which renders them as potential sources for thermally controlled optoelectronic applications due to their sizes in the micrometer range.

2. Experiments

2.1. Materials

Lutetium acetate tetrahydrate ($Lu(Ac)_3 \cdot 4H_2O$) and oleylamine (OLAM, 90%) were purchased from Sigma Aldrich. Thulium acetate hydrate ($Tm(Ac)_3 \cdot H_2O$, 99.99%) was purchased from Apollo Scientific. Holmium acetate hydrate ($Ho(Ac)_3 \cdot H_2O$, 99.99%), oleic acid (OLAC, 90%), 1-octadecene (ODE, 90%), potassium tungstate (K_2WO_4, 99.9%) and n-hexane (99%), were purchased from Alfa Aesar. Absolute ethanol was purchased from VWR.

2.2. Synthesis of undoped $KLu(WO_4)_2$ and Ho^{3+}, Tm^{3+} doped $KLu(WO_4)_2$ rods

$KLu(WO_4)_2$ and Ho, Tm:$KLu(WO_4)_2$ rods were synthesized via a thermal decomposition-assisted method. In a typical synthesis, 0.4 mmol of $Lu(Ac)_3 \cdot 4H_2O$ were added into a mixture of 12 mmol OLAC, 12 mmol OLAM and 24 mmol ODE. The mixture was heated at 423 K to achieve the complexation of the lutetium precursor with the organic surfactants, prior of cooling down naturally

at room temperature. Then, 0.8 mmol K_2WO_4 were added dropwise ensuring a molar ratio of K:Lu:W=4:1:2 and organic surfactants to Lu(III) precursor of 40:1. The mixture was heated at 373 K under vacuum for 0.5 h to remove residual oxygen species. After switching to protective nitrogen atmosphere, the reaction mixture was heated at 573 K using a rate of 10 K min^{-1} and maintained at this temperature for 2 h. The products of the reaction were precipitated in ethanol and recovered by centrifugation at 6500 rpm for 5 minutes. The precipitates were redispersed in n-hexane and ethanol was added again. A second purification cycle was carried out to remove the excess of ligands and impurities, resulting in the formation of a white precipitate (hereafter seeds). These seeds were calcined at 1023 K for different times (0.5, 1 and 2 h) to ensure the formation of the desired final product. The synthesis of Ho, Tm:$KLu(WO_4)_2$ rods, was similar, except for the addition of $Ho(Ac)_3{\cdot}H_2O$ and $Tm(Ac)_3{\cdot}H_2O$ as dopants with molar ratios 3 mol% Ho^{3+}, 5 mol% Tm^{3+} and 1 mol% Ho^{3+}, 10 mol% Tm^{3+}, substituting Lu^{3+} ions in the KLuW host. These doping ratios were selected because they were found to exhibit the highest photoluminescence intensity and photothermal conversion efficiencyin the NIR.[8]

2.3. Characterizations

The crystalline structure of these materials was investigated via X-ray powder diffraction (XRPD). These measurements were made using a Siemens D5000 diffractometer (Bragg-Brentano parafocusing geometry and vertical θ-θ goniometer) fitted with a curved graphite diffracted-beam monochromator, incident and diffracted-beam Soller slits, a 0.06° receiving slit and a scintillation counter as detector. The angular 2θ diffraction range was set between 5 and 70°. The data were collected with an angular step of 0.05° at 3 s per step and sample rotation. Cu K_α radiation was obtained from a Copper X-ray tube operated at 40 kV and 30 mA.

The size and shape of the synthesized materials were determined by transmission electron microscopy (TEM), using a JEOL JEM-1011 electron microscope operating at an accelerating voltage of 100 kV. The seeds were dispersed in n-hexane, whereas the final products of the reactions were dispersed in distilled water, followed by a deposition of 10 μL of the corresponding dispersion on the surface of a Copper grid covered by a holey Carbon film (HD200 Copper Formvar/Carbon). The size of the particles was analyzed using the ImageJ software.

The Raman active vibrational modes of the materials were recorded via micro-Raman analysis, using a Renishaw inVia Reflex microscope with the unpolarized light from a 514 nm argon laser focused on the sample by a 50× Leica objective in the range 200-2000 cm^{-1}, using a grating with 2400 lines per mm and an exposure time of 10 s.

Fourier Transform Infrared (FT-IR) spectra were recorded in the range of 400-4000 cm^{-1} on a FT-IR IluminatIR II Smith spectrophotometer, to investigate the presence of the organic surfactants on the surface of the samples.

The photoluminescence of the doped materials in the range from 450 nm to 2200 nm was recorded with a Yokogawa AQ6373 (for the visible) and a Yokogawa AQ6375 (for the NIR) optical spectrum analyzer with a resolution of 2 nm and an integration time of 1 s. The particles were excited by a 808 nm fiber-coupled diode laser with a power density of ~100 Wcm^{-2}. The scattered excitation radiation was eliminated by using a 850 nm longpass dichroic filter (Thorlabs). For the temperature-photoluminescence dependence analysis, the setup was the same, except that the nanocrystals were introduced inside a heating stage (Linkam, THMS 600) equipped with a boron disk for improved temperature distribution. The performance of these rods as thermometers was analyzed in a wide range of temperatures from 293 K to 473 K.

The photothermal conversion efficiency of these particles was investigated by the integrated sphere method.[25] A glass cuvette containing an aqueous dispersion of the doped particles with a concentration of 1 gL^{-1} was placed inside the integrating sphere, perpendicular to the laser irradiation provided by the 808 nm fiber-coupled diode laser with a power of 200 mW. The laser from the fiber tip was collimated to a spot size of 5 mm in diameter on the sample. The power signals of the empty cuvette, the solvent and the sample, were collected using a powermeter Ophir Nova II.

3. Results and Discussion

3.1. Synthesis of monoclinic $KLu(WO_4)_2$ microrods

The thermal decomposition-assisted method was implemented for the synthesis of $KLu(WO_4)_2$ and Ho, Tm:$KLu(WO_4)_2$ particles. The methodology consists on the decomposition of lutetium (III) acetate tetrahydrate (and the corresponding Ho (III) and Tm (III) acetates for the case of doped rods) in the presence of organic surfactants (OLAC, OLAM and non-coordinating 1-octadecene (ODE)) at 573 K under a protective inert nitrogen atmosphere, followed by a final step of calcination at 1023 K for 2 hours (see Scheme 1). The reaction parameters applied in this reaction, such as the ratios between organic surfactants, the ratios between organic surfacants and Lu (III) precursors, or the ratios between Lu (III) precursors and potassium precursors, the reaction time, and the calcination temperature, were inspired from synthesis of the same material via solvothermal methodologies, with slight modifications.[24]

Scheme 1. Synthesis of monoclinic KLuW rods via the thermal decomposition-assisted method.

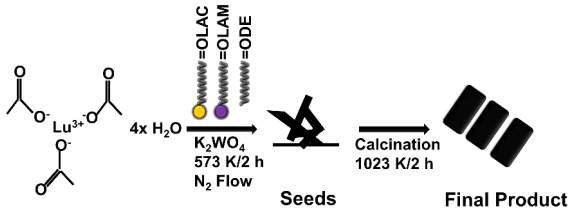

The seeds and the final products of the thermal decomposition-assisted reaction were structurally and morphologically analyzed. The XRPD pattern of the seeds is characterized by the appearance of very broad peaks (see Figure S1 at Supporting Information). They seem to be formed by a mixture of different compounds, among which monoclinic KLuW with a low degree of crystallinity, as some of the more intense peaks observed in this pattern seem to coincide with the position of the most intense peaks of the KLuW reference pattern (JCPDS file 54-1204). The XRPD patterns of the final products (see Figure 1), regardless of the calcination time, reveal that the crystalline structure obtained belongs to monoclinic $KLu(WO_4)_2$, crystallizing in the space group *C2/c*.[26] Transmission electron microscopy (TEM) images show that the seeds have nanorod morphology with an average length and width distribution of 124 ± 5.2 nm and 24 ± 3 nm, respectively (see Figure S2 at Supporting Information). Additionally, the nanorods seems to have a tendency to agglomerate.

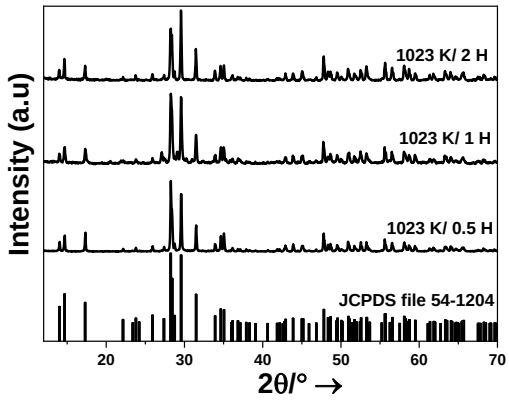

Figure 1. XPRD of monoclinic KLuW synthesized via the thermal decomposition-assisted method at a calcination temperature of 1023 K and different calcination times (0.5 h, 1 h and 2 h). The reference pattern of monoclinic KLuW (JCPDS 54-1204) is included for comparison.

The size and shape of the final products was investigated as a function of the calcination time, keeping the calcination temperature (1023 K) unchanged. With the increase of the calcination time, there is a tendency to generate more regular rods. Hence, when the rods were calcined for 0.5 h, they tended to agglomerate (see Figure 3 (a)), with an average length of 2620 ± 91 nm and an average width of 885 ± 40 nm (see Figure S3 (a), (b) and Figure S4 (a) at Supporting Information). By increasing the calcination time at 1 h, rods with a better defined morphology were obtained (see Figure 3 (b)) with lower length sizes (~1600 ± 140 nm) and widths (~370 ± 25 nm) (see Figure S3 (c), (d) and Figure S4 (b) at Supporting Information).

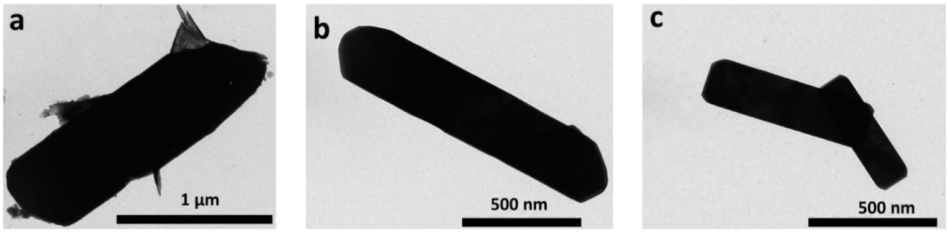

Figure 2. TEM images of monoclinic KLuW synthesized at 1023 K for: (a) 0.5 h, (b) 1 h and (c) 2h.

Nevertheless, it should be highlighted here that the final product obtained after calcination for 1 h included agglomerated particles, combined with these rods (see Figure S4 (b) at the Supporting Information). When the calcination time was increased to 2 h, the final products displayed a more homogeneous shape in the form of regular rods (see Figure 3 (c)) with length sizes of 1103 ± 50 nm and widths of 180 ± 5 nm (see Figure S3 (e), (f) at Supporting Information). Besides the length of the rods, also their width decreased as the calcination time increased (see Figure S3 (b), (d) and (f) at Supporting Information) Furthermore, the aspect ratio of these rods increased as the calcination time increased, with a maximum value of around 6 for the case of the rods calcined for 2 h. These regular rods represent a well-defined shape for the monoclinic KLuW material, in contrary to those obtained by the modified sol-gel Pechini,[6-8, 22] and solvothermal methodologies.[24] Furthermore, the obtained shape for these KLuW microrods is very similar to the shape that can be predicted by using SHAPE software, based on the Donnay-Harker theory (see Figure S5 at Supporting Information).[27] Hence, for what follows, we focused on the characterization of the rods calcined for 2 h at 1023 K.

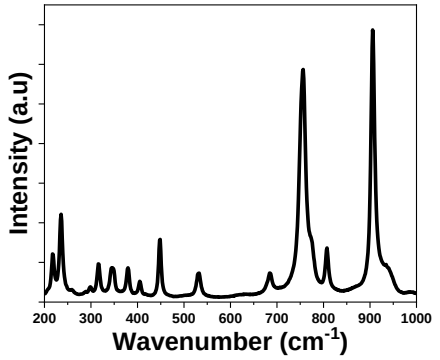

Figure 3. Unpolarized Raman spectra of the obtained KLuW rods by the thermal decomposition-assisted method measured at room temperature.

We also analyzed the vibrational modes of the KLuW rods via Raman spectroscopy. The vibrational modes (see Figure 3) match with the profiles of bulk KLuW,[9, 28] and nanocrystals.[8] The most intense peak observed at 905 cm^{-1} is attributed to the stretching mode of the W-O bond. The second most intense peak, lying at 755 cm^{-1}, is assigned to the coupling between the

stretching mode of the W-O bond and the oxygen-doubled bridged group (WOOW).[8, 9, 28] The ranges between 270-400 cm^{-1} and 400-1000 cm^{-1} belong to the bending modes and the stretching modes of the WO_6 group in the double tungstates.[9] The phonons below 270 cm^{-1} are associated to the translational modes of the cations (K^+, Lu^{3+} and W^{6+}) and the rotational motion of the WO_6 group in the unit cell.[8, 9, 28]

We studied also which organic surfactants are attached, if any, on the surface of the seeds and the final product via FT-IR. The FT-IR spectra reveal that the seeds are coated with the oleic acid moieties that were not found in the final products, confirming that the organic coating is removed after calcination (see Figure 4). The FT-IR spectrum of the seeds reveals that the nanorods are not coated either with free OLAC or OLAM, since the characteristic peaks of OLAC (1709 cm^{-1}) and OLAM (1593 and 3300 cm^{-1}) are missing.[29] However, they are coated with oleic acid moieties. This is confirmed from the broad band observed at around 3400 cm^{-1}, attributed to the O-H stretching mode of oleic acid.[30]

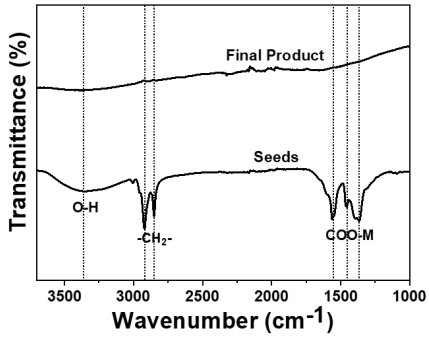

Figure 4. FT-IR spectra of the seeds and final product obtained in the synthesis of KLuW rods by the thermal decomposition-assisted method.

Further, asymmetric and symmetric stretching vibrations of the $-CH_2$ group of oleic acid, are observed at 2930 cm^{-1} and 2850 cm^{-1},[30] respectively. Last, the metal carboxylates bands, assigned either to the antisymmetric and symmetric stretching vibrations of the deprotonated COO^- group, are present at around 1300-1600 cm^{-1}. The difference in between these two bands, reveals the type of coordination between the metal ions and the COO^- group.[31] This difference for the nanorods is around 150 cm^{-1}, revealing a bidentate binding between the metal ions and the carboxylates.[31]

3.2. Photoluminescence of Ho, Tm:$KLu(WO_4)_2$ rods

By doping monoclinic KLuW with Ho^{3+} and Tm^{3+} and illuminating with NIR light (808 nm wavelength), generation of photoluminescence and heat due to radiative and non-radiative processes can occur simultaneously.[8] Further, upon this excitation wavelength, emissions located at the visible and NIR, can be generated.

The generation of photoluminescence within these spectral ranges in the KLuW rods was analyzed by introducing 3 mol% Ho, 5 mol% Tm and 1 mol% Ho, 10 mol% Tm as dopants, substituting Lu^{3+} ions in the KLuW host. These doping ratios have been reported to be the ones exhibiting the highest photoluminescence intensity in the NIR (3 mol% Ho, 5 mol% Tm) and the highest photothermal conversion efficiency (1 mol% Ho, 10 mol% Tm).[8] The incorporation of dopants (Ho^{3+} and Tm^{3+}) into KLuW does not affect to the crystalline structure, vibrational modes, and morphology (see Figure S6 at Supporting Information), when compared to the undoped material. It should be stated that in terms of the length and width of the rods, a slight increase is observed (see Figure S6 (d) and Figure S6 (b) at Supporting Information), which is related to the effect of the dopants in the lattice parameters of the monoclinic phase.

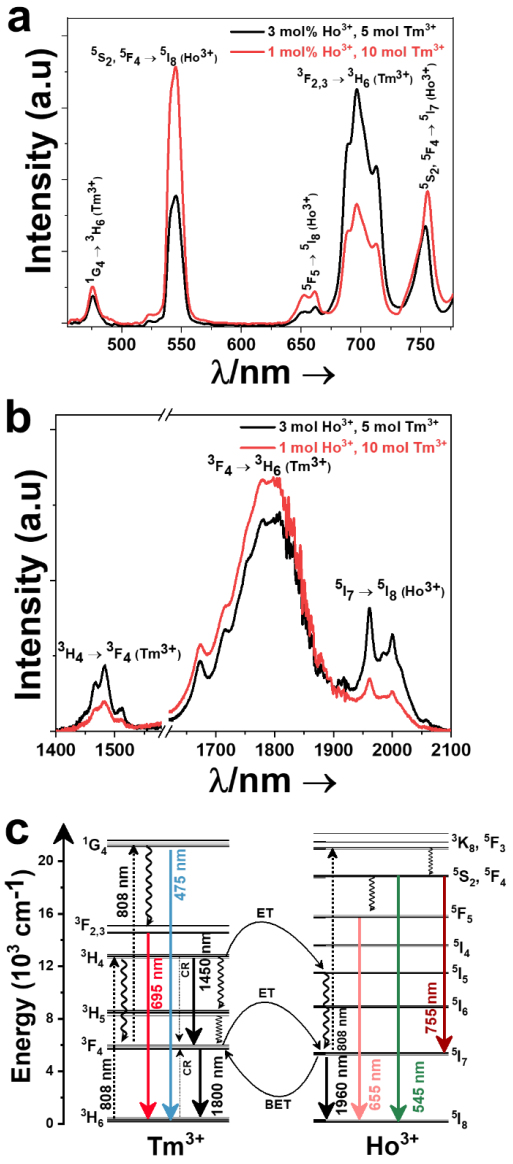

Figure 5. (a) Upconversion emissions in the visible recorded at room temperature for Ho, Tm:KLuW microrods. (b) Downshifting emissions in the NIR recorded at room temperature. (c) Mechanism of the generation of emission bands located within the visible and NIR regions, after excited with 808 nm wavelength. Solid arrows indicate radiative processes. The red arrow indicate the absorption process excited by the 808 nm laser. The black arrows indicate the three radiative emissions: $^3H_4 \rightarrow {}^3F_4$, $^3F_4 \rightarrow {}^3H_6$ and $^5I_7 \rightarrow {}^5I_8$. Curved arrows indicate non-radiative multiphonon decays processes. The dashed arrows stands for the cross relaxation (CR) process in Tm^{3+} ($^3H_6$, $^3H_4$) $\leftrightarrow$ ($^3F_4$, $^3F_4$).

The photoluminescence spectrum recorded in the visible, consists on the emission bands located at the blue ($^1G_4 \rightarrow {}^3H_6$, Tm^{3+}), green ($^5S_2$, $^5F_4 \rightarrow {}^5I_8$, Ho^{3+}), and red ($^5F_5 \rightarrow {}^5I_8$ and $^5S_2$, $^5F_4 \rightarrow {}^5I_7$ of Ho^{3+}, and $^3F_{2,3} \rightarrow {}^3H_6$ of Tm^{3+}) (see Figure 5 (a)).[7] The 808 nm excitation source is absorbed from Tm^{3+}, which promotes its electrons from the ground state to the $^3H_4$ energy level, followed by a non-radiative decay to the $^3F_4$ energy level. A second photon absorbed at 808 nm, promotes the

electrons to the $^1G_4$ excited state. From this excited energy level, a radiative decay at the ground state generates the emission located at 475 nm (blue). The emission located at 695 nm (red) is generated after a non-radiative decay from the $^1G_4$ state to the $^3F_{2,3}$ state prior to relaxing radiatively to the ground state (see Figure 5 (c)). The emissions assigned to Ho^{3+} ions, are generated due to energy transfer (ET) processes from Tm^{3+} ions.[7, 32, 33] From the $^3H_4$ and $^3F_4$ levels of Tm^{3+}, ET processes can lead to the population of the $^5I_5$ and $^5I_7$ levels of Ho^{3+} (see Figure 5 (c)). From the $^5I_7$ level of Ho^{3+} also a back energy transfer (BET) process can take place towards the $^3F_4$ level of Tm^{3+}. The $^5I_7$ level of Ho^{3+}, can also be populated through a non-radiative decay from the $^5I_5$ level of the same ion. In addition, in the $^5I_7$ level of Ho^{3+}, the energy transfer from Tm^{3+} promotes the electrons of Ho^{3+} to the higher energy levels $^3K_8$ and $^5F_3$.[7, 32, 33] From these levels, non-radiative decays populate the $^5S_2$ and $^5F_4$ levels resulting in a radiative transition towards the $^5I_8$ ground state, generating the emission at 545 nm (green) and towards the $^5I_7$ level, generating the emission at 755 nm (red). Finally, a radiative transition from the $^5F_5$ level, which is populated from the non-radiative relaxation of the $^3K_8$ and $^5F_3$ levels, to the $^5I_8$ ground state generated the emission at 655 nm (red).

In terms of the brightness of the emissions generated from the two different doping concentrations analyzed, in general, the 1 mol% Ho, 10 mol% Tm doping concentration enhances the emissions located at 545 nm, 655 nm and 755 nm, whereas for the 3 mol% Ho, 5 mol% Tm doping concentration generates high intensity of the 695 nm emission. The photoluminescence spectrum recorded in the NIR, after exciting the microrods at 808 nm, consist in three emission bands assigned to the: $^3H_4 \rightarrow {}^3F_4$ (1.45 μm) and $^3F_4 \rightarrow {}^3H_6$ (1.8 μm) electronic transitions of Tm^{3+} and the $^5I_7 \rightarrow {}^5I_8$ (1.96 μm) electronic transition of Ho^{3+} (see Figure 5 (b)).

Upon excitation at 808 nm, Tm^{3+} absorbs this energy provided by the excitation source and promotes its electrons from the $^3H_6$ ground state to the $^3H_4$ excited state. From this energy level, electrons can decay radiatively to the $^3F_4$ level, generating the emission of this ion at 1.45 μm. Furthermore, from the $^3F_4$ level, the electrons can relax radiatively back to the ground state, leading to the generation of the second emission of Tm^{3+} located at 1.8 μm (see Figure 5 (c)). The $^3F_4$ level could also be populated via cross-relaxation processes like $^3H_4$, $^3H_6 \leftrightarrow {}^3F_4$, $^3F_4$ due to the energy resonance between these two processes.[8] In addition, the $^3F_4$ level of Tm^{3+} is resonant in energy with the $^5I_7$ level of Ho^{3+}, which allows for ET and BET processes to take place as indicated above, resulting in the promotion of the electrons of Ho^{3+} to this excited state from the ground state. Then, the electrons of Ho^{3+} relax radiatively to the $^5I_8$ ground state, giving rise to the emission band at 1.96 μm.

In terms of brightness of the generated emissions, clearly, in general, the 3 mol% Ho, 5 mol% Tm doping concentration exhibits the highest intensities for all the emissions, with a more pronounced effect in the emissions located at 1.45 μm and 1.96 μm, whereas the 1 mol% Ho, 10 mol% Tm, doping concentration enhances the 1.8 μm emission of Tm^{3+}.

3.3. Ho, Tm:$KLu(WO_4)_2$ microrods as luminescent thermometers

The intensity of the emissions exhibited by these microrods within these spectral ranges changes with the temperature, as can be seen in Figure S7 in the Supporting Information from room temperature to 473 K, meaning that these microrods can be used as luminescent thermometers. The performance of these thermometers, can be evaluated and compared with that of other luminescent thermometers, by analyzing: (i) the intensity ratio (Δ); (ii) the absolute thermal sensitivity (S_{abs}); (iii) the relative thermal sensitivity (S_{rel}); and (iv) the temperature resolution (δT). With the increase of the temperature, the intensity of all the emissions bands decreases significantly, probably due to thermal activation of luminescence quenching mechanisms.[34] For the emissions located in the visible this decrease in the intensity of the emissions is highly pronounced, leading to a low signal-to-noise ratio at the highest temperatures analyzed, with the exception of the emissions located at the 695 nm and 755 nm that maintain a good signal-to-noise ratio, which allows their application as luminescent thermometers. The same situation is observed for the emissions in the NIR.

Hence, to extract the thermometric performance of these microrods, we investigated the intensity ratio between the 695 nm and 755 nm emission bands. Figure 6 (a) shows the temperature

dependence of the intensity of these two emissions. Despite both decrease as the temperature increase, the intensity of the emission located at 695 nm (generated by Tm^{3+}) decreases faster than that of the emission located at 755 nm generated by Ho^{3+}). The experimental data of the intensity ratio between these two bands were fitted to an empirical exponential growing equation of the type:[7, 35, 36]

$$\Delta = \Delta_0 + B\exp(\alpha T) \quad (1)$$

where Δ_0, B and α are constants to be determined by the fitting. From this equation, we can extract the expression of the absolute thermal sensitivity:[37]

$$S_{abs} = \frac{\partial \Delta}{\partial T} = B\alpha\exp(\alpha T) \quad (2)$$

The relative thermal sensitivity is used as a figure of merit to compare the performance of different thermometers, independently of their nature.[38] Thus, S_{rel} in our case is:

$$S_{rel} = \frac{1}{\Delta}\left|\frac{\partial\Delta}{\partial T}\right| x\ 100\% = \frac{B\ \alpha\exp(\alpha T)}{\Delta_0 + B\exp(\alpha T)} x\ 100\% \quad (3)$$

Besides S_{rel}, also the temperature resolution allows for a comparison of the performance of different thermometers.[39] The temperature resolution is defined as the smallest temperature change that can be detected in a given measurement and we can determined from:

$$\delta T = \frac{1}{S_{rel}}\frac{\delta\Delta}{\Delta} = \left|\frac{\Delta_0 + B\exp(\alpha T)}{B\ \alpha\exp(\alpha T)}\right| \frac{\delta\Delta}{\Delta} \quad (4)$$

where $\frac{\delta\Delta}{\Delta}$ = 0.5% is the relative error in the determination of the thermometric parameter for the acquisition setup used.[7] The smaller the temperature resolution, the better the thermometric performance.

For the NIR, the temperature dependence of the intensity of the emissions reveals a general decrease with the increase of the temperature, as can be seen in Figure 6 (b). However, the intensity of the emission bands located at 1.8 μm (generated by Tm^{3+}) and 1.96 μm (generated by Ho^{3+}) decreases faster, as the temperature increases than the intensity of the emission band located at 1.45 μm (generated by Tm^{3+}).

Here, three different intensity ratios could be calculated: 1.45 μm/1.8 μm, 1.45 μm/1.96 μm and 1.8 μm/1.96 μm. Among these three intensity ratios, we investigated which of them displayed the highest change with temperature, following a model for dual emitting centers in lanthanide-based luminescent thermometers, assuming that the exponential term dominates in the intensities of the transitions involved and applying a single deactivation channel:[39-41]

$$\Delta = \Delta_0 \frac{\alpha_{2i}}{\alpha_{1i}} \frac{exp\left(-\frac{\Delta E_2}{k_B T}\right)}{exp\left(-\frac{\Delta E_1}{k_B T}\right)} = B\exp\left(\frac{\Delta E_1 - \Delta E_2}{k_B T}\right) = B\exp\left(\frac{-C}{T}\right) \quad (5)$$

where Δ_0 stands for the ratio between the two emission intensities at 0 K; α_{2i} and α_{1i} stands for the ratio between the non-radiative and radiative probabilities for the emitting levels of the electronic transitions 2 and 1, respectively; B and C are empirical constants to be determined by the fitting; $\Delta E_1 - \Delta E_2$ is the energy difference between the two activation energies for the thermally quenched processes arising from the excited levels involved in our process; and k_B is the Boltzmann constant (k_B = 0.695 cm^{-1}).

The 1.8 μm/1.96 μm intensity ratio is the most affected one (extracted from the highest slope after fitting the experimental data to Equation 5) by the increase of the temperature, regardless of the doping ratio (see Figure S8), compared to the other two ratios. The same behavior was previously observed in the Ho, Tm:KLuW nanocrystals synthetized by the modified sol-gel Pechini,[8] and solvothermal methodologies.[24]

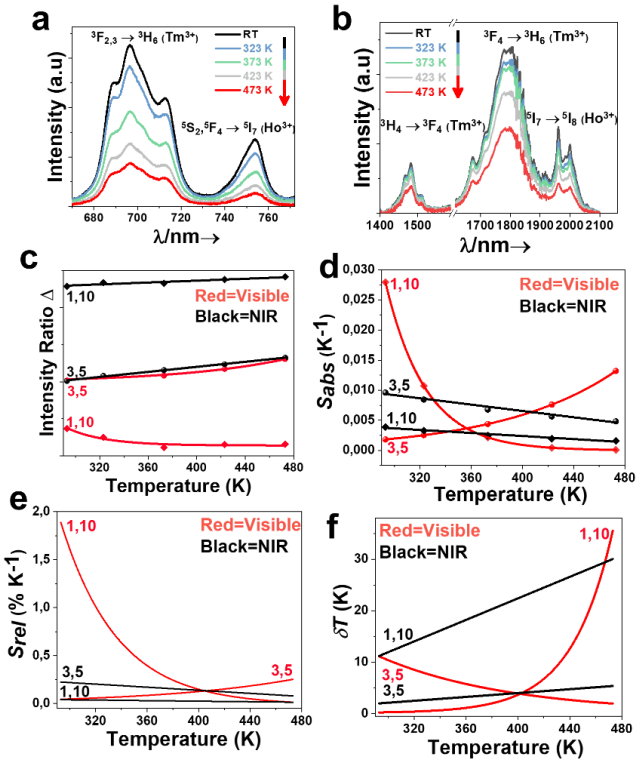

Figure 6. Temperature dependence of the emissions located in the (a) visible and (b) NIR (3 mol% Ho^{3+}, 5 mol% Tm^{3+} as an illustrative example). Variation of the (c) intensity ratios (scattered points represent experimental data and the lines represent fitting using Equation 1 and Equation 6 for the visible and NIR, respectively), (d) absolute thermal sensitivity, (e) relative thermal sensitivity, and (f) temperature resolution, as a function of the temperature and the doping concentrations. In red Ho, Tm:KLuW operating in the visible, in black Ho, Tm:KLuW operating in the NIR. The numbers under (c), (d), (e) and (f) stand for the doping ratios.

From Equation 5, we can determine the expressions of the absolute and relative thermal sensitivities, and the temperature resolution as follows:

$$S_{abs} = \frac{\partial\,\Delta}{\partial\,T} = \frac{B*C*\exp(-\frac{C}{T})}{T^2} \tag{6}$$

$$S_{rel} = \frac{1}{\Delta}\left|\frac{\partial\Delta}{\partial T}\right| x\ 100\% = \left|\frac{\Delta E}{k_B T^2}\right| x\ 100\% \tag{7}$$

$$\delta T = \frac{1}{S_{rel}}\frac{\delta\Delta}{\Delta} = \left|\frac{k_B T^2}{\Delta E}\right|\frac{\delta\Delta}{\Delta} \tag{8}$$

Having established the intensity ratios and the equations for the absolute and relative thermal sensitivities, and the temperature resolution, now we can compare the thermometric performance of these rods in the visible and in the NIR as a function of the doping ratio. In fact, the experimental data of these doped rods are recorded in the same experimental setup, and hence, we can use as a figure of merit all the parameters (S_{abs}, S_{rel} and δT) to make a full comparison between the performance of these rods within these spectral regions.

We fitted the experimental data with Equation 1 and Equation 5 (see Figure 6 (c)), respectively. The fitting parameters can be found in Table S1 in the Supporting Information. With the increase

of the temperature, the intensity ratio of the emissions in the NIR increased. Instead, the evolution of the intensity ratio of the emissions located in the visible depends on the doping concentration. While for the microrods containing 3 mol% Ho^{3+}, 5 mol% Tm^{3+} the intensity ratio increased as the temperature increased, that of the microrods containing 1 mol% Ho^{3+}, 10 mol% Tm^{3+}decreased.

The microrods containing 1 mol% Ho, 10 mol% Tm displayed the highest S_{abs}, with a value ~0.028 K^{-1}, achieved at room temperature in the visible (see Figure 6 (d)). This value is approximately 7 times higher than the one obtained in the NIR. Instead, the microrods containing 3 mol% Ho, 5 mol% Tm exhibited a higher absolute thermal sensitivity when operating in the NIR.

The same trends are also observed for the relative thermal sensitivity. The highest S_{rel} is achieved in the visible for the microrods containing 1 mol% Ho, 10 mol% Tm, with a value of 1.9% K^{-1} at 293 K, almost 45 times higher than the one obtained in the NIR (see Figure 6 (e) and Table S1 in the Supporting Information). Instead, for the microrods containing 3 mol% Ho, 5 mol% Tm similar values for the relative thermal sensitivity were obtained both in the visible (0.25% K^{-1}) and NIR (0.24% K^{-1}), although in the first case the maximum value was achieved at 473 K, while in the NIR the maximum value was obtained at room temperature.

The variation of the temperature resolution with the increase of the temperature follows the inverse trend of the relative thermal sensitivity. Thus, the higher the relative thermal sensitivity, the smaller (and better) the temperature resolution (see Figure 6 (f)). The lowest δT is obtained for the microrods containing 1 mol% Ho, 10 mol% Tm operating in the visible, with a remarkable value of 0.26 K at room temperature. Generally, this parameter increases as the temperature increases. This trend, however, is in the opposite for the case of the microrods containing 3 mol% Ho, 5 mol% Tm operating in the visible.

Hence, from these results, it can be clearly observed the thermometric performance of these microrods is higher in the visible than in the NIR. Nevertheless, the intensity of the emissions generated in the visible is very low when compared to the ones obtained in the NIR. Hence, in other words, the quantum yield that these microrods exhibit in the NIR is higher than that exhibited in the visible. This would imply that the generation of these emission bands can be produced with smaller laser excitation powers, which is beneficial to avoid damaging the samples where these microrods can be embedded, and at the same time, the detection of these emission bands can be done with much simple detectors to obtain the same thermometric performance. So, given the benefits of thermal sensing in NIR, next we focus on the thermal sensing properties of these rods in this spectral range. In this spectral regime, we intend to draw some conclusions regarding the effect of the size and shape of the different Ho, Tm:KLuW particles synthesized by different methodologies, including modified sol-gel Pechini (hereafter P), microwave-assisted solvothermal method (hereafter MW), and conventional autoclave solvothermal method (hereafter CA), on their temperature sensing properties.

The Ho, Tm:KLuW particles synthesized by the P, MW and CA methodologies were also recorded under the same experimental conditions, which allows us to fully compare all the thermometric parameters analyzed in this paper. The variation of the different the intensity ratios as a function of the different Ho, Tm:KLuW nanoparticles and doping concentrations are presented in Figure 7 (a) and in Table S2 in the Supporting Information.

If we compare the effect of the different doping levels, the microrods containing 1 mol% Ho, 10 mol% Tm in general exhibit a higher variation of the intensity ratio with the temperature. The reason why the nanocrystals with the 3 mol% Ho, 5 mol% Tm doping level exhibit lower thermometric performance than the 1 mol% Ho, 10 mol% Tm doping level, might be related to the fact that other thermally activated processes such as diffusion among lanthanide (Ln^{3+}) ions are happening, and also multiphonon non-radiative decays might become more important, thus affecting the electronic population balance between the $^3F_4$ and $^5I_7$ levels.[8]

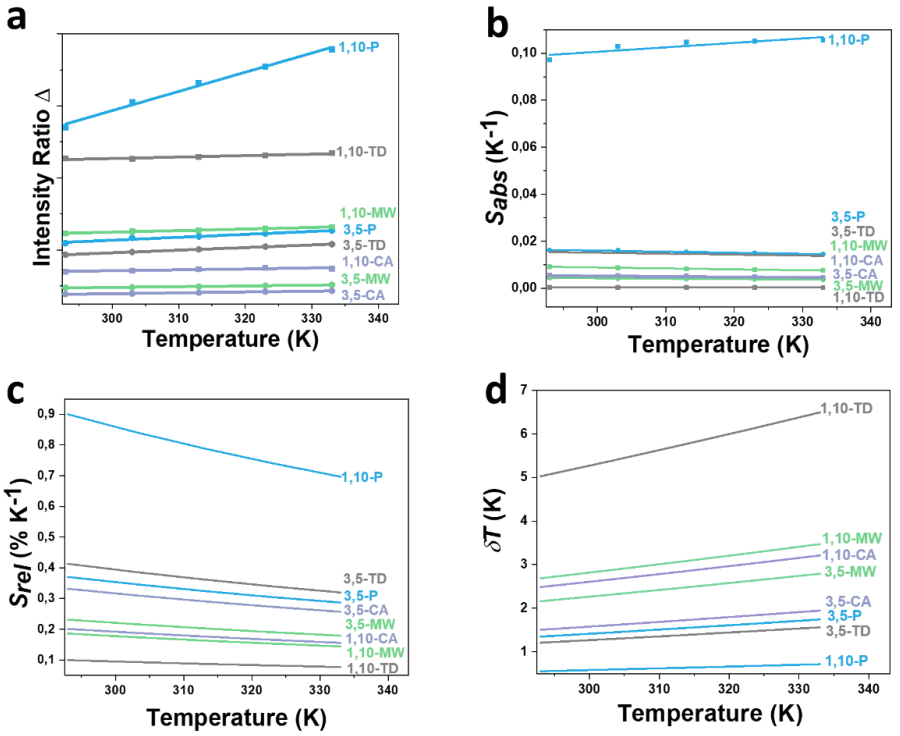

Figure 7. Temperature-dependence of: (a) intensity ratio (experimental data in scattered point and fitting according to Equation 5 in lines), (b) absolute thermal sensitivity, (c) relative thermal sensitivity, and (d) temperature resolution, as a function of the different doping concentrations and different synthetic methodologies by which Ho, Tm:KLuW particles have been produced. The numbers represent the doping concentrations (in mol%) of Ho^{3+} and Tm^{3+}, respectively, and the letters stand for the synthetic methodologies: P for the modified sol-gel Pechini method (blue lines and symbols); MW for microwave-assistend solvothermal method (green lines and symbols); CA for conventional autoclave solvothermal method (violet lines and symbols); and TD for thermal decomposition-assisted method (grey lines and symbols).

If we focus now on the effect of the size of these Ho, Tm doped KLuW particles on their performance as luminescent thermometers, it can be clearly seen that with the increase of the size of the particles, their thermometric performance increases (see in Figure 7 (b)-(d)). Figure S10 in the Supporting Information shows a comparison of the sizes of the Ho, Tm:KLuW particles synthesized by the different methods. The particles produced by the Pechini method, with sizes around 2 microns,[8] exhibit the highest S_{abs} (see Figure 7 (b)), S_{rel} (see Figure 7 (c)), and smallest δT (see Figure 7 (d)). On the other hand, the nanocrystals synthesized by the MW solvothermal method, with the smallest size among all these particles in the range of 12 nm,[24] tend to exhibit some of the lowest performances. However, this is more true for the particles containing 3 mol% Ho, 5 mol% Tm. A possible explanation relies on the fact that with the decrease of the size of the particles, the amount of the luminescent active ions close to their surfaces is increased due to the bigger surface to volume ratio. These ions can interact with the ligands attached to the surface of the nanoparticles, leading to quenching processes that would affect to their thermal sensitivity.[35, 42]

Finally, if we analyze the effect of the shape of these particles on their thermometric performance, Ho, Tm doped KLuW materials with non-precise shapes appear to exhibit a better thermometric performance than those with well-defined shapes. As it is known, the interaction of the light with the matter, depends on the size and shape of the matter.[43-45] Different sizes and shapes lead to different surface-to-volume ratio. Hence, for these Ho, Tm doped KLuW materials, the

thermometric performance will depend on their surface-to-volume ratio. As the size of particles is decreased, the surface-to-volume ratio increases. As this ratio changes, so does the ratio of the active ions in the surface versus the active ions within the core of the particles. Hence, MW particles have the highest surface-to-volume ratio, whereas the particles synthesized from the sol-gel Pechini methodology, exhibit the lowest one. The smaller the surface to volume ratio, the better the absorption, and the smaller the scattering. In addition, the probability of radiative and non-radiative processes to take place, should be taken into account. Overall, it appears that for the particles synthesized from the sol-gel Pechini methodology, these two parameters effect positively their thermometric performance.

3.4. Ho, Tm:KLu(WO_4)$_2$ rods as photothermal agents

When a material is illuminated by light, part of this light will be absorbed and another part will be scattered. The part of the light which is absorbed can be transformed in photoluminescence or released as heat. In lanthanide doped materials, this transformation into heat is due to the non-radiative processes that can occur within the electronic structure of the lanthanide ions. In this case, we are interested in measuring the fraction of the light absorbed that is converted into heat. For this, the photothermal conversion efficiency, *i.e.* the ability of the nanocrystals to convert the absorbed light into heat, was determined using the integrating sphere method.[25]

In this method, the photothermal conversion efficiency η is calculated by the expression:

$$\eta = \left|\frac{P_{blank} - P_{sample}}{P_{empty} - P_{sample}}\right| x\ 100\% \qquad (9)$$

where P_{blank}, P_{empty} and P_{sample} are the power values measured for the solvent (distilled water in this case), the empty cuvette, and a dispersion of the doped Ho, Tm:KLuW rods in distilled water, respectively.

The photothermal conversion efficiency of the Ho, Tm:KLuW microrods was analyzed by exciting a distilled water dispersion of the microrods with a concentration of 1 g L^{-1} with the 808 nm laser at a power that changed from 200 mW to 800 mW. Figure 8 (a) shows the photothermal conversion efficiency obtained for the Ho,Tm:KLuW microrods together with the other Ho, Tm:KLuW nanoparticles synthesized by other methods as a function of the excitation power. According to the results, and as expected, the photothermal conversion efficiency is independent of the excitation power used. The rods containing 3 mol% Ho, 5 mol% Tm exhibit the highest light-to-heat conversion efficiency among all the Ho, Tm:KLuW nanoparticles with a value of η=66 ± 2%. Concerning the 1 mol% Ho, 10 mol% Tm doping concentration, this efficiency is clearly lower of about η=41 ± 2%.

In general, from the doping concentration point of view, the photothermal conversion efficiency is strictly related to the processes of ET and BET (see Figure 5 (c)) due to the fact that the $^3F_4$ level of Tm^{3+} and the $^5I_7$ level of Ho^{3+} are not exactly resonant in energy, thus, part of the energy provided, is released as heat.[8] At higher concentration of Tm^{3+}, these ET and BET would be favored and hence more heat will be released.

The dependence of the photothermal conversion efficiency with the size of the particles could be established for the Ho, Tm:KLuW particles containing 1 mol% Ho, 10 mol% Tm. It looks like with the decrease of the size of these particles, the photothermal conversion efficiency increased (see Figure 8 (a) and Table S2 at Supporting Information). A possible explanation about this observation might be related to the surface-to-volume ratio of the particles. With the decrease of the size, this ratio increases, and thus, the portion of the surface of the materials exposed to the interaction with the light, is bigger, which favors the interaction with surface ligands that cause quenching effects, and thus the release of heat.[43, 45] We must stress here that other factors, including the doping ratios or the quenching centers, might have a crucial role. The conclusions reached for the influence of the size of particles on their photothermal conversion efficiency, could be correlated also to the effect of shape. Nevertheless, for the case of 3 mol% Ho, 5 mol% Tm, the situation is more complex. These particles in shape of rods, generate more heat than the others. We do believe that besides the afore mentioned factors, such as ET and BET transfer

between Tm^{3+} and Ho^{3+} ions, and the fact that the energy levels involved are not totally resonant, an additional factor might be the presence of hot spots on the rods. These hot spots can be generated due to the presence of corners on the rods. Despite this, we do believe that also the surface-to-volume ratio, might play a role. Having a relatively role surface-to-volume ratio, render these rods to better absorb and less scatter the energy source, which are key factors on improving the photothermal conversion efficiency.

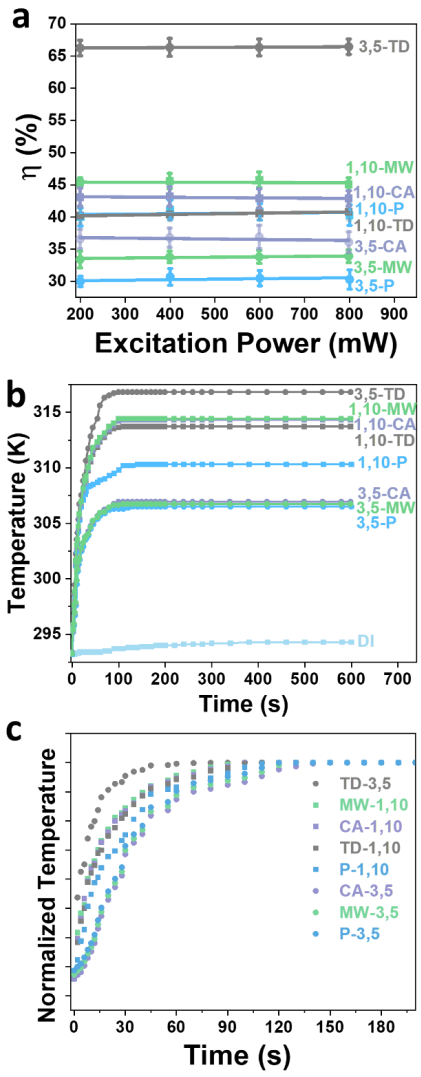

Figure 8. (a) Photothermal conversion efficiency of different Ho, Tm: KLuW particles synthesized via four different synthetic methodologies, as a function of the excitation power. (b) Time-dependent temperature profile of Ho, Tm doped KLuW materials synthesized via different synthetic methodologies achieved in aqueous solutions when illuminated with 808 nm laser. Numbers present the doping ratios in mol%, where the letters stand for the synthetic methodologies: modified sol-gel Pechini method are labelled as P and in blue lines and symbols, solvothermal methods (microwave-assisted, labelled as MW in green lines and symbols, and conventional autoclave labelled as CA in pink lines and symbols) and thermal decomposition-assisted methods as TD in grey lines and symbols. (c) Normalized maximum temperature reached from each particles within the corresponding aqueous solutions.

The value achieved for the photothermal conversion efficiency of 3 mol% Ho, 5 mol% Tm:KLuW microrods, represents the highest light-to-heat conversion ability reported for lanthanide-doped tungstates and for Ho, Tm co-doped materials. Compared to other classes of photothermal conversion agents, these microrods exhibit values higher than those of FePt,[46] Cu_9S_5,[47] graphene oxide,[25] Au/AuS nanoparticles or Au/SiO_2 nanoshells (see Table S3 at the Supporting Information).[48] The photothermal conversion efficiency reported here is in same range of that reported for graphene in DMF,[25] and Au nanoshells or nanorods.[49] However, the ability of Au nanostars,[49] or core@shell@shell $NaNdF_4$@$NaYF_4$@Nd:$NaYF_4$ nanoparticles,[50] to generate heat is still higher when compared to that of Ho, Tm doped KLuW microrods.

The ability of the Ho, Tm:KLuW microrods to convert light into heat is further proved by monitoring the temperature generated by a dispersion of these particles in distilled water with a concentration of 1 g L^{-1}, after being excited at 808 nm with a power of 200 mW and a beam spot diameter of ~10 μm on the external surface of the vial, while recording the photoluminescence spectrum to determine the temperature inside the liquid by the luminescent thermometer. Figure 8 (b) illustrates the temperature evolution generated by the water dispersion of the different Ho, Tm doped KLuW particles prepared by the different synthetic methodologies. To ensure that this increase of temperature is due to the heat generated by the Ho, Tm:KLuW particles, the same experiment was undertaken using water only illuminated under the same conditions, observing only an increase of 1 K. The KLuW microrods containing 3 mol% Ho and 5 mol% Tm allows getting a maximum temperature in the liquid of 316.8 K, which represents an increase of around 24 K. The general tendency for the temperature evolution observed for all the nanoparticles analyzed is a fast increase in the first 25-30 s, and then a slow tendency until reaching the temperature plateau after approximately 100 s. In addition, within these 100 s, we plotted the normalized maximum value of the temperature reached from the corresponding aqueous solutions of each particle (see Figure 8 (c)). It can be concluded that within this time, the particles with the doping levels 3 mol% Ho and 5 mol% Tm, reach faster the maximum temperature exhibited by them (316.8 K). These results are assigned to the ability of each particle to generate heat. Higher photothermal conversion efficiency, implies higher heating velocity. Despite the higher photothermal conversion efficiency displayed by the microrods, the increase of temperature in the solution is just a couple of degrees higher than the other particles, for example the MW particles. A possible explanation about this, might be due to the relatively large size of the microrods. Being large, implies that these microrods tend to flocculate faster within the aqueous dispersion. We investigated the flocculation time of all the particles as a function of time. Results, summarized in Figure S11 at the Supporting Information, confirm that these microrods flocculate faster than the other particles, for a time of less than 0.5 h. Particles synthesized from the MW methodology, that are much smaller, rest in suspension for a longer. In this way, the MW particles favor reaching a higher temperature in the solution. This implies that for practical applications of the microrods, it would be required to disperse them in a polymer.

4. Conclusions

$KLu(WO_4)_2$ particles with precise rod morphology with an average length of 1100 nm and width of 180 nm were synthesized via a novel thermal decomposition-assisted method in the presence of organic surfactants (OLAC, OLAM and ODE), followed by a calcination process at 1023 K for 2 h. The successful formation of monoclinic $KLu(WO_4)_2$ was confirmed by X-ray diffraction and Raman spectroscopy. The microrods could be easily doped with Ho^{3+} and Tm^{3+} without affecting their crystalline structure, morphology and vibrational modes. The ability to dope KLuW rods with Ho^{3+} and Tm^{3+} opens the possibility to use them as temperature sensors in the visible and the NIR, and also as photothermal conversion agents. In the NIR, the maximum relative thermal sensitivity achieved with the Ho^{3+} and Tm^{3+} doped $KLu(WO_4)_2$ microrods was 0.41% K^{-1}, lower than the one that can be achieved with the non-defined and agglomerated Ho^{3+} and Tm^{3+} doped $KLu(WO_4)_2$ particles that could be obtained by the modified sol-gel Pechini method, but higher than that of the same particles obtained by solvothermal methodologies. Instead, the photothermal conversion efficiency of 3 mol% Ho and 5 mol% Tm doped KLuW microrods is 66

± 2%, the highest ever achieved with Ho, Tm:KLuW particles, and comparable with the one obtained in graphene in DMF and Au nanoshells or nanorods.

From the comparison of the results obtained from the thermal sensing and photothermal conversion efficiency experiments, doping ratio, size and shape are key factors affecting these applications. Doping ratios manipulate the ET/BET processes, thus proper selection should be considered. Regarding the size and shape, the interplay between the surface-to-volume ratio, and the radiative and non-radiative processes, crucially influence the performance, either as thermal sensor or as photothermal agent. Overall, the performance of agglomerated particles synthesized from modified sol-gel Pechini methodology as thermal sensors is higher compared to the other particles. In terms of photothermal agents, the rods display better performance, which is comparable to that of gold nanoparticles. We underline the fact that based on the size and shape of the materials, one can tune and control the ability to sense the temperature and to convert light into heat by selecting one of the reported synthetic methodologies to produce Ho, Tm:KLuW particles. A precise control of these properties, is crucial, for example, in optoelectronic applications, to adjust the performance of the corresponding device.

These findings confirm the possible potential application of this material as luminescent temperature sensors and photothermal conversion agents and opens up their use in applications like optoelectronic, since their large sizes would restrict their use in biomedical applications.

5. Acknowledgements

This work was supported by the Spanish Government under projects MAT2016-75716-C2-1-R (AEI/FEDER, UE) and by the Generalitat de Catalunya under project 2017SGR755. A.N acknowledges financial support from the Generalitat de Catalunya under grant 2017FI_B00620, 2018FI_B100161 and 2019 FI_B200154.

6. References

1. Jambunathan, V.; Mateos, X.; Pujol, M.; Carvajal, J.; Aguiló, M.; Díaz, F.; Griebner, U.; Petrov, V., Diode-pumped Ho-doped $KLu(WO_4)_2$ laser at 2.08 μm. *Applied Physics Express* **2011**, 4, 072601-072604.
2. Mateos, X.; Petrov, V.; Liu, J.; Pujol, M. C.; Griebner, U.; Aguilo, M.; Diaz, F.; Galan, M.; Viera, G., Efficient 2 μm continuous-wave laser oscillation of Tm^{3+}:$KLu(WO_4)_2$. *IEEE Journal of Quantum Electronics* **2006**, 42, (10), 1008-1015.
3. Jambunathan, V.; Mateos, X.; Pujol, M. C.; Carvajal, J. J.; Aguiló, M.; Díaz, F.; Griebner, U.; Petrov, V., Optimization of dopant concentration in Ho:$KLu(WO_4)_2$ laser achieving ~70% slope efficiency. *Laser Physics* **2013**, 23, (12), 125801-125806.
4. Bolanos, W.; Carvajal, J.; Mateos, X.; Aguilo, M.; Diaz, F., Exploring waveguiding properties of heavily doped Yb^{3+}: $KLu(WO_4)_2$ epitaxial layers. *Photonics Journal, IEEE* **2010**, 2, 482-489.
5. Bolaños, W.; Carvajal, J. J.; Cinta Pujol, M.; Mateos, X.; Lifante, G.; Aguiló, M.; Díaz, F., Epitaxial growth of lattice matched $KY_{1-x-y}Gd_xLu_y(WO_4)_2$ thin films on $KY(WO_4)_2$ substrates for waveguiding applications. *Crystal Growth & Design* **2009**, 9, (8), 3525-3531.
6. Savchuk, O. A.; Carvajal, J. J.; Pujol, M. C.; Barrera, E. W.; Massons, J.; Aguilo, M.; Diaz, F., Ho,Yb:$KLu(WO_4)_2$ aanoparticles: A versatile material for multiple thermal sensing purposes by luminescent thermometry. *Journal of Physical Chemistry C* **2015**, 119, (32), 18546-18558.
7. Savchuk, O. A.; Carvajal, J. J.; Brites, C. D. S.; Carlos, L. D.; Aguilo, M.; Diaz, F., Upconversion thermometry: a new tool to measure the thermal resistance of nanoparticles. *Nanoscale* **2018**, 10, (14), 6602-6610.
8. Nexha, A.; Carvajal, J. J.; Pujol, M. C.; Díaz, F.; Aguiló, M., Short-wavelength infrared self-assessed photothermal agents based on Ho,Tm: $KLu(WO_4)_2$ nanocrystals operating in the third biological window (1.45-1.96 μm wavelength range). *Journal of Materials Chemistry C* **2020**, 8, (1), 180-191.
9. Petrov, V.; Cinta Pujol, M.; Mateos, X.; Silvestre, Ò.; Rivier, S.; Aguiló, M.; Solé, R. M.; Liu, J.; Griebner, U.; Díaz, F., Growth and properties of $KLu(WO_4)_2$, and novel ytterbium and thulium lasers based on this monoclinic crystalline host. **2007**, 1, (2), 179-212.
10. Loiko, P.; Serres, J. M.; Mateos, X.; Yumashev, K.; Kuleshov, N.; Petrov, V.; Griebner, U.; Aguiló, M.; Díaz, F., In-band-pumped Ho: $KLu(WO_4)_2$ microchip laser with 84% slope efficiency. *Optics Letters* **2015**, 40, (3), 344-347.
11. Kifle, E.; Mateos, X.; de Aldana, J. R. V.; Ródenas, A.; Loiko, P.; Choi, S. Y.; Rotermund, F.; Griebner, U.; Petrov, V.; Aguiló, M.; Díaz, F., Femtosecond-laser-written Tm:$KLu(WO_4)_2$ waveguide lasers. *Optics Letters* **2017**, 42, (6), 1169-1172.

12. Weissleder, R., A clearer vision for in vivo imaging. *Nature Biotechnology* **2001**, 19, (4), 316-317.
13. Hemmer, E.; Benayas, A.; Légaré, F.; Vetrone, F., Exploiting the biological windows: current perspectives on fluorescent bioprobes emitting above 1000 nm. *Nanoscale Horizons* **2016**, 1, (3), 168-184.
14. Shi, L.; Sordillo, L. A.; Rodríguez-Contreras, A.; Alfano, R., Transmission in near-infrared optical windows for deep brain imaging. *Journal of Biophotonics* **2016**, 9, (1-2), 38-43.
15. Naczynski, D. J.; Tan, M. C.; Zevon, M.; Wall, B.; Kohl, J.; Kulesa, A.; Chen, S.; Roth, C. M.; Riman, R. E.; Moghe, P. V., Rare-earth-doped biological composites as in vivo shortwave infrared reporters. *Nature Communications* **2013**, 4, (1), 2199.
16. Mohammadi Pouyan, S.; Miri, M.; Sheikhi, M. H., Design of a CMOS compatible dual polarization four-level optical modulator based on thermally-actuated phase transition of vanadium dioxide. *Photonics and Nanostructures-Fundamentals and Applications* **2019**, 35, 100710.
17. Vicente, C. M. S.; Lima, P. P.; Bermudez, V. d. Z.; Carlos, L. D.; André, P. S.; Ferreira, R. A. S., Fabrication of low-cost thermo-optic variable wave plate based on waveguides patterned on di-ureasil hybrids. *Optics Express* **2014**, 22, (22), 27159-27168.
18. Xing, H.; Li, J.; Shi, Y.; Guo, J.; Wei, J., Thermally driven photonic actuator based on silica opal photonic crystal with liquid crystal elastomer. *ACS Applied Materials & Interfaces* **2016**, 8, (14), 9440-9445.
19. Qian, X.; Zou, J.; Shi, M.; Yang, B.; Li, Y.; Wang, Z.; Liu, Y.; Liu, Z.; Zheng, F., Development of optical-thermal coupled model for phosphor-converted LEDs. *Frontiers of Optoelectronics* **2019**, 12, (3), 249-267.
20. Marciniak, L.; Bednarkiewicz, A.; Strek, W., The impact of nanocrystals size on luminescent properties and thermometry capabilities of Cr, Nd doped nanophosphors. *Sensors and Actuators B: Chemical* 2017, 238, 381-386.
21. Marciniak, L.; Prorok, K.; Bednarkiewicz, A., Size dependent sensitivity of Yb^{3+},Er^{3+} up-converting luminescent nano-thermometers. *Journal of Materials Chemistry C* **2017**, 5, (31), 7890-7897.
22. Galceran, M.; Pujol, M. C.; Aguiló, M.; Díaz, F.; Technology, Sol-gel modified Pechini method for obtaining nanocrystalline $KRE(WO_4)_2$ (RE= Gd and Yb). *Journal of Sol-Gel Science Technology* **2007**, 42, (1), 79-88.
23. Savchuk, O.; Carvajal, J. J.; De la Cruz, L. G.; Haro-González, P.; Aguiló, M.; Díaz, F., Luminescence thermometry and imaging in the second biological window at high penetration depth with $Nd:KGd(WO_4)_2$ nanoparticles. *Journal of Materials Chemistry C* **2016**, 4, (31), 7397-7405.
24. Nexha, A.; Carvajal, J. J.; Pujol, M. C.; Díaz, F.; Aguiló, M., Effect of size and shape of Ho, $Tm:KLu(WO_4)_2$ nanocrystals in the performance as simultaneous luminescent nanothermometers operating in the third biological window and as photothermal agents. *Submitted at Journal of Alloys and Compounds.*
25. Savchuk, O. A.; Carvajal, J. J.; Massons, J.; Aguiló, M.; Díaz, F., Determination of photothermal conversion efficiency of graphene and graphene oxide through an integrating sphere method. *Carbon* **2016**, 103, 134-141.
26. Pujol, M. C.; Aznar, A.; Mateos, X.; Solans, X.; Massons, J.; Suriñach, S.; Díaz, F.; Aguiló, M., Structural redetermination, thermal expansion and refractive indices of $KLu(WO_4)_2$. *Journal of Applied Crystallography* **2006**, 39, (2), 230-236.
27. Shape Software, link: http://www.shapesoftware.com/00_Website_Homepage/
28. Jambunathan, V.; Mateos, X.; Pujol, M. C.; Carvajal, J. J.; Massons, J.; Aguiló, M.; Díaz, F., Near-infrared photoluminescence from Ho^{3+}-doped monoclinic $KLu(WO_4)_2$ crystal codoped with Tm^{3+}. *Journal of Luminescence* **2009**, 129, (12), 1882-1885.
29. Shukla, N.; Liu, C.; Jones, P. M.; Weller, D., FTIR study of surfactant bonding to FePt nanoparticles. *Journal of Magnetism and Magnetic Materials* **2003**, 266, (1), 178-184.
30. Zhang, L.; He, R.; Gu, H. C., Oleic acid coating on the monodisperse magnetite nanoparticles. *Applied Surface Science* **2006**, 253, (5), 2611-2617.
31. Deacon, G. B.; Phillips, R. J., Relationships between the carbon-oxygen stretching frequencies of carboxylato complexes and the type of carboxylate coordination. *Coordination Chemistry Reviews* **1980**, 33, (3), 227-250.
32. Li, Y. F.; Wang, Y. Z.; Yao, B. Q.; Liu, Y. M., Upconversion spectrum of $Tm,Ho:GdVO_4$ pumped by pulse and CW laser at 800 nm. *Laser Physics Letters* **2008**, 5, (8), 597-599.
33. Payne, S. A.; Smith, L. K.; Kway, W. L.; Tassano, J. B.; Krupke, W. F., The mechanism of Tm to Ho energy transfer in $LiYF_4$. *Journal of Physics:Condensed Matter* **1992**, 4, (44), 8525-8542.
34. Riseberg, L. A.; Moos, H. W., Multiphonon Orbit-Lattice Relaxation of Excited States of Rare-Earth Ions in Crystals. *Physical Review* **1968**, 174, (2), 429-438.
35. Brandão-Silva, A. C.; Gomes, M. A.; Novais, S. M. V.; Macedo, Z. S.; Avila, J. F. M.; Rodrigues, J. J.; Alencar, M. A. R. C., Size influence on temperature sensing of erbium-doped yttrium oxide nanocrystals exploiting thermally coupled and uncoupled levels' pairs. *Journal of Alloys and Compounds* **2018**, 731, 478-488.
36. Lojpur, V.; Nikolić, G.; Dramićanin, M. D., Luminescence thermometry below room temperature via up-conversion emission of $Y_2O_3:Yb^{3+},Er^{3+}$ nanophosphors. *Journal of Applied Physics* **2014**, 115, (20), 203106.
37. Santos, P. V. d.; Araujo, M. T. d.; Gouveia-Neto, A. S.; Neto, J. A. M.; Sombra, A. S. B., Optical temperature sensing using upconversion fluorescence emission in Er^{3+}/Yb^{3+}-codoped chalcogenide glass. *Applied Physics Letters* **1998**, 73, (5), 578-580.
38. Brites, C. D. S.; Lima, P. P.; Silva, N. J. O.; Millán, A.; Amaral, V. S.; Palacio, F.; Carlos, L. D., Thermometry at the nanoscale. *Nanoscale* **2012**, 4, (16), 4799-4829.

39. Brites, C. D. S.; Millán, A.; Carlos, L. D., Chapter 281-Lanthanides in Luminescent Thermometry. In *Handbook on the Physics and Chemistry of Rare Earths*, Jean-Claude, B.; Vitalij K, P., Eds. Elsevier: 2016; Vol. 49, pp 339-427.
40. Duarte, M.; Martins, E.; Baldochi, S. L.; Vieira, N. D.; Vieira, M. M. F., De-excitation mechanisms of $BaLiF_3:Co^{2+}$ crystals. *Optics Communications* **1999**, 159, (4), 221-224.
41. Mott, N. F., On the absorption of light by crystals. *Proceedings of the Royal Society A* **1938**, 167, (930), 384-391.
42. Savchuk, O. A.; Carvajal, J. J.; Cesteros, Y.; Salagre, P.; Nguyen, H. D.; Rodenas, A.; Massons, J.; Aguiló, M.; Díaz, F., Mapping temperature distribution generated by photothermal conversion in graphene film using $Er,Yb:NaYF_4$ nanoparticles prepared by microwave-assisted solvothermal method. *Frontiers in Chemistry* **2019**, 7, 88-99.
43. Jain, P. K.; Lee, K. S.; El-Sayed, I. H.; El-Sayed, M. A., Calculated absorption and scattering properties of gold nanoparticles of different size, shape, and composition: Applications in biological imaging and biomedicine. *Journal of Physical Chemistry B* **2006**, 110, (14), 7238-7248.
44. Hao, E.; Schatz, G. C.; Hupp, J. T., Synthesis and optical properties of anisotropic metal nanoparticles. *Journal of Fluorescence* **2004**, 14, (4), 331-341.
45. Lee, K. S.; El-Sayed, M. A., Dependence of the enhanced optical scattering efficiency relative to that of absorption for gold metal nanorods on aspect ratio, size, end-cap shape, and medium refractive index. *Journal of Physical Chemistry B* **2005**, 109, (43), 20331-20338.
46. Baffou, G.; Quidant, R.; Girard, C., Heat generation in plasmonic nanostructures: Influence of morphology. *Applied Physics Letters* **2009**, 94, (15), 153109.
47. del Rosal, B.; Rocha, U.; Ximendes, E. C.; Martín Rodríguez, E.; Jaque, D.; Solé, J. G., Nd^{3+} ions in nanomedicine: Perspectives and applications. *Optical Materials* **2017**, 63, 185-196.
48. Chen, C. L.; Kuo, L. R.; Lee, S. Y.; Hwu, Y. K.; Chou, S. W.; Chen, C. C.; Chang, F. H.; Lin, K. H.; Tsai, D. H.; Chen, Y. Y., Photothermal cancer therapy via femtosecond-laser-excited FePt nanoparticles. *Biomaterials* **2013**, 34, (4), 1128-1134.
49. Tian, Q.; Jiang, F.; Zou, R.; Liu, Q.; Chen, Z.; Zhu, M.; Yang, S.; Wang, J.; Wang, J.; Hu, J., Hydrophilic Cu_9S_5 nanocrystals: A photothermal agent with a 25.7% heat conversion efficiency for photothermal ablation of cancer cells in vivo. *ACS Nano* **2011**, 5, (12), 9761-9771.
50. Cole, J. R.; Mirin, N. A.; Knight, M. W.; Goodrich, G. P.; Halas, N. J., Photothermal efficiencies of nanoshells and nanorods for clinical therapeutic Aapplications. J*ournal of Physical Chemistry C* **2009**, 113, (28), 12090-12094.
51. Maestro, L. M.; Haro-González, P.; Sánchez-Iglesias, A.; Liz-Marzán, L. M.; García Solé, J.; Jaque, D., Quantum dot thermometry evaluation of geometry dependent heating efficiency in gold nanoparticles. *Langmuir* **2014**, 30, (6), 1650-1658.
52. Marciniak, L.; Pilch, A.; Arabasz, S.; Jin, D.; Bednarkiewicz, A., Heterogeneously Nd^{3+} doped single nanoparticles for NIR-induced heat conversion, luminescence, and thermometry. *Nanoscale* **2017**, 9, (24), 8288-8297.

Supporting Information

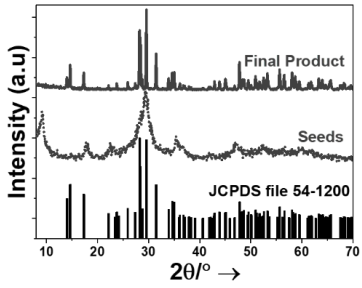

Figure S1. XRPD patterns of the seeds and the final products (calcined at 1023 K for 2 h as an example) obtained in the synthesis of KLuW particles via the thermal decomposition-assisted method. The KLuW reference pattern (JCPDS file 54-1200) is included for comparison.

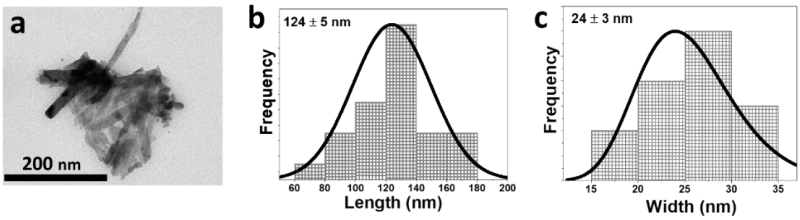

Figure S2. (a) Transmission electron microscopy image of the seeds obtained at 573 K for 2 h, and their lognormal distribution for (b) length, and (c) width.

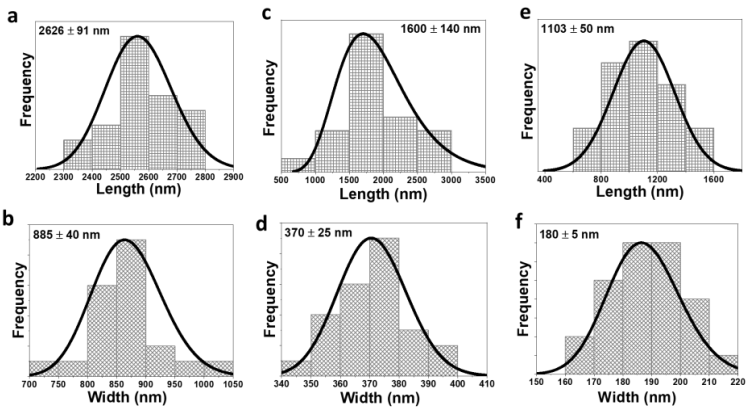

Figure S3. Lognormal length and width distribution of the rods as a function of the calcination time: (a), (b) 0.5 h, (c), (d) 1 h, and (e), (f) 2 h, respectively.

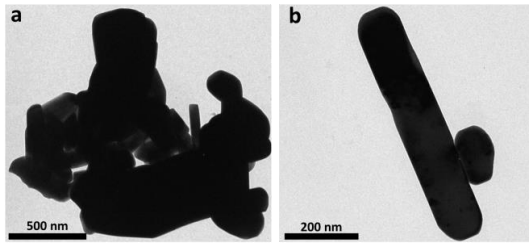

Figure S4. Transmission electron microscopy image of the final products calcined at 1023 K for (a) 0.5 h and (b) 1 h.

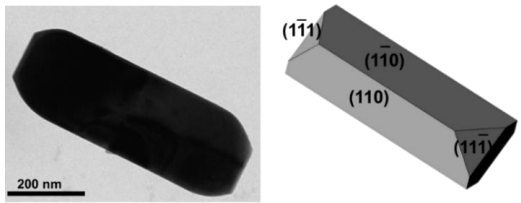

Figure S5. Crystalline habit of the undoped KLuW rods, transmission electron microscopic image and morphology predicted by the SHAPE software.

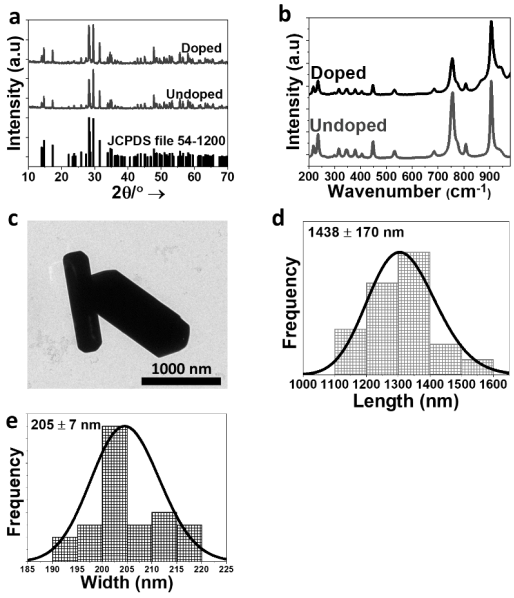

Figure S6. (a) XRPD pattern of undoped KLuW and doped Ho, Tm:KLuW microrods. (b) Raman spectroscopy of undoped KLuW and doped Ho, Tm:KLuW microrods. (c) TEM image doped Ho, Tm:KLuW microrods, and their corresponding length (d) and (e) width distribution.

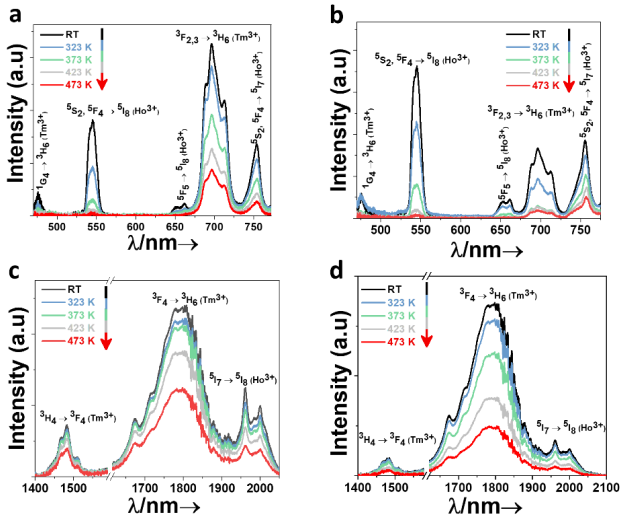

Figure S7. Evolution with temperature of the intensity of the emission bands in the visible of Ho, Tm:KLuW microrods containing: (a) 3 mol% Ho^{3+}, 5 mol% Tm^{3+}, and (b) 1 mol% Ho^{3+}, 10 mol% Tm^{3+}. Evolution with temperature of the intensity of the emission bands in the NIR of Ho, Tm:KLuW rods containing: (c) 3 mol% Ho^{3+}, 5 mol% Tm^{3+} and (d) 1 mol% Ho^{3+}, 10 mol% Tm^{3+}.

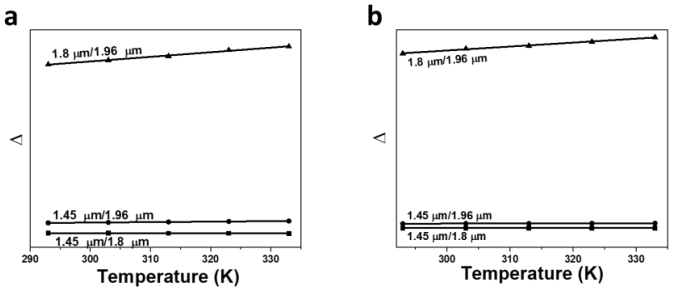

Figure S8. Temperature dependence of the three possible intensity ratios in the NIR of Ho, Tm:KLuW microrods containing: (a) 3 mol% Ho^{3+}, 5 mol% Tm^{3+} and (b) 1 mol% Ho^{3+}, 10 mol% Tm^{3+}.

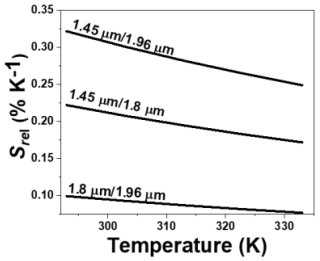

Figure S9. Temperature dependence of the relative thermal sensitivity of 1 mol% Ho^{3+}, 10 mol% Tm^{3+}:KLuW microrods, operating as luminescent thermometers in the NIR, calculated for the three possible intensity ratios in this spectral region.

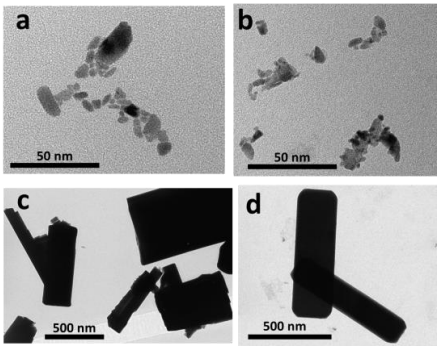

Figure S10. TEM images of Ho, Tm:KLuW particles synthesized via four different synthetic methodologies: (a) MW= microwave-assisted solvothermal method, (b) CA=conventional autoclave solvothermal method, (c) P=modified sol-gel Pechini method, and (d) TD = thermal decomposition-assisted method.

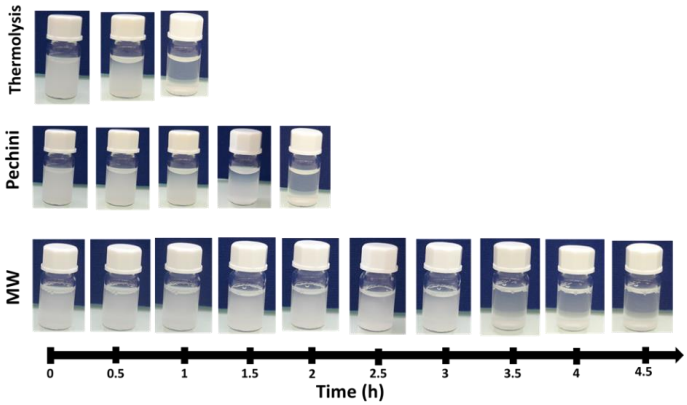

Figure S11. Sedimentation test of Ho, Tm:KLu(WO$_4$)$_2$ nanocrystals synthesized from the modified sol-gel Pechini, solvothermal (MW as an example) and thermolysis methodologies

Table S1. Fitting parameters and thermometric performance of Ho, Tm:KLuW microrods synthesized via the thermal decomposition-assisted method, operating in different spectral regimes and on the temperature range 293 K-473 K.

Based on Equation 1

Doping level (mol%)	Regime	Δ_0	B	α	R^2	S_{abs} (K^{-1})	S_{rel} (% K^{-1})	δT (K)
3 Ho, 5 Tm	VIS	3.95	0.0066	0.011	0.98	0.013	0.25	1.97
1 Ho, 10 Tm	VIS	0.55	10312	0.032	0.94	0.028	1.9	0.26

Based on Equation 5

Doping level (mol%)	Regime	B	C	$\Delta E_1 - \Delta E_2$ (cm^{-1})	R^2	S_{abs} (K^{-1})	S_{rel} (% K^{-1})	δT (K)
3 Ho, 5 Tm	NIR	8.07	203.9	141.7	0.99	0.0096	0.24	2.1
1 Ho, 10 Tm	NIR	10.38	36.6	25.4	0.90	0.0039	0.04	11.7

Table S2. Fitting parameters, thermometric performance, and photothermal conversion efficiency of Ho, Tm:KLuW particles synthesized via four different synthetic methodologies (P=modified sol-gel Pechini method; MW=microwave-assisted solvothermal method; CA=conventional autoclave solvothermal method; and TD=thermal decomposition-assisted method).

Doping (mol%)	Synthesis	Size (nm)	R^2	B	C	$\Delta E_1 - \Delta E_2$ (cm^{-1})	S_{abs} (K^{-1})	S_{rel} (% K^{-1})	δT (K)	η (%)	Ref.
1 Ho, 10 Tm	P	2000	0.99	155 ± 15	773 ± 31	537	0.097	0.90	0.55	40	1
1 Ho, 10 Tm	MW	12	0.98	8 ± 0.3	159 ± 10	111	0.0091	0.18	2.6	45	2
1 Ho, 10 Tm	CA	16	0.99	5 ± 0.7	172 ± 44	120	0.0056	0.20	2.4	43	24
1 Ho, 10 Tm	**TD**	**1480**	**0.92**	**12 ± 0.6**	**173 ± 17**	**60**	**0.009**	**0.1**	**5**	**41**	**This Work**
3 Ho, 5 Tm	P	2000	0.95	13 ± 1	318 ± 29	221	0.016	0.37	1.34	30	1
3 Ho, 5 Tm	MW	12	0.98	3 ± 0.1	199 ± 11	138	0.0044	0.23	2.1	33	24
3 Ho, 5 Tm	CA	16	0.99	4 ± 0.1	285 ± 10	198	0.0051	0.33	1.5	36	24
3 Ho, 5 Tm	**TD**	**1480**	**0.99**	**12 ± 0.2**	**354 ± 5**	**247**	**0.015**	**0.41**	**1.2**	**66**	**This Work**

Table S3. Comparison of photothermal conversion efficiency (η) in different materials. The excitation wavelength (λ_{exc}) of the laser and the method used to extract η are included for comparison. The **Ho, Tm:KLu(WO_4)$_2$** particles are labelled according to the synthetic method by which they were produced (P=modified sol-gel Pechini method; MW=microwave-assisted solvothermal method; CA=conventional autoclave solvothermal method; and TD=thermal decomposition-assisted method).

Material	**Method**	**λ_{exc} (nm)**	**η (%)**	**Ref.**
Au nanostars	Double Beam Fluorescence Thermometry	808	102	3
Au nanorods	Double Beam Fluorescence Thermometry	808	95	3
$NaNdF_4$@$NaYF_4$@ Nd:$NaYF_4$	Thermal Relaxation	808	72.7	4
$NdVO_4$ in water	Thermal Relaxation	808	72.1	5
Au nanoshells	Double Beam Fluorescence Thermometry	808	68	3
Graphene in DMF	Integrating Sphere	808	67	6
Ho, Tm:KLu(WO_4)$_2$-TD	**Integrating Sphere**	**808**	**66**	**This work**
Au nanorods	Double Beam Fluorescence Thermometry	808	63	3
Au nanorods	Thermal Relaxation	815	61	7
Au/AuS nanoshells	Thermal Relaxation	815	59	7
Graphene Oxide in water	Integrating Sphere	808	58	6
Ho, Tm:KLu(WO_4)$_2$-MW	Integrating Sphere	808	45	2
Ho, Tm:KLu(WO_4)$_2$-CA	Integrating Sphere	808	43	2
Ho, Tm:KLu(WO_4)$_2$-P	Integrating Sphere	808	41	1
Au/SiO_2 nanoshells	Thermal Relaxation	815	34	7
FePt nanoparticles	$P_{converted\ to\ heat}/P_{excitation}$	800	30	8
Cu_9S_5	Thermal Relaxation	980	25.7	9
Au nanoshells	Thermal Relaxation	808	25	10

References

1. Nexha, A.; Carvajal, J. J.; Pujol, M. C.; Díaz, F.; Aguiló, M., Short-wavelength infrared self-assessed photothermal agents based on Ho,Tm:KLu(WO_4)$_2$ nanocrystals operating in the third biological window (1.45-1.96 μm wavelength range). *Journal of Materials Chemistry C* **2020,** 8, (1), 180-191.
2. Nexha, A.; Carvajal, J. J.; Pujol, M. C.; Díaz, F.; Aguiló, M.,, Effect of size and shape of Ho, Tm:KLu(WO_4)$_2$ nanocrystals in the performance as simultaneous luminescent nanothermometers operating in the third biological window and as photothermal agents. *Submitted at Journal of Alloys and Compounds*
3. Maestro, L. M.; Haro-González, P.; Sánchez-Iglesias, A.; Liz-Marzán, L. M.; García Solé, J.; Jaque, D., Quantum dot thermometry evaluation of geometry dependent heating efficiency in gold nanoparticles. *Langmuir* **2014,** 30, (6), 1650-1658.
4. Marciniak, L.; Pilch, A.; Arabasz, S.; Jin, D.; Bednarkiewicz, A., Heterogeneously Nd^{3+} doped single nanoparticles for NIR-induced heat conversion, luminescence, and thermometry. *Nanoscale* **2017,** 9, (24), 8288-8297.
5. del Rosal, B.; Pérez-Delgado, A.; Carrasco, E.; Jovanović, D. J.; Dramićanin, M. D.; Dražić, G.; de la Fuente, Á. J.; Sanz-Rodriguez, F.; Jaque, D., Neodymium-based stoichiometric ultrasmall nanoparticles for multifunctional deep-tissue photothermal therapy. *Advanced Optical Materials* **2016,** 4, (5), 782-789.
6. Savchuk, O. A.; Carvajal, J. J.; Massons, J.; Aguiló, M.; Díaz, F., Determination of photothermal conversion efficiency of graphene and graphene oxide through an integrating sphere method. *Carbon* **2016,** 103, 134-141.
7. Cole, J. R.; Mirin, N. A.; Knight, M. W.; Goodrich, G. P.; Halas, N. J., Photothermal efficiencies of nanoshells and nanorods for clinical therapeutic applications. *Journal of Physical Chemistry C* **2009,** 113, (28), 12090-12094.
8. Chen, C. L.; Kuo, L. R.; Lee, S. Y.; Hwu, Y.K.; Chou, S.W.; Chen, C. C.; Chang, F. H.; Lin, K. H.; Tsai, D. H.; Chen, Y. Y., Photothermal cancer therapy via femtosecond-laser-excited FePt nanoparticles. *Biomaterials* **2013,** 34, (4), 1128-1134.
9. Tian, Q.; Jiang, F.; Zou, R.; Liu, Q.; Chen, Z.; Zhu, M.; Yang, S.; Wang, J.; Wang, J.; Hu, J., Hydrophilic Cu_9S_5 nanocrystals: A photothermal agent with a 25.7% heat conversion efficiency for photothermal ablation of cancer cells in vivo. *ACS Nano* **2011,** 5, (12), 9761-9771.
10. Pattani, V. P.; Tunnell, J. W., Nanoparticle-mediated photothermal therapy: A comparative study of heating for different particle types. *Lasers in Surgery and Medicine* **2012,** 44, (8), 675-684.

Chapter IV

Multimorphological Ho, Tm:Y_2O_3 colloidal nanocrystals operating in the III-BW

Engineering synthetic methodologies for colloidal nanocrystals with precise control on their size, shape and crystal structure, is of paramount importance for understanding and properly tuning their chemical, physical and optical properties. These nanocrystals exhibit properties which cannot be achieved by their corresponding bulk counterparts. In addition, proper design of the size and shape of the nanocrystals allows the optimization for their application in nanoelectronics, optics, photovoltaics and biomedicine. Here, we explore synthesis of lanthanide sesquioxide nanocrystals, based on thermolysis reaction, and the applications of these lanthanide doped yttrium sesquioxide (Y_2O_3) colloidal nanocrystals as nanothermometers and nanohearts tuned as a function of their size and shape.

Cubic yttrium sesquioxide exhibits a wide range of properties, including a broad optical transparency range (0.2-8 μm) with an optical band gap of 5.6 eV, high thermal conductivity, high refractive index and low phonon energy, which have made it an attractive choice as host material for lanthanide ions for optical applications. Nevertheless, the majority of applications developed up to now have been designed for the bulk cubic Y_2O_3 materials, hence, no control on their morphology can be obtained. Nanocrystalline sesquioxide have been used as starting material to obtain optical transparent ceramic material for laser applications. We opted for wet chemical synthesis of undoped Y_2O_3 and lanthanide doped Y_2O_3 nanoparticles to produce diverse morphological habits of this compound, with the goal to determine the role of their sizes and shapes on the nanothermometer and nanoheater applications.

Thermolysis reactions and digestive ripening processes, in the presence of organic coordinating agents and directing controlling agents, ensure proper control on the size and shape of the final product. In the thermolysis reaction, the introduction of sodium nitrate ($NaNO_3$), among other agents including sodium chloride (NaCl), potassium chloride (KCl) and potassium nitrate (KNO_3), resulted in the formation of nanotriangles with sizes of ~23 nm, and nanohearts with sizes of ~32 nm, just by tuning the reaction time. In addition, we attempted the formation of core@shell and layer-by-layer nanoarchitectures by seeded growth addition (the seeds were composed of Ho, Tm doped Y_2O_3). The core@shell structures were obtained by adding the already prepared seeds (lanthanide doped Y_2O_3) to the reaction solution at room temperature for the growth of the shell. The layer-by-layer structures were obtained by hot-injection of the seeds at the crystallization temperature of the reaction.

On the other hand, Y_2O_3 colloidal nanocrystals were also obtained by, in this case, altering slightly the synthesis methodology by adding digestive ripening processes. In this case, the products are self-assembled nanodics with sizes ranging from 8-30 nm, and ultrathin, with thicknesses down to the unit cell (1 ± 0.2 nm) of this crystalline structure. Different directing agents were applied to test the effect of cations and anions in the crystalline habit of the product. This methodology is easily applicable to other sesquioxides like Yb_2O_3 and Gd_2O_3.

Upon doping with holmium (Ho^{3+}) and thulium (Tm^{3+}), Y_2O_3 colloidal nanocrystals with different morphological habits, were tested as temperature sensors operating in the third biological window and as photothermal agents. The thermometric performance determined for 3 mol% Ho^{3+} and 5 mol% Tm^{3+} doped nanotriangles, nanohearts, core@shell, layer-by-layer and self-assembled nanodics, demonstrate that the self-assembled nanodics are the nanoparticles influenced the most by the change of temperature, displaying a relative thermal sensitivity of 0.92% K^{-1} and a temperature resolution of 0.54 K at the lowest temperature under investigation (313 K), despite the emission generated by the core@shell nanoparticles is the brightest among them. Concerning the photothermal conversion efficiency, evaluated by using the integrated sphere method, the core@shell nanoarchitectures exhibited the highest value of 34%, two fold higher than the one obtained for the other Y_2O_3 colloidal nanocrystals. The higher photothermal conversion efficiency observed in the core@shell nanoarchitectures is explained by the effective non-radiative relaxation processes taking place, favored by the presence of the coating shell.

Paper V

Controlling the growth of colloidal rare earth oxides via wet chemical methodologies

Albenc Nexha, Maria Cinta Pujol,* Joan J. Carvajal, Francesc Díaz, Magdalena Aguiló
Universitat Rovira i Virgili, Departament Química Física i Inorgànica,
Física i Cristal·lografia de Materials i Nanomaterials (FiCMA-FiCNA)-EMaS, Campus Sescelades, E-43007, Tarragona, Spain
*mariacinta.pujol@urv.cat

Abstract

Rare earth oxide colloidal nanocrystals were synthesized via wet chemical methodologies (thermolysis and thermolysis reaction assisted by digestive ripening processes) using capping organic surfactants (oleic acid (OLAC) and oleylamine (OLAM)) in the absence or presence of structure-directing agents. The influence of the absence or the presence of these agents on the morphological and structural characteristics of the synthesized colloidal nanocrystals was investigated. Fine-tuning of the size and shape of the rare earth oxide nanocrystals can be achieved upon changing the nature of the structure-directing agents or the condition of the reactions. The role of the cations (Na^+, K^+) or the anions (NO_3^- or Cl^-) of these agents on the size, shape and the crystalline structure of the final product of the wet chemical methodologies were highlighted. Mechanisms explaining the formation of these monodisperse rare earth oxide nanocrystals were proposed, considering also the surface analysis characterizations (FT-IR and ^{1}H NMR).

1. Introduction

Development of new methodologies for the synthesis of colloidal nanocrystals with controllable size, shape and crystalline structure, are of paramount importance in understanding and tuning their chemical, physical and optical properties.[1, 2] Tailoring the size, shape and crystalline structure of these colloidal nanocrystals, not only provides new properties which cannot be achieved by their bulk counterparts,[3-5] but also enables optimized designs for applications in nanoelectronics, optics, photovoltaics and biomedicine.[6-11] Hence, elucidating the mechanisms that governs the shape and size control of colloidal nanocrystals is crucial.[12-14] Uniform colloidal nanocrystals are produced via wet chemical synthesis,[15] and the control over their sizes and shapes is achieved by various methods, including seed-mediated growth,[16] control of the reaction kinetics,[17] oriented attachment,[18] selective passivation by organic surfactants,[19] sequential cation exchange processes,[20, 21] and presence of structure-directing agents, also known as additives.[22] In this way, a plethora of different sizes and shapes with multifunctional applications, are generated.

Lately, high quality rare earth functional based colloidal nanocrystals have emerged extensive curiosity due to their peculiar optical properties.[23] Lanthanide's up- and down-converting mechanisms, arising from their 4f electrons,[24] have boosted their applications in fields like luminescence devices, photocatalysis, optical transmission, medical diagnosis and biosensing.[23, 25] Among different classes of rare earth compounds, rare earth oxides (RE_2O_3) are probe to continuous investigations to fine-tune their size, shape and crystal structures via the wet chemical methodologies.[26-28] Still, question marks lie ahead concerning the establishment of suitable wet chemical techniques for the preparation of uniform RE_2O_3 with easy control over their size, shape and crystal structure.

The introduction of structure-directing agents has tremendously improved the ability to precise control the crystalline phases, shapes and sizes of rare earth functional based colloidal nanocrystals and furthermore endow their electronic, magnetic and optical properties. This strategy is intensely devoted in the synthesis of rare-earth fluoride based colloidal nanocrystals. For example, Chen *et al*.[29] induced a phase transformation at low temperature (down to 403 K) from cubic-to-hexagonal (α→β) $NaYF_4$ by using Ti^{4+} ions. Similarly, the introduction of Mn^{2+},[30] and alkali-earth metals Ca^{2+} and Sr^{2+},[31] provided control over the size, shape and the desired crystalline phase. Zhao *et al*.[32] and Yin *et al*.[33] reported enhancement of the upconversion luminescence intensity of $NaYF_4$ by introducing into the reaction mixture additives of Li^+ and Mo^{3+} ions, respectively. In another report, the addition of Fe^{3+} ions in the Er^{3+}/Yb^{3+}: β-$NaGdF_4$ boosted the upconversion luminescence intensity of the green and the red.[34] Using as additives inorganic salts such as NaCl, KCl, LiCl and $BaCl_2$, Fu *et al*.[35] synthesized truncated octahedral, walnut-like and bundle-like morphologies of orthorhombic YF_3.

Regardless, the incorporation of these agents and the investigation of the underlying mechanism that govern the morphological and structural control on the synthesis of RE_2O_3 colloidal nanocrystals are scarce.[26, 27, 36, 37] Examples of the incorporation of additives in the synthesis of RE_2O_3 colloidal nanocrystals via the wet chemical methodologies, involve alkali ions such as the lithium hydroxide (LiOH), potassium hydroxide (KOH) and sodium hydroxide (NaOH) shape controlled synthesis of tripodal and triangular cubic Gd_2O_3 via thermal decomposition,[26, 36, 37] sodium diphosphate ($Na_4P_2O_7$) and sodium nitrate ($NaNO_3$) for tuning the shape of two-dimensional nanoplates and increase the yield of the thermolysis reactions,[27] Co^{2+} and Cd^{2+} in the form of acetylacetonate for the synthesis of RE_2O_3 nanodiscs via a digestive ripening reactions.[38]

Here, inspired by these works and the lack of a general understanding of the role of the structure-directing (hereafter X) agents in the synthesis of uniform RE_2O_3 colloidal nanocrystals via the wet chemical methodologies, we investigated the role of the absence or presence of these agents on the size, shape and the crystalline structure of the final product of the wet chemical methodologies. The effect of the cations (Na^+, K^+) or the anions (NO_3^- or Cl^-) from which these X agents are composed was highlighted. In addition, surface chemistry analysis of the final products were undertaken with the goal of elucidating the mechanism behind these synthetic methodologies.

2. Experiments

2.1. Materials

Yttrium acetate hydrate ($Y(CH_3CO_2)_3{\cdot}H_2O$ as $Y(Ac)_3{\cdot}H_2O$, purity 99.99%), gadolinium acetate hydrate ($Gd(CH_3CO_2)_3{\cdot}H_2O$ as $Gd(Ac)_3{\cdot}H_2O$, purity as 99.99%), oleylamine ($C_{18}H_{35}NH_2$, as OLAM, purity 70%) and potassium chloride (KCl, purity 99%) were purchased from Sigma Aldrich. Ytterbium acetate ($Yb(CH_3CO_2)_3$, as $Yb(Ac)_3$, purity 99.99%) was purchased from Apollo Scientific. Oleic acid ($CH_3(CH_2)_7CH{=}CH(CH_2)_7COOH$, as OLAC, purity 90%), 1-octadecene ($CH_3(CH_2)_{15}CH{=}CH_2$ as ODE, purity 90%), n-hexane ($CH_3(CH_2)_4CH_3$, purity 90%), sodium nitrate ($NaNO_3$, purity 99%) and potassium nitrate (KNO_3, purity 99%) were purchased from Alfa Aesar. Sodium chloride (NaCl) and ethanol (CH_3CH_2OH) were purchased from Merck and VWR, respectively.

2.2. Thermolysis reactions for rare earth sesquioxide Y_2O_3 colloidal nanocrystal synthesis

In a typical synthesis of Y_2O_3 colloidal nanocrystals through thermolysis reaction, 2.5 mmol of $Y(Ac)_3{\cdot}H_2O$ were added in a mixture of 25 mmol OLAC, 25 mmol OLAM and 15 mmol ODE. The reaction mixture was heated at 393 K under vacuum and held at this temperature for 0.5 h. The reaction mixture was then heated at 583 K using a ramp of 15 K min^{-1} and kept at this temperature for a time interval between 0.5 h and 2 h. After cooling down to room temperature, the reaction mixture was purified by washing with an excess of ethanol, followed by centrifugation at 5000 rpm for 10 minutes. Then, the supernatant was discarded and the precipitate was redispersed in an apolar solvent (n-hexane or toluene). The purification cycle was repeated for three times and the

final product was either stored in a solution dispersed in an apolar solvent or stored as a solid powder product after drying it in a muffle furnace at 333 K for 4 h.

When a structure-directing agent was used, the synthesis methodology was the same, but adding 4 mmol of the structure-directing agent ($NaNO_3$, KNO_3, NaCl or KCl) in the first solution.

2.3. Thermolysis reaction assisted by digestive ripening process for rare earth sesquioxide (RE=Y, Gd and Yb) colloidal nanocrystal synthesis

In a typical synthesis of rare earth sesquioxide colloidal nanocrystals through thermolysis reaction assisted by a digestive ripening process, 0.2 mmol of $Y(Ac)_3 \cdot H_2O$ (or $Gd(Ac)_3 \cdot H_2O$ or $Yb(Ac)_3$, 99.99%), were mixed and dissolved in 45 mmol of OLAM under nitrogen atmosphere. The solution was heated at 553 K using a ramp of 15 K min^{-1}. Once the temperature reached 553 K, 15 mmol of OLAC were swiftly injected into the reaction flask. The solution temperature was held at 553 K for 1 h. After the reaction, the solution was naturally cooled down to room temperature. The product of the reaction was extracted by adding an excess of ethanol to the solution, followed by centrifugation at 4500 rpm for 10 min, after which the supernatant was discarded and the precipitate was redissolved in an apolar solvent (n-hexane or toluene). The purification cycle was repeat until the supernatant was colorless. The rare earth sesquioxide colloidal nanocrystals obtained can be either stored in an apolar solvent dispersion or as a solid powder after drying it in a muffle furnace at 333 K for 4 h.

When a structure-directing agent was used, the synthesis methodology was the same, but adding 0.1 mmol of the structure-directing agent (NaCl, KCl, $NaNO_3$ or KNO_3) in the starting reaction mixture.

2.4. Characterization

X-ray powder diffraction (XRPD) measurements were made using a Siemens D5000 diffractometer (Bragg-Brentano parafocusing geometry and vertical θ-θ goniometer) fitted with a curved graphite diffracted-beam monochromator, incident and diffracted-beam Soller slits, a 0.06° receiving slit and a scintillation counter as detector. The angular 2θ diffraction range was set between 5 and 70°. The data were collected with an angular step of 0.05° at 3s per step and sample rotation. Cu K_α radiation was obtained from a Copper X-ray tube operated at 40 kV and 30 mA.
The colloidal nanocrystals size and shape were examined by a JOEL JEM-1011 transmission electron microscope (TEM) operating at an accelerating voltage of 100 kV or with a JEM-2100 high resolution transmission electron microscopy (HRTEM) operating at 300 kV. For the preparation of the TEM or HRTEM grids, around 7 µL of a diluted dispersion of the colloidal nanocrystals in n-hexane or toluene, were placed on the surface of a Copper grid covered by a holey Carbon film (HD200 Copper Formvar/Carbon).
Fourier Transform Infrared (FT-IR) spectra of the colloidal nanocrystals in powder form, were recorded in the range of 400-4000 cm^{-1} on a FT-IR IluminatIR II, Smith spectrophotometer, to investigate the presence of different functional groups on the surface of the nanoparticles that can be associated with the surfactants used in their synthesis.
Nuclear magnetic resonance (NMR) samples were prepared by dispersing 5 mg of the nanocrystals in 0.5 mL of deuterated chloroform, provided from Sigma Aldrich. NMR measurements were measured at room temperature and recorded on a Bruker Avance Neo spectrometer operating at a ^1H frequency of 400 MHz and featuring a BBI probe.

3. Results and discussion

3.1. Thermolysis reactions for rare earth sesquioxide colloidal nanocrystal synthesis

Upon tuning the operating parameters of thermolysis reactions, different morphological habits ranging from polyhedra, plates, discs, tripodal and triangular rare earth sesquioxide colloidal nanocrystals, can be produced.[26, 27, 39] Among the different rare earth sesquioxide, we focused our attention particularly in the preparation of yttrium sesquioxide particles. Yttrium sesquioxide nanocrystals represent a highly attractive host material for lanthanide ions, with potential

applications in the lighting industry,[40] displays,[41] and *in vivo* biological imaging.[42] In addition, the nanodimensional size of yttria particles, may promote their applications. For example, doped yttria nanocrystals compared to their corresponding bulk part, exhibit enhanced emission lifetimes,[43, 44] and increased luminescence efficiencies,[45] due to phonon confinement effects.

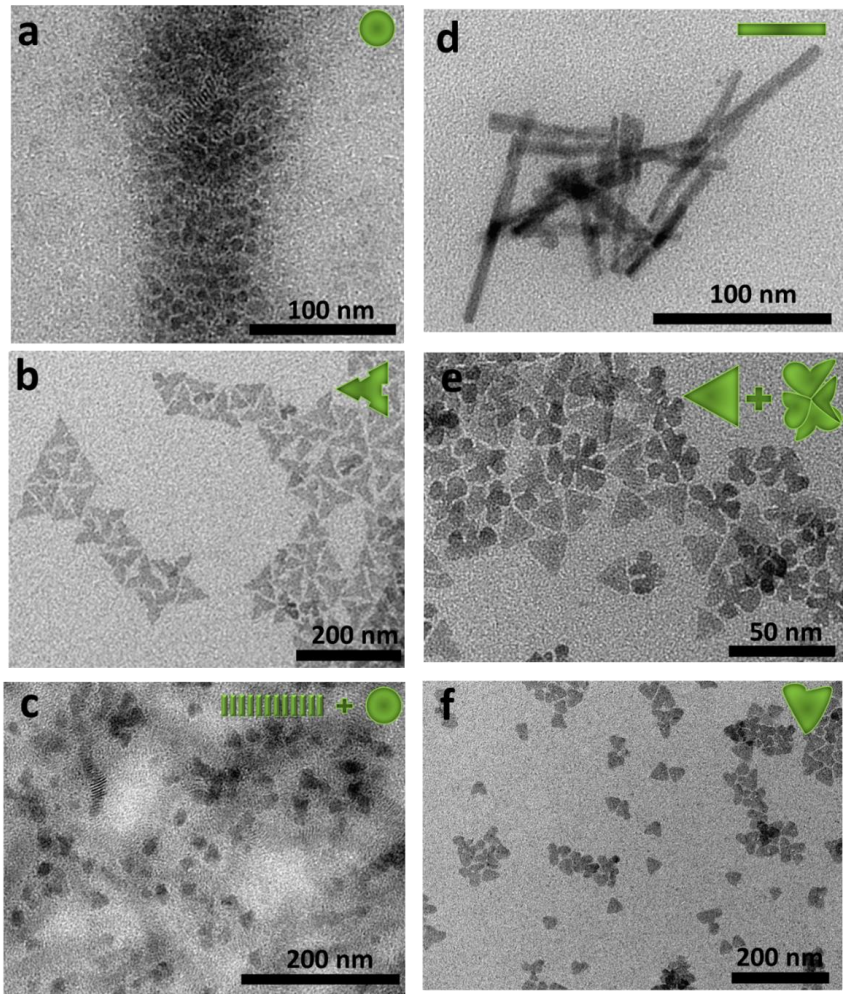

Figure 1. TEM images of Y_2O_3 colloidal nanocrystals synthesized via the thermolysis reaction at 583 K for 0.5 h using: (a) no X agents, (b) $NaNO_3$, (c) NaCl, (d) KCl, and at 583 K using $NaNO_3$ as X agents for: (e) 1 h and (f) 2 h reaction time, respectively. The sketchs portray the shape of the nanocrystals.

We synthesized yttrium sesquioxide colloidal nanocrystals via the thermal decomposition of yttrium (III) acetate precursor in the presence of OLAC and OLAM as capping ligands, ODE as a non-coordinating ligand, followed by the presence or not of X agent, adapting a synthetic methodology reported previously.[27] $Y(Ac)_3{\cdot}H_2O$ is selected as precursor for yttrium due to its fast thermal decomposition rate when compared with other yttrium complex precursors, such as acetylacetonates and benzoylacetonates.[28] The molar ratio between Y^{3+}:OLAM used in this synthesis was 1:10, regardless if X agents have been used. When these agents are used, the ratio among Y^{3+}:OLAM:X was 1:10:1.6. Among the organic surfactants, the molar ratios were OLAC:OLAM:ODE=10:10:6. The reaction temperature and time were set at 583 K and 0.5 h, respectively, following the parameters stablished in the literature for the synthesis of Gd_2O_3 and Y_2O_3 nanoparticles with triangular morphology.[27]

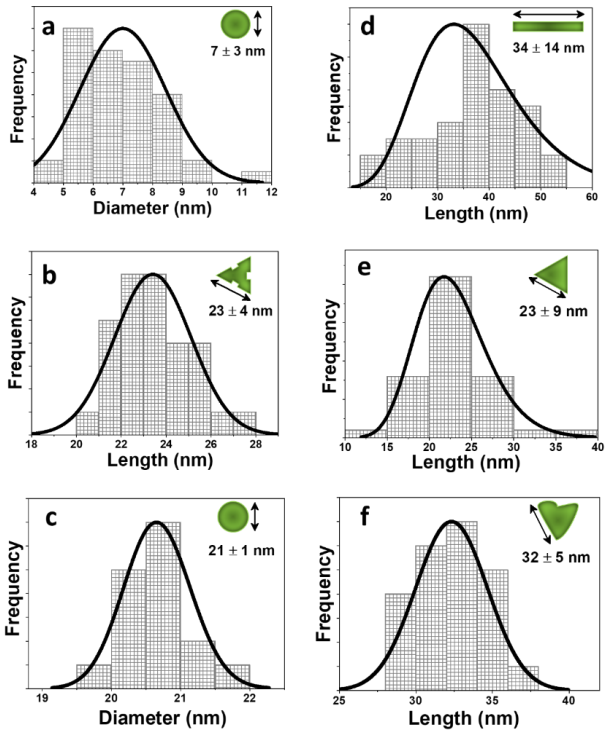

Figure 2. Lognormal size distribution of Y_2O_3 colloidal nanocrystals synthesized via the thermolysis reaction at 583 K for 0.5 h using: (a) no X agents, (b) $NaNO_3$, (c) NaCl, (d) KCl, and at 583 K using $NaNO_3$ as X agents for: (e) 1 h and (f) 2 h, respectively. The arrows aside the drawings stand for the parameter measured to determine their sizes.

The effect of the X agents on the morphology was investigated also by substituting $NaNO_3$ with KCl and KNO_3 to understand if the effect observed is due to the cations or anions. When KCl was introduced as X agent, the morphology of the final product changed to nanorods (see Figure 1 (d)). This result suggest that there is a cooperative effect between the cation (K^+) and the anion (Cl^-) that governs the morphology of the final product. On the other hand, surprisingly, KNO_3 did not reacted in the mixture, remaining at the bottom of the vial (see Figure S1 in the Supporting Information). The reason for that is not clear, but a possible explanation could be related to the relatively large ionic radii of K^+ ion compared to that of Na^+.

In terms of sizes, nanocrystals formed by nucleation, condensation, and particle growth are expected to yield lognormal size distributions.[46, 47] According to that, the mean sizes and the corresponding standard deviations have been obtained by fitting a lognormal distribution to the histograms of Figures 2 (b), (c) and (d), extracted after analyzing over 100 nanoparticles for each sample with the ImageJ software. The branched nanotriangles obtained in the presence of $NaNO_3$, have an average lateral length of 23 ± 4 nm (see Figure 2 (b)). The average diameter of the nanodiscs obtained when NaCl was used as X agent is around 21 ± 1 nm (see Figure 2 (c)), whereas their length is 21 ± 5 nm (see Figure S2 at Supporting Information). The nanorods synthesized using KCl have an average length of 34 ± 14 nm (see Figure 2 (d)). Clearly, the introduction of these structure-directing agents causes a modification of the size and shape of the yttria nanocrystals. In terms of monodispersity level, the nanodiscs obtained without X agents are comparable with those from using $NaNO_3$. From, the other side, the nanocrystals synthesized in the presence of KCl are less monodisperse compared to the other nanoparticles synthesized without and with X agents.

The XRPD patterns of the obtained products, in general, exhibit a poor degree of crystallinity. This is why the diffraction peaks appear very broad (see Figure 3). The thermolysis synthesis in

the absence of X agents, from its side, does not exhibit any peak at all (see Figure 3), indicating that an amorphous material seems to be obtained. As noted by Wawrzynczyk *et al.*,[36] and other authors,[26, 39, 48] not all the diffraction peaks are so broad, but some appear as sharper peaks. The most accepted explanation for this observation seems to be related to the preferential crystal growth orientation.[26, 39, 48] By comparison with the previous results published in the literature.[26, 36, 39, 48] The XRPD patterns obtained for the colloidal nanocrystals seem to indicate that they crystallize in the cubic system, with space group *Ia* $\bar{3}$, regardless of the X agent used. When comparing the different X agents used in these thermolysis reactions, clearly, the product of the reaction with $NaNO_3$ exhibits an enhanced intensity of the peaks corresponding to the {222} and {440} crystalline planes when compared to the pattern profile of the product with NaCl and KCl. Significantly, the diffraction peak corresponding to the (400) plane is also present in the diffraction pattern of the product obtained with $NaNO_3$ as X agent. Comparing the final product of the reaction with NaCl and KCl, both of them exhibit broad XR pattern profiles, nevertheless for the former one, it can be noted a sharp peak at the (440) plane, whereas for the latter one a sharp peak at the (222) plane. These different behaviors might be related to the different cations (Na^+ and K^+) since the anions source is the same (Cl^-). Hence, a combinatory effect between the cation and the anion present in the X agent, greatly influences the growth direction of a nanocrystals.

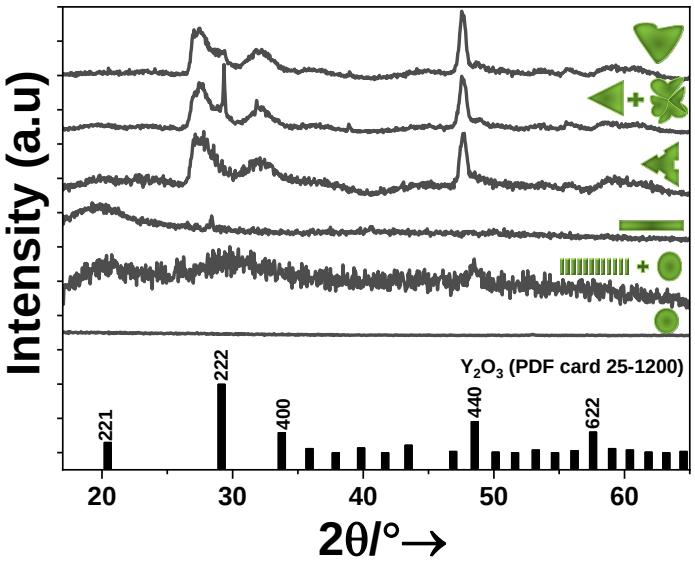

Figure 3. XRPD patterns of Y_2O_3 colloidal nanocrystals synthesized via the thermolysis reaction at 583 K for 0.5 h using no X agents and X agents ($NaNO_3$, NaCl and KCl), and at 583 K using $NaNO_3$ as X agents for reaction times of 1 h and 2 h. The reference pattern (PDF card 25-1200) of the cubic yttrium sesquioxide is included for comparison.

When we increased the reaction time from 0.5 to 2 h in the presence of $NaNO_3$, while keeping the other conditions unchanged (reaction temperature 583 K, Y^{3+}:OLAM:X ratio as 1:10:1.6 and OLAC:OLAM:ODE ratio as 10:10:6), the morphology of the nanocrystals evolved to a mixture flower-like nanocrystals and regular nanotriangles when the reaction time was set to 1 h, and to nanohearts when the reaction time was set to 2 h (see Figure 1 (e) and (f)). This increase of the reaction time also affected to the size of the crystals, that increase, for the case of the nanohearts to 32 ± 5 nm (see Figure 2 (f)), and the number of nanocrystals that can be seen in the pictures decreased. This is because, with the increase of the reaction time, smaller nanocrystals are sacrificed towards bigger nanocrystals, due to ripening processes.[49] For the reaction time of 1 h, the nanocrystals display a size of 23 ± 9 nm for the regular nanotriangles (see Figure 2 (e)) and the flower-like type nanocrystals have an average diameter of 29 ± 4 nm (see Figure S3 at Supporting Information).

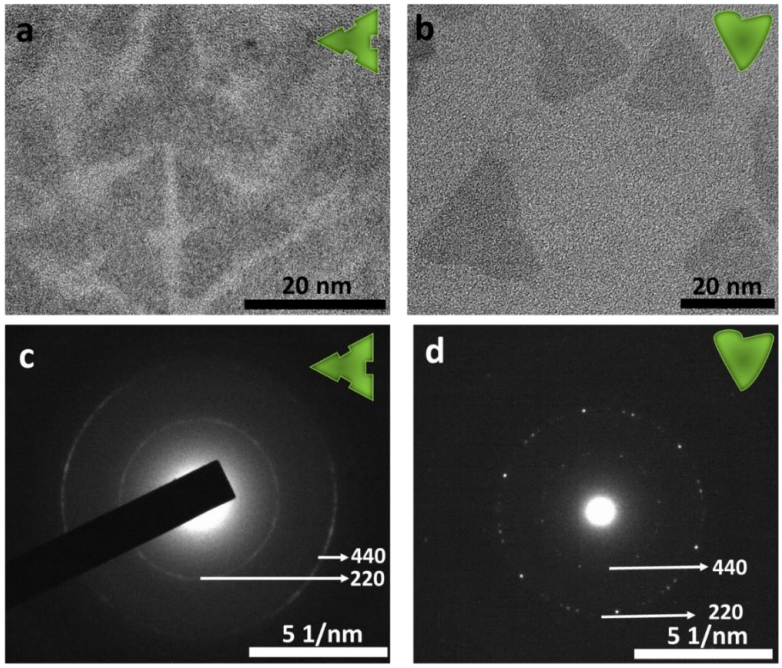

Figure 4. HRTEM images and SAED patterns of Y_2O_3 colloidal nanocrystals synthesized via the thermolysis reaction at 583 K, using $NaNO_3$ as X agent and different reaction time: (a) and (c) 0.5 h. and (b) and (d) 2 h.

The XRPD patterns of these colloidal nanocrystals reveal that the crystalline phases obtained belong to cubic Y_2O_3 with space group *Ia* $\bar{3}$, regardless of the reaction time (see Figure 3). The XRPD patterns also show the coexistence of sharp and broad peaks. Significantly, the diffraction peak (400) is present in all the diffractograms. The singular XRPD pattern obtained for the product synthesized at 1 h of reaction time, should be related to the presence of two morphologies populations, observed also from TEM (see Figure 1 (e)). There is the presence of a sharp {110} peak and a broad {111} peak. The displacement of the broad one could be related to the expansion of the crystallographic net, when the planes are strongly confined in one dimensional (1D). Our hypothesis is that the two coexistent morphologies are assigned to a two different crystallographic orientations, such as {111} confinement for the triangular shapes, and the {100} for the flower type.
High resolution TEM images (Figure 4 (a) and (b)) reveal the clear morphology of the nanocrystals synthesized via thermolysis reactions in the presence of $NaNO_3$ as X agents at a reaction time of 0.5 h and 2 h. At 0.5 h, the morphology is that of a clear branched nanotriangles (see Figure 4 (a)), whereas at 2 h reaction time, nanohearts are obtained (see Figure 4 (b)). In addition, the confinement of the plates in the {111} crystalline plane for the ternary symmetric morphologies can be confirmed also by the selected area electron diffraction (SAED) patterns obtained which is in the [111] zone (see Figure 4 (c) and (d) for the branched nanotriangles and nanohearts, respectively). The values of d-spacing calculated from the SAED patterns agreed with the cubic crystalline phase of yttrium sesquioxides.

3.2. Thermolysis reactions assisted by digestive ripening processes for the synthesis of rare earth sesquioxide colloidal nanocrystal in the absence or presence of structure-directing agents

Jeong *et al*.,[38] reported a thermolysis reaction assisted by digestive ripening process for sub-10 nm rare earth sesquioxide nanodiscs in the presence of Co^{2+} and Cd^{2+} as X agents in the form of acetylacetonate and OLAC as ripening agent. However, the incorporation of Co^{2+}/Cd^{2+} compounds portrays serious drawbacks related to their cost and more critical to their high

toxicity.[50, 51] Influenced from this work, we implemented a similar methodology to synthesize rare earth sesquioxide nanodiscs with the goal of avoiding the addition of these toxic elements. To achieve this goal, we attempted, the synthesis of yttria colloidal nanocrystals via thermolysis reaction assisted by digestive ripening process, in the absence and presence of a non-toxic and cheap X agents.

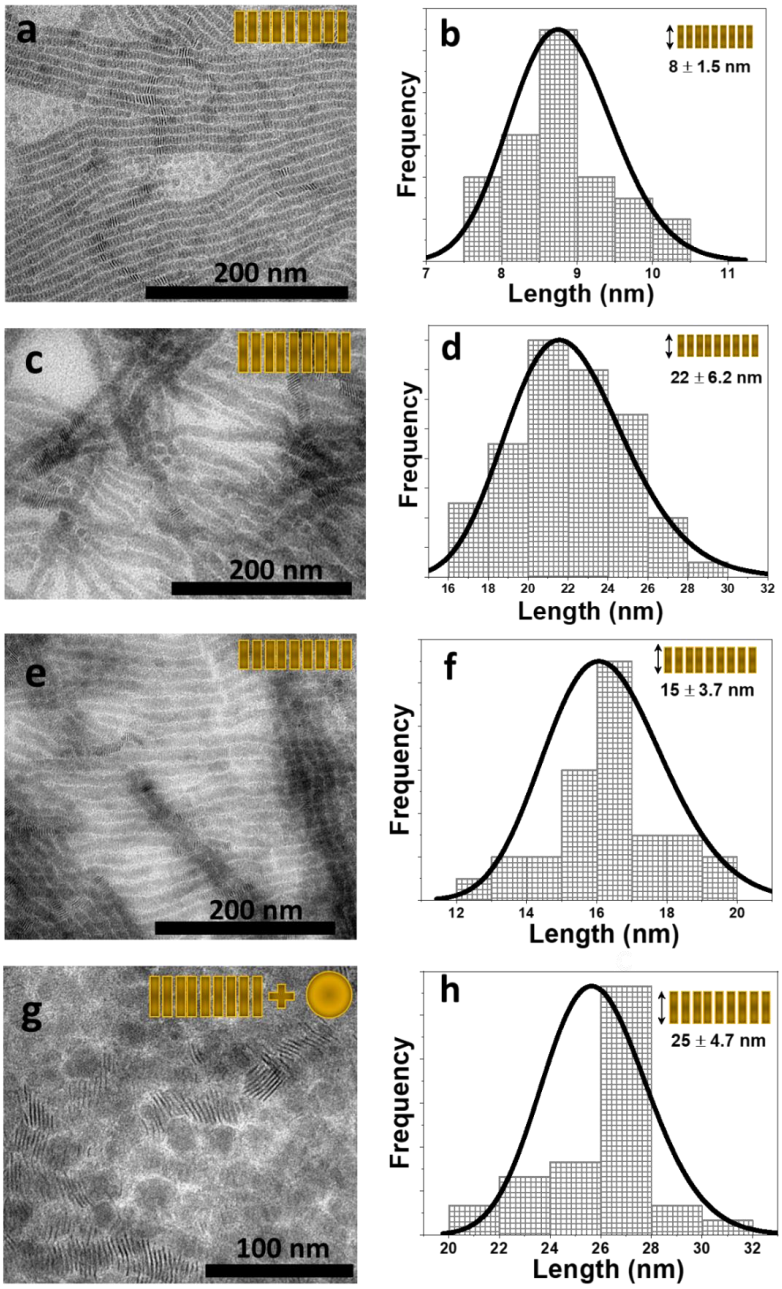

Figure 5. TEM images and lognormal size distribution of yttrium sesquioxide colloidal nanocrystals synthesized using: (a) and (b) no additives, (c) and (d) NaCl, (e) and (f) $NaNO_3$, and, (g) and (h) KCl, as X agents, respectively, by thermolysis assisted reaction by digestive ripening process. The sketchs portray the shape of the nanocrystals, whereas the arrows aside these sketchs stands for the parameter taken into account to determine the size of the nanocrystals.

Before exploring the effect of these agents, a few details have been considered, such as the type of precursor applied, the molar ratio between all the reagents, the temperature and time of the reaction. For the precursor, we opted for the acetates ($RE(Ac)_3$), since they are probe to faster thermal decomposition rates compared with acetylacetonates and benzoylacetonates precursors.[28] The $RE(Ac)_3$ precursor was thermally decomposed in the presence of OLAM with or without X agents in an oxygen-free atmosphere. The decomposition of the precursor was confirmed by the change of the colour of the reaction mixture from transparent colourless to olive-like, while the reaction temperature is raised at 553 K. The molar ratio between RE(III):OLAM:X used was 2:450:1, as already reported and optimized for the case of RE^{3+}:OLAM:Me, being Me=Cd^{2+} or Co^{3+}.[38]

Concerning the RE^{3+}:X ratio, we established the ratio 2:1, to achieve high crystalline nanocrystals followed by a well-defined shape and low size distribution, as demonstrated previously.[36] In the absence of X agent in the synthesis, the molar ratio RE^{3+}:OLAM was kept at 2:450. At the temperature of 553 K, with the swift injection of OLAC, there was a fast slight decrease of the temperature down to 533 K, changing the olive-like transparent color of the reaction mixture to turbid gray. After 1 min, the desired temperature (553 K) was recovered and the color of the reaction mixture changed to transparent yellowish. The OLAM:OLAC molar ratio used here was 3:1, in accordance with previous optimizations.[38] A further increase of this ratio can lead to smaller nanocrystals, due to enhancement of the rate of nucleation when OLAM is increased.[28] The reaction mixture was maintained at this temperature for 1 h as an adequate temperature and time for total decomposition of the precursor.[38] The colloidal nanocrystals were obtained after purifying the cooled-down reaction mixture with excessive amount of ethanol and dispersing it in apolar solvent (n-hexane or toluene), and dried in a conventional oven operating in open air conditions. All the dried colloidal nanocrystals were structurally investigated via XRPD and morphologically via TEM and HRTEM.

First, we analyzed the final product obtained in the absence of X agents. The resulted final product is composed of nanodiscs with high tendency of self-assembly (see Figure 5 (a)). These nanodiscs are highly uniform and monodisperse with average size 8 ± 1.5 nm (see Figure 5 (b)). Comparing with the same product synthesized from the thermolysis reaction without additives, in terms of the size they are similar but the formed colloidal nanocrystals are more uniform and monodisperse, probably due to the focusing in size exhibited from the digestive ripening process. Eu^{3+} doped Y_2O_3 self-assembled nanodiscs synthesized in the absence of X agents, were reported,[52] nevertheless, there an additional organic surfactants, such as trioctylamine, besides OLAM and OLAM, was implemented in the methodology, and glacial acetic acid was added to catalyse the reaction. Moreover, clearly the major morphological habit reported from them are the pure nanodiscs with slight tendency to generated self-assembled fibre-like structure. We believe this is due to the incorporation of the dopant (Eu^{3+}), which may disturb the self-organization of these nanodiscs. For these Eu^{3+} doped Y_2O_3 nanodiscs, the average size obtained was in the range of 30 nm-35 nm.

In the presence of X agents, we could extract only one report, the one achieved from Jeong *et al.*,[38] nevertheless, it should be stated that they do not report self-assembly in Y_2O_3 colloidal nanodiscs. Among the lanthanide sesquioxides, the Ho_2O_3 colloidal nanodiscs are the ones exhibit the self-assembly conduct. The average sizes of these nanodiscs are in the range 6.4 ± 0.3 nm. We cannot make a conclusive statement about the size comparison with the methodology that we have implemented without X agents, however, the sizes are comparable. From the other side, we underline that the size (the shape as well) of the final products obtained via wet chemical methodologies, are strictly related to the synthetic methodology applied. Thus, to the best our knowledge, this is the first synthetic methodology displaying this high degree of self-assembly for Y_2O_3 colloidal nanocrystals using thermolysis reaction assisted by digestive ripening processes.

For our methodology, we explored furthermore the effect of the X agents on the self-assembly conduct of Y_2O_3 colloidal nanodiscs. We investigated the effect of different anions and cations present in the X agents on the thermolysis reaction assisted by digestive ripening. In general, we observed the nanodiscs are still self-assembled, but changes in their degree of self-assembly and their sizes are detected.

We started to analyze the effect of anion, by implementing two X agents: NaCl and $NaNO_3$, while keeping the other parameters unchanged. In this way, we exclude the effect of the cation, by keeping it the same (Na^+), and observe if the different anions (NO_3^- and Cl^-) will exhibit any change in the morphological habit of the final product. Both X agents, maintain the self-assemble property of the nanodiscs (see Figure 5 (c) and (e)). Nevertheless, in terms of size, the nanodiscs synthesized in the presence of NO_3^-, are smaller and further slightly more uniform and monodisperse compared to the ones synthesized via Cl^-. In the presence of Cl^-, nanodiscs with length around 22 ± 6.2 nm (see Figure 5 (d)) are produced, whereas using NO_3^- the length is around 15 ± 3.7 nm (see Figure 5 (f)). The same behavior in terms of the size obtained of the colloidal nanocrystals, was also observed for the thermolysis reactions.

Last, maintaining the reaction conditions unchanged, the effect of different cations (K^+ instead of Na^+) was analyzed by substituting NaCl with KCl. In this case, the self-assembly conduct achieved from K^+, started to be disassemble, although still present, and pure nanodiscs are appearing (see Figure 5 (g)). This observation could be related to the relatively higher ionic radii of the K^+ compared to the Na^+ ion.[53] Concerning the size of the nanodiscs in the self-assembly conduct in the reaction with KCl, they appear larger compared to the ones obtained with NaCl or $NaNO_3$, reaching a value of 25 ± 4.7 nm (see Figure 5 (h)), whereas the pure form of nanodiscs have a diameter around 28 ± 2.2 nm (see Figure S4 at Supporting Information). In addition, these nanodiscs are less uniform and less monodispersed compared to the cases of other additives (see Figure 5 (h)).

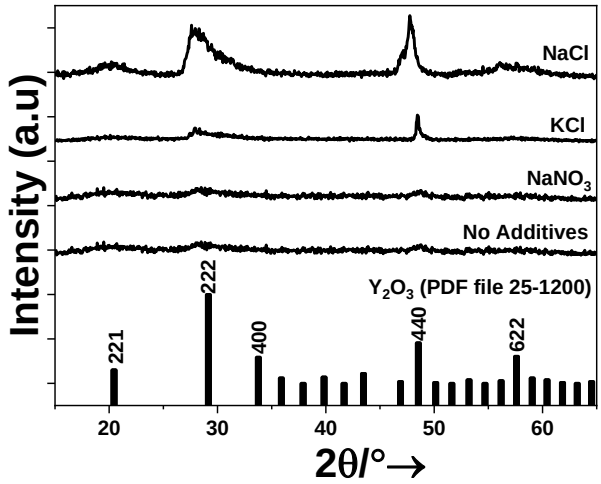

Figure 6. XRPD patterns of Y_2O_3 self-assembled nanodiscs synthesized in the absence and presence of X agents.

The crystalline structure of all the obtained nanodiscs was analyzed using XRPD. From Figure 6, some pattern do not exhibit clear diffraction peaks, implying poor crystallinity. The XRPD patterns of the product synthesized without additives or when using $NaNO_3$ as X agents, exhibit similar profiles including relatively low degree of crystallinity. When introducing NaCl as X agent, a clear improvement of the crystallinity of the final product is detected, related to the presence of high intensity diffraction peaks. The patterns ca be assigned to the cubic phase of yttria with space group *Ia* $\bar{3}$. Clearly, for the reactions in the absence of the additives and when $NaNO_3$ was included, very broad XRPD profiles are detected. On the contrary, the addition of NaCl, ensures sharp patterns, towards (111) and (110) plane (see Figure 6). Further, in general, it can be noted the disappearance of the peak at {400}. A possible explanation may rely on the crystalline orientation of the particles, influenced by the presence of the Cl^- ions during the synthesis or the digestive ripening effect. We speculate that the presence of Cl^- is more prone to be responsible of the change of the crystalline orientation.

Hence, given the clear crystalline profile of the nanodiscs synthesized when applying NaCl as X agent, for what follows, we focus to the synthesis of other rare earth sesquioxides in the presence of this agent. We explored the possibility of synthesizing other rare earth based sesquioxides by using their acetates as precursor, keeping unchanged all the molar ratios and treating the reaction mixture at a temperature of 583 K and time of 1 h, in the presence of NaCl as X agent. We investigated the size, shape and crystalline structure of the RE_2O_3 ($RE=Gd^{3+}$ and Yb^{3+} as illustrative examples) colloidal nanocrystals synthesized in the presence of NaCl. For both examples, the shape of the final products obtained are those of ultrathin nanomaterials, in the form of nanodiscs, as can be seen from the acquired TEM images (see Figure 7 (a) and (b)). Gadolinium sesquioxide colloidal nanocrystals are formed in the shape of nanodiscs with a mean size of 19 ± 7 nm (see Figure 7 (c)). Ytterbium sesquioxide is composed of nanodiscs with a mean size of 9 ± 3.3 nm (see Figure 7 (d)). Similar results were also observed for the thermolysis reactions assisted by digestive ripening processes in the presence of Co^{2+}/Cd^{2+} precursors as X agents.[38]

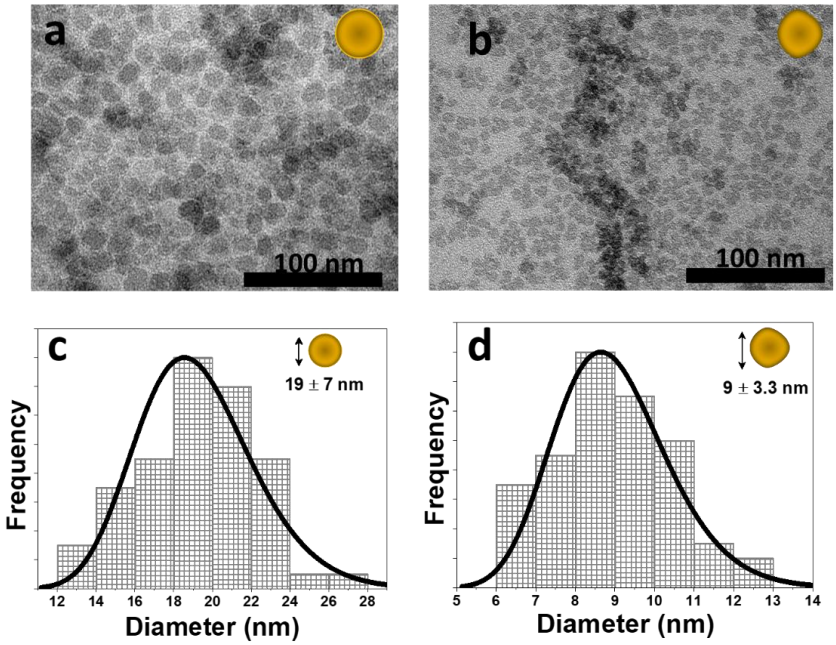

Figure 7. TEM images and lognormal size distribution of rare earth sesquioxide colloidal nanocrystals: (a) and (c) Gd_2O_3, (b) and (d) Yb_2O_3, synthesized by thermolysis reaction assisted by digestive ripening process with NaCl as X agent. The drawings portray the shape of the nanocrystals, whereas the arrow stands for the parameter taken into account to determine their sizes.

Having synthesized gadolinium and ytterbium sesquioxides, now we can compare our methodology with the implying Co^{3+} or Cd^{2+} precursors as X agents.[38] First, we compare from the morphological point of view. Morphologically, the nanodiscs obtained using NaCl in the present manuscript, are slightly larger, when comparing to the ones grown by the presence of Co^{3+} or Cd^{2+} precursors. Further, in our methodology, a higher influence of the RE^{3+} ion in the final size of the nanodiscs can be deduced, leading to a 2-fold increase in size of these nanocrystals for Gd_2O_3 and Y_2O_3, compared with Yb_2O_3. Contrarily, Jeong *et al.* reported similar diameters for Gd^{3+} and Yb^{3+} sesquioxides, in the range of 6 nm and 7.9 nm, respectively.[38] We speculate that the larger differences in size among the different rare earth sesquioxides, could be related either to a required optimization of the amount of NaCl applied for each sesquioxide synthesis, or NaCl as X agent is more sensitive to the RE^{3+} ion than Co^{3+} or Cd^{2+} precursors. The different response of NaCl to the different ions could be related to their ionic size.[27] Nevertheless, the monodispersity of the rare-earth sesquioxides achieved from NaCl is higher compared with

those achieved from Co^{3+} or Cd^{2+} precursors.[38] Y_2O_3 and Gd_2O_3 nanocrystals display larger variation of the sizes (see Figure 5 (d) and Figure 7 (c)) compared to Yb_2O_3 discs (see Figure 7 (d)). In the other hand, the sub-10 nm lanthanide sesquioxides in the presence of Co^{3+} or Cd^{2+} precursors, exhibit a monodispersibility level of <10%, without specifying particular lanthanide elements.[38]

Another appealing remark of the thermolysis reaction assisted by digestive ripening processes, is the capacity of the yttrium sesquioxide nanodiscs, compared to the nanodiscs of Gd_2O_3 and Yb_2O_3, to self-assemble into long fiber-like superstructures with length ranging from nanometers up to few micrometers. As pointed out also above, this phenomena was also encountered in the case of Eu^{3+} doped Y_2O_3 synthesized via a thermolysis reaction in the presence of a triple organic surfactants (trioctylamine, OLAM and OLAC), and glacial acetic acid, acting as a catalyze,[52, 54] and for the synthesis of rare earth nanocrystals via digestive ripening process in the initial presence of OLAM and Co^{2+}/Cd^{2+} precursors as X agents, and later, at the desired temperature (583 K), the swift injection of OLAC.[38] Surprisingly, the work from Engelsen *et al.*[52] for the synthesis Eu^{3+} doped Y_2O_3 self-assembled nanodiscs, was originally inspired from another paper, in which it was attempted the preparation of Eu_2O_3 nanoparticles, resulting in nanoplatelets,[54] instead of self-assembled nanodiscs. More appealing, the work from Jeong *et al.* reported self-assembly conducts in almost all the rare earth sesquioxides, nevertheless they did not reveal if Y_2O_3 nanocrystals are self-assembled or not.[38] Clearly, in the synthetic methodology that we apply here, are only Y_2O_3 colloidal nanocrystals that exhibit this self-assembly conduct. The reason after this observation is unclear and further in depth studies are required. Concerning the reason why these nanocrystals self-assemble, the authors stated that this conduct could be attributed to the combinatory effect of the van der Waals attractions and the steric repulsion of oleate ligands capping the nanodiscs.[38, 52] The nanodiscs-to-nanodiscs (hereafter inter-discs) distance in these self-assembled nanoarchitectures, is equal to a value of 3.9 nm,[52] matching with the almost two time projected distance of cis oleic acid.[55] In our methodology, an inter-disc distance around 3.8 nm was determined, as detected from the acquired HRTEM image in Figure S5 (a) at Supporting Information.

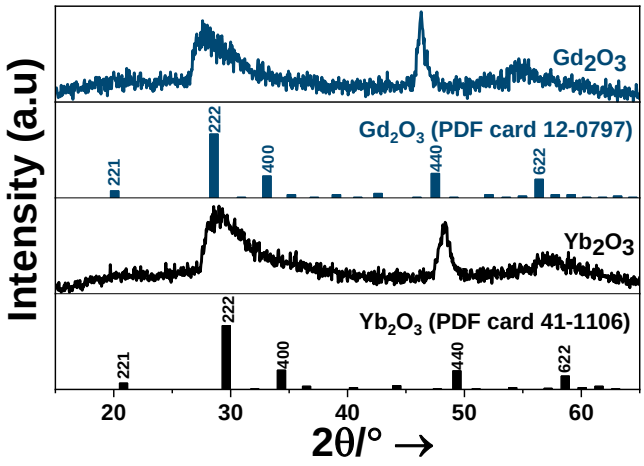

Figure 8. XRPD patterns of RE_2O_3 (RE=Gd and Yb) colloidal nanocrystals synthesized via the thermolysis reaction assisted by digestive ripening process. The corresponding reference patterns, PDF card 41-1106 and PDF card 12-0797 for Yb_2O_3 and Gd_2O_3 are included for comparison.

In terms of the crystalline structure of the colloidal nanocrystals obtained by thermolysis reactions assisted by digestive ripening processes, clearly all the diffractograms exhibit patters with broad peaks (see Figure 8), related probably to the relative low size of the nanocrystals. The peaks can be assigned to the cubic structures with space group *Ia* $\bar{3}$ of the sesquioxides, with lattice constant of a=10.4 Å for Yb_2O_3, with PDF card 41-1106 and a=10.8 Å for Gd_2O_3 PDF card 12-0797.

Nevertheless, as it has been pointed out in other references, not all of the diffraction peaks are broadened, some of them are sharper and this could be explained by the preferential crystal growth direction.[26, 28, 36, 48] For our methodology, the sharpening of the peaks is more significant for the (440) peak and the effect is more intense for Y_2O_3 colloidal nanodiscs. We assume that the confined plane in the nanodiscs is the {100}, related to the disappearance of the diffraction peak {400}, and with a preferential growth along the [110] crystallographic directions, due to the sharpness of this peak. In literature, it was been proposed the possibility that the alkali ion is intercalating in the crystalline structure, arguing that this effect will be favoured by a similarity of ionic radii and as the ratio of Me^+ ion versus RE^{3+} is increased.[36] The most similar radii in the systems studied in our methodology, is for the Gd^{3+} (ionic radii 1.053 Å, coordination number 8) and for the Na^+ (ionic radii 1.13-1.53 Å). For the case of Y^{3+} and Yb^{3+} synthesis, the Na^+ ionic radii is too large. Furthermore, the ratio RE^{3+}:Na^+ used in our methodology, is 1/0.5, which is rather low. Therefore, we can discard the existence of the $NaREO_2$ compound in the synthesized samples.
Continuing with the ratio RE^{3+}:Na^+ and comparing our Gd_2O_3 nanodiscs with the Gd_2O_3 nanoparticles produced from Wawrzynczyk *et al.*,[36] we can state that the outcome is similar. We recall that the reaction parameters, involving the Gd^{3+}:Na^+ ratio, the precursors ($Gd(Ac)_3$ and NaCl) and the organic surfactants (OLAC, OLAM) are identical. In terms of reaction time and temperature, our methodology consists in 553 K during 1 h, whereas Wawrzynczyk *et al.*, produced Gd_2O_3 nanoparticles at 583 K for 0.75 h.[36] Still, in the XRPD pattern presented in Figure 8, the peak {400} has disappeared totally, on the contrary of the diffraction patterns reported by them, in which this diffraction peak was present. A possible explanation may rely on the crystalline orientation of the particles, influenced by the presence of the Cl^- ions during the synthesis or the digestive ripening effect. We speculate that the presence of Cl^- is more prone to be responsible of the change of the crystalline orientation.
The Eu^{3+} doped Y_2O_3 self-assembled nanodiscs reported from Engelsen *et al.*[52] and the RE_2O_3 colloidal nanocrystals from Jeong *et al.*,[38] barely show any diffraction peaks. The authors attributed this outcome due to a possible modification of the atomic structure due to the change in surface energy, stabilizing ligand effects and the presence of defects and strains when comparing the ultra-small sized particles with their bulk counterparts. Still, also our Y_2O_3 self-assembled nanodiscs rely in the ultra-small regime of dimensions with average sizes of 20 nm and thickness of 1 ± 0.3 nm (see Figure S5 (b) at Supporting Information), but their diffractogram exhibits a sharp and intense diffraction peak corresponding to the {100} crystallographic plane (see Figure 6), which might be assigned again to the effect of the X agent. As stressed above, this would again reaffirm the statement that the plane of the nanodiscs is confined in the {100} planes, and the crystal is growing along the [110] directions.

3.3. Surface characterizations of colloidal nanocrystals prepared via the wet chemical synthesis

Generally, the synthesis of colloidal nanocrystals via the wet chemical methodologies in the presence of the organic surfactants, implies twofold role of the organic surfactants, when the product is already formed: the dispersion of the final product in organic solvent (*i.e.* hydrophobic nature of the final products) and surface passivation.[56] Thus, the final product of the wet chemical synthesis are expected to be coated with organic surfactants.

We analyzed the presence of the organic surfactants on the surface of our already-dried final products of the digestive ripening process and the thermolysis reaction via Fourier Transform Infrared. Figure 9 (a) presents the spectra recorded for the self-assembled Y_2O_3 nanodiscs produced from the digestive ripening reaction and for the branched Y_2O_3 nanotriangles synthesized from the thermal decomposition.

In both methodologies, the peaks at 2850 and 2924 cm^{-1} are assignable to the symmetric and the antisymmetric methylene group stretches (ν_s (CH_2) and (ν_{as} (CH_2)) of OLAC and OLAM.[57, 58] A very weak shoulder around 2924 cm^{-1} is attributed to the antisymmetric methyl stretch ν_{as} (CH_3). The characteristic bands of OLAC at 1710 cm^{-1} of ν(C=O) stretch and of OLAM at 1595 cm^{-1} for the bending δ(NH_2),[59] could not be detected neither in the digestive ripening or the thermal decomposition method, which confirms the absence of unreacted -COOH and -NH_2 groups of OLAC and OLAM absorbed on the surface of synthesized colloidal nanocrystals.

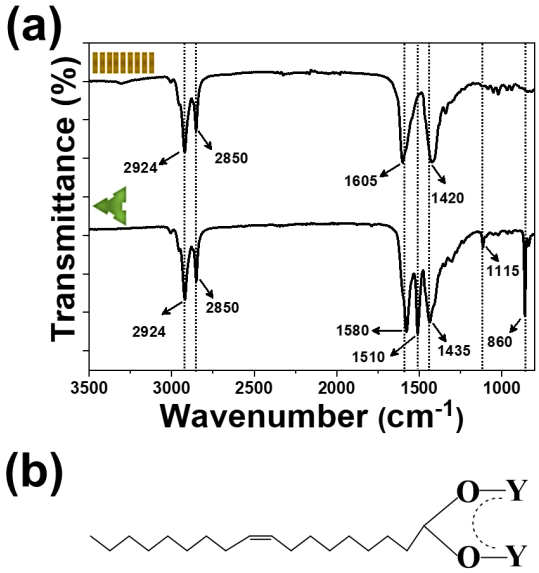

Figure 9. (a) FT-IR spectra of the organic surfactants coated yttrium oxide nanocrystals synthesized via the thermolysis reaction and digestive ripening methodologies. (b) Proposed coordination of the oleic acid moiety to yttrium atoms.

The peak at 1710 cm^{-1} of ν(C=O) stretch for unreacted OLAC, in the case of the thermal decomposition, is replaced by two characteristic bands at 1580 cm^{-1} and 1435 cm^{-1}, and in the case of digestive ripening by bands at 1605 cm^{-1} and 1420 cm^{-1}, ascribed to the antisymmetric and symmetric stretching vibrations of the deprotonated carboxylic group (COO^-), indicating that the OLAC molecules were deprotonated and presented carboxylates anions due to the promotion of OLAM.[60] In addition, these predominantly oleate species in both methodology confirm the successful chemisorption of oleic acid as a carboxylate in the surface of the colloidal nanocrystals. The absence of the oleylamine is expected because of the high electron affinity of the oleic acid and the presence of three different binding motifs (monodentrate, bidentate or bridging)[61] when compared to only the amine headgroup of oleylamine. This observation is in agreement with other articles published that show that no FTIR spectral features are found that are characteristics of an amine-containing species,[58, 60, 62] even when at the reaction is incorporated only OLAM.[63] Although the reason why OLAM is not found in surface of the colloidal nanocrystals is unclear, Harris *et al*.[64] stated that OLAM helps for the formation of an acid base complex with OLAC, thus more OLAC molecules have dissociated hydroxyl groups that promote the adsorption of OLAC on the surface of the nanocrystals. This, was furthermore proved in reactions when only OLAC was used as an organic surfactant, as shown from He *et al*.[62] the typical 1710 cm^{-1} peak of C=O stretching mode is absent, indicating so a complete chemisorption of OLAC on the surface of the nanocrystals.

Thus, the separation between this two bands, reveals the type of binding of the carboxylic group into the surface of the colloidal nanocrystals.[61] So, for a monodentrate ligand a separation of >200 cm^{-1} is expected, <110 cm^{-1} for a bidentate and 140-200 cm^{-1} for a bridging ligand.[61] The separation of the two bands is 145 cm^{-1} and 185 cm^{-1} for the thermal decomposition and the digestive ripening reaction, respectively. Although this separation lies in the region of the bridging ligand (two oxygen atoms from carboxylates are coordinated symmetrical to two different Y atoms), is hard to distinguish from FTIR whether the oleic acid is of bridged nature or purely ionic, as depicted in Figure 9 (b).

The incorporation of the ligands on the surface of the colloidal nanocrystals was furthermore studied from ^1H NMR analysis. The dried nanocrystals were dispersed in deuterated chloroform ($CDCl_3$) and analyzed via proton NMR. The results obtained from ^1H NMR for the Y_2O_3

nanocrystals synthesized via the thermolysis and the digestive ripening reactions, are shown in Figure 10 (a) and (b). Both spectrum consists of similar behavior and conclude that the only ligand that is attached to the surface of the colloidal nanocrystals is the oleic acid.

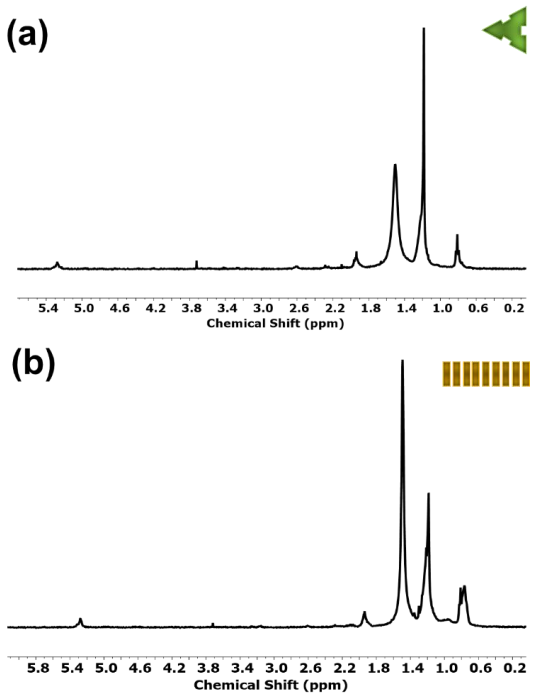

Figure 10. ^{1}H NMR spectrum of the (a) branched nanotriangles and (b) the self-assembled nanodiscs synthesized from the thermolysis and digestive ripening reactions, respectively.

Thus, typical chemical shifts (δ) of oleylamine such as the multiplet 2.6 ppm of the methylene group close to the NH_2 or the triplet of the hydrogen on the amine group at 1.17 ppm (see Figure S3 at Supporting Information) are not observed in either of the patterns of the two different synthetic approaches. Typical patterns of oleic acid moieties, such as the vinyl group at δ=5.28 ppm, the allyl group at δ=2 ppm and the methylene group at δ=0.89 ppm (see Figure S3 at Supporting Information for the ^{1}H NMR pattern of oleic acid) are typically observed on the pattern of the synthesized nanocrystals. As in accordance with other studies of the oleic acid capped colloidal nanocrystals, the ^{1}H NMR peaks did not shifted, however they exhibit a significantly breaded or disappeared.[65] Regarding the integrals of the peaks, they do not match with that of the pure oleic acid and a possible reasoning for that might be because the signals of the hydrogen atoms located near the surface of the nanoparticles are affected in the strongest way from the broadening phenomena.[66]

3.4. Mechanisms of the synthesis of colloidal nanocrystals

During the thermolysis reaction, an achievement of a transparent liquid mixture, as reported also elsewhere, is a proof of the fact that a ligand-exchange reaction has taken place,[67] thus in our case, the rare earth acetates were exchanged with the OLAC ligand. The just formed $RE(OLAC)_3$ complex cannot undergo thermal decomposition until 673 K,[28] thus the basic compound OLAM catalyzes the *in situ* transformation of the $RE(OLAC)_3$ complex into RE_2O_3.[28] During this step, the initial RE_2O_3 nuclei formed and by the presence of $NaNO_3$ as X agent, a preferential crystallographic growth along <110> orientation occurred. A schematic presentation of the mechanism of the formation of the rare earth sesquioxide nanocrystals *via* the thermolysis reaction is illustrated in Figure 11 (a).

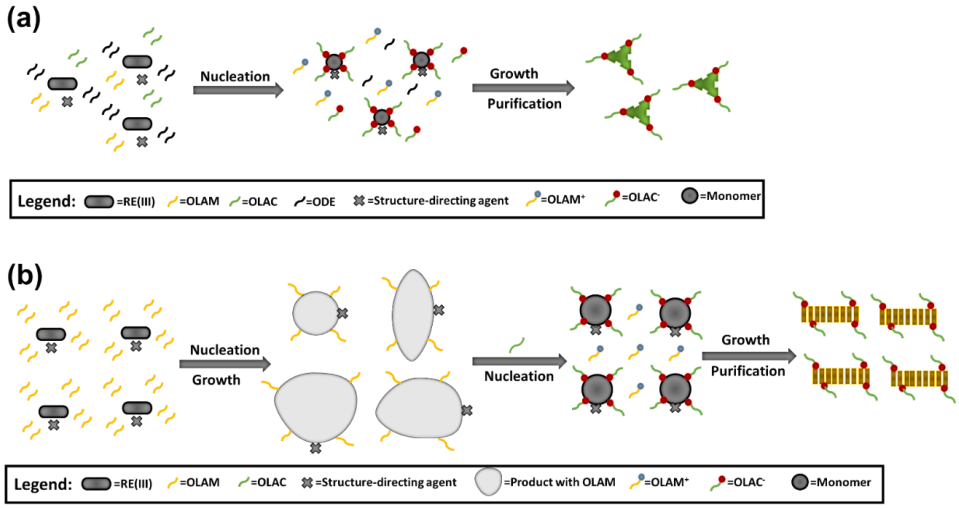

Figure 11. Proposed mechanism for the synthesis of rare earth oxide colloidal nanocrystals via: (a) thermolysis and (b) digestive ripening reactions.

During the digestive ripening process, OLAM is the compound that is initially weakly bounded and forms the $RE(OLAM)_3$ complex with the rare earth precursor and a "sacrificial" non-uniform and aggregated monomer (highly reactive monomer species that induce the nucleation and process the growth of nanocrystals),[68] is formed (see Figure 11 (b)), which morphology is dictated from the X agents NaCl. When OLAC is swiftly injected, due to his highly electron donating ability,[69] replaces the existing weakly bounded OLAM species and bind to the surface of the nanocrystals, thus regrowing on the "sacrificial" monomer, leading to the formation of well-defined colloidal nanocrystals.[68]

Taking into account the data from the FT-IR and HNMR analysis, one can rule out that the ligand bonded to the surface of the nanocrystals is oleic acid moiety. However, taking into account these surface functionalization techniques, no traces of the X agents were observed neither in FT-IR or H NMR, thus the possible explanation relies on the fact that the X agents, initially bounded to a certain crystallographic direction, and during the purification process could be partially washed out or remain undetected into the colloidal solution.[35, 38]

4. Conclusions

Highly monodisperse cubic rare earth oxide colloidal nanocrystals were synthesized via wet chemical synthesis, mainly thermolysis and digestive ripening processes. Control over the characteristics of the final products can be achieved by tuning the reaction conditions or involving structure-directing agents in the synthesis. The sizes and shapes, crystalline structure and the surface chemistry of these nanocrystals were investigated using electronic microscopy (TEM and HRTEM), power XRD, and FT-IR and ^{1}H NMR, respectively. Within these wet chemical synthesis, different types of structure-directing agents, including NaCl, $NaNO_3$, KCl and KNO_3, are employed. For the digestive ripening process, the obtained nanocrystals are in shape of nanodiscs with a tendency to be self-assembled in the form of fiber-like structures. When these agents where applied in thermolysis reactions, the shape of the final product is varied among branched nanotriangles, nanodiscs and nanorods. In addition, when exposed into longer reaction times, the branched nanotriangles are converted into nanohearts. In all the wet chemical methodologies applied, the crystalline structure of the final product of the reactions, resembles that of the cubic phase. Surface characterization techniques Fourier Transform Infrared (FT-IR) and proton Nuclear Magnetic Resonance (^{1}H NMR) revealed that oleic acid was the organic surfactant bonded to the surface of the colloidal nanocrystals on both synthetic methodologies.

Based on these findings, mechanisms for the generation of these colloidal nanocrystals via wet chemical methodologies, were proposed. On the thermolysis reaction, OLAM acts as a catalyst to thermally decompose the rare earth-OLAC complex. On the digestive ripening process, the preformed rare earth-OLAM complex act as a "sacrificial" monomer on which the stronger binder OLAC is added and furthermore control the size and shape of the final formed colloidal nanocrystals. These synthetic methodologies have the potential to be applied for the synthesis of other type of materials, including transition metal oxides.

5. Acknowledgements

This work was supported by the Spanish Government under projects MAT2016-75716-C2-1-R (AEI/FEDER, UE) and by the Generalitat de Catalunya under project 2017SGR755. A.N acknowledges financial support from the Generalitat de Catalunya under grant 2017FI_B00620, 2018FI_B100161 and 2019 FI_B200154.

6. References

1. Murphy, C. J.; Sau, T. K.; Gole, A. M.; Orendorff, C. J.; Gao, J.; Gou, L.; Hunyadi, S. E.; Li, T., Anisotropic metal nanoparticles: Synthesis, assembly, and optical applications. *Journal of Physical Chemistry B* **2005,** 109 (29), 13857-13870.
2. Xia, Y.; Xiong, Y.; Lim, B.; Skrabalak, S. E., Shape-controlled synthesis of metal nanocrystals: Simple chemistry meets complex physics? *Angewandte Chemie International Edition* **2009,** 48 (1), 60-103.
3. Li, X.; Wang, M.; Shen, H.; Zhang, Y.; Wang, H.; Li, L. S., Inorganic Sn-X-complex-induced 1D, 2D, and 3D copper sulfide superstructures from anisotropic hexagonal nanoplate building blocks. *Chemistry An European Journal* **2011,** 17 (37), 10357-10364.
4. Li, X.; Si, H.; Niu, J. Z.; Shen, H.; Zhou, C.; Yuan, H.; Wang, H.; Ma, L.; Li, L. S., Size-controlled syntheses and hydrophilic surface modification of Fe_3O_4, Ag, and Fe_3O_4/Ag heterodimer nanocrystals. *Dalton Transactions* **2010,** 39 (45), 10984-10989.
5. Li, X.; Niu, J. Z.; Shen, H.; Xu, W.; Wang, H.; Li, L. S., Shape controlled synthesis of tadpole-like and heliotrope seed-like $AgInS_2$ nanocrystals. *CrystEngComm* **2010,** 12 (12), 4410-4415.
6. Talapin, D. V.; Lee, J.-S.; Kovalenko, M. V.; Shevchenko, E. V., Prospects of colloidal nanocrystals for electronic and optoelectronic applications. *Chemical Reviews* **2010,** 110 (1), 389-458.
7. Kamat, P. V., Quantum Dot Solar Cells. Semiconductor nanocrystals as light harvesters. *Journal of Physical Chemistry C* **2008,** 112 (48), 18737-18753.
8. Algar, W. R.; Susumu, K.; Delehanty, J. B.; Medintz, I. L., Semiconductor quantum dots in bioanalysis: Crossing the valley of death. *Analytical Chemistry* **2011,** 83 (23), 8826-8837.
9. Nozik, A. J.; Beard, M. C.; Luther, J. M.; Law, M.; Ellingson, R. J.; Johnson, J. C., Semiconductor quantum dots and quantum dot arrays and applications of multiple exciton generation to third-generation photovoltaic solar cells. *Chemical Reviews* **2010,** 110 (11), 6873-6890.
10. Konstantatos, G.; Sargent, E. H., Nanostructured materials for photon detection. *Nature Nanotechnology* **2010,** 5 (6), 391-400.
11. Labrador-Páez, L.; Ximendes, E. C.; Rodríguez-Sevilla, P.; Ortgies, D. H.; Rocha, U.; Jacinto, C.; Martín Rodríguez, E.; Haro-González, P.; Jaque, D., Core-shell rare-earth-doped nanostructures in biomedicine. *Nanoscale* **2018,** 10 (27), 12935-12956.
12. Kwon, S. G.; Hyeon, T., Colloidal chemical synthesis and formation kinetics of uniformly sized nanocrystals of metals, oxides, and chalcogenides. *Accounts of Chemical Research* **2008,** 41 (12), 1696-1709.
13. Grzelczak, M.; Pérez-Juste, J.; Mulvaney, P.; Liz-Marzán, L. M., Shape control in gold nanoparticle synthesis. *Chemical Society Reviews* **2008,** 37 (9), 1783-1791.
14. Jun, Y.; Choi, J.; Cheon, J., Shape control of semiconductor and metal oxide nanocrystals through nonhydrolytic colloidal routes. *Angewandte Chemie International Edition* **2006,** 45 (21), 3414-3439.
15. Park, J.; Joo, J.; Kwon, S. G.; Jang, Y.; Hyeon, T., Synthesis of monodisperse spherical nanocrystals. *Angewandte Chemie International Edition* **2007,** 46 (25), 4630-4660.
16. Xia, Y.; Gilroy, K. D.; Peng, H. C.; Xia, X., Seed-mediated growth of colloidal metal nanocrystals. *Angewandte Chemie International Edition* **2017,** 56 (1), 60-95.
17. Petroski, J. M.; Wang, Z. L.; Green, T. C.; El-Sayed, M. A., Kinetically controlled growth and shape formation mechanism of platinum nanoparticles. *Journal of Physical Chemistry B* **1998,** 102 (18), 3316-3320.
18. Lee, E. J. H.; Ribeiro, C.; Longo, E.; Leite, E. R., Oriented attachment: An effective Mechanism in the formation of anisotropic nanocrystals. *Journal of Physical Chemistry B* **2005,** 109 (44), 20842-20846.
19. Gao, J.; Bender, C. M.; Murphy, C. J., Dependence of the gold nanorod aspect ratio on the nature of the directing surfactant in aqueous solution. *Langmuir* **2003,** 19 (21), 9065-9070.

20. van der Stam, W.; Bladt, E.; Rabouw, F. T.; Bals, S.; Donega, C. d. M., Near-infrared emitting $CuInSe_2/CuInS_2$ dot core/rod shell heteronanorods by sequential cation exchange. *ACS Nano* **2015,** 9 (11), 11430-11438.
21. Li, H.; Zanella, M.; Genovese, A.; Povia, M.; Falqui, A.; Giannini, C.; Manna, L., Sequential cation exchange in nanocrystals: Preservation of crystal phase and formation of metastable phases. *Nano Letters* **2011,** 11 (11), 4964-4970.
22. Guria, A. K.; Pradhan, N., Doped or Not Doped: Ionic impurities for influencing the phase and growth of semiconductor nanocrystals. *Chemistry of Materials* **2016,** 28 (15), 5224-5237.
23. Gai, S.; Li, C.; Yang, P.; Lin, J., Recent progress in rare earth micro/nanocrystals: Soft chemical synthesis, luminescent properties, and biomedical applications. *Chemical Reviews* **2014,** 114 (4), 2343-2389.
24. Moeller, T., The Lanthanides. In *The Chemistry of the Lanthanides*,Ed. Pergamon: 1973; pp 1-101.
25. Sarkar, D.; Ganguli, S.; Samanta, T.; Mahalingam, V., Design of lanthanide-doped colloidal nanocrystals: Applications as phosphors, sensors, and photocatalysts. *Langmuir* **2019,** 35 (19), 6211-6230.
26. Paik, T.; Gordon, T. R.; Prantner, A. M.; Yun, H.; Murray, C. B., Designing tripodal and triangular gadolinium oxide nanoplates and self-assembled nanofibrils as potential multimodal bioimaging probes. *ACS Nano* **2013,** 7 (3), 2850-2859.
27. Wang, D.; Kang, Y.; Ye, X.; Murray, C. B., Mineralizer-assisted shape-control of rare earth oxide nanoplates. *Chemistry of Materials* **2014,** 26 (22), 6328-6332.
28. Si, R.; Zhang, Y. W.; Zhou, H. P.; Sun, L. D.; Yan, C. H., Controlled-synthesis, self-assembly behavior, and surface-dependent optical properties of high-quality rare-earth oxide nanocrystals. *Chemistry of Materials* **2007,** 19 (1), 18-27.
29. Chen, D.; Huang, P.; Yu, Y.; Huang, F.; Yang, A.; Wang, Y., Dopant-induced phase transition: a new strategy of synthesizing hexagonal upconversion $NaYF_4$ at low temperature. *Chemical Communications* **2011,** 47 (20), 5801-5803.
30. Tian, G.; Gu, Z.; Zhou, L.; Yin, W.; Liu, X.; Yan, L.; Jin, S.; Ren, W.; Xing, G.; Li, S.; Zhao, Y., Mn^{2+} Dopant-controlled synthesis of $NaYF_4$:Yb/Er upconversion nanoparticles for in vivo imaging and drug delivery. *Advanced Materials* **2012,** 24 (9), 1226-1231.
31. Chen, X.; Peng, D.; Wang, F., Tuning $NaYF_4$ nanoparticles through alkaline earth doping. *Nanomaterials* **2013,** 3 (4), 583-591.
32. Zhao, C.; Kong, X.; Liu, X.; Tu, L.; Wu, F.; Zhang, Y.; Liu, K.; Zeng, Q.; Zhang, H., Li^+ ion doping: an approach for improving the crystallinity and upconversion emissions of $NaYF_4$:Yb^{3+},Tm^{3+} nanoparticles. *Nanoscale* **2013,** 5 (17), 8084-8089.
33. Yin, D.; Wang, C.; Ouyang, J.; Song, K.; Liu, B.; Cao, X.; Zhang, L.; Han, Y.; Long, X.; Wu, M., Enhancing upconversion luminescence of $NaYF_4$:Yb/Er nanocrystals by Mo^{3+} doping and their application in bioimaging. *Dalton Transactions* **2014,** 43 (31), 12037-12043.
34. Ramasamy, P.; Chandra, P.; Rhee, S. W.; Kim, J., Enhanced upconversion luminescence in $NaGdF_4$:Yb,Er nanocrystals by Fe^{3+} doping and their application in bioimaging. *Nanoscale* **2013,** 5 (18), 8711-8717.
35. Fu, Z.; Cui, X.; Cui, S.; Qi, X.; Zhou, S.; Zhang, S.; Jeong, J. H., Uniform Eu^{3+}-doped YF_3 microcrystals: inorganic salt-controlled synthesis and their luminescent properties. *CrystEngComm* **2012,** *14* (11), 3915-3922.
36. Wawrzynczyk, D.; Samoć, M.; Nyk, M., Controlled synthesis of luminescent Gd_2O_3:Eu^{3+} nanoparticles by alkali ion doping. *CrystEngComm* **2015,** 17 (9), 1997-2003.
37. Liu, Y.; Li, Y.; Jeong, S.; Wang, Y.; Chen, J.; Ye, X., Colloidal Synthesis of Nanohelices via Bilayer Lattice Misfit. *Journal of the American Chemical Society* **2020,** 142 (29), 12777-12783.
38. Jeong, J.; Kim, N.; Kim, M. G.; Kim, W., Generic synthetic route to monodisperse sub-10 nm lanthanide oxide nanodisks: A modified digestive ripening process. *Chemistry of Materials* **2016,** 28 (1), 172-179.
39. Si, R.; Zhang, Y. W.; You, L. P.; Yan, C. H., Rare-Earth Oxide Nanopolyhedra, Nanoplates, and Nanodisks. *Angewandte Chemie International Edition* **2005,** 44 (21), 3256-3260.
40. Schmechel, R.; Kennedy, M.; Seggern, H.; Winkler, H.; Kolbe, M.; Fischer, R. A.; Xaomao, L.; Benker, A.; Winterer, M.; Hahn, H., Luminescence properties of nanocrystalline Y_2O_3:Eu^{3+} in different host materials. *Journal of Applied Physics* **2001,** 89 (3), 1679-1686.
41. Dhanaraj, J.; Jagannathan, R.; Kutty, T. R. N.; Lu, C. H., Photoluminescence characteristics of Y_2O_3:Eu^{3+} nanophosphors prepared using sol-gel thermolysis. *Journal of Physical Chemistry B* **2001,** 105 (45), 11098-11105.
42. Kim, S.; Lim, Y. T.; Soltesz, E. G.; De Grand, A. M.; Lee, J.; Nakayama, A.; Parker, J. A.; Mihaljevic, T.; Laurence, R. G.; Dor, D. M.; Cohn, L. H.; Bawendi, M. G.; Frangioni, J. V., Near-infrared fluorescent type II quantum dots for sentinel lymph node mapping. *Nature Biotechnology* **2004,** 22 (1), 93-97.
43. Yang, H. S.; Feofilov, S. P.; Williams, D. K.; Milora, J. C.; Tissue, B. M.; Meltzer, R. S.; Dennis, W. M., One phonon relaxation processes in Y_2O_3:Eu^{3+} nanocrystals. *Physica B: Condensed Matter* **1999,** 263-264, 476-478.
44. Yang, H. S.; Hong, K. S.; Feofilov, S. P.; Tissue, B. M.; Meltzer, R. S.; Dennis, W. M., Electron-phonon interaction in rare earth doped nanocrystals. *Journal of Luminescence* **1999,** 83-84, 139-145.
45. Wakefield, G.; Holland, E.; Dobson, P. J.; Hutchison, J. L., Luminescence Properties of Nanocrystalline Y_2O_3:Eu. *Advanced Materials* **2001,** 13 (20), 1557-1560.

46. Granqvist, C. G.; Buhrman, R. A., Ultrafine metal particles. *Journal of Applied Physics* **1976,** *47* (5), 2200-2219.
47. Söderlund, J.; Kiss, L. B.; Niklasson, G. A.; Granqvist, C. G., Lognormal size distributions in particle growth processes without coagulation. *Physical Review Letters* **1998,** 80 (11), 2386-2388.
48. Yang, H.; Lee, H.; Holloway, P. H., Anisotropic growth of luminescent Eu^{3+}-or Er^{3+}-doped Gd_2O_3 nanocrystals. *Nanotechnology* **2005,** 16 (12), 2794-2798.
49. Kwon, S. G.; Hyeon, T., Formation mechanisms of uniform nanocrystals via hot-injection and heat-up methods. *Small* **2011,** 7 (19), 2685-2702.
50. Ali, Z.; Waheed, H.; Kazi, A. G.; Hayat, A.; Ahmad, M., Chapter 16-Duckweed: An efficient hyperaccumulator of heavy metals in water bodies. In *Plant Metal Interaction*, Ahmad, P., Ed. Elsevier: 2016; pp 411-429.
51. Leyssens, L.; Vinck, B.; Van Der Straeten, C.; Wuyts, F.; Maes, L., Cobalt toxicity in humans-A review of the potential sources and systemic health effects. *Toxicology* **2017,** 387, 43-56.
52. den Engelsen, D.; Fern, G. R.; Ireland, T. G.; Hudry, D.; Abeykoon, A. M. M.; Nykypanchuk, D.; Dickerson, J. H.; Silver, J., Ultrathin Y_2O_3:Eu^{3+} nanodiscs: spectroscopic investigations and evidence for reduced concentration quenching. *Nanotechnology* **2018,** 29 (45), 455703.
53. Shannon, R. D., Revised effective ionic radii and systematic studies of interatomic distances in halides and chalcogenides. *Acta Crystallographica Section A* **1976,** 32 (5), 751-767.
54. Hudry, D.; Abeykoon, A. M. M.; Hoy, J.; Sfeir, M. Y.; Stach, E. A.; Dickerson, J. H., Ultrathin europium oxide nanoplatelets: "Hidden" parameters and controlled synthesis, unusual crystal structure, and photoluminescence Properties. *Chemistry of Materials* **2015,** 27 (3), 965-974.
55. den Engelsen, D.; de Koning, B., Ellipsometric study of organic monolayers. Part 1. Condensed monolayers. *Journal of the Chemical Society, Faraday Transactions 1: Physical Chemistry in Condensed Phases* **1974,** 70 (0), 1603-1614.
56. Yin, Y.; Alivisatos, A. P., Colloidal nanocrystal synthesis and the organic-inorganic interface. *Nature* **2005,** 437 (7059), 664-670.
57. Ahrenstorf, K.; Heller, H.; Kornowski, A.; Broekaert, J. A. C.; Weller, H., Nucleation and growth mechanism of Ni_xPt_{1-x} nanoparticles. *Advanced Functional Materials* **2008,** 18 (23), 3850-3856.
58. Zhang, L.; He, R.; Gu, H. C., Oleic acid coating on the monodisperse magnetite nanoparticles. *Applied Surface Science* **2006,** 253 (5), 2611-2617.
59. Perez De Berti, I. O.; Cagnoli, M. V.; Pecchi, G.; Alessandrini, J. L.; Stewart, S. J.; Bengoa, J. F.; Marchetti, S. G., Alternative low-cost approach to the synthesis of magnetic iron oxide nanoparticles by thermal decomposition of organic precursors. *Nanotechnology* **2013,** 24 (17), 175601-175613.
60. Klokkenburg, M.; Hilhorst, J.; Erné, B. H., Surface analysis of magnetite nanoparticles in cyclohexane solutions of oleic acid and oleylamine. *Vibrational Spectroscopy* **2007,** 43 (1), 243-248.
61. Deacon, G. B.; Phillips, R. J., Relationships between the carbon-oxygen stretching frequencies of carboxylato complexes and the type of carboxylate coordination. *Coordination Chemistry Reviews* **1980,** 33 (3), 227-250.
62. He, J.; Kanjanaboos, P.; Frazer, N. L.; Weis, A.; Lin, X. M.; Jaeger, H. M., Fabrication and Mechanical Properties of Large-Scale Freestanding Nanoparticle Membranes. *Small* **2010,** 6 (13), 1449-1456.
63. Smolensky, E. D.; Park, H. Y. E.; Berquó, T. S.; Pierre, V. C., Surface functionalization of magnetic iron oxide nanoparticles for MRI applications-effect of anchoring group and ligand exchange protocol. *Contrast Media and Molecular Imaging* **2011,** 6 (4), 189-199.
64. Harris, R. A.; Shumbula, P. M.; van der Walt, H., Analysis of the interaction of surfactants oleic acid and oleylamine with iron oxide nanoparticles through molecular mechanics modeling. *Langmuir* **2015,** 31 (13), 3934-3943.
65. Ji, X.; Copenhaver, D.; Sichmeller, C.; Peng, X., Ligand bonding and dynamics on colloidal nanocrystals at room temperature: The case of alkylamines on CdSe nanocrystals. *Journal of the American Chemical Society* **2008,** 130 (17), 5726-5735.
66. Hostetler, M. J.; Wingate, J. E.; Zhong, C. J.; Harris, J. E.; Vachet, R. W.; Clark, M. R.; Londono, J. D.; Green, S. J.; Stokes, J. J.; Wignall, G. D.; Glish, G. L.; Porter, M. D.; Evans, N. D.; Murray, R. W., Alkanethiolate gold cluster molecules with core diameters from 1.5 to 5.2 nm: Core and monolayer properties as a function of core size. *Langmuir* **1998,** 14 (1), 17-30.
67. Hyeon, T., Chemical synthesis of magnetic nanoparticles. *Chemical Communications* **2003**, 8 , 927-934.
68. Shimpi, J. R.; Sidhaye, D. S.; Prasad, B. L. V., Digestive ripening: A fine chemical machining process on the nanoscale. *Langmuir* **2017,** 33 (38), 9491-9507.
69. Li, Y.; Liu, J.; Wang, Y.; Wang, Z. L., Preparation of monodispersed Fe-Mo nanoparticles as the catalyst for CVD synthesis of carbon nanotubes. *Chemistry of Materials* **2001,** 13 (3), 1008-1014.

Supporting Information

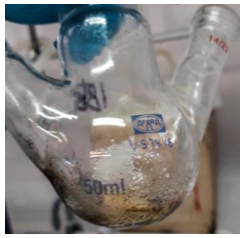

Figure S1. KNO_3 as X agent non-reacting during the thermolysis reaction.

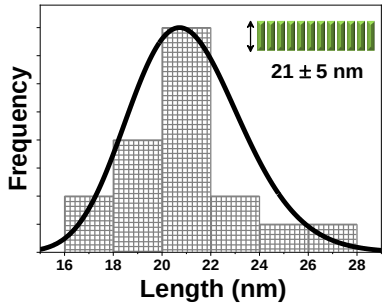

Figure S2. Lognormal length distribution of the nanodiscs produced via thermolysis reaction using NaCl as X agent.

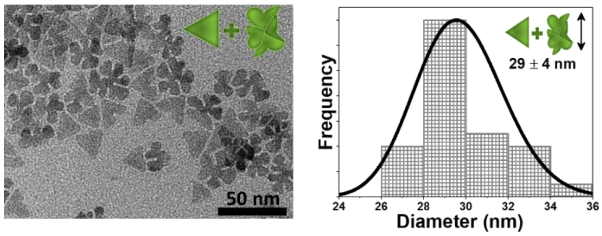

Figure S3. TEM image and lognormal size distribution of Y_2O_3 nanocrystals synthesized via the thermolysis methodology during 1 h reaction time.

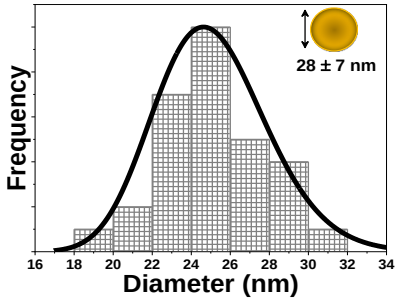

Figure S4. Lognormal size distribution of the diameter of only nanodiscs synthesized in the presence of KCl as X agent. The drawing depicts the shape of the nanocrystals, whereas the arrow stands for the parameter taken into account to determine their sizes.

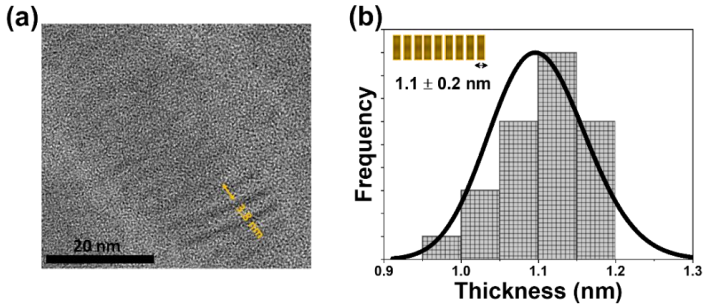

Figure S5. High resolution TEM image of self-assembled Y_2O_3 nanodiscs synthesized via thermolysis reaction assisted by digestive ripening process in the presence of NaCl as X agent.

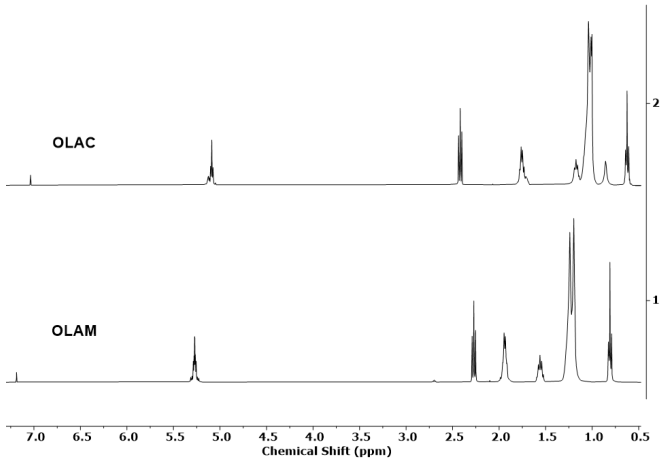

Figure S6. ^{1}H NMR spectrum of oleic acid (OLAC) and oleylamine (OLAM) used during the thermolysis and digestive ripening synthesis of rare earth colloidal nanocrystals.

Paper VI

Evaluating the performance of Ho^{3+}, Tm^{3+} doped Y_2O_3 nanotriangles, nanohearts and self-assembled nanodiscs as luminescent nanothermometers and photothermal agents as a function of the morphology

Albenc Nexha, Joan J. Carvajal,* Maria Cinta Pujol, Francesc Díaz, Magdalena Aguiló
Universitat Rovira i Virgili, Departament Química Física i Inorgànica,
Física i Cristal·lografia de Materials i Nanomaterials (FiCMA-FiCNA)-EMaS, Campus Sescelades, E-43007, Tarragona, Spain
**joanjosep.carvajal@urv.cat*

Abstract

Thermal decomposition and digestive ripening synthesis of Ho^{3+} and Tm^{3+} doped yttrium oxide in the shape of nanotriangles (length ~44 nm), nanohearts (length ~53 nm), and self-assembled nanodiscs (diameter ~21 nm and down-to-unit cell thickness), were tested as potential nanothermometers and photothermal conversion agents, operating in the third biological window (III-BW) regime. The generated photoluminescence in these colloidal nanocrystals, after excitation with 808 nm lying in the first biological window (I-BW), includes three bands attributed to the electronic transitions: $^3H_4 \rightarrow {}^3F_4$ (1.5 µm) and $^3F_4 \rightarrow {}^3H_6$ (1.85 µm, composed by two Stark sublevels with emissions lying at 1.8 µm and 1.96 µm) of Tm^{3+}, and $^5I_7 \rightarrow {}^5I_8$ (2.1 µm) of Ho^{3+}.

The performance of these nanocrystals as nanothermometers, investigated at the temperature range from 313 K-373 K, was evaluated by considering the intensity ratios between non-thermally coupled levels (1.5 µm/1.85 µm, 1.5 µm/2.1 µm and 1.85 µm/2.1 µm) and between thermally coupled levels (1.8 µm/1.96 µm). The performance based on the fluorescence intensity ratio of the thermally coupled levels was influenced the most from the change of temperature and among these nanocrystals, the self-assembled nanodiscs displayed the highest thermal sensing properties for a value of the relative thermal sensitivity and temperature resolution of 0.92% K^{-1} and 0.54 K at the lowest temperature under investigation. This value represents, up to day, the best thermometric performance for materials operating in the III-BW regime. From the results, a proportional relationship between the size of the nanocrystals and their performance as nanothermometers is concluded: smaller the size, higher the performance.

Concerning the applicability of these nanocrystals as photothermal agents, the best light-to-heat conversion ability is assigned to the nanotriangles for a value of 15 ± 2%, independent of the power of the 808 nm laser applied. These shape of nanocrystals exhibit more effective non-radiative mechanisms than the nanohearts and self-assembled nanodiscs. This photothermal conversion efficiency is comparable with other lanthanide doped materials, nevertheless lower than that of metallic plasmonic nanoparticles.

1. Introduction

The synthesis of nanocrystals with well-defined shapes is of paramount importance, as the size, shape, surface area and crystal structure, radically influences the chemical, physical and optical

properties of the nanocrystals.[1-3] Development of nanosized materials with pretailored properties and functionalities have boosted their application in several research fields such as electronics,[4] optics,[5-7] catalysis,[8-11] magnetics,[12] and nanomedicine.[13] In the field of nanomedicine, these materials offer new possibilities on imaging, diagnosis and therapy.[10] Typical examples of the applications of the nanomaterials in nanomedicine involve the treatment of brain tumors,[14] cardiovascular diagnosis,[14-16] selective drug delivery,[14, 15] and deep-tissue optical imaging,[14, 17] that can be complemented with temperature reading within biological tissue when luminescent nanothermometers are used.[18]

Luminescent nanothermometers are a class of non-contact thermometers, constituted by luminescent nanomaterials whose luminescent properties are temperature dependent. These nanothermometers provide fast and accurate temperature reading at the nanoscale and have, nowadays, emerged as an effective replacement for conventional contact thermometers.[18] Although several types of luminescent nanothermometers have been reported (polymers[19-21], organic dyes[22, 23], quantum dots[24, 25], and metallic nanoparticles[26-28], among others), lanthanide doped nanothermometers have attracted significant interest attributed to their outstanding luminescent properties covering an important part of the electromagnetic spectrum, their photochemical stability and their low or scarce toxicity.[29]

Concerning their luminescent properties, when excited by a light source, the lanthanide ion can transform the absorbed light into luminescence and heat due to the radiative and non-radiative decay processes, generated within their electronic levels.[30] These two processes make that lanthanide doped luminescent nanothermometers can be employed, simultaneously, as thermal probes and photothermal conversion agents.[31] However, despite the enormous research devoted to lanthanide doped luminescent nanothermometers, a lot of challenges are still to be faced. One of these challenges addresses the understanding of the effect of different shapes of nanosized materials in the thermal sensing and photothermal conversion properties of lanthanide based luminescent nanothermometers.

In this paper, we investigate the effect of the shape of holmium (Ho^{3+}) and thulium (Tm^{3+}) doped yttrium oxide (Y_2O_3) colloidal nanocrystals in their thermal sensing and light-to-heat conversion efficiency. Ho^{3+} and Tm^{3+} were chosen as dopant ions due to the presence of radiative (responsible for luminescence, thus, thermal reading) and non-radiative (responsible for heat generation) decay processes, after absorption of light in the first biological window (I-BW), and due to their emissions in the third biological window (III-BW) or short-wavelength infrared region (SWIR).[32] In this last spectral region, light transmits more effectively (up to three times) through specific biological tissues like those containing melanin or oxygenated blood, achieving higher light penetration depths and thus, deeper temperature readings.[33] Y_2O_3, with a broad transparency range (0.2-8 μm), a large band gap (5.6 eV), a high thermal conductivity, a high refractive index, and a low phonon energy, is an attractive choice as host material for Ho^{3+} and Tm^{3+} for luminescent applications.[34, 35] Nanotriangles, nanohearts and self-assembled nanodiscs of Ho^{3+}, Tm^{3+} doped Y_2O_3 nanoparticles, with an average size below 50 nm, were synthesized by using thermolysis and digestive ripening in the presence of additives to control their shapes. For temperature sensing, we analyzed the emission bands at 1.5 μm and 1.85 μm of Tm^{3+} and the 2.1 μm emission band of Ho^{3+}, after excitation at 808 nm, and we evaluated their photothermal conversion at this particular excitation wavelength by using the integrated sphere method.[36]

2. Experiments

2.1. Materials

Yttrium acetate hydrate ($Y(Ac)_3 \cdot H_2O$, 99.99%) and oleylamine (OLAM, > 70%) were purchased from Sigma Aldrich. Thulium acetate hydrate ($Tm(Ac)_3 \cdot H_2O$, 99.99%) was purchased from Apollo Scientific. Holmium acetate hydrate ($Ho(Ac)_3 \cdot H_2O$, 99.99%), oleic acid (OLAC, 90%), 1-octadecene (ODE, 90%), n-hexane (99%) and sodium nitrate ($NaNO_3$, 99%) were purchased from Alfa Aesar. Sodium chloride (NaCl) and ethanol (EtOH) were purchased from Merck and VWR, respectively.

2.2. Synthesis of Ho, Tm doped Y_2O_3

3 mol% Ho^{3+} and 5 mol% Tm^{3+} doped Y_2O_3 colloidal nanocrystals in the shape of nanotriangles and nanohearts were synthesized by a thermal decomposition method reported from Wang *et al.* with modification,[37] whereas self-assembled nanodiscs were synthesized using a digestive ripening mechanisms as previously reported.[38] The doping ratio chosen for better comparison with another work, where these ions were embedded in another type of host and generated the highest intensity of the emissions in the III-BW.[31]

In a typical thermolysis synthesis of 3 mol% Ho^{3+} and 5 mol%Tm^{3+} doped Y_2O_3 colloidal nanotriangles, 2.3 mmol of $Y(Ac)_3{\cdot}H_2O$, 0.075 mmol of $Ho(Ac)_3{\cdot}H_2O$, 0.125 mmol of $Tm(Ac)_3{\cdot}H_2O$ and 4 mmol of $NaNO_3$, were dissolved into a solution containing 25 mmol of OLAC, 25 mmol of OLAM and 15 mmol of ODE. The reaction mixture was heated under vacuum at 413 K for 30 min. After switching to nitrogen flow, the reaction temperature was increased to 583 K and held at this temperature for 30 min, prior to cooling down naturally at room temperature. To extract the desired nanocrystals, a purification cycle was applied by adding an excess of EtOH in the cooled solution, followed by centrifugation at 5000 rpm for 10 minutes and redispersion in n-hexane. This purification cycle was repeated three times. The final product of the reaction was stored as powder by evaporating the solvent.

The synthesis of 3 mol% Ho^{3+} and 5 mol% Tm^{3+} doped Y_2O_3 colloidal nanohearts was the same as that followed for the nanotriangles, except that the reaction time was extended to 2 h.

In a typical digestive ripening synthesis of self-assembled 3 mol% Ho^{3+} and 5 mol% Tm^{3+} doped Y_2O_3 colloidal nanodiscs , 0.184 mmol of $Y(Ac)_3{\cdot}H_2O$, 0.006 mmol of $Ho(Ac)_3{\cdot}H_2O$, 0.01 mmol of $Tm(Ac)_3{\cdot}H_2O$ and 0.1 mmol of NaCl were mixed and dissolved in 45 mmol of OLAM under nitrogen atmosphere. The solution was heated at 553 K using a ramp of 15 K/min. Once the temperature reached 553 K, 15 mmol of OLAC were swiftly injected into the reaction flask. The solution temperature was held at 553 K for 1 h. After the reaction, the solution was naturally cooled down to room temperature. The product of the reaction was extracted by adding an excess of ethanol to the solution, followed by centrifugation at 4000 rpm for 10 min, after which the supernatant was discarded and the precipitate was redissolved in n-hexane. This separation step was repeated three times. The final product of the reaction was stored as powder by evaporating the solvent.

2.3. Characterization

Powder X-ray diffraction (XRD) measurements were made using a Siemens D5000 diffractometer (with Bragg-Brentano parafocusing geometry and a vertical θ-θ goniometer) fitted with a curved graphite diffracted-beam monochromator, incident and diffracted-beam Soller slits, a 0.06º receiving slit, and scintillation counter as detector. The angular 2θ diffraction range was set between 5 and 70º. The data were collected with an angular step of 0.05º at 3s per step with sample rotation to increase the statistics of the signal collected. Cu K_α radiation was obtained from a Copper X-ray tube operated at 40 kV and 30 mA.

For the morphological characterization, transmission electron microscopy (TEM) images were recorded using a JEOL JEM-1011 electron microscope operating at an accelerating voltage of 100 kV. For the preparation of the TEM grids, the nanocrystals were dispersed in n-hexane. Around 7 µL of the diluted n-hexane dispersion were placed on the surface of a Copper grid covered by a holey Carbon film (HD200 Copper Formvar/Carbon).

Fourier Transform Infrared (FT-IR) spectra were recorded in the range of 400-4000 cm^{-1} in a FT-IR IluminatIR II, Smith spectrophotometer, to investigate the presence of different functional groups in the samples.

For the photoluminescence analysis of the nanocrystals, the emission spectra were recorded in a Yokogawa AQ6375 optical spectrum analyzer in the range from 1350 nm to 2200 nm, with a resolution of 2 nm and an integration time of 20 s. The nanoparticles were excited by a 808 nm

fiber-coupled diode laser (Thorlabs) with a power of 800 mW and the beam was focused on the sample using a 20× microscope objective (N.A=0.4) bringing a spot size of ~10^{-6} m in the sample. This would bring an excitation power density of ~400 W/cm^2, being below the limit of the level of the power density used in biomedical applications.[39, 40] The scattered excitation radiation was eliminated by using a 850 nm longpass dichroic filter (Thorlabs). For the analysis of the dependence of the photoluminescence with temperature, the same methodology was used, except that the nanocrystals were introduced inside a heating stage (Linkam, THMS 600) equipped with a boron disk for improved temperature distribution, and a thermocouple for the external reading of temperature, that provided an accuracy of 0.1 K.

The photothermal conversion efficiency was investigated by applying the method of the integrating sphere.[36] A glass cuvette containing 3 mol% Ho^{3+} and 5 mol% Tm^{3+} doped Y_2O_3 colloidal nanocrystals dispersed in n-hexane with a concentration of around 1 g/L was placed inside the integrating sphere, perpendicular to the laser irradiation provided by the 808 nm fiber-coupled diode laser. The sample was illuminated at different excitation powers. The laser from the fiber tip was collimated to a spot size of 5 mm in diameter on the sample. A baffle was introduced in the integrating sphere, between the sample and the detector, in order to prevent the direct reflections from the sample to the detector. The generated signals, such as the scattered, reflected, transmitted light and part of the light that is absorbed and converted into another light wavelength, were collected by an Ophir Nova II powermeter.[36] In addition, this integrated sphere, was used to compare the intensity of the emission generated by the nanocrystals, applying the same fiber and optic spectrometer, as described in the photoluminescence measurements.

3. Results and Discussion

3.1. Morphological and structural characterization of Ho^{3+}, Tm^{3+} doped Y_2O_3 colloidal nanocrystals

3 mol% Ho^{3+}, 5 mol% Tm^{3+} doped Y_2O_3 colloidal nanocrystals with different sizes and shapes, were synthesized using thermolysis and digestive ripening reactions in the presence of additives. The shape and size of the nanocrystals obtained via the thermolysis reaction was examined by TEM. From the thermolysis reactions, branched nanotriangles and nanohearts were obtained using $NaNO_3$ as additive.

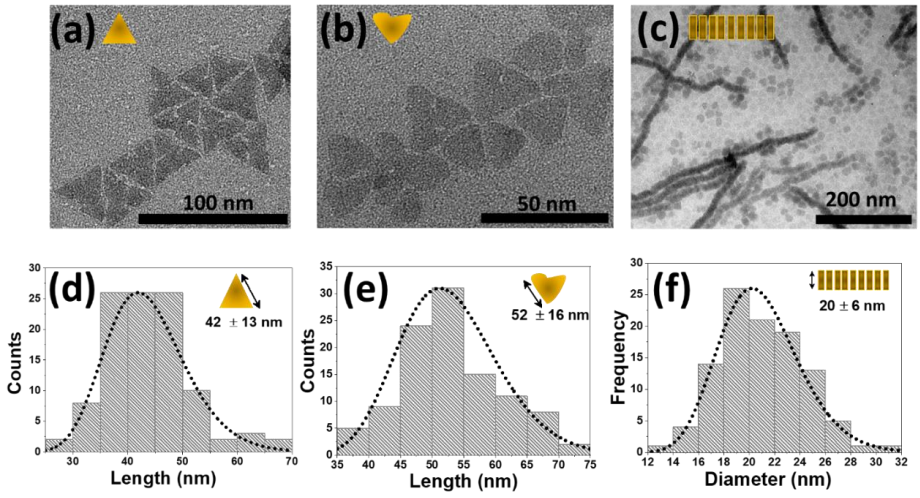

Figure 1. TEM images of the 3 mol% Ho^{3+}, 5 mol% Tm^{3+} doped Y_2O_3 colloidal nanocrystals obtained by thermolysis and digestive ripening in the presence of $NaNO_3$ and NaCl, respectively. (a) branched nanotriangles, (b) nanohearts and (c) self-assembled nanodiscs. The insets in the figures depict the shape of the colloidal nanocrystals obtained. Log-normal size distribution of the nanocrystals obtained: (d)

nanotriangles, (e) nanohearts, and (f) self-assembled nanodiscs. The sketch within the images stands for the shape of the nanocrystals. The arrows aside the sketchs of the nanocrystals stands for the parameters measured to determine their size distribution.

For a reaction time of 0.5 h, branched nanotriangles (see Figure 1 (a)) with an average length of 42 ± 13 nm (see Figure 1 (d)) were obtained. By increasing the reaction time to 2 h, the branched nanotriangles evolved to nanohearts (see Figure 1 (b)) with an average length of 52 ± 16 nm (see Figure 1 (e)). Compared to the corresponding undoped nanocrystals,[38] there is a tendency of increase of the size of these colloidal particles, which clearly arises due to the disturbance of the lattice constant from the dopants.[41-47]

From the digestive ripening reaction, 3 mol% Ho^{3+}, 5 mol% Tm^{3+} doped Y_2O_3 self-assembled nanodiscs (see Figure 1 (c)) were obtained when using NaCl as additive. The self-assembled nanodiscs are characterized with a thickness of the order of a single unit cell (1 ± 0.2 nm, determined from the high resolution TEM image in Figure S1 at Supporting Information) and an average length of 20 ± 6 nm (see Figure 1 (f)). The dimensions of all nanocrystals were determined after processing the images of over 100 nanocrystals with the Image J software. The average sizes have been obtained by fitting a lognormal distribution to the histogram of the Figure 1 (d)-(f). Nanocrystals formed by nucleation, condensation, and particle growth are expected to yield lognormal size distributions.[48, 49]

The crystal structure of the 3 mol% Ho^{3+}, 5 mol% Tm^{3+} doped Y_2O_3 colloidal nanocrystals was examined by X-ray powder diffraction. The nanocrystals obtained crystallized in the cubic system with $Ia\bar{3}$ spatial group, as compared to the reference pattern JCPDS file 25-1200 shown in Figure 2. A general trend observed in the XRD patterns is the significant broadening of the peaks attributed to the small size of the nanocrystals, as observed previously from other authors when synthesizing small sized rare earth colloidal nanocrystals and coexistence with other sharp peaks.[37, 50, 51] These broad peaks are low-angle shifted in comparison with the bulk reference pattern.[52] This fact could be related to an expansion of the crystallographic net due to the strong 1D confinement in the crystallographic planes responsible of these broad diffraction peaks.[52] Taking into account our previous observations,[38] the absence or presence of the {400} peak, can be an indication of the crystallographic orientation of the morphologies observed. When the obtained morphology are the self-assembled nanodisk, the {400} peak is absent (see Figure 2). On the contrary, when the obtained morphologies are governed by a ternary rotation symmetry, the {400} peak appears in the diffraction spectra. Our hypothesis is that the two different crystallographic orientations are a 1D {111} confinement for the nanotriangles and nanoheart shapes, and the {100} for the nanodiscs type.

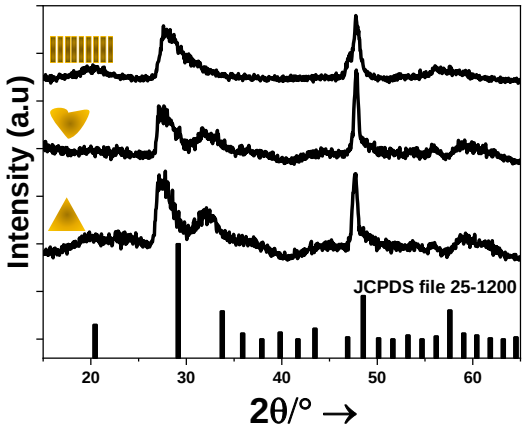

Figure 2. XRD patterns of 3 mol% Ho^{3+}, 5 mol% Tm^{3+} doped Y_2O_3 colloidal nanocrystals synthesized via thermolysis and digestive ripening. The reference pattern of cubic Y_2O_3 (JCPDS file 25-1200) is included for comparison.

3.2. Photoluminescence of Ho^{3+}, Tm^{3+} doped Y_2O_3 colloidal nanocrystals

The emission spectra in the III-BW of 3 mol% Ho^{3+}, 5 mol% Tm^{3+} doped Y_2O_3 colloidal nanocrystals (nanotriangles, nanohearts and self-assembled nanodiscs) was recorded after excitation at 808 nm with a power of excitation of 800 mW. The emission spectra, presented in Figure 3 (a), consist of three emission bands assigned to the: $^3H_4 \rightarrow {}^3F_4$ (1.5 µm) and $^3F_4 \rightarrow {}^3H_6$ (1.85 µm) electronic transitions of Tm^{3+}, and $^5I_7 \rightarrow {}^5I_8$ (2.1 µm) electronic transition of Ho^{3+}.[31, 53]

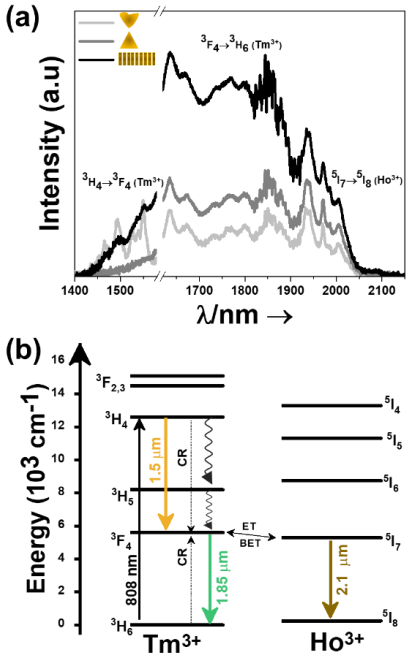

Figure 3. (a) Luminescent emissions in the III-BW recorded at room temperature for the 3 mol% Ho^{3+}, 5 mol% Tm^{3+} doped Y_2O_3 colloidal nanocrystals, excited at 808 nm. Please note that part of the graph from 1580 nm to 1620 nm was removed due to the second harmonic of the 808 nm laser source. (b) Energy level diagram of Ho^{3+} and Tm^{3+} ions in Ho,Tm:Y_2O_3 and the mechanisms of generation of their SWIR emission lines. The red arrow indicate the absorption process excited by the 808 nm laser. The black arrows indicate the three radiative emissions: $^3H_4 \rightarrow {}^3F_4$ (Tm^{3+}), $^3F_4 \rightarrow {}^3H_6$ (Tm^{3+}) and $^5I_7 \rightarrow {}^5I_8$ (Ho^{3+}). Curved arrows indicate non-radiative multiphonon decays processes. Dashed arrows stand for the cross relaxation (CR) process in Tm^{3+} ($^3H_6$,$^3H_4$) ↔ ($^3F_4$,$^3F_4$). The double headed arrow indicates the ET-BET process between Tm^{3+} and Ho^{3+}.

The location of these bands in Ho, Tm:Y_2O_3 materials is misleading. Hence, for Tm^{3+}: Y_2O_3, the location of thulium's bands is related to the type of material. For single crystals, the band at 1.5 µm is either not present,[54] or centered at 1.55 µm,[55] whereas the band at 1.85 µm consists of a broad emission band extending from ~1.6 to above 2 µm, with the maximum intensity located at around 1.95 µm.[55] For nanopowders, the band at 1.5 µm is absent, whereas the band at 1.85 µm has a similar shape than that observed for Tm^{3+}:Y_2O_3 single crystals.[56] For Ho^{3+} doped Y_2O_3 materials, experimental reports about their emissions are not reported. The only data available are related to calculated stimulated emission cross-section, reported for the case of ceramics, with two emission bands, one located at around 1.93-1.94 µm, with a higher intensity, and another broad band with lower intensity centered at around 2.1 µm.[57] Thus, the different Ho^{3+}, Tm^{3+}:Y_2O_3 colloidal nanocrystals reported here, represent the first Y_2O_3 nanoparticles dually doped with Ho^{3+} and Tm^{3+}. In these nanocrystals, the bands of Tm^{3+} are enhanced in intensity (1.5 µm) and changed substantially the shape (1.85 µm) by enhancing the intensity of the peaks lying at short

wavelengths and decreasing the intensity of the peaks located at longer wavelengths. Hence, this band can be considered composed of two Stark sublevels located at 1.8 μm and 1.96 μm. Concerning the band of Ho^{3+} (2.1 μm), is clearly visible, regardless of low intensity. Comparing the intensity of the emissions among these three different colloidal nanocrystals, the self-assembled nanodiscs generate the highest emission compared to that of the nanotriangles and nanohearts. For example, the intensity of the emissions of the self-assembled nanodiscs is approximately 2 fold and 2.5 fold higher compared to that of the nanotriangles and nanohearts, respectively. Although, the reason behind this observation is not evident, we observe a trend on the emission's intensity of these nanostructures: the smaller the size, the higher the emission intensity.

The generation of these emission bands involves the absorption of the 808 nm excitation light from the $^3H_6$ electronic ground state level of Tm^{3+}, promoting the electrons to the $^3H_4$ excited state. The 1.5 μm emission band is produced from the radiative decay of the electrons from the $^3H_4$ excited state to the $^3F_4$ manifold. A further radiative decay to the ground state, give rise to the second thulium emission band at 1.85 μm. Tm^{3+} ions might undergo a cross-relaxation (CR) process into the $^3F_4$ excited state, when one of the ions initially into the upper $^3H_4$ excited state exchange the energy with an electron in the $^3H_6$ ground state. Due to the energy resonance between the $^3F_4$ level of Tm^{3+} and the $^5I_7$ level of Ho^{3+}, energy transfer (ET) and back energy transfer (BET) processes might take place, promoting the electrons of Ho^{3+} to this excited state from its ground state. Then, the electrons of Ho^{3+} relax radiatively to the $^5I_8$ ground state, giving rise to the holmium emission band at 2.1 μm.[31, 53] The detailed mechanism of the generation of the emission bands in the III-BW is depicted in Figure 3 (b).

3.3. Ho, Tm:Y_2O_3 colloidal nanocrystals as luminescent nanothermometers

The synthesized 3 mol% Ho^{3+}, 5 mol% Tm^{3+} doped Y_2O_3 colloidal nanocrystals were tested as luminescent nanothermometers in the III-BW. The temperature dependence of the three emission bands was recorded in the range 313-373 K (see Figure 4 for the self-assembled nanodiscs as an example). With the increase of the temperature, the intensity of the emission decreases. This phenomenon is explained by the thermal activation of the luminescence quenching mechanisms, such as the increase of the non-radiative decay rates.[30]

The performance of different shaped Ho, Tm:Y_2O_3 colloidal nanocrystals as luminescent nanothermometers was determined by taking into account the evolution of four parameters: (i) the integrated intensity ratio (Δ or FIR), (ii) the absolute thermal sensitivity (S_{abs}); (iii) the relative thermal sensitivity (S_{rel}); and (iv) the temperature resolution (δT). The integrated intensity ratio Δ and FIR are used as thermometric parameters to evaluate the dependence of the ratio of two intensities from temperature. The difference between these parameters rely on the fact that Δ relates the intensity ratio of two non-thermally coupled levels, whereas fluorescence intensity ratio FIR is designed to relate the intensity ratio between two thermally coupled levels, i.e, levels arising from the same emitter and an energy difference between the transition in the range from 200-2000 cm^{-1}.[58] For Ho, Tm:Y_2O_3 colloidal nanocrystals, Δ is applied for: (i) 1.45 μm/1.8 μm, (ii) 1.45 μm/1.96 μm and (iii) 1.45 μm/2.1 μm, and FIR for (iv) 1.8 μm/1.96 μm ratios, where the $^3F_4 \rightarrow {}^3H_6$ (centered at 1.85 μm) transition is considered to be composed of two Stark sublevels located at 1.8 μm and 1.96 μm.

Here, in more details, we investigated the evolution of the FIR of the Stark sublevels thermally coupled bands (1.8 μm and 1.96 μm), being this the ratio that is influenced the most by the temperature change (see Figure 5 (a)). The other intensity ratios based on non-thermally coupled levels, have also been investigated, and the results are presented in Figure S1 in the Supporting Information. From the figure, is clearly observed that the highest slope, i.e. highest thermometric performance, is assigned to the thermally coupled levels, instead of the non-thermally coupled ones. These results follow the same trend that we have shown in our previously reported paper for Ho, Tm doped $KLu(WO_4)_2$ nanocrystals.[31]

The temperature dependence of FIR is expressed as:[59, 60]

$$FIR = \frac{I_1}{I_2} = \frac{g_1 \vartheta_1 A_1}{g_2 \vartheta_2 A_2} \exp\left(-\frac{\Delta E}{k_B T}\right) = B \exp\left(-\frac{\Delta E}{k_B T}\right) \qquad (1)$$

where I_1 and I_2 stand for the integrated intensity of the Stark sublevels of the $^3F_4 \rightarrow {}^3H_6$ transitions located at 1.8 μm and 1.96 μm, g_1 and g_2 are the degeneracy of the Stark sublevels, respectively; ϑ_1, ϑ_2, A_1 and A_2 are the frequencies and spontaneous emission rates corresponding to these levels; B is the pre-exponential constant; ΔE is the energy gap between the Stark sublevels in the particular host; k_B is the Boltzmann's constant (k_B=0.695 cm^{-1}) and T is the absolute temperature.

From the graph (see Figure 5 (a)), it can be observed that the change in temperature affects more to the intensity ratio of the nanotriangles and the self-assembled nanodiscs, whereas the nanohearts are almost insensitive. Equation 1 can be transformed into a logarithmic form of:

$$\ln(FIR) = \ln(B) + \left(\frac{\Delta E}{k_B T}\right) = \ln(B) + \left(-\frac{C}{T}\right) \qquad (2)$$

where B and C represent constants determinate from experimental fitting of the dependence of the intensity ratio with the change of temperature. The variation of logarithmic form of FIR in the range of 298 K-373 K obeys to a linear tendency (see Figure 5 (b)). From this fitting, the values of the intercept, the slope and the energy gap for each type of nanocrystals, are calculated and presented in Table 1. Knowing these values, allows us to determine the thermal sensing properties of these nanocrystals.

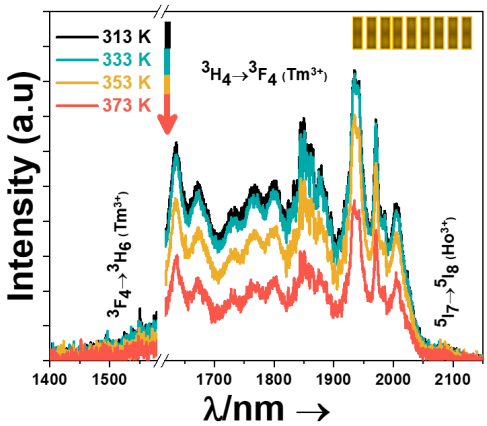

Figure 4. Temperature dependence of the intensity of the emission bands in the III-BW of the 3 mol% Ho^{3+}, 5 mol% Tm^{3+} doped Y_2O_3 colloidal self-assembled nanodiscs, excited at 808 nm. Please note that part of the graph from 1580 nm to 1630 nm was removed due to the second harmonic of the 808 nm laser source.

The thermal sensing properties of Ho,Tm:Y_2O_3 colloidal nanocrystals is evaluated by calculating the value of the absolute thermal sensitivity (S_{abs}), relative thermal sensitivity (S_{rel}) and temperature resolution (δT).

S_{abs}, a term introduced from dos Santos *et al.*[61], related to the sample's characteristics such as the absorption and lifetime and the experimental setup used to record the spectra, is calculated from Equation 3:

$$S_{abs} = \frac{\partial FIR}{\partial T} = FIR \, \frac{\Delta E}{k_B T^2} \qquad (3)$$

The dependence of S_{abs} from the temperature is presented in Figure 5 (c). The nanotriangles show the highest absolute thermal sensitivity with a value of 0.024 K^{-1} at 313 K, which is approximately 10 times higher than that of the nanohearts (S_{abs}=0.0033 K^{-1}) at the same temperature. The self-assembled nanodiscs from their side, exhibit an absolute thermal sensing

comparable with that of the nanotriangles, for a value of 0.021 K^{-1}. Interesting both these materials, display the same variation of these parameter, there is initially a decrease with the increase of the temperature, then an increase reaching a maximum value with that comparable with the maximum value at the initial 313 K (see Figure 5 (c)), demonstrating that these nanocrystals display an almost flat response over the temperature range analyzed, indicating that these nanothermometers (including the nanohearts too) are equally sensitive in this temperature range.

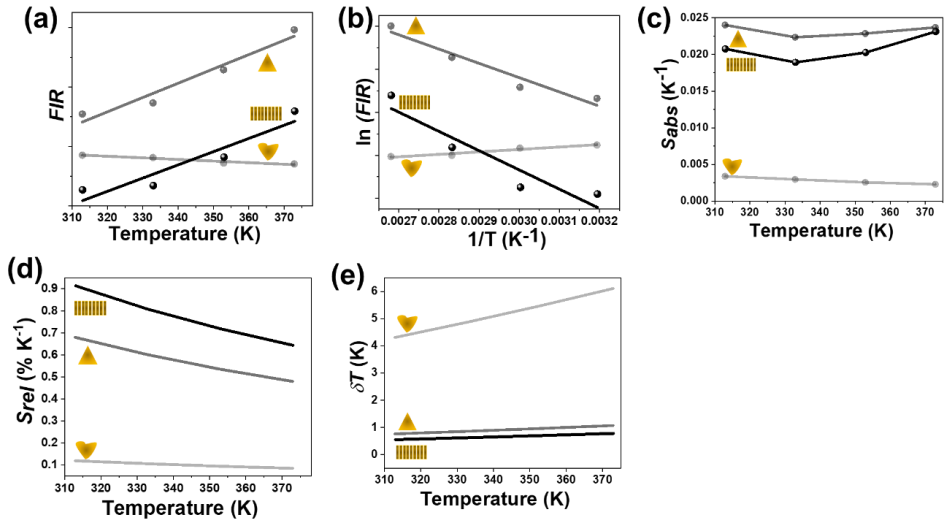

Figure 5. (a) Temperature dependence of the intensity ratio FIR (experimental data and linear fitting according to Equation 1 for the 1.8 μm/1.96 μm intensity ratio calculated for Ho,Tm:Y_2O_3 colloidal nanocrystals with different morphologies. (b) Variation of the logarithmic form of FIR with the inverse of temperature. (c) Absolute thermal sensitivity (S_{abs}), (d) relative thermal sensitivity (S_{rel}), and (e) temperature resolution (δT) for Ho,Tm:Y_2O_3 colloidal nanocrystals with different morphologies.

Brites *et al.* defined the relative thermal sensitivity (S_{rel}) as the maximum change in the intensity ratio for each temperature degree, expressed as:[62]

$$S_{rel} = \frac{1}{FIR}\left|\frac{\partial FIR}{\partial T}\right| x\ 100\% \qquad (4)$$

which is converted to the following expression:

$$S_{rel} = \left|\frac{\Delta E_2 - \Delta E_1}{k_B T^2}\right| x\ 100\% \qquad (5)$$

after substituting the expression of FIR as expressed in Equation 1.

Thus, S_{rel} can be used as a figure of merit to compare the thermal sensing properties of different luminescent nanothermometers, regardless of their nature. The variation of S_{rel} with temperature for Ho, Tm:Y_2O_3 colloidal nanocrystals with different morphologies in the III-BW is provided in Figure 5 (c). From the three different Ho, Tm:Y_2O_3 colloidal nanocrystals, the self-assembled nanodiscs exhibited the maximum relative thermal sensitivity with a value of S_{rel}=0.92% K^{-1}, whereas the nanotriangles had a value of 0.67% K^{-1} and the nanohearts showed the minimum thermal sensitivity with a value of 0.12% K^{-1}, all obtained at the lowest temperature under investigation (313 K). The relative thermal sensitivity was found to be inversely proportional to the change of temperature, for example, it decreases as the temperature increased. In the case of the self-assembled nanodiscs, it decreased from 0.92% K^{-1} at 313 K to 0.64% K^{-1} at 373 K.

In addition to S_{rel}, the temperature resolution (δT) is also applied as a parameter for the evaluation of the thermometric performance of different luminescent nanothermometers.[62] The

temperature resolution is defined as the smallest temperature change that can be resolved in a given measurement and it is estimated according to the following equation:[62]

$$\delta T = \frac{1}{S_{rel}} \frac{\delta \Delta}{\Delta} = \left| \frac{k_B T^2}{\Delta E_2 - \Delta E_1} \right| \frac{\delta \Delta}{\Delta} \quad (6)$$

where $\frac{\delta \Delta}{\Delta}$ is the relative error in the determination of the thermometric parameter. This parameter depends on the acquisition setup used in the experiment with a typical value for conventional detectors of 0.5%.[63] Hence, by applying this value and the calculated value of S_{rel} from Equation 5, the minimum temperature resolution for the self-assembled nanodiscs was determined to be 0.54 K at 313 K. At the same temperature, for the nanotriangles and the nanohearts, the temperature resolution was 0.69 K and 4.3 K, respectively.

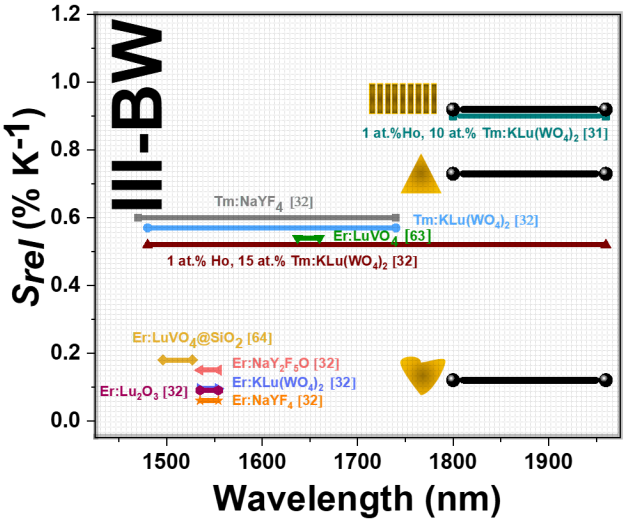

Figure 6: Thermometric performance of the lanthanide doped luminescent nanothermometers operating in the III-BW in terms of relative thermal sensitivity. The numbers in brackets represent the corresponding reference from which the data were extracted: 1 at:% Ho, 10 at.%:$KLu(WO_4)_2$ from 31; Er:Lu_2O_3, Tm and Er:$NaYF_4$, Er:NaY_2F_5 and Er and 1 at.% and 15 at. Tm: $KLu(WO_4)_2$ from 32, Er: $LuVO_4$ from 63; and Er:$LuVO_4$@SiO_2 from 64. The data interval represents the wavelength region used to evaluate their thermal performance.

Table 1 summarizes the thermometric performance of different Ho.Tm:Y_2O_3 colloidal nanocrystals, resolved from the intensity ratio between the thermally coupled levels. Taking into account the thermal sensing data and the characterization of these nanocrystals, it can be concluded that, as the size of the nanocrystals decreases, the thermometric performance is enhanced.

Table 1. Fitting parameters, S_{abs}, S_{rel} and δT of different Ho,Tm:Y_2O_3 colloidal nanocrystals, calculated from the ratio between the thermally coupled levels.

Material	B	C	$\Delta E_2 - \Delta E_1$ (cm^{-1})	R^2	S_{abs} (K^{-1})	S_{rel} (% K^{-1})/313 K	δT (K)
Nanohearts	1.97	114.1	78.9	0.95	0.0033	0.12	4.3
Nanotriangles	5.75	663.9	461.4	0.95	0.024	0.67	0.73
Nanodiscs	36.96	895.02	622.1	0.90	0.021	0.92	0.54

Taking into account the values of S_{rel} and δT for the different shaped Ho, Tm:Y_2O_3 colloidal nanocrystals provided here, now we can compare their thermometric performance with that of

other nanothermometers operating in the III-BW. Figure 6 presents the relative thermal sensing values for a series of lanthanide doped luminescent nanothermometers operating in the III-BW. From the figure, it can be concluded that the self-assembled nanodiscs, display the highest value of relative thermal sensitivity in this spectral region.

3.4. Photothermal conversion efficiency of Ho, Tm:Y_2O_3 colloidal nanocrystals

The ability of materials to convert the absorbed light into heat is defined as the photothermal conversion efficiency. For the determination of this photothermal conversion efficiency (η) of our Ho, Tm:Y_2O_3 colloidal nanocrystals, we used the method of the integrated sphere.[36] Figure 7 (a) shows a simplified scheme of this method. Generally, when a material (as an illustrative example we show in Figure 7 (a), a cuvette filled with 1 g/L Ho, Tm:Y_2O_3 nanotriangles dispersed in cyclohexane) is illuminated by light (with a wavelength of 808 nm in this case), the light can be absorbed by our nanotriangles (showed as red spheres), scattered (showed in green arrows), and reflected (showed in gold arrows) from the surface of our nanotriangles or the cuvette, or transmitted through them (showed in violet arrows).[36] All the light that is not absorbed by the sample is reflected by the walls of the integrating sphere several times until it reaches the detector (a powermeter). Also, the part of the light that after being absorbed by the sample is converted into light at another wavelength, as we have seen in the previous sections, is detected by the powermeter. The only part of the light absorbed by the sample that cannot be detected by the powermeter is just the part that is transformed into heat. Thus, by determining the light with which the sample is illuminated (P_{input}), and the part of the light that is not transformed into heat (P_{output}), we can determine the photothermal conversion efficiency of a particular material, without knowing any of the thermal parameters of the material in advance, as requested by other techniques.[36] This method has been validated previously for metallic plasmonic nanoparticles, graphene flakes, and inorganic dielectric materials.[31, 36, 63]

Thus, to calculate the photothermal conversion efficiency (η), we need to measure the power values measured for the solvent (cyclohexane in this case) (P_{blank}), the empty cuvette (P_{empty}) and the dispersion of Ho, Tm:Y_2O_3 nanocrystals (nanotriangles, nanohearts or self-assembled nanodiscs) in cyclohexane (P_{sample}), From these values we can calculate η using the following equation:

$$\eta = \left|\frac{P_{blank} - P_{sample}}{P_{empty} - P_{sample}}\right| x\ 100\% \qquad (7)$$

We estimated the light-to-heat conversion ability of Ho, Tm:Y_2O_3 nanocrystals by exposing them to different laser powers. The results are summarized in Figure 7 (b). From the graph, it can be observed that the ability of the nanocrystals to convert the absorbed light into heat is independent of the laser power provided, within the experimental errors determined, as it would be expected for the photothermal conversion efficiency. The nanotriangles exhibit the highest photothermal conversion efficiency, with a value of η =15 ± 2%, whereas the nanohearts and the self-assembled nanodiscs show lower efficiencies, 10 ± 1% and 8 ± 2%, respectively. Thus, taking into account these results, the nanotriangle morphology compared to the nanohearts and self-assembled nanodiscs, seems to favor the transformation of light into heat.

According to the light generation efficiency, presented in Figure 3 (a), one would expect that the self-assembled nanodiscs would show the minimum heat generation ability, since they present the highest emission intensity among the nanocrystals analyzed, as it is the case here. Nevertheless, according to this figure, the nanohearts would have to show the highest photothermal conversion efficiency, and this is not the case. To clarify this discrepancy among the nanohearts and the nanotriangles, we evaluated the ability of lanthanide doped materials to generate heat, by investigating the effectiveness of the non-radiative processes, the main responsible factor of heat generation in these compounds.[31] Hence, in these colloidal nanocrystals, the non-radiative mechanisms will be strictly related to the intra-ions or inter-ions interactions and the surface interactions among the nanocrystals and their coating ligands. An effective non-radiative emission, *i.e.* a higher ability to generate heat, will be displayed by a fast decrease in the intensity of the emissions with the increase of the temperature.

To proof the effectiveness of non-radiative processes, in these two nanocrystals, we monitored the decrease of the intensity of the three emission bands (1.5 μm, 1.85 μm and 2.1 μm) as temperature increase from 313 K to 373 K. As the temperature increases, all bands of the nanotriangles decay faster than those of nanohearts (Figure 8 (a)-(c)). The nanotriangles bands decrease approximately 40% of the initial value. Two of the most important bands will be the 1.5 μm and 1.85 μm. Hence, the intensity of the 1.5 μm band, would be affect by the non-radiative processes between the $^3H_4$ to $^3F_4$ state (see Figure 3 (b)), and since the intensity is decreased faster in the nanotriangles (see Figure 8 (b)), is a proof of a more effective mechanism taking place on these nanocrystals. On the other hand, the intensity of the 1.85 μm band is affected by the energy transfer (ET) between the quasi-resonant energy levels of $^3F_4$ level of Tm^{3+} and the $^5I_7$ level of Ho^{3+}, and when this ET process takes place, part of the energy is transferred into heat, which according to Figure 8 (b), is again more effective in the nanotriangles and as an outcome, more heat in generated from these particles.

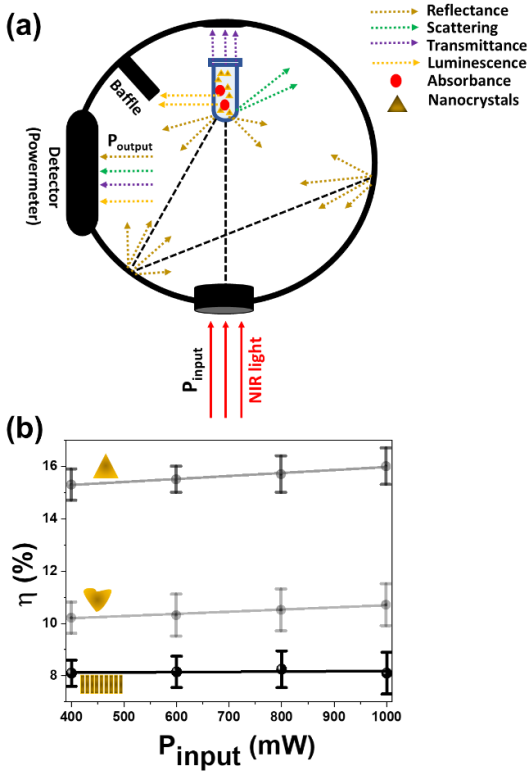

Figure 7. (a) Schematic representation of the basis of the integrated sphere method for the determination of the photothermal conversion efficiency (η). (b) Photothermal conversion efficiency determined for Ho, Tm:Y_2O_3 colloidal nanocrystals versus the input laser power (P_{input}). Error bars are included for each measurement. The lines represent an eye guide for the reader.

Although this explanation provided here, cannot draw a final conclusion regarding the effect of size and shape on the light-to-heat conversion efficacy, in general, as seen for the case of self-assembled nanodiscs, smaller sized particles provide higher brightness (Figure 3 (a)), better thermal sensing properties (Figure 5 (e)), but smaller heat generation (Figure 7 (b)). In the contrary, one cannot properly correlate the effect of the size and shape of lanthanide doped materials on the intra-ions or inter-ions interactions and the surface interactions in the heat generation process.

In any case, the nanotriangles obtained show a low photothermal conversion efficiency when compared to other lanthanide doped materials for which this ability has been demonstrated

previously. For instance, $NaNdF_4$@$NaYF_4$@ Nd:$NaYF_4$ nanostructures with η =72.7%,[65] $NdVO_4$ nanocrystals with η=72.1%,[66] or Ho, Tm:$KLu(WO_4)_2$ nanoparticles with η =40 ± 2%,[31] show very low efficiency, are much more efficient than the nanocrystals analyzed here. Nevertheless, our nanotriangles have a similar efficiency to that reported for 20 mol% Nd^{3+}:$NaYF_4$ (η =15%), 3 mol% Nd^{3+}:$LiYF_4$ (η =16%) and NdF_3 nanoparticles (η=10%).[67] However, this is the first time that the morphology of the nanocrystals is taken into account to analyze its influence on the photothermal conversion efficiency of a particular material. As it can be seen according to the results obtained, the morphology seems to play a major role in this parameter.

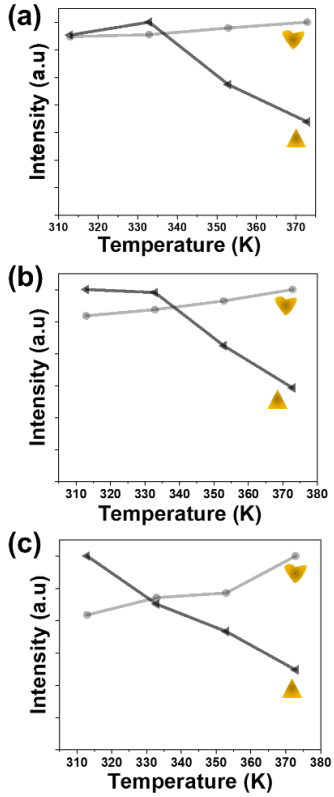

Figure 8. Variation of the intensity of the emissions: (a) 1.5 μm, (b) 1.85 μm and (c) 2.1 μm, with the temperature for nanotriangles and nanohearts. The lines represent a guide for the eyes of the readers.

4. Conclusions

Nanotriangles, nanohearts and self-assembled nanodiscs yttrium oxide colloidal nanocrystals doped with 3 mol% Ho^{3+}, 5 mol% Tm^{3+} with sizes ~42 nm, 52 nm and 20 nm, were tested as luminescent nanothermometers operating in the third biological window and as photothermal conversion agents. By exciting these nanocrystals with NIR light source, located at the first biological window, three emission bands in the third biological window were detected: 1.5 μm, 1.85 μm (composed of two Stark sublevels located at 1.85 μm and 1.96 μm) and 2.1 μm, attributed to the $^3H_4 \rightarrow {}^3F_4$, $^3F_4 \rightarrow {}^3H_6$ electronic transitions of Tm^{3+} and the $^5I_7 \rightarrow {}^5I_8$ electronic transition of Ho^{3+}, respectively. Self-assembled nanodiscs, the brightest among these particles, achieved the best thermometric performance for a value of relative thermal sensitivity of 0.92% K^{-1} and a temperature resolution 0.54 K, at 313 K, extracted from the fluorescence intensity ratio between thermally coupled levels of 1.8 μm and 1.96 μm. The best light-to-heat conversion efficiency was assigned to the nanotriangles with a value of η = 15 ± 2%, comparable with that of other lanthanide

doped materials. According to these results, the morphology of a particular material seems to play a major role in the thermometric performance and as their potentiality as photothermal agent. Thus, in the future, this parameter must to be taken into account when optimizing these properties.

5. Acknowledgements

This work was supported by the Spanish Government under projects MAT2016-75716-C2-1-R (AEI/FEDER, UE) and by the Generalitat de Catalunya under project 2017SGR755. A.N acknowledges financial support from the Generalitat de Catalunya under grant 2017FI_B00620, 2018FI_B100161 and 2019FI_B200154.

6. References

1. Murray, C. B.; Kagan, C. R.; Bawendi, M. G., Synthesis and characterization of monodisperse nanocrystals and close-packed nanocrystal assemblies. *Annual Review of Materials Science* **2000,** 30, (1), 545-610.
2. Murphy, C. J.; Sau, T. K.; Gole, A. M.; Orendorff, C. J.; Gao, J.; Gou, L.; Hunyadi, S. E.; Li, T., Anisotropic metal nanoparticles: Synthesis, assembly, and optical applications. *Journal of Physical Chemistry B* **2005,** 109, (29), 13857-70.
3. Xia, Y.; Xiong, Y.; Lim, B.; Skrabalak, S. E., Shape-controlled synthesis of metal nanocrystals: simple chemistry meets complex physics? *Angewandte Chemie International Edition* **2009,** 48, (1), 60-103.
4. Peng, X.; Manna, L.; Yang, W.; Wickham, J.; Scher, E.; Kadavanich, A.; Alivisatos, A. P., Shape control of CdSe nanocrystals. *Nature* **2000,** 404, (6773), 59-61.
5. Sun, Y.; Xia, Y., Shape-controlled synthesis of gold and silver nanoparticles. *Science* **2002,** 298, (5601), 2176-2179.
6. Dhanaraj, J.; Jagannathan, R.; Kutty, T. R. N.; Lu, C. H., Photoluminescence characteristics of Y_2O_3:Eu^{3+} nanophosphors prepared using sol-gel thermolysis. *Journal of Physical Chemistry B* **2001,** 105, (45), 11098-11105.
7. Ye, X.; Collins, J. E.; Kang, Y.; Chen, J.; Chen, D. T.; Yodh, A. G.; Murray, C. B., Morphologically controlled synthesis of colloidal upconversion nanophosphors and their shape-directed self-assembly. *Proceedings of the National Academy of Sciences of the United States of America* **2010,** 107, (52), 22430-22435.
8. Feng, X.; Sayle, D. C.; Wang, Z. L.; Paras, M. S.; Santora, B.; Sutorik, A. C.; Sayle, T. X.; Yang, Y.; Ding, Y.; Wang, X.; Her, Y. S., Converting ceria polyhedral nanoparticles into single-crystal nanospheres. *Science* **2006,** 312, (5779), 1504-1508.
9. Habas, S. E.; Lee, H.; Radmilovic, V.; Somorjai, G. A.; Yang, P., Shaping binary metal nanocrystals through epitaxial seeded growth. *Nature Materials* **2007,** 6, (9), 692-697.
10. Lee, I.; Delbecq, F.; Morales, R.; Albiter, M. A.; Zaera, F., Tuning selectivity in catalysis by controlling particle shape. *Nature Materials* **2009,** 8, (2), 132-138.
11. Bratlie, K. M.; Lee, H.; Komvopoulos, K.; Yang, P.; Somorjai, G. A., Platinum nanoparticle shape effects on benzene hydrogenation selectivity. *Nano Letters* **2007,** 7, (10), 3097-3101.
12. Song, Q.; Ding, Y.; Wang, Z. L.; Zhang, Z. J., Formation of orientation-ordered superlattices of magnetite magnetic nanocrystals from shape-segregated self-assemblies. *Journal of Physical Chemistry B* **2006,** 110, (50), 25547-25550.
13. Mensah, F.; Seyoum, H.; Misra, P., Nanomaterials in Nanomedicine. In *Applied Spectroscopy and the Science of Nanomaterials*, Misra, P., Ed. Springer Singapore: Singapore, 2015; pp 253-277.
14. Boisselier, E.; Astruc, D., Gold nanoparticles in nanomedicine: preparations, imaging, diagnostics, therapies and toxicity. *Chemical Society Reviews* **2009,** 38, (6), 1759-82.
15. Zhang, X. Q.; Lam, R.; Xu, X.; Chow, E. K.; Kim, H. J.; Ho, D., Multimodal nanodiamond drug delivery carriers for selective targeting, imaging, and enhanced chemotherapeutic efficacy. *Advanced Materials* **2011,** 23, (41), 4770-5.
16. Dvir, T.; Bauer, M.; Schroeder, A.; Tsui, J. H.; Anderson, D. G.; Langer, R.; Liao, R.; Kohane, D. S., Nanoparticles targeting the infarcted heart. *Nano Letters* **2011,** 11, (10), 4411-4.
17. Jiang, S.; Gnanasammandhan, M. K.; Zhang, Y., Optical imaging-guided cancer therapy with fluorescent nanoparticles. *Journal of the Royal Society Interface* **2010,** 7, (42), 3-18.
18. Jaque, D.; Vetrone, F., Luminescence nanothermometry. *Nanoscale* **2012,** 4, (15), 4301-4326.
19. Uchiyama, S.; Kawai, N.; de Silva, A. P.; Iwai, K., Fluorescent polymeric AND logic gate with temperature and pH as inputs. *Journal of the American Chemical Society* **2004,** 126, (10), 3032-3033.
20. Okabe, K.; Inada, N.; Gota, C.; Harada, Y.; Funatsu, T.; Uchiyama, S., Intracellular temperature mapping with a fluorescent polymeric thermometer and fluorescence lifetime imaging microscopy. *Nature Communications* **2012,** 3, 705-714.

21. Uchiyama, S.; Matsumura, Y.; de Silva, A. P.; Iwai, K., Fluorescent molecular thermometers based on polymers showing temperature-induced phase transitions and labeled with polarity-responsive benzofurazans. *Analytical Chemistry* **2003,** 75, (21), 5926-35.
22. Low, P.; Kim, B.; Takama, N.; Bergaud, C., High-spatial-resolution surface-temperature mapping using fluorescent thermometry. *Small* **2008,** 4, (7), 908-914.
23. Paviolo, C.; Clayton, A. H.; McArthur, S. L.; Stoddart, P. R., Temperature measurement in the microscopic regime: a comparison between fluorescence lifetime- and intensity-based methods. *Journal of Microscopy* **2013,** 250, (3), 179-88.
24. Lee, J.; Govorov, A. O.; Kotov, N. A., Nanoparticle assemblies with molecular springs: a nanoscale thermometer. *Angewandte Chemie International Edition* **2005,** 44, (45), 7439-42.
25. Kalytchuk, S.; Zhovtiuk, O.; Kershaw, S. V.; Zboril, R.; Rogach, A. L., Temperature-dependent exciton and trap-related photoluminescence of CdTe quantum dots embedded in a NaCl matrix: Implication in thermometry. *Small* **2016,** 12, (4), 466-76.
26. Shang, L.; Stockmar, F.; Azadfar, N.; Nienhaus, G. U., Intracellular thermometry by using fluorescent gold nanoclusters. *Angewandte Chemie International Edition* **2013,** 52, (42), 11154-11157.
27. Back, M.; Trave, E.; Ueda, J.; Tanabe, S., Ratiometric optical thermometer based on dual near-infrared emission in Cr^{3+}-doped bismuth-based gallate host. *Chemistry of Materials* **2016,** 28, (22), 8347-8356.
28. McLaurin, E. J.; Vlaskin, V. A.; Gamelin, D. R., Water-soluble dual-emitting nanocrystals for ratiometric optical thermometry. *Journal of the American Chemical Society* **2011,** 133, (38), 14978-14980.
29. Quintanilla, M.; Benayas, A.; Naccache, R.; Vetrone, F., Chapter 5: Luminescent nanothermometry with lanthanide-doped nanoparticles. In 2016; pp 124-166.
30. Riseberg, L. A.; Moos, H. W., Multiphonon orbit-lattice relaxation of excited states of rare-earth ions in crystals. *Physical Review* **1968,** 174, (2), 429-438.
31. Nexha, A.; Carvajal, J. J.; Pujol, M. C.; Díaz, F.; Aguiló, M., Short-wavelength infrared self-assessed photothermal agents based on Ho,Tm:$KLu(WO_4)_2$ nanocrystals operating in the third biological window (1.45-1.96 μm wavelength range). *Journal of Materials Chemistry C* **2020,** 8, (1), 180-191.
32. Savchuk, O. A.; Carvajal, J. J.; Haro-Gonzalez, P.; Aguiló, M.; Díaz, F., Luminescent nanothermometry using short-wavelength infrared light. *Journal of Alloys and Compounds* **2018,** 746, 710-719.
33. Naczynski, D. J.; Tan, M. C.; Zevon, M.; Wall, B.; Kohl, J.; Kulesa, A.; Chen, S.; Roth, C. M.; Riman, R. E.; Moghe, P. V., Rare-earth-doped biological composites as in vivo shortwave infrared reporters. *Nature Communications* **2013,** 4, 2199.
34. Vetrone, F.; Boyer, J. C.; Capobianco, J. A.; Speghini, A.; Bettinelli, M., Effect of Yb^{3+} codoping on the upconversion emission in nanocrystalline Y_2O_3:Er^{3+}. *Journal of Physical Chemistry B* **2003,** 107, (5), 1107-1112.
35. Dikovska, A. O. G.; Atanasov, P. A.; Jiménez de Castro, M.; Perea, A.; Gonzalo, J.; Afonso, C. N.; García López, J., Optically active Er^{3+}-Yb^{3+} codoped Y_2O_3 films produced by pulsed laser deposition. *Thin Solid Films* **2006,** 500, (1), 336-340.
36. Savchuk, O. A.; Carvajal, J. J.; Massons, J.; Aguiló, M.; Díaz, F., Determination of photothermal conversion efficiency of graphene and graphene oxide through an integrating sphere method. *Carbon* **2016,** 103, 134-141.
37. Wang, D.; Kang, Y.; Ye, X.; Murray, C. B., Mineralizer-assisted shape-control of rare earth oxide nanoplates. *Chemistry of Materials* **2014,** 26 (22), 6328-6332.
38. Nexha, A.; Pujol, M. C.; Carvajal, J. J.; Díaz, F.; Aguiló, M., Controlling the growth of colloidal rare earth oxides via wet chemical methodologies. *To be submitted.*
39. Williams, C. G.; Malik, A. N.; Kim, T. K.; Manson, P. N.; Elisseeff, J. H., Variable cytocompatibility of six cell lines with photoinitiators used for polymerizing hydrogels and cell encapsulation. *Biomaterials* **2005,** 26, (11), 1211-1218.
40. del Rosal, B.; Ximendes, E.; Rocha, U.; Jaque, D., In vivo luminescence nanothermometry: from materials to applications. *Advanced Optical Materials* **2017,** 5, (1), 1600508-1600522.
41. Liu, D.; Xu, X.; Du, Y.; Qin, X.; Zhang, Y.; Ma, C.; Wen, S.; Ren, W.; Goldys, E. M.; Piper, J. A.; Dou, S.; Liu, X.; Jin, D., Three-dimensional controlled growth of monodisperse sub-50 nm heterogeneous nanocrystals. *Nature Communications* **2016,** 7, (1), 10254-10262.
42. Homann, C.; Krukewitt, L.; Frenzel, F.; Grauel, B.; Würth, C.; Resch-Genger, U.; Haase, M., $NaYF_4$:Yb,Er/$NaYF_4$ core/shell nanocrystals with high upconversion luminescence quantum yield. *Angewandte Chemie International Edition* **2018,** 57, (28), 8765-8769.
43. Kömpe, K.; Borchert, H.; Storz, J.; Lobo, A.; Adam, S.; Möller, T.; Haase, M., Green-emitting $CePO_4$:Tb/$LaPO_4$ core-shell nanoparticles with 70% photoluminescence quantum yield. *Angewandte Chemie International Edition* **2003,** 42, (44), 5513-5516.
44. Kim, S. Y.; Jeong, J. S.; Mkhoyan, K. A.; Jang, H. S., Direct observation of the core/double-shell architecture of intense dual-mode luminescent tetragonal bipyramidal nanophosphors. *Nanoscale* **2016,** 8, (19), 10049-10058.
45. Vetrone, F.; Naccache, R.; Mahalingam, V.; Morgan, C. G.; Capobianco, J. A., The active-core/active-shell approach: A strategy to enhance the upconversion luminescence in lanthanide-doped nanoparticles. *Advanced Functional Materials* **2009,** 19, (18), 2924-2929.
46. Quintanilla, M.; Ren, F.; Ma, D.; Vetrone, F., Light management in upconverting nanoparticles: Ultrasmall core/shell architectures to tune the emission color. *ACS Photonics* **2014,** 1, (8), 662-669.

47. Peng, D.; Ju, Q.; Chen, X.; Ma, R.; Chen, B.; Bai, G.; Hao, J.; Qiao, X.; Fan, X.; Wang, F., Lanthanide-doped energy cascade nanoparticles: Full spectrum emission by single wavelength excitation. *Chemistry of Materials* **2015,** 27, (8), 3115-3120.
48. Granqvist, C. G.; Buhrman, R. A., Ultrafine metal particles. *Journal of Applied Physics* **1976,** 47, (5), 2200-2219.
49. Söderlund, J.; Kiss, L. B.; Niklasson, G. A.; Granqvist, C. G., Lognormal size distributions in particle growth processes without coagulation. *Physical Review Letters* **1998,** 80, (11), 2386-2388.
50. Si, R.; Zhang, Y. W.; Zhou, H. P.; Sun, L. D.; Yan, C. H., Controlled-synthesis, self-assembly behavior, and surface-dependent optical properties of high-quality rare-earth oxide nanocrystals. *Chemistry of Materials* **2007,** 19, (1), 18-27.
51. Jeong, J.; Kim, N.; Kim, M. G.; Kim, W., Generic synthetic route to monodisperse sub-10 nm lanthanide oxide nanodisks: A modified digestive ripening process. *Chemistry of Materials* **2016,** 28 (1), 172-179.
52. Si, R.; Zhang, Y. W.; You, L. P.; Yan, C. H., Rare-earth oxide nanopolyhedra, nanoplates, and nanodisks. *Angewandte Chemie International Edition* **2005,** 44, (21), 3256-3260.
53. Jambunathan, V.; Mateos, X.; Pujol, M. C.; Carvajal, J. J.; Massons, J.; Aguiló, M.; Díaz, F., Near-infrared photoluminescence from Ho^{3+}-doped monoclinic $KLu(WO_4)_2$ crystal codoped with Tm^{3+}. *Journal of Luminescence* **2009,** 129, (12), 1882-1885.
54. Mun, J. H.; Jouini, A.; Novoselov, A.; Guyot, Y.; Yoshikawa, A.; Ohta, H.; Shibata, H.; Waseda, Y.; Boulon, G.; Fukuda, T., Growth and characterization of Tm-doped Y_2O_3 single crystals. *Optical Materials* **2007,** 29, (11), 1390-1393.
55. Guyot, Y.; Moncorgé, R.; Merkle, L. D.; Pinto, A.; McIntosh, B.; Verdun, H., Luminescence properties of Y_2O_3 single crystals doped with Pr^{3+} or Tm^{3+} and codoped with Yb^{3+}, Tb^{3+} or Ho^{3+} ions. *Optical Materials* **1996,** 5, (1), 127-136.
56. Sidorowicz, A.; Wajler, A.; Węglarz, H.; Nakielska, M.; Orliński, K.; Diduszko, R.; Olszyna, A., Preparation and characterization of thulium doped yttrium oxide ($Tm:Y_2O_3$) powders. *Journal of Alloys and Compounds* **2017,** 709, 293-298.
57. Newburgh, G. A.; Word-Daniels, A.; Michael, A.; Merkle, L. D.; Ikesue, A.; Dubinskii, M., Resonantly diode-pumped Ho^{3+}: Y_2O_3 ceramic 2.1 μm laser. *Optics Express* **2011,** 19, (4), 3604-3611.
58. Wade, S. A.; Collins, S. F.; Baxter, G. W., Fluorescence intensity ratio technique for optical fiber point temperature sensing. *Journal of Applied Physics* **2003,** 94, (8), 4743-4756.
59. Brites, C. D. S.; Lima, P. P.; Silva, N. J. O.; Millán, A.; Amaral, V. S.; Palacio, F.; Carlos, L. D., Thermometry at the nanoscale. *Nanoscale* **2012,** 4, (16), 4799-4829.
60. Santos, P. V. d.; Araujo, M. T. d.; Gouveia-Neto, A. S.; Neto, J. A. M.; Sombra, A. S. B., Optical temperature sensing using upconversion fluorescence emission in Er^{3+}/Yb^{3+}-codoped chalcogenide glass. *Applied Physics Letters* **1998,** 73, (5), 578-580.
61. Brites, C. D. S.; Millán, A.; Carlos, L. D., Chapter 281-Lanthanides in Luminescent Thermometry. In *Handbook on the Physics and Chemistry of Rare Earths*, Jean-Claude, B.; Vitalij K, P., Eds. Elsevier: 2016; Vol. 49, pp 339-427.
62. Savchuk, O. A.; Carvajal, J. J.; Brites, C. D. S.; Carlos, L. D.; Aguilo, M.; Diaz, F., Upconversion thermometry: a new tool to measure the thermal resistance of nanoparticles. *Nanoscale* **2018,** 10, (14), 6602-6610.
63. Ma, Y.; Xiang, G.; Zhang, J.; Liu, Z.; Zhou, P.; Liu, W.; Tang, X.; Jiang, S.; Zhou, X.; Li, L.; Luo, Y.; Jin, Y., Upconversion properties and temperature sensing behaviors in visible and near-infrared region based on fluorescence intensity ratio in $LuVO_4:Yb^{3+}/Er^{3+}$. *Journal of Alloys and Compounds* **2018,** 769, 325-331.
64. Xiang, G.; Liu, X.; Zhang, J.; Liu, Z.; Liu, W.; Ma, Y.; Jiang, S.; Tang, X.; Zhou, X.; Li, L.; Jin, Y., Dual-mode optical thermometry based on the fluorescence intensity ratio excited by a 915 nm wavelength in $LuVO_4:Yb^{3+}/Er^{3+}@SiO_2$ nanoparticles. *Inorganic Chemistry* **2019,** 58, (12), 8245-8252.
65. Marciniak, L.; Pilch, A.; Arabasz, S.; Jin, D.; Bednarkiewicz, A., Heterogeneously Nd^{3+} doped single nanoparticles for NIR-induced heat conversion, luminescence, and thermometry. *Nanoscale* **2017,** 9, (24), 8288-8297.
66. del Rosal, B.; Pérez-Delgado, A.; Carrasco, E.; Jovanović, D. J.; Dramićanin, M. D.; Dražić, G.; de la Fuente, Á. J.; Sanz-Rodriguez, F.; Jaque, D., Neodymium-based stoichiometric ultrasmall nanoparticles for multifunctional deep-tissue photothermal therapy. *Advanced Optical Materials* **2016,** 4, (5), 782-789.
67. Wu, X.; Yeow, E. K. L., Tuning the NIR downconversion luminescence and photothermal conversion efficiencies of $MNd_xY_{1-x}F_4$ (M=Na and Li) nanocrystals for use in anti-counterfeiting labels with opposite displays. *Nanoscale* **2019,** 11, (32), 15259-15269.

Supporting Information

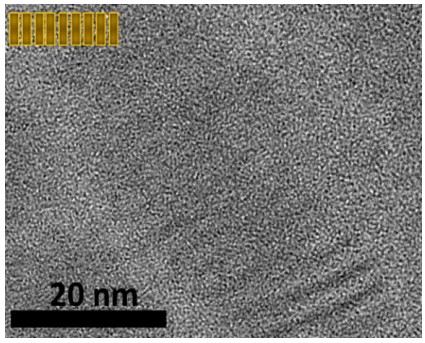

Figure S1. High resolution TEM image of self-assembled Y_2O_3 nanodiscs.

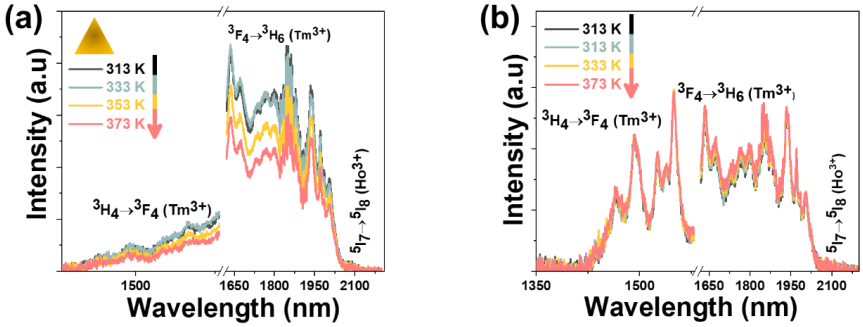

Figure S2. Temperature dependence of the intensity of the emission bands in the III-BW of the 3 mol% Ho^{3+}, 5 mol% Tm^{3+} doped Y_2O_3 colloidal: (a) nanotriangles and (b) nanohearts, excited at 808 nm. Please note that part of the graph from 1580 nm to 1630 nm was removed due to the second harmonic of the 808 nm laser source.

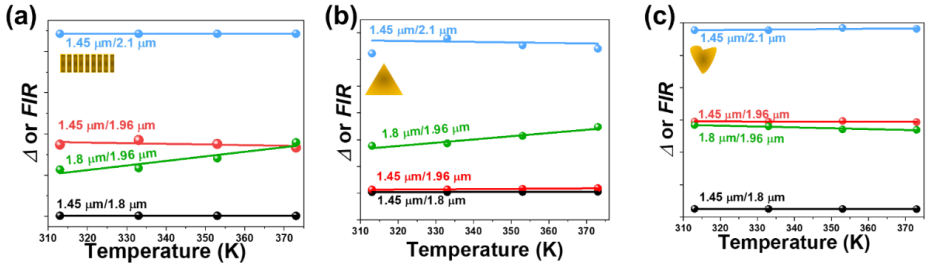

Figure S3. Temperature-dependence of the intensity ratio (Δ or FIR) of the four emission bands of: (a) self-assembled nanodiscs, (b) nanotriangles and (c) nanohearts.

Paper VII

Effect of the core@shell and layer-by-layer nanoarchitectures on the thermal sensing and photothermal conversion efficiency in triangular Ho^{3+}, Tm^{3+}:Y_2O_3 colloidal nanocrystals operating in the third biological window

Albenc Nexha, Joan J. Carvajal,* Maria Cinta Pujol, Francesc Díaz and Magdalena Aguiló
Universitat Rovira i Virgili, Departament de Química Física i Inorgànica,
Física i Cristal·lografia de Materials i Nanomaterials (FiCMA-FiCNA)-EMaS, Campus Sescelades, E-43007, Tarragona, Spain
*joanjosep.carvajal@urv.cat

Abstract

Thermal decomposition methodologies were applied to synthesize monodisperse core, core@shell and layer-by-layer Ho, Tm:Y_2O_3 colloidal nanocrystals. The structure, morphology and surface linked molecules of the synthesized nanocrystals, were investigated by X-ray diffraction, transmission electron microscopic techniques and FT-IR. The photoluminescence properties of the synthesized colloidal nanocrystals were recorded in the third biological window (III-BW) region after excitation at 808 nm source, lying also within the biological windows. Regardless of the nature of the nanocrystals, three emission bands were detected, attributed to the: $^3H_4 \rightarrow {}^3F_4$ (1.5 µm) and $^3F_4 \rightarrow {}^3H_6$ (1.85 µm) electronic transitions of Tm^{3+} and $^5I_7 \rightarrow {}^5I_8$ (2.1 µm) attributed to the electronic transition of Ho^{3+}. The core only, core@shell and layer-by-layer Ho, Tm:Y_2O_3 colloidal nanocrystals were tested as luminescent nanothermometers and as photothermal conversion agents. The highest relative thermal sensitivity was achieved from the Ho, Tm:Y_2O_3 core only nanomaterials with a value of S_{rel}=0.68% K^{-1}, and the best light-to-heat conversion efficiency from the core@shell nanocrystals with a η=34%. The temperature sensing properties are reduced for the core@shell nanocrystals due to the hampering of the quenching mechanisms from the surrounding ligands by the coating shell, although this shell ensures brighter emission compared to the core only and layer-by-layer structures. The layer-by-layer structures, instead, display the lowest intensity of the emissions, having so, lower quantum efficiency and lower thermometric performance. The higher photothermal conversion efficiency observed in the core@shell nanoarchitectures is explained by the effective non-radiative relaxation processes taking place, favoured by the presence of the coating shell.

1. Introduction

Establishing control over the morphology of nanocrystals is one of the main paths to design their properties for specific requirements and applications. Different examples involve changing the size and shape of nanocrystals to adjust the plasmonic nature of metal nanoparticles (Au[1, 2] and Ag[3, 4]), tuning the band gap and polarizability of semiconductors,[5, 6] and reshape the optical and magnetic properties of lanthanide based nanocrystals.[7, 8] The incorporation of an additional shell, forming core shell nanocrystals (hereafter core@shell), allows for a further optimization of the properties of the core materials and of the combination with new properties.[9-13]

In lanthanide doped core@shell nanocrystals, the proper design of the shell (or multishells) covering the core, led to the discovery of novel properties. Single core lanthanide doped nanocrystals often exhibit low photoluminescence yield as a result of energy-transfer (ET)

processes to the surface through adjacent dopant ions or because the luminescence of surface dopant ions is quenched.[14, 15] Growing an inert or active shell into the core lanthanide doped nanocrystals might lead to enhanced photoluminescence yields attributed to the protecting effect on of the luminescent ion from quenching due to the surrounding environment (*e.g.*, stabilizing ligands, solvent molecules, surface defects, etc.).[16]

Thus, for example, the preparation of a core@shell nanoarchitectures by growing an inert shell ($LaPO_4$) around an optically active core ($Tb:CePO_4$), led to an increase of the photoluminescence yield from 43% for core only nanocrystals up to 70% after the shell deposition.[17] A similar effect on the photoluminescence yield and resistance towards cerium oxidation was reported for the highly monodisperse active core@inert shell $Ce,Tb:NaGdF_4@NaYF_4$ colloidal nanocrystals compared to $Ce,Tb:NaGdF_4$ core only nanoparticles.[18] The replacement of the active core@inert shell with an active core@active shell might provide, brighter nanophosphors, as demonstrated in the case of $Er,Yb:NaGdF_4@Yb:NaGdF_4$, in which the role of the active shell was to absorb more near infrared (NIR) light to subsequently transfer it to the activator (Er) located in the core.[19] Additional benefits of implementing core@shell nanoarchitectures have been demonstrated in the preparation of upconverting multishell nanocrystals, such as active core@active shell@inert shell $Tm,Yb:NaGdF_4@A:NaGdF_4@NaFY_4$, in which A=Dy, Sm, Tb and Eu.[20] The basic principle of the multishell active core@active shell@inert shell nanocrystals is dedicated to the so-called *"controlled gadolinium network-mediated energy migration"* to tune the output color.[20, 21] These multishell upconverting nanocrystals have been implemented for temporal full color tuning through nonsteady-state upconversion,[12] multicolor emission modulated by laser power,[22] lifetime regulation,[23, 24] and orthogonal excitation-emission upconversion.[25]

Lanthanide doped nanocrystals, upon near infrared (NIR) excitation, can generate radiative and nonradiative processes, which are responsible for their simultaneously application as luminescent nanothermometers and as photothermal agents.[26-29] Thus, lanthanide doped nanocrystals, can behave as self-assessed photothermal agents, *i.e.* they can simultaneously generate luminescence and heat. Luminescent nanothermometry refers to a non-contact based thermometric technique which aims to extract temperature knowledge at the nanoscale from the temperature dependent properties of the luminescence generated by the materials used,[30] bypassing the drawbacks of the traditional contact thermometers.[31] Luminescent nanothermometers allow to achieve temperature readings through temperature-associated changes in their emission properties, including variations in intensity, peak position, polarization anisotropy, fluorescence lifetime, or band shape.[30] This field of nanothermometry combines high relative thermal sensitivity (>1% K^{-1}) and high spatial resolution (<10 μm) in short acquisition times (<1 ms), and, as it operates remotely, works even in biological fluids, fast-moving objects, and strong electromagnetic fields.[30-33] Successful examples of the effect of the core@shell nanostructures in thermal sensing as luminescent nanothermometers achieved with lanthanide doped core@shell nanocrystals involve: (i) active core@active shell $Yb,Tm:LaF_3@Er,Yb:LaF_3$ nanocrystals exhibited a 7-fold higher thermal sensitivity compared to core only nanoparticles a value ~ 5% K^{-1},[34] (ii) the preparation via a thermal decomposition reaction of core@shell $Pr,Er,Yb:NaGdF_4@Yb:NaYF_4$ nanocrystals with a thermal sensitivity of 9.52% K^{-1} thermal sensing in the low temperature range (83 K),[35] or (iii) thermal sensing in wide temperature ranges from 300 K to 900 K achieved in $Er,Yb:NaYF_4@SiO_2$ nanocrystals.[36] The introduction of impurities in core@shell nanocrystals, allows for further tuning of their thermal sensing properties. A typical example is using active core@active shell $Yb,Ho:NaGdF_4@Yb,Tm:NaYF_4$ nanostructures, presenting a maximum thermal sensitivity of 2.4% K^{-1} when the intensity ratio of the red emission (Ho: $^5F_5 \rightarrow {}^5I_8$ and Tm: $^1G_4 \rightarrow {}^3F_4$ transitions) and the green emission (Ho: $^5S_2$, $^5F_4 \rightarrow {}^5I_8$ transition) was considered.[37] The introduction of Ce in the core as impurity, tuned the thermal sensitivity between 0.7 and 4.4% K^{-1} via the efficient cross relaxation processes between Ce and Ho ions.[37]

Photothermal agents refers to materials that have the ability to absorb light and convert it into heat.[38] The ultimate goal of a photothermal agent is to induce cellular hyperthermia, a technique used for the treatment of tumoral diseases at temperatures above 314 K (41 °C).[38] Thus, a more effective ability of a material to convert light into heat, allows to use them as potential photothermal agent. Successful examples of the boost on the photothermal conversion efficiency of the core@shell (or multishell) structures compared to the core only nanoparticles (or core with one

shell layer) include: (i) thermal decomposition synthesized Er,Yb:$NaYF_4$@ Tm,Yb:$NaYF_4$ nanomaterials synthesized by thermal decomposition exhibit a net temperature increment of 7 K when compared to the core only Er,Yb:$NaYF_4$ nanoparticles,[39] (ii) core@shell@shell $NaNdF_4$@$NaYF_4$@$NaYF_4$:Nd nanoarchitectures were able to increase the temperature of a chloroform solution from room temperature to 318 K, whereas the core@shell only $NaYF_4$@$NaYF_4$:Nd nanoparticles increased the temperature by only 3 K,[27] and (iii) Er,Yb:LaF_3@Nd:LaF_3 core@shell structures exhibited a heating capability 10% higher than Er, Yb,Nd:LaF_3 nanoparticles, after exciting these nanocrystals at 808 nm, and assigning these properties to the ability of Nd to absorb the light and transfer it to Er and Yb with a different efficiency in the two cases.[40] However, the nanosized control over the formation of this colloidal, is generally achieved via the incorporation of capping/coordination organic surfactants, such as oleic acid and oleylamine,[41-43] and structure-directing agents such as LiOH,[44] $NaNO_3$ and $Na_4P_2O_7$,[45] chloride or bromide salts,[46] or transition metal salts,[47-51] which may lead to generation of surface defects and lattice disorders, influencing their radiative (responsible for luminescent nanothermometry) and non-radiative (responsible for photothermal conversion efficiency) processes. These processes at their time are responsible for their corresponding nanothermometry, upconversion, bioimaging and optical sensing.[52] Thus, producing core@shell nanocrystals is not always a guarantee for enhanced thermal sensing performances. For example, core@shell Er,Yb:$NaYF_4$@Tm,Yb:$NaYF_4$ nanoparticles, exhibited a lower relative thermal sensitivity when compared to the core only Er,Yb:$NaYF_4$ nanoparticles,[39] similar to what has been observed in Er,Yb:$NaGdF_4$@$NaYF_4$ core@shell and Er,Yb:$NaGdF_4$ core only nanoparticles,[53] and Pr:LaF_3@LaF_3 core@shell and Pr:LaF_3 core only nanoparticles.[54]

The enhanced dual functionality (as nanothermometers and photothermal agents) of the lanthanide doped core@shell nanocrystals, shifted the focus towards their application in nanomedicine,[55] specially when the emission of the nanocrystals lies on the so-called biological windows (BWs), in which the biological tissues become partially transparent due to a simultaneous reduction in both absorption and scattering of light.[56] Different biological windows have been defined: (i) the first biological window (I-BW) lying in the range 650-950 nm, (ii) the second biological window (II-BW) extending from 950 to 1350 nm, (iii) the third biological window (III-BW) from 1350 nm to 2000 nm, and (iv) the fourth biological window centered at 2200 nm.[57] Compared to the other BWs, the III-BW has gained significant interest because light transmits more effectively (up to three times) through specific biological tissues like those containing melanin,[58] while the scattering of the light is increasingly reduced as the wavelength increases,[57] achieving higher deeper light penetration depths in the biological tissues, a critical parameter is these nanoparticles want to found a real application in the biomedical field.

In this communication, we test the possibility of applying Ho,Tm:Y_2O_3 as core only, core@shell Ho,Tm:Y_2O_3@Y_2O_3 and layer-by-layer Ho,Tm:Y_2O_3/Y_2O_3 nanoarchitectures, as potential self-assessed photothermal agents. These nanocrystals were synthesized using a thermal decomposition methodology. The crystalline structure, and morphological characteristics all the colloidal nanocrystals obtained were analyzed. Their abilities as luminescent nanothermometers operating in the III-BW were analyzed by studying the temperature-dependence on the intensity ratio of the three emission bands generated in this region (1.45 μm and 1.8 μm by Tm and 1.96 μm by Ho) revealing that the maximum thermal sensitivity could be assigned to the core only nanocrystals. The highest photothermal conversion efficiency instead, determined by the integrated sphere method,[59] was achieved for the core@shell nanocrystals.

2. Experiments

2.1. Materials

Yttrium acetate hydrate ($Y(Ac)_3 \cdot H_2O$, 99.99%) and oleylamine (OLAM, > 70%) were purchased from Sigma Aldrich. Thulium acetate hydrate ($Tm(Ac)_3 \cdot H_2O$, 99.99%) was purchased from Apollo Scientific. Holmium acetate hydrate ($Ho(Ac)_3 \cdot H_2O$, 99.99%), oleic acid (OLAC, 90%), 1-octadecene (ODE, 90%), n-hexane (99%) and sodium nitrate ($NaNO_3$, 99%) were purchased from Alfa Aesar. Ethanol (EtOH) was purchased from VWR.

2.2. Synthesis of Y_2O_3 and Ho, Tm:Y_2O_3 colloidal nanocrystals by thermolysis

Undoped Y_2O_3 and 3 mol% Ho, 5 mol% Tm:Y_2O_3 colloidal nanocrystals were synthesized via a thermal decomposition reaction.[60]

In a typical thermolysis synthesis of Y_2O_3 colloidal nanocrystals, 2.5 mmol of $Y(Ac)_3 \cdot H_2O$ and 4 mmol of $NaNO_3$, were dissolved into a solution containing 25 mmol of OLAC, 25 mmol of OLAM and 15 mmol of ODE. The reaction mixture was heated under vacuum at 413 K for 30 min to remove residual water and oxygen. After switching to nitrogen flow, the reaction temperature was increased to 583 K and held at this temperature for 30 min, prior to cooling it down naturally at room temperature. To extract the desired nanocrystals, a purification cycle was applied by adding an excess of EtOH in the cooled solution, followed by centrifugation at 5000 rpm for 10 min and redispersion in cyclohexane. This purification cycle was repeated three times. The final product of the reaction can either be stored in solution by dispersing the nanocrystals in an apolar organic solvent or as powders by evaporating totally the solvent.

The synthesis of the 3 mol% Ho, 5 mol% Tm:Y_2O_3 colloidal nanocrystals, was performed following the same methodology as that of undoped of Y_2O_3 colloidal nanocrystals, except that 3 mol% Ho^{3+} (0.075 mmol of $Ho(Ac)_3 \cdot H_2O$) and 5 mol% Tm^{3+} (0.125 mmol of $Tm(Ac)_3 \cdot H_2O$) were added at the beginning of the experiment, while the concentration of $Y(Ac)_3 \cdot H_2O$ was reduced to 2.3 mmol.

2.3. Synthesis of active core@inert shell (Ho, Tm:Y_2O_3@Y_2O_3) colloidal nanocrystals by thermolysis

For the synthesis of the active core@inert shell Ho, Tm:Y_2O_3@Y_2O_3 colloidal nanocrystals, 2.5 mmol of $Y(Ac)_3 \cdot H_2O$, 4 mmol of $NaNO_3$ and 0.25 g/mL (total volume 4 mL) of the already prepared Ho^{3+}, Tm^{3+}:Y_2O_3 nanocrystals dispersed in n-hexane, were dissolved into a solution containing 25 mmol of OLAC, 25 mmol of OLAM and 15 mmol of ODE with vigorous stirring. The reaction mixture was heated at 353 K for 30 min to remove n-hexane. The mixture was heated under vacuum at 413 K for 30 min to remove residual water and oxygen. After switching to nitrogen flow, the reaction temperature was increased to 583 K and held at this temperature for 30 min. After the reaction was completed, the final solution was cooled down to room temperature naturally. Three purification cycles were performed to extract the final products, stored either as powders or in solution.

2.4. Seeded growth synthesis of layer-by-layer Ho, Tm:Y_2O_3/Y_2O_3 colloidal nanocrystals

For the seeded growth synthesis of layer-by-layer Ho, Tm^{3+}:Y_2O_3/Y_2O_3 colloidal nanocrystals, 2.5 mmol of $Y(Ac)_3 \cdot H_2O$ and 4 mmol of $NaNO_3$ were dissolved in a solution containing 25 mmol of OLAC, 17.5 mmol of OLAM and 15 mmol of ODE with vigorous stirring. The mixture was heated under vacuum at 413 K for 30 min to remove residual oxygen. After switching to nitrogen flow, the reaction temperature was increased to 583 K. At this point, 0.3 g/mL of Ho^{3+}, Tm^{3+}:Y_2O_3 nanocrystals predissolved in 12.5 mmol OLAM for a total volume of 4 mL, were added at the mixture with a rate of 0.5 mL/min, controlled by a syringe pump. After complete injection of the Ho^{3+}, Tm^{3+}:Y_2O_3 (approximately 10 min), the reaction was continued for 30 min more. After the reaction was completed, the final solution was cooled down to room temperature naturally. Three purification cycles were performed to extract the final product, stored either as powders or in solution.

2.5. Characterization

X-ray powder diffraction (XRPD) measurements were performed using a Siemens D5000 diffractometer (Bragg-Brentano parafocusing geometry and vertical θ-θ goniometer) fitted with a curved graphite diffracted-beam monochromator, incident and diffracted-beam Soller slits, a 0.06° receiving slit and a scintillation counter as detector. The angular 2θ diffraction range was set between 5 and 70°. The data were collected with an angular step of 0.05° at 3s per step with sample rotation to increase the statistics of the measurement. Cu K_α radiation was obtained from a copper X-ray tube operated at 40 kV and 30 mA.

Nanoparticles size and shape were examined by a JEOL JEM-1011 transmission electron microscope (TEM) operating at an accelerating voltage of 100 kV or with a JEOL JEM-2100 high resolution transmission electron microscope (HRTEM) operating at 300 kV. For the preparation of the TEM or HRTEM grids, the nanocrystals were dispersed in n-hexane using ultrasounds and around 7 µL of diluted dispersion of the nanocrystals in n-hexane, were placed on the surface of a copper grid covered by a holey carbon film (HD200 Copper Formvar/carbon). The size distribution of the colloidal nanocrystals was investigated via ImageJ software by counting around 100 nanocrystals.

Fourier Transform Infrared (FT-IR) spectra were recorded in the range of 400-4000 cm^{-1} on a FT-IR IluminatIR II, Smith spectrophotometer, to investigate the presence of the different functional groups in the samples to determine which surfactant species are attached onto the surfaces of the nanocrystals.

For the photoluminescence analysis, the emission spectra of the nanocrystals were recorded in a Yokogawa AQ6375 optical spectrum analyzer in the range from 1350 nm to 2200 nm, with a resolution of 2 nm and an integration time of 20 s. The nanoparticles were excited by a 808 nm emission fiber-coupled diode laser (Thorlabs) with a power of 800 mW and the beam was focused on the sample using a 20× microscope objective (numerical aperture=0.4) and bringing a spot size of 1 µm in the sample. The excitation density is around 400 W/cm^2. The scattered excitation radiation was eliminated by using a 850 nm longpass dichroic filter (Thorlabs). For the temperature-photoluminescence dependence, the methodology was the same, except that the nanocrystals were placed inside a heating stage (Linkam, THMS 600) equipped with a boron disk for improved temperature distribution.

The photothermal conversion efficiency was investigated by applying the method of the integrating sphere.[59] A glass cuvette containing a cyclohexane solution of the colloidal nanocrystals with a concentration of around 1 g/L was placed inside an integrating sphere, perpendicular to the laser beam provided by the 808 nm fiber-coupled diode laser (Thorlabs), and was illuminated with different excitation powers (from 0.4 W to 1 W). The laser from the fiber tip was collimated to a spot size of ~5 mm in diameter on the sample. The power density used under these conditions ranges from 0.8 to 2 W/cm^2. A baffle was introduced in the integrating sphere, between the sample and the detector, in order to prevent the direct reflections from the sample to the detector. The signal (the power of the empty cuvette, the power of the cuvette containing the solvent only, and the power of the cuvette containing the solvent and the nanocrystals) was collected using an Ophir Nova II powermeter.

In addition, this integrated sphere, was used to compare the intensity of the emission generated by the nanocrystals, applying the same fiber and optic spectrometer, as described in the photoluminescence measurements.

3. Results and discussion

3.1. Characterization of the Y_2O_3 based colloidal nanocrystals

The crystal structure of all synthesized colloidal nanocrystals, resembles the cubic phase with *Ia* $\bar{3}$ spatial group (JCPDS card 25-1200) (see Figure 1). Their patterns are composed of broad peaks due to their low size, as observed previously in other reports of rare earth sesquioxides synthesized by thermal decomposition methods.[44, 45, 61-63] The average crystallite size of the colloidal nanocrystals, calculated using the Debye-Scherrer equation,[64] applied to the (440) reflection, were 13.2, 14.5, 17.5 and 14.3 nm for the undoped Y_2O_3, core only Ho, Tm:Y_2O_3, core@shell Ho, Tm:Y_2O_3@Y_2O_3 and layer-by-layer structures Ho, Tm:Y_2O_3/Y_2O_3, respectively.

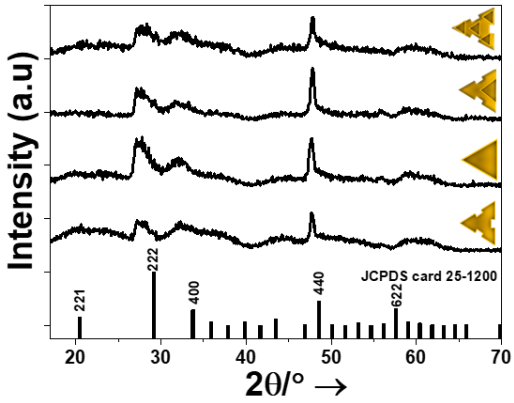

Figure 1. Powder X-ray diffraction patterns of the undoped Y_2O_3, core only Ho, Tm:Y_2O_3, core@shell Ho, Tm:Y_2O_3@Y_2O_3 and layer-by-layer structures Ho, Tm:Y_2O_3/Y_2O_3. The sketchs within the patterns stands for the shape of the colloidal nanocrystals.

Representative TEM images of every kind of nanocrystals obtained are presented in Figure 2. The colloidal Y_2O_3 nanocrystals, grown in the absence of dopants, present a branched broken-edge nanotriangular morphology, monodisperse in size, (see Figure 2 (a)) with an average lateral length of 23 ± 5 nm (see Figure 3). Ho, Tm:Y_2O_3 colloidal nanocrystals exhibit a more complete triangular morphology (see Figure 2 (b)), again monodisperse in size, with an average size than increase to 42 ± 13 nm (see Figure 3).

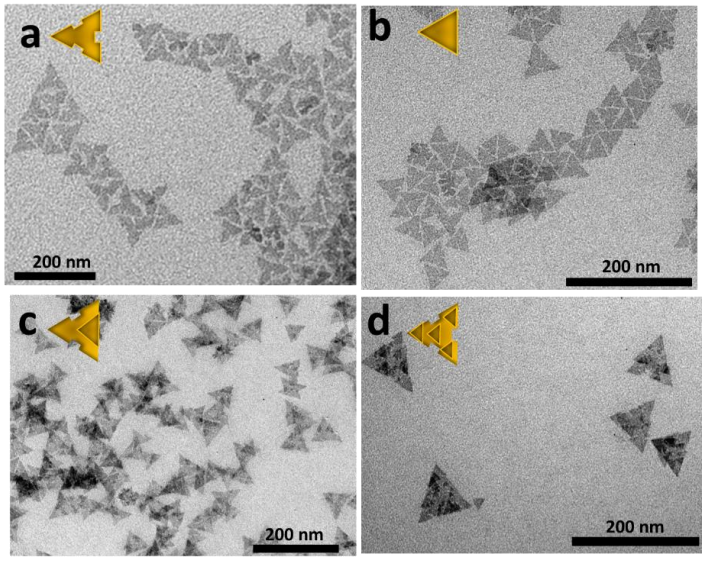

Figure 2. Transmission electron microscopy (TEM) images of (a) undoped, (b) doped with Ho^{3+} and Tm^{3+}, (c) core@shell and (d) layer-by-layer yttrium oxide colloidal nanocrystals.

The core@shell Ho, Tm:Y_2O_3@Y_2O_3 nanocrystals exhibit also a triangular morphology (see Figure 2 (c)) with an average size distribution of 73 ± 18 nm (see Figure 3). Finally, the colloidal nanocrystals prepared by injecting the crystal seeds during the synthesis process exhibit a combination of complete nanotriangles morphology and branched broken-edge nanotriangles in the form of layer-by-layer structure, with the complete nanotriangles growing on top of the broken-edge nanotriangles (see Figure 2 (d)). The complete nanotriangles and the branched broken-

edge nanotriangles have different size distributions with mean sizes of 39 ± 10 nm (see Figure S1 in the Supporting Information) and 100 ± 20 nm (see Figure 3), respectively. This difference in the size of the two morphological habits indicate that the cores and the shells nucleate independently, and probably in a later stage they got attached together. All obtained morphologies show a ternary symmetry, which could correspond to the ternary axis in the cubic system along the [111] crystallographic direction. These morphologies can indicate that the triangular plate is parallel to the crystalline plane.

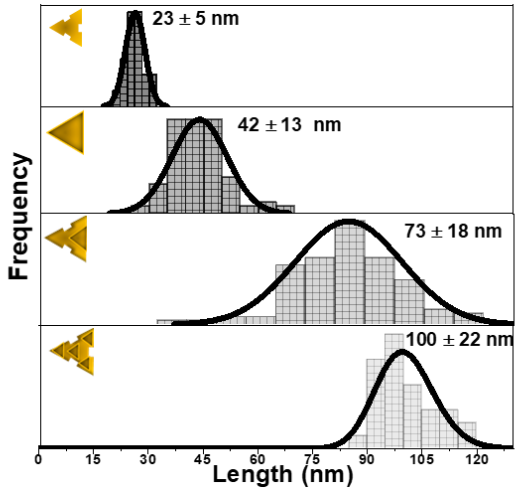

Figure 3. Lateral length side distribution, standard deviation and lognormal fitting of undoped Y_2O_3 nanocrystals, Ho, Tm:Y_2O_3 nanocrystals, core@shell and layer-by-layer yttrium oxide colloidal nanocrystals.

As observed in the XRPD patterns in Figure 1, the (222) reflection peak is very broad, which will be in agreement with the thin thickness of the particle parallel to this crystallographic plane, furthermore the larger shift of this peak in comparison with the reference pattern could be also associated to the confinement of this plane.[44, 45, 60]

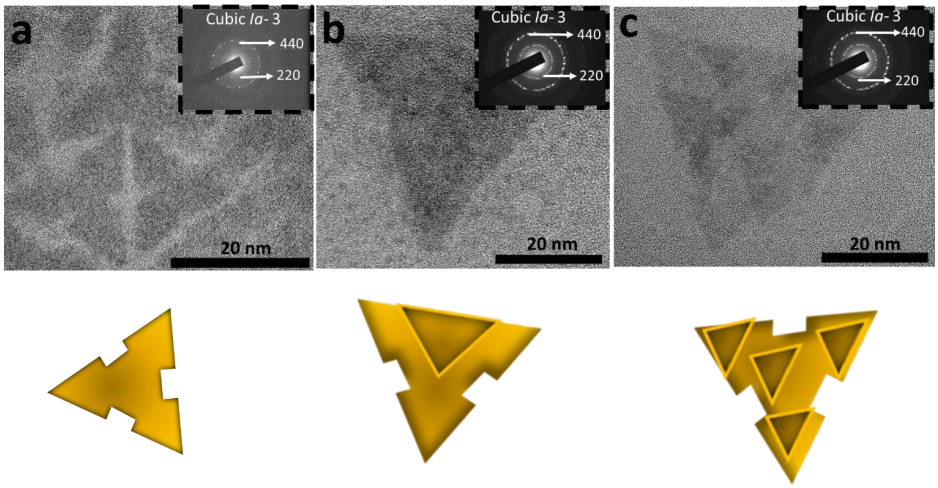

Figure 4. High resolution transmission electron microscopy (HRTEM) images and the corresponding selected area electron diffraction (SAED) patterns of (a) undoped, (b) core@shell and (c) layer-by-layer yttrium oxide based colloidal nanocrystals. The alignment of the sketch is included for better understanding of the structures.

The size of the nanocrystals determined from the TEM images is higher than the crystallite size calculated from the Scherrer equation (see Table S1 at Supporting Information) due to the fact that the Scherrer equation measures the size of the crystallite, whereas the TEM images give information about the size of the particles.[65, 66] However, both methods confirm that with the introduction of the dopants and the preparation of the core@shell and layer-by-layer structures, the sizes increase. The increase in the length of the colloidal nanotriangles from the core only to the core@shell structures, is an indirect proof of the incorporation of the additional growing shell, covering the core material and the formation of the core@shell nanocrystals.[17, 67-72] While undoped nanocrystals exhibit a sharp size distribution, it broadens when introducing the dopants, and especially when the core@shell structures are formed. In the case of the layer-by-layer structure, the sizes of the nanotriangles formed only by the shells have similar sizes than those of the undoped Y_2O_3 nanocrystals, indicating that in fact they have the same composition. Instead, when undoped and doped nanocrystals attach together, their sizes increase substantially from around 80 nm to 120 nm.

The HRTEM images and the selected area electron diffraction (SAED) of the different colloidal nanocrystals obtained are presented in the Figure 4 (a)-(c). The SAED patterns of all nanocrystals, reveal the presence of the (220) and (440) crystallographic planes.[60] The lattice fridges of core@shell and layer-by-layer colloidal nanocrystals could be hardly observed via HRTEM due to relative little thickness of the materials, whereas for the undoped and doped nanocrystals could not be observed because of their smaller sizes. The lattice fridges of core@shell and the layer-by-layer nanocrystals, are separated by 0.306 nm, corresponding to the (222) crystallographic plane (see Figure S2 at Supporting Information for layer-by-layer nanocrystals as an illustrative example). In the case of the core@shell, it is impossible to distinguish between the core (Ho^{3+}, Tm^{3+}:Y_2O_3) and the shell (Y_2O_3) since the two of them have similar lattice constants and the concentration of dopants is too low to show a certain contrast in the figures due to the different atomic weight.[70, 71, 73, 74]

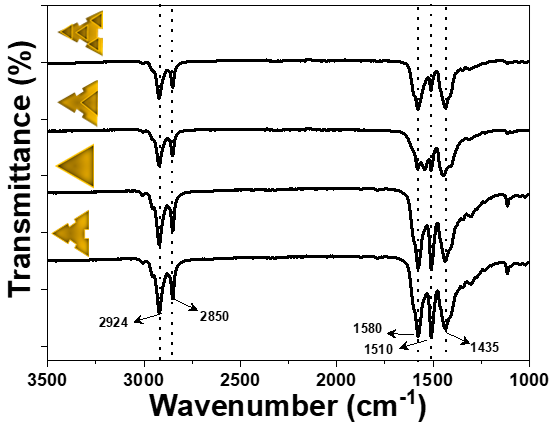

Figure 5. FT-IR spectra of yttrium oxide based colloidal nanocrystals synthesized via the thermal decomposition reactions in this work.

The presence of organic surfactants coating the surface of the obtained colloidal nanocrystals was investigated using Fourier Transform Infrared (FTIR) spectroscopy (see Figure 5). The FTIR analysis reveal that the surface of these colloidal nanocrystals is coated with oleic acids moieties in the form of a bridging or an ionic ligand.[60] The absence of the typical vibrational bands of OLAC and OLAM such as the ν(C=O) stretching band located at 1710 cm^{-1} and the bending δ (NH_2) band located at 1595 cm^{-1}, and the presence of bands located at 1580 cm^{-1}, 1510 cm^{-1} and 1435 cm^{-1}, ascribed to the antisymmetric and symmetric stretching vibrations of the deprotonated carboxylic group (COO^-), indicate that the OLAC molecules were deprotonated and transformed into carboxylate anions, catalyzed by OLAM.[75] Thus, the oleate-capping ligand renders the

nanocrystals to be hydrophobic and, as a result, they are dispersible in apolar organic solvents, forming clear transparent stable solutions (check Figure S3 at Supporting Information).

Scheme 1. Scheme proposed to explain the thermal decomposition synthesis of the different Y_2O_3 colloidal nanocrystal: A. Experimental setup applied. Synthesis of: B. core Ho, Tm:Y_2O_3. C. core@shell Ho, Tm:Y_2O_3@Y_2O_3. D. layer-by-layer Ho, Tm:Y_2O_3/Y_2O_3 colloidal nanoarchitectures.

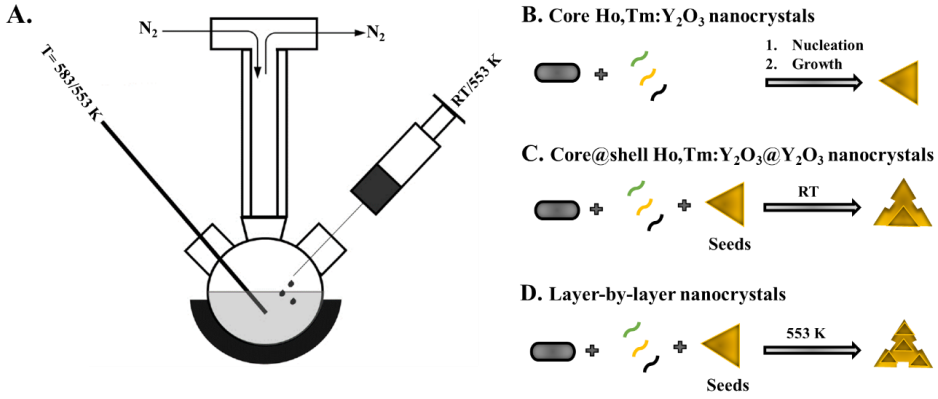

Scheme 1 displays a general sketch of the seeded-growth thermolysis methodologies used to synthesize the core, core@shell and layer-by-layer Ho, Tm:Y_2O_3@Y_2O_3 colloidal nanocrystals. The core nanocrystals act as seeds for the synthesis of core@shell nanocrystals, by being added at room temperature (RT), dispersed in an apolar organic solvent (cyclohexane in our case) and for the synthesis of layer-by-layer Ho, Tm:Y_2O_3/Y_2O_3 colloidal nanocrystals by being injected at the crystallization temperature (583 K). The same scheme is applied also for the synthesis of layer-by-layer structures, with the difference that the core material is injected at 583 K after being predissolved in oleylamine.

3.2. Photoluminescence of the yttrium oxide based colloidal nanocrystals

The emissions in the III-BW of the core, core@shell and the layer-by-layer Ho^{3+}, Tm^{3+}:Y_2O_3 colloidal nanocrystals were recorded after exciting the nanocrystals with a NIR 808 nm light source, using a power of 800 mW. The emissions, presented in Figure 6 (a), regardless of the nature of the nanocrystals, consist of three emission bands: the ones centered at around 1.5 µm and 1.85 µm, attributed to the $^3H_4 \rightarrow {}^3F_4$ and $^3F_4 \rightarrow {}^3H_6$ electronic transitions of Tm^{3+}, respectively, and a small band located at around 2.1 µm, attributed to the $^5I_7 \rightarrow {}^5I_8$ electronic transition of Ho^{3+}.The intensity of the emissions generated by the core@shell nanocrystals is the highest recorded, whereas the intensity for the core only nanocrystals decreased around 1.2 times. The layer-by-layer nanocrystals exhibited the lowest intensity in the III-BW, among the nanocrystals analyzed.

The location of the bands of Tm^{3+} and Ho^{3+} in Y_2O_3, is contradictory in literature. For example, for singly doped Tm^{3+}:Y_2O_3 single crystals, the band at 1.5 µm is either not present,[76] or centered at 1.55 µm,[77] whereas the band at 1.85 µm consists of a broad emission band extending from ~1.6 to above 2 µm, with the maximum intensity located at around 1.95 µm.[77] For Tm^{3+} doped Y_2O_3 nanopowders, the band at 1.5 µm has not been reported previously, whereas the band at 1.85 µm has a similar shape than that observed for Tm^{3+}:Y_2O_3 single crystals.[78] For Ho^{3+} doped Y_2O_3 materials, no reports about their experimental emissions can be found in the literature, and only the calculated stimulated emission cross-section has been reported for the case of ceramics, with two emission bands, one located at around 1.93-1.94 µm, with a higher intensity, and another broad band with lower intensity centered at around 2.1 µm.[79]

Thus, according to the results previously reported in the literature, the Ho^{3+}, Tm^{3+}:Y_2O_3 colloidal nanocrystals reported here, represent the first Y_2O_3 nanoparticles dually doped with Ho^{3+} and Tm^{3+}. From our observations, the presence of Ho^{3+} in the crystals seems to enhance the intensity

of the first emission band of Tm^{3+} (1.5 µm), and changes substantially the shape of the band at 1.85 µm, enhancing the intensity of the peaks lying at short wavelengths and decreasing the intensity of the peaks located at longer wavelengths. In this way, the maximum intensity is not encountered at ~1.95 µm, but at ~1.85 µm. This band, in fact, would overlap the emission band of Ho^{3+} located at around 1.93-1.94 µm, and they cannot be distinguished. But what is sure, is that the presence of this band does not reinforce the intensity of the peaks lying at longer wavelengths, but the opposite. From another side, the band at 2.1 µm can be clearly seen in our case, although with a lower intensity for the case of the core only nanocrystals.

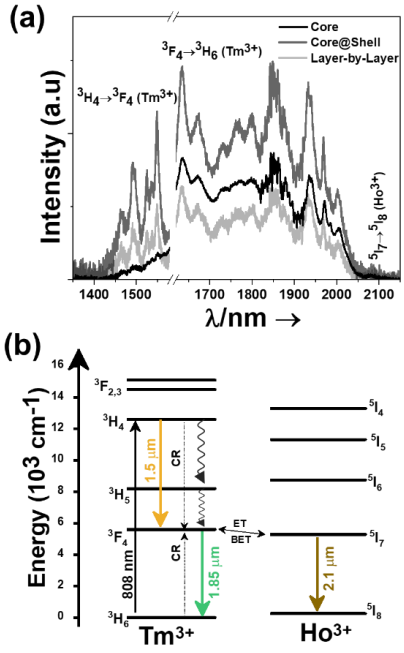

Figure 6. (a) Emissions in the III-BW recorded at room temperature for the core only, core@shell and the layer-by-layer Ho, Tm:Y_2O_3 colloidal nanocrystals, excited at 808 nm. Please note that part of the graph from 1580 nm to 1620 nm was removed due to the presence of a higher harmonic order of the 808 nm laser source. (b) Energy level diagram of Ho^{3+} and Tm^{3+} ions in Y_2O_3 and the mechanisms of generation of their emission lines in the III-BW. Solid arrows indicates radiative processes. The red arrow indicate the absorption process excited by the 808 nm laser. The black arrows indicate the radiative emissions. Curved arrows indicate non-radiative multiphonon decays processes. The dashed arrows stands for the cross relaxation (CR) process in Tm^{3+}. Finally, the double sided arrow stands for the energy transfer and back energy transfer processes that can take place between Ho^{3+} and Tm^{3+} ions.

A representation of the mechanism of the generation of the emission lines in these nanocrystals is presented in Figure 6 (b). The generation of these emission bands involves the absorption of the NIR 808 nm excitation light from the $^3H_6$ electronic ground state level of Tm^{3+}, promoting the electrons to the $^3H_4$ excited state. The 1.5 µm emission band is produced from the radiatively decay of the electrons from the $^3H_4$ excited state to the $^3F_4$ manifold. Further decay to the ground state, give rise to the second thulium emission band at 1.85 µm. Tm^{3+} ions also undergo a cross-relaxation (CR) process into the $^3F_4$ excited state, involving one ion excited in the upper $^3H_4$ excited state and another ion in its $^3H_6$ ground state. Furthermore, and due to the energy resonance between the $^3F_4$ level of Tm^{3+} and the $^5I_7$ level of Ho^{3+}, an energy transfer (ET) and back energy transfer (BET) processes might take place, promoting the electrons of Ho^{3+} to this excited state from the ground state. Then, the electrons of Ho^{3+} relax radiatively to the $^5I_8$ ground state, giving rise to the holmium emission band at 2.1 µm.[80] The existence of this last energy transfer mechanism would explain the reduction of intensity of the emission band of Tm^{3+} located

at 1.85 μm observed in our nanocrystals in benefit of the 2.1 μm emission band of Ho^{3+}, and as a consequence, the increase we observed of the intensity of the emission band located at 1.5 μm.

The higher intensity of the emission generated by the core@shell when compared to the emission of the only core nanocrystals is another evidence of the successful formation of the core shell nanoarchitectures.[80-81] Thus, these results confirm that the core@shell structures are beneficial for the improvement of the emission of this kind of crystals, due to the reduction of the probability of quenching mechanisms at the surface of the crystals to occur, by the creation of this inert shell layer that protects the active ions from being deexcited by their interaction with the surrounding medium. From another side, the fact that the layer-by-layer structures exhibited the smallest emission intensity would probe the fact that the active core is not protected by an inert layer, but instead, they grow one on the top of the other. Thus, in this case, the reduction of the emission intensity, might be explained by the increase of the surface to volume ratio, which exposes more active ions to the surrounding medium, due to the higher size of these nanostructures.

3.3. Thermal sensing capacity in the III-BW of the triangular Ho^{3+}, Tm^{3+} doped yttrium oxide colloidal nanocrystals

The thermal sensing capacity in the III-BW of the triangular Ho, Tm:Y_2O_3 colloidal nanocrystals, including core, core@shell and layer-by-layer nanocrystals, was determined from the evolution of the intensity ratio of the emissions in this region with the increase of the temperature from 313 K to 373 K, in the biological range of temperatures.[38] Increasing the temperature resulted in a decrease of the intensity of the emissions in core only and core@shell nanocrystals (see Figure S4 (a) at Supporting Information) as presented in Figure 7 (a), mainly due to the thermal activation of the luminescence quenching mechanisms.[82] For the layer-by-layer nanostructures, the increase of the temperature resulted in increase of the intensity of the emissions, especially of the 1.85 μm band (see Figure S4 (b) at Supporting Information). The intensity ratio was calculated from the integrated intensity for the 1.5 μm, the Stark sublevels of the $^3F_4 \rightarrow {}^3H_6$ transitions located at 1.8 μm and 1.96 μm, and the 2.1 μm, at different temperatures. Four different intensity ratios were calculated corresponding to the ratio between the non-thermally coupled emissions located at: (i) 1.45 μm/1.8 μm, (ii) 1.45 μm/1.96 μm, (iii) 1.45 μm/2.1 μm, and between the thermally coupled emissions located at: (iv) 1.8 μm/1.96 μm. Thermally coupled levels represent transition with energy gap (ΔE) of the order of 200 cm^{-1} to 2000 cm^{-1}.[83]

Figure 7 (b) shows the evolution of these four intensity ratios with the temperature for the core only nanocrystals, and in Figure S5 (a) and (b) in the Supporting Information for the core@shell and the layer-by-layer structures. From this figures, it is evident that the intensity ratio arising from the Stark sublevels (1.8 μm/1.96 μm) is the one showing the biggest slope, *i.e.* the intensity ratio that is affected the most by the change of the temperature.

Figure 7 (c) compares the evolution of the 1.8 μm/1.96 μm intensity ratio with the temperature for the core only, core@shell and layer-by-layer Ho^{3+}, Tm^{3+} doped yttrium oxide colloidal nanocrystals. From the graph, it can be observed that we obtain a bigger slope for the core only nanocrystals, making them the more thermal sensible, and thus, the best choice to develop a luminescent nanothermometer based on these structures.

In fact, the core@shell structures, in which the active lanthanide ions are protected by the inert shell layer from the environment, show the smallest slope. This would indicate that, despite the inert shell contributes to have a brighter emission, it is also hampering the quenching mechanisms from the surrounding ligands and solvent molecules, which seem to be activated as the temperature increases. From another side, if we compare the slope of the core only nanocrystals with that of the layer-by-layer structures, we can see that the slope of the latter is much smaller that the former. This might be due to two different parameters. On the first hand, the fact that the intensity of these structures is the smallest among the analyzed colloidal nanocrystals (see Figure 6 (a)) indicates that their quantum efficiency is smaller also, influencing their thermal sensing performance. On the second hand, the fact that one side of the nanocrystals, at least, is in contact with the inert layer grown in the second step of the synthesis process reduces the contact area of the solvent molecules with the active nanocrystals (and maybe also the concentration of

surfactant molecules attached to the surfaces in contact with the active ions), making that the thermal quenching mechanisms are not as effective as in the first case.

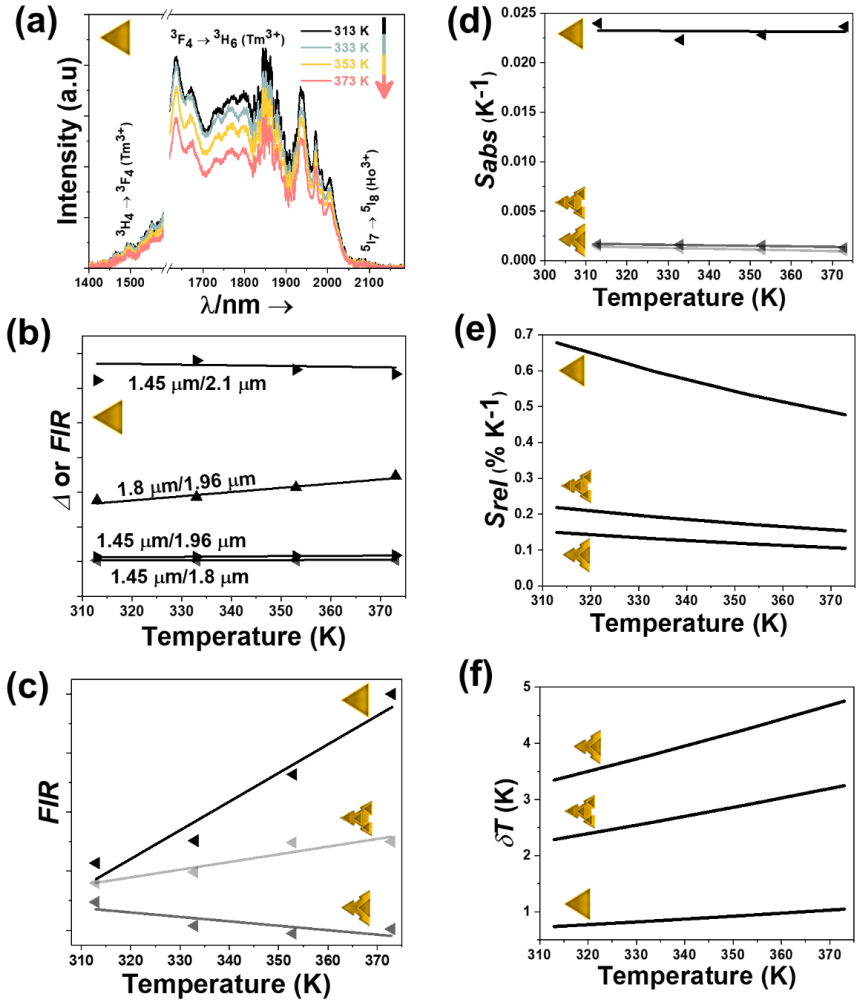

Figure 7. (a) Variation of the emission bands of the Ho, Tm:Y_2O_3 core only nanocrystals with the increase of the temperature. (b) Temperature-dependence of the intensity ratio (Δ or FIR) of the four emission bands of Ho, Tm:Y_2O_3 core only nanocrystals. (c) Temperature dependence of FIR (experimental data and linear fitting according to Equation 3 for 1.8 μm/1.96 μm) for core, core@shell and layer-by-layer colloidal nanocrystals. (d) Determination of the absolute thermal sensitivity (S_{abs}), (e) Determination of the relative thermal sensitivity (S_{rel}), and (f) Determination of the temperature resolution (δT) for core, core@shell and layer-by-layer Ho, Tm doped yttrium oxide based colloidal nanocrystals, from the 1.8 μm/1.96 μm ratio.

The relation between the intensity ratio (Δ) and the temperature between the non-thermally coupled levels considers the total transition probability of an emitting level is the sum of the radiative and non-radiative transition probabilities,[84] and relating the integrated luminescence intensity to the inverse of the total transition probability,[85] this relationship is expressed as:

$$\Delta = \frac{I_1}{I_2} = \Delta_0 \frac{1+\sum_i \alpha_{2i}\, exp\left(-\frac{\Delta E_{2i}}{k_B T}\right)}{1+\sum_i \alpha_{1i}\, exp\left(-\frac{\Delta E_{1i}}{k_B T}\right)} \qquad (1)$$

where 1 and 2 are the two emissions whose intensities are used to estimate the thermometric performance (either 1.45 μm/1.8 μm, 1.45 μm/1.96 μm or 1.45 μm/2.1 μm); Δ_0 stands for the ratio between the I_{01}/I_{02} at 0 K for 1 and 2 emissions; α_{2i} and α_{1i} stands for the ratio between the non-radiative and radiative probabilities for the emitting level of the electronic transitions 1 and 2, respectively; and the sum sign extends from *i*= 1 to *n*, being *n* all possible non-radiative process deactivation channels of transitions with intensities I_1 and I_2. Finally, ΔE_{2i} and ΔE_{1i} are the activation energies for the thermally quenched processes of transitions 1 and 2.

In a scenario in which the exponential term dominates in the intensities of the transitions involved, as it is our case, and assuming a single deactivation channel ($1 \ll \alpha_j \exp(-\Delta E_j/k_B T)$, Equation 1 could be transformed into:

$$\Delta = \Delta_0 \frac{\alpha_{2i}}{\alpha_{1i}} \frac{exp\left(-\frac{\Delta E_2}{k_B T}\right)}{exp\left(-\frac{\Delta E_1}{k_B T}\right)} = B \exp\left(\frac{\Delta E_1 - \Delta E_2}{k_B T}\right) = B \exp\left(\frac{-C}{T}\right) \quad (2)$$

where $B=\Delta_0 \frac{\alpha_{2i}}{\alpha_{1i}}$ is an empirical constant to be determined by fitting and $C = \frac{\Delta E_1 - \Delta E_2}{k_B}$ is the energy difference between the two activation energies for the thermally quenched processes, while k_B is the Boltzmann constant expressed in cm^{-1} (k_B=0.695 cm^{-1}).

The intensity ratio between the thermally coupled levels can be related to the temperature by the so-called fluorescence intensity ratio (FIR), expressed as:[86-87]

$$FIR = \frac{I_1}{I_2} = \frac{g_1 \vartheta_1 A_1}{g_1 \vartheta_1 A_1} \exp\left(-\frac{\Delta E}{k_B T}\right) = B \exp\left(-\frac{\Delta E}{k_B T}\right) \quad (3)$$

where I_1 and I_2 stand for the integrated intensity of the Stark sublevels of the $^3F_4 \rightarrow {}^3H_6$ transitions located at 1.8 μm and 1.96 μm, g_1 and g_1 are the degeneracy of the Stark sublevels, respectively; ϑ_1, ϑ_1, A_1 and A_1 are the frequencies and spontaneous emission rates corresponding to these levels; B is the pre-exponential constant; ΔE is the energy gap between the Stark sublevels in the particular host; k_B is the Boltzmann's constant (k_B=0.695 cm^{-1}) and T is the absolute temperature.

By fitting Equation 1 to the experimental integrated area of 1.45 μm/1.8 μm, 1.45 μm/1.96 μm, 1.45 μm/2.1 μm, the value of the constants B and C are deduced. Table S2 at the Supporting Information summarizes the values of the constants, together with the fitting parameter and their thermal sensing capacity of all non-thermally coupled levels, depending on the morphology of the nanocrystals employed.

Equation 3 can be rewritten in the logarithmic form as:

$$\ln(FIR) = \ln(B) + \left(\frac{\Delta E}{k_B T}\right) = \ln(B) + \left(-\frac{C}{T}\right) \quad (4)$$

where B and C represent constants determinate from experimental calibration of the dependence of the intensity ratio with the change of temperature. The variation of logarithmic form of FIR in the range of 298 K-373 K obeys to a linear tendency (check Figure S6 at the Supporting Information). From this fitting, the values of the intercept, the slope and the energy gap for each type of nanocrystals, are calculated and presented in Figure S6 at the Supporting Information. Knowing these values, allows us to determine the thermometric performance of each nanocrystals.

The thermal sensing performance of the nanothermometers we developed, can be evaluated by estimating the absolute thermal sensitivity (S_{abs}), the relative thermal sensitivity (S_{rel}), and the temperature resolution (δT). These parameters are strictly proportional to the slope obtained from the intensity ratio equations (Equation 2 and Equation 3), thus, since the slope derived from the experimental data of the intensity ratio between the thermally coupled levels is higher compared to the non-thermally coupled levels, in the following, we present the performance of these nanocrystals as a function of this ratio.

The absolute thermal sensitivity is defined as the change of the intensity ratio with the temperature:[88]

$$S_{abs} = \frac{\partial FIR}{\partial T} \qquad (5)$$

Substituting Equation 3, the value of the absolute thermal sensitivity for the case of the thermally coupled levels, is expressed as:

$$S_{abs} = FIR\ \frac{\Delta E}{k_B T^2} \qquad (6)$$

Despite the absolute thermal sensitivity is frequently applied in the literature, cannot be used to compare the performance of luminescent thermometers of different nature, as it depends on the sample characteristics (absorption and lifetimes) and on the experimental setup used.[31] Thus, S_{abs} allows to compare the performance of these different Ho^{3+}, Tm^{3+}:Y_2O_3 colloidal nanocrystals as luminescence nanothermometers only among them. Figure 7 (c) shows that the core only colloidal nanocrystals exhibit the highest absolute thermal sensitivity, for a value of 0.0048 K^{-1} at the lowest temperature under investigation.

However, S_{abs} does not allow for comparison with other thermal nanoprobes, thus, the relative thermal sensitivity was introduced as a figure of merit.[31] Compared to S_{abs}, the relative thermal sensitivity S_{rel} presents the critical advantage to be independent of the nature of the thermometer, allowing direct and quantitative comparison between different samples.[31] The relative thermal sensitivity expresses the maximum change in the FIR for each temperature degree and it is defined as:[31]

$$S_{rel} = \frac{1}{FIR}\left|\frac{\partial FIR}{\partial T}\right| x\ 100\ \% \qquad (7)$$

Substituting Equation 2, the value of the absolute thermal sensitivity for the case of the thermally coupled levels, is expressed as:

$$S_{rel} = \frac{\Delta E}{k_B T^2}\ x\ 100\ \% \qquad (8)$$

The highest relative thermal sensitivity among the different Ho^{3+}, Tm^{3+}:Y_2O_3 colloidal nanoarchitectures investigated corresponds again to the core only Ho^{3+}, Tm^{3+}:Y_2O_3 nanocrystals with a value of 0.68% K^{-1} at 313 K. The lowest one corresponds to the core@shell nanostructures, achieving a relative thermal sensitivity of 0.15% K^{-1} at 313 K, whereas the layer-by-layer nanocrystals present a relative thermal sensitivity of 0.22% K^{-1} at 313 K (Figure 7 (d)). A general trend observed in the evolution of the relative thermal sensitivity, is its decrease as the temperature increased.

Additionally, the temperature resolution (δT) is also another parameter to determine the thermometer's performance. The temperature resolution is defined as the smallest temperature change that can be resolved in a given measurement and it is estimated as:[31]

$$\delta T = \frac{1}{S_{rel}}\frac{\delta\Delta}{\Delta} \qquad (9)$$

where $\frac{\delta\Delta}{\Delta}$ is the relative error in the determination of the thermometric parameter. This parameter depends on the acquisition setup used, and a typical value that can be used for conventional detection system is 0.5 %.[89] Substituting the expression of relative thermal sensitivity (Equation 8) to Equation 9, the value of the temperature resolution for the case of the thermally coupled levels, is expressed as:

$$\delta T = \frac{k_B T^2}{\Delta E}\frac{\delta\Delta}{\Delta} \qquad (10)$$

The core only Ho, Tm:Y_2O_3 colloidal nanocrystals exhibits the smallest temperature resolution with a value of 0.73 K at the lowest temperature studied (see Figure 7 (e)). The core@shell and the layer-by-layer nanoarchitectures present higher temperature resolution values (3.33 K and 2.28 K, respectively) at 313 K. A general trend observed in the evolution of the temperature resolution, is its increase as the temperature increased. Table 1 summarizes all the parameters used to determine the thermometric performance of the Ho, Tm:Y_2O_3 colloidal nanoartichectures based on the ratio between the thermally coupled levels 1.8 μm/1.96 μm. Following the same strategy, also the performance of these nanocrystals based on the non-thermally coupled levels can be evaluated, by simply substituting Equation 2 to the expression of S_{abs}, S_{rel} and δT. These results are summerised in Table S2 at the Supporting Information. As expected, due to the highest slope obtained from the thermally coupled 1.8 μm/1.96 μm levels, their performance is relatively higher compared to the performance of non-thermally coupled levels. In addition, the thermometric performance of non-thermally coupled levels are also based on the weak intensity emission at 2.1 μm, which results in low value of fitting parameters and may provide uncertainty of the calculation of thermal sensing parameters, as the performance is highly dependent on the strength of the signal.[31,90]

Table 1. Fitting parameters, S_{abs}, S_{rel} and δT of different Ho,Tm:Y_2O_3 colloidal nanocrystals, calculated from the ratio between the thermally coupled levels.

Material	B	C	ΔE (cm^{-1})	R^2	S_{abs} (K^{-1})	S_{rel} (% K^{-1})	δT (K)
Core	5.75	663.9	461.4	0.95	0.024	0.67	0.73
Core@Shell	2.45	146.4	101.8	0.75	0.0014	0.15	3.34
Layer-by-Layer	1.33	214.3	148.9	0.92	0.0015	0.22	2.28

Knowing the thermometric performance of the core, core@shell and layer-by-layer based Ho, Tm:Y_2O_3 colloidal nanocrystals, now we can compare their performance with other nano/microcrystals operating also in the III-BW as possible thermometers. The results of this comparison can be seen in Figure 8, in which the temperature resolution (the smallest temperature change that can be determined with the nanothermometers) is presented.

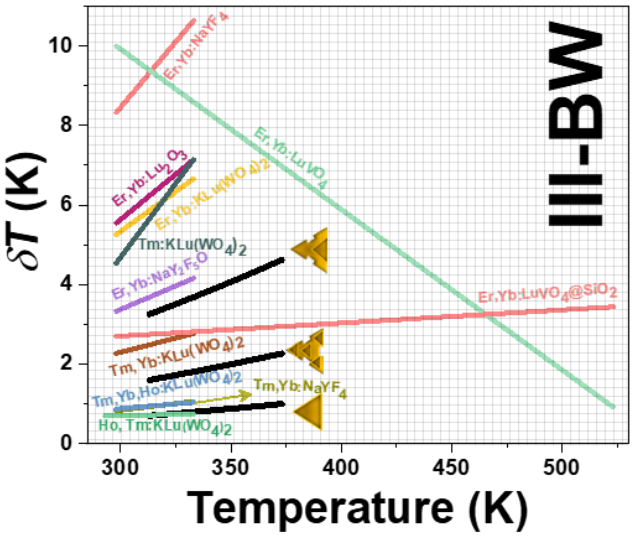

Figure 8. Comparison of the performance of the lanthanide doped luminescent nanothermometers operating in the III-BW. The core, core@shell and layer-by-layer Ho, Tm:Y_2O_3 colloidal nanocrystals are depicted in thick black lines and in their corresponding shapes.

The core only nanotriangles show a temperature resolution comparable with that of Ho, Tm:$KLu(WO_4)_2$ nanocrystals synthesized via a sol-gel method,[26] and the Tm,Ho,Yb: $KLu(WO_4)_2$ and Tm, Yb: $NaYF_4$,[91] which are among the nanothermometers with the best performances in the III-BW. In general, core@shell and layer-by-layer Ho, Tm:Y_2O_3 colloidal nanocrystals exhibit thermometric performances comparable to those of Er, Yb doped materials: $LuVO_4@SiO_2$,[92] and NaY_2F_5O,[91] and Tm, Yb:$KLu(WO_4)_2$.[91] The performance of these nanoarchitectures is better than that of other Er, Yb doped materials ($LuVO_4$,[93] $NaYF_4$,[91] and Lu_2O_3,[91] and Tm:$KLu(WO_4)_2$).[91] It should be admitted here that in the case of Er^{3+} doped materials: $LuVO_4$,[92] and $LuVO_4@SiO_2$,[93] their performance is evaluated in an wide range of temperatures from 298-523 K (including also the physiological range). Their maximum temperature resolution at the physiological range are 2.7 and 10 K for $LuVO_4@SiO_2$ and $LuVO_4$, respectively.

3.4. Photothermal conversion efficiency of Ho, Tm:Y_2O_3 colloidal nanocrystals

When excited with NIR 808 nm excitation light, the nanocrystals can absorb light and convert it either to luminescence or to heat. The part of the absorbed light that is converted into heat can be defined as photothermal conversion. Normally, this conversion of light into heat, due to non-radiative processes, has been avoided traditionally in luminescent materials through the design of the material to maximize their luminescent properties. However, in the last years it has been seen as an opportunity tool for the treatment of different diseases, as cancer, through light-activated hyperthermia processes.[38] Even more, if this release of heat can be controlled at a local scale through the measurement of the temperature with the same tool, developing the so called self-assessed photothermal conversion agents, it makes these nanotools as one of the most promising strategies for the treatment of several diseases in nanomedicine.[26] The best way to measure the performance of the material for these purposes is by measuring its photothermal conversion efficiency.[38]

We determined the photothermal conversion efficiency of different Ho^{3+}, Tm^{3+}:Y_2O_3 colloidal nanocrystals via the integrated sphere method (see Figure 9 (a)).[59, 81, 82] The integrated sphere method, and accounting as a benefit in comparison with other methods used to measure the photothermal conversion efficiency, accounts for the portion of light converted into another emission of light, and the scattered, reflected and transmitted portions of the original light source with which the sample has been illuminated. Thus, just by comparing the power of the initial light source and that after interacting with the sample, we can know which portion has been converted into heat.[59]

When the different Ho, Tm:Y_2O_3 colloidal nanocrystals (show in Figure 9 (a)), are illuminated with 808 nm light source, the light can be absorbed by the nanocrystals (represented as red spheres), scattered (represented as green arrows) and reflected (represented as gold arrows) from the surface of our nanocrystals or the cuvette or transmitted (represented as violet arrows). To calculate the photothermal conversion efficiency (η), we used the following expression:[59]

$$\eta = \left|\frac{P_{blank} - P_{sample}}{P_{empty} - P_{sample}}\right| x\ 100\% \qquad (11)$$

where P_{blank}, P_{empty} and P_{sample} are the radiation power values measured for the solvent (cyclohexane in this case), the empty cuvette and the dispersion of colloidal nanocrystals (core, core@shell and layer-by-layer Ho, Tm:Y_2O_3 colloidal nanocrystals) in cyclohexane, respectively.

The photothermal conversion efficiency of the core only, core@shell and layer-by-layer nanoarchitectures as a function of the laser power is presented in Figure 9 (b). As can be seen, the light-to-heat conversion of the nanocrystals is independent of the laser power applied. The core only nanotriangles, which demonstrated the best thermal sensing ability, exhibit a value of photothermal conversion efficiency ~15%, similar to that exhibited by the layer-by-layer based structures. The highest photothermal conversion efficiency was obtained for the core@shell nanocrystals, with a value of 34%, which is more than two times higher than that of the other nanocrystals.

The ability of a lanthanide doped compounds to convert the absorbed light into heat, is attributed to the effectiveness of the non-radiative processes.[26] Comparing the ability of the core@shell with the core only particles, as two of the best nanoheaters among the tested colloidal nanocrystals tested here, a defined and paramount effect is attributed to the presence of the shell layer. So, for the core@shell nanoparticles, the non-radiative mechanisms would be governed by the intra-ions or inter-ions interactions also with the crystalline host. For the case of core only nanoparticles, besides these interactions, additional non-radiative processes can take place at the surface of the material by their interaction with the surrounding ligands. In order to determine where these mechanisms are more effective, the variation of the intensity of the emission bands with the temperature should be taken into account. A fast decrease in the intensity of the emission with the increase of the temperature, will indicate a very effective non-radiative emission and as a consequence, a higher ability of generating heat.

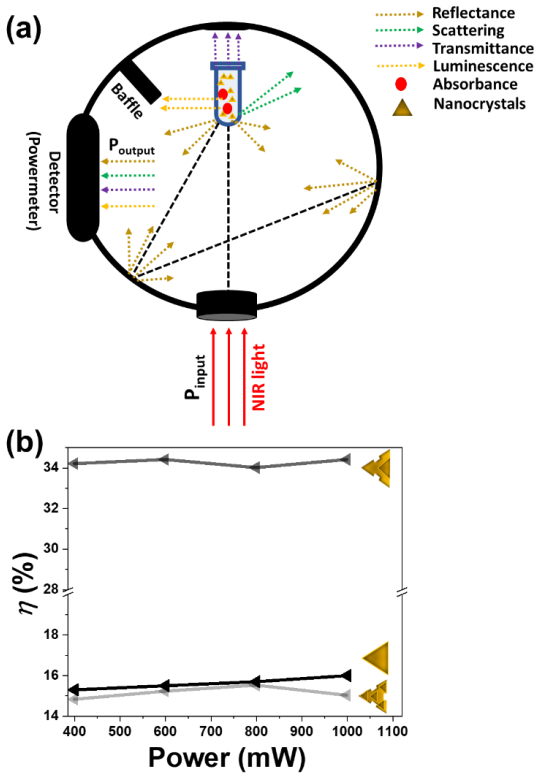

Figure 9. (a) Schematic representation of the setup used for the determination of the photothermal conversion efficiency of Ho, Tm:Y_2O_3 colloidal nanocrystals by the integrating sphere method,[59] and (b) Evolution of the photothermal conversion efficiency of core only, core@shell and layer-by-layer Ho, Tm:Y_2O_3 colloidal nanoarchitectures with the power of the excitation laser.

To proof this statement, for the core only and core@shell, we monitored the decrease of the intensity of the three emission bands (1.5 μm, 1.85 μm and 2.1 μm) with the increase of the temperature from 313 to 373 K. For core@shell nanoparticles, the intensity of the bands at 1.5 μm (Figure 10 (a)) and 1.85 μm (Figure 10 (b)), decrease faster than for the core only nanoparticles, while the band at 2.1 μm (Figure 10 (c)) decreases slowly. The effect of the temperature is more evident for the 1.85 μm band, with an overall decrease down to almost 30%. The non-radiative process happening from the $^3H_4$ to $^3F_4$ (see Figure 6 (b)), would affect to the intensity of the 1.5 μm band and a faster decrease of this emission band in core@shell compared to core only, is an indication of a more effective mechanism on these particles. For the emission band located at 1.85 μm, would be affected by the energy transfer between the quasi-resonant energy levels of $^3F_4$ level of Tm^{3+} and the $^5I_7$ level of Ho^{3+}. When the energy transfer process is

produced, part of the energy is lost in the form of heat, and according to Figure 10 (b), this process is more effective for the core@shell nanoartichectures, indicating yet again that more heat is released from these particles.

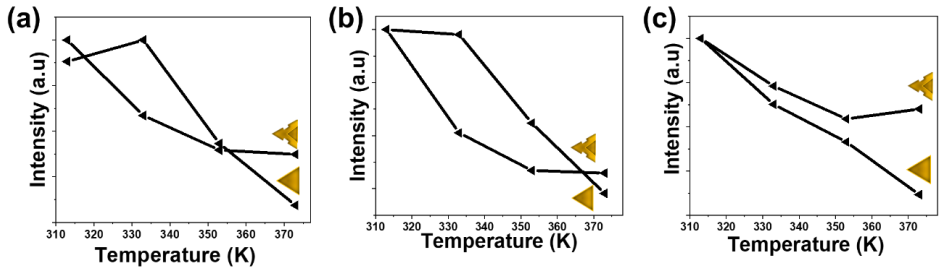

Figure 10. Variation of the intensity of the emissions: (a) 1.5 μm, (b) 1.85 μm and (c) 2.1 μm with the temperature for core and core@shell nanoartichectures. The lines represent a guide for the eyes of the readers.

These comparisons on the temperature-dependence of intensity of the emission bands, proofs a novel methodology to underline the effects arising from the incorporation of the shell on the generation of heat. These explanation could be also applied in other type of materials, for example active core@active shell Er,Yb:$NaYF_4$@Tm, Yb:$NaYF_4$ nanoparticles, in which the thermal sensing of the core only is higher than that of the active core@active shell, but the light-to-heat conversion ability of the later ones, exhibit a net temperature increment of 7 K when compared to the core only Er,Yb:$NaYF_4$ nanoparticles.[39] The dual performance of these particles (as thermal sensors and photothermal agents) was determined from the green emission of Er^{3+} ions ($^4S_{3/2}$ and $^2H_{11/2}$), after excitation with NIR 980 nm excitation. If we observe the decrease of the intensity of the emission bands, it is clear that the band of $^2H_{11/2}$ in the core@shell particles is highly influences from the temperature compared to the core only particles.[39] Thus, by applying our novel methodology, a reasoning behind these observation, can be given.

Comparing the photothermal conversion efficiency of this core@shell nanocrystals with other photothermal agents reported in the literature, the Ho, Tm:Y_2O_3@Y_2O_3 colloidal nanocrystals exhibit a higher photothermal conversion efficiency than other metallic such as Au nanoshells (η ~ 25%)[94] and semiconductor nanocrystals including $Cu_{2-x}Se$ (η ~ 22%),[95] Cu_9S_5 (η ~ 25.7%),[96] and FePt (η ~ 30%).[97] The efficiency of these nanocrystals is even higher than that of some other lanthanide based materials including hexagonal Nd^{3+}:$NaYF_4$ (η ~ 21.3%),[98] orthorhombic NdF_3 (η ~ 10.3%),[98] and tetragonal Nd:$LiYF_4$ (η ~ 1.6%).[98] The ability of the core@shell to convert light into heat is similar to that of Au/SiO_2 nanoshells (η ~ 34%).[99] However, when compared to the performance of other lanthanide based nanomaterials, involving Ho, Tm doped $KLu(WO_4)_2$ with η ~ 40%,[26] $NdVO_4$ with η ~ 72.1%,[28] or core@shell@shell $NaNdF_4$@$NaYF_4$@$NaYF_4$:Nd with η ~ 72.7%,[27] the performance of this core@shell colloidal nanocrystals is lower. Their performance is lower when compared also carbon based materials, such as graphene (η ~ 64%),[59] or gold nanocrystals such as nanorods (η ~ 95%),[100] or nanostars (η ~ 102%).[100]

4. Conclusions

Core, core@shell and layer-by-layer structures based on cubic Ho, Tm doped Y_2O_3 nanoarchitectures were synthesized via thermal decomposition methodologies in the presence of coordinating organic surfactants (oleic acid and oleylamine) and $NaNO_3$ as a structure directing agent. These colloidal nanocrystals nanoarchitectures were applied as potential luminescent nanothermometers in the III-BW and as photothermal conversion agents, after excitation with a NIR 808 nm light source, lying in the I-BW. Despite the brightest emission in the III-BW was obtained for the core@shell structures, due to the protecting effect of the shell layer against quenching mechanisms generated by solvent molecules and ligands attached to the surface of the nanocrystals, the best thermal sensing performance was observed in the core only

nanocrystals with a value of 0.68% K^{-1} and temperature resolution of 0.73 K at the lowest temperature analyzed, 313 K. For the the photothermal conversion efficiency, the core@shell nanocrystals exhibited the highest conversion η=34%, two times higher than that of the core only and layer-by-layer nanoarchitectures. This value of the photothermal conversion efficiency is assigned to the effectiveness of the non-radiative processes occurring in the core@shell particles, due to the presence of the shell.

5. Acknowledgments

This work was supported by the Spanish Government under projects MAT2016-75716-C2-1-R (AEI/FEDER, UE) and by the Generalitat de Catalunya under project 2017SGR755. A.N acknowledges financial support from the Generalitat de Catalunya under grant 2017FI_B00620, 2018FI_B100161 and 2019FI_B200154.

6. References

1. Rogobete, L.; Kaminski, F.; Agio, M.; Sandoghdar, V., Design of plasmonic nanoantennae for enhancing spontaneous emission. *Optics Letters* **2007,** 32 (12), 1623-1625.
2. Jain, P. K.; Lee, K. S.; El-Sayed, I. H.; El-Sayed, M. A., Calculated absorption and scattering properties of gold nanoparticles of different size, shape, and composition: applications in biological imaging and biomedicine. *Journal of Physical Chemistry B* **2006,** 110 (14), 7238-7248.
3. Ye, S.; Song, J.; Tian, Y.; Chen, L.; Wang, D.; Niu, H.; Qu, J., Photochemically grown silver nanodecahedra with precise tuning of plasmonic resonance. *Nanoscale* **2015,** 7 (29), 12706-12712.
4. Cassar, R. N.; Graham, D.; Larmour, I.; Wark, A. W.; Faulds, K., Synthesis of size tunable monodispersed silver nanoparticles and the effect of size on SERS enhancement. *Vibrational Spectroscopy* **2014,** 71, 41-46.
5. Hu, J.; Li, L.; Yang, W.; Manna, L.; Wang, L.; Alivisatos, A. P., Linearly polarized emission from colloidal semiconductor quantum rods. *Science China Materials* **2001,** 292 (5524), 2060-2063.
6. Li, L.; Hu, J.; Yang, W.; Alivisatos, A. P., Band gap variation of size- and shape-controlled colloidal CdSe quantum rods. *Nano Letters* **2001,** 1 (7), 349-351.
7. Johnson, N. J.; Oakden, W.; Stanisz, G. J.; Scott Prosser, R.; van Veggel, F. C., Size-tunable, ultrasmall $NaGdF_4$ nanoparticles: insights into their T1 MRI contrast enhancement. *Chemistry of Materials* **2011,** 23 (16), 3714-3722.
8. Boyer, J. C.; Van Veggel, F. C., Absolute quantum yield measurements of colloidal $NaYF_4$: Er^{3+}, Yb^{3+} upconverting nanoparticles. *Nanoscale* **2010,** 2 (8), 1417-1419.
9. Homann, C.; Krukewitt, L.; Frenzel, F.; Grauel, B.; Würth, C.; Resch-Genger, U.; Haase, M., $NaYF_4$:Yb,Er/ $NaYF_4$ core/shell nanocrystals with high upconversion luminescence quantum yield. *Angewandte Chemie International Edition* **2018,** 57 (28), 8765-8769.
10. Zhang, Y.; Zhang, L.; Deng, R.; Tian, J.; Zong, Y.; Jin, D.; Liu, X., Multicolor barcoding in a single upconversion crystal. *Journal of the American Chemical Society* **2014,** 136 (13), 4893-4896.
11. Fischer, S.; Bronstein, N. D.; Swabeck, J. K.; Chan, E. M.; Alivisatos, A. P., Precise tuning of surface quenching for luminescence enhancement in core-shell lanthanide-doped nanocrystals. *Nano Letters* **2016,** *16* (11), 7241-7247.
12. Deng, R.; Qin, F.; Chen, R.; Huang, W.; Hong, M.; Liu, X., Temporal full-colour tuning through non-steady-state upconversion. *Nature Nanotechnology* **2015,** 10 (3), 237-242.
13. Savchuk, O. A.; Carvajal, J. J.; Cascales, C.; Aguiló, M.; Díaz, F., Benefits of silica core-shell structures on the temperature sensing properties of Er,Yb:$GdVO_4$ up-conversion nanoparticles. *ACS Applied Materials & Interfaces* **2016,** *8* (11), 7266-7273.
14. Huignard, A.; Gacoin, T.; Boilot, J. P., Synthesis and luminescence properties of colloidal YVO_4:Eu phosphors. *Chemistry of Materials* **2000,** 12 (4), 1090-1094.
15. Hebbink, G. A.; Stouwdam, J. W.; Reinhoudt, D. N.; Van Veggel, F. C., Lanthanide (III)-doped nanoparticles that emit in the near-infrared. *Advanced Materials* **2002,** 14 (16), 1147-1150.
16. Wang, F.; Wang, J.; Liu, X., Direct evidence of a surface quenching effect on size-dependent luminescence of upconversion nanoparticles. *Angewandte Chemie International Edition* **2010,** 49 (41), 7456-7460.
17. Kömpe, K.; Borchert, H.; Storz, J.; Lobo, A.; Adam, S.; Möller, T.; Haase, M., Green-emitting $CePO_4$:Tb/$LaPO_4$ core-shell nanoparticles with 70% photoluminescence quantum yield. *Angewandte Chemie International Edition* **2003,** 42 (44), 5513-5516.
18. Boyer, J. C.; Gagnon, J.; Cuccia, L. A.; Capobianco, J. A., Synthesis, characterization, and spectroscopy of $NaGdF_4$: Ce^{3+}, Tb^{3+}/ $NaYF_4$ core/shell nanoparticles. *Chemistry of Materials* **2007,** 19 (14), 3358-3360.

19. Vetrone, F.; Naccache, R.; Mahalingam, V.; Morgan, C. G.; Capobianco, J. A., The active-core/active-shell approach: A strategy to enhance the upconversion luminescence in lanthanide-doped nanoparticles. *Advanced Functional Materials* **2009,** 19 (18), 2924-2929.
20. Su, Q.; Han, S.; Xie, X.; Zhu, H.; Chen, H.; Chen, C. K.; Liu, R. S.; Chen, X.; Wang, F.; Liu, X., The effect of surface coating on energy migration-mediated upconversion. *Journal of the American Chemical Society* **2012,** 134 (51), 20849-20857.
21. Wang, F.; Deng, R.; Wang, J.; Wang, Q.; Han, Y.; Zhu, H.; Chen, X.; Liu, X., Tuning upconversion through energy migration in core-shell nanoparticles. *Nature Materials* **2011,** *10* (12), 968-973.
22. Zhang, C.; Yang, L.; Zhao, J.; Liu, B.; Han, M. Y.; Zhang, Z., White-light emission from an integrated upconversion nanostructure: toward multicolor displays modulated by laser power. *Angewandte Chemie International Edition* **2015,** 54 (39), 11531-11535.
23. Zuo, J.; Sun, D.; Tu, L.; Wu, Y.; Cao, Y.; Xue, B.; Zhang, Y.; Chang, Y.; Liu, X.; Kong, X., Precisely tailoring upconversion dynamics via energy migration in core-shell nanostructures. *Angewandte Chemie International Edition* **2018,** 57 (12), 3054-3058.
24. Zhou, L.; Fan, Y.; Wang, R.; Li, X.; Fan, L.; Zhang, F., High-capacity upconversion wavelength and lifetime binary encoding for multiplexed biodetection. *Angewandte Chemie International Edition* **2018,** 57 (39), 12824-12829.
25. Li, X.; Guo, Z.; Zhao, T.; Lu, Y.; Zhou, L.; Zhao, D.; Zhang, F., Filtration shell mediated power density independent orthogonal excitations-emissions upconversion luminescence. *Angewandte Chemie International Edition* **2016,** 55 (7), 2464-2469.
26. Nexha, A.; Carvajal, J. J.; Pujol, M. C.; Díaz, F.; Aguiló, M., Short-wavelength infrared self-assessed photothermal agents based on Ho,Tm:KLu$(WO_4)_2$ nanocrystals operating in the third biological window (1.45-1.96 μm wavelength range). *Journal of Materials Chemistry C* **2020,** 8 (1), 180-191.
27. Marciniak, L.; Pilch, A.; Arabasz, S.; Jin, D.; Bednarkiewicz, A., Heterogeneously Nd^{3+} doped single nanoparticles for NIR-induced heat conversion, luminescence, and thermometry. *Nanoscale* **2017,** 9 (24), 8288-8297.
28. del Rosal, B.; Pérez-Delgado, A.; Carrasco, E.; Jovanović, D. J.; Dramićanin, M. D.; Dražić, G.; de la Fuente, Á. J.; Sanz-Rodriguez, F.; Jaque, D., Neodymium-based stoichiometric ultrasmall nanoparticles for multifunctional deep-tissue photothermal therapy. *Advanced Optical Materials* **2016,** 4, (5), 782-789.
29. Rocha, U.; Kumar, K. U.; Jacinto, C.; Ramiro, J.; Caamaño, A. J.; Solé, J. G.; Jaque, D., Nd^{3+} doped LaF_3 nanoparticles as self-monitored photo-thermal agents. *Applied Physics Letters* **2014,** 104 (5), 53703-53709.
30. Jaque, D.; Vetrone, F., Luminescence nanothermometry. *Nanoscale* **2012,** 4 (15), 4301-4326.
31. Brites, C. D. S.; Millán, A.; Carlos, L. D., Chapter 281-Lanthanides in Luminescent Thermometry. In *Handbook on the Physics and Chemistry of Rare Earths*, Jean-Claude, B.; Vitalij K, P., Eds. Elsevier: 2016; Vol. 49, pp 339-427.
32. Brites, C. D.; Lima, P. P.; Silva, N. J.; Millán, A.; Amaral, V. S.; Palacio, F.; Carlos, L. D., Thermometry at the nanoscale. *Nanoscale* **2012,** 4 (16), 4799-4829.
33. Wang, X.; Wolfbeis, O. S.; Meier, R. J., Luminescent probes and sensors for temperature. *Chemical Society Reviews* **2013,** 42 (19), 7834-7869.
34. Ximendes, E. C.; Rocha, U.; Sales, T. O.; Fernández, N.; Sanz-Rodríguez, F.; Martín, I. R.; Jacinto, C.; Jaque, D., In vivo subcutaneous thermal video recording by supersensitive infrared nanothermometers. *Advanced Functional Materials* **2017,** 27 (38), 1702249.
35. Rodrigues, E. M.; Gálico, D. A.; Lemes, M. A.; Bettini, J.; T. Neto, E.; Mazali, I. O.; Murugesu, M.; Sigoli, F. A., One pot synthesis and systematic study of the photophysical and magnetic properties and thermal sensing of α and β-phase $NaLnF_4$ and β-phase core@shell nanoparticles. *New Journal of Chemistry* **2018,** 42 (16), 13393-13405.
36. Geitenbeek, R. G.; Prins, P. T.; Albrecht, W.; van Blaaderen, A.; Weckhuysen, B. M.; Meijerink, A., $NaYF_4$:Er^{3+},Yb^{3+}/SiO_2 core/shell upconverting nanocrystals for luminescence thermometry up to 900 K. *Journal of Physical Chemistry C* **2017,** 121 (6), 3503-3510.
37. Xu, M.; Chen, D.; Huang, P.; Wan, Z.; Zhou, Y.; Ji, Z., A dual-functional upconversion core@shell nanostructure for white-light-emission and temperature sensing. *Journal of Materials Chemistry C* **2016,** 4 (27), 6516-6524.
38. Jaque, D.; Martínez Maestro, L.; del Rosal, B.; Haro-Gonzalez, P.; Benayas, A.; Plaza, J. L.; Martín Rodríguez, E.; García Solé, J., Nanoparticles for photothermal therapies. *Nanoscale* **2014,** 6 (16), 9494-9530.
39. Zhang, Y.; Chen, B.; Xu, S.; Li, X.; Zhang, J.; Sun, J.; Zheng, H.; Tong, L.; Sui, G.; Zhong, H.; Xia, H.; Hua, R., Dually functioned core-shell $NaYF_4$:Er^{3+}/Yb^{3+}@$NaYF_4$:Tm^{3+}/Yb^{3+} nanoparticles as nano-calorifiers and nano-thermometers for advanced photothermal therapy. *Scientific Reports* **2017,** 7 (1), 11849-11861.
40. Ximendes, E. C.; Rocha, U.; Jacinto, C.; Kumar, K. U.; Bravo, D.; López, F. J.; Rodríguez, E. M.; García-Solé, J.; Jaque, D., Self-monitored photothermal nanoparticles based on core-shell engineering. *Nanoscale* **2016,** 8 (5), 3057-3066.
41. Yin, Y.; Alivisatos, A. P., Colloidal nanocrystal synthesis and the organic-inorganic interface. *Nature* **2005,** 437 (7059), 664-670.
42. Chang, J.; Waclawik, E. R., Colloidal semiconductor nanocrystals: controlled synthesis and surface chemistry in organic media. *RSC Advances* **2014,** 4 (45), 23505-23527.

43. Naccache, R.; Yu, Q.; Capobianco, J. A., The Fluoride host: Nucleation, growth, and upconversion of lanthanide-doped nanoparticles. *Advanced Functional Materials* **2015,** 3 (4), 482-509.
44. Paik, T.; Gordon, T. R.; Prantner, A. M.; Yun, H.; Murray, C. B., Designing tripodal and triangular gadolinium oxide nanoplates and self-assembled nanofibrils as potential multimodal bioimaging probes. *ACS Nano* **2013,** 7 (3), 2850-2859.
45. Wang, D.; Kang, Y.; Ye, X.; Murray, C. B., Mineralizer-assisted shape-control of rare earth oxide nanoplates. *Chemistry of Materials* **2014,** 26 (22), 6328-6332.
46. Murali, G.; Mishra, R. K.; Lee, J. M.; Chae, Y. C.; Kim, J.; Suh, Y. D.; Lim, D.; Lee, S. H., Aspect-ratio controlled synthesis and tunable luminescence of YF_3:Yb^{3+}/Er^{3+} upconversion nanocrystals. *Crystal Growth & Design* **2017,** *17* (6), 3055-3061.
47. Yin, D.; Wang, C.; Ouyang, J.; Song, K.; Liu, B.; Cao, X.; Zhang, L.; Han, Y.; Long, X.; Wu, M., Enhancing upconversion luminescence of $NaYF_4$:Yb/Er nanocrystals by Mo^{3+} doping and their application in bioimaging. *Dalton Transactions* **2014,** 43 (31), 12037-12043.
48. Ramasamy, P.; Chandra, P.; Rhee, S. W.; Kim, J., Enhanced upconversion luminescence in $NaGdF_4$:Yb,Er nanocrystals by Fe^{3+} doping and their application in bioimaging. *Nanoscale* **2013,** 5 (18), 8711-8717.
49. Zhu, Y.; Zhao, S.; Zhou, B.; Zhu, H.; Wang, Y., Enhancing upconversion luminescence of $LiYF_4$:Yb,Er nanocrystals by Cd^{2+} doping and core-shell structure. *Journal of Physical Chemistry C* **2017,** 121 (34), 18909-18916.
50. Luo, Y.; Zhang, W.; Liao, Z.; Yang, S.; Li, X.; Zuo, F.; Luo, J., Role of Mn^{2+} doping in the preparation of core-shell structured Fe_3O_4@upconversion nanoparticles and their applications in T_1/T_2-weighted magnetic resonance imaging, upconversion luminescent imaging and near-infrared activated photodynamic therapy. *Nanomaterials* **2018,** 8 (7), 466-481.
51. Nannuri, S. H.; Kulkarni, S. D.; K, S. C.; Chidangil, S.; George, S. D., Post annealing induced manipulation of phase and upconversion luminescence of Cr^{3+} doped $NaYF_4$:Yb,Er crystals. *RSC Advances* **2019,** 9 (17), 9364-9372.
52. van Hest, J. J. H. A.; Blab, G. A.; Gerritsen, H. C.; de Mello Donega, C.; Meijerink, A., Probing the influence of disorder on lanthanide luminescence using Eu-doped $LaPO_4$ nanoparticles. *Journal of Physical Chemistry C* **2017,** 121 (35), 19373-19382.
53. Chen, D.; Xu, M.; Huang, P., Core@shell upconverting nanoarchitectures for luminescent sensing of temperature. *Sensors and Actuators B: Chemical* **2016,** 231, 576-583.
54. Pudovkin, M. S.; Koryakovtseva, D. A.; Lukinova, E. V.; Korableva, S. L.; Khusnutdinova, R. S.; Kiiamov, A. G.; Nizamutdinov, A. S.; Semashko, V. V., Luminescence nanothermometry based on Pr^{3+} LaF_3 single core and Pr^{3+} LaF_3/LaF_3 core/shell nanoparticles, *Advances in Materials Science and Engineering* **2019,** 14, 2618307-218321.
55. Labrador-Páez, L.; Ximendes, E. C.; Rodríguez-Sevilla, P.; Ortgies, D. H.; Rocha, U.; Jacinto, C.; Martín Rodríguez, E.; Haro-González, P.; Jaque, D., Core-shell rare-earth-doped nanostructures in biomedicine. *Nanoscale* **2018,** 10 (27), 12935-12956.
56. Weissleder, R., A clearer vision for in vivo imaging. *Nature Biotechnology* **2001,** 19 (4), 316-317.
57. Shi, L.; Sordillo, L. A.; Rodríguez-Contreras, A.; Alfano, R., Transmission in near-infrared optical windows for deep brain imaging. *Journal of Biophotonics* **2016,** 9 (1-2), 38-43.
58. Naczynski, D. J.; Tan, M. C.; Zevon, M.; Wall, B.; Kohl, J.; Kulesa, A.; Chen, S.; Roth, C. M.; Riman, R. E.; Moghe, P. V., Rare-earth-doped biological composites as in vivo shortwave infrared reporters. *Nature Communications* **2013,** 4 (1), 2199-209.
59. Savchuk, O. A.; Carvajal, J. J.; Massons, J.; Aguiló, M.; Díaz, F., Determination of photothermal conversion efficiency of graphene and graphene oxide through an integrating sphere method. *Carbon* **2016,** 103, 134-141.
60. Nexha, A.; Pujol, M. C.; Carvajal, J. J.; Díaz, F.; Aguiló, M., Controlling the growth of colloidal rare earth oxides via wet chemical methodologies. *To be submitted.*
61. Douglas, F. J.; MacLaren, D. A.; Renero-Lecuna, C.; Peacock, R. D.; Valiente, R.; Murrie, M., Self-assembly of ultra-thin lanthanide oxide nanowires via surfactant-mediated imperfect oriented attachment of nanoparticles. *CrystEngComm* **2012,** 14 (21), 7110-7114.
62. Cao, Y. C., Synthesis of square gadolinium oxide nanoplates. *Journal of the American Chemical Society* **2004,** 126 (24), 7456-7457.
63. Si, R.; Zhang, Y. W.; Zhou, H. P.; Sun, L. D.; Yan, C. H., Controlled-synthesis, self-assembly behavior, and surface-dependent optical properties of high-quality rare-earth oxide nanocrystals. *Chemistry of Materials* **2007,** 19 (1), 18-27.
64. Patterson, A. L., The Scherrer formula for X-ray particle size determination. *Physical Review* **1939,** 56 (10), 978-982.
65. James, A. R.; Subrahmanyam, J.; Yadav, K. L., Structural and electrical properties of nanocrystalline PLZT ceramics synthesized via mechanochemical processing. *Journal of Physics D: Applied Physics* **2006,** 39 (10), 2259-2263.
66. Goel, P.; Yadav, K. L., Substitution site effect on structural and dielectric properties of La-Bi modified PZT. *Journal of Materials Science* **2007,** 42 (11), 3928-3935.
67. Liu, D.; Xu, X.; Du, Y.; Qin, X.; Zhang, Y.; Ma, C.; Wen, S.; Ren, W.; Goldys, E. M.; Piper, J. A.; Dou, S.; Liu, X.; Jin, D., Three-dimensional controlled growth of monodisperse sub-50 nm heterogeneous nanocrystals. *Nature Communications* **2016,** 7 (1), 10254-10262.

68. Homann, C.; Krukewitt, L.; Frenzel, F.; Grauel, B.; Würth, C.; Resch-Genger, U.; Haase, M., $NaYF_4$:Yb,Er/ $NaYF_4$ core/shell nanocrystals with high upconversion luminescence quantum yield. *Angewandte Chemie International Edition* **2018,** 57 (28), 8765-8769.
69. Kim, S. Y.; Jeong, J. S.; Mkhoyan, K. A.; Jang, H. S., Direct observation of the core/double-shell architecture of intense dual-mode luminescent tetragonal bipyramidal nanophosphors. *Nanoscale* **2016,** 8 (19), 10049-10058.
70. Vetrone, F.; Naccache, R.; Mahalingam, V.; Morgan, C. G.; Capobianco, J. A., The active-core/active-shell approach: A strategy to enhance the upconversion luminescence in lanthanide-doped nanoparticles. *Advanced Functional Materials* **2009,** 19 (18), 2924-2929.
71. Quintanilla, M.; Ren, F.; Ma, D.; Vetrone, F., Light management in upconverting nanoparticles: Ultrasmall core/shell architectures to tune the emission color. *ACS Photonics* **2014,** 1 (8), 662-669.
72. Peng, D.; Ju, Q.; Chen, X.; Ma, R.; Chen, B.; Bai, G.; Hao, J.; Qiao, X.; Fan, X.; Wang, F., Lanthanide-doped energy cascade nanoparticles: Full spectrum emission by single wavelength excitation. *Chemistry of Materials* **2015,** 27 (8), 3115-3120.
73. Li, Y.; Chen, B.; Tong, L.; Zhang, X.; Xu, S.; Li, X.; Zhang, J.; Sun, J.; Wang, X.; Zhang, Y.; Sui, G.; Zhang, Y.; Zhang, X.; Xia, H., A temperature self-monitoring $NaYF_4$:Dy^{3+}/Yb^{3+}@ $NaYF_4$:Er^{3+}/Yb^{3+} core-shell photothermal converter for photothermal therapy application. *Results in Physics* **2019,** 15, 102704-102711.
74. Abel, K. A.; Boyer, J. C.; Veggel, F. C. J. M. v., Hard proof of the $NaYF_4$/$NaGdF_4$ nanocrystal core/shell structure. *Journal of the American Chemical Society* **2009,** 131 (41), 14644-14645.
75. Klokkenburg, M.; Hilhorst, J.; Erné, B. H., Surface analysis of magnetite nanoparticles in cyclohexane solutions of oleic acid and oleylamine. *Vibrational Spectroscopy* **2007,** 43 (1), 243-248.
76. Mun, J. H.; Jouini, A.; Novoselov, A.; Guyot, Y.; Yoshikawa, A.; Ohta, H.; Shibata, H.; Waseda, Y.; Boulon, G.; Fukuda, T., Growth and characterization of Tm-doped Y_2O_3 single crystals. *Optical Materials* **2007,** 29 (11), 1390-1393.
77. Guyot, Y.; Moncorgé, R.; Merkle, L. D.; Pinto, A.; McIntosh, B.; Verdun, H., Luminescence properties of Y_2O_3 single crystals doped with Pr^{3+} or Tm^{3+} and codoped with Yb^{3+}, Tb^{3+} or Ho^{3+} ions. *Optical Materials* **1996,** 5 (1), 127-136.
78. Sidorowicz, A.; Wajler, A.; Węglarz, H.; Nakielska, M.; Orliński, K.; Diduszko, R.; Olszyna, A., Preparation and characterization of thulium doped yttrium oxide (Tm:Y_2O_3) powders. *Journal of Alloys and Compounds* **2017,** 709, 293-298.
79. Newburgh, G. A.; Word-Daniels, A.; Michael, A.; Merkle, L. D.; Ikesue, A.; Dubinskii, M., Resonantly diode-pumped Ho^{3+}:Y_2O_3 ceramic 2.1 μm laser. *Optics Express* **2011,** 19 (4), 3604-3611.
80. Jambunathan, V.; Mateos, X.; Pujol, M.; Carvajal, J.; Massons, J.; Aguiló, M.; Díaz, F., Near-infrared photoluminescence from Ho^{3+}-doped monoclinic $KLu(WO_4)_2$ crystal codoped with Tm^{3+}. *Journal of Luminescence* **2009,** 129, 1882-1885.
81. Nexha, A.; Carvajal, J. J.; Pujol, M. C.; Díaz, F.; Aguiló, M., Ho^{3+}, Tm^{3+} doped Y_2O_3 nanotriangles, nanohearts and self-assembled nanodiscs for luminescence nanothermometry and photothermal conversion efficiency. *To be submitted.*
82. Riseberg, L. A.; Moos, H. W., Multiphonon orbit-lattice relaxation of excited etates of rare-earth ions in crystals. *Physical Review* **1968,** 174 (2), 429-438.
83. Wade, S. A.; Collins, S. F.; Baxter, G. W., Fluorescence intensity ratio technique for optical fiber point temperature sensing. *Journal of Applied Physics* **2003,** 94 (8), 4743-4756.
84. Mott, N. F., On the absorption of light by crystals. *Proceedings of the Royal Society A* **1938,** 167 (930), 384-391.
85. Duarte, M.; Martins, E.; Baldochi, S. L.; Vieira, N. D.; Vieira, M. M. F., De-excitation mechanisms of $BaLiF_3$:Co^{2+} crystals. *Optics Communications* **1999,** 159 (4), 221-224.
86. Wade, S. A.; Collins, S. F.; Baxter, G. W., Fluorescence intensity ratio technique for optical fiber point temperature sensing. *Journal of Applied Physics* **2003,** 94 (8), 4743-4756.
87. Brites, C. D. S.; Lima, P. P.; Silva, N. J. O.; Millán, A.; Amaral, V. S.; Palacio, F.; Carlos, L. D., Thermometry at the nanoscale. *Nanoscale* **2012,** 4 (16), 4799-4829.
88. Santos, P. V.; Araujo, M. T.; Gouveia-Neto, A. S.; Neto, J. A. M.; Sombra, A. S. B., Optical temperature sensing using upconversion fluorescence emission in Er^{3+}/Yb^{3+}-codoped chalcogenide glass. *Applied Physics Letters* **1998,** 73 (5), 578-580.
89. Savchuk, O. A.; Carvajal, J. J.; Brites, C. D. S.; Carlos, L. D.; Aguilo, M.; Diaz, F., Upconversion thermometry: a new tool to measure the thermal resistance of nanoparticles. *Nanoscale* **2018,** 10 (14), 6602-6610.
90. Rocha, U.; Jacinto, C.; Kumar, K. U.; López, F. J.; Bravo, D.; Solé, J. G.; Jaque, D., Real-time deep-tissue thermal sensing with sub-degree resolution by thermally improved Nd^{3+}:LaF_3 multifunctional nanoparticles. *Journal of Luminescence* **2016,** 175, 149-157.
91. Savchuk, O. A.; Carvajal, J. J.; Haro-Gonzalez, P.; Aguiló, M.; Díaz, F., Luminescent nanothermometry using short-wavelength infrared light. *Journal of Alloys and Compounds* **2018,** 746, 710-719.
92. Xiang, G.; Liu, X.; Zhang, J.; Liu, Z.; Liu, W.; Ma, Y.; Jiang, S.; Tang, X.; Zhou, X.; Li, L.; Jin, Y., Dual-Mode Optical Thermometry Based on the Fluorescence Intensity Ratio Excited by a 915 nm Wavelength in $LuVO_4$:Yb^{3+}/Er^{3+}@SiO_2 Nanoparticles. *Inorganic Chemistry* **2019,** 58 (12), 8245-8252.
93. Ma, Y.; Xiang, G.; Zhang, J.; Liu, Z.; Zhou, P.; Liu, W.; Tang, X.; Jiang, S.; Zhou, X.; Li, L.; Luo, Y.; Jin, Y., Upconversion properties and temperature sensing behaviors in visible and near-infrared

region based on fluorescence intensity ratio in $LuVO_4:Yb^{3+}/Er^{3+}$. *Journal of Alloys and Compounds* **2018,** 769, 325-331.
94. Pattani, V. P.; Tunnell, J. W., Nanoparticle-mediated photothermal therapy: A comparative study of heating for different particle types. *Lasers in Surgery and Medicine* **2012,** 44 (8), 675-684.
95. Hessel, C. M.; Pattani, V. P.; Rasch, M.; Panthani, M. G.; Koo, B.; Tunnell, J. W.; Korgel, B. A., Copper selenide nanocrystals for photothermal therapy. *Nano Letters* **2011,** 11 (6), 2560-2566.
96. Tian, Q.; Jiang, F.; Zou, R.; Liu, Q.; Chen, Z.; Zhu, M.; Yang, S.; Wang, J.; Wang, J.; Hu, J., Hydrophilic Cu_9S_5 nanocrystals: A photothermal agent with a 25.7% heat conversion efficiency for photothermal ablation of cancer cells in vivo. *ACS Nano* **2011,** 5, (12), 9761-9771.
97. Chen, C. L.; Kuo, L. R.; Lee, S. Y.; Hwu, Y. K.; Chou, S. W.; Chen, C. C.; Chang, F. H.; Lin, K. H.; Tsai, D. H.; Chen, Y. Y., Photothermal cancer therapy via femtosecond-laser-excited FePt nanoparticles. *Biomaterials* **2013,** 34 (4), 1128-1134.
98. Wu, X.; Yeow, E. K. L., Tuning the NIR downconversion luminescence and photothermal conversion efficiencies of $MNd_xY_{1-x}F_4$ (M =Na and Li) nanocrystals for use in anti-counterfeiting labels with opposite displays. *Nanoscale* **2019,** 11 (32), 15259-15269.
99. Cole, J. R.; Mirin, N. A.; Knight, M. W.; Goodrich, G. P.; Halas, N. J., Photothermal efficiencies of nanoshells and nanorods for clinical therapeutic applications. *Journal of Physical Chemistry C* **2009,** 113, (28), 12090-12094.
100. Maestro, L. M.; Haro-González, P.; Sánchez-Iglesias, A.; Liz-Marzán, L. M.; García Solé, J.; Jaque, D., Quantum dot thermometry evaluation of geometry dependent heating efficiency in gold nanoparticles. *Langmuir* **2014,** 30 (6), 1650-1658.

Supporting Information

Table S1. Size of the colloidal nanocrystals calculated from the Scherrer equation and from the TEM images

Type of nanocrystals	Size (Scherrer equation)	Size (TEM images)
Undoped	13.2	23.5
Core	14.5	43.7
Core@Shell	17.5	72.1
Layer-by-layer	14.3	100.5 (branched) and 39.5 (complete)

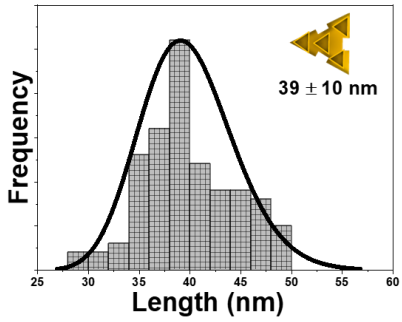

Figure S1. Lognormal side distribution of the complete nanotriangles in the layer-by-layer structure

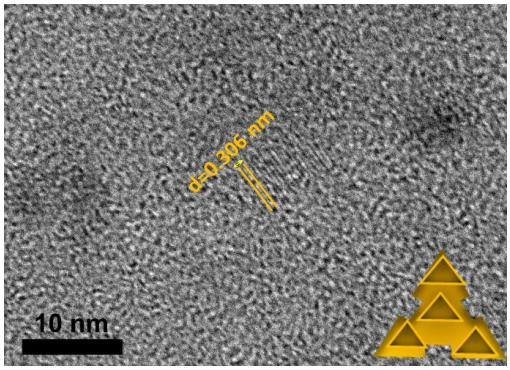

Figure S2. High resolution transmission electron microscopy (HRTEM) of layer-by-layer colloidal nanocrystals with lattice fringes separation of 0.306 nm.

Figure S3. Dispersion of undoped colloidal nanocrystals in apolar solvent (n-hexane).

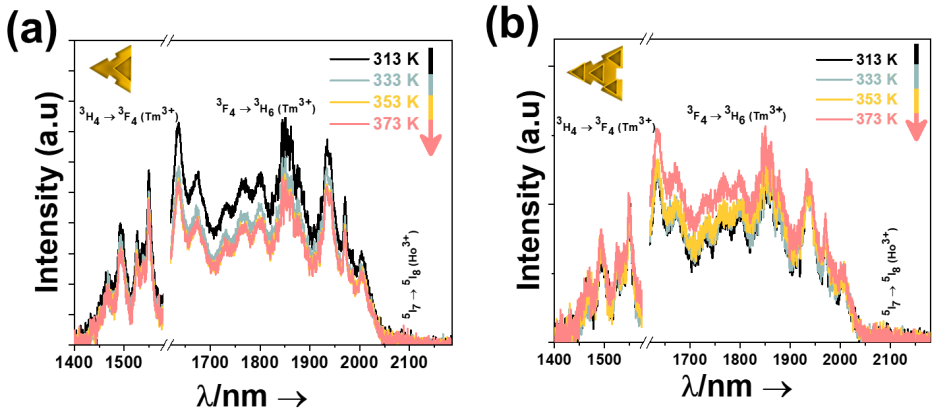

Figure S4. Variation of the emission bands of the: (a) core@shell and (b) layer-by-layer nanostructures with the increase of the temperature.

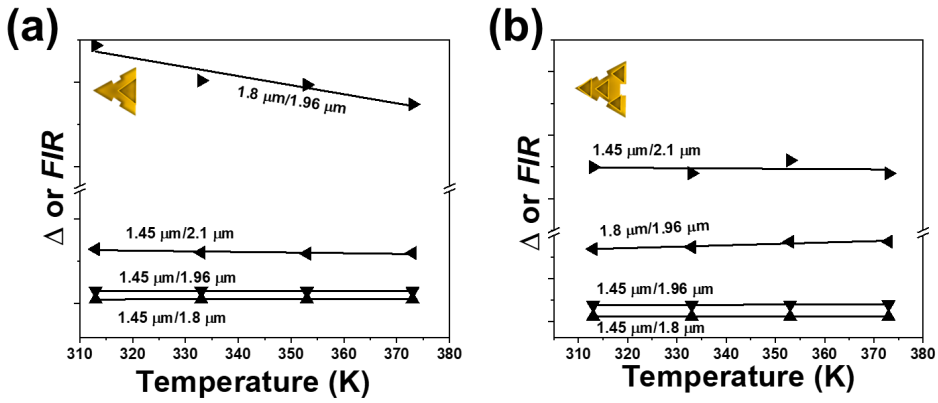

Figure S5. Temperature-dependence of the intensity ratio of the three emission bands of: (a) core@shell and (b) layer-by-layer nanocrystals.

Table S2. Fitting parameters, S_{abs}, S_{rel} and δT of different Ho.Tm:Y_2O_3 colloidal nanocrystals, calculated from the ratio between the non-thermally coupled levels.

Material	Ratio	B	C	ΔE (cm^{-1})	R^2	S_{abs} (K^{-1})	S_{rel} (% K^{-1})	δT (K)
Core	1.45/1.8	0.043	-92.6	64.4	0.31	$5 \cdot 10^{-4}$	0.09	5.3
Core@Shell	1.45/1.8	0.21	46.74	32.4	0.37	$8 \cdot 10^{-4}$	0.05	10.4
Layer-by-Layer	1.45/1.8	0.135	-73.5	51.1	0.45	$1.2 \cdot 10^{-3}$	0.07	6.6
Core	1.45/1.96	10.65	-20.4	14.2	0.01	0.02	0.02	24
Core@Shell	1.45/1.96	16.35	-209.3	145.5	0..91	0.068	0.08	2.3
Layer-by-Layer	1.45/1.96	66.4	160.9	111.8	0.02	0.022	0.16	3
Core	1.45/2.1	243.3	72.5	50.4	0.05	0.135	0.07	6.7
Core@Shell	1.45/2.1	76.9	-261.9	182	0.81	0.48	0.27	1.8
Layer-by-Layer	1.45/2.1	473.2	221.1	153.6	0.04	0.45	0.22	2.2

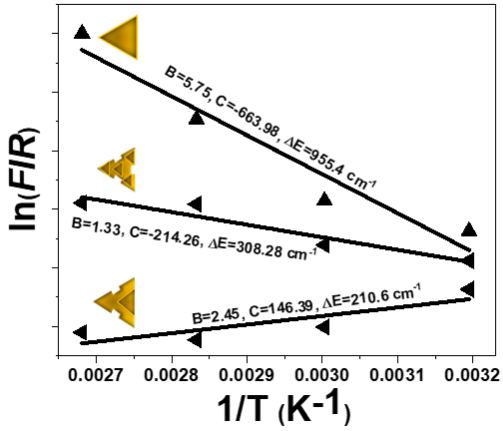

Figure S6. Plot of the logarithmic form of FIR as a function of the inverse of temperature for the intensity ratio of 1.8 μm/1.96 μm for all the type of colloidal nanocrystals. For each plot, the values of the intercept, slope and the energy gap, are given.

Chapter V

Other applications of lanthanide oxide nanocrystals

Lanthanide doped crystalline nanoparticles can exhibit a wide variety of applications governed by their peculiar electronic configuration, and morphological characteristics that can be achieved by using a precise synthetic methodology. Among these multifunctionalities, we investigated the ability to generate white light and to scavenge harmful hydroxyl radicals, both multifunctionalities are present by yttrium sesquioxide nanocrystals synthesized by the wet chemical methodologies.

For the white light generation, rare earth oxides (REO_2 and RE_2O_3, being RE a rare earth cation) portray probably the most explored class of materials to exhibit this broad emission. Particular attention for the white light emitters have emerged due to their broad range of applications in solar energy conversion technologies, lighting sources, backlight, full-color displays and biomedical imaging. Several types of rare earth oxide materials have been implemented for the generation of white light, ranging from PrO_2 and TbO_2, Sm_2O_3 and Tm_2O_3, La_2O_3, Er_2O_3, Yb_2O_3, Gd_2O_3, and Y_2O_3. Despite the high number of works devoted to these materials, these nanocrystals are generally synthesized via sol-gel Pechini or other solvothermal methodologies, which involve calcination of their precursors (chlorides, nitrates, oxalates, hydroxides, amongst others), which leads to the inability to have monodisperse particles and agglomerated final products are achieved. Instead, we implemented the thermal decomposition methodologies, to control the size and shape of the nanocrystals by using organic surfactants during the synthesis, and also getting attached on their surfaces. In addition, we doped the nanocrystals by active RE^{3+} ions, with the aim of enhancing the white light emission by the introduction of dopants. By doing so, we achieved for the generation of white light from a rare earth oxide material coated with organic surfactants. In addition, we explored the effect on the white light generation by factors like the power of the laser applied, time of the recording of the spectrum, the temperature on which these nanocrystals are exposed. Taking advantage of the temperature-dependent properties of the emitted white light, the applicability for luminescent nanothermometry was considered. The results reveal that these nanocrystals have high sensitivity, in the range of 2.65% K^{-1} at high temperatures, around 473 K.

Nanosized material have the ability to prevent the formation of harmful reactive oxygen species within mediums. Most of the attention is placed on ceria nanocrystals, due to their ability to switch between Ce^{3+} and Ce^{4+}. We studied the application of yttrium sesquioxide nanocrystals as potential hydroxyl scavenger. It is believed that the antioxidant properties of yttria nanocrystals are assigned to their nonstoichiometric nature. In fact, studies comparing the ability of ceria and yttria to protect nerve cells from oxidative stress, suggest that yttria has superior antioxidant properties compared to ceria. We evaluate the hydroxyl radical scavenging properties of yttrium sesquioxide nanocrystals as a function of their sizes and shapes. Yttria nanocrystals were synthesized by applying wet chemical methodologies, including thermal decomposition and digestive ripening- assisted methodologies. Thermal decomposition led to two different shapes such as branched nanotriangles and nanohearts, obtaining one of them by tuning the temperature of the reaction. From digestive ripening-assisted synthesis, ultrathin nanodiscs with thicknesses down-to-unit cell were obtained. To render these nanoparticles compatible for hydroxyl

scavenging analysis, water dispersable particles were prepared by treating the as-synthesized nanoparticles under acidic conditions. The hydroxyl radical scavenging assay was based on a Fenton reaction, using methyl violet as a chromogenic agent. The effect of different sizes and shapes of yttria nanocrystals on their antioxidant properties was tested. In addition, we explored the effect of the RE^{3+} dopants in the yttria host, on their radical scavenging capacity. We concluded with an *ex-vivo* experiments with the goal of determine if yttria can prevent the generation of harmful hydroxyl radical species, by monitoring by photometric methods and by thermal profiles, the reaction of liver catalase with hydrogen peroxide.

Paper VIII

Luminescent nanothermometry via white light emission generated from Ho^{3+}, Tm^{3+}:Y_2O_3 colloidal nanocrystals

Albenc Nexha, Maria Cinta Pujol,* Joan J. Carvajal, Francesc Díaz, Magdalena Aguiló
Universitat Rovira i Virgili, Departament Química Física i Inorgànica,
Física i Cristal·lografia de Materials i Nanomaterials (FiCMA-FiCNA)-EMaS, Campus Sescelades, E-43007, Tarragona, Spain
*mariacinta.pujol@urv.cat

Abstract

Cubic Ho^{3+} and Tm^{3+} doped Y_2O_3 colloidal nanotriangles with sizes ~43 nm, were synthesized via thermal decomposition. These colloidal nanocrystals, upon high power excitation at 808 nm, generate white light. The crystalline structure, size and shape, and the surface of the colloidal nanocrystals, were investigated before and after being exposed to laser excitation. Factors that might affect the generation of white light, such as the excitation power, the stability of the white light generated with time, and the temperature at which the colloidal nanocrystals were exposed, are analyzed. The white light changed with temperature, allowing the application of these nanocrystals as luminescent nanothermometers over a wide range of temperatures, from room temperature to 473 K. The relative thermal sensitivity and the temperature resolution of these luminescent nanothermometers are 2.65% K^{-1} and 0.18 K, respectively, at the maximum temperature investigated, allowing to demonstrate a new highly sensitive mechanism for luminescence thermometry.

1. Introduction

White light emitters are of interest for a broad range of applications, such as solar energy conversion technologies, lighting sources, backlight, full-color displays and biomedical imaging.[1-8] A large variety of materials have been reported as white light emitters, including quantum dots,[9-13] semiconductor nanocrystals,[14-16] small organic molecules,[17-19] polymers,[20-23] lanthanide complexes,[24-29] and lanthanide doped inorganic materials.[30-37]

Due to high luminescence efficiency of the lanthanide materials (either embedded in a crystalline or amorphous host, or as part of oganometallic complexes), the generation of the white light by these materials attracted the attention of the scientific community. Rare earth sesquioxides (RE_2O_3) represent, probably, the most widely investigated systems to generate white light, including Y_2O_3,[38-41] Er_2O_3,[42-44] Yb_2O_3,[45, 46] Gd_2O_3,[47, 48] La_2O_3,[49] Sm_2O_3 and Tm_2O_3,[45] PrO_2 and TbO_2.[50] In addition, RE_2O_3 have also potential for applications in bioimaging,[51-53] diagnosis and therapy,[53-55] and sensing.[56-61]

Nevertheless, the mechanism of the generation of white light in rare earth based materials, continues to be a subject of discussion. Mechanisms such as photon avalanche,[62, 63] oxygen vacancy emission,[64] electron-hole recombination,[65] dispersive optical bistability,[66, 67] and blackbody radiation,[2, 50, 63, 68] have been proposed. However, there is no yet a general agreement on what triggers the production of white light in the rare earth-based emitters. Additional factors that might affect to the white light emission and that should be considered involve parameters such as the stability of the white light generation with time and the temperature on which the emitting materials are exposed to.

We have chosen yttrium sesquioxide colloidal nanocrystals to investigate their potentiality as white light emitters, mainly due to their broad transparency range (0.2-8 μm) with a band gap of 5.6 eV, high thermal conductivity, high refractive index and low phonon energy, which have made

of it, traditionally, an attractive choice as host material for lanthanide ions for optical applications.[69, 70] We doped these colloidal nanocrystals with Ho^{3+} and Tm^{3+} ions. It is believed that dopants can enhance the quality of the generated white light in Y_2O_3 by reducing its thermal conductivity.[71] To the best of our knowledge, these nanocrystals portray the first ever RE_2O_3 colloidal based materials to be able to generation white light, while excited with near infrared (hereafter NIR) light.

Here, we explore the ability of highly monodispersed cubic Ho^{3+} and Tm^{3+} doped Y_2O_3 colloidal nanotriangles to generate white light under excitation at 808 nm. Factors affecting the white light emission, including the power of the laser applied, its stability with time, the temperature on which the emitters are exposed, are analyzed. Taking advantage of the temperature-dependent properties of the white light, we explored the possibility of using these colloidal nanotriangles for luminescence nanothermometry, obtaining values of relative thermal sensitivity and temperature resolution, of 3.8% K^{-1} and 0.13 K, respectively, at the maximum temperature under investigation (473 K), indicating that these materials act as highly sensitive luminescent nanothermometers

2. Experimental Section

2.1. Materials

Yttrium acetate hydrate ($Y(CH_3CO_2)_3 \cdot H_2O$ as $Y(Ac)_3 \cdot H_2O$, purity 99.99%) and oleylamine ($C_{18}H_{35}NH_2$, as OLAM, purity 70%) were purchased from Sigma Aldrich. Thulium acetate hydrate ($Tm(CH_3CO_2)_3 \cdot H_2O$ as $Tm(Ac)_3 \cdot H_2O$, purity 99.99%) was purchased from Apollo Scientific. Holmium acetate hydrate ($Ho(CH_3CO_2)_3 \cdot H_2O$ as $Ho(Ac)_3 \cdot H_2O$, purity 99.99%)), oleic acid ($CH_3(CH_2)_7CH=CH(CH_2)_7COOH$, as OLAC, purity 90%), 1-octadecene ($CH_3(CH_2)_{15}CH=CH_2$ as ODE, purity 90%), n-hexane (99%), cyclohexane (90%) and sodium nitrate ($NaNO_3$, 99%) were purchased from Alfa Aesar. Absolute ethanol (EtOH) was purchased from VWR.

2.2. Synthesis of Ho^{3+} and Tm^{3+} doped Y_2O_3 colloidal nanocrystals

Thermal decomposition was applied to synthesize Ho^{3+} and Tm^{3+} doped Y_2O_3 colloidal nanocrystals in the shape of nanotriangles. In a typical thermolysis synthesis for obtaining 3 mol% Ho^{3+} and 5 mol% Tm^{3+} doped Y_2O_3 colloidal nanotriangles,[57, 61] 2.3 mmol of $Y(Ac)_3 \cdot H_2O$, 0.075 mmol of $Ho(Ac)_3 \cdot H_2O$, 0.125 mmol of $Tm(Ac)_3 \cdot H_2O$ and 4 mmol of $NaNO_3$ were mixed in a solution containing 25 mmol of OLAC, 25 mmol of OLAM and 15 mmol of ODE. The reaction mixture was heated to 413 K and degassed to remove residual oxygen for 0.5 h. After switching to nitrogen flow, the reaction temperature was increased to 583 K and held at this temperature for an additional 0.5 h, prior to letting it cool down naturally to room temperature. The nanotriangles were extracted by adding an excess of EtOH, followed by centrifugation at 5000 rpm for 10 minutes and redispersion in n-hexane. This purification cycle was repeated until the discarded supernatant was colorless. The final product of the reaction can be either stored as a solution by dispersing in an apolar solvent (n-hexane or cyclohexane) or as powder by evaporating the solvent.

2.3. Characterization

X-ray powder diffraction (XRPD) measurements were made using a Siemens D5000 diffractometer (Bragg-Brentano parafocusing geometry and vertical θ-θ goniometer) fitted with a curved graphite diffracted-beam monochromator, incident and diffracted-beam Soller slits, a 0.06° receiving slit and a scintillation counter as a detector. The angular 2θ diffraction range was set between 5 and 70°. The data were collected with an angular step of 0.05° at 3 s per step. The sample was rotated to increase the statistics of the signal collected. Cu K_α radiation was obtained from a Copper X-ray tube operated at 40 kV and 30 mA.

For the morphological characterization, transmission electron microscopy (TEM) images were recorded using a JEOL JEM-1011 electron microscope operating at an accelerating voltage of 100 kV. For the preparation of the TEM grids, the nanocrystals were dispersed in n-hexane using ultrasounds, and around 7 μL of the diluted dispersion were drop casted on the surface of a Copper grid covered by a holey Carbon film (HD200 Copper Formvar/Carbon).

Fourier Transform Infrared (FT-IR) spectra were recorded in the range of 400-4000 cm^{-1} on a FT-IR IluminatIR II, Smith spectrophotometer, to investigate the presence of the different functional groups on the samples to determine which surfactant species are attached onto the surfaces of the nanocrystals.

The white light generated by the doped nanocrystals was recorded in a range from 400 nm to 2200 nm. The emission was recorded as three independent spectra: 400 nm-800 nm, using a 750

nm shortpass dichroic filter (Thorlabs) to avoid the laser excitation; 850 nm-1200 nm using a 850 nm longpass dichroic filter (Thorlabs) to avoid the laser excitation; and 1200 nm-2200 nm using a 850 nm longpass dichroic filter (Thorlabs). The first two spectra were collected using a Yokogawa AQ6373 optical spectrum analyzer, while the last one was recorded using a Yokogawa AQ6375 optical spectrum analyzer, operating in all cases with a resolution of 2 nm and an integration time of 1 s. The nanoparticles were excited by a 808 nm fiber-coupled diode laser operating at different powers. The laser beam was focused on the sample using a 20× microscope objective (numerical aperture 0.4), generating a spot of approximately 10^{-6} m in diameter on the sample. To record the temperature dependence of the spectra the set-up was the same, except that the nanocrystals were introduced inside a heating stage (Linkam, THMS 600) equipped with a boron disk for improved temperature distribution.

3. Results and Discussion

3.1. White light generated by Ho^{3+} and Tm^{3+} doped Y_2O_3 colloidal nanocrystals

3 mol% Ho^{3+} and 5 mol% Tm^{3+} doped Y_2O_3 colloidal nanotriangles, in powder form, were excited at 808 nm using laser power ranging from 0.6 W to 1 W. This doping ratio was chosen in previous works of our group since they exhibit the brightest emissions for Ho^{3+} and Tm^{3+} in the near infrared (NIR).[72] Irradiation with the 808 nm laser generated white light emission in these nanocrystals. We recorded the emission spectrum over a wide range of wavelengths from 400 nm to 2200 nm, but avoiding the signal of the 808 nm energy source with the corresponding filters. For that, we split the collection range into three intervals: 400 nm-750 nm (in which we used a 750 nm shortpass dichroic filter), 850 nm-1200 nm (in which we used a 850 nm longpass dichroic filter), and 1200 nm-2200 nm (in which we used again the 850 nm longpass dichroic filter).

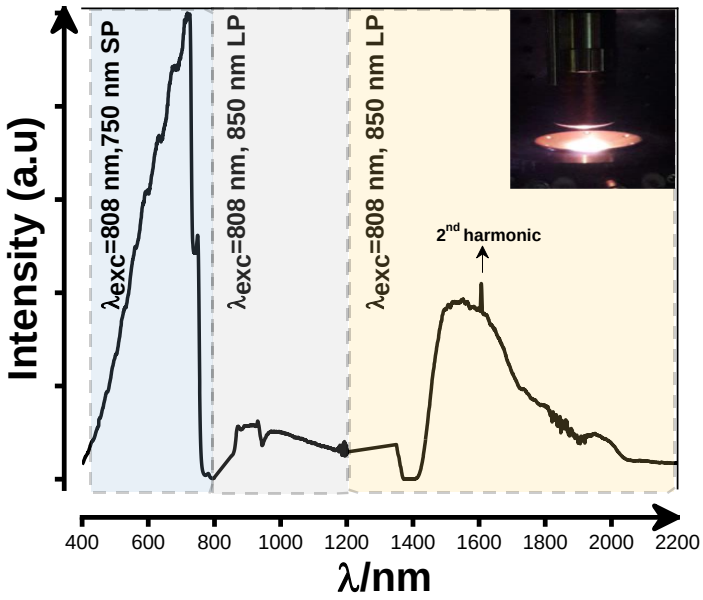

Figure 1. Emission generated by the Ho^{3+}, Tm^{3+}:Y_2O_3 nanotriangles in the 400 to 2200 nm spectral range, after excitation at 808 nm with a power of 0.6 W. The inset displays a picture of the white light generated. The different intervals of collection of the spectrum are marked, SP stands for short pass filter, and LP for long pass filter used to avoid the excitation laser signal.

The collected signals, after excitation with a power of 0.6 W, were normalized to properly compare and to identify were the maximum intensity of the white light is displayed. The results, summarized in Figure 1, reveal the shape of the white emission through all the 400 nm to 2200 nm range. The emission spectra of the nanocrystals display a very broad band extending from the visible to the

near infrared spectral regions. The inset in Figure 1 shows a picture of the white light emission obtained, showing its high brightness. In general, the spectral shape of the emission consists of a broad unstructured band that increase monotonically, notably in the visible range interval from 400-750 nm. The second interval from 850-1200 nm displays a constant intensity of the light. The last interval, from 1200-2200 nm also displays a similar profile as the interval from 400-800 nm, nevertheless here the increase is slightly lower.

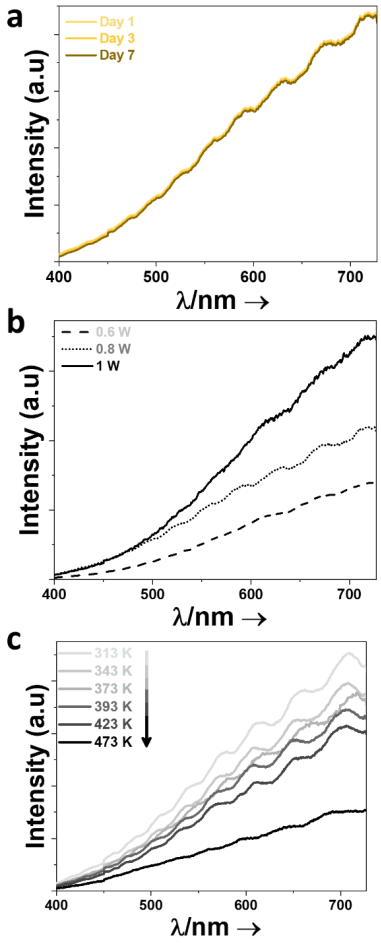

Figure 2. The effect of: (a) stability with time, (b) power of the excitation laser, and (c) temperature at which the nanocrystals were exposed, on the generation of white light.

We should stress here that to trigger the generation of white light and keep it stable, the nanocrystals have to be exposed to high laser powers and a temperature of around 313 K. After these pretreatments, the white light remains stable through time. Taking into account the pretreatments we have to apply, it seems that the mechanism after the generation of white light in Ho^{3+} and Tm^{3+}:Y_2O_3 nanotriangles can be related to thermal radiation. Nevertheless, as stated above, a wide variety of mechanisms have been proposed[2, 50, 62-68] and this topic is still under debate.

Given the high intensity of the emission generated within the visible region and the fact most of the applications for these white light emitters take profit only of the emissions located in this region,[1-8] we focused our attention on this spectral region. Hence, within the 400-750 nm range, we investigated the effect of several factors, such as the stability with time, the excitation laser power, and the temperature at which the nanocrystals were exposed, on the generated white light emission.

Concerning the stability of the spectrum with time, the white light emission generated by Ho^{3+} and Tm^{3+}:Y_2O_3 nanotriangles after 1, 3 and 7 days, recorded at an excitation power of 0.6 W, remains unchanged (see Figure 2 (a)), which implies that the effect generating the white light emission is highly stable.

Next, we observed the effect of the power of the 808 nm laser excitation source on the intensity of the white light emission. The power of the laser was increased from 0.6 W to 1 W. The results, shown in Figure 2 (b), indicated that it exist a linear relationship (see also Figure S1 at Supporting Information displaying the variation of the maximum intensity of the emission with the power of the laser) between the emission intensity and the laser power applied.

Finally, to analyze the dependence of the white light emission with the temperature, the colloidal nanocrystals were introduced in a heating stage to control the temperature in the range from 313 to 473 K. It is generally accepted that the emissions rising from rare earth-based particles are temperature-dependent, regardless of their operating range.[72-76] We observed that above 473 K the white light emission was ceased. Hence, upon excitation at 808 nm with 1 W to maximize the intensity of the white light emission, we recorded the evolution of the spectra over the 400-800 nm range. The results, presented in Figure 2 (c) indicate a clear decrease of the intensity of the white light, with a more pronounced effect above 423 K. The important dependence of the intensity of the white light emission with the temperature allowed us to explore the possibility of using this emission for luminescence nanothermometry applications.

3.2. Luminescent nanothermometry with white light emission

To explore the application as luminescent nanothermometers of the white light emission nanotriangles in the visible, we selected three different spectral regions according to RGB criteria within the temperature range from 313 K to 473 K. Hence, we defined the blue region, in the wavelength interval from 450 nm to 480 nm, the green region from 510 nm to 550 nm, and the red region from 650 nm to 700 nm, as indicated in Figure 3 (a). This strategy would allow us, in the future, use a RGB digital color sensor to develop fast, compact, low-cost and non-invasive temperature nanosensors as we reported previously for other less efficient lanthanide doped luminescent nanoparticles with emissions in the different RGB regions.[77]

It can be observed that as the temperature increases, the emission intensity in the red region is decreasing faster than in the other two regions (see Figure 3 (b)). From its side, the emission intensity in the green region is also decreasing faster than in the blue region, although not as fast as the emission intensity in the red region. Last, the emission intensity in the blue region, barely exhibits any change with the temperature (see Figure 3 (b)), which indicated that we can use the emission intensity in this region as an internal reference for the luminescent thermometer developed. Thus, these characteristics indicates that we can develop a ratiometric luminescent thermometer by calculating the intensity ratio between two out of these three emitting regions.

According to that, we analyzed the evolution of the intensity ratio, calculated from the integrated intensity in these different RGB regions, as blue vs green, blue vs red, and green vs red. The data included in Figure 3 (c), show two different behaviors for the intensity ratios. At temperatures below 423 K, they exhibit a flat behavior almost independent of the temperature, while above this temperature an important growth model is observed.

Hence, we applied two different fitting models: linear fitting for the region from room temperature to 423 K, and polynomial fitting for the region from room temperature to 473 K. For the linear model, an equation of the form of:

$$\Delta = A * T + B \qquad (1)$$

is applied, whereas for polynomial model, the equation is expressed in the following way:

$$\Delta = A + B * T + C * T^2 \qquad (2)$$

where A, B and C are constants to be determined from the fitting, and T stands for the absolute temperature.

Having established the fitting equations, now we can analyze the thermometric performance of these nanocrystals by evaluating their absolute and relative thermal sensitivities, and their temperature resolution. The absolute sensitivity would allow us to compare the performance of the three different luminescent nanothermometers we propose in this paper, since their

temperature-dependence emission properties are recorded under the same conditions. It is defined as the first derivative of the intensity ratio:[78]

$$S_{abs} = \frac{\partial \Delta}{\partial T} \qquad (3)$$

By substituting the equations on the intensity ratios (Equation 1 and Equation 2), the final equation to determine the absolute sensitivity (either in the linear of polynomial model) of the white light generated from yttria nanocrystals, is as follows:

$$S_{abs} = A \qquad (4)$$

for the linear model, and

$$S_{abs} = B + C * T \qquad (5)$$

for the polynomial model.

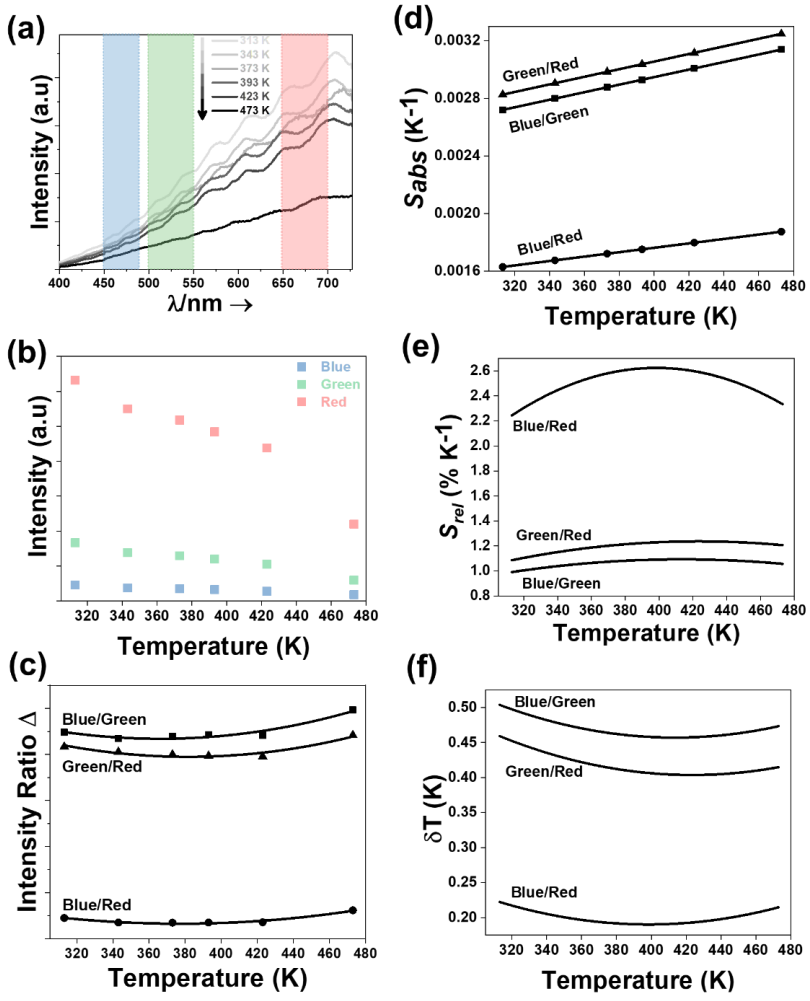

Figure 3. (a) Evolution of the intensity of the emission of the white light in the 400-750 nm region as a function of temperature. The selected wavelength regions for luminescent nanothermometry (blue region (450-480 nm), green region (510-550 nm) and red region (650-700 nm)) are also indicated. Effect of the temperature in: (b) the emission intensity in the blue, green and red region (scattered point stand for experimental data, the lines are guide for the eyes), (c) intensity ratios among the RGB regions (scattered

point are the experimental data and lines are the fitting curves), (d) absolute thermal sensitivity (S_{abs}), (e) relative thermal sensitivity (S_{rel}), and (f) temperature resolution (δT).

On the other hand, the relative thermal sensitivity, used normally as a figure of merit to compare the performance of different thermometers, expresses the maximum change in the intensity ratio for each temperature degree and it is defined as:[76]

$$S_{rel} = \frac{1}{\Delta}\left|\frac{\partial \Delta}{\partial T}\right| x\ 100\% \qquad (6)$$

By substituting the equations on the intensity ratios, the final expression to determine the relative thermal sensitivity of white light in yttria nanocrystals, is as follows:

$$S_{rel} = \frac{A}{A * T + B}\ x\ 100\% \qquad (7)$$

for the linear model, and

$$S_{rel} = \frac{B + C * T}{A + B * T + C * T^2}\ x\ 100\% \qquad (8)$$

for the polynomial model.

And finally, the temperature resolution, defined as the smallest temperature change that can be resolved in a given measurement, is another parameter that can determine the thermometric performance of a thermometer, expressed as:[76]

$$\delta T = \frac{1}{S_{rel}}\frac{\delta \Delta}{\Delta} \qquad (9)$$

where $\frac{\delta \Delta}{\Delta}$ stands for the uncertainty in the determination of the intensity ratio (0.5% in the common situations).[76] Hence, as smallest the value of δT, the better the thermometric performance of a thermometer. Having determined the equations for S_{abs}, S_{rel} and δT, now we can compare the performance of Ho^{3+} and Tm^{3+}:Y_2O_3 nanotriangles as a function of the wavelength regimes (blue vs green, blue vs red, and green vs red).

For the linear model, the results summarized in Figure S2 at the Supporting Information, clearly underline that the thermometric performance is dependent on the slope of the fitting. The higher the slope, the better the performance. Hence, the intensity ratio between the green vs red displays the highest slope, and as a consequence higher S_{abs} (0.000324 K^{-1} constant through all the temperature range) and S_{rel} (0.076% K^{-1} at 423 K), and smallest δT (6.5 K at 423 K) compared to the blue vs green or blue vs red (see Figure S2 at the Supporting Information).

On the other hand, the thermometric performance of these colloidal nanocrystals based on the polynomial model, reveals that the performance based on the blue vs red (in terms of S_{rel} and δT) is higher compared to the other two ratios. Results are summarized in Figure 3 (c), (d) and (e). Hence, the highest S_{abs} for a value of 0.000325 K^{-1} at 473 K, is attributed to the green vs red, whereas those based on blue vs green and blue vs red are 0.00314 K^{-1} and 0.00817 K^{-1}, respectively (see Figure 3 (d)). Concerning S_{rel}, the blue vs red exhibits a value of around 2.65% K^{-1} (see Figure 3 (e)), relatively quite high compared to the blue vs green (1.11% K^{-1}), and green vs red (1.26% K^{-1}) at the temperature of 423 K. δT evolution with the temperature, presented in Figure 3 (f), demonstrated the blue vs red ratio can sense temperature changes down to 0.18 K, whereas the blue vs green, and green vs red, down to 0.45 K and 0.39 K at 423 K, respectively. Hence, overall these nanothermometers are highly sensitivity to temperature changes and stand for potential candidates for white light applications.

3.3. Characterization of Ho^{3+} and Tm^{3+} doped Y_2O_3 colloidal nanocrystals

We investigated the crystalline structure, the morphological characteristics (size and shape) and the functional groups attached to the surface of the Ho^{3+} and Tm^{3+} doped Y_2O_3 colloidal nanocrystals, before and after generation of the white light. The XRPD pattern of the as synthesized nanocrystals by the thermal decomposition methodology show broad diffraction peaks, indicating poor crystallinity (see Figure 4, gray line). Nevertheless, some sharper peaks are detected, as well, that might be related to preferential growth orientations.[79, 80] The pattern matched with the cubic crystalline structure of yttria with space group *Ia* $\bar{3}$, with a slight shifting of

the position of the diffraction peaks towards lower angles when compared to the reference pattern, due to the expansion of the structure by the substitution of Y^{3+} by Ho^{3+} and Tm^{3+} in the structure.

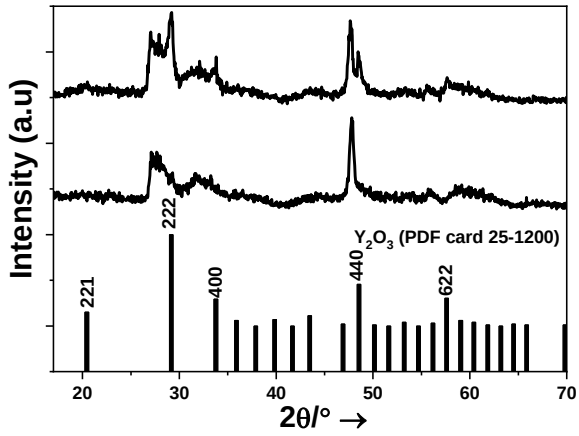

Figure 4. XRPD patterns of Ho^{3+} and Tm^{3+} doped Y_2O_3 colloidal nanocrystals, before (bottom line) and after (upper line) white light generation. The reference pattern of Y_2O_3 (PDF card 25-1200) is included for comparison.

After the white light generation experiments, the data reveal that the crystallinity of the sample has improved (see Figure 4, black line), since the diffraction peaks appear sharper. It can be seen that different new sharp peaks start to appear, mainly at the positions corresponding to the (222) and (440) planes, whereas the intensity of the (221), (400) and (622) peaks increased slightly. We presume that because of the high laser powers applied (a necessary condition for the white light generation) and the temperature-dependence experiments, the heat provided to the sample lead to an improved degree of crystallinity in the sample. In previous examples of white light emitting yttria particles,[38-41] and other lanthanide oxides[44, 47-49, 81] reported in the literature, such structural investigation after the generation of the white light has not been undertaken. Thus, we cannot know if the structural effects observed are due to the laser exposure or the heating process, up to 473 K during ~2 h, that was applied to the samples during the luminescence nanothermometry experiments.

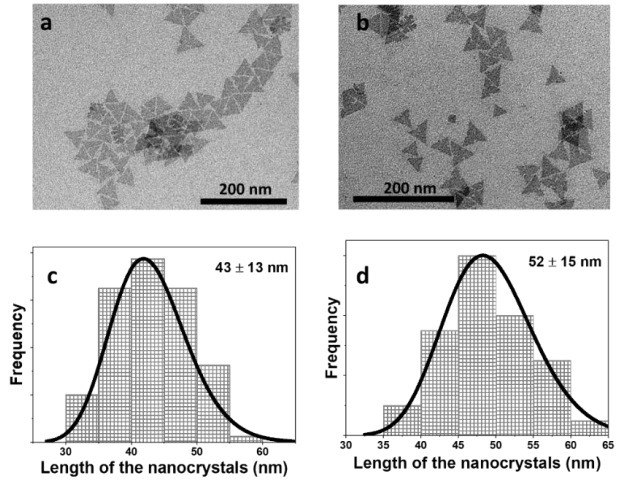

Figure 5. TEM images and lognormal size distribution of the lateral length of Ho^{3+} and Tm^{3+} doped Y_2O_3 nanocrystals: (a) and (c) as-synthesized, and (b) and (d) after the white light generation experiments

We also examined the size and shape of the colloidal nanocrystals before and after the white light generation experiments, via TEM. The Ho^{3+} and Tm^{3+} doped Y_2O_3 colloidal nanocrystals prepared by the thermal decomposition synthesis show a triangular morphology (see Figure 5 (a)). Their average length size is 43 ± 13 nm (see Figure 5 (c)), deduced after analyzing over 100 nanocrystals through the ImageJ software.

Finally, we recorded IR spectra of these nanocrystals via FTIR spectroscopy, with the goal to study the presence of the coating organic surfactants on their surfaces. FTIR data, summarized in Figure 6, demonstrate that there are no changes in the nanocrystals before or after the white light generation experiments, and that they are in both cases coated with oleic acids moieties in the form of bridging or ionic ligands, as previously investigated.[61, 79] The absence of the typical vibrational bands of OLAC and OLAM such as the ν(C=O) stretching band located at 1710 cm^{-1} and the bending δ (NH_2) band located at 1595 cm^{-1}, and the presence of bands located at 1580 cm^{-1}, 1510 cm^{-1} and 1435 cm^{-1}, ascribed to the antisymmetric and symmetric stretching vibrations of the deprotonated carboxylic group (COO^-), respectively, indicate that the OLAC molecules were deprotonated and transformed into carboxylate anions, catalyzed by OLAM.[38-41] An additional observation that confirms that the nanocrystals after the white light generation experiments are coated with organic surfactant is their ability to be dispersed in apolar solvents, such as n-hexane or cyclohexane.

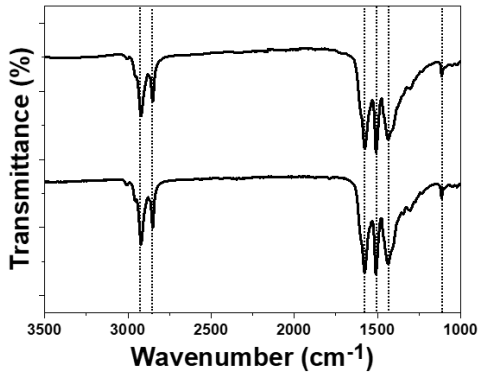

Figure 6. FTIR analysis of Ho^{3+} and Tm^{3+} doped Y_2O_3 nanocrystals as-synthesized (bottom line) and after the white light generation experiments (upper line).

4. Conclusions

In summary, we have reported for the first time the generation of white light emission from highly monodisperse Ho^{3+} and Tm^{3+} doped Y_2O_3 colloidal nanotriangles, synthesized by thermal decomposition. We investigated different factors affecting the generation of white light emission, including the stability of the spectrum with time, the excitation laser power applied, and the temperature at which the nanocrystals were exposed. Since the intensity of the emission of these Ho,Tm:Y_2O_3 nanocrystals in the visible regime is highly dependent on the temperature, we explored their potential applicability as luminescent thermometers. This is the first time, to the best of our knowledge, that white light emitter nanophosphors have been used for this purpose. These nanothermometers are highly sensitive to the change of temperature, exhibit high values of the relative thermal sensitivity (2.65% K^{-1}) and temperature resolution (0.18 K) at high temperatures (473 K), within the wavelength range from 400 nm to 750 nm. Finally, the effects of the high laser powers used for the excitation of these nanoparticles to generate white light on their crystalline structure, size, shape, and ligands attached to their surfaces have been analyzed.

5. Acknowledgments

This work was supported by the Spanish Government under projects MAT2016-75716-C2-1-R (AEI/FEDER, UE) and by the Generalitat de Catalunya under project 2017SGR755. A.N acknowledges financial support from the Generalitat de Catalunya under grant 2017FI_B00620, 2018FI_B100161 and 2019FI_B200154.

6. References

1. Ye, H.; Bogdanov, V.; Liu, S.; Vajandar, S.; Osipowicz, T.; Hernández, I.; Xiong, Q., Bright photon upconversion on composite organic lanthanide molecules through localized thermal radiation. *Journal of Physical Chemistry Letters* **2017,** 8 (23), 5695-5699.
2. Wang, J.; Ming, T.; Jin, Z.; Wang, J.; Sun, L. D.; Yan, C. H., Photon energy upconversion through thermal radiation with the power efficiency reaching 16%. *Nature Communications* **2014,** 5 (1), 5669-5678.
3. Sakr, E. S.; Zhou, Z.; Bermel, P., High efficiency rare-earth emitter for thermophotovoltaic applications. *Applied Physics Letters* **2014,** 105 (11), 111107-111111.
4. Yang, X.; Zhou, G.; Wong, W. Y., Recent design tactics for high performance white polymer light-emitting diodes. *Journal of Materials Chemistry C* **2014,** 2 (10), 1760-1778.
5. Kim, S. H.; Park, S.; Kwon, J. E.; Park, S. Y., Organic light-emitting diodes with a white-emitting molecule: emission mechanism and device characteristics. *Advanced Functional Materials* **2011,** 21 (4), 644-651.
6. Sava, D. F.; Rohwer, L. E. S.; Rodriguez, M. A.; Nenoff, T. M., Intrinsic broad-band white-light emission by a uuned, corrugated metal-organic framework. *Journal of the American Chemical Society* **2012,** 134 (9), 3983-3986.
7. Bünzli, J. C. G., Lanthanide luminescence for biomedical analyses and imaging. *Chemical Reviews* **2010,** 110 (5), 2729-2755.
8. Kamtekar, K. T.; Monkman, A. P.; Bryce, M. R., Recent advances in white organic light-emitting materials and devices (WOLEDs). *Advanced Materials* **2010,** 22 (5), 572-582.
9. Wang, C.; Xu, S.; Wang, Y.; Wang, Z.; Cui, Y., Aqueous synthesis of multilayer Mn:ZnSe/Cu:ZnS quantum dots with white light emission. *Journal of Materials Chemistry C* **2014,** 2 (4), 660-666.
10. Bowers, M. J.; McBride, J. R.; Rosenthal, S. J., White-Light emission from magic-sized cadmium selenide nanocrystals. *Journal of the American Chemical Society* **2005,** 127 (44), 15378-15379.
11. Zhang, W. J.; Pan, C. Y.; Cao, F.; Yang, X., White-light-emitting Cu,Mn co-doped Zn-In-S/ZnS quantum dots with high stability and their electroluminescence. *Journal of Materials Chemistry C* **2017,** 5 (40), 10533-10542.
12. Zhang, W. J.; Pan, C. Y.; Cao, F.; Wang, H.; Yang, X., Highly bright and stable white-light-emitting cadmium-free Ag,Mn co-doped Zn-In-ZnS quantum dots and their electroluminescence. *Journal of Materials Chemistry C* **2018,** 6 (38), 10233-10240.
13. Panda, S. K.; Hickey, S. G.; Demir, H. V.; Eychmüller, A., Bright white-light emitting manganese and copper co-doped ZnSe quantum dots. *Angewandte Chemie International Edition* **2011,** 50 (19), 4432-4436.
14. Chen, H. S.; Hong, H. Y.; Kumar, R. V., White light emission from semiconductor nanocrystals by in situ colour tuning in an alternating thermodynamic-kinetic fashion. *Journal of Materials Chemistry* **2011,** 21 (16), 5928-5932.
15. Krause, M. M.; Mooney, J.; Kambhampati, P., Chemical and thermodynamic control of the surface of semiconductor nanocrystals for designer white light emitters. *ACS Nano* **2013,** 7 (7), 5922-5929.
16. Sapra, S.; Mayilo, S.; Klar, T. A.; Rogach, A. L.; Feldmann, J., Bright white-light emission from semiconductor nanocrystals: by chance and by design. *Advanced Materials* **2007,** 19 (4), 569-572.
17. Williams, E. L.; Haavisto, K.; Li, J.; Jabbour, G. E., Excimer-based white phosphorescent organic light-emitting diodes with nearly 100 % internal quantum efficiency. *Advanced Materials* **2007,** 19 (2), 197-202.
18. Sakai, K.; Ishikawa, T.; Akutagawa, T., A blue-white-yellow color-tunable excited state intramolecular proton transfer (ESIPT) fluorophore: sensitivity to polar-nonpolar solvent ratios. *Journal of Materials Chemistry C* **2013,** 1 (47), 7866-7871.
19. Nagarajan, N.; Velmurugan, G.; Prakash, A.; Shakti, N.; Katiyar, M.; Venuvanalingam, P.; Renganathan, R., Highly emissive luminogens based on imidazo[1,2-a]pyridine for electroluminescent applications. *Chemistry An Asian Journal* **2014,** 9 (1), 294-304.
20. Luo, J.; Li, X.; Hou, Q.; Peng, J. B.; Yang, W.; Cao, Y., High-efficiency white-light emission from a single copolymer: Fluorescent blue, green, and red chromophores on a conjugated polymer backbone. *Advanced Materials* **2007,** 19 (8), 1113-1117.
21. Wu, H.; Zhou, G.; Zou, J.; Ho, C. L.; Wong, W. Y.; Yang, W.; Peng, J.; Cao, Y., Efficient polymer white-light-emitting devices for solid-state lighting. *Advanced Materials* **2009,** 21 (41), 4181-4184.
22. Ravindran, E.; Somanathan, N., Efficient white-light emission from a single polymer system with “spring-like” self-assemblies induced emission enhancement and intramolecular charge transfer characteristics. *Journal of Materials Chemistry C* **2017,** 5 (19), 4763-4774.

23. Sahin, O.; Cinar, M. E.; Tekin, E.; Mucur, S. P.; Topal, S.; Suna, G.; Eroglu, M. S.; Ozturk, T., White light emitting polymers possessing thienothiophene and boron units. *Chemistry Select* **2017,** 2 (10), 2889-2894.
24. Shunmugam, R.; Tew, G. N., White-light emission from mixing blue and red-emitting metal complexes. *Polymers for Advanced Technologies* **2008,** 19 (6), 596-601.
25. Balamurugan, A.; Reddy, M. L. P.; Jayakannan, M., Single polymer photosensitizer for Tb^{3+} and Eu^{3+} ions: An approach for white light emission based on carboxylic-functionalized poly(m-phenylenevinylene)s. *Journal of Physical Chemistry B* **2009,** 113 (43), 14128-14138.
26. Cuan, J.; Yan, B., Cool-white light emitting hybrid materials of a resin-mesoporous silica composite matrix encapsulating europium polyoxometalates through an ionic liquid linker. *RSC Advances* **2013,** 3 (43), 20077-20084.
27. Tang, Q.; Liu, S.; Liu, Y.; He, D.; Miao, J.; Wang, X.; Ji, Y.; Zheng, Z., Color tuning and white light emission via in situ doping of luminescent lanthanide metal-organic frameworks. *Inorganic Chemistry* **2014,** 53 (1), 289-293.
28. He, G.; Guo, D.; He, C.; Zhang, X.; Zhao, X.; Duan, C., A color-tunable europium complex emitting three primary colors and white light. *Angewandte Chemie International Edition* **2009,** 48 (33), 6132-6135.
29. Ma, X.; Li, X.; Cha, Y. E.; Jin, L. P., Highly thermostable one-dimensional lanthanide(III) coordination polymers constructed from benzimidazole-5,6-dicarboxylic acid and 1,10-phenanthroline: Synthesis, structure, and tunable white-light emission. *Crystal Growth & Design* **2012,** 12 (11), 5227-5232.
30. Ramakrishna, P. V.; Murthy, D. B. R. K.; Sastry, D. L., White-light emitting Eu^{3+} co-doped $ZnO/Zn_2SiO_4:Mn^{2+}$ composite microphosphor. *Spectrochimica Acta Part A: Molecular and Biomolecular Spectroscopy* **2014,** 125, 234-238.
31. Mao, Z.; Wang, D.; Lu, Q.; Yu, W.; Yuan, Z., Tunable single-doped single-host full-color-emitting $LaAlO_3$:Eu phosphorvia valence state-controlled means. *Chemical Communications* **2009,** 3, 346-348.
32. Mahalingam, V.; Naccache, R.; Vetrone, F.; Capobianco, J. A., Enhancing upconverted white light in $Tm^{3+}/Yb^{3+}/Ho^{3+}$-doped $GdVO_4$ nanocrystals via incorporation of Li^+ ions. *Optics Express* **2012,** 20 (1), 111-119.
33. Xing, L.; Yang, W.; Lin, J.; Huang, M.; Xue, Y., Enhanced and stable upconverted white-light emission in $Ho^{3+}/Yb^{3+}/Tm^{3+}$-doped $LiNbO_3$ single crystal via Mg^{2+} ion doping. *Scientific Reports* **2017,** 7 (1), 14725-14732.
34. Rai, M.; Kaur, G.; Singh, S. K.; Rai, S. B., Probing a new approach for warm white light generation in lanthanide doped nanophosphors. *Dalton Transactions* **2015,** 44 (13), 6184-6192.
35. Wang, T.; Yu, H.; Siu, C. K.; Qiu, J.; Xu, X.; Yu, S. F., White-light whispering-gallery-mode lasing from lanthanide-doped upconversion $NaYF_4$ hexagonal microrods. *ACS Photonics* **2017,** 4 (6), 1539-1543.
36. Singh, N. S.; Sahu, N. K.; Bahadur, D., Multicolor tuning and white light emission from lanthanide doped $YPVO_4$ nanorods: energy transfer studies. *Journal of Materials Chemistry C* **2014,** 2 (3), 548-555.
37. Barrera, E. W.; Pujol, M. C.; Carvajal, J. J.; Mateos, X.; Solé, R.; Massons, J.; Speghini, A.; Bettinelli, M.; Cascales, C.; Aguiló, M.; Díaz, F., White light upconversion in Yb-sensitized (Tm, Ho)-doped $KLu(WO_4)_2$ nanocrystals: the effect of Eu incorporation. *Physical Chemistry Chemical Physics* **2014,** *16* (4), 1679-1686.
38. Bilir, G.; Di Bartolo, B. J. O. M., Production of bright, wideband white light from Y_2O_3 nano-powders induced by laser diode emission. *Optical Materials* **2014,** 36 (8), 1357-1360.
39. Bilir, G.; Özen, G.; Collins, J.; Cesaria, M.; Di Bartolo, B., Unconventional production of bright white light emission by Nd-doped and nominally un-doped Y_2O_3 nano-powders. *IEEE Photonics Journal* **2014,** 6, 8200518.
40. Cesaria, M.; Collins, J.; Di Bartolo, B., On the efficient warm white-light emission from nano-sized Y_2O_3. *Journal of Luminescence* **2016,** 169, 574-580.
41. Lin, C.; Zhang, C.; Lin, J., Sol-gel derived Y_2O_3 as an efficient bluish-white phosphor without metal activator ions. *Journal of Luminescence* **2009,** *129* (12), 1469-1474.
42. Tabanli, S.; Yilmaz, H. C.; Bilir, G.; Erdem, M.; Eryurek, G.; Di Bartolo, B.; Collins, J., Broadband, white light emission from doped and undoped insulators. *ECS Journal of Solid State Science and Technology* **2018,** 7 (1), 3199-3210.
43. Wang, J.; Hao, J. H.; Tanner, P. A., Persistent luminescence upconversion for Er_2O_3 under 975 nm excitation in vacuum. *Journal of Luminescence* **2015,** 164, 116-122.
44. Tabanli, S.; Eryurek, G.; Di Bartolo, B., White light emission from Er_2O_3 nano-powder excited by infrared radiation. *Optical Materials* **2017,** 69, 207-213.
45. Wang, J.; Tanner, P. A., Upconversion for white light generation by a single compound. *Journal of the American Chemical Society* **2010,** 132 (3), 947-949.
46. Wang, J.; Hao, J. H.; Tanner, P. A., Luminous and tunable white-light upconversion for YAG ($Yb_3Al_5O_{12}$) and (Yb, Y)$_2O_3$ nanopowders. *Optics Letters* **2010,** 35 (23), 3922-3924.
47. Jayasimhadri, M.; Ratnam, B. V.; Jang, K.; Lee, H. S.; Yi, S. S.; Jeong, J. H., Conversion of green emission into white light in Gd_2O_3 nanophosphors. *Thin Solid Films* **2010,** 518 (22), 6210-6213.
48. Bilir, G.; Erguzel, O., Up-conversion emission properties and unexpected white light emission from Er^{3+}/Yb^{3+} doped Gd_2O_3 nanophosphors. *Materials Research Express* **2016,** 3 (10), 106201-106214.
49. Singh, A.; Singh, S.; Kumar, D.; Rai, D.; Rai, S.; Kumar, K., Light-into-heat conversion in $La_2O_3:Er^{3+}$-Yb^{3+} phosphor: an incandescent emission. *Optics Letters* **2012,** 37 (5), 776-778.

50. Silva Filho, C. I.; Oliveira, A. L.; Pereira, S. C. F.; de Sá, G. F.; da Luz, L. L.; Alves, S., Bright thermal (blackbody) emission of visible light from LnO_2 (Ln=Pr, Tb), photoinduced by a NIR 980 nm laser. *Dalton Transactions* **2019,** 48 (8), 2574-2581.
51. Paik, T.; Gordon, T. R.; Prantner, A. M.; Yun, H.; Murray, C. B., Designing tripodal and triangular gadolinium oxide nanoplates and self-assembled nanofibrils as potential multimodal bioimaging probes. *ACS Nano* **2013,** 7 (3), 2850-2859.
52. Hemmer, E.; Venkatachalam, N.; Hyodo, H.; Hattori, A.; Ebina, Y.; Kishimoto, H.; Soga, K., Upconverting and NIR emitting rare earth based nanostructures for NIR-bioimaging. *Nanoscale* **2013,** 5 (23), 11339-11361.
53. Dong, H.; Du, S. R.; Zheng, X. Y.; Lyu, G. M.; Sun, L. D.; Li, L. D.; Zhang, P. Z.; Zhang, C.; Yan, C. H., Lanthanide nanoparticles: From design toward bioimaging and therapy. *Chemical Reviews* **2015,** 115 (19), 10725-10815.
54. Teo, R. D.; Termini, J.; Gray, H. B., Lanthanides: Applications in cancer diagnosis and therapy. *Journal of Medicinal Chemistry* **2016,** 59 (13), 6012-6024.
55. Park, J. Y.; Chang, Y.; Lee, G. H., Multi-modal imaging and cancer therapy using lanthanide oxide nanoparticles: current status and perspectives. *Current Medicinal Chemistry* **2015,** 22 (5), 569-81.
56. Peng, Y.; Chen, X.; Gao, Z., Determination of trace amounts of mercury using hierarchically nanostructured europium oxide. *Talanta* **2010,** 82 (5), 1924-1928.
57. Nexha, A.; Carvajal, J. J.; Pujol, M.C.; Díaz, F.; Aguiló, M., Effect of the core@shell and layer-by-layer nanoarchitectures on the thermal sensing and photothermal conversion efficiency in triangular Ho, $Tm:Y_2O_3$ colloidal nanocrystals operating in the third biological window. *To be submitted.*
58. Aguilar-Vázquez, L.; Aguilar-Caballos, M. P.; Gómez-Hens, A., Development of an automatic high-throughput assay for tetracycline determination by using Eu_2O_3 nanoparticles and dry-reagent technology. *Talanta* **2014,** 119, 111-115.
59. Debasu, M. L.; Oliveira, H.; Rocha, J.; Carlos, L. D., Colloidal $(Gd_{0.98}Nd_{0.02})_2O_3$ nanothermometers operating in a cell culture medium within the first and second biological windows. *Journal of Rare Earths* **2020,** 38 (5), 483-491.
60. Jia, M.; Fu, Z.; Liu, G.; Sun, Z.; Li, P.; Zhang, A.; Lin, F.; Hou, B.; Chen, G., NIR-II/III luminescence ratiometric nanothermometry with phonon-tuned sensitivity. *Advanced Optical Materials* **2020,** 8 (6), 1901173-1901180.
61. Nexha, A.; Carvajal, J. J.; Pujol, M.C.; Díaz, F.; Aguiló, M., Evaluating the performance of Ho^{3+}, Tm^{3+} doped Y_2O_3 nanotriangles, nanohearts and self-assembled nanodiscs as luminescent nanothermometers and photothermal agents as a function of the morphology. *To be submitted.*
62. Marciniak, L.; Strek, W.; Hreniak, D.; Guyot, Y., Temperature of broadband anti-Stokes white emission in $LiYbP_4O_{12}$:Er nanocrystals. *Applied Physics Letters* **2014,** 105 (17), 173113-173118.
63. Chen, Z.; Jia, H.; Sharafudeen, K.; Dai, W.; Liu, Y.; Dong, G.; Qiu, J., Up-conversion luminescence from single vanadate through blackbody radiation harvesting broadband near-infrared photons for photovoltaic cells. *Journal of Alloys and Compounds* **2016,** 663, 204-210.
64. Zhu, Y.; Xu, W.; Li, C.; Zhang, H.; Dong, B.; Xu, L.; Xu, S.; Song, H., Broad White Light and Infrared Emission Bands in YVO_4:Yb^{3+},Ln^{3+} (Ln^{3+}=Er^{3+}, Tm^{3+}, or Ho^{3+}). *Applied Physics Express* **2012,** 5 (9), 92701-92705.
65. Miao, C.; Liu, T.; Zhu, Y.; Dai, Q.; Xu, W.; Xu, L.; Xu, S.; Zhao, Y.; Song, H., Super-intense white upconversion emission of Yb_2O_3 polycrystals and its application on luminescence converter of dye-sensitized solar cells. *Optics Letters* **2013,** 38 (17), 3340-3343.
66. Joshi, A.; Sharaby, Y. A.; Hassan, S. S., Temperature-induced optical bistability with Kerr-nonlinear blackbody reservoir. *Optics Communications* **2016,** 359, 387-392.
67. Redmond, S. M.; Rand, S. C.; Oliveira, S. L., Bistable emission of a black-body radiator. *Applied Physics Letters* **2004,** 85 (23), 5517-5519.
68. Redmond, S.; Rand, S. C.; Ruan, X. L.; Kaviany, M., Multiple scattering and nonlinear thermal emission of Yb^{3+}, Er^{3+}:Y_2O_3 nanopowders. *Journal of Applied Physics* **2004,** 95 (8), 4069-4077.
69. Vetrone, F.; Boyer, J. C.; Capobianco, J. A.; Speghini, A.; Bettinelli, M., Effect of Yb^{3+} Codoping on the Upconversion Emission in Nanocrystalline Y_2O_3:Er^{3+}. *The Journal of Physical Chemistry B* **2003,** 107 (5), 1107-1112.
70. Dikovska, A. O. G.; Atanasov, P. A.; Jiménez de Castro, M.; Perea, A.; Gonzalo, J.; Afonso, C. N.; García López, J., Optically active Er^{3+}-Yb^{3+} codoped Y_2O_3 films produced by pulsed laser deposition. *Thin Solid Films* **2006,** 500 (1), 336-340.
71. Bilir, G.; Eryürek, G., The role played by dopant ions for the production of broadband white light emission from metal oxide nano-powders under laser diode excitation. *Ceramics International* **2016,** 42 (5), 6065-6071.
72. Nexha, A.; Carvajal, J. J.; Pujol, M. C.; Díaz, F.; Aguiló, M., Short-wavelength infrared self-assessed photothermal agents based on Ho,Tm:$KLu(WO_4)_2$ nanocrystals operating in the third biological window (1.45-1.96 μm wavelength range). *Journal of Materials Chemistry C* **2020,** 8 (1), 180-191.
73. Jaque, D.; Vetrone, F., Luminescence nanothermometry. *Nanoscale* **2012,** 4 (15), 4301-26.
74. Savchuk, O. A.; Carvajal, J. J.; Cascales, C.; Aguiló, M.; Díaz, F., Benefits of silica core-shell structures on the temperature sensing properties of Er,Yb:$GdVO_4$ up-conversion nanoparticles. *ACS Applied Materials & Interfaces* **2016,** *8* (11), 7266-7273.

75. Savchuk, O. A.; Haro-González, P.; Carvajal, J. J.; Jaque, D.; Massons, J.; Aguiló, M.; Díaz, F., Er:Yb:NaY_2F_5O up-converting nanoparticles for sub-tissue fluorescence lifetime thermal sensing. *Nanoscale* **2014,** 6 (16), 9727-9733.
76. Brites, C. D. S.; Millán, A.; Carlos, L. D., Chapter 281-Lanthanides in Luminescent Thermometry. In *Handbook on the Physics and Chemistry of Rare Earths*, Jean-Claude, B.; Vitalij K, P., Eds. Elsevier: 2016; Vol. 49, pp 339-427.
77. Savchuk, O. A.; Carvajal, J. J.; Massons, J.; Cascales, C.; Aguiló, M.; Díaz, F., Novel low-cost, compact and fast signal processing sensor for ratiometric luminescent nanothermometry. *Sensors and Actuators A: Physical* **2016,** 250, 87-95.
78. Santos, P. V. d.; Araujo, M. T. d.; Gouveia-Neto, A. S.; Neto, J. A. M.; Sombra, A. S. B., Optical temperature sensing using upconversion fluorescence emission in Er^{3+}/Yb^{3+}-codoped chalcogenide glass. *Applied Physics Letters* **1998,** 73 (5), 578-580.
79. Nexha, A.; Pujol, M. C.; Carvajal, J. J.; Díaz, F.; Aguiló, M., Controlling the growth of colloidal rare earth oxides via wet chemical methodologies. *To be submitted.*
80. Wang, D.; Kang, Y.; Ye, X.; Murray, C. B., Mineralizer-assisted shape-control of rare earth oxide nanoplates. *Chemistry of Materials* **2014,** 26 (22), 6328-6332.
81. Wang, J.; Tanner, P. A., Upconversion for white light generation by a single compound. *Journal of the American Chemical Society* **2009,** 132 (3), 947-949.

Supporting Information

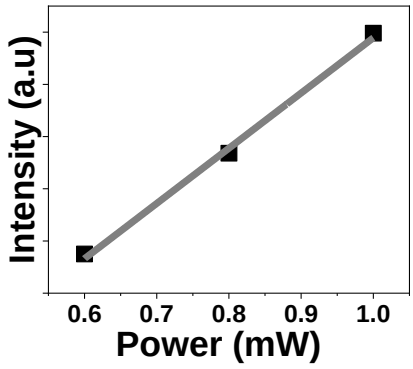

Figure S1. Variation of the maximum intensity of the white light emission with the power of the laser.

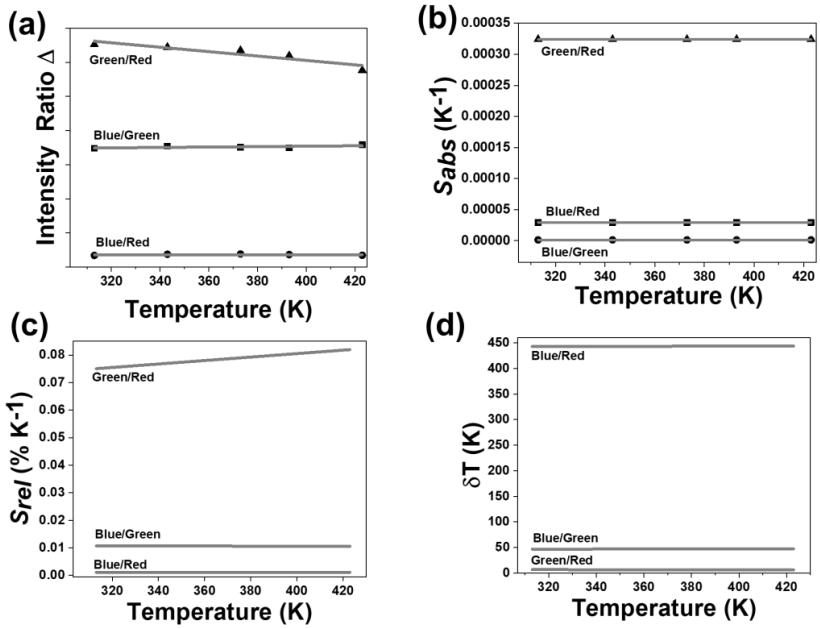

Figure S2. Thermometric performance of the white light (based on blue/green, blue/red and green/red ratios) generated from Ho, Tm doped Y_2O_3 colloidal nanocrystals based on the linear model: (a) temperature-dependence of the intensity ratio, (b) the absolute thermal sensitivity, (c) the relative thermal sensitivity and (d) temperature resolution.

Paper IX

Engineering yttrium oxide antioxidant nanoagents

Albenc Nexha, Joan J. Carvajal,* Maria Cinta Pujol, Francesc Díaz, Magdalena Aguiló
Universitat Rovira i Virgili, Departament Química Física i Inorgànica,
Física i Cristal·lografia de Materials i Nanomaterials (FiCMA-FiCNA)-EMaS, Campus Sescelades, E-43007, Tarragona, Spain
*joanjosep.carvajal@urv.cat

Abstract

Cubic yttrium oxide nanocrystals with different sizes and shapes, were synthesized via thermal decomposition and digestive ripening methodologies. From the thermal decomposition methodology, monodispersed-size nanotriangles and nanohearts, with lateral size around 23 nm and 32 nm, were produced. Self-assembled nanodiscs with diameter length up to 22 nm and thickness down to their unit cell, were produced from the digestive ripening-assisted methodology. After rendering these nanocrystals water soluble, their ability to scavenge harmful hydroxyl radicals, were tested as a function of their sizes and shapes, by applying a Fenton reaction in the presence of methyl violet as a chromogenic agent. Further, the effect of lanthanide dopants on their antioxidant properties, incorporated in yttrium sesquioxide host, was explored, leading to enhanced properties. Finally, the antioxidant properties of the best performing antioxidant nanoagent among the three different types of yttria nanocrystals, the lanthanide doped nanotriangles, were tested in an *ex-vivo* experiment, concluding that these particles can prevent the formation of hydroxyl radical species within the biological medium.

1. Introduction

Reactive oxygen species (hereafter ROS) are chemically reactive chemical species containing oxygen.[1] These species can be generated in organisms, including humans, during metabolic and immune system functions.[1] They can display a beneficial role at certain concentration in phagocytosis, apoptosis, and necrosis.[1] Nevertheless, when the concentration of these species increases above a certain limit, a chain of damages can be initiated. Typical ROS species involve superoxides (O_2^-), nitric oxide (NO), peroxynitrite ($ONOO^-$) and hydroxyl radical (•OH).[1, 2]

Among these species, hydroxyl radicals are considered as the highest reactive type of ROS, whose disbalance between generation and elimination can lead to accumulation of irreversible damages to proteins, lipids, and DNA, prolonged further to oxidative stress, mutations and cell death.[3-8] Within the human body, hydrogen peroxide, due to its longer longevity and compartmentalization can react with biomolecules containing metals, for example Cu^+ or Fe^{2+}, leading to the formation of hydroxyl radicals.[1, 2, 5, 7, 8] Due to the critical contribution of these ions to hydroxyl radical formation, whatever increases the levels of free copper or iron in the cells, such as chronic alcoholic consumption,[9] promotes the generation of ROS species. Thus, quantification and regulation of •OH species under physiological relevant conditions, is a crucial yet challenging task.

Strategies to prevent the generation of hydroxyl radicals involve the so-called antioxidant therapies. Antioxidants portray those materials, which neutralize the effect and action of the ROS species.[1, 10] Potential candidates for antioxidant therapies, during decades, involved vitamin E and C molecules.[11-13] Nevertheless, these small molecules are inherently unstable and possess limited active sites. Antioxidants are also applied in other areas. For example, they are key components in food technologies by preserving the quality of fats and oils and lipid-containing foods by suppressing oxidation reactions of their unsaturated components.[14] Further, antioxidants

are commonly used as stabilizers in fuels and lubricants to prevent oxidation, and in gasolines to prevent the polymerization, a process that leads to the formation of engine-fouling residues.[15] Therefore, the development of new antioxidant materials as potential candidates for antioxidant therapies is highly demanded.

The main class of new antioxidant compounds that have been extensively investigated are defective metal oxide based nanoparticles by virtue of their rich active sites and excellent stability.[1, 10] Typical models of metal oxide nanoparticles applied as antioxidants involve transition,[16-22] and rare-earth metals.[23-30] Among these antioxidants, rare-earth based oxides have attracted substantial focus, with the main key material being cerium oxide (also known as ceria). Ceria particles constitute a unique antioxidant material, attributed to the ability to switch between Ce^{4+} and Ce^{3+} oxidation states on their surfaces.[26, 27, 31] At the same time, their good biocompatibility properties have allowed researchers to apply ceria nanoparticles to prevent retinal degradation induced by intracellular peroxide molecules,[32] protection from radiation-induced pneumonitis,[33] treat hepatocellular carcinoma,[34] and generate cardio protective effects.[35] It has been suggested that the antioxidant properties of ceria particles are highly related to their particle size and shape, the surface electrical charge and surface coatings which affects the biodistribution of ceria, doping, oxygen vacancies distribution (nonstoichiometry) and other external factors including the pH of the medium or the nature of the buffer.[36]

The antioxidant properties of materials are often evaluated by their ability to scavenge hydroxyl radicals from Fenton reagents in a methyl violet solution. In this reaction, the decomposition of hydrogen peroxide in the presence of reducible metal ions such as iron (II), copper (I) or chromium (III), leads to the generation of hydroxyl radicals.[1, 37, 38] The result of this reaction is manifested by a decoloration of the methyl violet solution. When the antioxidant agent is added, it prevents the decoloration of the methyl violet solution by scavenging the hydroxyl radicals. This reaction can be simply followed by absorption spectroscopy.

In this paper we analyze the antioxidant properties of yttrium oxide nanocrystals as a potential hydroxyl scavenger. Yttrium oxide (Y_2O_3, also known as yttria) is an attractive choice as host material for lanthanide doping ions for photodynamic therapy and biological imaging applications,[39-43] due to its broad transparency range (0.2-8 μm), with a wide band gap of 5.6 eV, high thermal conductivity, high refractive index and low phonon energy.[44, 45] In addition, yttrium oxide based nanoparticles are benign in *in-vitro*,[46] or *in-vivo* systems,[47] which renders them a potential candidate for biomedical applications. Yttria, as ceria, displays some degree of nonstoichiometry.[48] The nonstoichiometric characteristics of yttria are exhibited under normal conditions of temperature and pressure,[49] and can be visualized through the absorption of water and carbon dioxide from the atmosphere.[50] Up to date, it is believed that are these nonstoichiometric characteristics that renders yttria its antioxidant properties.

The antioxidant properties of yttria are already demonstrated. Schubert *et al*. not only highlighted the ability of yttrium oxide to protect nerve cells from oxidative stress, but concluded that yttria particles have superior antioxidant properties compared to ceria.[46] Additional studies suggest that yttria particles prevent photoreceptors death in a light-damage model of retinal degeneration,[28] and reduce the severity of acute pancreatitis caused by cerulein hyperstimulation.[29] Yttrium oxide nanoparticles functionalized with ethylene glycol methacrylate phosphate were investigated as prophylactic and therapeutic antioxidant agents on heat stressed model.[51] Concerning antioxidant experiments based on absorption spectroscopy, the ability of yttria particles to scavenge 2,2-diphenyl-1-picrylhydrazyl (•DPPH) radicals, was reported.[52] Nevertheless, the synthetic methodologies for these particles are based on annealing of the yttrium (III) precursors at high temperatures, such as 723 K,[51] 973 K or 1173 K,[52] which can result in agglomerated particles with no control on their size or shape. In addition, up to now, there is no report evaluating the antioxidant properties of yttria nanoparticles as a function of their sizes and shapes. Furthermore, to the best of our knowledge, studies evaluating the hydroxyl radical scavenging properties of yttrium oxide nanocrystals via Fenton reactions, are not reported up to day. By analyzing the antioxidant properties of yttria particles with this method, would allow for a better comparison with already reported ceria antioxidants.

We evaluate the hydroxyl radical scavenging properties of yttrium oxide nanocrystals through the Fenton reaction assay, as a function of their sizes and shapes. Different size and shape yttria nanocrystals were synthesized by applying wet chemical methodologies, including thermal decomposition and digestive ripening reactions. In addition, we explored the effect of the

lanthanide dopants, embedded within the yttria host, on the radical scavenging capacity. We concluded with an *ex-vivo* experiments with the goal to determine if yttria can prevent the generation of harmful hydroxyl radical species inside of the body, by monitoring through photometric methods and thermal profiles, the reaction of liver catalase with hydrogen peroxide.

2. Experiments

2.1. Materials

Yttrium acetate hydrate ($Y(CH_3CO_2)_3 \cdot H_2O$ as $Y(Ac)_3 \cdot H_2O$, purity 99.99%), erbium acetate tetrahydrate ($Er(CH_3CO_2)_3 \cdot 4H_2O$ as $Er(Ac)_3 \cdot 4H_2O$, purity 99.99%), oleylamine ($C_{18}H_{35}NH_2$, as OLAM, purity 70%), methyl violet (MV), iron sulfate pentahydrate $FeSO_4 \cdot 7H_2O$, Tris-HCl buffer (pH=4.5), were purchased from Sigma Aldrich. Ytterbium acetate tetrahydrate ($Yb(CH_3CO_2)_3 \cdot 4H_2O$ as $Yb(Ac)_3 \cdot 4H_2O$, purity 99.99%), was purchased from Apollo Scientific. Oleic acid ($CH_3(CH_2)_7CH=CH(CH_2)_7COOH$, as OLAC, purity 90%), 1-octadecene ($CH_3(CH_2)_{15}CH=CH_2$ as ODE, purity 90%), n-hexane (99%), sodium nitrate ($NaNO_3$, 99%) were purchased from Alfa Aesar. Sodium chloride (NaCl), H_2O_2 (30 wt.%) and ethanol (EtOH), were purchased from Merck and VWR Chemicals, respectively.

2.2. Synthesis of colloidal yttrium sesquioxide nanocrystals

Yttrium sesquioxide nanocrystals with the shape of branched nanotriangles and nanohearts, were synthesized via a thermal decomposition method, as previously reported.[53, 54] In a typical synthesis of undoped Y_2O_3 branched nanotriangles, 2.5 mmol of $Y(Ac)_3 \cdot H_2O$ and 4 mmol of $NaNO_3$ were added to a mixture of 25 mmol OLAC, 25 mmol OLAM and 15 mmol ODE in a three neck flask. The reaction mixture was degassed at 393 K for 0.5 h to ensure the removal of residual oxygen species and complexation of rare earth ions with the organic surfactants. After switching to nitrogen atmosphere, the mixture was heated at 583 K and maintained at this temperature for a period of 0.5 h. The reaction was cooled down naturally to room temperature. Purification is conducted through the addition of an excess of ethanol, followed by centrifugation at 5000 rpm during 10 min and redispersion of the precipitates in an apolar solvent (n-hexane). The purification cycle was repeated three times. The final product can be stored as a dispersion in n-hexane or as a solid product, after evaporation of the solvent in a muffle furnace at 333 K for 4 h. For the synthesis of doped nanotriangles, the methodology was the same, except that 2 mol% $Er(Ac)_3 \cdot 4H_2O$ and 10 mol% $Yb(Ac)_3 \cdot 4H_2O$ (or 4 mol% $Er(Ac)_3 \cdot 4H_2O$ and 4 mol% $Yb(Ac)_3 \cdot 4H_2O$), were introduced as dopants at the beginning of the reaction.

For the synthesis of undoped yttrium sesquioxide nanohearts, the methodology was identical, except that the reaction mixture was treated at 583 K for a period of 2 h.

Yttrium sesquioxide nanocrystals with the shape of self-assembled nanodiscs were synthesized via a digestive ripening method.[53] In a typical synthesis, 0.2 mmol $Y(Ac)_3 \cdot H_2O$, 0.1 mmol of NaCl and 45 mmol of OLAM, were added to a three neck flask and heated at 553 K using a ramp of 15 $Kmin^{-1}$ under protective nitrogen atmosphere. At 553 K, 15 mmol of OLAC were swiftly injected in the reaction flask and the reaction mixture was allowed to age for 1 h, prior to cooling down naturally at room temperature. The product of the reaction was extracted by adding an excess of ethanol to the solution, followed by centrifugation at 4000 rpm for 10 min, after which the supernatant was discarded and the precipitate was redissolved in n-hexane. The purification cycles were repeated until the discarded supernatant was colorless. The final product of the reaction can be either stored as a dispersion in n-hexane or as a powder by evaporating the solvent.

2.3. Preparation of water dispersible yttrium sesquioxide nanocrystals

Water dispersible yttrium oxide nanocrystals were prepared by treating the as-synthesized particles obtained by the thermal decomposition and digestive ripening methods under acidic conditions, as reported elsewhere.[55] Shortly, around 60 mg of the as-synthesized nanoparticles were dispersed in 30 mL of a solution of HCl and ethanol with pH adjusted to 1.0. The mixture was sonicated for 1 h. Ligand free nanoparticles were obtained after centrifugation at 6500 rpm for 10 min and washing with a HCl/ethanol solution, with pH adjusted to 4.0. Several washing

cycles with ethanol and distilled water, lead to the final dispersion of these nanoparticles in distilled water.

2.4. Hydroxyl radical scavenging properties

The antioxidant properties of yttrium oxide nanocrystals were analyzed by investigating their capability to scavenge the hydroxyl radicals from Fenton reagents in a methyl violet (MV) solution. Stock solutions of methyl violet (1 mM), Tris-HCl buffer (0.5 M), $FeSO_4 \cdot 7H_2O$ (0.45 mM), H_2O_2 (2 M) and water dispersible yttrium oxide nanoparticles of different shapes (nanotriangles, nanohearts or nanodiscs with 20 mg/mL concentration each) were prepared separately before the photometric analysis. A reaction solution with a final volume of 4 mL was prepared, composed by $1.2 \cdot 10^{-5}$ M MV, 0.15 mM $FeSO_4 \cdot 7H_2O$, 1.0 M of H_2O_2, 0.1 M Tris-HCl buffer,[23, 24, 31] to which 0.1 to 2 mg/mL water dispersible yttrium oxide nanoparticles were added. The reaction solution was thoroughly mixed by sonicating it for 5 minutes prior to the UV-VIS absorbance measurements using a UV-VIS-NIR Cary 5000 spectrophotometer. .

2.5. *Ex-vivo* antioxidant properties of yttrium sesquioxide nanocrystals

For the *ex-vivo* experiment, the decomposition of hydrogen peroxide by liver catalase and the role of the yttrium oxide nanoparticles as antioxidant agents were explored. Within these experiments, an exothermic reaction takes place when liver catalase reacts with hydrogen peroxide, accompanied by the formation of foam.[56] In the experiments we used fat pig liver, distilled water, yttria nanoparticles and hydrogen peroxide. In a typical *ex-vivo* experiment, different quantities of fat pig liver, distilled water, yttria nanoparticles and hydrogen peroxide, were added in this order, and were optimized in the absence of a reference model. The optimal quantities were evaluated by tracking the reaction solution through absorbance measurements in a UV-VIS-NIR Cary 5000 spectrophotometer, with the goal of observing the evolution of the absorption band of liver catalase, and by recording the temperature within the solution through a platinum and platinum-10% rhodium thermocouple connected to a digital multimeter. Fat pig liver was smashed by a blender. A certain quantity of smashed liver was dispersed in distilled water by sonicating it for a period of 0.5 h. Analysis were acquired within a period of time of 5 min to avoid flocculation of the smashed liver within the solution. After establishing the proper weight of smashed liver and volume of distilled water for proper absorbance analyses, we initially tested the effect of different volumes of hydrogen peroxide, and monitored the absorbance of liver. In addition, here an exothermic reaction takes place. The temperature changes within a period of 5 min were recorded using the thermocouple. After that we tested the effect of the addition of undoped and Er, Yb doped yttria nanoparticles on the reaction to analyze their antioxidant properties in this biological system.

2.6. Characterization

The crystalline structure of the as-synthesized and acid treated particles were investigated by X-ray powder diffraction (XRPD). The measurements were made using a Siemens D5000 diffractometer (with Bragg-Brentano parafocusing geometry and a vertical θ-θ goniometer) fitted with a curved graphite diffracted-beam monochromator, incident and diffracted-beam Soller slits, a 0.06° receiving slit, and a scintillation counter as detector. The angular 2θ diffraction range was set between 5° and 70°. The data were collected with an angular step of 0.05° at 3 s per step with sample rotation to increase the statistics of the signal collected. Cu K_α radiation was obtained from a Copper X-ray tube operated at 40 kV and 30 mA.

The size and shape of the nanoparticles were investigated by transmission electron microscopy (TEM). The images were acquired using a JEOL JEM-1011 electron microscope operating at an accelerating voltage of 100 kV. For the preparation of the TEM grids, the nanocrystals were dispersed in n-hexane in the case of the as-synthesized nanoparticles, and in distilled water for the acid treated nanoparticles. Around 7 µL of the solutions were placed on the surface of a Copper grid covered by a holey Carbon film (HD200 Copper Formvar/Carbon).

The ligands present on the surfaces of the as-synthesized and acid treated nanoparticles were investigated using Fourier Transform Infrared (FT-IR) spectroscopy. The spectra were recorded in the range of 400-4000 cm^{-1} in a FT-IR IluminatIR II, Smith spectrophotometer.

3. Results and Discussion

3.1. Synthesis of yttrium oxide nanocrystals

The sizes and shapes, the crystalline structures and the surfaces of the yttrium oxide nanoparticles, as-synthesized from the wet chemical methodologies, and after acid treatment, were examined. By applying thermal decomposition and digestive ripening synthesis in the presence of $NaNO_3$ and NaCl as additives, different sizes and shapes of the nanocrystals could be obtained.[53] The size and shape of the yttrium oxide nanocrystals obtained were examined by TEM and their size distribution was determined using the Image J software after analyzing over 100 nanocrystals.

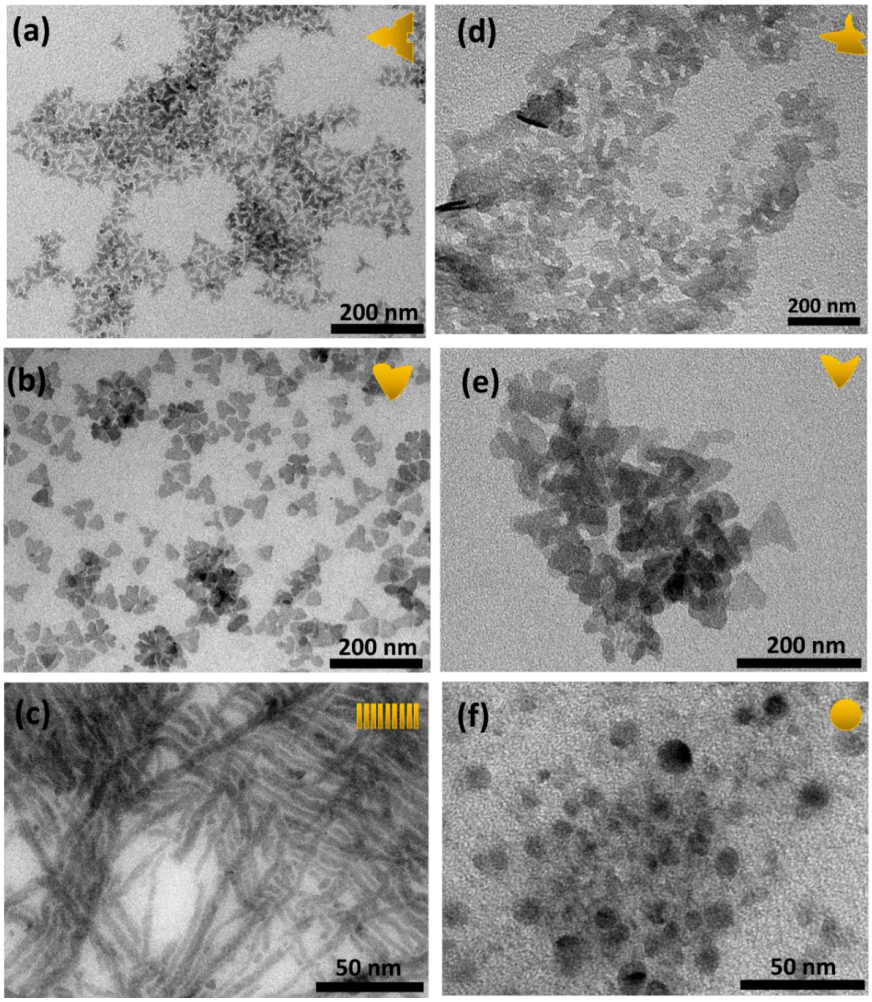

Figure 1. TEM images of the as-synthesized and acid treated nanocrystals: (a), (d) branched nanotriangles, (b), (e) nanohearts, and (c), (f) nanodiscs. The sketch in the figures depict the shape of the colloidal nanocrystals obtained.

The shape of the nanocrystals obtained through the thermal decomposition reaction in the presence of $NaNO_3$ as a structure-directing agent can be described as branched nanotriangles (see Figure 1 (a), and Figure S1 at Supporting Information for a high resolution TEM image clarifying the branched shape of the nanocrystals) and nanohearts ((see Figure 1 (b)), for reaction times of 0.5 h and 2 h, respectively, while keeping the reaction temperature unchanged (583 K). The branched nanotriangles have an average lateral dimension of 23 ± 3.1 nm (see Figure 2 (a)), whereas the nanohearts are in the range of 32 ± 5.8 nm (see Figure 2 (b)), confirming that with the increase of the reaction time, the nanocrystals grow bigger.[53]

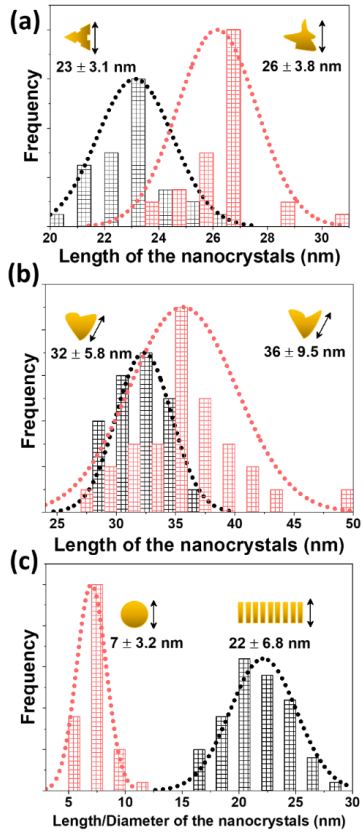

Figure 2. Lognormal size distribution of the as-synthesized (in black) and acid treated (in red) nanocrystals: (a) branched nanotriangles, (b) nanohearts, and (c) nanodiscs. The arrows within the sketch of the shape of the nanoparticles stands for the parameter taken into account to determine their dimensions.

For the nanocrystals synthesized via the digestive ripening method in the presence of NaCl as structure-directing agent, the shape matches that of self-assembled nanodiscs (see Figure 1 (c)), with a mean diameter of 22 ± 6.8 nm (see Figure 2 (c)) and a thickness similar to the unit cell dimensions (1.02 ± 0.1 nm), as determined by high resolution TEM images (see Figure S2 in the Supporting Information) and previously reported.[53]

In order to make these nanocrystals compatible for radical scavenging assays in biological environments, water dispersible particles should be prepared.[1] To achieve this goal, the as-synthesized nanocrystals, were treated under acidic conditions in a HCl/ethanol solution at pH=1.0.[55] The sizes and shapes of the organic surfactant-free nanocrystals obtained under this treatment were examined by TEM. It is clear that the acidic treatment affected substantially to the shapes and sizes of the nanoparticles. For the branched nanotriangles, their shape has changed to an almost irregular one, with the edges totally vanished (see Figure 1 (d)). In addition, these nanoparticles have a tendency to assemble, probably due to the absence of coating organic surfactants. Concerning the size, they are bigger than the initial nanotriangles, with size ~26 ± 3.5 nm as can be seen in Figure 2 (a), where a comparison of the lognormal size distribution of the nanocrystals before and after acidic treatment is presented. Instead, the shape of the nanohearts is maintained (see Figure 1 (e)), although they also tend to aggregate. Their sizes increased slightly to 36 ± 9.5 nm (see Figure 2 (b)).

Self-assembled nanodiscs display the major changes in terms of their sizes and shape. After the acidic treatment, the nanodiscs have lost their ability to self-assemble (see Figure 1 (f)). It is

accepted in the literature that the self-assembly behavior of these nanodiscs is maintained because of the oleate surfactants that capped their surfaces,[53, 57, 58] confirmed by the nanodisc-to-nanodisc distance (3.8 nm),[53, 57] which matches with the double of the projected distance of the cis-oleic acid molecule, indicating that there these molecules are attached in both sides of the discs.[59] With the treatment under acidic conditions, the oleic acid organic surfactants are removed from the surface of the nanodiscs, which in turn, disassemble. As a result, disc shaped particles with average sizes around 7 ± 3.2 nm are obtained (see Figure 2 (c)).

Regardless of the shape and size of the nanocrystals and if they have been treated with acid or not, they crystallized in the cubic system with *Ia* $\bar{3}$ spatial group, (see Figure 3). In general, the XRPD patterns are composed of broad peaks, attributed to the small sizes of the colloidal nanocrystals. In addition, it could be observed the absence (in the self-assembled nanodiscs) or the presence (in the branched nanotriangles and nanohearts) of the (400) peak, as we have previously reported, which indicates the crystallographic orientation of the observed morphologies.[53] For the branched nanotriangles and nanohearts, this orientation belongs to a one dimensional (1D) [111] confinement, whereas for the self-assembled nanodiscs, the orientation is towards the [100] confinement.[53] Therefore, the nanoparticles are, from the crystal structure point of view, stable.

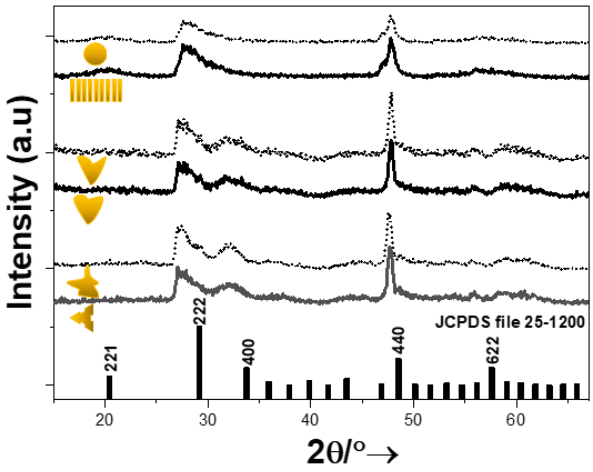

Figure 3. XRPD patterns of the as-synthesized (solid black line) and acid treated (dashed black line) Y_2O_3 nanocrystals. The reference pattern of cubic Y_2O_3 (JCPDS file 25-1200) is included for comparison.

We also analyzed the surface of the yttrium oxide nanocrystals to investigate the presence of organic surfactant coating molecules by using Fourier Transform Infrared spectroscopy (FT-IR). The colloidal nanocrystals synthesized by thermal decomposition and digestive ripening methods present oleic acid moieties on their surfaces. Oleic acid does not appear in its pure form, as can be confirmed by the absence of the characteristic band of the C=O stretching mode appearing at 1710 cm^{-1}. This band is replaced by a band appearing at 1580 cm^{-1} and 1435 cm^{-1} for the branched nanotriangles and nanohearts, respectively, whereas for the self-assembled nanodiscs by bands appearing at 1605 cm^{-1} and 1420 cm^{-1} (see black solid lines in Figure 4), ascribed to the antisymmetric and symmetric stretching vibrations of the deprotonated carboxylic group (COO^-), indicating that the OLAC molecules were deprotonated into carboxylates anions due to the promotion of OLAM.[60] The absence of OLAM is expected, as the role of this surfactant is to catalyze the deprotonation of OLAC.[61] This observation is in agreement with other articles published that illustrate that no FTIR spectral features characteristics of an amine-containing species are observed,[60, 62, 63] even when in the reaction only OLAM is used.[64] The peaks at 2850 and 2924 cm^{-1} are assignable to the symmetric and the antisymmetric methylene group stretches

(ν_s (CH_2) and (ν_{as} (CH_2)) of OLAC and OLAM.[62, 65] A very weak shoulder around 2924 cm^{-1} is attributed to the antisymmetric methyl stretch ν_{as} (CH_3).

For the particles treated under acidic conditions, the FT-IR spectrum reveal that most of the bands are weakened. For example, the shoulder band at around 2924 and 2850 cm^{-1} or the carboxylate bands at 1580 cm^{-1} and 1435 cm^{-1} have decreased (see dotted lines in Figure 4), as reported previously.[55] In addition, the appearance of a broad bands around 3400 cm^{-1} is detected. This band is assigned to the O-H stretching band of water.[66] These results seem to ensure that we modified the surface of the nanoparticles to facilitate their dispersibility in water.

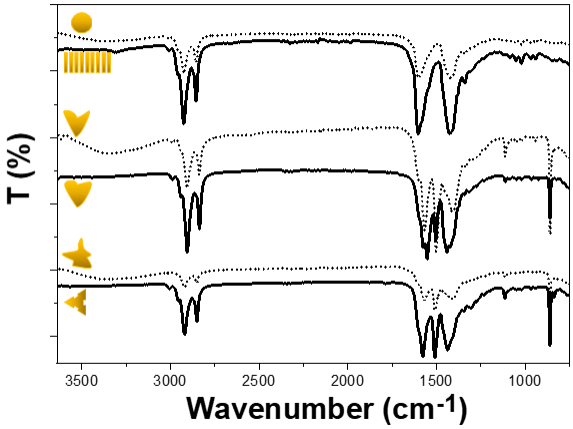

Figure 4. FT-IR spectra of the as-synthesized (black solid lines) and acid treated (dashed black lines) yttria nanocrystals.

3.2. Hydroxyl radical scavenging properties of yttrium sesquioxide nanocrystals

Antioxidant properties of water dispersible yttrium oxide nanocrystals were determined by their ability to scavenge hydroxyl radicals produced in the Fenton reaction, using methyl violet as a chromogenic agent. MV, dissolved in water, displays a purple color with a maximum absorbance located at around 590 nm.[67] The Fenton reagents, Fe^{2+} ions and H_2O_2 under acidic, neutral or basic conditions,[24, 37, 38, 68] can react to generate hydroxyl radicals. These radicals can quickly interact with MV by attacking its –C=C– bond, oxidizing the purple MV into colorless MV.[24, 37, 38, 68] This oxidation process is manifested by a decrease of the absorbance of MV.[23, 26, 31] The antioxidant properties of yttria nanocrystals will be assessed if they can protect MV from being attacked by •OH radicals when added to the solution, visualized through an avoidance of the reduction of the intensity of the maximum of absorbance of MV.

For the UV-Vis photometric experiments, first, we determined the absorbance of MV, dispersed in distilled water with a concentration of $1.2 \cdot 10^{-5}$ M, as a function of time. The results reveal that, within a time frame of at least 30 min, long enough to perform the Fenton reaction, no change on the absorbance of MV could be detected (see Figure S3 (a) in the Supporting Information). Then, a new solution containing MV, H_2O_2 (1 M concentration) and Y_2O_3 (nanotriangles with a concentration 0.01 mg/mL), in the absence of the Fenton reagents, was prepared and the absorbance was measured. No changes were observed to respect of MV in distilled water only (see Figure S3 (b) at Supporting Information), indicating that in the absence of Fe^{2+} ions no Fenton reaction can take place, and thus, no free hydroxyl radicals could be generated.

When Fe^{2+} ions are introduced into a new solution with MV, H_2O_2 and Y_2O_3 (same concentrations as above), in the form of $FeSO_4 \cdot 7H_2O$ under acidic conditions, the Fenton reaction takes place and •OH radicals can be generated within the medium. Figure 5 (a) shows the comparison of the absorbance spectra of a solution containing only MV in distilled water, a solution containing MV, Fe^{2+} ions at a 0.15 mM concentration, and H_2O_2 at a 1 M concentration (Fenton reaction), and a

Fenton reaction solution to which yttria nanotriangles were added with a concentration of 0.01 mg/mL, inspired from previously reported investigations on ceria.[23, 24, 31] The incubation time in all cases has been less than 2 min. Clearly, a decrease in the intensity of the maximum of absorbance after the Fenton reaction was observed (see red line in Figure 5 (a)), suggesting that the MV molecules have been oxidized. When yttria nanoparticles are introduced into the solution, the intensity of the maximum of absorbance recovers part of its value (see purple line in Figure 5 (a)). These results prove the ability of our yttria nanoparticles to scavenge part of •OH radicals and protect MV from further oxidation.

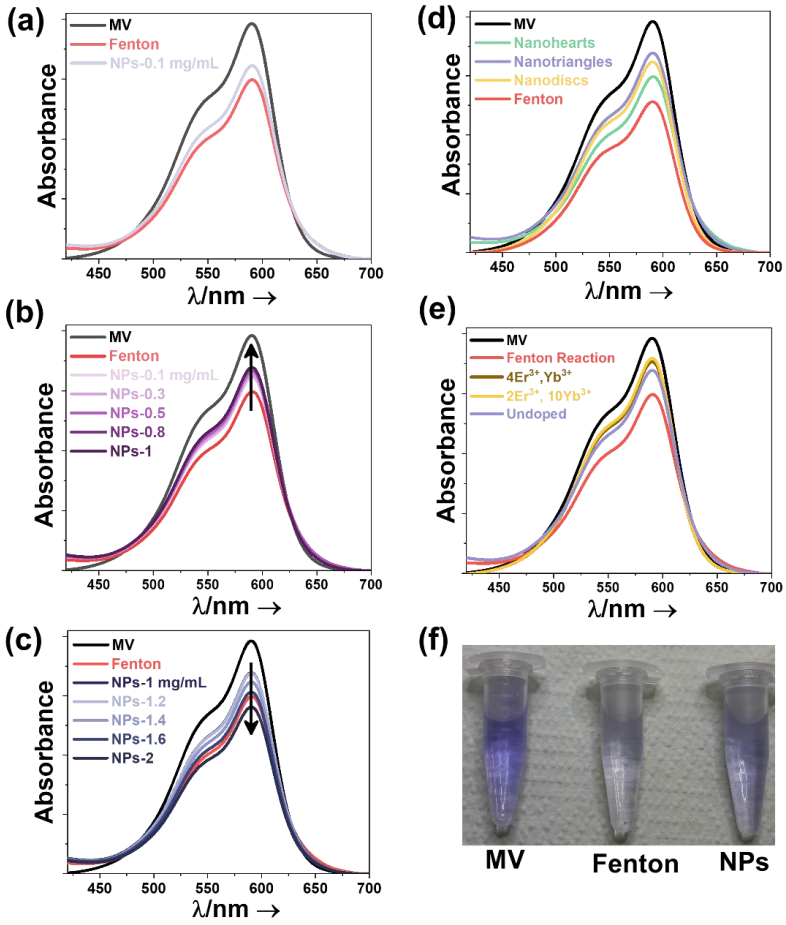

Figure 5. Absorbance spectra of methyl violet: (a) in distilled water, in the Fenton reaction solution, and with the addition of yttria nanoparticles; (b) tuning the concentration of yttria nanoparticles in the Fenton reaction solution from 0.1 mg mL^{-1} to 1 mg mL^{-1}; (c) tuning the concentration of yttria nanoparticles in the Fenton reaction solution from 1 mg mL^{-1} to 2 mg mL^{-1}; (d) size and shape of the yttrium oxide nanoparticles (nanotriangles with average sizes of 26 ± 3.5 nm, nanohearts with average sizes of 36 ± 9.5 nm and nanodiscs with an average diameter of 7 ± 3.2 nm; (e) doping ions incorporated in the yttria nanotriangles(4 mol% Er^{3+},4 mol% Yb^{3+} and 2 mol% Er^{3+},10 mol% Yb^{3+}), and (f) Pictures displaying the change in color of the methyl violet in distilled water (labelled "MV"), in the Fenton reaction solution without yttria nanoparticles (labelled "Fenton") and with 2 mol% Er^{3+}, 10 mol% Yb^{3+} doped yttria nanotriangles (labelled "NPs").

It has been reported recently that several factors can significantly affect the antioxidant activity of the nanocrystals.[69] One of these factors is the concentration of nanocrystals added in the reaction. Lu *et al.* found that when increasing the concentration of ceria nanoparticles up to 20 μM, the antioxidant properties exhibited by these nanoparticles are enhanced. Nevertheless, an additional

increase of the concentration until 50 μM lead to disappearance of the antioxidant properties, and instead, an enhancement of the oxidant activity was observed.[69] Following this idea, we tuned the concentration of yttria nanotriangles to determine which concentration scavenge most effectively the formation of •OH radicals in the Fenton reaction.

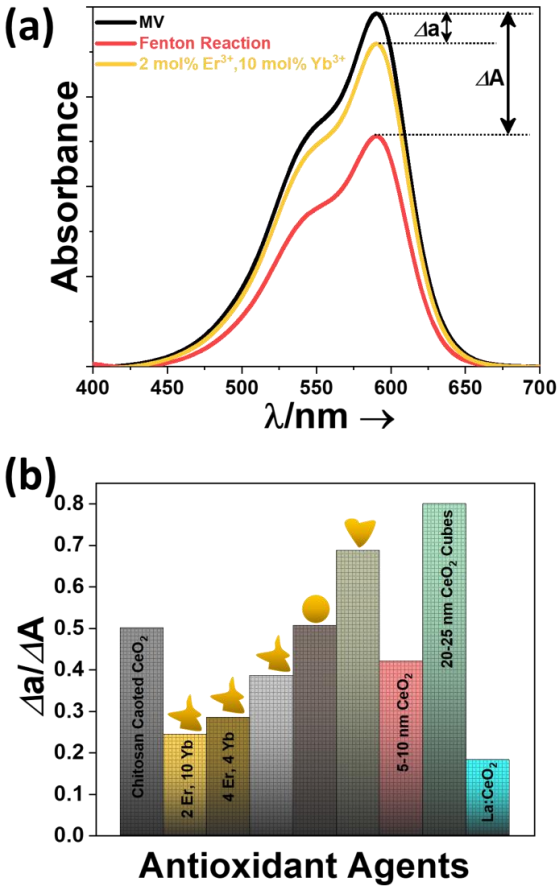

Figure 6. (a) Scheme portraying the model for the determination of the antioxidant capacity of the nanocrystals by taking into account the changes in the maximum of absorbance for MV, using as an example 2 mol% Er^{3+},10 mol% Yb^{3+} doped yttria nanotriangles. (b) Data chart displaying the antioxidant performance of the different nanocrystals based on the ratio between Δa and ΔA. On the data chart are included yttria based nanocrystals within this study showed with their corresponding shapes, and cerium oxide nanocrystals: 5-10 nm CeO_2 nanoparticles and 20-25 nm CeO_2 nanocubes,[69] chitosan coated CeO_2 nanoparticles,[70] and 10 mol% lanthanum doped ceria nanocubes.[26]

The results reveal that the antioxidant properties of Y_2O_3 nanoparticles depend on their concentration (see Figures 5 (b) and (c)). For concentrations up to 1 mg mL^{-1}, their capacity to prevent the generation of hydroxyl radicals increases, achieving as maximum of the antioxidant activity for a concentration of 1 mg mL^{-1} (see Figure 5 (b)). Instead, a further increase of the concentration up to 2 mg mL^{-1}, causes a reduction in the antioxidant activity of the nanoparticles (see Figure 5 (c)) until they disappear totally, and a further oxidation of methyl violet is observed. Thus, a concentration of 1 mg mL^{-1} seems to be the optimal concentration to maximize the antioxidant activity of the yttria nanotriangels.

We also analyzed the effect of the shape and size of the yttria nanoparticles of their antioxidant properties, fixing their concentrations to 1 mg mL^{-1}. Distorted nanotriangles exhibited the better

antioxidant properties compared with the other morphologies (see Figure 5 (d)). Nanohearts exhibited the smallest antioxidant capacity. We believe the reason for this behavior might be related with the oxygen vacancies present in the yttria nanoparticles. Despite we did not determine the concentration of oxygen vacancies in our nanocrystals, it is generally accepted that irregular nanocrystals tend to accumulate more oxygen vacancy defects on their surfaces,[1, 23] which in turn would increase the scavenging of hydroxyl radicals.

Having established nanotriangles as the best antioxidant agent among the yttria nanocrystals synthesized, we finally, analyzed if the incorporation of lanthanide dopants in the nanoparticles plays any role on the antioxidant properties of exhibited by them. It has been reported that yttrium oxide can incorporate lanthanide ions as dopants within its structure replacing Y^{3+} ions.[71, 72] It has also been reported that the introduction of lanthanide dopants in ceria nanoparticles enhanced their antioxidant properties.[25, 26]

We tested the antioxidant properties of Er^{3+} and Yb^{3+} co-doped yttria nanotriangles. The doped particles were synthesized through the same thermal decomposition method, and no changes were observed in the crystalline structure (see Figure S4 (a) in the Supporting Information). However, when comparing morphologically the undoped and doped nanocrystals, clearly, for the doped ones, slight distortions from the general branched nanotriangle shape, are detected (see Figure S4 (b) at Supporting Information for a comparison between the two shapes), suggesting that dopants can induce irregularities in shape. We explored two different doping concentrations, 4 mol% Er^{3+},4 mol% Yb^{3+} and 2 mol% Er^{3+},10 mol% Yb^{3+}. It has been reported that dopants can generate changes in the lattice constants of the host matrices, leading to irregularities and to an increase of the concentration of oxygen vacancies, causing eventually an enhancement of their antioxidant properties.[25, 26, 36] Indeed, we observed an increase of the antioxidant properties of the Er^{3+} and Yb^{3+} doped yttria nanotriangles when compared to the undoped ones, and these antioxidant properties were slightly better when the quantity of dopants was higher (see Figure 5 (e)). These results support the idea that the introduction of dopants increases the morphological irregularities in the nanoparticles, and as a consequence, also the concentration of oxygen vacancies, leading to better antioxidant properties.

To compare the performance of our yttria nanoparticles with that of other ceria nanoparticles as antioxidant agents reported in the literature, we considered the comparison between the maximum intensity of the absorption band of MV under the different reaction conditions, as proposed previously by Lu *et al*..[69] Taking as reference the value of the maximum intensity of the absorption band of MV in distilled water, ΔA is defined as the drop in the intensity of this peak under the Fenton reaction conditions (see Figure 6 (a)). From another side, Δa corresponds to the decrease in the intensity of this peak when the antioxidant particles are added to the solution (see Figure 6 (a)). Then, the evaluation of the performance of the nanoparticles as antioxidant agents is based on the ratio between Δa and ΔA.[31, 69] If the nanoparticles can prevent the formation of •OH radicals, the value of Δa should be smaller than ΔA.[31, 69] Therefore, the smaller the value of this ratio, the stronger the hydroxyl radical scavenging properties of the nanocrystals.[31, 69]

Figure 6 (b) shows the values of $\Delta a/\Delta A$ ratio for our yttria nanoparticles, together with that of other ceria nanoparticles reported in the literature. Several remarks can be drawn from this figure. First, doped nanoparticles, including 2 mol% Er^{3+},10 mol% Yb^{3+} and 4 mol% Er^{3+},4 mol% Yb^{3+} doped yttria, and 10 mol% lanthanum doped ceria,[26] exhibit lower values for this ratio, *i.e.* better antioxidant properties, compared to the corresponding undoped particles. Hence, the use of lanthanide doped ceria or yttria nanoparticles can be clearly underlined as a promising strategy for the future development of antioxidant nanoagents with improved performance. Second, the geometrical characteristics of the antioxidant nanoparticles, such as their sizes and shapes, greatly influence their performance. Smaller particles seem to exhibit better performances (see the values of the $\Delta a/\Delta A$ ratio in Figure 6 (b) for 5-10 nm CeO_2 nanoparticles and 20-25 nm CeO_2 nanocubes,[69] with the former one being more effective). Third, it can be also deduced from the data provided in Figure 6 (b), that coating the particles with biocompatible molecules as chitosan, can affect to the antioxidant properties, reducing them, probably because the active sites of the antioxidant nanoparticles are hampered by these coating molecules.[27, 36] But the main conclusion

that we can extract from these results is that yttria nanoparticles exhibit similar antioxidant properties with those reported up to now for ceria nanoparticles, thus opening the door to this application for yttria nanoparticles.

3.3. *Ex-vivo* antioxidant properties of yttrium oxide nanocrystals

To demonstrate the possibility of using yttrium oxide nanocrystals as antioxidant agents in biological/biomedical applications, we designed an *ex-vivo* experiment to monitor the reaction of the catalase enzyme that can be encountered in liver with hydrogen peroxide. Catalase consists of a tetramer of four polypeptide chains, each over 500 amino acids long, with four iron-containing heme groups.[73] When hydrogen peroxide enters in contact to the liver, an exothermic chemical reaction, followed by the creation of foams, occurs, leading to the generation of oxygen and water molecules.[56] This reaction is promoted by the catalase enzyme. Hence, catalase can eliminated hydrogen peroxide either by promoting a reaction between two hydrogen peroxide molecules resulting in the formation of water and oxygen, or by promoting the interaction of hydrogen peroxide with compounds such as alcoholic beverages that serve as hydrogen donors, so that the hydrogen peroxide can be converted to one molecule of water, and the reduced donor becomes oxidized (a process called the peroxidatic activity of catalase).[56, 74]

Hence, this enzyme prevents from the generation of harmful ROS species, such as •OH radicals, within the liver. We underline the similarities between the reactions of iron ions in the Fenton assay with the one of catalase with hydrogen peroxide. In both reactions, the presence of iron species allows for the generation of ROS radicals. Thus, the reaction of catalase with hydrogen peroxide mimics the Fenton assay.

Thus, the goal of the *ex-vivo* experiment was to investigate the antioxidant properties of yttrium oxide nanocrystals on the reaction of liver catalase with hydrogen peroxide. If yttria nanocrystals do exhibit antioxidant properties within this biological system, the heat released by the interaction of catalase with hydrogen peroxide during the experiment, will be reduced compared to the reaction in the absence of these nanoparticles. The reaction was also monitored through spectrophotometric analysis.

In a solution of the smashed pork liver in distilled water, were added different amount of H_2O_2, and both, the absorbance of the dispersion and the temperature generated during the exothermic reaction were monitored. To obtain substantial enough changes in both parameters to monitor the potential activity of the antioxidant nanoparticles in the subsequent experiments, 2 mL of H_2O_2 had to be added to the solution. Smaller amounts of H_2O_2 generated a change in temperature too small to see any effect from the antioxidant nanoparticles (see Figures 7 (a)), while bigger amounts of H_2O_2 cause the absorption bands of catalase to disappear (see Figures 7 (b)). We also monitored the temperature in the dispersion of liver only in distilled water for control purposes. The temperature within this solution remained constant at room temperature for the monitored period of 5 min. Thus, the increase of temperature observed occurs only when the reaction of liver catalase with hydrogen peroxide occurs. In addition, to obtain a good spectrum of absorbance of the smashed pork liver in distilled water it was necessary to generate a dispersion of 70 mg of smashed liver in 5.5 mL of distilled water. In this dispersion, we were able to observe the presence of three absorbance bands, located at 415 nm, 540 nm and 575 nm (see Figure 7 (b)). The 415 nm band, is the so-called Soret band, and is assigned to the π-π^* transition of the porphyrin hosting iron band, the bands located at 540 nm and 575 nm are attributed to metal-to-ligand charge transfer processes.[75, 76]

When yttria nanotriangles were added to the solution, in the sequence: 70 mg liver, 5.5 mL of distilled water, undoped yttria nanotriangles (from 2 mg to 10 mg) and 2 mL of H_2O_2, the antioxidant effect of the yttria nanoparticles could be analyzed. The temperature changes allowed us to monitor more precisely what is happening in the solution for the different quantities of yttria nanoparticles added. When 4-10 mg of yttria nanotriangles were added, the temperature of the solution is similar or increased above the temperature recorded in the reaction without the presence of the yttria particles (see Figure 7 (c)). Thus, this would imply that at these quantities, the yttria nanocrystals act as an oxidant. When only 2 mg of yttria nanoparticles were added, the antioxidant properties were manifested, as the temperature decreased to 302 K, below the temperature obtained only with H_2O_2 (see Figure 7 (c)). In the meanwhile, the absorbance of the

catalase in the presence of 2 mg of yttria nanoparticles, increased slightly compared to that observed in the solution containing others, the catalase and H_2O_2 only (Figure 7 (d) displays in scattered point the maximum absorbance for 415 nm, 540 nm and 575 nm bands as a function of different amount of undoped particles, while the full absorbance spectrum is presented in Figure S5 (a) at the Supporting Information). For the other concentrations, the absorbance of the catalase is decreased, even lower the one of the solution of the liver with distilled water and hydrogen peroxide (see Figure 7 (d) and Figure S5 (a) at Supporting Information), probably because at these concentration oxidant properties are manifested instead of the antioxidants. Hence, we established 2 mg nanotriangles as the optimal amount of yttria nanoparticles to be added into the solution mixture to reduce the effects of the reaction between catalase and H_2O_2.

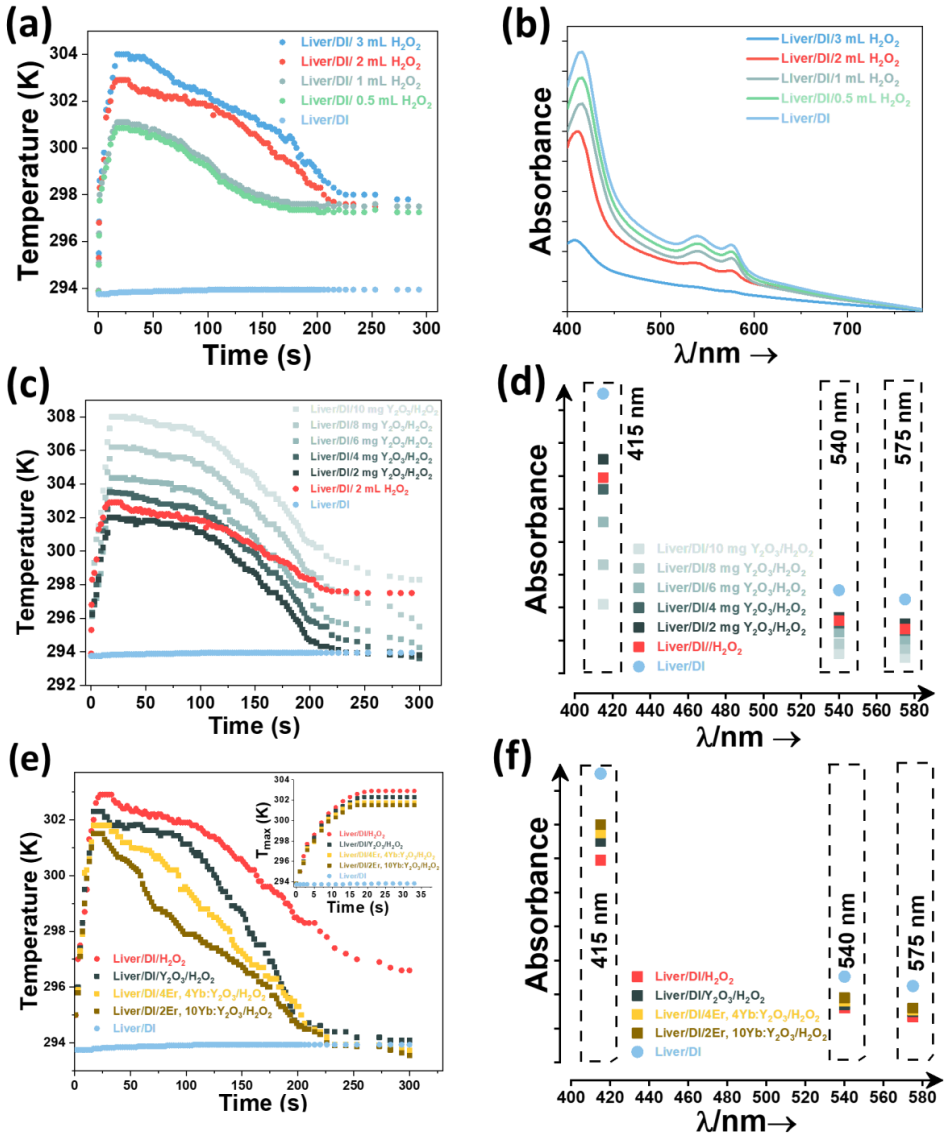

Figure 7. Absorbance (scattered point of the maximum absorbance for each band in (d) and (f)) and temperature profiles recorded in a solution composed of liver and: (a) and (b) distilled water and different quantities of hydrogen peroxide; (c) and (d) distilled water, 2 mL hydrogen peroxide and different quantities of undoped yttria nanotriangles; and (e) and (f) distilled water, 2 mL hydrogen peroxide 2 mg of Er^{3+} and

Yb^{3+} co-doped yttria nanotriangles with different doping concentrations. The inset under figure (e) displays the maximum temperature reached within the first 30 seconds of the reaction.

Finally, when we introduce Er^{3+} and Yb^{3+} as dopants in the yttria nanoparticles, since the doped yttria nanoparticles exhibited better antioxidant properties in the Fenton reaction than the undoped ones, we observed that the temperature increase is lower than when undoped nanoparticles where used (see Figure 7 (e)). Among the doped nanoparticles, the highest temperature reached for the 4 mol% Er^{3+},4 mol% Yb^{3+} yttria nanoparticles is ~301.5 K, whereas for the 2 mol% Er^{3+},10 mol% Yb^{3+} doping concentration is ~301 K (see the inset of Figure 7 (e) which displays the maximum temperature reached for the nanoparticles within the first 30 seconds of the reactions), 0.5 and 1 K lower than the temperature achieved with the undoped nanotriangles (see Figure 7 (c)). These results seem to demonstrate that the increase of the doping concentration favors the antioxidant properties in these particles. Also, as can be seen in Figure 7 (e), the temperature profile of the doped nanoparticles decreases faster from the maximum when compared to that of the undoped nanoparticles. This might indicate that the process of reducing the effects of the reaction between catalase and H_2O_2 develops faster using these nanoparticles, and the liver recovers faster its normal temperature. These results were corroborated through the better recovery of the intensity of the absorption bands of catalase observed when doped yttria nanoparticles are added to the reaction, as can be seen in Figure 7 (f) where scattered point display the maximum absorbance of each band (or in Figure S5 (b) with the full spectrum of the absorbance for each case). Thus, we can conclude that the yttria nanoparticles we developed here might be implemented as antioxidant nanoagents within biological media, catalyzing in this way the elimination of hydrogen peroxide molecules from the medium and preventing the formation of harmful ROS species.

4. Conclusions

As we proved in this paper, nanodimensional cubic yttrium oxide particles treated in acidic conditions display antioxidant properties by scavenging hydroxyl radicals, both in biological and non-biological media. Their antioxidant properties depend highly on their morphological characteristics, especially their shapes, influenced by the formation of irregularities that we attribute to a deviation from the stoichiometry of the structure. Yttrium oxide nanotriangles, nanohearts and nanodiscs, synthesized via wet chemical methodologies (thermolysis and digestive ripening), were tested. Among them, nanotriangles displayed the better antioxidant levels of scavenging hydroxyl radicals due to the presence of morphological related irregularities on their structures. Besides the shape and defects, the introduction of lanthanide ions, such as Er^{3+} and Yb^{3+} and their concentration also influenced the ability to scavenge hydroxyl radicals. The antioxidant properties are enhanced with the introduction of dopants at larger concentrations. An additional reason for introducing these doping ions is that a luminescent thermometer can be built with them (see Supporting Information), to monitor the increase of temperature during the reaction process, especially in the *ex-vivo* experiment, allowing the development of a self-assessed antioxidant agent. However, the low quantum yield in the generation of the emissions from these ions in these nanoparticles hampered this possibility due to the low concentration of the nanoparticles dispersed in the solutions.

5. Acknowledgements

This work was supported by the Spanish Government under projects MAT2016-75716-C2-1-R (AEI/FEDER, UE) and by the Generalitat de Catalunya under project 2017SGR755. A.N acknowledges financial support from the Generalitat de Catalunya under grant 2017FI_B00620, 2018FI_B100161 and 2019FI_B200154.

6. References

1. Valgimigli, L.; Baschieri, A.; Amorati, R., Antioxidant activity of nanomaterials. *Journal of Materials Chemistry B* **2018,** 6 (14), 2036-2051.
2. Orient, A.; Donkó, Á.; Szabó, A.; Leto, T. L.; Geiszt, M., Novel sources of reactive oxygen species in the human body. *Nephrology Dialysis Transplantation* **2007,** 22 (5), 1281-1288.
3. Cadet, J.; Wagner, J. R., Oxidatively generated base damage to cellular DNA by hydroxyl radical and one-electron oxidants: Similarities and differences. *Archives of Biochemistry and Biophysics* **2014,** 557, 47-54.
4. Morry, J.; Ngamcherdtrakul, W.; Yantasee, W., Oxidative stress in cancer and fibrosis: Opportunity for therapeutic intervention with antioxidant compounds, enzymes, and nanoparticles. *Redox Biology* **2017,** 11, 240-253.
5. Rhee, S. G., H_2O_2, a necessary evil for cell signaling. *Science* **2006,** 312 (5782), 1882-1883.
6. Finkel, T.; Serrano, M.; Blasco, M. A., The common biology of cancer and ageing. *Nature* **2007,** 448 (7155), 767-774.
7. Phaniendra, A.; Jestadi, D. B.; Periyasamy, L., Free radicals: Properties, sources, targets, and their implication in aarious diseases. *Indian Journal of Clinical Biochemistry* **2015,** 30 (1), 11-26.
8. Scheibmeir, H. D.; Christensen, K.; Whitaker, S. H.; Jegaethesan, J.; Clancy, R.; Pierce, J. D., A review of free radicals and antioxidants for critical care nurses. *Intensive and Critical Care Nursing* **2005,** 21 (1), 24-28.
9. Wu, D.; Cederbaum, A. I., Alcohol, oxidative stress, and free radical damage. *Alcohol research & health : the journal of the National Institute on Alcohol Abuse and Alcoholism* **2003,** 27 (4), 277-84.
10. Karakoti, A.; Singh, S.; Dowding, J. M.; Seal, S.; Self, W. T., Redox-active radical scavenging nanomaterials. *Chemical Society Reviews* **2010,** 39 (11), 4422-4432.
11. Brown, B. G.; Zhao, X. Q.; Chait, A.; Fisher, L. D.; Cheung, M. C.; Morse, J. S.; Dowdy, A. A.; Marino, E. K.; Bolson, E. L.; Alaupovic, P.; Frohlich, J.; Serafini, L.; Huss-Frechette, E.; Wang, S.; DeAngelis, D.; Dodek, A.; Albers, J. J., Simvastatin and niacin, antioxidant vitamins, or the combination for the prevention of coronary disease. *The New England Journal of Medicine* **2001,** 345 (22), 1583-1592.
12. Valko, M.; Rhodes, C. J.; Moncol, J.; Izakovic, M.; Mazur, M., Free radicals, metals and antioxidants in oxidative stress-induced cancer. *Chemico-Biological Interactions* **2006,** 160 (1), 1-40.
13. Valko, M.; Leibfritz, D.; Moncol, J.; Cronin, M. T. D.; Mazur, M.; Telser, J., Free radicals and antioxidants in normal physiological functions and human disease. *The International Journal of Biochemistry & Cell Biology* **2007,** 39 (1), 44-84.
14. Senanayake, S. N., Wanasundara, P.J.P. and Shahidi, F. , Antioxidants: Science, technology, and applications. In *Bailey's Industrial Oil and Fat Products*, 2020; pp 1-61.
15. Boozer, C. E.; Hammond, G. S.; Hamilton, C. E.; Sen, J. N., Air oxidation of hydrocarbons. II. The stoichiometry and fate of inhibitors in benzene and chlorobenzene. *Journal of the American Chemical Society* **1955,** 77 (12), 3233-3237.
16. Paul, S.; Saikia, J. P.; Samdarshi, S. K.; Konwar, B. K., Investigation of antioxidant property of iron oxide particlesby 1′-1′diphenylpicryl-hydrazyle (DPPH) method. *Journal of Magnetism and Magnetic Materials* **2009,** 321 (21), 3621-3623.
17. Shah, S. T.; A Yehya, W.; Saad, O.; Simarani, K.; Chowdhury, Z.; A Alhadi, A.; Al-Ani, L. A., Surface functionalization of iron oxide nanoparticles with gallic acid as potential antioxidant and antimicrobial agents. *Nanomaterials* **2017,** 7 (10), 306-323.
18. Purkayastha, D. D.; Das, N.; Bhattacharjee, C. R., Synthesis and antioxidant activity of cupric oxide nanoparticles accessed via low-temperature solid state thermal decomposition of bis(dimethylglyoximato) copper(II) complex. *Materials Letters* **2014,** 123, 206-209.
19. Das, D.; Nath, B. C.; Phukon, P.; Dolui, S. K., Synthesis and evaluation of antioxidant and antibacterial behavior of CuO nanoparticles. *Colloids and Surfaces B: Biointerfaces* **2013,** 101, 430-433.
20. Madhu, G.; Bose, V. C.; Aiswaryaraj, A. S.; Maniammal, K.; Biju, V., Defect dependent antioxidant activity of nanostructured nickel oxide synthesized through a novel chemical method. *Colloids and Surfaces A: Physicochemical and Engineering Aspects* **2013,** 429, 44-50.
21. Madhu, G.; Biju, V., Nanostructured amorphous nickel oxide with enhanced antioxidant activity. *Journal of Alloys and Compounds* **2015,** 637, 62-69.
22. Saikia, J. P.; Paul, S.; Konwar, B. K.; Samdarshi, S. K., Nickel oxide nanoparticles: A novel antioxidant. *Colloids and Surfaces B: Biointerfaces* **2010,** 78 (1), 146-148.
23. Wang, Y. J.; Dong, H.; Lyu, G. M.; Zhang, H. Y.; Ke, J.; Kang, L. Q.; Teng, J. L.; Sun, L. D.; Si, R.; Zhang, J.; Liu, Y. J.; Zhang, Y. W.; Huang, Y. H.; Yan, C. H., Engineering the defect state and reducibility of ceria based nanoparticles for improved anti-oxidation performance. *Nanoscale* **2015,** 7 (33), 13981-13990.
24. Fisher, T. J.; Zhou, Y.; Wu, T. S.; Wang, M.; Soo, Y. L.; Cheung, C. L., Structure-activity relationship of nanostructured ceria for the catalytic generation of hydroxyl radicals. *Nanoscale* **2019,** 11 (10), 4552-4561.
25. Olvera Salazar, A.; García Hernández, M.; López Camacho, P. Y.; López Marure, A.; Reyes de la Torre, A. I.; Morales Ramírez, Á. d. J.; Hernández Santiago, F.; Aguilera Vázquez, L., Influence of Eu^{3+} doping content on antioxidant properties of Lu_2O_3 sol-gel derived nanoparticles. *Materials Science and Engineering: C* **2016,** 69, 850-855.

26. Fernandez-Garcia, S.; Jiang, L.; Tinoco, M.; Hungria, A. B.; Han, J.; Blanco, G.; Calvino, J. J.; Chen, X., Enhanced hydroxyl radical scavenging activity by doping lanthanum in ceria nanocubes. *Journal of Physical Chemistry C* **2016,** 120 (3), 1891-1901.
27. Lee, S. S.; Song, W.; Cho, M.; Puppala, H. L.; Nguyen, P.; Zhu, H.; Segatori, L.; Colvin, V. L., Antioxidant properties of cerium oxide nanocrystals as a function of nanocrystal diameter and surface coating. *ACS Nano* **2013,** 7 (11), 9693-9703.
28. Mitra, R. N.; Merwin, M. J.; Han, Z.; Conley, S. M.; Al-Ubaidi, M. R.; Naash, M. I., Yttrium oxide nanoparticles prevent photoreceptor death in a light-damage model of retinal degeneration. *Free Radical Biology and Medicine* **2014,** *75*, 140-148.
29. Khurana, A.; Anchi, P.; Allawadhi, P.; Kumar, V.; Sayed, N.; Packirisamy, G.; Godugu, C., Yttrium oxide nanoparticles reduce the severity of acute pancreatitis caused by cerulein hyperstimulation. *Nanomedicine: Nanotechnology, Biology and Medicine* **2019,** 18, 54-65.
30. Abuid, N. J.; Gattás-Asfura, K. M.; Schofield, E. A.; Stabler, C. L., Layer-by-layer cerium oxide nanoparticle coating for antioxidant protection of encapsulated beta cells. *Advanced Healthcare Materials* **2019,** 8 (12), 1801493-1801503.
31. Xue, Y.; Luan, Q.; Yang, D.; Yao, X.; Zhou, K., Direct evidence for hydroxyl radical scavenging activity of cerium oxide nanoparticles. *Journal of Physical Chemistry C* **2011,** 115 (11), 4433-4438.
32. Chen, J.; Patil, S.; Seal, S.; McGinnis, J. F., Rare earth nanoparticles prevent retinal degeneration induced by intracellular peroxides. *Nature Nanotechnology* **2006,** 1 (2), 142-150.
33. Colon, J.; Herrera, L.; Smith, J.; Patil, S.; Komanski, C.; Kupelian, P.; Seal, S.; Jenkins, D. W.; Baker, C. H., Protection from radiation-induced pneumonitis using cerium oxide nanoparticles. *Nanomedicine: Nanotechnology, Biology and Medicine* **2009,** 5 (2), 225-231.
34. Fernández-Varo, G.; Perramón, M.; Carvajal, S.; Oró, D.; Casals, E.; Boix, L.; Oller, L.; Macías-Muñoz, L.; Marfà, S.; Casals, G.; Morales-Ruiz, M.; Casado, P.; Cutillas, P. R.; Bruix, J.; Navasa, M.; Fuster, J.; Garcia-Valdecasas, J. C.; Pavel, M. C.; Puntes, V.; Jiménez, W., Bespoken nanoceria: A new effective treatment in experimental hepatocellular carcinoma. *Hepatology* **2020,** 72, 1267-1282.
35. Niu, J.; Azfer, A.; Rogers, L. M.; Wang, X.; Kolattukudy, P. E., Cardioprotective effects of cerium oxide nanoparticles in a transgenic murine model of cardiomyopathy. *Cardiovascular Research* **2007,** 73 (3), 549-559.
36. Dong, H.; Du, S. R.; Zheng, X. Y.; Lyu, G. M.; Sun, L. D.; Li, L. D.; Zhang, P. Z.; Zhang, C.; Yan, C. H., Lanthanide nanoparticles: From design toward bioimaging and therapy. *Chemical Reviews* **2015,** 115 (19), 10725-10815.
37. Yang, X.; Tian, P.; Zhang, X.; Yu, X.; Wu, T.; Xu, J.; Han, Y., The generation of hydroxyl radicals by hydrogen peroxide decomposition on FeOCl/SBA-15 catalysts for phenol degradation. *AIChE Journal* **2015,** 61 (1), 166-176.
38. Attri, P.; Kim, Y. H.; Park, D. H.; Park, J. H.; Hong, Y. J.; Uhm, H. S.; Kim, K. N.; Fridman, A.; Choi, E. H., Generation mechanism of hydroxyl radical species and its lifetime prediction during the plasma-initiated ultraviolet (UV) photolysis. *Scientific Reports* **2015,** 5 (1), 9332.
39. Shih, S. J.; Yu, Y. J.; Wu, Y. Y., Manipulation of dopant distribution in yttrium-doped ceria particles. *Journal of Nanoscience and Nanotechnology* **2012,** 12 (10), 7954-7962.
40. Chang, M.; Tie, S., Fabrication of novel luminor Y_2O_3:Eu^{3+}@SiO_2@YVO_4:Eu^{3+} with core/shell heteronanostructure. *Nanotechnology* **2008,** 19 (7), 75711-75719.
41. Andelman, T.; Gordonov, S.; Busto, G.; Moghe, P. V.; Riman, R. E., Synthesis and cytotoxicity of Y_2O_3 nanoparticles of various morphologies. *Nanoscale Research Letters* **2009,** 5 (2), 263-273.
42. Setua, S.; Menon, D.; Asok, A.; Nair, S.; Koyakutty, M., Folate receptor targeted, rare-earth oxide nanocrystals for bi-modal fluorescence and magnetic imaging of cancer cells. *Biomaterials* **2010,** 31 (4), 714-729.
43. Traina, C. A.; Dennes, T. J.; Schwartz, J., A Modular monolayer coating enables cell targeting by luminescent yttria nanoparticles. *Bioconjugate Chemistry* **2009,** 20 (3), 437-439.
44. Dikovska, A. O. G.; Atanasov, P. A.; Jiménez de Castro, M.; Perea, A.; Gonzalo, J.; Afonso, C. N.; García López, J., Optically active Er^{3+}-Yb^{3+} codoped Y_2O_3 films produced by pulsed laser deposition. *Thin Solid Films* **2006,** 500 (1), 336-340.
45. Vetrone, F.; Boyer, J. C.; Capobianco, J. A.; Speghini, A.; Bettinelli, M., Effect of Yb^{3+} codoping on the upconversion emission in nanocrystalline Y_2O_3:Er^{3+}. *Journal of Physical Chemistry B* **2003,** 107 (5), 1107-1112.
46. Schubert, D.; Dargusch, R.; Raitano, J.; Chan, S. W., Cerium and yttrium oxide nanoparticles are neuroprotective. *Biochemical and Biophysical Research Communications* **2006,** 342 (1), 86-91.
47. Lim, S. F.; Riehn, R.; Ryu, W. S.; Khanarian, N.; Tung, C.; Tank, D.; Austin, R. H., In vivo and scanning electron microscopy imaging of upconverting nanophosphors in caenorhabditis elegans. *Nano Letters* **2006,** 6 (2), 169-174.
48. Bevan, D. J. M.; Kordis, J., Mixed oxides of the type MO_2 (fluorite)-M_2O_3-I oxygen dissociation pressures and phase relationships in the system CeO_2-Ce_2O_3 at high temperatures. *Journal of Inorganic and Nuclear Chemistry* **1964,** 26 (9), 1509-1523.
49. Kofstad, P., Nonstoichiometry, diffusion, and electrical conductivity in binary metal oxides. *Wiley Interscience (J. Wiley & Sons, Inc.)* **1972**.
50. Kilbourn, B. T., Yttria. In *Concise Encyclopedia of Advanced Ceramic Materials*, Brook, R. J., Ed. Pergamon: Oxford, 1991; pp 521-522.

51. Kassem, S.; Mohamed, M.; Sayour, H.; Canfarotta, F.; Piletsky, S.; Soliman, M. A. M., Functionalized core-shell yttrium oxide nanoparticles as antioxidants agents in heat stressed rats. *Biological Trace Element Research* **2020**, 198, 189-197.
52. Mellado-Vázquez, R.; García-Hernández, M.; López-Marure, A.; López-Camacho, P. Y.; De Jesús Morales-Ramírez, Á.; Beltrán-Conde, H. I., Sol-Gel synthesis and antioxidant properties of yttrium oxide nanocrystallites incorporating P-123. *Materials* **2014,** 7 (9), 6768-6778.
53. Nexha, A.; Pujol, M.C.; Carvajal, J. J.; Díaz, F.; Aguiló, M., Controlling the growth of colloidal rare earth oxides via wet chemical methodologies. *To be submitted.*
54. Wang, D.; Kang, Y.; Ye, X.; Murray, C. B., Mineralizer-assisted shape-control of rare earth oxide nanoplates. *Chemistry of Materials* **2014,** 26 (22), 6328-6332.
55. Li, Z.; Liang, T.; Lv, S.; Zhuang, Q.; Liu, Z., A rationally designed upconversion nanoprobe for in vivo detection of hydroxyl radical. *Journal of the American Chemical Society* **2015,** 137 (34), 11179-11185.
56. Heck, D. E.; Shakarjian, M.; Kim, H. D.; Laskin, J. D.; Vetrano, A. M., Mechanisms of oxidant generation by catalase. *Annals of the New York Academy of Sciences* **2010,** 1203 (1), 120-125.
57. den Engelsen, D.; Fern, G. R.; Ireland, T. G.; Hudry, D.; Abeykoon, A. M. M.; Nykypanchuk, D.; Dickerson, J. H.; Silver, J., Ultrathin Y_2O_3:Eu^{3+} nanodiscs: spectroscopic investigations and evidence for reduced concentration quenching. *Nanotechnology* **2018,** *29* (45), 455703-455718.
58. Jeong, J.; Kim, N.; Kim, M. G.; Kim, W., Generic synthetic route to monodisperse sub-10 nm lanthanide oxide nanodisks: A modified digestive ripening process. *Chemistry of Materials* **2016,** 28 (1), 172-179.
59. den Engelsen, D.; de Koning, B., Ellipsometric study of organic monolayers. Part 1. Condensed monolayers. *Journal of the Chemical Society, Faraday Transactions 1: Physical Chemistry in Condensed Phases* **1974,** *70* (0), 1603-1614.
60. Klokkenburg, M.; Hilhorst, J.; Erné, B. H., Surface analysis of magnetite nanoparticles in cyclohexane solutions of oleic acid and oleylamine. *Vibrational Spectroscopy* **2007,** 43 (1), 243-248.
61. Si, R.; Zhang, Y. W.; Zhou, H. P.; Sun, L. D.; Yan, C. H., Controlled-synthesis, self-assembly behavior, and surface-dependent optical properties of high-quality rare-earth oxide nanocrystals. *Chemistry of Materials* **2007,** 19 (1), 18-27.
62. Zhang, L.; He, R.; Gu, H. C., Oleic acid coating on the monodisperse magnetite nanoparticles. *Applied Surface Science* **2006,** 253 (5), 2611-2617.
63. He, J.; Kanjanaboos, P.; Frazer, N. L.; Weis, A.; Lin, X. M.; Jaeger, H. M., Fabrication and mechanical properties of large-scale freestanding nanoparticle membranes. *Small* **2010,** 6 (13), 1449-1456.
64. Smolensky, E. D.; Park, H. Y. E.; Berquó, T. S.; Pierre, V. C., Surface functionalization of magnetic iron oxide nanoparticles for MRI applications-effect of anchoring group and ligand exchange protocol. *Contrast Media and Molecular Imaging* **2011,** 6 (4), 189-199.
65. Ahrenstorf, K.; Heller, H.; Kornowski, A.; Broekaert, J. A. C.; Weller, H., Nucleation and growth mechanism of Ni_xPt_{1-x} nanoparticles. *Advanced Functional Materials* **2008,** 18 (23), 3850-3856.
66. Nicolaisen, F. M., IR absorption spectrum (4200–3100 cm^{-1}) of H_2O and $(H_2O)_2$ in CCl_4. Estimates of the equilibrium constant and evidence that the atmospheric water absorption continuum is due to the water dimer. *Journal of Quantitative Spectroscopy and Radiative Transfer* **2009,** 110 (18), 2060-2076.
67. Korppi-Tommola, J.; Yip, R. W., Solvent effects on the visible absorption spectrum of crystal violet. *Canadian Journal of Chemistry* **1981,** 59 (2), 191-194.
68. Yao, S. Y.; Xu, W. Q.; Johnston-Peck, A. C.; Zhao, F. Z.; Liu, Z. Y.; Luo, S.; Senanayake, S. D.; Martínez-Arias, A.; Liu, W. J.; Rodriguez, J. A., Morphological effects of the nanostructured ceria support on the activity and stability of CuO/CeO_2 catalysts for the water-gas shift reaction. *Physical Chemistry Chemical Physics* **2014,** 16 (32), 17183-17195.
69. Lu, M.; Zhang, Y.; Wang, Y.; Jiang, M.; Yao, X., Insight into Several Factors that Affect the Conversion between Antioxidant and Oxidant Activities of Nanoceria. *ACS Applied Materials & Interfaces* **2016,** 8 (36), 23580-23590.
70. Zhai, Y.; Zhou, K.; Xue, Y.; Qin, F.; Yang, L.; Yao, X., Synthesis of water-soluble chitosan-coated nanoceria with excellent antioxidant properties. *RSC Advances* **2013,** 3 (19), 6833-6838.
71. Nexha, A.; Carvajal, J. J.; Pujol, M.C.; Díaz, F.; Aguiló, M.,, Effect of the core@shell and layer-by-layer nanoarchitectures on the thermal sensing and photothermal conversion efficiency in triangular Ho, $Tm:Y_2O_3$ colloidal nanocrystals operating in the third biological window. *To be submitted.*
72. Nexha, A.; Carvajal, J. J.; Pujol, M.C.; Díaz, F.; Aguiló, M., Evaluating the performance of Ho^{3+}, Tm^{3+} doped Y_2O_3 nanotriangles, nanohearts and self-assembled nanodiscs as luminescent nanothermometers and photothermal agents as a function of the morphology. *To be submitted.*
73. Chance, B., The composition of catalase-peroxide complexes. *The Journal of biological chemistry* **1949,** 179 (3), 1311-1330.
74. Albano, E., Alcohol, oxidative stress and free radical damage. *Proceedings of the Nutrition Society* **2006,** 65 (3), 278-290.
75. Deisseroth, A.; Dounce, A. L., Catalase: Physical and chemical properties, mechanism of catalysis, and physiological role. *Physiological Reviews* **1970,** 50 (3), 319-375.
76. Dos Santos, W. G.; Pacheco, I.; Liu, M. Y.; Teixeira, M.; Xavier, A. V.; LeGall, J., Purification and characterization of an iron superoxide dismutase and a catalase from the sulfate-reducing reducing bacterium desulfovibrio gigas. *Journal of Bacteriology* **2000,** 182 (3), 796-804.

Supporting Information

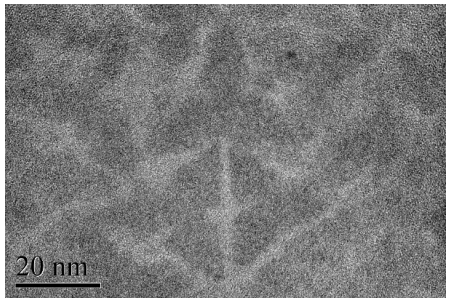

Figure S1. High resolution TEM image of the branched Y_2O_3 nanotriangles synthesized via thermal decomposition methodology.

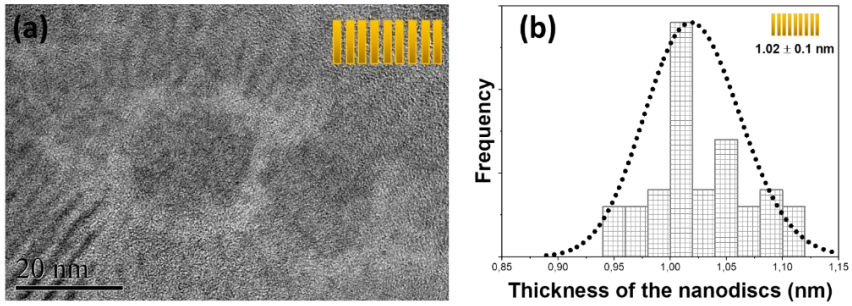

Figure S2. (a) High resolution TEM image and (b) corresponding thickness of the self-assembled Y_2O_3 nanodiscs synthesized via digestive ripening methodology.

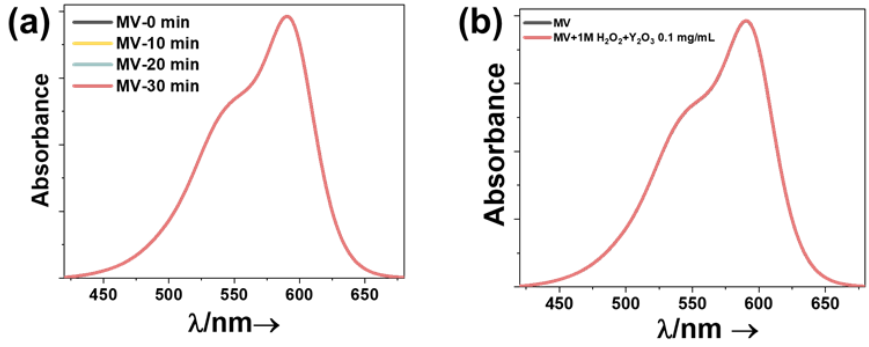

Figure S3. (a) Absorbance of methyl violet as a function of time and (b) Absorbance of a solution of methyl violet in water, and a mixture of MV, H_2O_2, and Y_2O_3 with the concentrations indicated in the graph.

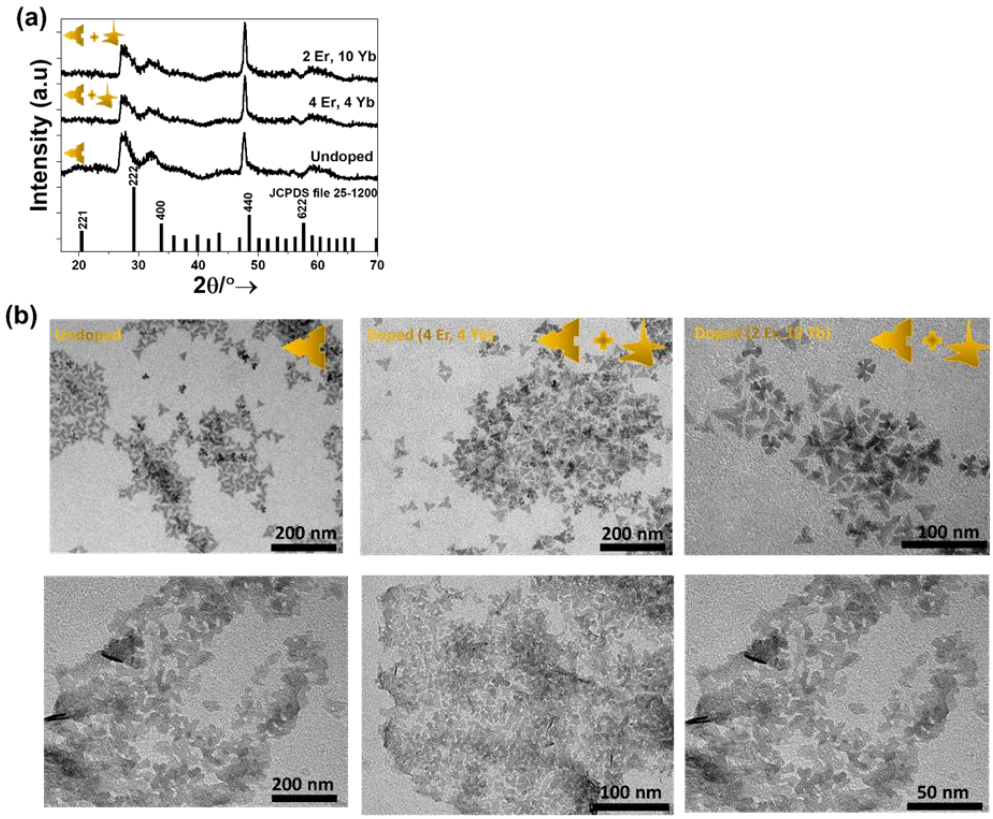

Figure S4. (a) XRPD pattern and (b) TEM images of the as-synthesized (above) and of the corresponding acid treated (below) undoped and doped (4 mol% Er^{3+}, 4 mol% Yb^{3+} and 2 mol% Er^{3+}, 10 mol% Yb^{3+}) yttrium oxide nanocrystals.

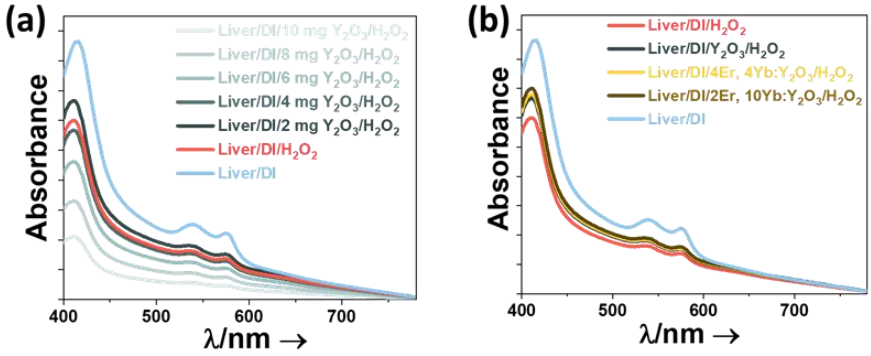

Figure S5. Absorbance recorded in a solution composed of liver and: (a) distilled water, 2 mL hydrogen peroxide and different quantities of undoped yttria nanotriangles; and (b)distilled water, 2 mL hydrogen peroxide 2 mg of Er and Yb co-doped yttria nanotriangles with different doping concentrations.

Luminescent Nanothermometers based on the green emissions arising from Er, Yb:Y_2O_3 colloidal nanocrystals after excitation with 980 nm light source

Taking as an example 4 mol% Er^{3+} and 4 mol% Yb^{3+} colloidal yttrium oxide nanodiscs, the ability of these colloidal nanocrystals to sense the temperature is demonstrated. Using a single emitting center based on

the two green emissions of Er^{3+} from these colloidal nanocrystals, as a source of the ratio of the emission intensities of two distinct transitions, the thermometric parameter (Δ) or fluorescence intensity ratio (FIR), can be described as:[1,2]

$$\Delta = FIR = \frac{I_H}{I_S} = \frac{g_H \vartheta_H A_H}{g_S \vartheta_S A_S} \exp\left(-\frac{\Delta E}{k_B T}\right) = B \exp\left(-\frac{\Delta E}{k_B T}\right) \qquad (1)$$

where I_H and I_S stand for the integrated intensity of the two green emissions arising the two $^2H_{11/2}$ and $^4S_{3/2}$ emitting levels, respectively; g_H and g_S are the degeneracy of the $^2H_{11/2}$ and $^4S_{3/2}$ levels, respectively; ϑ_H, ϑ_S, A_H and A_S are the frequencies and spontaneous emission rates corresponding to these levels; B is the pre-exponential constant; ΔE is the energy gap between the $^2H_{11/2}$ and $^4S_{3/2}$ levels in the particular host; k_B is the Boltzmann's constant and T is the absolute temperature.

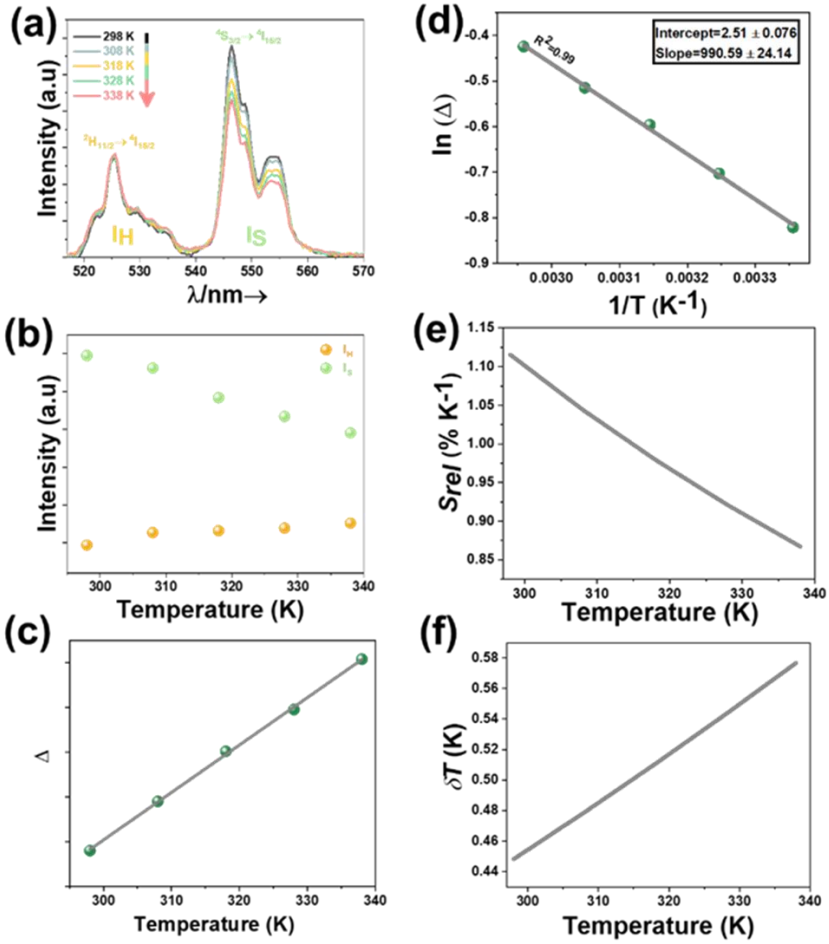

Figure S6. (a) Temperature dependence of the green emissions lines of the self-assembled Er^{3+}, Yb^{3+}:Y_2O_3 upconverting nanodiscs. (b) Variation of the integrated emission intensities with temperature. (c) Influence of the temperature on the thermometric parameter Δ or FIR. (d) Plot of the logarithmic form of FIR as a function of the inverse of temperature. (e) Relative thermal sensitivity of the self-assembled nanodiscs as a function of the temperature. (f) The temperature uncertainty of the self-assembled nanodiscs as a function of the temperature.

The thermometric performance of 4 mol% Er^{3+} and 4 mol% Yb^{3+}:Y_2O_3 upconverting colloidal nanocrystals was investigated by analyzing the effect of the increase of the temperature in the physiological range on the intensity ratio of thermally coupled green emissions of Er^{3+} (525 nm and 550 nm emissions), after exciting the nanocrystals with a 980 nm laser operating with a power of 4.54 W. Figure S6 (a) illustrates the temperature dependence of the 525 nm and 550 nm green emissions of the self-assembled Er^{3+}, Yb^{3+}:Y_2O_3

nanodiscs in the physiological range of temperatures from 298 K-338 K. Increasing the temperature between 298 and 338 K, results in a significant variation of the intensity of the green emissions (Figure S6 (b)). The intensity of the 550 nm emission decreases the most with the increase of the temperature, while the intensity of the 525 nm emission is nearly constant. This decrease in intensity is related to the thermal activation of the luminescence quenching mechanisms, such as the increase of the non-radiative decay rates.[3] Consequently, with the variation of the green emissions with temperature, also their ratio is temperature-dependent.

Thus, the intensity ratio Δ or FIR of the two green transitions is based on the validity of the Boltzmann distribution between the $^2H_{11/2}$ and $^4S_{3/2}$ levels and is evaluated by Equation 1.[4] FIR is proportional to the change of the temperature (Figure S6 (c)). Equation 1 can be rewritten in the logarithmic form as:

$$\ln(\Delta) = \ln(FIR) = \ln(B) + \left(\frac{\Delta E}{k_B T}\right) = \ln(B) + \left(-\frac{C}{T}\right) \qquad (2)$$

where B and C represent constants determinate from experimental calibration of the dependence of the intensity ratio with the change of temperature. The variation of logarithmic form of FIR in the range of 298 K-338 K obeys to a linear tendency, exhibiting a fitting regression factor over 99% (check Figure S6 (d)). From this fitting, the values of the slope (990.59 ± 24.14) and the intercept (2.51 ± 0.076) are deduced. Knowing these values, allows us to extract the value of the pre-exponential term B and the energy gap ΔE between the Er^{3+} $^2H_{11/2}$ and $^4S_{3/2}$ thermally coupled levels and furthermore, determine the thermometric performance of the self-assembled nanodiscs. The corresponding value of the pre-exponential term and the energy gap are 12.30 and 688 cm^{-1}, respectively.

The figures of merit usually used to compare the performance of nanothermometers, independent of their nature, are the relative thermal sensitivity (S_{rel}) and the temperature resolution (δT).[5] The relative thermal sensitivity of the self-assembled Er^{3+}, Yb^{3+}:Y_2O_3 upconverting nanodiscs is calculated:[1,5]

$$S_{rel} = \frac{1}{\Delta}\left|\frac{\partial \Delta}{\partial T}\right| * 100\% = \frac{\Delta E}{k_B T^2} * 100\% \qquad (3)$$

Thus, by applying Equation 4, the relative thermal sensitivity of the self-assembled nanodiscs is in the range of 1.11% K^{-1} at 298 K. The evolution of S_{rel} as a function of temperature is presented in Figure 5 (e). S_{rel} shows an inverse relationship with the temperature, as temperature increases, the values of S_{rel} decreases gradually.

The temperature resolution of the nanothermometers is defined as:[5]

$$\delta T = \frac{1}{S_{rel}}\frac{\delta \Delta}{\Delta} \qquad (4)$$

where $\frac{\delta \Delta}{\Delta}$ is the relative error in the determination of the thermometric parameter. This parameter depends on the acquisition setup, and a typical value that can be used is 0.5%.[6] The calculated temperature uncertainty of the self-assembled Er^{3+}, Yb^{3+}:Y_2O_3 upconverting nanodiscs is 0.44 K at 298 K. This parameter has a linear relationship with the temperature, as the temperature increases, the temperature resolution increases, reaching a maximum value of 0.57 K at 338 K (Figure S6 (f)).

References

1. Wade, S. A.; Collins, S. F.; Baxter, G. W. Fluorescence intensity ratio technique for optical fiber point temperature sensing. *Journal of Applied Physics* **2003,** 94 (8), 4743-4756.
2. Brites, C. D. S.; Lima, P. P.; Silva, N. J. O.; Millán, A.; Amaral, V. S.; Palacio, F.; Carlos, L. D. Thermometry at the nanoscale. *Nanoscale* **2012,** 4 (16), 4799-4829.
3. Riseberg, L. A.; Moos, H. W. Multiphonon orbit-lattice relaxation of excited states of rare-earth ions in crystals. *Physical Review* **1968,** 174 (2), 429-438.
4. Shinn, M.; Sibley, W.; Drexhage, M.; Brown, R. Optical transitions of Er^{3+} ions in fluorozirconate glass. *Physical Review B* **1983,** 27 (11), 6635-6649.
5. Brites, C. D. S.; Millán, A.; Carlos, L. D. In *Handbook on the Physics and Chemistry of Rare Earths*; Jean-Claude, B., Vitalij K, P., Ed.; Elsevier: 2016; Vol. 49, pp 339-427.
6. Savchuk, O. A.; Carvajal, J. J.; Brites, C. D. S.; Carlos, L. D.; Aguilo, M.; Diaz, F. Upconversion thermometry: a new tool to measure the thermal resistance of nanoparticles. *Nanoscale* **2018,** 10 (14), 6602-6610.

Conclusions

To summarize, we underlined key factors that might influence the optical properties and the potential application of lanthanide doped materials. We first conducted a revision of all the works published on luminescence thermometry within the biological windows. The conclusions that we can extract from this revision are:

- Lanthanide doped luminescent materials have triggered the development of highly sensitive thermometers, particularly if the operating regime of their emissions is located within the biological windows (I-BW: 650-950 nm, II-BW: 1000-1350 nm, III-BW: 1400-2000 nm and IV-BW: centered at 2200 nm). In this review, several strategies towards obtaining better temperature sensing performances within the biological windows have been analyzed.

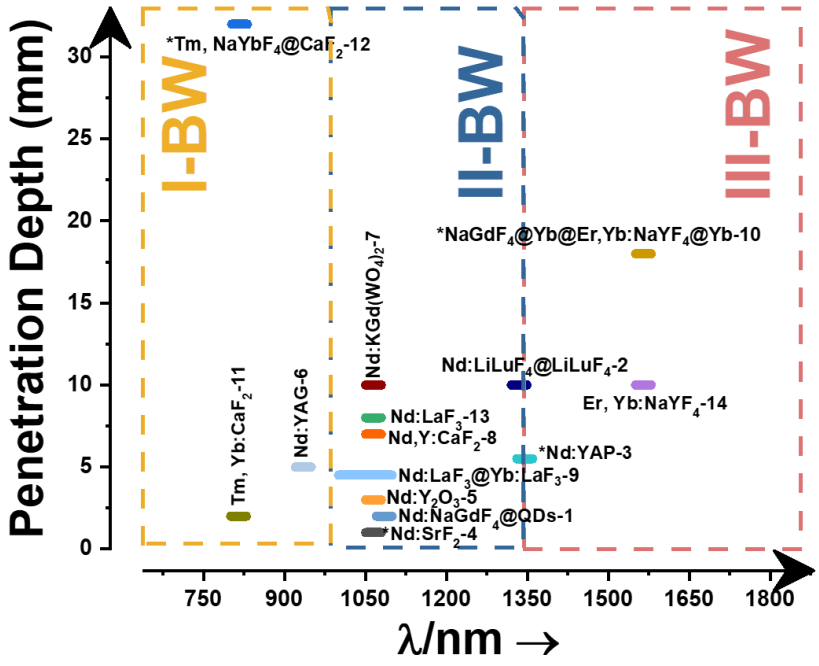

Figure 6.1. Penetration depth in biological windows reported for lanthanide doped luminescent nanomaterials. The intervals represent the operating wavelength regimes for the corresponding nanothermometer, whereas the star mark (*) indicates only one reported wavelength. The numbers indicate the references.

Hence, for the choice of the excitation wavelength, the selection of a NIR source is highly recommended, allowing for deeper penetration depths and better thermal readings, implying no phototoxicity or photobleaching effects, enhancing significantly the interest of these luminescent thermometers in biological/biomedical applications. Related to the choice of hosts for the lanthanide ions, a strategy that results in highly sensitive thermometers is the use of active core@active shell nanostructures. Another choice is the combination of the emissions of lanthanide ions with those arising from transition metal ions or quantum dots, acting as reference and highly thermally quenched probes, respectively. Also coating lanthanide doped nanothermometers with an inert shell can result in higher intensities and better temperature sensing performances due to the

reduced thermal quenching resulting from the influence of surface defects. Related to the choice of the lanthanide ions, a proper selection upon the concentration of the ion to be used and the operating biological window in which one wants to work is required. The intentional introduction of impurities inside the hosts (such as the case of Y^{3+} in Nd^{3+}:CaF_2) might lead to reduced thermal quenching effects, and upon a proper selection of the concentration of these impurities, to a better thermometric performance. In terms of lanthanide ions included as emitters, Nd^{3+} and Tm^{3+} are the ones that attracted most of the attention (see Table 1.1 for example). Nevertheless, a better choice for efficient luminescent nanothermometers is that constituted by dual emitting centers, since they provide better thermal sensitivity and allow incorporating multifunctionality in these nanoparticles.

Despite the big number of works devoted to the development of luminescent thermometers operating in the biological windows spectral ranges, and the demonstration of amazing applications for them, there are still challenges that remain unsolved. From the synthetic point of view, a vast amount of research is devoted to the synthesis of fluoride doped hosts, either in the form of bare, core@shell or multishell nanostructures, through the thermal decomposition of trifluoroacetate precursors to achieve control of their sizes and shapes. This synthetic approach suffers from the toxicity of the by-products and final products generated in the reactions, and an additional surface functionalization of the obtained nanoparticles is required for their potential use in biomedical applications. Therefore, new synthetic routes towards biocompatible nanomaterials are highly desirable. Furthermore, new choices for hosts for the lanthanide ions should also be proposed.

Concerning the thermometric performance of the lanthanide based luminescent nanothermometers, clearly some discrepancies towards the evaluation of their performances (calculation of the thermometric parameter or S_{rel}) appear. In this way, it would be recommended that all the authors follow the same procedures in order to be able to compare properly the performance of the different luminescent thermometers proposed. In addition, besides the S_{rel} and δT, a minority of publications report about their resolution (spatial or temporal), reproducibility and repeatability. These parameters are also important to facilitate the implementation of the lanthanide based luminescent thermometers in real biological/biomedical applications outside of the laboratories. Another very important parameter that should be taken into account when developing a novel luminescent thermometer is their quantum yield, both absolute and relative. A good quantum yield would allow for an easier detection scheme for the emissions generated by the luminescent thermometers by using cheaper detectors and lower laser excitation powers, simplifying also the protocols of use of these luminescent nanoparticles, and facilitating their use by non-experts in these subjects. As can be seen in this revision, the absolute quantum yield has not been yet reported for any lanthanide based luminescent thermometers, and is a much reduced number of publications the relative quantum yield has been taken into account. Thus, an additional effort is required by the research teams devoted to the development of novel luminescent thermometers to take this parameter into account. In addition, here it should be stated that just a few reports tried to understand the effect of the different sizes and shapes of the nanoparticles in their thermometric performance.

From the biological/biomedical and other applications point of view, the studies published up to now are mostly focused in the II-BW spectral region. Clearly, the high numbers of reports in the II-BW are devoted to their high penetration depths, however, according to Naczynski *et al*.[14] and other recent publications this parameter should be better displayed at longer wavelength,[15] of BW in the III-BW and IV-BW spectral ranges. Therefore, these regimes should be further explored in the future. In addition, for the biological/biomedical applications, the biological tissues in which these luminescent thermometers have been applied are different (chicken breast, pork fat, phantom tissue or mice), leading, of course, to different penetration depths (see Figure 6.1) due to the different responses to the interaction with the light of their biological components. Thus, an extensive research work should be developed to understand similarities and differences towards the interaction of light with the different biological tissues to extract reliable conclusions in this area.

Nevertheless, and regardless of the nature of the biological tissue, when operating at longer wavelengths, in general, the penetration depth increased, considering only these examples in which chicken breast is used as a subject of study, as can be seen in Figure 6.1. From Figure 6.1, it can be extracted as well that the majority of the luminescent nanothermometers developed up to now operating within the biological windows spectral ranges, including also these materials used only to determine the penetration depth in biological tissues, are based on Nd^{3+} doped materials, when other choices are also possible, like the combination of Ho^{3+} and Tm^{3+} ions, for instance, to develop multifunctional nanoparticles such as self-assessed photothermal agents.

Furthermore, in *in-vitro* applications, concepts related to the temperature flocculation at the nanoscale, the disagreement between the calculated and the experimental temperature, and the understanding of the thermal conductivity in a cell,[16] should be addressed. In fact, theoretically, the discrepancies in *in-vitro* applications, could also affect to the in-vivo applications.[16]

Finally, another research direction that should be taken into account would be exploring the application of these luminescent thermometers outside the biological/biomedical fields, since their reported applicability in this direction is scarce.

We studied the effect of morphological characteristics of the same host where the lanthanide ions were embedded, on their ability to sense the temperature within the III-BW, to act as photothermal and as antioxidant agents. Different sizes and shapes of the host were engineered by applying well-established sol-gel methodologies, novel solvothermal and wet chemical methodologies. We opted for hosts including monoclinic double tungstates and rare earth cubic sesquioxides.

Related to the Ho^{3+} and Tm^{3+} embedded in monoclinic double tungstates, in $KLu(WO_4)_2$ particles, for applications in luminescent nanothermometry in the III-BW and photothermal agents:

- We proved their ability to act as self-assessed photothermal agents in the III-BW, upon illumination with near infrared light, located as well within the biological windows regions (808 nm, I-BW). These materials, synthesized from a well-established modified sol-gel Pechini methodology, result in the aggregation of the nanocrystals and a wide size distribution ranging from 150 ± 25 nm to 1.8 µm. The Ho^{3+} and Tm^{3+} doped particles can release heat that will increase the temperature of the environment in which they are embedded, and emit light that allows determining the temperature *in situ* without incorporating an external thermal probe. The emissions lines located at 1.45 µm, 1.8 µm and 1.96 µm, attributed to the $^3H_4 \rightarrow {}^3F_4$ and $^3F_4 \rightarrow {}^3H_6$ electronic transitions of Tm^{3+} and the $^5I_7 \rightarrow {}^5I_8$ electronic transition of Ho^{3+}, respectively, were taken into account to elucidate their self-assessing photothermal properties. Different doping concentrations were tested with the goal of achieving optimal self-assessing photothermal properties. The results revealed that the 3 mol% Ho^{3+}, 5 mol% Tm^{3+} doping concentration generated the brightest emissions in the III-BW. In terms of applications, 1 mol% Ho^{3+}, 10 mol% Tm^{3+} doped $KLu(WO_4)_2$ nanoparticles exhibited the best self-assessed photothermal properties among all the different concentrations tested. Concerning the temperature sensing performance, the intensity ratio between the 1.8 µm and 1.96 µm bands generated the highest relative thermal sensitivity with a value 0.90% K^{-1} and the smallest temperature resolution (0.55 K) at 293 K. Regarding their ability to generate heat, the photothermal conversion efficiency was determined to be around 40 ± 2%, higher than that of other photothermal agents such as metallic and semiconductor nanocrystals. The self-assessing photothermal ability of these particles was further tested in an *ex-vivo* experiment, revealing that the particles can exhibit this ability within a penetration of 2 mm inside biological tissues.

- Novel solvothermal methodologies, namely conventional autoclave and microwave-assisted, in the presence of organic surfactants, resulted in time and energy-effective routes for the synthesis of non-agglomerated, close-to-spherical, and nanodimensional monoclinic $KLu(WO_4)_2$ particles. The formation of the monoclinic crystalline phase was confirmed by X-ray powder diffraction and Raman dispersion. Microwave-assisted and

conventional autoclave solvothermal methodologies generated particles with sizes of around 12 nm and 16 nm, respectively. These two methodologies may provide some guidance in the preparation of other type of nanomaterials including vanadates, carbonates, molybdates and phosphates. By doping the product of each solvothermal synthesis with 3 mol% Ho^{3+}, 5 mol% Tm^{3+} and 1 mol% Ho^{3+}, 10 mol% Tm^{3+}, inspired from the results obtained for the modified sol-gel Pechini method, these nanocrystals can act as self-assessed photothermal agents. In terms of their applications as temperature sensors and nanoheaters, within the particles obtained by solvothermal methodologies, those prepared by the microwave-assisted method are luminescent thermometers not as good as those prepared by the conventional autoclave method, but generate more heat. When compared to the agglomerated particles produced by the modified sol-gel Pechini methodology, we reached the conclusion that particles with smaller sizes generate more heat (45 $\pm$ 2%), but are worse luminescent thermometers (0.33% K^{-1}). These particles would be optimal for biomedical applications, due to their nanodimensional sizes, the fact of not being agglomerated and their water dispersibility for prolonged times.

- We engineered well-shape-defined monoclinic $KLu(WO_4)_2$ particles by applying a thermal decomposition-assisted methodology in the presence of organic surfactants. The successful formation of this crystalline phase was confirmed by X-ray powder diffraction and Raman dispersion. Transmission electron microscopy images revealed a precise rod morphology with an average length of 1100 nm and widths of 180 nm. The ability to dope these rods with Ho^{3+} and Tm^{3+} ions allowed us to compare their temperature sensing properties over a wide range of temperatures, and covering the spectral ranges of the visible and the NIR. We underlined the advantages of performing their ability to sense the temperature within the NIR region. Furthermore, we evaluated the performance of these rods as temperature sensors and photothermal agents, and compared it with the those of the other $KLu(WO_4)_2$ nanoparticles prepared by the other synthetic methods. Different factors including the doping concentration (3 mol% Ho^{3+}, 5 mol% Tm^{3+} and 1 mol% Ho^{3+}, 10 mol% Tm^{3+}), sizes and shapes of the doped particles, were taken into account. We concluded that for the thermometric performance in particles doped with 1 mol% Ho^{3+}, 10 mol% Tm^{3+}, bigger and agglomerated particles exhibit better temperature sensing properties. Instead, for the photothermal conversion efficiency in particles doped with 3 mol% Ho^{3+}, 5 mol% Tm^{3+}, bigger and well-shape-defined particles, generate more heat. The rods doped with 3 mol% Ho^{3+}, 5 mol% Tm^{3+} ions exhibit a photothermal conversion efficiency of 66 $\pm$ 2%, the highest ever achieved with Ho, Tm:KLuW particles, and comparable with the one obtained for graphene in DMF and Au nanoshells or nanorods. We emphasized that these rods can be used in temperature dependent optoelectronic applications, since their large sizes would restrict their use in biomedical applications.

In regard of the results obtained for the sesquioxides for applications as luminescent nanothermometers in the III-BW and photothermal agents:

- We devoted special attention on controlling the size and shape of these oxides by implementing wet chemical methodologies with the ultimate goal of achieving high monodisperse colloidal nanocrystals. We opted for thermal decomposition and digestive ripening processes in the presence of organic surfactants and structure-directing agents. Via digestive ripening reactions by incorporating OLAC and OLAM as organic surfactants, and NaCl as structure-directing agent, rare earth oxide nanodiscs, with thickesses down to a unit cell, were synthesized. This digestive ripening methodology was successful for several rare earth sesquioxides (Gd_2O_3, Yb_2O_3 and Y_2O_3), with Y_2O_3 nanodiscs displaying the ability to self-assemble. Upon tuning the reaction time of thermal decomposition methodologies, branched nanotriangles with mean length sizes of 23 $\pm$ 4 nm and nanohearts with mean sizes of 32 $\pm$ 5 nm were produced, using OLAC, OLAM and ODE as organic surfactants and $NaNO_3$ as structure-directing agent.

The role that the presence of different structure-directing agents might apply were elucidated by analyzing the structures, morphologies and surface chemistry of the final products. Based on these findings, mechanisms for the synthesis of these nanocrystals were proposed.

- The ability of yttrium oxide colloidal nanocrystals to sense the temperature within the III-BW and generate heat, were analyzed by doping them with Ho^{3+} and Tm^{3+}. By exciting these doped nanotriangles, nanohearts and self-assembled nanodiscs with 808 nm light, three emission bands in the third biological window were detected: 1.5 μm, 1.85 μm (composed of two bands arising from different Stark sublevels located at 1.85 μm and 1.96 μm) and 2.1 μm, attributed to the $^3H_4 \rightarrow {}^3F_4$, $^3F_4 \rightarrow {}^3H_6$ electronic transitions of Tm^{3+} and the $^5I_7 \rightarrow {}^5I_8$ electronic transition of Ho^{3+}, respectively. Self-assembled nanodiscs, the brightest among these particles, achieved the best thermometric performance with a value of relative thermal sensitivity of 0.92% K^{-1} and a temperature resolution of 0.54 K, at 313 K, extracted from the fluorescence intensity ratio between the emission bands of Tm^{3+} ions, located at 1.8 μm and 1.96 μm, arising from thermally coupled electronic levels. The best light-to-heat conversion efficiency was obtained for the nanotriangles with a value of 15 ± 2 %.

- We synthesized core@shell and layer-by-layer nanoarchitectures taking the Ho^{3+} and Tm^{3+} doped nanotriangles as basis. For the core@shell structures of the type active core@inert shell, the pre-synthesized Ho^{3+} and Tm^{3+} doped nanotriangles, acting as seeds, were injected at room temperature. For the layer-by-layer structures, these seeds were added during the crystallization process. The results highlighted the advantages of these nanoarchitectures on producing brighter emissions and enhancing the ability to generate more heat when excited with a NIR light source.

Referring to other applications of rare earth sesquioxides:

- We reported for the first time the generation of white light emission and the applicability as luminescent nanothermometers from colloidal yttrium oxide nanocrystals. Highly monodisperse Ho^{3+} and Tm^{3+} doped Y_2O_3 nanotriangles, upon exposure to high 808 nm excitation powers, can generated white light. We investigated the effect of this process in their crystalline structure, size and shape, and ligands attached to their surface. Furthermore, factors affecting to the white light generation, including the stability of the spectrum with time, the excitation power and the temperature at which the nanocrystals were exposed, were explored. The intensity of the white light emission, recorded within the visible regime, is highly influenced by the temperature, which allowed to use these nanocrystals as luminescent nanothermometers. White light based nanothermometers exhibited high values of the relative thermal sensitivity (2.65% K^{-1}) with a temperature resolution (0.18 K) at high temperature (473 K).

- We explored the possibilities of using nanodimensional cubic yttrium oxide particles as antioxidant agents. Their antioxidant properties were evaluated considering factors like their sizes and shapes, and their doping levels. We reached the conclusion that the antioxidant properties, tested via a Fenton reaction using methyl violet as a chromogenic agent, were enhanced with the introduction of dopants. As a final test, we analyzed the antioxidant properties of these nanoagents in an *ex-vivo* experiment, confirming that the yttria nanoparticles can prevent the formation of hydroxyl radical species within this *ex-vivo* system.

References

1. Cerón, E. N.; Ortgies, D. H.; del Rosal, B.; Ren, F.; Benayas, A.; Vetrone, F.; Ma, D.; Sanz-Rodríguez, F.; Solé, J. G.; Jaque, D.; Rodríguez, E. M., Hybrid nanostructures for high-sensitivity luminescence nanothermometry in the second biological window. *Advanced Materials* **2015,** 27, 4781-4787.
2. Skripka, A.; Morinvil, A.; Matulionyte, M.; Cheng, T.; Vetrone, F., Advancing neodymium single-band nanothermometry. *Nanoscale* **2019,** 11, 11322-11330.
3. Hernández-Rodríguez, M. A.; Lozano-Gorrín, A. D.; Martín, I. R.; Rodríguez-Mendoza, U. R.; Lavín, V., Comparison of the sensitivity as optical temperature sensor of nano-perovskite doped with Nd^{3+} ions in the first and second biological windows. *Sensors and Actuators B: Chemical* **2018,** 255, 970-976.
4. Pedroni, M.; Cortelletti, P.; Cantarelli, I. X.; Pinna, N.; Canton, P.; Quintanilla, M.; Vetrone, F.; Speghini, A., Colloidal nanothermometers based on neodymium doped alkaline-earth fluorides in the first and second biological windows. *Sensors and Actuators B: Chemical* **2017,** 250, 147-155.
5. Kolesnikov, I. E.; Kalinichev, A. A.; Kurochkin, M. A.; Mamonova, D. V.; Kolesnikov, E. Y.; Kurochkin, A. V.; Lähderanta, E.; Mikhailov, M. D., Y_2O_3:Nd^{3+} nanocrystals as ratiometric luminescence thermal sensors operating in the optical windows of biological tissues. *Journal of Luminescence* **2018,** 204, 506-512.
6. Benayas, A.; del Rosal, B.; Pérez-Delgado, A.; Santacruz-Gómez, K.; Jaque, D.; Hirata, G. A.; Vetrone, F., Nd:YAG Near-Infrared Luminescent Nanothermometers. *Advanced Optical Materials* **2015,** 3, 687-694.
7. Savchuk, O.; Carvajal, J. J.; De la Cruz, L. G.; Haro-González, P.; Aguiló, M.; Díaz, F., Luminescence thermometry and imaging in the second biological window at high penetration depth with Nd:KGd$(WO_4)_2$ nanoparticles. *Journal of Materials Chemistry C* **2016,** 4, 7397-7405.
8. Quintanilla, M.; Zhang, Y.; Liz-Marzán, L. M., Subtissue plasmonic heating monitored with CaF_2:Nd^{3+},Y^{3+} nanothermometers in the second biological window. *Chemistry of Materials* **2018,** 30, 2819-2828.
9. Ximendes, E. C.; Santos, W. Q.; Rocha, U.; Kagola, U. K.; Sanz-Rodríguez, F.; Fernández, N.; Gouveia-Neto, A. d. S.; Bravo, D.; Domingo, A. M.; del Rosal, B.; Brites, C. D. S.; Carlos, L. D.; Jaque, D.; Jacinto, C., Unveiling in vivo subcutaneous thermal dynamics by infrared luminescent nanothermometers. *Nano Letters* **2016,** 16, 1695-1703.
10. Wang, R.; Li, X.; Zhou, L. and Zhang, F., Epitaxial seeded growth of rare-earth nanocrystals with efficient 800 nm near-infrared to 1525 nm short-wavelength infrared downconversion photoluminescence for in vivo bioimaging. *Angewandte Chemie International Edition* **2014**, 53, 12086-12090.
11. Dong, N. N.; Pedroni, M.; Piccinelli, F.; Conti, G.; Sbarbati, A.; Ramírez-Hernández, J. E.; Maestro, L. M.; Iglesias-de la Cruz, M. C.; Sanz-Rodriguez, F.; Juarranz, A.; Chen, F.; Vetrone, F.; Capobianco, J. A.; Solé, J. G.; Bettinelli, M.; Jaque, D.; Speghini, A., NIR-to-NIR two-photon excited CaF_2:Tm^{3+},Yb^{3+} nanoparticles: multifunctional nanoprobes for highly penetrating fluorescence bio-imaging. *ACS Nano* **2011,** 5, 8665-8671.
12. Chen, G.; Shen, J.; Ohulchanskyy, T. Y.; Patel, N. J.; Kutikov, A.; Li, Z.; Song, J.; Pandey, R. K.; Ågren, H.; Prasad, P. N.; Han, G., (α-$NaYbF_4$:Tm^{3+})/CaF_2 core/shell nanoparticles with efficient near-infrared to near-Infrared upconversion for high-contrast deep tissue bioimaging. *ACS Nano* **2012,** 6, 8280-8287.
13. Rocha, U.; Kumar, K. U.; Jacinto, C.; Villa, I.; Sanz-Rodríguez, F.; del Carmen Iglesias de la Cruz, M.; Juarranz, A.; Carrasco, E.; van Veggel, F. C. J. M.; Bovero, E.; Solé, J. G.; Jaque, D., Neodymium-doped LaF_3 nanoparticles for fluorescence bioimaging in the second biological window. *Small* **2014,** 10, 1141-1154.
14. Naczynski, D. J.; Tan, M. C.; Zevon, M.; Wall, B.; Kohl, J.; Kulesa, A.; Chen, S.; Roth, C. M.; Riman, R. E.; Moghe, P. V., Rare-earth-doped biological composites as in vivo shortwave infrared reporters. *Nature Communications* **2013,** *4*, 2199-2209.
15. Shi, L.; Sordillo, L. A.; Rodríguez-Contreras, A.; Alfano, R., Transmission in near-infrared optical windows for deep brain imaging. *Journal of Biophotonics* **2016,** 9, 38-43.
16. Suzuki, M.; Plakhotnik, T., The challenge of intracellular temperature. *Biophysical Reviews* **2020,** *12*, 593-600.

UNIVERSITAT ROVIRA I VIRGILI
SYNTHESIS AND CHARACTERIZATIONS OF MULTIFUNCTIONAL LUMINESCENT LANTHANIDE DOPED MATERIALS
Albenc Nexha

UNIVERSITAT ROVIRA I VIRGILI
SYNTHESIS AND CHARACTERIZATIONS OF MULTIFUNCTIONAL LUMINESCENT LANTHANIDE DOPED MATERIALS
Albenc Nexha

UNIVERSITAT
ROVIRA i VIRGILI